DOCTOR OF PHILOSOPHY

Routes towards low-cost renewable hydrogen production

Dixon, Christopher Ross

Award date:
2015

Awarding institution:
University of Dundee

Routes towards low-cost renewable hydrogen production

Christopher Ross Dixon

The thesis submitted to the Division of Physics, University of Dundee, in fulfilment of the requirement for the degree of Doctor of Philosophy (PhD)

May 2015

Contents

List of Figures and Tables

Acknowledgements

I would like to thank Dr David Rodley, my supervisor and mentor throughout most of this research. Dr Rodley has a very broad range of knowledge and experience within renewable energy disciplines, providing effective supervision for the topics included in this thesis. Dr Rodley also kept me involved with renewable energy projects at the university and within the community, and with local energy conferences.

I would also like to thank Prof Mervyn Rose (former Head of Division, Electronic Engineering & Physics), my former supervisor. Prof Rose provided insight and direction into research areas, such as involving laser processing and nanoscale materials.

My exceptional gratitude also goes to Dr Stephen Reynolds and Dr Yongchang Fan. Their supporting knowledge and advice for certain areas of my research was immensely helpful. Advice from Dr Reynolds was sought in areas such as solar energy and microelectronics, both of which he holds expertise. Dr Fan guided me through SEM microscopy, EDX, materials analysis and excimer laser processing. Dr Fan is an expert in these areas of science.

I also wish to thank the other academic members of staff who provided advice and support with theory, experimental work, and those who also employed me for lecturing and project supervision; these were very rewarding experiences and opportunities to develop teaching skills.

Other staff within the division that provided assistance were Callum Moore (microelectronics), Stuart Anthony (materials processing) and Grant Kidd (technical assistance). Their technical support and knowledge was greatly appreciated throughout this research, for the construction of electronic devices, materials processing, synthesis of CNTs, and for general electrical/mechanical work.

Finally I would also like to thank former research students Dr Jin Yao and Dr Qammar Goher who provided practical assistance with materials processing.

Signed Declaration

I, Christopher Ross Dixon, declare that I am the author of the thesis, that all references cited have been consulted by me, that the work of which this thesis is a record has been done by me, and that it has not been previously accepted for a higher degree.

Christopher Ross Dixon

May 2015

Nomenclature

AC – Activated carbon

a-C – Amorphous carbon

ADC – Analogue-to-digital convertor

AFM – Atomic Force Microscopy

AG – Asynchronous (or induction) generator

AM – Airmass

APR – Aqueous phase reforming

ATR – Autothermal reforming

BG – Biomass gasification

BSE – Backscattered electrons

BtL – Biomass to liquid

CB – Conduction band

CFRP – Carbon fibre reinforced plastic

CG – Coal gasification

CHP – Combined heat and power

CNT – Carbon nanotube

CoG – Combined coal/biomass gasification

CtL – Coal to liquid

CPOX – Catalytic partial oxidation

CVD – Chemical vapour deposition

EDX – Energy-dispersive X-ray spectroscopy

E-H – Electron-hole

ES – Electrolyser stack

FHL – Formate hydrogenlyase enzyme complex

FIT – Feed-in tariff

FSG – Frank Sargent Group (College of Life Sciences, UoD)

FSV – Fuel cell vehicle

F-T – Fischer-Tropsch

GC – Gas chromatography

GNF – Graphite nanofibres

GtL – Gas to liquid

HAWT – Horizontal axis wind turbine

HCS – Hill-climb search

HDS – Hydrosuphurisation

HER – Hydrogen evolution reaction

HGMs – Hollow glass microspheres

HTFT – High temperature Fischer Tropsch

ICE – Internal combustion engine

INC – Incremental conductance

LB – Lysogeny broth (growing media)

LEC – Levy Exemption Certificate

LH_2 – Liquid H_2

LTFT – Low temperature Fischer Tropsch

MCS – Microgeneration Certification Scheme

MEA – Membrane electrode assembly

MEC – Microbial electrolytic cell

MFC – Microbial fuel cell

MOF – Metal organic framework

MPP/MPPT – Maximum power point/maximum power point tracking

MS – Mass spectrometry

MWCNT – Multi-walled carbon nanotube

NMRL – Nanoscale Materials Research Lab, University of Dundee

OER – Oxygen evolution reaction

P&O – Perturb and observe

PCWS – Photocatalytic water splitting

PEC – Photoelectrochemical cell

PECVD – Plasma-enhanced CVD

PEM – Polymer electrolyte membrane/proton exchange membrane

PEN – DuPont Teijin Teonex Q65HA polyethylene naphthalate (half-treated) film

PGM – Platinum-group metal

PMSG – Permanent magnet synchronous generator

POX – Partial oxidation

ppm – Parts per million

ppmv – Parts per million by volume

PrOx – Preferential oxidation

PSA – Pressure swing adsorption

PV – Photovoltaic(s)

ROC – Renewable Obligation Certificate

SE – Secondary electrons

SEM – Scanning electron microscopy

SOEC/SOFC – Solid oxide electrolyser cell/solid oxide fuel cell

SQAG/WRAG – Squirrel cage/wound rotor type asynchronous generator

SR/SMR – Steam reforming/Steam methane reforming

SR – Synchronous rectification

STP – Standard temperature and pressure

SWCNT – Single-walled carbon nanotube

TD – Thermal decomposition

TEM – Transmission Electron microscopy

TSR (or λ) – Tip-speed ratio

USDoE – US Dept. of Energy

VAWT – Vertical axis wind turbine

VB – Valence band

WGS – Water gas shift

WT – Wind turbine

XPS – X-ray photoelectron spectroscopy

α – Axial induction

A – Area

B – Flux density

c – Velocity of light

C – Capacitance

C_{GS} – Gate-source capacitance

C_H – H concentration

Cp – Component of power

C_F – Component of force

D – Duty cycle (%)

D_{MPP} – Duty value at which maximum power point occurs

ε_0 – Permittivity of free space

e – Electron charge

E – Energy

E_G – Band gap energy

E_S – Solar irradiance/energy

E_W – Wind energy

f – Frequency

F – Faraday constant

F – Force

η – Efficiency

η (rated) – Efficiency at rated power (or max power)

η (max) – Maximum efficiency

η_{Alt} – Alternator efficiency

η_C – Overall power converter efficiency

η_{Conv} – Power transfer conversion efficiency

η_{EC} – Electrolyser cell efficiency

η_{Elec} – Wind turbine electrical output power efficiency

$\eta_{ES\text{-}R}$ – Relative electrolyser efficiency (compared to the same power with 8 active cells)

η_{Eng} – Engine efficiency

η_{ES} – Electrolyser stack efficiency

η_F – Faraday (current) efficiency

η_{FC} – Fuel cell efficiency

η_{MPPT} – Maximum power point tracking efficiency

η_{PV} – PV efficiency

η_V – Voltage efficiency

h – Planck's constant

h – Height

ΔH – Enthalpy change

ΔH_{M} – Enthalpy change per unit mass

ΔH_{V} – Enthalpy change per unit volume

ΔH_{Vap} – Enthalpy of vapourisation

ΔG – Gibbs energy change

$\Delta G_{(g)}$ – Gibbs energy change forming gas as product

I – Current

I_d – Diode current

I_{DS} – Drain-source current

I_{ES} – Electrolyser stack current

I_{In} – Input current

I_{MPP} – Current at the maximum power point

I_{Out} – Input current

I_p – Maximum cell photocurrent

I_s – Reverse saturation current

I_{SC} – Short circuit current

I_{WT} – Wind turbine current

j – Current density

k – Boltzmann constant

λ – Wavelength

l – Length

L – Inductance

m_e – Electron rest mass

M_M – Molar mass

n – Number (such as number of cells)

n – Intrinsic carrier density

n_A/n_D – Acceptor/donor dopant concentrations

N – Number of turns

N_A – Avogadro's number

p – Pressure

P – Power

P_{Ctrl} – Controller power demand

P_{Elec} – Electrical power (output, i.e. from a wind turbine)

P_{ES} – Electrolyser stack power

P_{Mech} – Mechanical power

P_{MPP} – Maximum power point (e.g. of a wind turbine at a certain wind velocity)

P_{WT} – Wind turbine power

q – Heat transfer

ρ – Density

r – Radius/distance

R – Gas constant

R_{DS} – Drain-source resistance

R_L – Inductor resistance

R_s – Effective series resistance

R_{sh} – Shunt resistance

R_{th} – Rydberg constant

ΔS – Entropy change

τ – Torque

T – Temperature

T_C – Critical temperature

T_{Cell} – Cell temperature

u – Relative molecular mass

ΔU – Internal energy change

ω – Rotational velocity

φ – Incident photon flux with energy above the band gap

v – Wind velocity

v_{RMC} – Root-mean-cube velocity

V – Voltage (or emf in the case of Eq 5.17)

V_{Act} – Activation voltages

V_{Cell} – Cell voltage

V_D – Diffusion voltage

V_{DS} – Drain-source voltage

V_{ES} – Electrolyser stack voltage

V_{GS} – Gate-source voltage

V_{In} – Input voltage

V_{MPP} – Voltage at the maximum power point

V_{OC} – Open circuit voltage

V_{Out} – Output voltage

V_R – Reversible voltage

V_{Stack} – Stack voltage

V_{Th} – Thermoneutral voltage

V_{WT} – Wind turbine voltage

Vol_F – Fuel consumed

Vol_{H2} – Volumetric production rate

Vol_M – Molar volume

w – Work transfer

W – Number of states in a system

Ø – Diameter

Summary

The transition from declining conventional fossil fuel energy to renewables is one of the most significant challenges facing humanity. Hydrogen is anticipated as the key future energy vector. This is sought to bring more value and utility to renewable energy resources, and eventually providing an energy storage medium to replace fossil fuels such as for automotive applications. This thesis contains an investigation of hydrogen production through renewable low-cost and low-carbon processes.

Literature reviews of conventional and renewable H_2 production methods and storage (compression, liquefaction, adsorption materials and hydrides) are presented in detail (in appendices). Particular attention has been given to energy efficiency, cost and practicality of processes. Electrolysis of water is investigated in detail. Wind turbines and solar photovoltaics are reviewed and physically investigated as key renewable electrical energy sources for renewable H_2 production via electrolysis. Conventional and novel electrical power control is investigated and tested to support low-cost wind/solar-powered electrolysis.

Biological H_2 production from mixed-acid fermentation of *Escherichia coli* is practically investigated from the energy-physics perspective and considered as one possible route to permit renewable H_2 production in the long-term. Photocatalytic materials are also investigated as additional future routes for renewable H_2 production; in this work they are investigated using nanoscale materials processing and surface analysis techniques.

This thesis has an energy-focussed, applied and practical theme, achieving a broad investigation of the topics herein. Experimental investigations were chosen based upon relevance, practicality, concurrent research, availability of resources, and for application of novel nanoscale materials processing. Power control elements for wind-powered H_2 production have for example been optimised by complete investigation of supply/load characteristics rather than adopting the more conventional power electrical/electronic approach. Ultimately the work here aims to demonstrate (at small-scale) that renewable H_2 production can be achieved at relatively low cost, e.g. by wind-powered electrolysis, inferring that pathways can be established within existing means to produce much larger quantities of renewable H_2 economically.

1. Introduction

1.1 Renewable Hydrogen

1.1.1 Climate Change

Atmospheric carbon dioxide has been increasing steadily since the beginning of the industrial revolution (c.a. 1800) and sharply since the 1950s [1]. As shown in Figure 1.1.1, global levels were approximately 280 ppmv in pre-industrial times (for around 11,000 years). By 1957 they reached 315 ppmv and by 2013, 400 ppmv [2] (varying cyclically by season). In the G8 summit of July 2009, it was recognised that the costs of inaction on climate change would outweigh the costs for the development of reduced carbon societies. It was also recognised that energy security was essential for social and economic development. At approx. 450 ppmv a critical point could be reached, with what is described as 'serious climate implications' [3]. These include detrimental ecological and sociological changes [4]:

- Extreme weather and temperature
- Snow cover and sea level variation (presently 15-23 cm as a result of emissions)
- Greater incidence and magnitude of hurricanes, floods, and droughts, which will affect productivity, ecosystems, agriculture, forestry, and society.

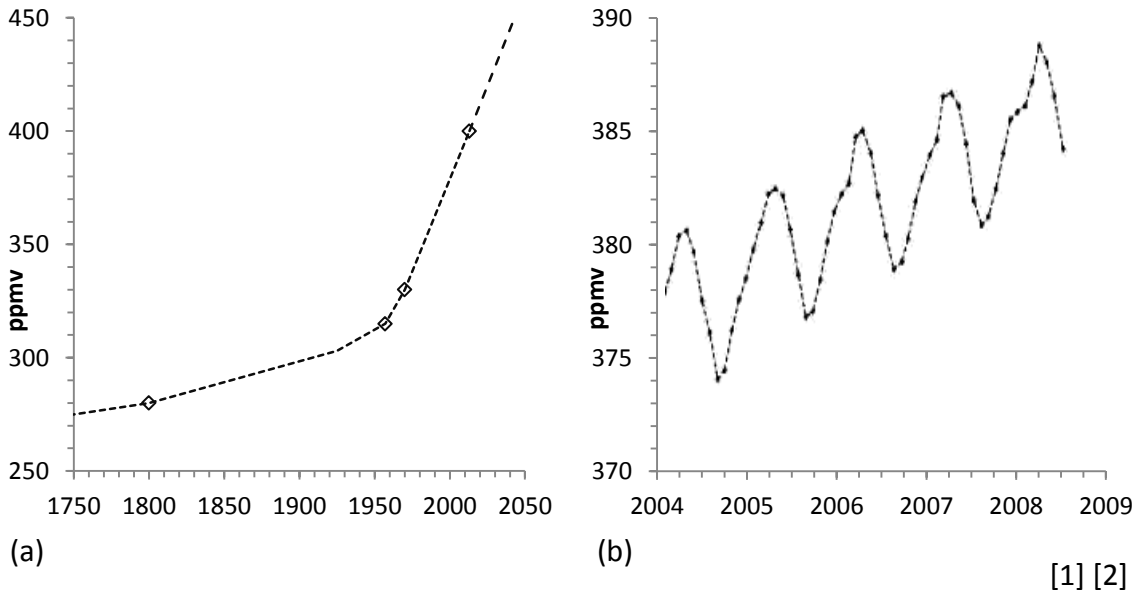

Figure 1.1.1 – Example Data for Historical Global CO_2 Levels (ppm by volume)
Data in (a) highlights that CO_2 levels have been observed to rise steeply since the 1950s, and (b) varying cyclically by season (this example data is from a tropical region).

It was agreed that a global average temperature above pre-industrial levels should not be allowed to exceed 2°C, indicating that global CO_2 emissions will peak but then must start to decline by around 2020. The rate at which CO_2 emissions are currently growing indicates the critical point will be reached before 2050. In response, G8 leaders expressed their willingness to support a goal of reducing greenhouse gas (GHG) emissions by 80% by 2050 (compared to 1990 levels of approx. 352 ppm) [5]. However, the International Energy Agency (IEA) has estimated that 80% of the total CO_2 emissions permissible by 2035 in order to stabilise below 450 ppm are already 'locked-in' by our current energy infrastructure, with a possible case scenario being an increase of 3.5°C, or worst case scenario of 6°C if no significant new policies are implemented [6].

Anthropogenic conventional energy-related activities are also responsible for increased atmospheric CH_4 (methane, being far more significant GHG per molecule than CO_2) and N_2O (nitrous oxide), which are the third and fourth most significant GHGs; the second being H_2O vapour [4]. According to the Intergovernmental Panel on Climate Change (IPCC) reports of 2001 and 2007, global surface temperatures have increased by 0.8°C through the 1900s, and Earth's mean temperature is predicted to increase by 1.4-5.8°C during this century [7] [8]. The uncertainty represents both modelling limits and various mitigation scenarios.

Combustion of fossil fuels and deforestation have released carbon stocks and decreased the capacity of carbon sinks. Fossil fuel reserves are finite. Global warming and climate change are real threats to humanity, undoubtedly linked to increased CO_2 levels from use of fossil fuels [9]. Replacing conventional carbon-releasing fossil fuel energy systems is therefore essential. Vastly increasing use of renewable energy is part of the solution (coupled with more efficient use of energy resources etc). Within this lies energy storage requirement. This may be satisfied with renewable H_2 production, storage and end-use energy cycles.

1.1.2 Future Carrier of Renewable Energy

The use of H_2 as an energy storage medium, taking a share of the current fossil fuel energy industry, is a renewable and sustainable solution to the impending climate change and energy crisis. It is therefore inevitable that future use of H_2 will progress,

although the amount and timescale are still uncertain [3] [10-12]. Currently the largest challenges for renewable H_2 energy are to develop competitive renewable/low-carbon/sustainable production processes, convenient physical storage, infrastructure for distribution, markets for end use/demand, and to address concerns about safety [5] [13] [14]. There presently exists a global industry for H_2, dominated by reforming of hydrocarbons (carbon-releasing processes) producing H_2 for industrial markets such as ammonia synthesis. Renewable H_2 is yet to properly penetrate into existing energy markets and gain cost parity [15-17]. This is currently viewed as the most reasonable and beneficial pathway towards creating an energy carrier of the future, suitable for a number of roles. Renewable H_2 is therefore a very worthy topic for research, since it is likely to become a significant future energy vector, also potentially improving electricity grid stability with increasing renewables penetration.

1.1.3 Renewable Hydrogen Production

Renewable hydrogen production refers to the use of renewable energy resources to enable the decomposition of H_2O into H_2 (and O_2) or release H_2 from renewable biomass. This includes electrolysis of H_2O, fermentation of sugars, thermochemcical, photoelectrochemical/photocatalytic or photobiological processes [3] [18]. Any additional energy required to build or drive these processes should also be offset or provided by a renewable energy resource.

H_2 is not naturally abundant in Earth's atmosphere (3.5×10^{-6} % of air mass) [19], although hydrogen is the most abundant element in the universe (75%) [15]. Most hydrogen on Earth's surface is in the form of H_2O in the oceans, approx. 11% of mass (1.5×10^{8} GT) [20], also being the 10th most abundant substance within Earth's crust (0.006%) [21]. Hydrogen exists in many natural substances, namely hydrocarbons, but also sustainable reserves such as wood and waste biomass/carbohydrates [5] [22-25]. Water bodies alone, although not abundant in every region, can provide an ample physical source of hydrogen. In addition to climate change and energy security, local air quality and international competitiveness are two other significant drivers for the development of H_2 energy [3]. Therefore, with the use of a renewable energy resource such as solar, wind, marine or hydro energy to drive a H_2O decomposition process, or biological/thermal/photolysis processes such as the decomposition of waste biomass

via fermentation, there is a near-endless supply of a transportable renewable fuel in the form of H_2 potentially available.

The key aspect of this work has been to investigate low-cost routes towards renewable H_2 production. This may involve several methods, which have been investigated and discussed throughout this work. In order to substantiate the use of H_2 as a future renewable energy vector, it is essential that renewable production pathways develop (i.e. 'clean' pathways) to move away from unsustainable industrialised carbon-realising production processes involving hydrocarbons (i.e. 'dirty' pathways) [5] [10]. Existing renewable production methods are typically small-scale, in early or prototype stages of development [13] [15] [18]. Many are yet to reach reasonable scale in order to become established and recognised as financially viable. Investigation in this work seeks to better understand the physical principles underlying these processes and the multiple steps involved, identifying reasons why they may be costly or inefficient, and investigating ways of improving cost and efficiency such as by reducing and simplifying process steps. Processes have been physically investigated from the 'bottom up', i.e. micro/lab scale H_2 production, to enable practical research to be undertaken. Solving these challenges at small-scale could be the first steps towards implementing effective large-scale energy storage such as for grid networks**.** Findings in this work can therefore be inferred to larger scale systems, where economies of scale are more likely to make systems practical and commercially viable.

During this research it has been essential to fully understand the physical principles of hydrogen energy. Within literature there are various conventions in terms of measurement of energy, units, conditions etc. A correct energy-based convention has been held throughout this thesis. The physical principles of this and hydrogen energy have been extensively investigated and are included in Appendix A1.1 for further reference as necessary (supporting discussion of electrolyser/fuel cell processes). Atkins [26] and O'Hayre et al [27] provide definition and discussion of appropriate convention used within this thesis. Use of nanotechnology (electron microscopy and nanoscale material deposition processes etc) has been one aspect intended to be incorporated into this work to support novel research. Investigation and use of these systems has been central to parts of this research. These systems are discussed in Appendix A1.2 for the benefit of the reader as necessary.

1.2 The Present Hydrogen Economy

1.2.1 Overview

As discussed, a new energy vector is fundamental to the future of global energy and transport systems, replacing the existing system of convenient, energy-dense but carbon-intensive and declining fossil fuels. This is also necessary for development of variable/non-dispatchable renewable energy systems such as wind and solar. Hydrogen appears to be the most viable long-term option, although it is yet to receive full support and become established [3]. The concept of hydrogen as a fuel within a 'hydrogen economy' became properly recognised in the 1970s, partly due to the work of two individuals. These were an electrochemist J Bockris (who recently published a review paper [28] discussing these historical events) and his 1975 book *The Solar Hydrogen Alternative* where it was proposed that H_2 would become the automotive fuel of the future, and T Nejat Veziroglu who took a prominent role in the dissemination of similar concepts (becoming the president of the International Association for Hydrogen Energy and founder/editor of the International Journal of Hydrogen Energy). This coincided with the oil crisis of the same era, the end of the age of relatively cheap oil. The hydrogen economy essentially refers to the commercialised usage of hydrogen as an energy vector, including its production through to end-use, where it can replace hydrocarbon fuels and electrical energy [11] [25].

World energy-related annual CO_2 emission is expected to increase from 30.2×10^9 tonnes in 2008 to 43.2×10^9 tonnes in 2035 [29]. Reduced-carbon energy and depleting fossil fuels are therefore two significant factors driving markets and development of infrastructure for hydrogen. The hydrogen economy includes production, distribution/transportation, storage, and end-use (domestic, industrial and automotive markets) [11] [15] [30]. H_2 and electrical energy are similar in terms of being clean at the point of use, 'high grade' (i.e. convenient), and both must be produced. In the case of H_2 this requires energy and a physical H source [31]. Since 1900, H_2 has been used in several diverse industries such as steel cutting, vehicle fuel during the early 1940s (World War 2), and the US space programmes from the 1950s [3]. However, present use of H_2 for transportation and domestic energy is minimal. It is however expected that by 2050 hydrogen will have a significant role within energy systems, for transportation, industrial, commercial and domestic markets [30] [32].

1.2.2 Hydrogen Production

Production of H_2 is currently quite industrial and well established serving existing markets. This production is based almost exclusively upon reforming of hydrocarbons such as natural gas/methane (CH_4), heavier fractions/oils, and coal, which are carbon-releasing and non-renewable processes [33-35]. These processes presently dominate global H_2 production due to the relative abundance of cheap natural gas available in the United States and coal reserves in South Africa or China for example. The physical share of production by SMR is reported at approx. 48% globally [15], or the total use of CH_4/natural gas in all reforming processes possibly accounting for up to 75% [36] (there are frequent variations within literature, significant variation by country and often lack of specificity). Partial oxidation (POX) (of gaseous and liquid hydrocarbons/ oils) and coal gasification (CG) make up the bulk of the remainder (48%). Figure 1.2.1 shows an approx. distribution of global H_2 production by source (based upon data published in 2008) [15] [35], with fossil fuel resources accounting for some 96%. This illustrates the use of hydrocarbons in the direct conversion stage of the process (i.e. coal may be used in the local electricity grid to supply a natural gas reforming process, but the majority of the use of hydrocarbons in a particular process are for the physical reformation). Renewable H_2 (e.g. renewable-powered electrolysis of water or conversion of renewable biomass into H_2) forms only a negligible proportion of global H_2 production.

The established industrial processes are not remarkably energy efficient (although SMR being the most efficient of these, approx. 75%, up to 85% in cases [15] [33] [37]), so they do not lead to growth and interest in H_2 directly. It has not been seen as logical in pure energy conversion terms to produce H_2 through these techniques simply to combust at a later stage. The three main routes produce CO_2 in (minimum) proportions of 25%, 42% and 100% of the amount of H_2 in volumetric or molar terms for SMR, POX and CG respectively. In mass terms however, CO_2 accounts for (minimum) 84.6%, 90.2% and 95.7% of the total gas output, which is 7.3, 12.3 and 29.3 kg CO_2 kg^{-1} H_2 respectively if a total efficiency of 75% is assumed (and process energy sources are as per reforming/H_2 source) [35]. In recent years global H_2 production has been worth over £35 billion yr^{-1} (40-65 $\times 10^6$ tonnes) and has grown at above 10% yr^{-1} (reaching approx. 100 $\times 10^6$ tonnes yr^{-1} in 2013) [15] [36] [38] [39]. The development of

economical, renewable and sustainable H_2 production is arguably the most significant component for the development of the hydrogen economy in the long term [3] [11] [18]. There is extensive literature relating to H_2 production [33] [40-43], categorised in several ways:

1. Based on reforming (mainly hydrocarbons), or non-reforming processes
2. Renewable, or non-renewable processes
3. Carbon-intensive, low-carbon or carbon-neutral processes
4. Thermal, electrolytic, photolytic or other (such as dark fermentation) processes.

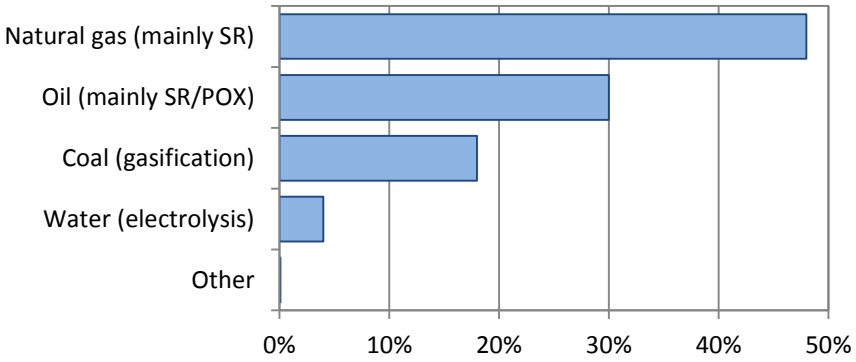

[15]

Figure 1.2.1 – Approximate Global Hydrogen Production by Source
Literature indicates SR of natural gas provides 48% of global H_2 production, another 48% from other conventional fuel reforming/gasification, and 4% from (potentially renewable) electrolysis methods.

The first categorisation is perhaps the most convenient. Main hydrocarbon reforming processes include: steam reforming (SR); partial oxidation (POX); autothermal reforming (ATR) (primary global H_2 production processes). Other reforming processes include: pyrolyis; plasma reforming; aqueous phase reforming (APR); ammonia reforming. Other processes include: gasification (of coal or biomass); biological hydrogen production (fermentation, biophotolysis, microbial cell, etc); electrolysis; thermolysis; photocatalytic water splitting/photoelectrolysis. Industrial reforming processes include at least one water-gas shift (WGS) stage, desulphurisation, and often pressure swing adsorption (PSA), preferential oxidation (PrOx) or methanation processes [33]. Thermal efficiency of these reforming processes has been shown to increase with higher H:C ratio, therefore CH_4 is the preferred hydrocarbon source [44]. These processes are reviewed and discussed in detail in Appendix A1.3.

1.2.4 Hydrogen Storage

Effective storage of H_2 is a significant challenge, particularly for the automotive industry, due to parameters such as the low volumetric and gravimetric density of H_2 [14] [45]. Current techniques include construction of high pressure lightweight storage tanks, liquefaction, storage in novel compounds (metal/chemical hydrides) and carbon nanostructures [14] [46]. In addition, $H_2 + CO_2$ may be converted into liquid fuels such as methanol through additional processing [12] [28], or H_2 + CO (syngas) can be converted into synthetic fuels through Fischer-Tropsch synthesis (following coal gasification etc) [44] [47]. These two chemical processes are potentially very significant alternative/indirect hydrogen storage methods within liquids, very relevant for automotive applications and the future development of renewable H_2. The main methods for hydrogen storage can be grouped by the following [46]:

- Conventional technologies based on compression, liquefaction, cryocompression
- Metal, complex and chemical hydrides of light elements (B, Li, N, Mg, Al etc)
- Carbon nanostructures and other adsorption materials
- Alternative approaches such as liquid fuel synthesis (Fischer-Tropsch)

Energy storage for automotive/mobile applications is arguably the most significant role for hydrogen in the near term; however, this has a relatively high level of energy storage expectation [14] [46]. Hydrogen is required to deliver the equivalent energy of conventional fuels, at the same weight, volume, and convenience [45]. Hydrogen storage is a therefore both a fundamental component and significant challenge for the development of the hydrogen economy.

Literature in this field is now abundant, particularly for automotive storage applications. Within which, it is evident that a large amount has been funded by the US Dept. of Energy (USDoE), who since 2003 (updated in 2009) established groups of targets and funding ($1200 million) for hydrogen storage for automotive applications [48]. These are applicable to light duty fuel cell vehicles (FSVs). The most recent targets at the time of writing are shown in Figure 1.2.2. A considerable amount of research to improve hydrogen storage has been published observing these targets [49]. Key challenges for automotive hydrogen storage systems may be grouped by the following components: capacity; thermodynamic stability and thermal conductivity; kinetics; reversibly; cost [50].

The gravimetric and volumetric energy densities are the primary components of capacity. These are the 'useable' amounts of hydrogen as a fraction of total system mass and volume. Useable refers to the actual amount of H_2 that can be released from the tank in normal conditions, since a small quantity must remain inside most storage systems. A tank is expected to hold enough H_2 to travel approx. 500 km between refills for example [46]. A FCV is assumed to be twice as efficient as an ICE vehicle and the energy requirement for H_2 becomes halved. H_2 is three times more energy dense than petroleum, therefore six times less physical H_2 is required. 5 kg H_2 (equating to a 30 L/30 kg petroleum tank) suggests a system of up to 91 kg and 125 L based on the USDoE 2017 targets. These parameters have proved difficult to achieve.

Thermodynamic issues for hydrogen storage are significant yet different from one storage system type to the next. Kinetics refers to the rate of charging/discharging of the storage system. In charging of a hydride system for example, the process involves several steps and the overall rate is determined by the slowest. Determining this is important and hence catalysis and refinement etc are important to reduce this sort of barrier [50]. The USDoE targets identify practical aspects such as a charging time of 200 seconds for storage of 5 kg of hydrogen (2017 targets). The system would also have to be stable in the presence of oxygen, with good thermal conductivity to dissipate heat during charge/discharge [50].

Reversibility usually refers to the easiness of charging/discharging the system. Energy will be lost in both actions when practical rates are applied [50]. This is particularly applicable to hydride storage, where there may be strong chemical bonds and energy barriers in order to uptake H. The cost of H_2 storage must not be an inhibiting factor for FCVs. Costs are expected to be high and it is not clear from literature how much of this would likely apply to a mass-produced H_2 storage concept in the future. While some storage methods may match capacity expectation, there are serious concerns and issues regarding kinetics, reversibility/stability, and cost for example [49]. Recharging may involve significant p, T, and more time than acceptable. Recharging may need to be carried out by tank exchange rather than on-board replenishment, to alleviate the charging time. NH_3 is one interesting example of a (chemical) hydride with high hydrogen density. This can potentially be reformed to H_2 on-demand, presenting a possible future storage method for H_2.

Parameter	2017	Ultimate
System gravimetric capacity, kg H_2 kg^{-1} system (MJ kg^{-1})	0.055 (7.8)	0.075 (10.6)
System volumetric capacity, kg H_2 L^{-1} system (MJ L^{-1} system)	0.040 (5.7)	0.070 (9.9)
Storage system cost, \$ MJ^{-1} (£ MJ^{-1})	2.8 (1.9)	1.9 (1.2)
Storage system gravimetric cost, \$ kg^{-1} H_2 stored (£ kg^{-1} H_2)	400 (264)	266 (176)
Target H_2 fuel cost, \$ kg^{-1} (£ kg^{-1})	2-4 (1.3-2.6)	
Operating ambient temperature, °C	-40/60	
Min/max delivery temperature, °C	-40/85	
1/4 tank to full operational life, cycles	1500	
Min delivery pressure from storage, bar abs	5	3
Max delivery pressure from storage system, bar abs	12	
Onboard efficiency, %	90	
'Well to powerplant' efficiency, %	60	
5 kg system fill time, s (kg H_2 s^{-1})	200 (0.025)	150 (0.033)
Minimum full flow rate, g s^{-1} kW^{-1}	0.02	
Start time to full flow (20 °C), s	5	
Start time to full flow (-20 °C), s	15	
Transient response at operating temperature (10%-90% and 90%-0%), s	0.75	
H_2 quality from storage, % H_2	SAE J2719 and ISO/PDTS 14687-2 (99.97% dry basis)	
Permeation, leakage, toxicity & safety	Meets or exceeds applicable Standards (SAE J2579 etc)	
Loss of usable H_2, g hr^{-1} kg^{-1} H_2 stored	0.05	

[51]

Table 1.2.2 – US Dept. of Energy Hydrogen Storage Targets and Guidelines
Data from USDoE publication in standard units (based on \$1 USD = £0.66 GBP).

Primarily due to gravimetric and volumetric energy density, at present there is not overwhelming confidence in a particular method to satisfy the needs of automotive markets. For stationary applications such as industrial storage for heating/chemical processes, compressed H_2 is adequate. A compact, safe, reliable, inexpensive and energy efficient method of storing H_2 for automotive use is required if FCVs are to become widespread.

Detailed technical literature reviews of the main hydrogen storage methods and recent research avenues have been included in Appendices A1.4-A1.7.

1.2.4 Hydrogen Infrastructure and Decentralised Generation

The infrastructure for the transportation and distribution of H_2 remains to be properly established [13] [30] [52]. Decentralised production may also be a feasible option to reduce transportation of H_2 [52]. This is an additional set of significant challenges for the development of H_2 energy. The transportation infrastructure will thus depend on the nature of the production, storage and demand. Therefore a range of different solutions may exist for one particular scenario. The infrastructure for new hydrogen energy systems will be based upon usage of H_2 for combustion (heating), turbines and ICEs, and in particular for fuel cell (FC) use. Infrastructure must therefore include H_2 production and sources, storage, transportation/ distribution, and commercial demand markets serving the energy roles mentioned above. A vast number of infrastructure models have been discussed in literature [52-54].

Growth of infrastructure requires investment, which requires perceived demand. Infrastructure for the hydrogen economy is yet to be properly deployed; it requires cheaper end-use systems, such as efficient and convenient storage tanks and practical FCs. Unfortunately, FCs are impeded primarily by the high cost of platinum-group metal (PGM) catalysts and for example issues of durability over long periods of heavy use [30] [55]. FCs are discussed in more detail in Chapter 2. Transportation of H_2 from production source to demand centres is generally accepted to use HGV trailers or dedicated H_2 pipelines [52].

It is reported that domestic mains gas networks have been successfully combined with H_2 feeds [56]. A recent study (in Germany, from 2013-2016) aims to establish how the gas network infrastructure would respond to this blended mixture. The H_2 has been produced at 3.5 bar by PEM electrolyser (315 kW). Blending may allow direct use of the gas mixture in existing markets, or extraction of H_2 from the network by purification technology. End-use is considered compatible with concentrations < 15%.

It is reported separately that the main issues with this strategy may be [57]:

- Material durability and integrity management
- Leakage
- Safety
- Downstream extraction or impact on existing/conventional end-use systems

Issues of steel embrittlement are discussed in literature [5] [28]. In the case of a review of pipework in the US, it is reported that the metallic pipework is primarily low-strength steel, generally not susceptible to hydrogen-induced embrittlement under normal operating conditions [57]. For Fe, Cu, or PE/PVC pipes, or elastomeric materials used in distribution systems, there is no concern under normal operating conditions. Leakage is reported to occur mainly at seals/joints, although these account for a negligible amount of pipe material. H_2 permeation through pipe walls is reported at 4-5 times faster than that of CH_4 [57]. With low mixtures this is not reported as a significant issue. Safety issues are reported to be considered minimal at low mixtures, although the present gas infrastructure is not suitable for mixtures of over 50%. However, this only applies to existing gas networks and non-dedicated H_2 pipelines. Therefore the H_2/gas blending strategy can potentially assist as a near-term transportation infrastructure and market for H_2, offsetting use of natural gas etc [56]. Importantly, blending H_2 within existing transportation and demand networks is one key strategy for the development of the hydrogen economy.

Decentralised H_2 refers to small/medium production centres near to sources of demand, therefore eliminating dedicated H_2 pipe networks. If the H source is initially stored in the form of a liquid fuel or gas and then reformed to H_2, it can also eliminate most of the H_2 storage issues. In this model, the feedstock could be transported to a distribution centre, where a (scaled-down) reforming process could take place. This is likely to cause a reduction to the reforming process efficiency, such as to around 68% in the case of SR [30]. ATR may be more suited to decentralised production, due to faster start-up and simplicity etc, or plasma reforming in the longer term. The overall aim for decentralised production or any alternative model is to provide H_2 in the near-term at the lowest cost, with minimal losses due to transportation/storage etc and preferably with some use of existing infrastructure/networks [57]. Finally, in order for H_2 to be sold commercially, it must be metered and distributed on forecourts for example. Kinetics of H_2 storage methods such as achieving very high pressures and fast H_2 uptake are therefore significant issues. These aspects are considered within the discussion of hydrogen storage in Appendices A1.4-A1.6.

1.2.5 Hydrogen Demand Markets

Neither automotive nor domestic H_2 energy markets are yet properly developed. For automotive markets in particular, the use of FCs as the mechanism of energy transfer from H_2 to electrical power is intended [11] [30]. The current global market for H_2 has grown quickly; 40-65 $\times 10^9$ kg yr^{-1} in 2008 to approx. 100 $\times 10^9$ kg yr^{-1} by 2013, mostly for industrial processes (with % of three largest demand markets shown) [15] [39]:

- Ammonia (NH_3) synthesis, other nitrogenated fertilizer synthesis (49%)
- Petroleum refining, upgrading, desulphurisation (hydrogenation reactions) (37%)
- Synthesis of methanol, ethanol, dimethyl ether (DME) (9%)
- Hydrogenation of hazardous wastes (dioxins, PCBs)
- Silicon deposition, crystal growing, soldering, copper film annealing in electronics manufacture
- Various other chemical, manufacturing and heat treatment (e.g. high temperature processes) such as in the metals/glass/ceramics/plastics industry, industrial furnace fuel, and other thermal/synthetic growth or synthesis processes
- Certain medical or biological procedures (for example some involve H_2 detection and may therefore involve H_2 sources for test/calibration purposes etc)
- Gas chromatography and monitoring, such as for flame ionisation and flame photometric detectors
- Food preparation (hydrogenation of amines and fatty acids etc)
- Alternative fuels synthesis (e,g, gas to liquid/F-T synthesis)
- Rocket engine/ICE/FC fuel
- Alternative heating fuel.

Near term demand for H_2 will be best satisfied by established hydrocarbon reforming (carbon-releasing processes), in order to provide commercial scale H_2 and remain competitive [32]. Use in automotive and transportation markets is slowly growing. A review of H_2 bus fleets indicates 121 fuel cell buses in use within 29 worldwide regions in 2014 [58], noting that this figure was based on data available in 2014 and some of these bus fleets may have revised their fleet size since that time. Select applications such as for a forklift truck or tugs (where weight and range is no issue) can already integrate with existing H_2 technology (such as Savannah River Technology Centre, USA) [59].

As previously discussed, mobile storage of H_2 is a significant issue when compared to liquid fuels. However, one interim possibility is the use of dual-fuel vehicles, to encourage use of H_2, such as a 'hythane' (H_2 + CH_4) engine [5] [60]. It is observed that an ICE can be adapted to operate fully on H_2 or on mixtures with CH_4. The main practical and design issues with significant use of H_2 in an ICE, due to its combustion properties being very different to conventional vehicle fuels, are reported to be [60-62]:

- The necessity of smaller spark plug gaps
- Pre-ignition/abnormal combustion/backfiring and engine timing issues
- High auto-ignition temperature (its effects on compression ratio)
- Selecting appropriate injection pressure
- Deterioration of the lubricating oil
- Issues regarding pistons, piston rings, crankcase ventilation, steel embrittlement
- Additional calibration of the oxygen sensors for the extremely lean mixtures
- A reduction in performance due to low energy density of H_2 fuel/air mix
- The advantage of lean mixtures to operate at low load conditions without a throttle valve, but with the disadvantage of increased hydrogen concentration in the exhaust gases at idling (mixture setting can act as a throttle to minimise issues relating to wide flammability limits of H_2).

Fuel cells are more efficient than ICEs, one of the driving forces for the use of H_2 [11] [30]. It is likely however that future energy systems will involve a mixture of platforms, involving H_2, electrical energy and hydrocarbons or combinations of these, allowing H_2 to penetrate markets. Use of a certain fuel or storage method such as batteries versus H_2 etc will be determined by practicality and cost to suit the individual needs of the system, etc. In the near term it will therefore be necessary to produce H_2 from established and competitive processes, based upon fossil fuels, whilst renewable H_2 technologies develop. This is one methodology to encourage the growth of H_2 into energy markets.

2. Electrolyser/Fuel Cell Materials Processing

Electrolyser cell (EC) and fuel cell (FC) devices have been briefly introduced in Chapter 1 and Appendix A1.3.9. Investigation of electrolysis in this work is in the context of using ECs for low-cost renewable H_2 production from wind and solar energy sources. PEM and alkaline ECs are considered here. Practical investigation of ECs/FCs and novel materials processing are presented in this chapter:

- Characterisation of trends/efficiency of a PEM EC/FC and alkaline electrolyser
- Testing of a custom PEM EC with Ni catalyst and the effects of novel laser processing of a Nafion PEM coated with an Ni catalyst
- Practical investigation of use of on-board H_2 in an ICE and its effects on efficiency

2.1.1 The Electrolyser/Fuel Cell Reaction

Understanding the reactions and electrochemistry that occur in PEM and alkaline cells has been critical in order to investigate electrical characteristics and efficiencies. This involves some complicated physical chemistry. Discussion in literature is often made purely from a chemistry aspect, rather than an energy aspect. There also remain some differences of convention in literature. These aspects have been investigated and are discussed here in the following two sections, from the practical energy physics context observing the fundamentals underpinning the cell electrical characteristics and efficiency. A literature review of EC/FC fundamentals and physical components has been provided in Appendix A2.1. In particular, A2.1.2 describes the function and physical layout of components and briefly describes the manufacturing/assembly processes.

Electrical potential across the cell electrodes permits the following two half-cell electrochemical reactions in PEM/acidic ECs [63]:

$$\text{Anode: } H_2O \rightarrow \tfrac{1}{2}O_2 + 2H^+ + 2e^-$$

$$\text{Cathode: } 2H^+ + 2e^- \rightarrow H_2$$

$$\text{Overall reaction: } H_2O \rightarrow H_2 + \tfrac{1}{2}O_2$$

With applied potential, H_2O forms weak bonds with the +ve anode (due to the electrical properties of H_2O), where the molecules come into contact with the catalyst.

When a sufficient potential is applied, H^+ (protons) can dissociate from H_2O. The remaining O^{2-} deposit electrons onto the anode, later forming O_2. The H^+ pass through the PEM to the –ve cathode, where they collect electrons, forming H_2 [63]. Current flows through the EC circuit as a result of these electron exchanges. The catalyst, mass transport and porosity aspects discussed in the previous section are therefore essential for optimised reaction kinetics.

For alkaline ECs, reactions involve OH^- ionic conduction. The basic reactions are [63]:

$$\text{Anode: } 2OH^- \rightarrow \tfrac{1}{2}O_2 + H_2O + 2e^-$$

$$\text{Cathode: } 2H_2O + 2e^- \rightarrow H_2 + 2OH^-$$

$$\text{Overall reaction: } H_2O \rightarrow H_2 + \tfrac{1}{2}O_2$$

Electrolytes are typically strong aqueous KOH or NaOH solutions (i.e. $H_2O + K^+ + OH^-$), of typically 25-30 wt% in industrial alkaline stacks [64]. With OH^- ions existing within the electrolyte, the anode reaction can proceed to form O_2, H_2O and release electrons onto the electrode. The cathode reaction proceeds with H_2O and electrons (from the power source), forming H_2 and OH^-.

The overall electrolysis reaction results in consumption of the H_2O in the cell, which must be replenished. Production of 1 kg H_2 (12,145 L at STP, from Table A1.1.1) requires 8.94 kg H_2O (with 7.94 kg O_2 produced) [26]. In the case of alkaline ECs, consumption of H_2O results in increased pH and requires management (and the reverse is the case for alkaline FCs). This may require circulation/mixing of the electrolyte, which can in turn mix small amounts of the dissolved gases and therefore is one cause of non-ideal H_2 purity in alkaline ECs [63].

2.1.2 Electrolyser/Fuel Cell Reaction Electrochemistry

Cell characteristics, specifically V, I, P and efficiency trends, are of the most significance when analysing EC or FC performance in the energy context. The FC reaction has been the subject of extensive research over recent decades. Much of the discussion of EC reactions and electrochemistry in literature has therefore been mapped over from FC research. This is often unhelpful, since there are distinct differences between the two reactions and the crossover has led to inconsistency and conventions that are not always helpful. For example, Zhang, Lin and Chen are some

of many authors who discuss and attempt to rationalise these conventions [65]. Atlam and Kolhe [66] model and discuss the performance of a simple PEM EC (which behaves like an EC and does not therefore obey FC convention), and for example they do not define fundamental cell voltages in the same way Zeng and Zhang [67].

Cell voltages are defined here from energy and charge required to perform the overall EC reaction, observing strict energy and electrochemistry convention applicable to electrolysis. As explained in Appendix A1.1, the reaction enthalpy for $H_2O \rightarrow H_2 + ½O_2$ can be calculated from the enthalpies of formation of the three species, resulting in ΔH = +285.87 kJ mol^{-1} at STP [26]. Since formation of H_2 requires two electrons, the molar charge that must pass through the cell per mol H_2 is $2F$ (where F is the Faraday constant, 96,485 C mol^{-1}). By defining reaction charge transfer and enthalpy, the *thermoneutral* voltage, V_{Th}, is simply

$$V_{Th} = \frac{\Delta H}{2F} \qquad \text{Eq 2.1}$$

where V_{Th} = 1.481 V at STP [68]. This represents the standard cell potential when the reaction is driven by electrical energy at STP. There may be net heat flow into the cell that changes the energy balance (H_2O can be split by heat, discussed in Appendix A1.3.11) and a *minimum reversible* voltage, V_R, is then defined from the Gibbs energy

$$V_R = \frac{\Delta G}{2F} \qquad \text{Eq 2.2}$$

where V_R = 1.229 V at STP and heat equivalent to $T\Delta S$ is supplied [68]. This heat may be considered in equivalent voltage terms from $T\Delta S$ / $2F$ = 0.252 V. In real EC operation at STP (accounting for various losses discussed in the next section), the reaction will proceed almost only when $V > V_{Th}$ since heat available to the reaction is negligible (and unfavourable) at 25°C [63]. In order to proceed at $V < V_{Th}$ the cell must absorb heat from an external source, maintaining a higher H_2O/cell temperature (T_{Cell}). The heat flow must remain if T_{Cell} is to be kept above ambient and to continue operation at $V < V_{Th}$. In the case where the cell components produce heat due to overvoltages, losses and irreversibilities etc this may then increase T_{Cell} and improve the reaction, but this heat is being supplied from the electrical source (some of which is being released to the surroundings) and is not 'free'. Hence T_{Cell} is a significant

aspect of efficiency [69]. PEM cells are usually operated at 80°C due to the optimal proton conductance of Nafion [70]. Alkaline cells may operate at slightly higher T_{Cell} although limited by the boiling point of the electrolyte and other practical issues [67]. Reaction enthalpy reduces to 281.7 kJ mol^{-1} at 80°C [27]. The Gibbs energy change reduces more significantly (this is illustrated in Figure A1.3.5 where $\Delta G \approx 0$ at 4400K) and this defines a more thermodynamically favourable reaction with an increased maximum thermal energy contribution ($T\Delta S$) permissible [63]. Cell voltages therefore decrease while operating at higher T_{Cell} (one of the reasons why FCs are less efficient than ECs) [27] [71]. V_R remains theoretically defined from ΔG with changes in T from external heat. Observing Eq. A1.1.12

$$\left(\frac{d(\Delta G)}{dT}\right)_p = -\Delta S \qquad \text{Eq 2.3}$$

and the change in V_R becomes

$$\Delta V_R = \frac{\Delta S(T_0 - T)}{2F} \qquad \text{Eq 2.4}$$

as T varies from the standard temperature, T_0 [27]. Considering $\Delta S \approx$ +163.4 J K^{-1} mol^{-1} (Appendix A1.1.4), a voltage decrease of 47 mV is indicated by increasing T_{Cell} from 25°C to 80°C. In real cell operation this may be observed to some extent, depending on the loss mechanisms and heat transfer coefficients. Pressure has the opposite effect. The Nernst equation (van't Hoff isotherm) can define ΔG and ΔV_R from the natural log of individual species partial pressures (where R = 8.314 J K^{-1} mol^{-1}) [71]:

$$\Delta V_R = \frac{RT}{2F} \ln\left(\frac{[\mathrm{H_2}][\mathrm{O_2}]^{½}}{[\mathrm{H_2O}]}\right) \qquad \text{Eq 2.5}$$

An ES is often operated where H_2 is produced at p > ambient and Eq. 2.5 is of practical use. At 10 atm, the change in V_R is indicated as +29.6 mV and this is likely a more energy-effective method for pressuring H_2 than other compression techniques, although observing the practical limitations of the ES. It is noted that Eq 2.5 only provides the effects of p at a certain T, not accounting for the separate effects of T. To form an expression for both p and T, Eq 2.5 must be rewritten with Eq 2.4 [27] [71]:

$$\Delta V_R = \frac{\Delta S(T_0 - T)}{2F} + \frac{RT}{2F} \ln\left(\frac{[\mathrm{H_2}][\mathrm{O_2}]^{½}}{[\mathrm{H_2O}]}\right) \qquad \text{Eq 2.6}$$

The log terms can represent simply the pressures of the species since they are normally isolated. More specifically, these substitute the activities of the species from the original Nernst equation [27]. Forms of this equation are more often written in the context of FCs. There are also other mathematical/empirical interpretations of p and T effects, explained elsewhere such as by Carmo et al [68]. The Nernst equation can also indicate the change in FC performance when operated with H_2 + air rather than H_2 + O_2, which is often the case [27]. Assuming O_2 partial pressure of 22% at STP, V_R reduces by 9.72 mV, giving a maximum theoretical FC voltage of 1.219 V.

The proportionality between cell current and H_2 formation was defined by Faraday [72]. The Faraday equations define the charge required per mol H_2 production = $2F$ [67]. For example, volumetric H_2 production rate (Vol_{H2}) in an EC, or H_2 consumption rate in a FC, is linked to I by the molar volume (Vol_M) (see Table A1.1.1) where

$$Vol_{H2} = \frac{nIVol_M}{2F} \qquad \text{Eq 2.7}$$

and the n term represents the number of series cells in the stack. With multiple cells, voltage increases proportionally and also the H_2 volume per unit of current. Eq 2.7 is almost exact, although there are some physical losses explained in the next section.

As discussed, the energy (work or heat) required to drive the EC reaction is defined from ΔH. In low temperature electrolysis this is usually entirely from the electrical source, since the cell materials/H_2O cannot conduct/permit heat equal to $T\Delta S$. This defines the (minimum) cell voltage, V_{Cell} = 1.481 V that must generally be applied *to* the EC reaction. As discussed in Appendix A1.1.4, the maximum energy delivered *from* the reaction as work (electrical) in the FC reaction is ΔG. The remainder of ΔH must result in heat ($\Delta H - \Delta G$ or $T\Delta S$). A FC reaction therefore provides (maximum) V_{Cell} = 1.229 V, always with waste heat [27]. This explains fundamental irreversibility and differences between the two reactions, and why it is not always appropriate to substitute FC electrochemistry into discussion of ECs. Similarly the temperature-related change in ΔG explains why high temperature electrolysis is thermodynamically favourable, and conversely keeping FCs cooled (≤ 80°C) is beneficial in electrical power terms.

2.1.3 Electrolyser/Fuel Cell Efficiency and Loss Mechanisms

Cell efficiency for electrolysis is defined from the electrical energy (input) and the energy transferred into chemical energy (ΔH) in the form of H_2 (output) [67] [68]. Likewise for FCs, it is defined from the H_2 reaction chemical potential energy (input) and electrical energy production (output) [27]. There are different conventions with cell efficiencies, such as discussed by O'Hayre et al [27] and Smolinka, Ojong and Garche [63]. The difference is in the definition of the chemical energy of the H_2-O_2 reaction. By correct definition, ΔH = 285.87 kJ mol^{-1} (141.80 MJ kg^{-1}) at STP [26] [27]. Since $\Delta G/\Delta H$ = 0.83, the FC reaction is limited to 83% in terms of maximum electrical energy from the reaction [27]. For ECs, this limit does not apply (maximum theoretical efficiency in a standard scenario is 100%). EC efficiency (η_{EC}) can be measured directly from the (electrical) energy required per unit of H_2 production, for example:

$$\eta_{EC} = \frac{141.8}{E_{ES}} \qquad \text{Eq 2.8}$$

where E_{ES} is the electrical energy (MJ) consumed per kg H_2 production. Similarly:

$$\eta_{FC} = \frac{E_{FC}}{141.8} \qquad \text{Eq 2.9}$$

where η_{FC} is the FC efficiency and E_{FC} is the electrical energy (MJ) produced from per kg H_2 consumed [27]. Volumetric measurement may be easier for small cells, where the electrical energy per litre (kJ) can be substituted and 11.67 kJ L^{-1} (at STP) for 141.8 MJ kg^{-1} respectively. As discussed in Appendix A1.1.4, electrolysis of H_2O in steam phase would not have to overcome the ΔH_{Vap} term (40.7 kJ mol^{-1}) [26] and has a significant advantage in electrical power terms (although +ΔH_{Vap} must come from another source and be considered in EC efficiency calculations, especially if not waste heat) [69] [71]. This permits an EC to operate with an apparent η_{EC} > 100% in electrical terms. EC efficiencies are often found erroneous, with ΔH replaced with that for steam (245.10 kJ mol^{-1} [27]), which is inconsistent with the reality of the normal process. In the FC reaction, the H_2O product may form as single molecules (since gaseous O_2 forms H_2O) with the phase change to liquid occurring later in the diffusion layer, releasing heat (-ΔH_{Vap}) and not contributing positively to the electrical part of the reaction. Maximum electrical energy available to the FC may therefore be equivalent to $\Delta G_{(g)}$ = 228.59 kJ mol^{-1} (the Gibbs energy when forming H_2O in gas

phase). This defines a maximum V_{Cell} = 1.185 V for a FC (leading to varying convention in literature) [63].

Efficiency can be separated into voltage efficiency (η_V) and current efficiency (η_F, the 'Faraday' efficiency) [63]. Current and H_2 flow rates are observed as not exactly proportional. Typically η_F = 98.5 to > 99.9% in normal ranges for alkaline and PEM cells [67] [73]. Loss is due to current crossover through the electrolyte/PEM/diaphragm (not forming H_2), H_2 leakage (some through the PEM/diaphragm), formation of radicals/H_2O_2, or H_2-O_2 recombination in the cell [67] [74]. η_F is calculated from H_2 production as a fraction of the theoretical H_2 production (the opposite for FCs) [72]:

$$\eta_F = \frac{Vol_{H2}(measured)}{Vol_{H2}(theoretical)} \qquad \text{Eq 2.10}$$

Near-ideal η_F allows η_V to indicate η_{EC} or η_{FC} to good accuracy. This is then calculated easily from V_{Cell} (or stack voltage, V_{Stack}, by multiplying the 1.481 term by n), where

$$\eta_{EC} \approx \frac{1.481}{V_{Cell}} = \frac{1.481n}{V_{Stack}} \qquad \text{Eq 2.11}$$

$$\eta_{FC} \approx \frac{V_{Cell}}{1.481} = \frac{V_{Stack}}{1.481n} \qquad \text{Eq. 2.12}$$

Importantly, for alkaline cells, fairly constant gas leakage thought the diaphragm is observed regardless of the operating current level. The amount of dissolved gases in the recirculating electrolyte also remains similar with different operating levels. For these two reasons an alkaline ES may have a lower current limit of 20% of the rated value, below which the η_F term and gas purity may start to decline quickly, inhibiting practical/efficient operation [63].

Cell/stack loss mechanisms are discussed extensively in literature for the FC reaction [27] [67]. Losses are generally considered as three types (as potentials, which may be quantified by effective resistances) including ohmic, mass transport and activation/electrochemical losses [63] [67]. Ohmic losses are from the small resistances of the stack conductive components and (particularly) of the ion-conducting diaphragm/membrane. Various physical mass transport losses occur within MEAs from concentrated gas/liquid counter flow within the porous current collector/diffusion layer. These mostly result from bubble formation restricting access

to conductive and activation sites (i.e. the catalyst on the PEM surface) [63] [67]. Hence quickly dispersing bubbles from PEM surfaces through the porous mesh layers is essential, whereas in the FC reaction the H_2O evolution must be quickly dispersed to allow O_2 to reach the PEM surface catalyst sites. Activation losses are more apparent in the FC reaction, particularly for the cathode reaction (OER) [27]. The EC/FC cell reactions appear simple but actually consist of several small steps, which include activation energy barriers (preventing the H_2O-forming reaction occurring spontaneously). The activation barrier is illustrated in Figure 2.1.3. Overpotentials are required to overcome these, known as activation voltages (V_{Act}). These have an exponential relation to current quantified by the Butler-Volmer equation [27] [63]:

$$I = I_e[\exp(\alpha 2FV_{Act}/RT) - \exp(-(1-\alpha)2FV_{Act}/RT)] \qquad \text{Eq 2.13}$$

The I_e term is known as exchange current and α is a charge transfer coefficient for each electrode (between 0-1) [27]. This is understood from the reaction steps, where energy is required to first break H-H and O-O bonds before new bonds are formed with net release of energy [27]. The principle of catalyst function is to reduce activation energy barriers by providing an alternative route of lower activation energy [26]. In FC electrochemistry, the three losses explain a typical V-j curve, such as Figure 2.1.4, with an activation region, ohmic region and mass transport region. Activation voltage loss quickly forms at low current due to the exponential relation, but does not then increase significantly through the current range. Ohmic voltage loss (IR) remains linear with current throughout the range. Mass transport significantly affects voltage at high current levels, when physical diffusion/bubbles impede the reaction. These separate factors make three regions become somewhat distinct.

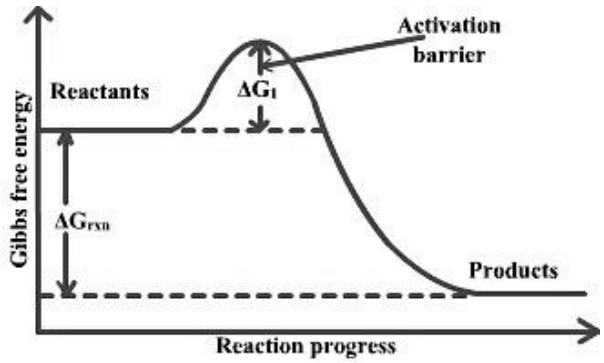

[27]

Figure 2.1.3 – Reaction Activation Barrier
An activation barrier is shown as ΔG_1 required above ΔG_{rxn} (the reaction Gibbs energy).

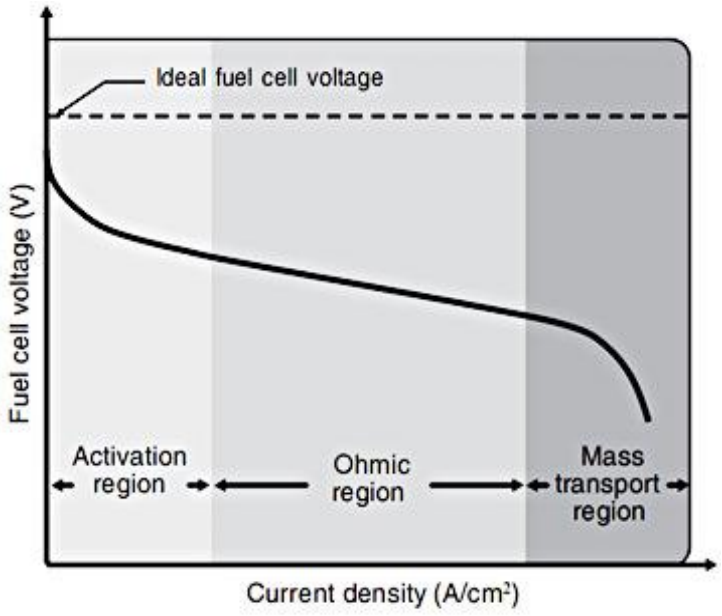

[27]

Figure 2.1.4 – Characteristic Fuel Cell Voltage-Current Density Curve
Three distinct loss regions are demonstrated for a typical FC.

Low temperature EC curves are in theory similar to FCs. As discussed, the reaction is not thermodynamically favourable at a significant rate until V_{Cell} > 1.481 V. Actual operating V_{Cell} values clearly vary with I and by device. Literature reports 1.5-2.2 V (typically 1.8-2.0 V) for PEM ECs, and 1.7-2.5 V (typically 1.8-2.4 V) for alkaline ECs [63] [67] [68]. PEM V_{Cell} values occur at much higher j ranges (up to 2.0 mA cm^{-2}), although typically 0.5-1.5 mA cm^{-2}, compared to < 0.5 A cm^{-2} for alkaline cells. The V_{Act} term may affect EC voltage, but this results in heating of the cell making the reaction more favourable, so is less apparent in ECs [69]. The dominant mass transport region may not be observed until very high currents (which may not be within the rating of the device). Pressure also has an effect on mass transport/bubble loss [75].

For FCs, V_{Cell} is much lower, typically 0.60-0.75 V for a PEM FC during normal use (ohmic range) [27]. As a result of these stated operating voltages, η_{FC} ≈ 40-50%. For alkaline ECs, η_{EC} ≈ 60-80%, and for PEM ECs, η_{EC} ≈ 75-80%. Considering that V_{Cell} is higher for an EC compared to a FC, an equivalent V_{Act} would not have the same reducing effect in terms of η_{EC} and η_{FC}. Figure 2.1.5 shows an ES V-j curve and magnitude of the loss components (overvoltages, of which the anode OER is the most significant) [63].

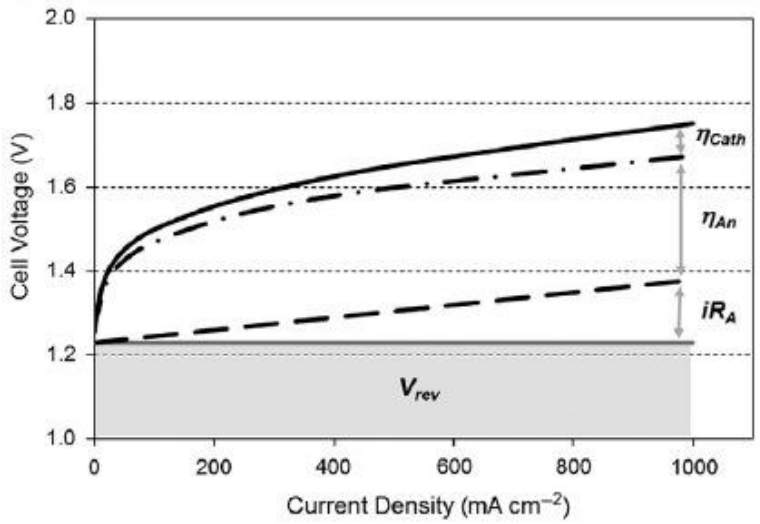

[63]

Figure 2.1.5 – PEM Electrolyser Voltage-Current Density Curve
Example apparent overvoltages from activation of the two half-cell reactions (η_{Cath}, η_{An}) and ohmic loss (iR_A) are shown comparatively for a range of current densities.

2.2 Electrolyser/Fuel Cell Testing

2.2.1 Cell Test Experimental Method

Three devices were tested to investigate real EC and FC trends. These were a Heliocentris PEM FC (dual-cell stack), PEM EC (single cell), and alkaline ES (eight-cell stack). The alkaline ES was of simple design and custom-built from a Ni/stainless steel plate kit, housed within a plastic case and with an electrolyte tank mounted above the stack. A diaphragm to separate the H_2 and O_2 was not available to this research. The alkaline ES was assembled in two layouts (producing mixed gases). One was a bipolar (series) layout of six cells fitted into four parallel channels (recommended by the supplier) (24 cells). The second layout consisted of eight cells built separately into the stack, electrically coupled in series.

The test cells are shown in Figures 2.2.1-2.2.3. Figure 2.2.3 shows the eight cell configuration of the alkaline ES. The stack was formed from eight individual cells, using polymer separating layers. This configuration was used to provide the test data. A channel existed at the top of each cell to permit gas flow and electrolyte replenishment. Cells were individually sealed by rubber O-rings. Copper strips provided series contact between cells, also allowing electrical access to individual cells.

Rated/max power: 1 W

Active surface area: 15.7 cm^2

Number of cells: 2

Anode catalyst: Pt

Cathode catalyst: Pt

Electrode material: stainless steel/Ti/C

η (rated/max power): 23% (0.34 V)

η (max): 57% (0.89 V)

Figure 2.2.1 – Heliocentris PEM Fuel Cell

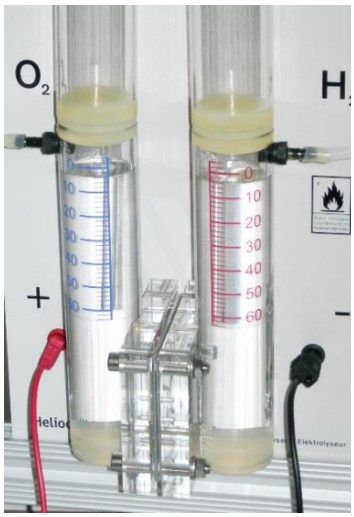

Rated power: 11 W

Active surface area: 30.3 cm^2

Number of cells: 1

Anode catalyst: Ir

Cathode catalyst: Pt

Electrode material: stainless steel/Ti/C

η (rated): 81% (1.90 V)

η (max): 95% (1.52 V)

Figure 2.2.2 – Heliocentris PEM Electrolyser

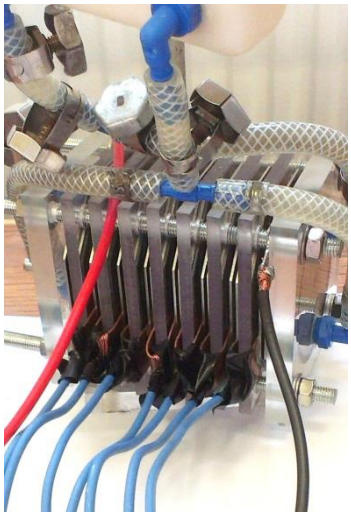

Rated power: 12 W per cell (96 W for 8 cells)

Active surface area: 39 cm^2 per cell (312 cm^2 for 8 cells)

Number of cells: 1-8

Anode catalyst: Ni

Cathode catalyst: Ni

Electrode material: Ni/Stainless steel

η (rated): 64% (2.30 V)

η (max): 77% (1.84 V)

Figure 2.2.3 – Custom (Variable Cell Number) Alkaline Electrolyser

A 24-cell configuration of the alkaline ES, which was not optimal, was used for later experimental work. Reasons for this and data are discussed in Subchapter 2.4. H_2 flow rates were measured volumetrically with flow metering and by physical water displacement, at varying temperature and ambient pressure due to the nature of the tests. Volumetric flow was adjusted for p and T in accordance with Eq A1.1.1 considered accurate to ±2%. Leakage due to the nature of the test set-up was measured in each case, and where avoidable this was compensated within the data (although these were generally negligible values for the test durations). Data for the EC/FC tests were subject to electrical measurement accuracy of ±1% from the metering.

In the FC tests, the stack was connected to variable loads from open to short-circuit. For the EC tests, a variable DC power supply was used. Measurements were taken at the cell terminals.

2.2.2 Cell Test Results and Discussion

Test data for the devices is shown in Figures 2.2.4-2.2.9. Data for V-j shows the theoretical voltages of 1.229 V and 1.481 V in each case. In Figure 2.2.4, the $\Delta G_{(g)}$ voltage of 1.185 V is also shown (which is not applicable to the EC data). Efficiency data displays η_V, η_F and η_{EC} or η_{FC}. The η_V term is a simple function of the voltage axis in these particular graphs, observing Eq 2.11 and Eq 2.12.

Data demonstrates that with near-ideal η_F the η_V term can indicate η_{EC} or η_{FC} accurately in normal ranges. The FC data indicates trends as expected from theory, although high current densities such as those reported from literature were not achieved. This was mainly due to T_{Cell} not reaching 80°C during the test, and the low catalyst loading on these test cells. Maximum P occurred towards the end of the 'ohmic' region, at V_{Cell} = 0.336 V. The (maximum) V_{OC} of 0.95 V is only slightly lower than what is typically reached by a commercial FC at STP (1.0 V) [73]. In Figure 2.2.4, since mass transport losses are negligible in the ohmic region, extrapolation of the linear ohmic trend to the voltage axis (≈ 0.79 V) indicates activation loss of approx. 0.40 V throughout most of the range.

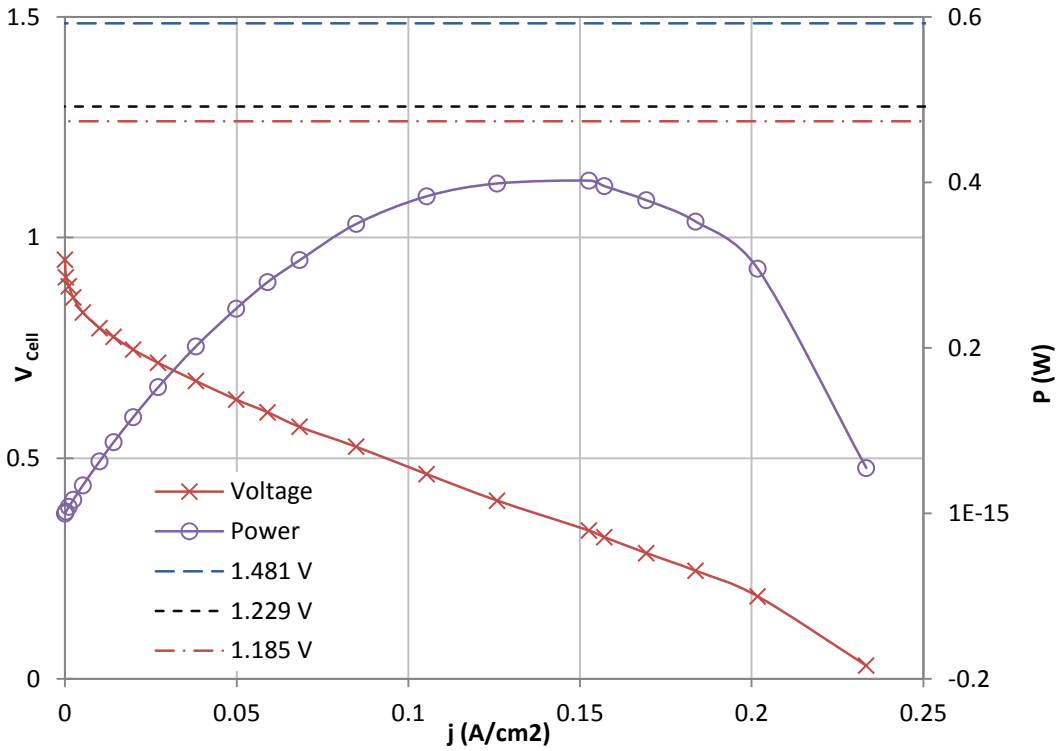

Figure 2.2.4 – Heliocentris PEM Fuel Cell Test Data (*V-j* and *P-j*)

Voltage- and power-current density data. V_{Th} (1.481 V), V_R (1.229 V) and V_R (ΔG) (1.185 V) are shown.

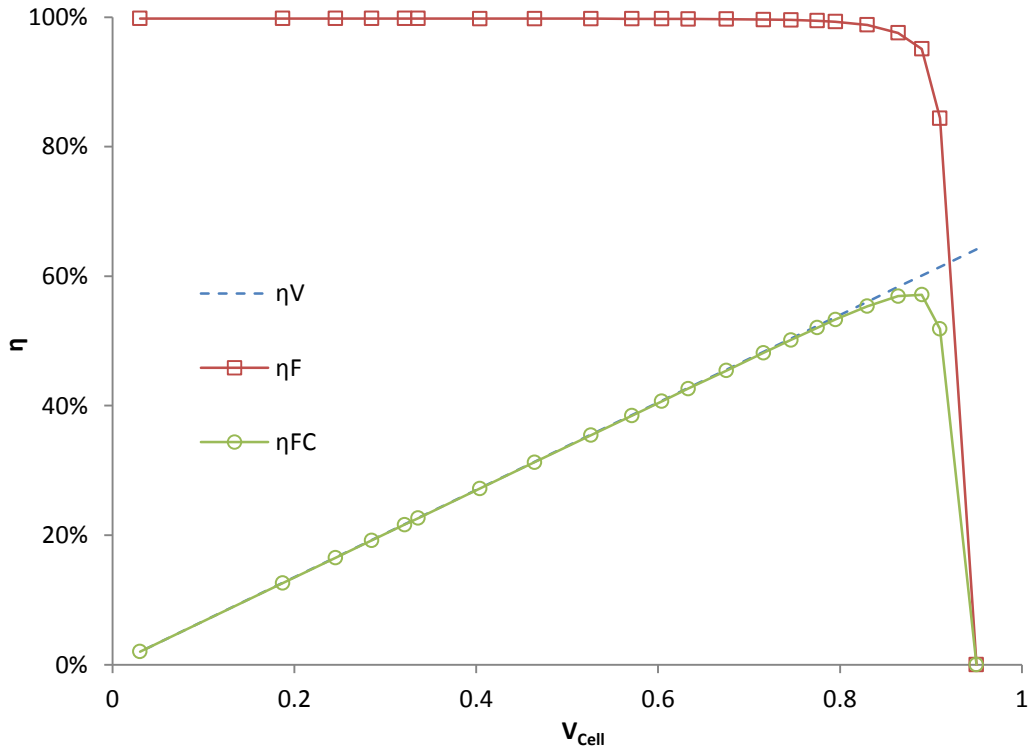

Figure 2.2.5 – Heliocentris PEM Fuel Cell Efficiency Test Data (η_V, η_F, η_{FC})

Cell efficiency-voltage data. η_V, η_F, η_{FC} are the voltage, current and energy efficiencies.

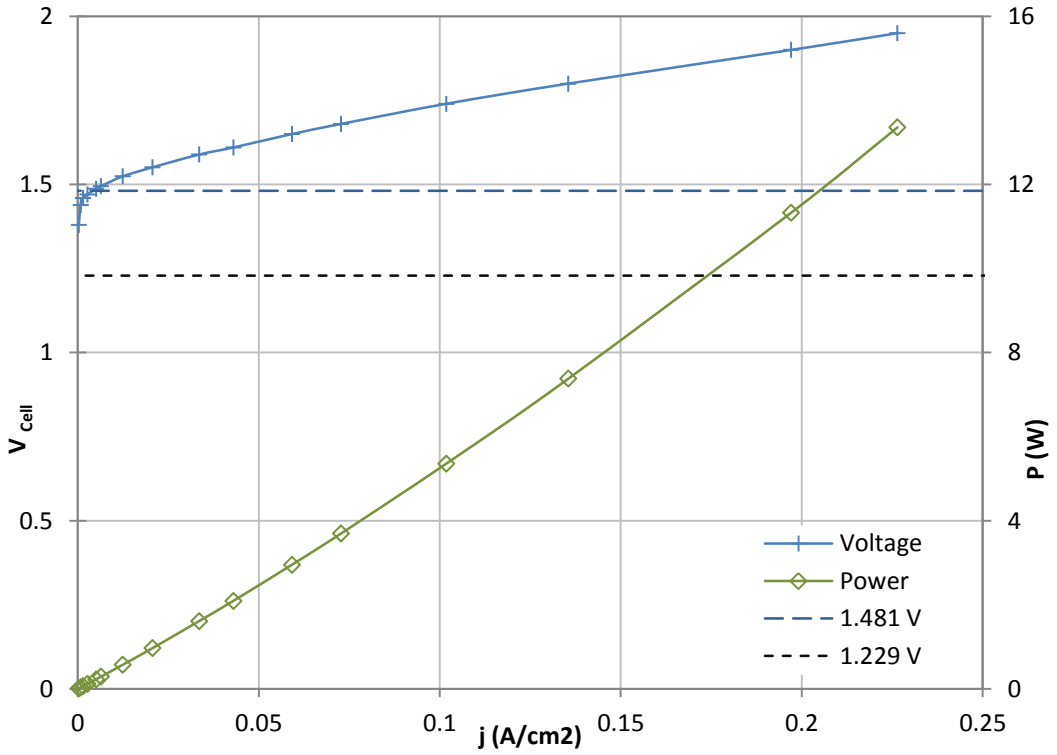

Figure 2.2.6 – Heliocentris PEM Electrolyser Test Data (*V-j* and *P-j*)
Voltage- and power-current density data. V_{Th} (1.481) and V_R (1.229) and are shown.

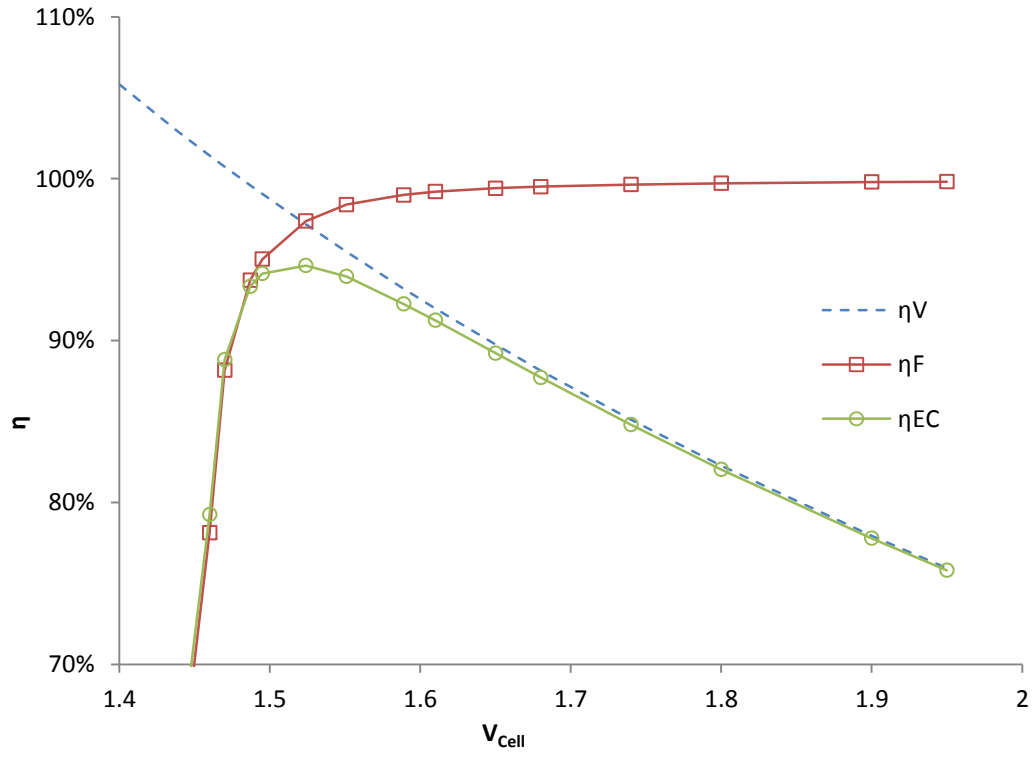

Figure 2.2.7 – Heliocentris PEM Electrolyser Efficiency Test Data (η_V, η_F, η_{EC})
Cell efficiency-voltage data. η_V, η_F, η_{EC} are the voltage, current and energy efficiencies.

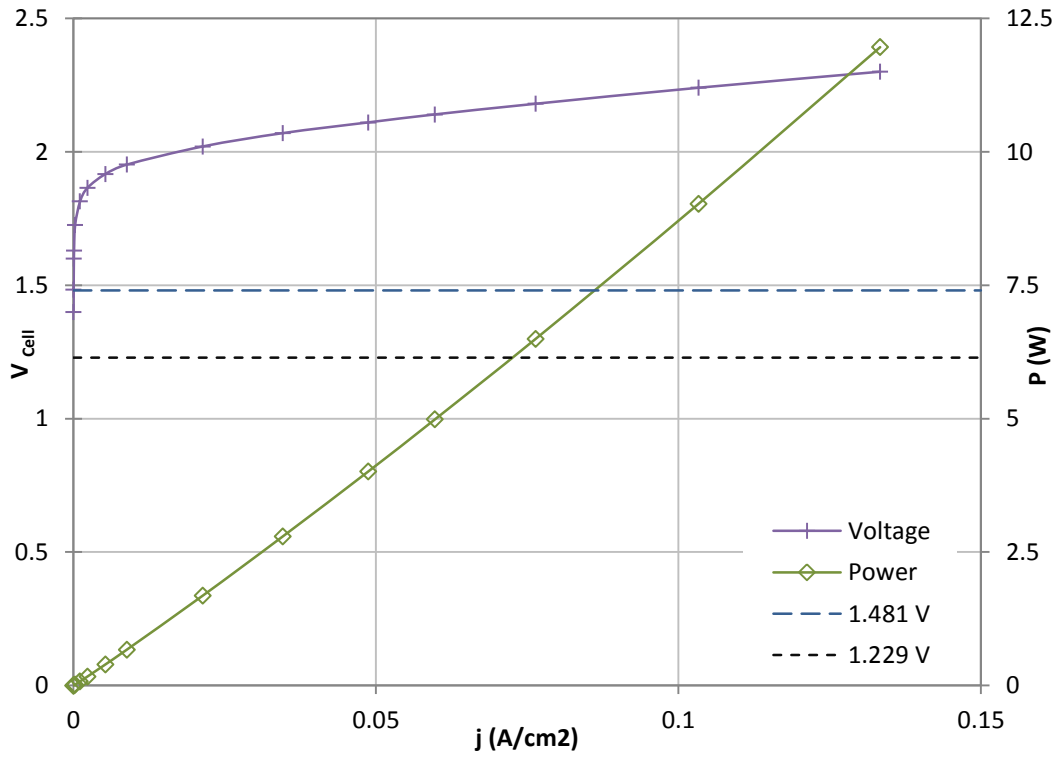

Figure 2.2.8 – Custom Alkaline Electrolyser Test Data (*V-j* and *P-j*)
Voltage- and power-current density data. V_{Th} (1.481) and V_R (1.229) and are shown.

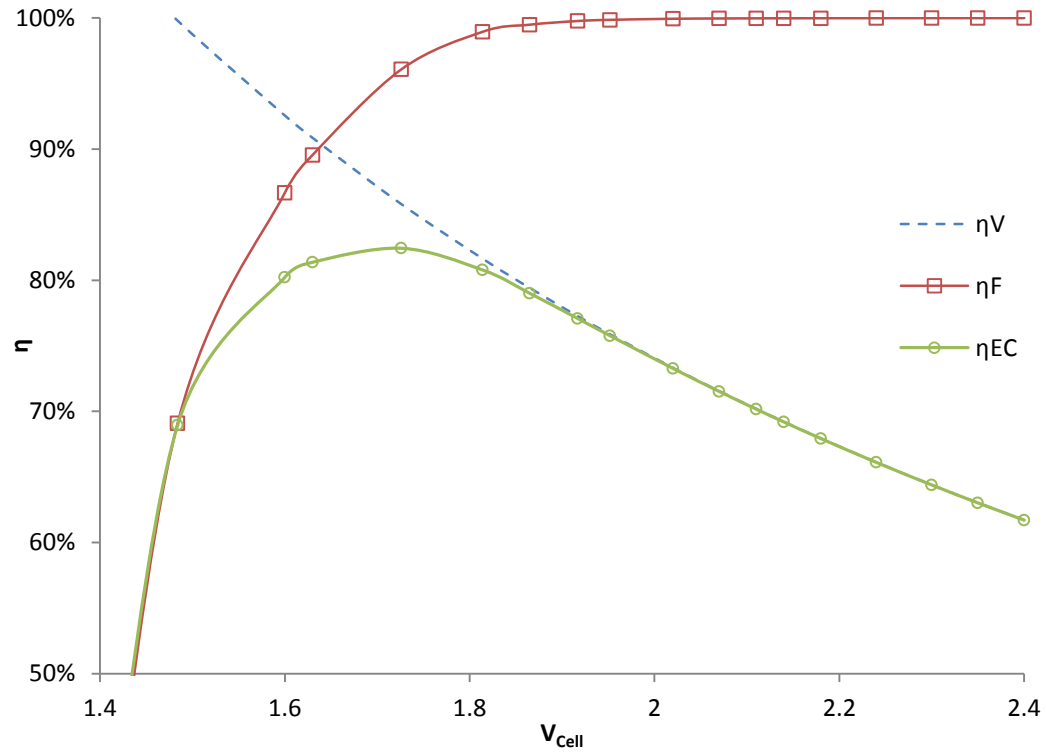

Figure 2.2.9 – Custom Alkaline Electrolyser Efficiency Test Data (η_V, η_F, η_{EC})
Cell efficiency-voltage data. η_V, η_F, η_{EC} are the voltage, current and energy efficiencies.

The PEM EC data demonstrates that production commences at a reasonable rate when V_{Cell} > 1.481 V as expected. The activation losses are not so apparent for thermodynamic reasons discussed previously. Unlike with the FC tested, where ohmic loss and activation (≈ 0.40 V) are almost equal at maximum power, in this EC the ohmic loss component is the only significantly noticeable factor apparent in the data. The cell does not reach mass transfer limitations in the test range. T_{Cell} increased towards 80°C during testing at higher j, which provided a slight reduction of the voltage gradient with further increase in j (although only slight due to increasing ohmic losses). T_{Cell} is in fact a current-limiting factor in this cell due to the lack of temperature control/cooling. The peak η_{EC} term occurred at very low j, although in practical ranges η_{EC} ≈ 78-92%. The η_F term is the governing factor for η_{EC} at very low j, whereas the η_V term becomes much more significant at higher ranges since η_F > 99%.

The alkaline ES showed an activation region due to its simple electrode surface/catalyst. Maximum η_{EC} was 82%, but where j was negligible. In practical ranges of j, η_{EC} ≈ 63-73%. Electrode surface and cross-section samples were examined by SEM/EDX, determining that the electrodes were homogenous Ni/stainless steel (with trace elements). Micrographs and EDX data are shown in Figures 2.2.10-2.2.11.

An interesting aspect of the PEM FC data is that the small increase in T_{Cell} reduces V_R but improves the Nafion performance. These two factors seem to be approx. equivalent from this test data and do not show significant adverse effects, although clearly this would vary between different cell types/designs. For the EC tests, increase of η_{EC} with reasonable increases in T_{Cell} was apparent in both cases. Further tests to operate these cells at more optimum temperatures with more exact monitoring would be helpful to clarify their performance, although this was not practical or required within this work. The PEM cells were simple test cells of micro scale and although representative of general theoretical trends they do not perform as efficiently and effectively as larger advanced cells with higher catalyst loadings. The alkaline ES was set-up to represent a typical state-of-the-art ES with a diaphragm. This was the case since although the ES was basic, the use of a diaphragm reduces η_{EC} (although without a diaphragm the ES can only be representative since the gases are mixed and of no practical use). Further references to cell performance trends will refer to that contained in literature where more applicable.

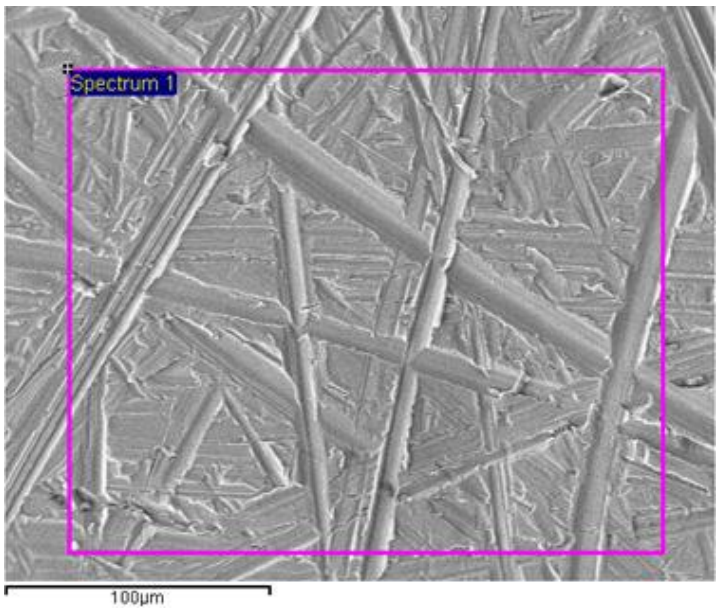

Element	Fe	Cr	C	Ni	O	S	Si
Weight %	61.52	16.51	11.46	6.01	2.77	1.08	0.65
Atomic %	46.98	13.54	21.34	8.32	7.40	1.44	0.98

Figure 2.2.10 – Alkaline Electrolyser Electrode SEM/EDX (Surface)
SEM micrograph of alkaline electrode surface and EDX data.

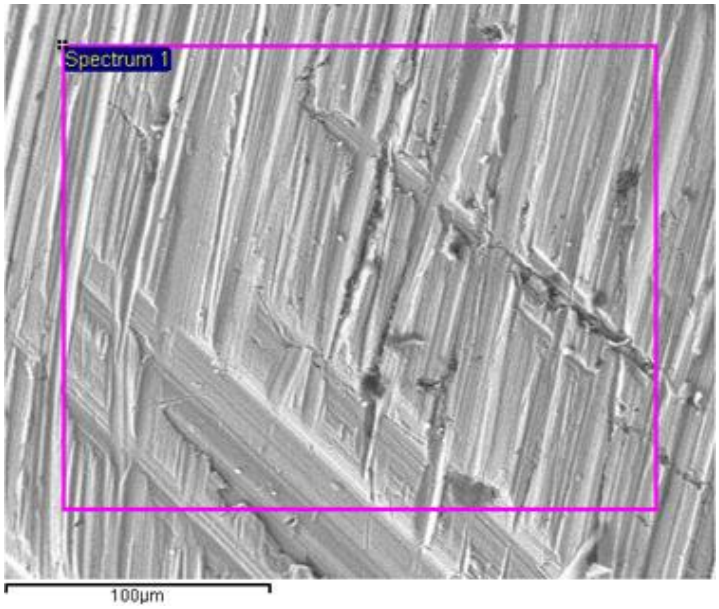

Element	Fe	Cr	C	Ni	O
Weight %	63.48	15.59	9.61	8.54	2.79
Atomic %	44.47	11.73	31.29	5.69	6.83

Figure 2.2.11 – Alkaline Electrolyser Electrode SEM/EDX (Cross-Section)
SEM micrograph of alkaline electrode cross-section and EDX data.

2.3 Nanoscale Deposition and Laser Processed Catalyst/PEM Work

2.3.1 Overview of Nanoscale Deposition and Laser Processing of Ni/Nafion

Nanoscale magnetron sputter deposition of Ni onto a Nafion PEM material was carried out to allow investigation of the effect of laser processing to form a more effective catalyst layer with increased surface area. The laser processing step was considered to facilitate the manufacturing of MEAs where a continuous (e.g. reel-to-reel), large-area process could potentially be carried out to produce enhanced catalyst-loaded PEM materials for FC/EC application. After the initial deposition process, laser processing could in theory be used as a single-step to form an enhanced catalyst layer. Magnetron sputter deposition processes have been widely used to form thin films for various applications, and recently for catalyst deposition for PEM EC/FC electrodes, either directly onto the PEM surface or current collectors [68] [76]. These are reported to provide excellent homogenous distributions of the catalyst material. There are however issues such as the small scale capacity of the process and cost [68]. There are several other conventional methods for catalyst deposition reported in literature. These include: Pechinie-Adams method; Adams fusion method; ethylene glycol colloidal method; sulphite complex method; sonochemical method. These are generally chemical-based and heat treatment processes. Brief explanations of these methods is provided by Carmo et al [68], who also identify that magnetron sputtering can potentially reduce and/or simplify the numerous necessary steps to fabricate catalysts or CCMs using the conventional methods (e.g. preparation of catalyst inks, spreading of the ink on the substrate, hot pressing of the catalytic layers on the PEM).

Ni is known to be a preferential catalyst in alkaline electrolysis for OER and HER reactions, for reasons of stability, catalytic activity and cost [67]. Ni is not commonly used in acidic/PEM reactions, due to the more preferential catalyst materials Ir, Pt and Ru. The reactions occurring in the OER and HER are complicated and there are a number of descriptions of these in the literature, where the OER in particular is more complex and may occur through various pathways [77]. The function and performance of single element and binary/tertiary catalysts have been studied extensively over the past decades, such as by cyclic voltammetric (CV) techniques [68] [78]. CV involves changing (ramping) voltages across electrodes and measuring current trends, with a potentiostat, which includes a reference electrode (REF), working electrode (WE) and

counter electrode (CE) [79]. These works have focussed on gauging the activity of different electrode materials and trying to understand the factors that determine this activity, much of which have been conducted in strong acid or alkaline solutions [78]. While there are numerous experimental data sets and various empirical and theoretical understandings of catalyst activity, there remains some uncertainty as to exactly the most appropriate catalysts and theoretical explanation for certain synergetic effects [76].

Various authors report voltammetric data in different format for single elements, such as that shown in Figures 2.3.1-2.3.2 [68] [79]. In Figure 2.3.1, data is presented by atomic number, as potential versus the standard hydrogen electrode potential (SHE), for OER and HER, in 0.1 mol L^{-1} H_2SO_4 solution at 80°C. The data source reports the HER activity order as Pd > Pt > Rh > Ir > Re > Os > Ru > Ni. For the OER, Ir ≈ Ru > Pd > Rh > Pt > Au > Nb [68]. Activity for Ni is not shown for the acidic OER in this data. It is also discussed that oxides of each catalyst are a dominant factor affecting their activities. In Figure 2.3.2, data is only present for the HER. The -log I term is current density and the $-\Delta H$ the catalyst-H intermediate bond enthalpy during the reaction. Data from the two sources are reasonably similar in terms of the general position/ranking of individual metals. Millet and Grigoriev [72] also analyse and present data with V-j curves for various catalysts. A typical CV circuit is shown in Figure 2.3.3, where E has been used to represent potentials [79].

Work in this part of the research aimed to utilise laser processing of a catalyst-loaded PEM substrate to improve the distribution and surface area of the sample, in order to improve the catalytic activity and ultimately cell performance. This was attempted by a simple processing technique that could, if practical, be later considered for larger area manufacturing processes. Cell performance was measured for the electrolysis reaction, where V-j trends were compared for different materials processing techniques. Use of the CV technique was not available to this research. Of the metals with known catalytic activity discussed here, only Ni was available to this part of the research. Therefore Ni was chosen as a test catalyst for the process and used for both the anode and cathode. Use of Ir and Pt would be preferential, although the aim of this work was to quantify the processing strategy and not the final performance. For this reason Ni was determined as a suitable test catalyst.

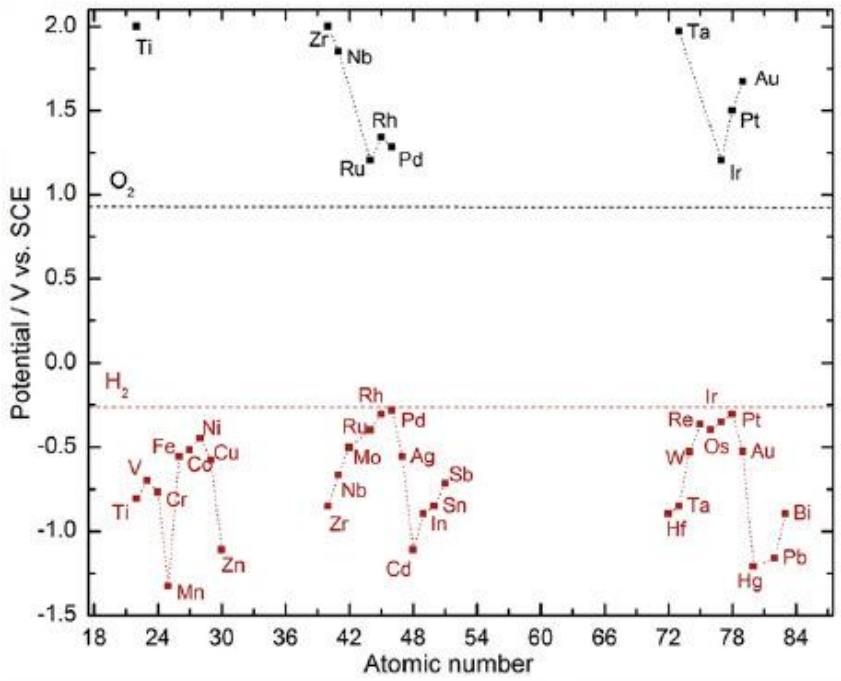

[68]

Figure 2.3.1 – Example Cyclic Voltammetry Data (Acidic OER/HER)
Catalyst potential versus standard hydrogen electrode potential is presented by atomic number, for OER and HER, in 0.1 mol L^{-1} H_2SO_4 solution at 80°C.

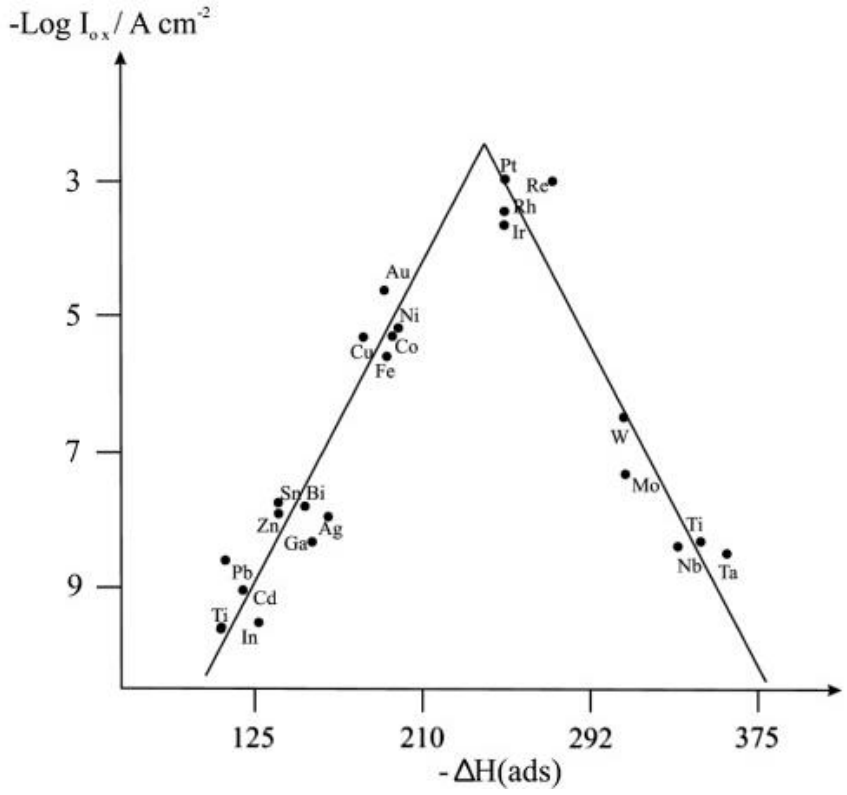

[78]

Figure 2.3.2 – Example Cyclic Voltammetry Data (Acidic HER)
Current density (-log I term) and the catalyst-H intermediate bond enthalpy ($-\Delta H$) for various catalysts.

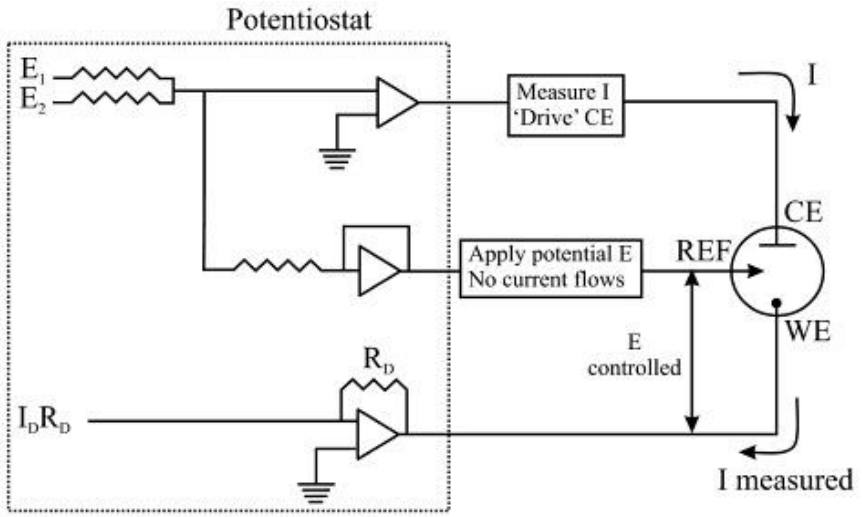

[78]

Figure 2.3.3 – Example Cyclic Voltammetry Circuit

Working electrode (WE) potential is cyclically ramped (linearly) versus a counter electrode (CE) to develop current through the cell. A reference electrode (REF) is used to measure WE voltages.

2.3.2 Cell Test Experimental Method

DuPont Nafion 115 samples (127 µm thickness) in 50×50 mm size where obtained from Sigma Aldrich. Samples were pre-treated in accordance with recommendation from DuPont datasheets to remove impurities and humidify (this includes various treatments depending upon application). For the work here, the samples were first cleaned and rinsed in distilled H_2O (dH_2O). Samples were then boiled in 3 wt% H_2O_2 solution (80°C) for 1 hr (to further remove any organic impurities), rinsed in boiling dH_2O for 1 hr, then boiled in 0.5 mol H_2SO_4 sulphuric acid (80°C) for 1 hr (to protonate the Nafion), and finally rinsed in boiling dH_2O to remove excess acid. Samples were stored in dH_2O at all times during preparation or when not in use to maintain humidity/protonation. Four Nafion samples were prepared. These included: plain Nafion; Nafion with 1nm Ni sputtered coating; Nafion with 2nm Ni sputtered coating; Nafion with 60 nm sputtered coating for laser processing. Previous laser processing experimental work was carried out with DuPont Teijin Teonex Q65HA polyethylene naphthalate half-treated film (known as 'PEN'), of 125 µm thickness. This was a cheaper film used to avoid excessive wastage of Nafion. It was observed that PEN was not transparent to UV laser photons, whereas Nafion was. Laser processing energy levels would therefore have to be later adjusted to suit Nafion. Several laser processing techniques were used to attain the correct intensity. This included

adjustment of beam energy (excitation voltage), pulse width, frequency and movement rate. Initial work on PEN is shown with SEM micrographs in Figure 2.3.4. EDX confirmed the composition of features. At 20%/40% intensities, the Ni coatings (the lighter regions of flaked appearance) were partially ablated (20% was the lowest energy setting of the excimer laser in this configuration). Almost entire ablation of the surface appeared at 60%/80%, leaving significant deformed regions/eruptions of the PEN surface due to the intensity of the laser beam. Increased material coatings and a covering layer were used in further work. Due to the diverging shape of the laser beam, moving the sample to a lower position (greater distance from laser emitter) enabled reduced beam energy, which was a technique used in the later work.

(a) 20%

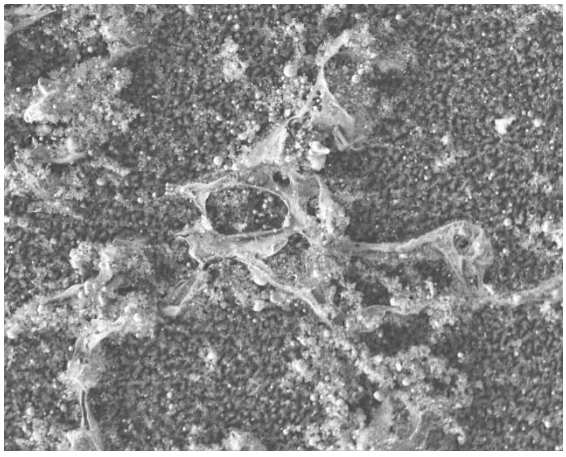

(b) 40%

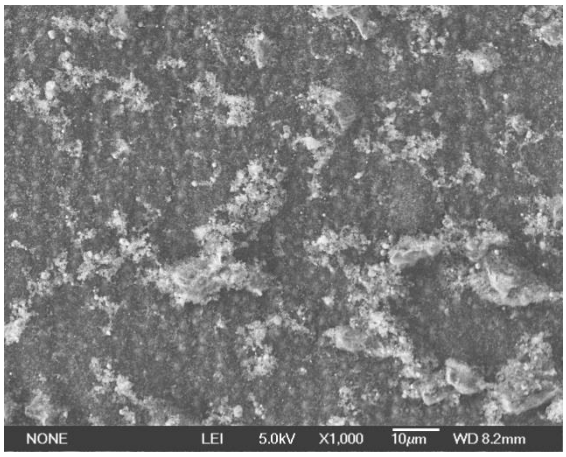

(c) 60%

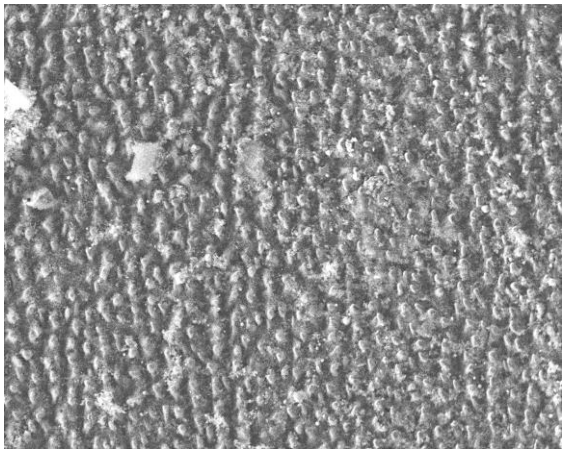

(d) 80%

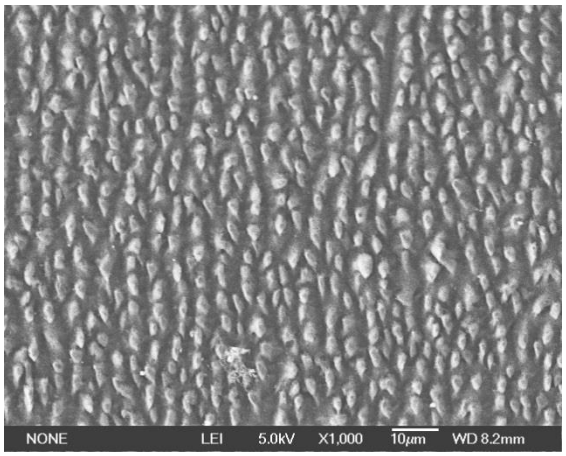

Figure 2.3.4 – SEM Micrographs of Excimer Laser Processed PEN (40 nm Ni coating)
Laser intensities (% of 404 mJ, at 17.2 kV): 20; 40; 60; 80. Pulse width: 20 ns. Frequency: 25 Hz. Movement rate: 2 mm s^{-1}. In (a) and (b) some Ni remains following laser processing at 20-40%. In (c) and (d) there is almost complete ablation (60-80%).

A test cell was assembled from two Perspex casing blocks, with two flat rubber seals around the edges of the inner surfaces. The MEA consisted of an electrode mesh layer current collector (0.3 mm stainless steel), electrode plate (1.4 mm stainless steel) pressed against either side of the Nafion. The MEA was fitted between the seals, which were sized at half of the thickness of the electrode plate and mesh to allow a precise fit. The Perspex casing had two holes drilled through to allow external electrical contacts to meet the (internal) electrodes. Further holes were drilled to allow inlet and exit port fittings for the H_2O, H_2 and O_2 and also to allow the case to be bolted together. A duplicate mesh layer was produced with a 40 nm Ni coating via sputter deposition. This was to allow testing of Ni catalyst and non Ni catalyst electrodes. The effective cell area was 9 cm^2. The test cell is shown in Figure 2.3.5.

Four experimental sets were carried out. The first set consisted of two experiments to determine the relative catalytic effects of the Ni as an electrode coating. This involved assembling the cell with the unprocessed Nafion sample and testing with Ni and then non Ni mesh electrodes. The next set of experiments was to test and compare the Ni coated Nafion to the above. This involved assembling the test cell with non Ni mesh and Nafion with 1nm Ni coating and then repeating with the cell assembled with Ni coated mesh. The third set copied the procedure of the second set, using Nafion with 2nm Ni coating. This aimed to determine how different Ni thicknesses layers onto Nafion affected performance. A laser processed Nafion sample was then produced and tested. This involved firstly the sputter deposition of 60 nm Ni onto the Nafion. The sample was then placed under an excimer laser and drawn through the beam in narrow strips, to eventually process the whole Nafion surface. To avoid significant material vaporisation loss, the sample was covered in another piece of Nafion during the processing. Laser settings were 20% and otherwise as stated in the earlier work (Figure 2.3.4). The result was expected to be a Nafion sample with distributed Ni sites, increased exposed Nafion and increased effective Ni surface area.

In all experiment sets both sides of the Nafion were coated/processed, allowing the Ni catalyst to be present in the OER and HER. The test procedure involved applying a range of voltages to the cell and measuring the current and gas flow. T_{Cell} was allowed to normalise to steady working values relevant to operation at the specific V/j etc (by allowing a short duration prior to taking measurement).

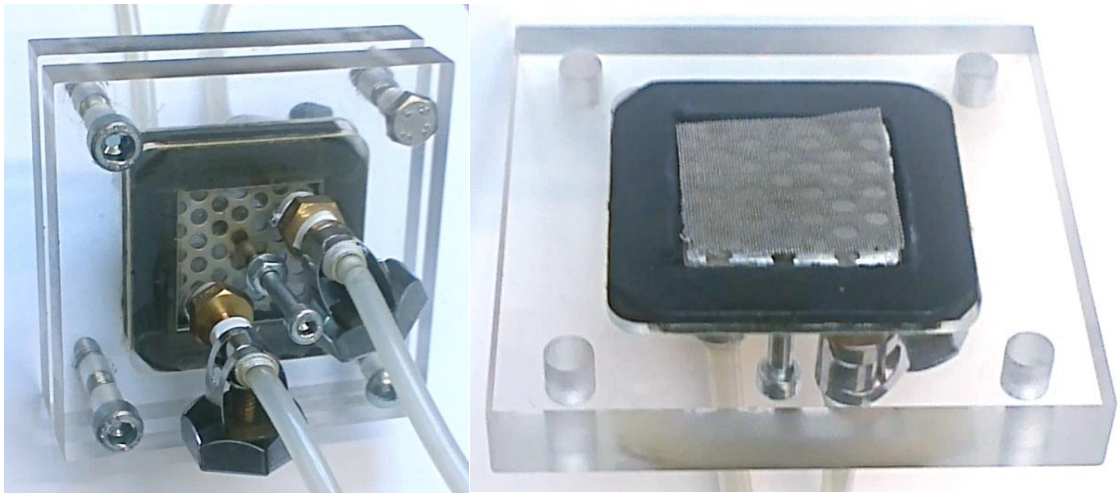

Figure 2.3.5 – Test Cell
FC cell using Perspex cases housing a Nafion sample and current collector/mesh layer.

2.3.3 Cell Test Experiment Results and Discussion

The first experiment set produced data for the EC with and without Ni as an electrode mesh catalyst. The next two sets were to determine whether direct deposition of Ni (1nm and 2 nm) onto Nafion improved cell performance, and to investigate two Ni coating thicknesses. This used the Ni and non Ni mesh to further support data from the previous experiment set. The experiment involving the laser processed Nafion was only carried out with the Ni-coated mesh, due to the instability of the Nafion coating noticed when the cell was disassembled following the first test. A significant amount of the Ni appeared to have removed, not permitting further representative experiments with the same Nafion sample. Graphical data for the seven experiments are shown in Figure 2.3.6, in the *j-V* form, which is more useful for later work in this thesis. This data indicates the 1nm Nafion samples to be the most effective overall (i.e. higher relative *j* values were evident in the upper voltage ranges).

From this work it was apparent that laser processing of Nafion samples requires further refinement to eliminate the weak Ni-surface bond. A stronger bond would be necessary to create a stable MEA of this sort. Small samples of the laser processed Nafion were removed prior to testing and SEM micrographs are shown in Figure 2.3.7. The dispersed Ni coating is clearly visible, which was the intention of the processing work. The flaked structure in the micrographs indicate the poor surface bonding of the Ni. Cracks in the Nafion surface (ranging from 0.03-0.8 µm) are likely the result of drying from the processing stage and prior to use in the SEM (vacuum).

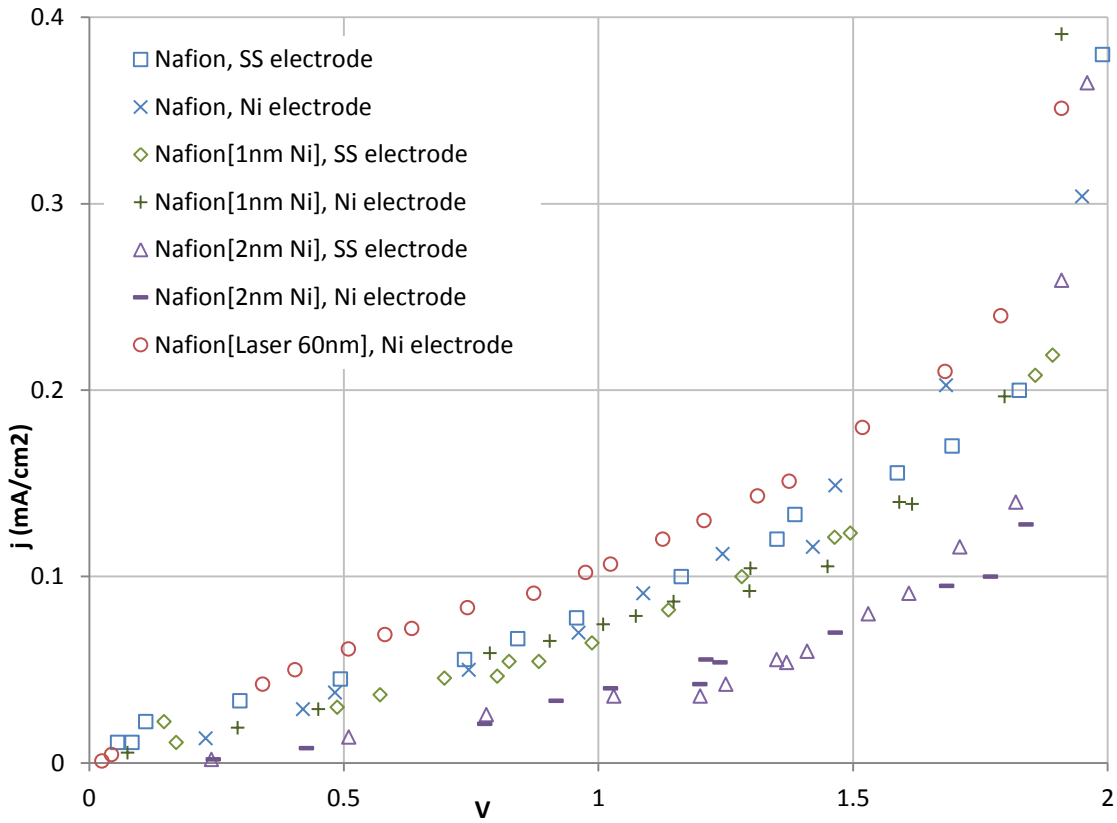

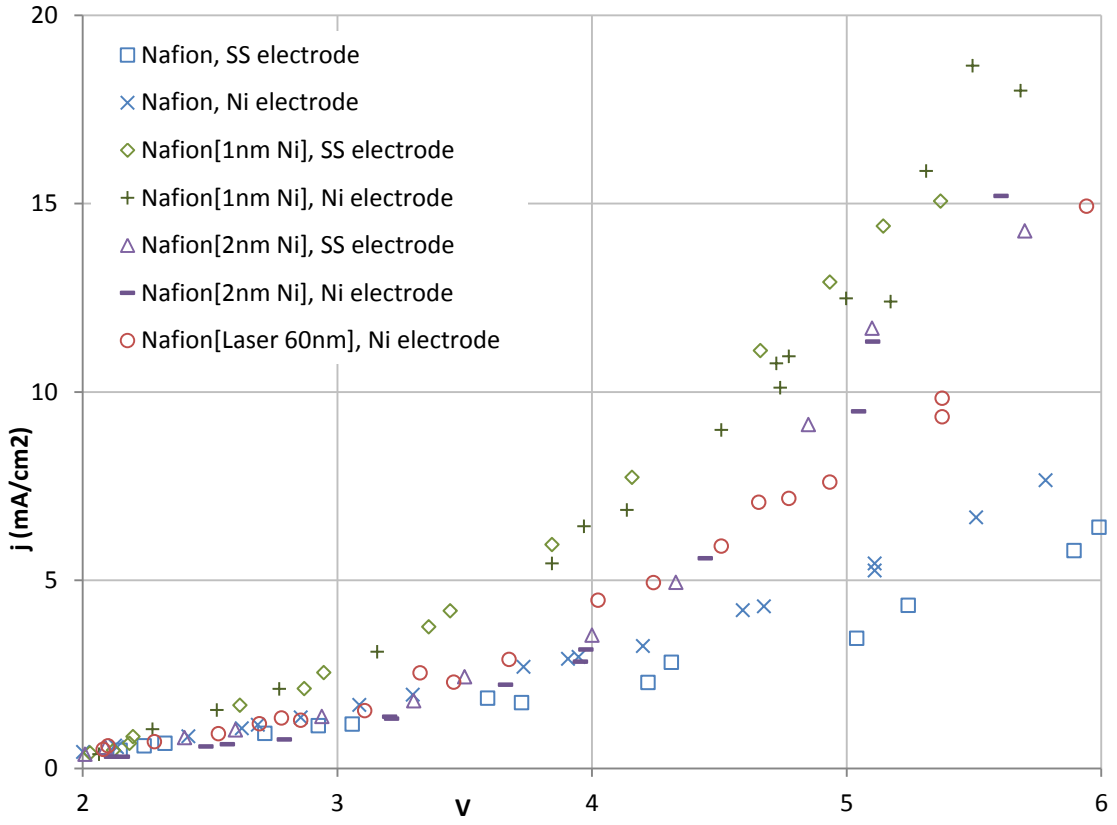

Figure 2.3.6 – Experimental Test Cell Data (*j*-*V*)

Current density-voltage data is shown in two regions for the various test cell materials/configurations. Current where V < 1.481 is due only to crossover (and gives indication of such, and therefore also cell integrity).

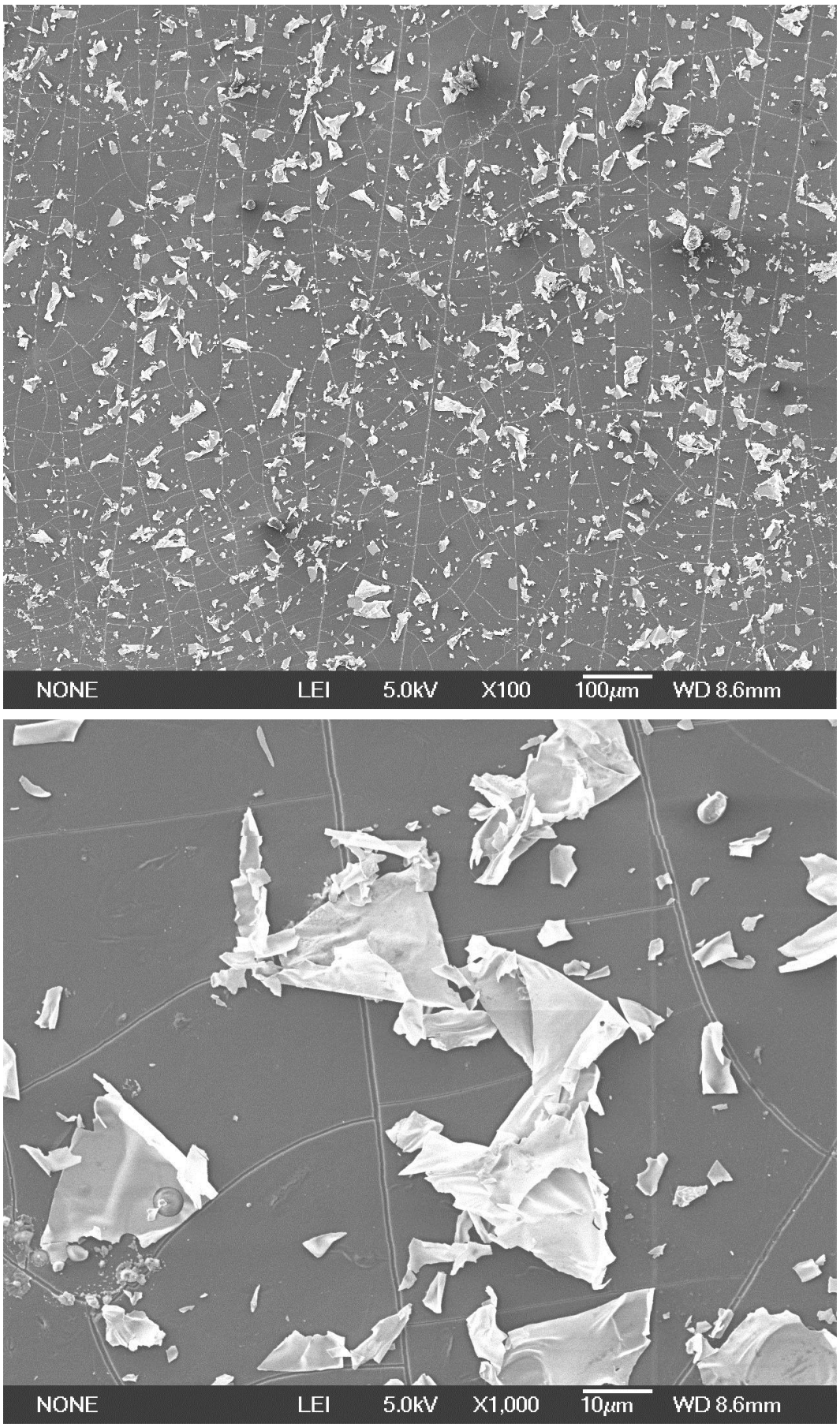

Figure 2.3.7 – SEM Micrographs of Excimer Laser Processed Nafion (60 nm Ni coating)
SEM imaging at two magnifications showing distributed (flaked) regions of Ni.

The laser processing of Nafion clearly resulted in a high surface area dispersed catalyst. This technique could be used as part of further materials processing such as growth of CNTs from the catalyst sites and use of catalytic deposition processes such as sputtering, both leading to further increased surface area.

Separate interesting features of the j-V performance data are apparent in the low voltage region (< 1.5 V), threshold region (1.5-2.0 V) and upper region (> 2.0 V). In these experiments, excessive V_{Cell} was required in order to reach significant j due to the simplicity of the cell and lack of PGMs. In the low V_{Cell} region, data gives a general indication of the cell conductivity/integrity. No H_2 forms when V_{Cell} < 1.5 V and any current data indicates electron conduction through the MEA. Nafion is not a perfect insulator and some electron crossover is expected (dependent upon Nafion thickness etc) [80]. This also gives a gauge of the surface contact between the mesh and Nafion. This range can assist with determining η_F since (once H_2 is being produced) only a negligible amount of H_2 will permeate through the Nafion in comparison to the electron crossover and total current, and the η_F will be mostly dependent on the electron crossover fraction of the total current (and leakage). The region < 1.5 V can be extrapolated to project the electron crossover as a function of voltage, indicating η_F. This has also been explained in literature such as by Atlam and Kolhe [66] and Shen et al [81]. The electron transport is in the opposite direction to the proton transport in an EC. For a FC the direction is the same, which indicates FCs being more prone to electron crossover. Since FCs operate at much lower V_{Cell} this phenomenon is not so apparent and may in fact be less than in ECs, directly affecting η_F in any case.

Figure 2.3.6 indicates H_2/O_2 evolution commencing between approx. 1.8-1.9 V. There are no significant apparent differences in the evolution voltages between the test configurations, although a small difference in the general trends are possible due to the different availability of Ni to the reaction sites and the different conductivity/ integrity of the cell in each experiment. For example, the laser processed sample appears to draw more current at low voltage and begin H_2 production at the lowest V_{Cell} of those tested, yet as V_{Cell} increases this cell does not perform as well as the 1 nm Nafion cells. In these experiments, H_2 production is only in tiny quantities and below the range of the volumetric measurement equipment until V_{Cell} > 2.5 V. At this point, $\eta_F \approx$ 70-88%. The relatively low η_F is a result of the low H_2 production in comparison to

the electron crossover. A linear region is observed in the data representing an 'ohmic' region. Mass transfer limitation was not likely to occur under the low *j* values in these tests. In the case of direct deposition onto Nafion, the surface must still permit proton transport through the metal catalyst layer. An optimal thickness would need to be sought and ideally with an appropriate PGM rather than Ni. At the optimal catalyst thickness, loading above would be too restrictive of the proton transport, whereas lower loading would not provide the most effective catalyst. Other work such as by Slavcheva et al [76] involving sputter deposition reports much higher loadings (and use of PGMs), with coatings of 250-1000 nm for example, representing loadings of 0.1-0.4 mg cm^{-2} Ir/IrO_2. In the work carried out here, much lower loadings were used (approx. 0.001-0.002 mg cm^{-2} Ni). From the data, the 2 nm Ni sample indicated decreased performance and for this reason and material limitations, further testing was not carried out to clarify whether further increased loadings would be beneficial. Figure 2.3.8 shows cell efficiencies for three of the test configurations, where η_{EC} reaches 43-53% at 2.2 V. The poor performance is generally due to the simple nature of the cell and the non-preferential catalyst (although Ni demonstrated some activity).

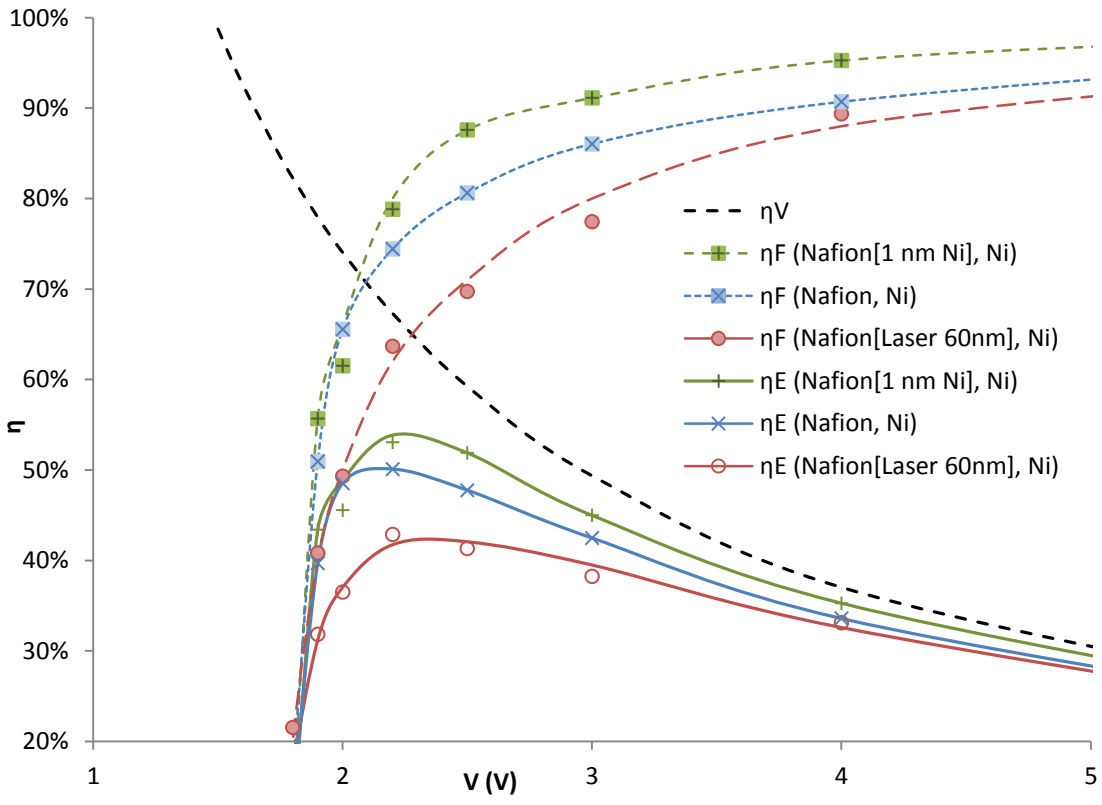

Figure 2.3.8 – Experimental Test Cell Efficiency Data
Voltage, current and energy efficiencies (η_V, η_F, η_E) from the various cell tests.

2.3.4 Cell Test Experiment Summary

Performance of Ni catalysts in an EC using nanoscale deposition and processing techniques was investigated. The key measurement is the j value for a given V_{Cell} (where a greater j represents superior performance). Work with Ni could help to profile the effects of laser processing and provide indicative data (from use of a cheap experimental catalyst) that could then be mapped over to similar work with PGMs in further research. Data suggests minimal but noticeable influence from Ni on the mesh current collectors in the unprocessed Nafion experiments. Ni has some catalytic activity in these reactions as suggested by literature although limited and not particularly significant in data here. The 1 nm Ni-Nafion configuration appears the most effective, with or without the Ni mesh. Variation of cell integrity (i.e. electrode-Nafion conductivity) appears to be the cause of the lower performance of the 2 nm Nafion sample, which was expected to be superior. This is implied from literature where thicker depositions are discussed. Nafion surface requires proton conductivity, and further work would be required to ascertain the most suitable thickness. In principle, the laser processed sample tested in this work was not successful, due to its instability. Also in comparison to the unprocessed Nafion with lower Ni loading, the laser processed sample had slightly lower performance. In general the test data here were prone to error (e.g. cell integrity variation), apparent in the low V_{Cell} region. Further work of this sort would require a more advanced test cell with a superior mesh layer and ideally Pt/Ir catalysts.

Laser processing requires further investigation to optimise the intensity to avoid material ablation and also investigate use of buffering metals or other techniques to increase bonding of the catalyst to the Nafion. Adjustment would likely be required when working with heavier PGM metals. Working with Nafion also requires extra attention to expansion/contraction with temperature/ humidity during processing stages. Importantly, the laser processing did produce a high surface area catalyst layer onto the Nafion and this processing approach may have significance in other nanoscale materials research work of this sort for ECs/FCs. SEM and EDX were used here to confirm material surface compositions and dispersion etc. EDX with 5 μm penetration into the Nafion did not permit easy identification of the surface Ni. XPS techniques would have been preferred, with 2 nm depth surface composition analysis.

2.4 Alkaline Electrolyser/Engine Experimental Work

2.4.1 Effects of On-board H_2 Production on Internal Combustion Engine Efficiency

An H_2 engine efficiency experiment was brought to the Division of Physics, UoD, in 2011. Assistance was required to determine whether on-board production of H_2 + O_2 fed into a vehicle engine could improve efficiency. The project had been set-up by a vehicle enthusiast claiming efficiency improvements, who had then been awarded local authority funding under an energy saving initiative. Work required was to:

- Test and optimise the efficiency of an alkaline electrolyser
- Measure the change in engine efficiency with on-board H_2 production

On-board H_2 production in this work refers to connecting an ES to an engine alternator to produce H_2 + O_2, fed directly into the engine air intake. From the outset, the thermodynamic limitations of the process were put forward and the idea was not considered feasible. The only circumstances where this might be of benefit would be where an alternator was faulty and dumping power when not loaded, which could possibly be recovered favourably by ES loading (not likely in a modern alternator). The other possibility was if the addition of H_2/O_2 gases into the fuel mixture were to improve the engine combustion/timing characteristics (due to high diffusivity etc [62]). These circumstances would not lead to significant improvement of ICE efficiency. No credible peer-reviewed data was found to demonstrate the effects of a set-up as described here.

Work to quantify the *losses* induced by this process was therefore carried out. This involved first optimising the ES supplied to the project and testing of an ICE and alternator to establish efficiencies. The system could then be tested with the ES powered by the alternator and the gases fed to the engine, to determine any change in performance/efficiency. Work here also allowed direct observation of the effects of feeding blended H_2 to an engine.

Efficiency is determined by fuel consumption and vice versa if the power output is known. CO_2/NO_x emissions are related directly to fuel consumption, and engine temperature in the case of NO_x. Losses in ICEs result from several relatively simple factors, including: friction; incomplete fuel combustion (incorrect stoichiometric mixture etc); thermodynamic/entropy losses; powering engine equipment such as

pumps/ignition etc. These also apply in the case of an H_2-fuelled ICE, as well as several other issues relating to the combustion characteristics when the ICE is not optimised for H_2 [60-62]. In-depth investigation of these factors is not essential here. Only a small few literature sources were found on the concept of on-board H_2 production. One is by Dülger, K R Özçelìk, who report of their own novel ES unit integrated with four vehicle ICEs [82]. They claim significant efficiency savings in city driving scenarios, although the data are very vague and appear circumstantial. They are not likely repeatable in normal combined driving tests. Yilmaz, Uludamar and Aydin provide a more recent and detailed report of a similar arrangement using an alkaline ES [83]. Their description of electrolysis and the overall process is simplified, and the relevance/conditions of the data are not clear. Vehicle efficiency is poorly defined in much of literature and there is also large natural variation and use of obsolete/undefined units (such as 'mpg' etc).

2.4.2 Electrolyser Stack Testing/Optimisation and ICE Experimental Methods

For this work, a simple alkaline ES kit was supplied for testing (materials from this kit were adapted and used to provide the ES for the experimental tests previously in Subchapter 2.2). The kit consisted of 25 Ni/stainless steel plates (plus spares), seals, tubing, water tank and Perspex end-pieces. No diaphragm was supplied or used for this experimental work. The ES was initially set-up and tested in a four parallel, six bipolar/series cell configuration (24 cells), as suggested by the kit supplier. The ES in this configuration is shown in Figure 2.4.1. The ES was extensively tested with 24 and 28 cells to determine performance with different configurations, and with temperature, electrolyte type/molarity, and cell spacing variation. The device was customisable and could in fact be assembled in configurations of 1-32 cells. The test engine was a bench-mounted Honda 50 cc 4-stroke, allowing fully manually operated throttle and fuel/air mixture adjustment. H_2/O_2 was fed into the air intake. The test alternator was coupled to the engine prop shaft via a custom fitting. Alternator loading was achieved using a 12 V battery and two heavy duty variable resistors. The test engine and alternator are shown in Figures 2.4.2-2.4.3. Fuel flow was measured volumetrically over time. The alternator electrical output was measured and converted to mechanical output power to allow efficiency calculations.

Rated power: approx. 220 W
Active surface area: 936 cm^2 (24 cells)
Number of cells: 24 (nominal), 1-32 (variable)
Anode catalyst: Ni
Cathode catalyst: Ni
Electrode material: Ni/Stainless steel
η (rated): 48 % (14.4 V, 15.0 A)
η (max): 54% (14.14 V)

Figure 2.4.1 – Alkaline Electrolyser 24-Cell Stack Configuration

Size: 50 cc
Max power: 1.5 kW (2 BHP) (117 rps)
Max torque: 2.7 Nm (75 rps)
Engine speed range: 25-200 rps
η (max): approx. 20%
η (typical): approx. 10-15%

Figure 2.4.2 – Honda 4-Stroke Test Engine

Rating: approx. 1.2 kW (90 A)
Type: electromagnet rotor, 3-phase rectified
Output: approx. 14.4 V (DC)
η (max): approx. 65%
η (typical): approx. 60%

Figure 2.4.3 – Test Alternator

Engine speed (ω) was measured in rps from the alternator ('w' terminal) by oscilloscope, as shown in Figure 2.4.4. Torque (τ) and engine power (P_{Mech}) were calculated from ω, electrical power (P_{Elec}) from the alternator and its efficiency (η_{Alt}):

$$\tau = \frac{P_{Elec}}{\eta_{Alt} 2\pi\omega} \quad \text{Eq 2.14}$$

$$P_{Mech} = \frac{P_{Elec}}{\eta_{Alt}} \quad \text{Eq 2.15}$$

A fixed value of 60% was used for η_{Alt} based on previous investigation/testing. Variable electrical load and throttle adjustment was used to vary τ and ω. The ES was operated at four H_2 generation rate to investigate changes to the engine performance and efficiency (η_{Eng}). The experimental work could then proceed to take engine efficiency data with and without H_2 generation. Although extensive ES testing was carried out, the focus in this work was at alternator voltages (typically 14.2-14.5 V). The project was informed that 15 A was the intended working range for this particular set-up for a vehicle engine. This would enable noticeable H_2 production but not cause significant load onto a vehicle alternator. In the case of the experimental testing, the engine was much smaller than that of a vehicle and current was reduced accordingly for better representation. Considering the engine size compared to a vehicle of 1500-2000 cc, ES currents of 0.5-3.0 A were used to represent 15-100 A, which would demonstrate clearly the effects of the process. The engine was loaded (by further alternator current) to represent typical engine conditions. For practical reasons the ES testing was focussed at the alternator voltage (14.4 V) and 15 A. Engine testing was representative of driving conditions and operated at relatively low throttle (relatively low ω, e.g. 66 rps). This was also due to practicalities such as the engine-alternator coupling strength. It was not necessary to characterise the test engine performance/ efficiency throughout its range. Variable loads were applied to the engine using the two variable resistors. One resistor was in series with the battery and the other across the alternator output, allowing approx. 0-4 A to flow as a result of battery charging and 0-10 A through the second resistor. Virtually identical conditions were then replicated but with the alternator providing additional power for the ES (feeding H_2 to the engine air intake). It was not practical to operate this particular ES directly from the alternator at low currents when optimised for 15 A, therefore the alternator received representative loading and a power supply was used to power the ES. The battery

provided a switch-operated excitation voltage to the alternator. For a fixed throttle, fuel consumption is almost proportional to engine speed, since the amount of fuel consumed is proportional to the engine displacement and the number of intakes. The mixture setting also allows variation of the fuel intake. For these tests the mixture setting was initially adjusted such that the engine performed optimally and then leaned slightly. This setting remained fixed throughout the experiment. The reason for leaning the mixture was to promote the use of the H_2/O_2 gas (so that any reduction in efficiency could not be attributed unduly to unfavourable mixture). Leaning the mixture allows more air and less fuel, which is beneficial for an engine where a significant portion of the air is a combustible fuel. Torque varies with engine loading and when increased the engine delivers more power, but engine speed is likely to decrease. Engine efficiency (η_{Eng}) should be approx. related to τ, since more P_{Mech} per unit fuel is likely with more τ for the specific throttle setting. Fuel enthalpy was considered 36 kJ mL^{-1} [26] for this work. η_{Eng} was calculated from fuel quantities in mL consumed over the experimental duration (Vol_F) and work delivered (from Eq 2.15):

$$\eta_{Eng} = \frac{P_{Mech}t}{36000\,Vol_F} = \frac{VIt}{21600\,Vol_F} \qquad \text{Eq 2.16}$$

Test durations were of the order of 10 minutes depending on conditions. Experimental work was focussed on first optimising the ES, and secondly engine efficiency measurement with and without the ES powered by the engine alternator.

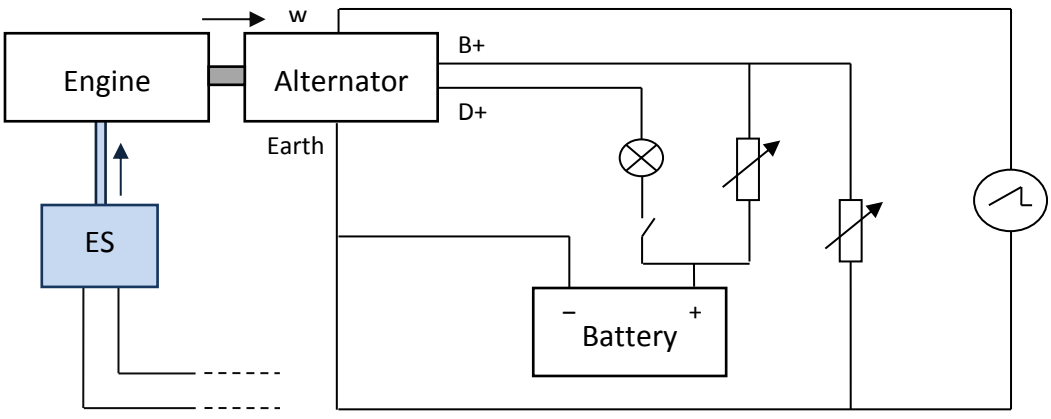

Figure 2.4.4 – Engine Test Circuit

The engine is shown mechanically linked to the alternator, which was loaded to the battery and heavy duty variable resistors (B+). Engine rps was monitored by oscilloscope via the alternator w terminal. D+ was for rotor excitation.

2.4.3 Electrolyser Optimisation Experiment Results and Discussion

Work to optimise the performance of a simple ES has been carried out previously such as by Nagaia et al [84]. In terms of cell spacing (without a diaphragm), it was reported by Nagaia that the minimum is optimal (which is to minimise ohmic losses through the electrolyte), but only to the extent before significant bubble loss occurs. At a certain spacing the maximum efficiency will occur, in terms of the lowest V_{Cell}, but the exact spacing will vary for different types of cells. For the work here, the spacing was physically limited only by the seals, in this case 2.0 mm O-rings, which could be compressed to a minimum size of 1.2 mm. Further reduction (with thinner seals) was not observed to enable increased efficiency at the 15 A range. With four parallel sets, 15 A equates to cell currents (I_{Cell}) of 3.75 A. As a baseline, 1.3 mm was used for further testing, avoiding significant stress on the ES components and O-ring failure.

Test electrolytes were NaOH and KOH aqueous solutions of 0.5-10 wt%. The electrolyte wt% had similar but opposite effect as cell spacing, where increased wt% led to increased current (due to more OH^-), and lower V_{Cell} to achieve 15 A. NaOH and KOH performed similarly. KOH appeared to produce slightly higher efficiencies and was used for continuing tests. The properties of KOH are published elsewhere such as by Allebrod et al [85], showing that conductivity increases with concentration and temperature. The maximum conductivity occurs at 25-30 wt% at 25°C. Temperature has an effect on conductivity, defining the wt% at which maximum conduction occurs. Conduction data by wt% and T are shown in Figure 2.4.5. Applying a DC potential to a KOH electrolyte creates a potential gradient, but current cannot flow unless chemical change occurs. Allebrod et al used an AC voltage (of varying frequency) to produce their data [85]. Industrial alkaline electrolysis uses concentrations of 25-30% (KOH) as stated previously [64]. Increasing wt% indicates increased efficiency from the ionic conductivity perspective, with lower ohmic loss in the cell. The simple ES tested here in the 24/28 cell configuration could not operate at these high wt% values due to the design of the plates. A normal ES will demonstrate significant current increase with a small change in V_{Cell} as observed in previous EC data in Section 2.2.2. This ES kit was designed for direct connection to various alternators expecting slightly different voltages, which would not be possible for a normal ES if expected to produce comparable currents in each case. Rather than use a DC-DC voltage converter (with

added cost, complexity and estimated loss of approx. 10%), the kit designer drilled holes in the electrode plates, shown in Figure 2.4.6, to effectively prevent rapid current increase. This created a significant loss within the cell. Although the holes allowed flow of gases/electrolyte between cells and the outlets, it also allowed electrolyte pathways to form between nearby plates, resulting in multiple additional effective cells forming in the ES. These holes caused very strange behaviour of the ES and significant losses, since some of the additional cells would be operating through long electrolyte pathways (with high ohmic loss) and at effective $V_{Cell} \approx 14.4$ V (where $\eta_{EC} \approx 10\%$).

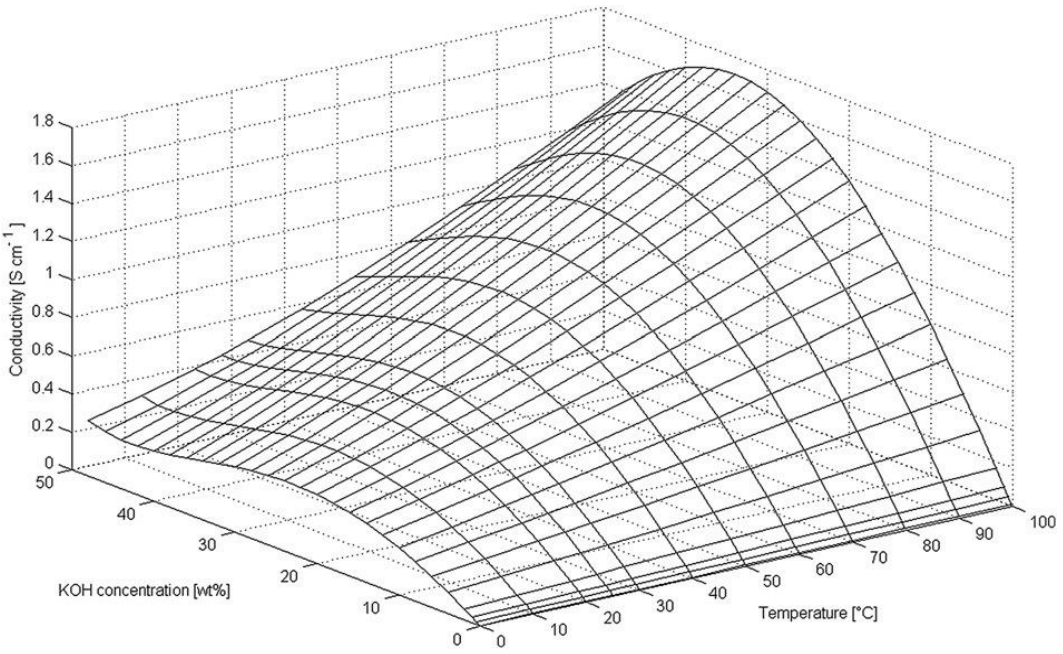

[85]

Figure 2.4.5 – 3D Plot of Aqueous KOH Conductivity by wt% and Temperature
Conductivity by KOH concentration (wt%) and temperature data are plotted.

Figure 2.4.6 – Electrode Plate from Alkaline Electrolyser Kit
Sample 'holed' plate from the alkaline ES (electrical connection is hole at top right).

Testing at conditions of 14.4 V, 15 A, 1.3 mm and at the normalised operating temperature then defined KOH of 2.0 wt% for 24 cells and 6.5% for 28 cells. The resulting η_{ES} values in these configurations were 48.1% and 50.4% for 24 and 28 cells respectively. Figures 2.4.7-2.4.8 show I_{ES} and η_{ES} data for cell spacing and KOH wt% variation. Data reported here include various practical optimisations to the basic kit, such as reducing certain pipe lengths, lowering the electrolyte/water tank (to reduce head pressure) and adjusting the O-ring position to minimise gas space in the cell (and maximise effective surface area). In Figure 2.4.6, the brown stain is due to K^+ bonding to the plate surface. The original O-ring position is indicated from this stain. Adjusting the position such that it is lowered with the top of the O-ring situated just above the top hole was found to be optimal in terms of still allowing gas to evacuate the cell but maximising cell area. Without modifications, the original kit (24-cell) was limited to η_{ES} ≈ 46% in initial tests. It was indicated that for operation at 15 A, it was preferable to first optimise the cell spacing (1.3 mm) and then the KOH wt% (the trends of these factors both appear linear within the test range). The ES here was limited to η_{ES} ≈ 50% by virtue of its simple design and as a result of the holes in the plates. As an obvious observation, by using an additional identical ES then two could be operated in parallel, each at 7.5 A. This would reduce current-based losses, allowing a more optimal arrangement, increasing η_{ES} to 54.0% (0.8 wt%) and 54.7% (2.5 wt%) for 24 and 28 cells respectively (and possibly reduced cell spacing and further gains in η_{ES}),.

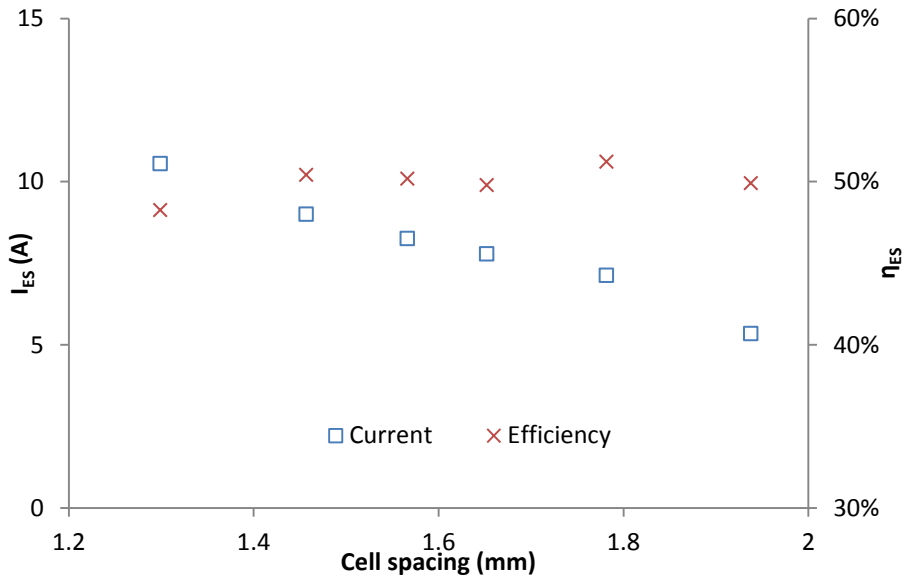

Figure 2.4.7 – Effects of Cell Spacing (24 cells, 14.4 V, 1wt% KOH)
Current and efficiency data are shown at various cell spacing values.

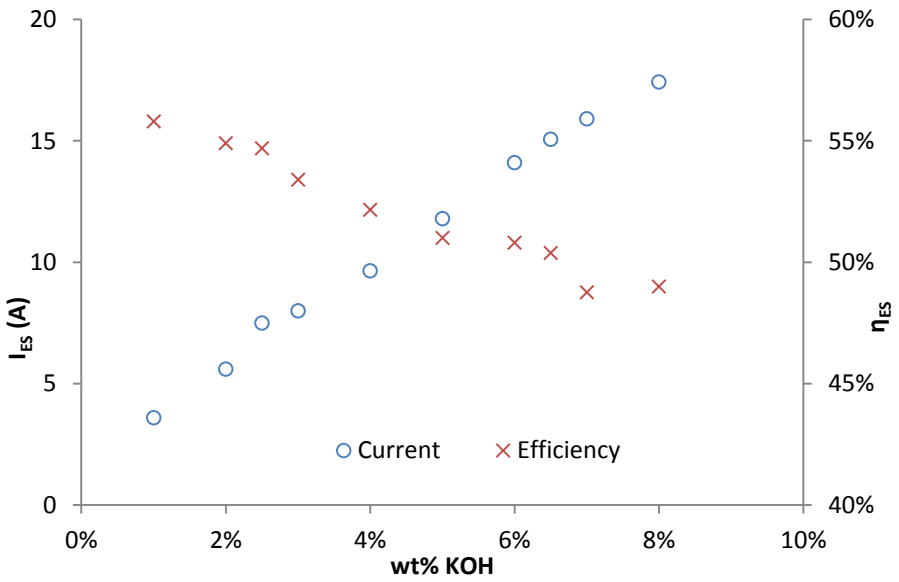

Figure 2.4.8 – Effects of KOH Concentration wt% (28 cells, 14.4 V)
Current and efficiency data are shown at various KOH concentrations (wt%).

The 28-cell configuration produced slightly higher efficiencies in this work and was used herein. With 24 cells (six series) at 14.4 V, V_{Cell} would be higher and therefore lower wt% values would always be required compared to when operated with 28 cells (seven series). Characteristic (optimised for 14.4 V) data by V_{Cell} is shown in Figure 6.4.9 for the final 28-cell configuration.

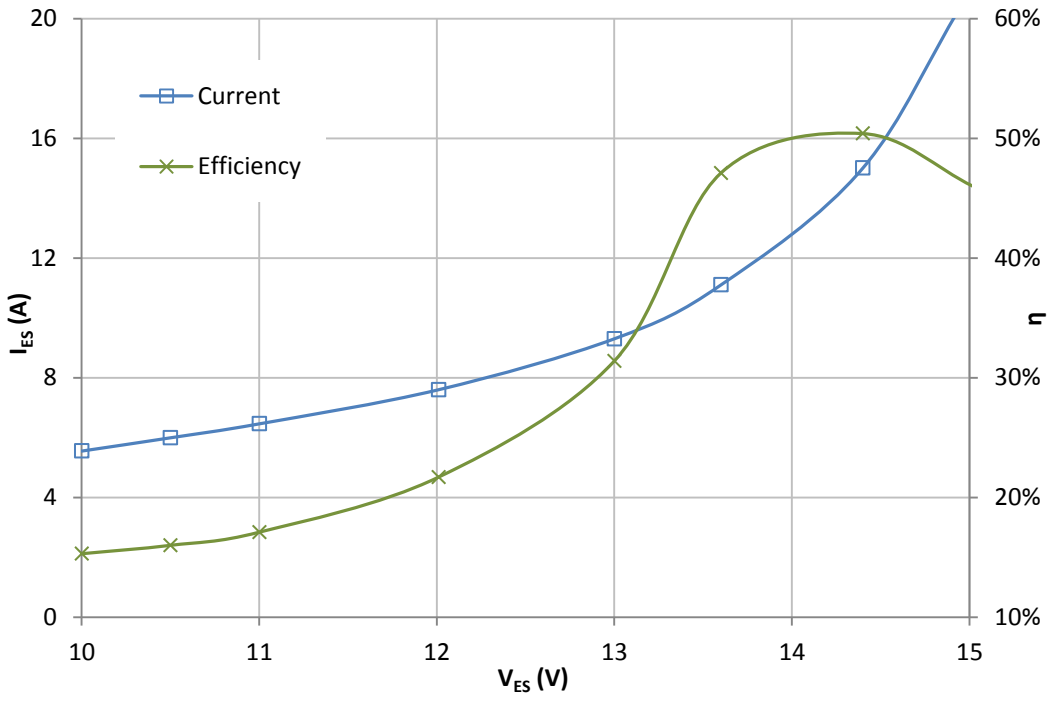

Figure 2.4.9 – Optimised Alkaline ES Efficiency Data (28 cells, 1.3 mm, 6.5 wt% KOH)
Test data for final ES configuration, now reaching peak efficiency (50%) at 14.4 V.

The η_F trend is not shown since for this ES with multiple cells it cannot be determined easily from volumetric measurement and current, or calculated characteristically as before. This is due to various secondary cells forming, operating at different V_{Cell}. The n term in the Faraday equation (Eq 2.11) basically cannot be defined easily and varies at different V_{Cell}. Measurement when V_{Cell} < 1.48 V indicates very high η_F per cell, as seen previously for the modified eight cell ES configuration in Figure 2.2.9.

2.4.3 Engine Test Experiment Results and Discussion

The engine was operated representing typical vehicle conditions with loading up to 285 W (mechanical) applied via the alternator to determine η_{Eng} values. Fuel consumption was carefully measured, to accuracy of ±5%. Conditions were replicated but with the additional alternator loads of 0.5-3 A to produce H_2 (assuming $\eta_{ES} \approx 50\%$). Data are shown in Figure 2.4.10. With significant H_2 load applied (e.g. 2 or 3 A), the engine speed reduced noticeably and the apparent η_{Eng} would therefore change. This would not be representative of the case in a vehicle (which would not be driven slower just because of use of the ES), so for this reason the throttle (via screw-operated idle position) was increased slightly to achieve the same ω and τ value in each comparable test. The value for P_{Mech} was derived from (useful) alternator current, ignoring current used for H_2 production. The fact that the engine ω decreased indicated that the process was detrimental to efficiency. The data also show that ES current led to a reduction in η_{Eng} and that on-board H_2 production was not beneficial. Loss is not obvious at 0.5 A, but reaches -1% at higher currents (which is quite significant when η_{Eng} < 10%). The H_2 quantities produced here were not observed to produce positive engine performance. Considering the engine at 66 rps, the intake of fuel/air would be 1.65 L s^{-1}. The ES at 1 A (14.3 W electrical output) would be producing only 0.61 mL s^{-1} (7.15 W H_2), based on the modified Eq 2.8. This is negligible even considering ΔH of the H_2/O_2 mix compared to fuel/air. As a data integrity check, the H_2 production was increased towards 15 A (from the power supply) while the alternator remained loaded at a condition such as 1 A and base load. In these cases, ω was not seen to increase until above 10 A (this is basically giving the engine free $H_2 + O_2$ into its air intake). It is not evident that H_2 modified the nature of the combustion positively. Considering that the ES load was causing reduction in ω is sufficient to confirm that the generated H_2 was not a substitute for the additional work required to power this load.

Vehicle efficiency loss at 15 A would be minimal but difficult to measure. Alternator loading and traces of electrolyte entering the engine would likely result in negating issues, such as alternator failure and engine wear. This concept would however have merit in a completely different set-up, where a stationary ICE could supply waste heat to a grid-powered ES. In this case, the ES would be operating efficiently and economically and the engine would simply be assisting the process with waste heat.

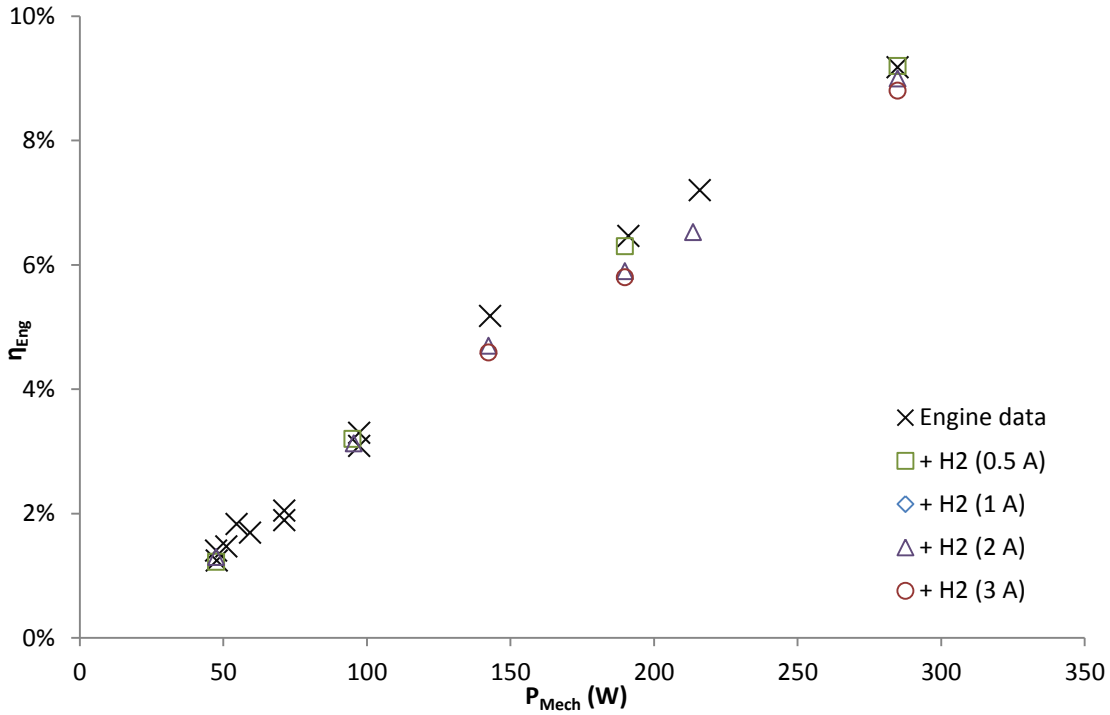

Figure 2.4.10 – Engine Test Data With/Without On-board H_2
Engine efficiency data with on-board H_2, showing losses with increasing ES current.

2.4.4 Alkaline Electrolyser/Engine Experiment Summary

This experiment investigated practical aspects of a simple alkaline ES from extensive testing, some of which would apply to a commercial alkaline ES. Data indicates that the basic ES supplied was limited to $\eta_{ES} \approx 50\%$. Slightly improved η_{ES} was observed with 28 cells, compared to 24 as expected due to lower j. ES performance was poor mainly due to the plate design. Engine testing demonstrated the effects of small H_2 fuel additions. Testing an engine in an on-board H_2 production arrangement was difficult. Data indicated reduction in η_{Eng} as anticipated from basic thermodynamics, of up to 1% in the case of excessive H_2 production. The system is therefore shown to be fundamentally flawed, due to inefficiencies of the three components.

2.5 Summary

EC/FC technologies have been investigated within the context of low-cost renewable H_2 production. These are shown to be responsive, modular and efficient, suitable for several applications [68]. The FC reaction has been discussed in literature to a much greater extent and there remain different conventions for cell efficiency and voltage etc. In particular, the fact that the EC reaction will proceed as favourable (with electrical power rather than heat) is often neglected. Inconsistency occasionally results in literature when FC electrochemistry is applied to ECs, where subtle differences in terms of H_2O state, conversion of electrical energy to and from ΔH and ΔG, and external heat are not considered (i.e. neglecting $V_{Th} \equiv 1.481$ V at STP).

Work here, comparable to literature, presents ECs operating practically at V_{Cell} = 1.6-2.4 V and η_{EC} = 75-80% (PEM), 60-80% (alkaline), or 0.5-0.8 V and η_{FC} = 35-55% for PEM FCs. While these factors are pertinent to the small devices tested and additional more complex issues may affect larger EC/FC devices, the basic functions and losses discussed here are analogous (i.e. current losses and activation, ohmic and mass transport voltage losses). Data from this work can be analysed with WT and PV data to practically investigate wind- and solar-powered H_2 production via electrolysis. Expedient use of EC-FC H_2 cycles for grid electrical energy storage is not presently feasible in most scenarios due to the low 'round-trip' efficiency of the process.

EC/FCs have been observed to require sophisticated electrode form, to enable porosity and conductivity. PEM cells rely on PGM catalysts, whereas Ni has good activity for alkaline cells and PEM cells to some extent (in the HER). This has been demonstrated here by 1nm deposited onto Nafion or a Ni coated mesh in a test EC, with the catalyst having the effect of reducing the reaction voltage thus improving efficiency. Laser processing was carried out on a 60 nm Ni-coated Nafion PEM to increase the effective Ni surface area. Laser processing successfully increased surface area but resulted in an unstable coating. Further work would be required to overcome this issue in order to produce a practical catalytic PEM from laser processing. Finally, investigation of on-board H_2 production via an EC connected to an engine's alternator demonstrated added loss when H_2 was produced and fed to the air intake, exactly as expected from basic thermodynamics.

3. Renewable H_2 from Wind and Solar Energy

The world has abundant renewable energy resources, providing 20% of global energy in 2013. In order of current usage they are bioenergy, hydro, wind, solar, geothermal, tidal, wave [39] [86] [87]. Resources originate mostly from the sun (solar), which powers thermal water vapour cycles (hydro), air pressure changes (wind, wave) and photobiological reactions (biomass). Additionally there are kinetic energies of the rotating earth and orbiting moon and gravitational interactions with one another and the sun forcing movement of water bodies (tidal), and then heat resources trapped or generated within the earth (geothermal) [88].

Global renewable electricity installed capacity (maximum power) was reported at 1560 GW in 2013 [87]. Wave energy is yet to make a significant contribution to the renewable mix mainly due to the present cost of the technology, lack of maturity and environmental practicalities [89] [90]. Tidal and hydro systems have excellent historical credibility. Tidal is predictable, although slightly restricted in terms of large-scale deployment. Hydro has the largest renewable electrical global installed capacity (1 TW in 2013), also an essential component for grid stability [87] [91] [92]. Hydro power with sufficient scale and edifice can provide economical dispatchable stored energy and is not considered for powering electrolysis. Geothermal energy is utilised on a reasonable scale in electrical (12 GW, 2013) and heat (3×10^{17} J yr^{-1}) generation, mostly in the USA, Iceland, Indonesia and Italy [87] [93]. Biomass provides the largest proportion of renewable energy (10% primary energy), mostly for heating [17] [94]. Wind turbine (WT) and solar photovoltaic (PV) systems are key renewables for electricity generation, although it is clear that an energy mix involving several technologies/locations provides better matching of grid supply/demand [95] [96].

This chapter presents renewable H_2 production via wind- and solar-powered electrolysis, including practical investigation and testing of the following:

- WTs and PV as renewable electrical energy sources
- Conventional/novel power converters and MPPT for connection of a WT to an ES
- Direct-connection of PV to an EC.

3.1 Renewable Electrical Energy from Wind Turbines

3.1.1 Micro Wind Turbine Test Experimental Method

WT testing was carried out with several micro HAWTs (up to 1 kW rating) and a micro VAWT during this work, to investigate electrical properties and to inform investigation of wind-powered electrolysis. A variable 1.5 kW fan was used in a test lab as a wind source. Observing various limits and loss factors this allowed WT testing to approx. 200 W. A detailed technical literature review of the physical principles and practical aspects of WTs has been included in Appendix A3.1, discussing power extraction and losses (i.e. of the rotor and generator), which can be referred to as necessary to support discussion in this chapter.

Three micro WTs were investigated extensively and the data are presented here in detail. These were an Eclectic Energy D400 HAWT (225 W rating at 12 ms^{-1}), a Marlec Rutland 910-F HAWT (120 W at 12 ms^{-1}) and a Forgen Ventus 30 Savonius VAWT (6 W at 12 ms^{-1}). All of the WTs tested had 3-phase PMSGs rectified internally to DC. Technical details for the three WTs are shown in Figures 3.1.1-3.1.3.

Simple 3-phase rectification used in these devices involving a bank of six Schottky diodes is explained by Lee and Chow [97]. A diode rectifier circuit is presented in Appendix Figure A3.1.8. There are also more advanced techniques involving synchronous rectification MOSFETs discussed elsewhere, which may be used in more efficient or larger rectifier units [98]. Six MOSFETs are used in the case of a 3-phase synchronous rectifier, replacing or supporting the six diodes in the simple circuit discussed above. The MOSFETs operate in pairs, inverted to each other, with three pairs operating out-of-phase by ⅔π from each other pair (in the case of a 3-phase rectifier). This requires additional control/PWM signals to operate each MOSFET and is not common for basic circuits or micro renewables. The synchronous rectified circuit is more efficient due to MOSFETs providing lower voltage drops than diodes due to the lower ON-state resistance. Schottky diodes for example exhibit a voltage drop ≈ 0.3 V at typical working currents. V and I measurements during WT testing here were therefore DC. Variable resistor banks of suitable power rating were used as test loads (0-1 kΩ).

Rated power: 225 W @ 12 ms^{-1}
Approx. cost: £1320 (2015)
Rotor: 5-blade
Ø / area: 1.10 m / 0.95 m^2
η (rated): 23%
η (max): 32%

[99]

Figure 3.1.1 – Eclectic Energy D400 Stealthgen HAWT (D400)

Rated power: 120 W @ 12 ms^{-1}
Approx. cost: £680 (2015)
Rotor: 6-blade
Ø / area: 0.91 m / 0.65 m^2
η (rated): 12%
η (max): 25%

[100]

Figure 3.1.2 – Marlec Rutland 910 Furlematic HAWT (910-F)

Rated power: 6 W @ 12 ms^{-1}
Approx. cost: £500 (2015)
Rotor: 3 Savonius drag scoops
Ø, height / area: 0.205 m, 0.305 m / 0.063 m^2
η (rated): 9%
η (max): 9%

[101]

Figure 3.1.3 – Forgen Ventus 30 Savonius VAWT (V30)

Three anemometer types were used for v measurement: a cupped anemometer; thermal mass flow measurement device; manometer. An accurate (but expensive) ultrasonic anemometer type was not available. These were investigated and are their function is explained in Appendix A3.2. All v data values reported are subject to error of ±5% due to natural variation and the particular measurement devices. In order to establish accurate test conditions the wind fan was set to constant power levels and v measured at the position where the centre of the WT would be during testing. Clearly

the WT could not be in position while establishing v readings, otherwise these would be offset by the physical obstruction of the WT. Due to basic properties of generators it was understood that $\omega \propto v \propto V$ (when the WT was not loaded), therefore acting like an anemometer. Once base v readings were established for each WT test, V_{OC} could then be used as a v reference. The trend of v-V_{OC} was established for each WT and is shown within data graphs in Appendix A3.3.

3.1.2 Micro Wind Turbine Test Experiment Results and Discussion

Data for each WT was used to investigate trends and performance up to the safe limits of the wind fan and equipment. Losses for each device were examined. The D400 was selected for wind-electrolysis tests and investigated in further detail. Readings of V and I were logged for a range of electrical loads, from open circuit to short circuit, and for a range of v values. Analysis of ω was carried out primarily by stroboscope. Direct readings for τ could not be established without interrupting the WT drive shaft. Rotor thrust could however be measured from backwards force on the WT mount, or τ from the rotational force component on the mount. A relation between I and τ could also be calculated from properties of the generator, since generator efficiency was known to a reasonable accuracy, although encountering some complex issues. Maximum electrical power (P_{Elec}) and I-V characteristics were sought and this relegated attention given to ω, τ and TSR (since as previously discussed there is not an exact relation between mechanical and electrical power trends due to generator losses etc [102]). Data for the D400 HAWT are shown in Figures 3.1.4 (I-V and P-V curves) and 3.1.5 (P-v curves). Test data for the 910-F HAWT and V30 VAWT are shown in Appendix A3.3. Electrical measurements were taken with accuracy of ±0.5%. WT losses were considered to result from the following:

- Non-ideal wind power extraction properties of the rotor
- Mechanical friction
- Generator losses
- Rectifier losses
- Other electrical losses
- It can be assumed that outside of a steady-state lab test scenario the WT may not constantly operate at its optimal power extraction condition, constituting a further loss factor (i.e. non ideal MPPT).

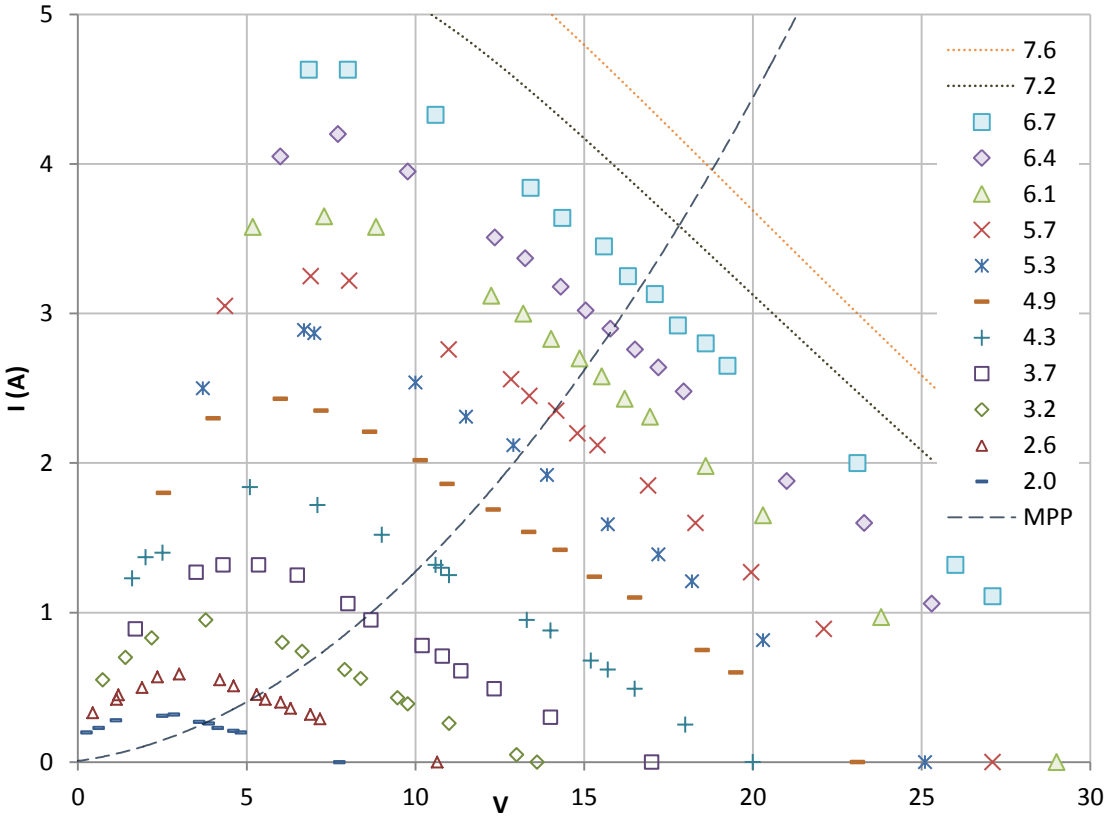

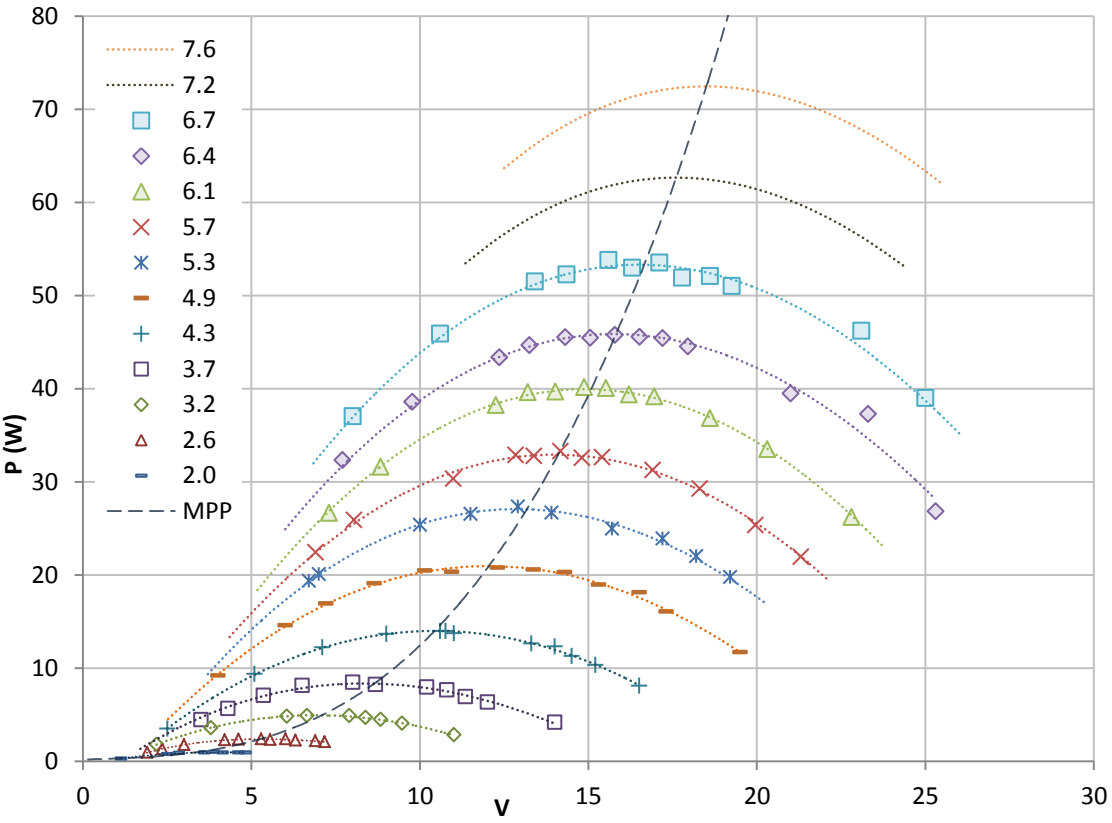

Figure 3.1.4 – D400 HAWT Test Data (*I*-*V* and *P*-*V*)

Current- and power-voltage test data are shown for the D400 WT, by wind velocity (2.0-7.6 ms^{-1}). The MPP trend through each wind velocity is overlaid.

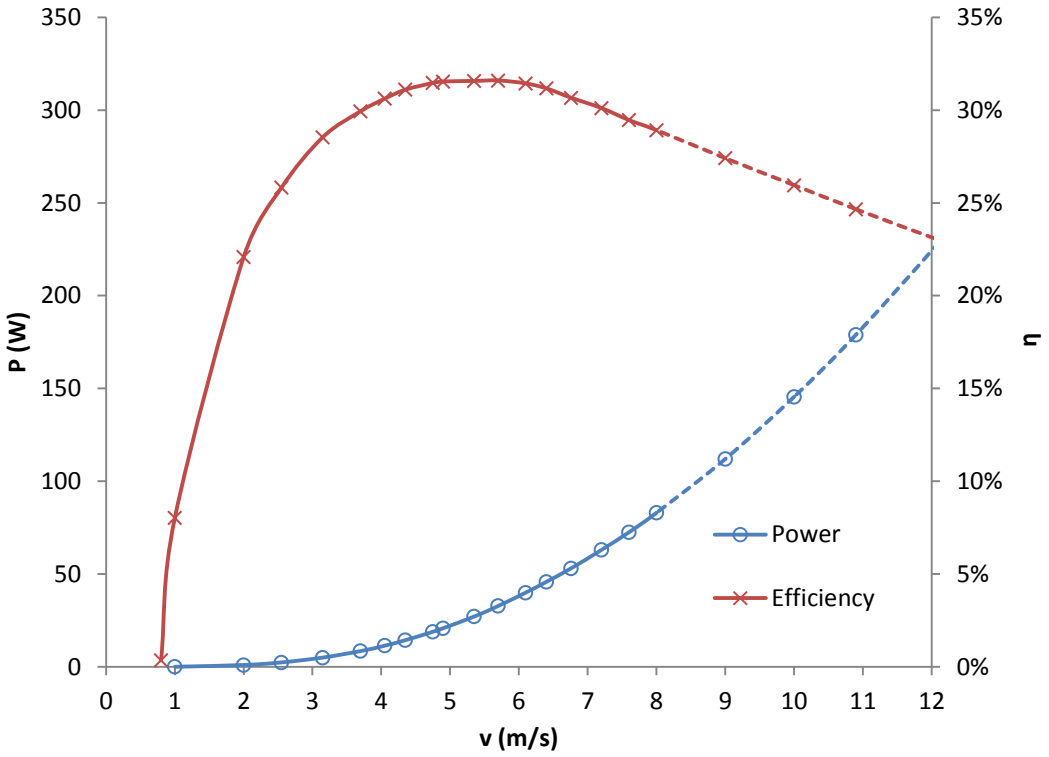

Figure 3.1.5 – D400 HAWT Test Data (P-v and v-V_{OC})
Power-velocity and efficiency test data are shown for the D400 WT.

The D400 has five blades and produces relatively high τ, low ω. The reason for five blades relates to relatively high currents and low voltage in 12 V battery charging roles (the D400 can be directly connected to a 12 V or 24 V battery and provide reasonably effective charging). It is rugged and designed for use on yachts where extremely high winds may occur, so it is assumed that a compromise between tip speed and thrust force onto the mountings must have been considered. Lower ω (and higher τ) also reduce friction loss in the device somewhat effectively at this scale of WT. The D400 was further investigated at 5.7 ms^{-1}, representing its (electrical) power efficiency (η_{Elec}) test limit ≈ 31.7% (33.4 W). The components of I, ω, τ, P_{Mech}, P_{Elec} and efficiencies for operation of the D400 at 5.7 ms^{-1} are shown in Figure 3.1.6. From data and inspection of the generator, rectifier and mechanical factors, the rotor itself was understood to be achieving approx. 36.7% extraction (38.5 W). The rotor in this case includes the mount bearings and its output is considered to be directly off the drive shaft. Slightly higher maximum rotor efficiency occurred at the mechanical limit of the rotor, observed at ω ≈ 4% lower (-0.2 rev s^{-1}) than the electrical limit. The maximum rotor efficiency was ≈ 36.8% (38.6 W). While there was no significant difference in this particular data set, it was clear from the graphical trend that a slight shift in optimum

ω exists between P_{Mech} and P_{Elec}, which would be more pronounced at higher v values. The remaining loss factor, effectively 13.3% loss of the rotor power, was calculated from (approx. compound values): 10.0% generator loss; 2.0% rectifier loss; 1.6% electrical loss from unavoidable wiring from the WT to the point of measure/use. Data excludes effects of measurement equipment, but some wiring would be necessary to use the WT in a real scenario and this was compensated in the testing. Graphical data above the test limits are calculated and shown dashed.

Friction from the shaft bearings was estimated by measuring the torque required to rotate the generator/rotor and comparing this to the torque values evident during operation. This loss component was considered shared amongst the generator and rotor efficiencies in this work. It would remain a fairly constant fraction of the WT power throughout normal (optimised) operation, due to τ and the friction force being proportional to v^2. At very low v (≈ 0.8 ms^{-1} in the case of the D400) the rotor may not overcome the static friction component of the generator/mount bearings. The bearing loss translates as a slight reduction in the τ value available to the generator relative to ω (and also slightly limits maximum ω at open circuit). The rectifier loss was based on a voltage drop ≈ 0.3 V in comparison to the generator output of 14.71 V (2.35 A) at the measured efficiency limit. This loss would tend to remain fairly constant during normal operation due to the properties of diodes, discussed in Subchapter 3.4 and Appendix A3.7 In 3-phase there are at least two diodes forward biased during operation and therefore current is shared. The rectifier and wire losses translate as the output voltage being slightly lower than that directly from the generator.

The rotor efficiency is understood to maintain η_{Rot} ≈ 36.6% through most of its working range of v. The exceptions are very low v (where for example rotor extraction and τ become very low and the various friction components rise disproportionately due to static friction etc), and at very high v (where for example the rotor may not properly align its yaw, and generator losses become very significant causing the rotor to operate significantly away from its optimal extraction). The generator in the D400 is of high quality and its efficiency understood to be approx. 90% at the limit [103] (efficiencies of some larger generators are understood to reach 98% [104]). Since $I \propto \tau$ and therefore $I \propto v^2$, but $V \propto v$, the generator efficiency declines at higher v values due to the increased I:V ratio. Generator loss is based upon two factors: iron losses (magnetic

flux losses); copper losses (conducting wires) [105]. Eddy currents are a significant component of the iron losses (dependent upon geometry) and also a slight component of the copper losses in a generator. During operation these effectively reduce both V and I from ideal. It was not possible to measure these factors exactly within this work. Importantly, generators have a limit to their current output based upon magnetic properties. Therefore an maximum power rating exists for a generator and efficiency will quickly decline when this is exceeded. For the D400 this is stated as 600W [99].

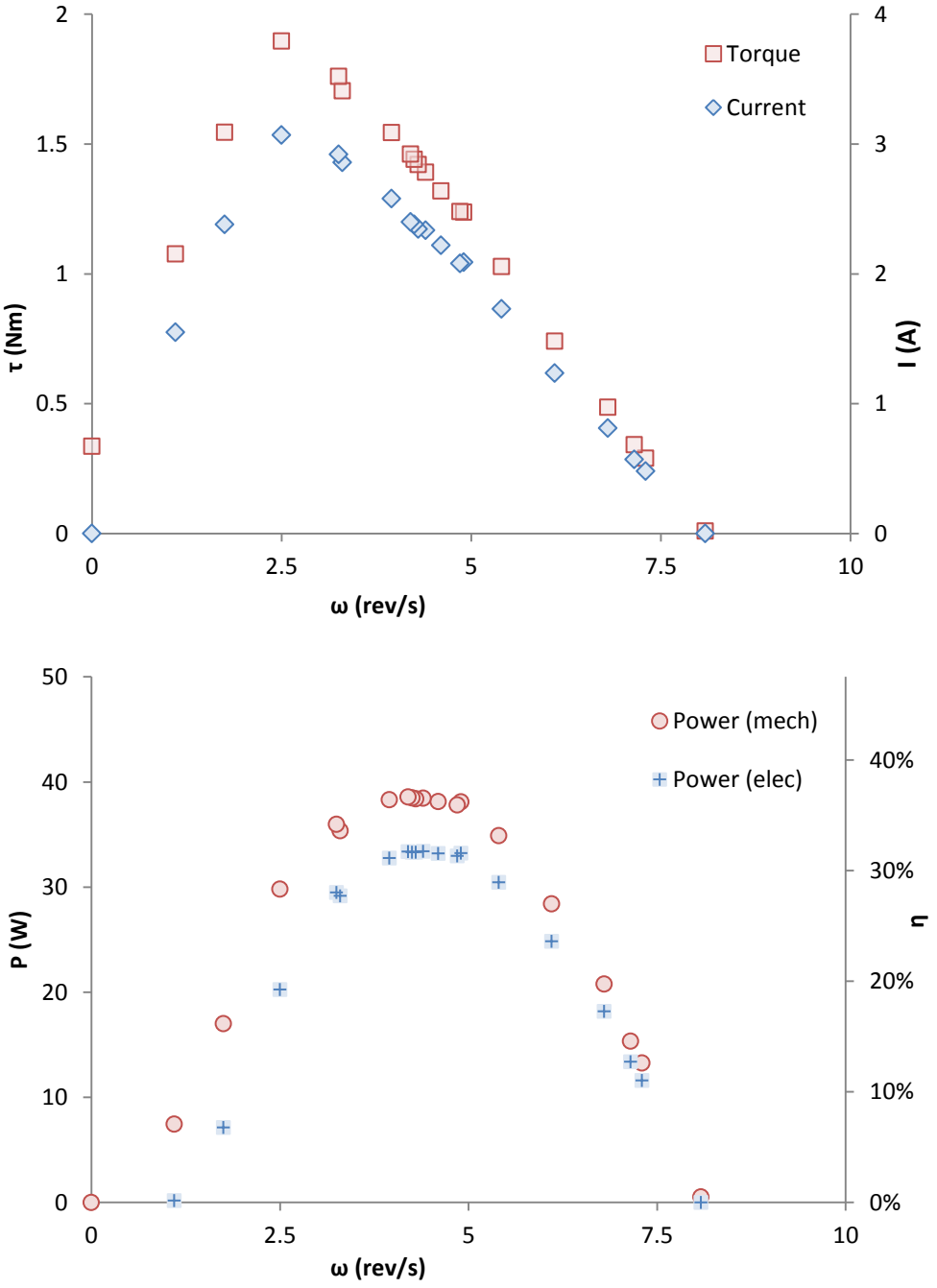

Figure 3.1.6 – D400 HAWT Current, Torque, Power and Efficiency Trends (5.7 ms^{-1})
Torque-, current-, power- and efficiency-rotational velocity data for the D400 WT.

Data for the 910-F HAWT (Appendix A3.3) show similar trends to the D400. The main exceptions are lower power and slightly higher $V{:}I$ ratio, due to the smaller rotor (and less optimal blade number) and differences between the generators coils etc. The 910-F was observed to operate at η_{Elec} < 27%. The generator is of slightly lower quality to that of the D400, with generator efficiency ≈ 85% typical for this size of WT. Observing the P-V and I-V trends for both HAWTs, blade stall occurs when the loading is high, where I and P suddenly decrease at low V or ω values. This does require a reasonable amount more current than when at the MPP, therefore the D400 and 910-F do not appear prone to entering stall easily during operation.

For the VAWT however, the interesting region is near short circuit loading since blade stall does not occur (there is no variable angle of attack). The drag-type rotor was therefore observed to deliver torque as a simple function of axial induction as indicated by theory, although at much lower levels. A slight current dip was observed at short-circuit due to very unfavourable I-V conditions for the generator. The VAWT has considerably lower I, P_{Elec} and η_{Elec}. The significant difference is due to smaller size and the drag-type rotor, rather than lift-type with variable angle of attack. The significant overall reduction in I (and τ) is due to the nature of the rotor, with one side opposing rotation. Since the rotor is drag-type and cannot benefit from lift, its power delivery is approx. halved compared to a lift-type rotor (based on $v \approx v_2$, considering discussion in Appendix A3.1.2), and due to the opposing action of the rotor this is further reduced significantly. Taking into consideration the theoretical limits and these practical aspects, the VAWT would be limited to η_{Elec} < 20% [106]. In fact the generator and overall build quality are not optimal in this device and η_{Elec} < 9% was observed. One advantage of a VAWT is not requiring yaw alignment and therefore they are reported to operate relatively better in very turbulent conditions (such as urban) compared to HAWTs (although still at much lower η_{Elec} than a HAWT) [106]. Darrieus lift-type VAWTS were not investigated practically but are understood to operate at efficiencies closer to HAWTs (approx. 40% for large Darrieus VAWTs, compared to 50% for large HAWTs at efficiency limits) [104] [107]. Testing of the V30 was carried out in an unenclosed environment, observing that the blocking effect explained elsewhere would otherwise offset data in a positive manner [108].

The MPP values of P, V, I (P_{MPP}, V_{MPP}, I_{MPP}) and trends are critical when considering connection to an electrolyser. Data demonstrates that $V_{MPP} \propto v$ and $I_{MPP} \propto v^2$ through the test range (although generator, rectifier and I^2R losses must be considered). Within the typical range v = 3-12 ms^{-1}, V_{MPP} must vary by a factor of 4 and I_{MPP} by a factor of 16 in order to maintain the MPP. The WT must therefore have dynamic loading such that V and I follow the MPP lines as shown in the data graphs. By convention for micro/small WTs this is achieved with variable DC-DC voltage stepping, creating variable generator loading and fairly steady output voltages from the converter (variable current). Power control to suit an electrolyser load, including two novel methods, are discussed in Subchapters 3.4, 3.6 and 3.7.

3.2 Renewable Electrical Energy from Solar Photovoltaics

3.2.1 Solar Photovoltaic Test Experimental Method

A polycrystalline PV module was tested in typical outdoor conditions in Dundee to determine I-V and P-V characteristics. The module consisted of four 5×10 cm series cells (area = 0.02 m^2) with 3 W rating. The objective was to assess the suitability of PV as an electrolysis power source for renewable H_2 production. A detailed technical literature review of the physical principles of PV cells has been included in Appendix A3.4, which can be referred to as necessary to support discussion in this chapter.

3.2.2 Solar Photovoltaic Test Experiment Results and Discussion

Test data is shown in Figure 3.2.1 for irradiances of 105-940 Wm^{-2}. Electrical measurements are with accuracy of ±0.5%. Irradiance intensity data was taken per unit of horizontal ground area from a nearby weather station [109] and adjusted (by a cosine function) to account for module tilt during test. Irradiance values are considered accurate to ±10%. The effect of cell temperature (T_{Cell}) on performance, particularly the reduction in V, is demonstrated in Appendix Figure A3.4.5. This is also evident in test data in Figure 3.2.1, since T_{Cell} increases with E. The MPP curve demonstrates that I_{MPP} increases proportionally with E and as an exponential function of V_{MPP}, but V_{MPP} may begin to decrease due to increase of T_{Cell}, which is foreseeable under higher irradiation conditions. This is in contradiction to constant T_{Cell} data sets encountered in literature; T_{Cell} varies in real PV installations during variable ambient conditions and changing solar irradiance, and this unavoidably skews V_{MPP} trends.

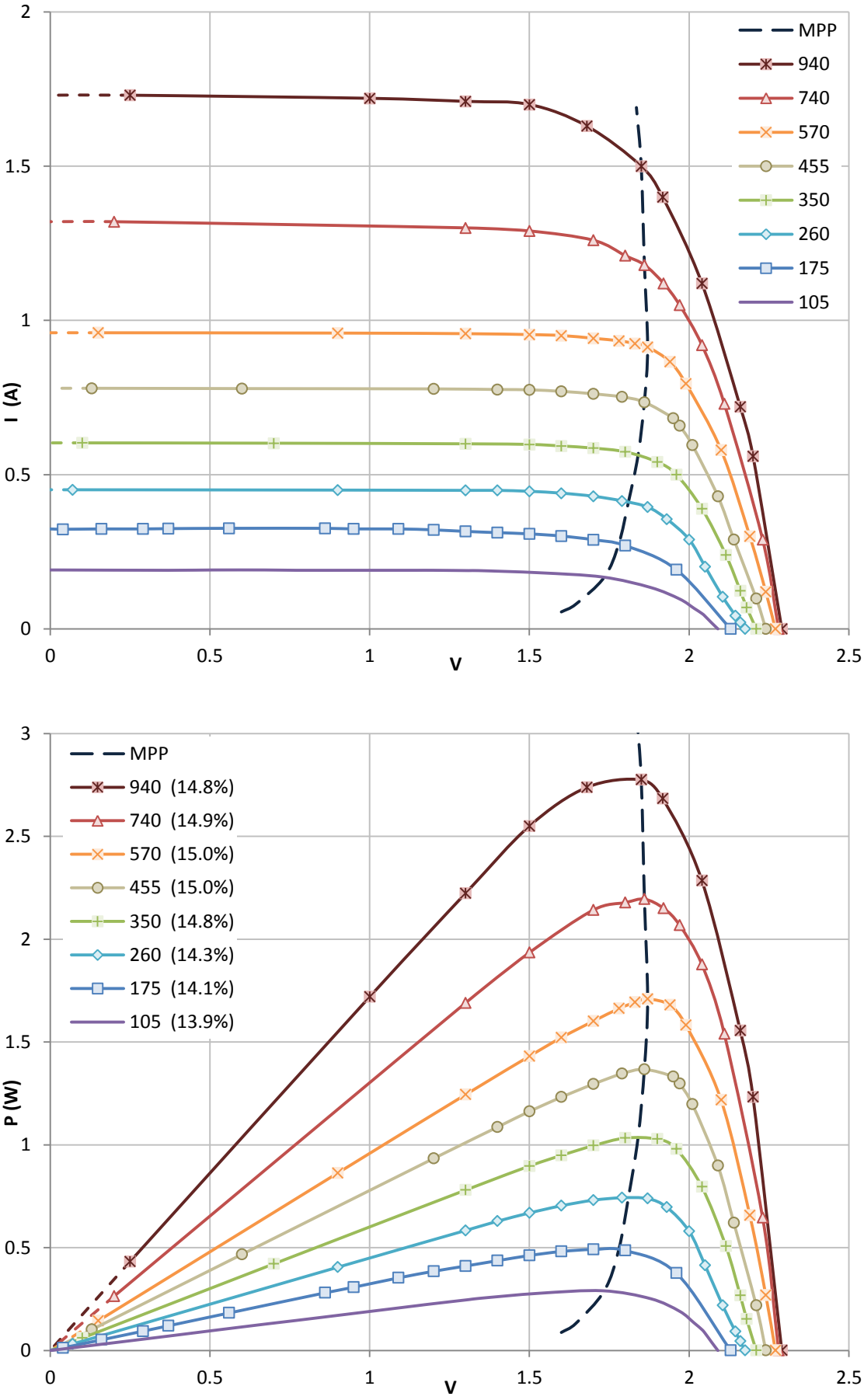

Figure 3.2.1 – Polycrystalline Photovoltaic Module Performance Data (*I-V*, *P-V*)
Current- and power-voltage data is shown for the test cell at 105-940 W m^{-2}.

PV efficiency (η_{PV}) was observed as fairly constant throughout the mid/upper test ranges, but T again becomes an influence since lower relative V_{MPP} is experienced with increased T. Relative efficiency can be almost determined by V_{MPP}, since I_{MPP} remains fairly proportional to E. Therefore η_{PV} appears to peak at approx. 15% at 565 W m^{-2}. However, a slight increase in I with T is also apparent (from Figure A3.4.5) and therefore η_{PV} appears to hold near 15% as $E \rightarrow$ 1000 W m^{-2}. For the test conditions at $E <$ 100 W m^{-2}, η_{PV} reduces below 14% (and $\eta_{PV} \rightarrow 0\%$ as $E \rightarrow 0$). Approx. η_{PV}% values are annotated on the P-V graph. Rated efficiency ≈ 14.7% (1000 W m^{-2}). The effects of increased T on the performance of thin film a-Si:H cells are reported to be much less severe and actually can be positive at low E values.

Dynamic tracking of the MPP is clearly critical for PV installations in grid-connection and electrolysis power roles. This is typically achieved with DC-DC converters and simple perturb and observe algorithms to find the MPP during changing E conditions. Variation in the E value is almost entirely related to air mass (AM), a measure of the amount of air in the atmosphere between the sun and the earth's surface, explained in Appendix A3.4. Another influence on E and P is the module orientation (zenith and azimuth). Having the module misaligned with a direct light source at a certain angle gives a simple geometric relation of $P \approx P_M \cos(a)$, where P_M is the maximum power found when maximally exposed to the light source and a the angle of deviation from this. In clear sky conditions with no landscape obstructions this simple function closely represents measured P as a function of a. Since maximum E is always sought, the module should ideally track the sun's position to maintain maximum P. However, importantly, surrounding landscape and cloud cover must be considered, since these obscure/reflect irradiance. Reflection from clouds was observed to account for a significant proportion of the irradiance during tests in overcast conditions, frequently occurring in the UK. In these conditions the module should be oriented more towards zenith; specifically it must find maximum E (and P), not necessarily directly towards the sun's position. Therefore physical PV tracking would ideally have a feedback loop to monitor changes in P with tilt/orientation, rather than rely solely on predetermined sun positions for example. Most small installations are of fixed angle and this should be set for an optimum average energy yield. In the UK this is aligned due south (or a few degrees west of south) and facing approx. 40° from zenith [110].

3.3 Wind and Solar Energy Economics

3.3.1 Review of Wind and Solar Energy Costs

The economics of renewable energy installations are of the most significance. These are briefly reviewed here from literature sources covering wind and solar energy. Wind energy is reported to be generally the cheapest renewable electrical energy appropriate for renewable H_2 production (e.g. excluding established hydro installations) [111] [112]. Presently 0.7% of global electricity is from solar, whereas 2.9% is from wind [87], which may be a reflection of cost. Larger WT and PV installations are more economical due to economies of scale, increased v in the case of high WT rotors (higher energy density), and lower power electronic component cost in relation to the overall cost and energy yields etc [87] [110]. However considering land costs, smaller scale (i.e. rooftop) installations may become more suitable.

With PV in particular, interest is split between cost per Watt and/or energy (over the installation lifetime) and cost per unit area (efficiency). In pure financial terms the former is of more importance. For limited spaces (rooftops) or extreme cases (satellites, airborne applications), there may be limited area and high demand, therefore cell efficiency is more critical. Market trends and demand have moved cells of low efficiency (most thin film) to slightly cheaper cost per Watt, although in recent years the fall in crystalline Si costs has put pressure on thin film and concentrating solar industries [87].

The energy costs over the lifetime of WT and PV installations vary significantly by size, type, location, year of commission, inflation and other economic factors, and are also reported differently across literature sources and at different times. In many cases the actual generation equipment cost may have been less than half of the overall installation cost [110]. The market has however become more competitive in recent years, which has reduced installation, consultant and labour cost components. A good list of status and characteristic costs for 2013 is provided for example by the Renewables 2014 Global Status Report [87]. Installations are generally considered over a 25-year lifetime. Large WT installations are reported to provide electricity at approx. 0.04-0.16 \$ kWh^{-1} onshore and 0.10-0.23 \$ kWh^{-1} offshore. PV is reported at 0.09-0.55 \$ kWh^{-1} [87] [112]. From European-only data PV figures are 0.14-0.38 \$ kWh^{-1} and continuing to decrease, such that in several countries the cost is below that

of grid electricity. Micro/small WT installations are reported at 0.15-0.35 $ kWh^{-1}. Installations of micro/small WTs may be three times higher than larger WTs and uneconomical (1900-6040 $ kW^{-1}) [87].

The cost per Watt (installed) for PV and WTs are both decreasing and may result in future cost parity in 2015-2020 (whereas conventional fuels are likely to increase in comparison) [113]. However, the capacity factor (percentage of maximum energy production) of WTs is typically higher than that of PV. In the UK and Northern Europe the capacity factor of PV may be 10.3%, or 17.1% in Southern Europe (22.8% with two-axis tracking), whereas WT capacity factors are typically 30-35% at large scale [39] [110]. Therefore the Watt-peak cost of PV must reduce to approx. half for cost parity with WTs.

Installed costs of PV vary by scale and location and are 2150-7000 $ kWp^{-1} for residential (< 5 kW), 2150-3800 $ kWp^{-1} for commercial (≈ 100 kW) and 1200-3800 $ kWp^{-1} for industrial (≈ 500 kW) (2013) [87]. In Europe these costs are towards the lower end and continue to decrease. MW-scale WTs report as 925-1950 $ kWp^{-1}. Large WT installations will therefore likely breakeven within seven years and PV within nine years (assuming export at 0.10 $ kWh^{-1}). PV cost remained fairly stable from 2013-2014 due to demand, despite significant reductions in the few years before, but support costs (inverters, installers etc) reduced. The actual cost of manufacturing PV in 2013 was reported at 0.50 $ W^{-1} [87].

3.3.2 Renewable Incentives and Microgeneration Certification Scheme

Large renewable electricity generation installations including PV and WTs are grid-connected to provide renewable energy into the national energy mix. For micro/small generation this also makes economic and efficiency sense, since there will be constant demand for the energy and optimal use of the equipment, unlike with finite battery storage or small off-grid loads etc. Grid connection is an important economic factor and is briefly discussed here. When grid-connected, the device can be metered at the site, and for example any demand at the site is first met and any excess is exported to the grid. For small-scale installations without metering, a fixed 50% export may be assumed.

In the UK, most renewable energy generation systems < 5MW can be eligible for feed-in tariffs (FITs) (after April 2010, formerly Renewable Obligation Certificates and Levy Exemption Certificates). The UK government's Department for Energy and Climate Change administrates the process and up-to-date details are found online [114] [115]. These currently consist of two components: generation tariff; export tariff. The generation tariff is a payment made by the owner's grid energy company to the owner for every unit of energy generated, whether used or exported to the grid. The source of the money is the energy supply company, but who claim the generation as their own and may see decreased future taxation etc due to renewable generation objectives, otherwise the cost will be absorbed by the energy company or simply passed on to bill payers.

The present generation tariffs (index linked) for PV and WTs are shown in Table 3.3.1. Generation tariffs vary by device type, scale, installation date and the nature of the installation. Rates are usually reviewed annually. For new installations these are said to be falling by 'degression', representing the falling cost of renewable energy technologies. Tariff payments reduce with increasing power rating, reflecting the economic differences of scale and thus supporting micro renewables. For PV, payments are classed as higher or medium level (separated by the dash in Table 3.3.1), depending on certain conditions for the installation.

In addition there is a flat lower rate (marked with * in Table 3.3.1) applicable to certain installations ≤ 250 kW and to all > 250 kW. The export tariff is a flat rate paid for units of energy exported to the grid (unused at the site), which is much lower than the generation tariff, currently 4.85p kWh^{-1} for all technologies as of 1 April 2015. Most developed countries have FITs and their general idea is to encourage growth of renewables. In the UK, micro/small WT and PV generation < 50 kW is covered by the Microgeneration Certification Scheme (MCS). This aims to ensure quality of installations and conformity to various guidelines. MCS-approved equipment and installers are required for micro/small installations to be eligible for FITs. Installers are expected to complete a training course in order to become certified. Similarly, equipment is tested for performance so that datasheets are accurate and for conformity. On one hand this has raised the level of overall competence of installers and improved datasheets, on the other hand it has increased the cost of installations.

Type	Rating	p kWh^{-1}
PV	≤ 4 kW	14.38 / 12.94
	4-10 kW	13.03 / 11.73
	10-50 kW	12.13 / 10.92
	50-150 kW	10.34 / 9.31
	150-250 kW	9.81 / 8.90
	≤ 5000 kW*	6.38
WT	≤ 100 kW	16.00
	100-500 kW	13.34
	500-1500 kW	7.24
	1500-5000 kW	3.07

[115]

Table 3.3.1 – PV and WT Feed-In Tariff Rates (November 2014)
An extract of FIT rates for PV and WT as of November 2014. PV is divided by a higher and medium rate. The lower PV rate is marked with *.

A vast amount of PV modules have undergone testing for MCS approval, whereas for micro WTs this has seen a slower uptake [115]. There are a significant amount of unapproved micro WTs on the market and generally of much lower cost to that of approved WTs. MCS may therefore be having unhelpful effects such as raising the price of micro WT installations, which due to their low efficiency and reduced wind velocities are barely profitable in a grid-feed set-up in most cases. A case study of a small/medium WT and PV installation was carried out at Cypex, a biological processing unit in Dundee. This is presented and discussed in Appendix A3.5. Data from this case study demonstrate that, while wind and solar energy can be quite economical and practical for energy generation, this is not assured and relies on the installer observing good practice and the overall installation costs being competitive.

3.4 Conventional Power Control and MPPT for Wind/Solar Electrolysis

3.4.1 Overview of DC-DC Converters and Conventional Power Control

Previous discussion of WT, PV and EC characteristic performance supports investigation of power conversion techniques to couple these devices for renewable H_2 production. Attention has been given to *I-V* data, efficiencies and practical issues etc. It was observed from practical work and literature that micro/small (fixed pitch) WTs ideally operate with variable voltage for maximum power extraction, resulting in a

requirement for a wide range of output voltages and currents (where $V \propto v$ and $I \propto v^2$) [116]. Also as observed, PV exhibit specific voltage and current conditions that must be considered to enable maximum power extraction, depending on irradiance and temperature etc [110]. Power conversion and MPPT strategies for micro/small renewables are central to this work. Conventional strategies for micro/small WT and PV systems involve inductive DC-DC converters with MPPT function (various types of) [116-119]. This provides suitable output for grid connection (with DC-AC conversion etc), battery charging, or other DC applications including powering an ES [102] [116] [120]. There are a multitude of topologies disused in literature for DC-DC voltage control depending on application and requirements (such as power reversal, isolation etc). Circuit topologies are explained and presented elsewhere such as by Lee and Chow [97]. Discussion of the most relevant aspects of the circuits is included in Appendix A3.6.

A more general review of power converter technologies for WTs has been provided by Baroudi, Dinavahi and Knight [116], where they consider micro/small (PMSG) up to large (AG) scale. Discussion of PV systems at micro/small scale is actually more apparent in literature since these are frequently deployed domestically, whereas conventional micro/small WT systems are not always economical for grid-connection at this scale [87]. Rectified WT voltage output can be coupled directly to a power converter, which may then involve step-down or step-up of DC voltage, or both. The objective here has been to produce a simple, low cost, practical and novel power controller with a MPPT function, demonstrating feasibly of wind/solar-powered electrolysis for renewable H_2 production at small scale, inferring more profitable H_2 production at larger scale. In the case of large grid-connected ES systems balancing WT/PV generation, the efficient conversion of grid AC power to DC ranges suitable for an ES is required. These large power electrical techniques have not been investigated in detail for this work. However, there exist established power control techniques for grid connection of large WT/PV installations and (separate) AC-DC converters in widespread use, thus providing the renewable energy source and capability for large grid-connected ES systems to be presently implemented for renewable H_2 production. For large WT systems, power is generally kept in AC and variable pitch/generator properties provide MPPT (maintaining voltage to suit the local grid) [116].

Investigation of power converters such as in the Cypex case study revealed expensive hardware being used (partly due to MCS requirements). Their function is quite refined due to the variable nature of the input/output I-V profiles [117]. Very simple control circuitry has been considered in this work for micro/small WTs.

ES systems benefit from grid connection (essential at large scale) to balance loading for optimal use of the ES and WT/PV [121] [122]. This assists with matching the ES rating to the available energy resource, avoiding use of an overrated ES for the amount of energy available etc. Crucially this could also assist with grid power balancing, by consuming excess from the grid to power the ES. Use of an ES system would therefore be of benefit to the grid and WT/PV markets in many circumstances, allowing increased renewable energy penetration [121]. The ultimate aim of any H_2 production system is to achieve the lowest cost per unit H_2, which will occur when maximum H_2 production is achieved for a particular system. Other issues in the case of balanced grid-connected H_2 production are maximum renewable energy capture (for maximum renewable H_2 production), efficient ES operation and improved grid economics from smart use/release of available renewable energy [122]. The H_2 unit cost over the lifetime of the installation becomes complicated when grid use is involved, since the grid may supply excess energy to the process at varying cost etc. In stand-alone systems, unit cost results from the total installation and maintenance cost divided by the total H_2 production over its lifetime. While work here applies directly to micro/small scale, the concepts involved support the credibility of renewable H_2 production from wind and solar resources that can be achieved more economically at larger scale.

3.4.2 Overview of MPPT Function

Much literature exists for MPPT strategies for WT and PV systems [102] [117] [123-141]. The function of these MPPT strategies is to dynamically track the power condition of the system and maintain operation at the MPP. For large WTs this variation may be actuated via blade pitch control, use of variable slip (to vary ω), or use of DC-DC power circuits [116] [117]. The latter is typically the case for smaller WTs and most PV systems. MPPT strategies may be with or without feedback sensors [102]. Feedback is usually from a hub-mounted anemometer in the case of large WTs. This indicates the v value, which is compared to known performance data, allowing

variation of the configuration (such as pitch) to optimise for the condition. Lookup data may simply be the optimal TSR (where the WT will attempt to maintain this with measurement of v and ω), or optimum τ (likewise it will refer to a known ideal τ ratio and attempt to maintain it). A further option is use of power signal feedback [128]. The latter two may not measure v directly (they typically measure ω) and this may cause a slight delay in the change of condition and small losses. In each case a lookup reference of for example the known optimal TSR, t-ω or P-ω trends are necessary [117]. The latter two techniques are shown to be practically the same [129]. The TSR method is simple but somewhat primitive. Importantly it should consider generator efficiency and its characteristics to establish the maximum electrical power output, which does not strictly occur at the same TSR through the operating range [102]

Micro/small WTs may use any of the above MPPT techniques although the hill-climb search (HCS) is common in these systems. There are also techniques involving ω and P_{Mech} etc [117]. HCS is a mathematical optimisation technique that searches for a maximum operating point [117]. Unlike the previously discussed MPPT techniques, HCS does not require predetermined data or feedback in the form of v, ω or τ etc. This is often preferable for smaller WT systems for simplicity. HCS typically takes V and I measurement to determine the circuit/inverter power. The controller makes a small variation to D (e.g. from 0% to 4%); the effect is either increased power production (moving toward the ideal I-V trend), or a decrease. With the former, the same direction of variation is repeated (e.g. from 4% to 8%). Otherwise the step is reversed (e.g. back to 0%). Over a few iterations the HCS algorithm finds the D value that achieves the MPP. Due to constant iteration the matching is inexact, since D will continually move to either side of the ideal MPP value [102] [117].

When powering an ES, measurement should ideally be of V_{ES} and I_{ES}, since circuit/converter losses may misalign the WT electrical power (P_{Elec}) and ES power (P_{ES}) as D varies. What may be experienced (such as with the experimental work here) is that measurement of V_{ES} may be somewhat unreliable when powered by a rectified 3-phase AC source, due to the ratio of variation and noise to actual positive variation of V_{ES} with correct iteration and the slight increase in P_{ES}. The V_{ES} value will not increase significantly with slight increase in P_{ES}. I_{ES} is more responsive, as shown in previous data in Figure 2.2.8 etc. Measurement of I_{ES} needs to maintain accuracy over a large

range of values and not add additional circuit loss. Appropriate sensing will therefore depend on the individual system.

With micro WTs, v may be very changeable. Due to this and rotor inertia, D may become quite erratic and often with erroneous iterations. The HCS circuit is not likely to maintain the MPP in these conditions. HCS benefits from use of variable D step size, so that large changes in v can be quickly compensated without several D iterations. Similarly, small changes in v do not then lead to unnecessary movement from the MPP. Some intelligence as to which direction to perturb is also sought, to avoid incorrect iterations during sudden changes of v, also considering the effects of rotor inertia [129] [130]. This requires more advanced HCS function, with use of an intelligent/fuzzy logic controller (FLC), further details of which have been discussed elsewhere [131] [132].
PV MPPT is easier since there is much less sudden variation and no inertia effects as experienced with WTs, especially when compared to similar MPPT techniques for micro/small WTs. There are several established techniques for MPPT of PV. These include: the beta method; perturb and observe (P&O, analogous to HCS); incremental conductance (INC); constant V and I ratio and V_{OC} and I_{SC} and sweep methods; use of a pilot cell; more complex methods based on dP/dV or dP/dI feedback control or use of FLCs and hybrid methods involving two of the above [133] [134]. The beta method and constant V and I ratio are the most simple. Additionally there is direct connection, which is often practical for battery charging and powering an ES, provided that it is properly set-up [142]. Use of a DC-DC converter at a fixed D value is a progression from a direct-connect circuit to accommodate mismatched components but maintaining simplicity [134]. The beta method involves a controller with a simple mathematical function that can determine the ideal I-V curve theoretically. With V and I measurement it then adjusts the circuit (such as D) to follow the ideal curve.

Constant V ratio control involves briefly isolating the PV to measure V_{OC} and then loading such that $V = k_V V_{OC}$, since $V_{MPP} \approx k_V V_{OC}$, where k_V is a predefined constant. Similarly, I_{SC} measurement can be used (with a different constant, k_I) where the PV is briefly short-circuited and $I_{MPP} \approx k_I I_{SC}$. Ratio methods are simple but inexact without measurement of T_{Cell} and cause unsteady outputs and power loss. Sweep techniques involve an occasional controller load sweep from V_{OC} to I_{SC} to locate the MPP. This method determines the MPP with accuracy but wastes power during the sweep and

between sweeps when conditions are changeable [134]. The pilot cell technique uses a small measurement cell identical to the main PV array, which is operated with the ratio method at V_{OC} or I_{SC} to provide data to determine the optimal configuration of the main PV array (V_{MPP} or I_{MPP}). This avoids the power loss and unsteady outputs from the main array that result from the constant ratio methods, but is not exact due to slight differences between the pilot and main components [134].

P&O is frequently used for MPPT of PV [135-137], identical to HCS previously discussed. It naturally benefits from the fact that irradiance is less changeable than wind and can generally maintain higher accuracy. Similarly it can also make use of variable step-size for improved performance during scattered cloud conditions etc. INC observes the trend of dP/dV by perturbation, in similar manner as P&O. The INC controller locates the point where dP/dV = 0, which occurs at the MPP [133] [134]. Recently, INC and P&O have been investigated and explained in detail, where they were shown to be the same in principle, producing identical results [137].

The main drawback with P&O/HCS techniques (even with variable step size etc) are constant iteration and error during changeable conditions. With a WT there is also the issue of component/mechanical stress from continual changing of the generator condition (from constant D variation) [130]. If v is gradually increasing yet the HCS algorithm has stepped in the wrong direction, it may read a false positive (since the output power has increased) and continue to progress erroneously. Rotor inertia will always benefit one direction of variation (where kinetic energy is extracted from the rotor, occurring with increased D in the case of step-up). This should ideally be accounted for within the algorithm. These issues have been investigated extensively and advanced control algorithms have been discussed such as by Kortabarria et al [130] and those reviewed by Raza Kazmi et al [129], involving FLCs and controllers with sophisticated function. MPPT algorithms based on lookup function are superior but require accurate data for the system, which may not be available or practical to measure. This may vary over time with changing ambient conditions (and specifically temperature, such as of an ES), component wear, or PV shading from tree growth etc. Raza Kazmi et al present a sophisticated multi-function algorithm to consider sensed data and a lookup reference, attempting to maintain a superior MPPT function [132].

3.4.3 DC-DC Power Converter Losses

Converter efficiency is a critical aspect of overall function. A considerable amount of literature discusses work on DC-DC converters to improve efficiency in various applications [123-127] [143] [144]. Circuit component non-ideality is often expressed as effective series resistance (ESR), resulting in I^2R losses. Power conversion efficiency (η_{Conv}) is calculated from the input and output voltage and current:

$$\eta_{Conv} = \frac{V_{Out}I_{Out}}{V_{In}I_{In}} = \frac{P_{ES}}{P_{WT}} \qquad \text{Eq 3.1}$$

This is dependent on conditions such as I:V ratio etc (high V and low I is preferable to minimise I^2R loss, although this is a system scaling/set-up issue and not necessary within the scope of the converter itself). In general η_{Conv} is reported from 88-99% [123-127] [143] [144], within which step-down is usually the most efficient and step-up/down the least. Ohmic/I^2R loss relates to the circuit wiring and specifically the four main components. Overall converter system efficiency (η_C) should consider the controller power demand and (in the case of WT/PV systems) the effectiveness of the MPPT function. This makes measurement of η_C complicated and somewhat inexact in real scenarios. Micro/small renewables may operate close to 240 V when grid-connected or 12/24/48 V in the case of battery charging. The magnitude of stepping adversely affects η_{Conv}. For micro/small renewables, the I:V ratio may be relatively high with for example a 1 kW device operating at 24 V (42 A). It may then be impractical to operate at large step-up to minimise losses in cabling etc, since this will reduce η_{Conv}. Large step-up (e.g. 10) may be achieved more efficiently with two or more converters linked together to make smaller step-ups (e.g. two step-ups of five with 'back-to-back' converters) rather than one single large step-up. Capacitive DC-DC converters [145] for large step-up are briefly discussed in Appendix A3.6.

The inductor and MOSFET are typically the most significant source of loss [127]. High capacitance (C) and inductance (L) provide more effective device function, also minimising hysteresis etc, but in the case of the inductor this increases R_L. Putting inductors in parallel to reduce R_L is not possible since this reduces L. Agbossou et al [143] demonstrate an impressive novel technique to effectively reduce R_L by placing multiple inductors (e.g. four) into separate circuits with a MOSFET and diode, reaching the same smoothing capacitor at the output. The MOSFETs are operated separately

(synchronised but out of sequence). This also reduces output ripple. Agbossou et al [143] provide a detailed discussion of this within the scope of an advanced controller used for a stand-alone renewable energy system. This consists of a WT and PV input and an ES providing H_2 production for later use in a FC to support and balance a small (renewable-powered) grid system. Samavatian and Radan also discuss a simple version of this described as an 'interleaved' low ripple convertor [144]. These topologies require multiple synchronised PWM signals, but potentially provide improved η_{Conv}. In general, good quality inductors with thick copper wire and iron/magnetic cores are preferred to minimise their adverse effects on η_{Conv}.

MOSFETs conduct electrons from source to drain when a sufficient gate-source voltage (V_{GS}) is applied. They have complicated characteristics, where their drain-source resistance (R_{DS}) is related to V_{GS} [146], and also to physical properties such as channel length, effective area, and doping [147]. There is a voltage threshold (typically between 1.8-4.0 V) at which a MOSFET begins to conduct (drain-source current, I_{DS}), as shown in Figure 3.4.1 [146]. Conductance is shown to increase with V_{GS} (and temperature). MOSFETs have a small gate-source capacitance (C_{GS}), which prevents instant change of V_{GS}. As a result, it is not possible to change from OFF-state to ON-state instantly and without passing through a region of relatively high R_{DS} for a matter of micro seconds. The switching signal must be square wave and deliver significant current at the instant where OFF- to ON-state occurs to quickly transfer charge to overcome this region. A MOSFET used in these circuits should be of suitable I_{DS} and V_{DS} (drain-source voltage) rating, of good quality, and ideally with relatively low C_{GS} (although this is generally linked to the maximum I_{DS} rating). Also, V_{GS} range (full ON-state) must be lower than the PWM signal voltage.

Diode function can be supported with use of a synchronous MOSFET, known as synchronous rectification (SR) [98] [127]. This is identical in principle to what has been discussed for AC-DC rectification circuits in Subchapter 3.1, offering very significant improvement to a basic power converter. SR requires a parallel MOSFET reaching ON-state when the diode is in forward bias, and OFF-state when reverse bias. This SR MOSFET has inverted but synchronised operation to that of the switching MOSFET. A MOSFET behaves like a reverse bias diode (by convention) and must be placed in reverse so that it only forward conducts in ON-state. Since Schottky diodes have a

voltage drop of approx. 0.3 V in normal current ranges, the SR MOSFET lowers this voltage drop considerably and almost eliminates losses from the diode part of the circuit [127]. An example SR circuit is shown in Figure 3.4.2 (in step-up topology). This requires another square wave signal, inverted to that of the first MOSFET. In the case of step-up using a signal generator with common ground to V_{In} this requires V_{GS} for the SR MOSFET to be effectively higher than V_{In} since the source pin is at a higher potential than ground (which prevents relatively basic controller set-up).

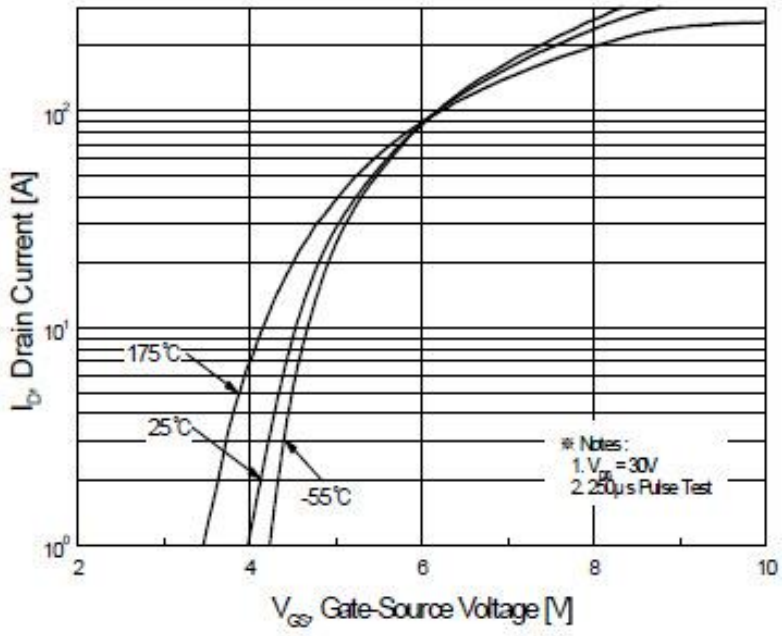

[146]

Figure 3.4.1 – MOSFET Drain-Source Current/Gate-Source Voltage Trend
The temperature-related I_{DS}-V_{GS} trend is shown from a MOSFET component datasheet.

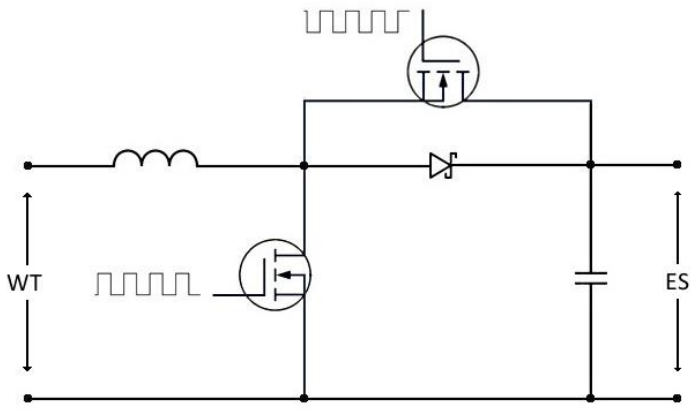

Adapted from [119]

Figure 3.4.2 – Example DC-DC Step-up Converter with Synchronous Rectification
The addition of a SR MOSFET is shown, supporting the diode in forward bias.

While powering an ES or battery charging there may be significant capacitance in the load and perfectly smooth DC voltage is not essential, so large capacitance may not be important in these applications. To minimise small reactive/ESR losses it may be preferable to use the largest capacitance as is practical in the device however (but observing any unhelpful effective inductance of the capacitor). Ceramic capacitors are preferred, due to high energy density, longer lifetimes, steady electrical performance, and lower ESR [148].

The PWM signal frequency (*f*) has an optimum value for a particular circuit. When the signal is HIGH the MOSFET will reach ON-state with delay (typically in µs) determined by the current limit of the signal generator and C_{GS}. When f is too high the MOSFET will not reach sufficient V_{GS} through the HIGH period and will not conduct optimally within the ON duration. When f is too low the circuit may not deliver a stable output, since the inductor and capacitor may become significantly discharged and cannot provide sufficient current to the load. As stated previously it becomes inefficient to operate the inductor/capacitor with significant charge/discharge cycles. The diode will also present a delay (in µs) before fully conducting [149] [150]. For these reasons, the circuit will require a PWM signal of a certain f value, depending on the PWM signal generator current limit and the four main circuit components.

3.4.3 Conventional DC-DC Converter Test Experimental Method

The D400 WT and eight-cell ES described earlier in this thesis were coupled via a DC-DC converter to investigate conventional micro WT-ES operation. Step-up topology (with and without SR) was chosen due to the voltage ranges of the WT and ES and the power available from the wind test facility, also tested with step-up/down topology for comparison. The controller unit was based on an Arduino Uno (5 V, 40 mA output), set to produce two synchronised PWM signals at 7.8 kHz and provide controller function including measurement of V and I. The converter circuit components and PWM frequency were chosen following investigation of their specific function, rating requirements and experimental testing. These were set-up to optimise power transfer efficiency (η_{Conv}) from the WT to ES in the test ranges (considering WT operation up to 12 ms^{-1}). The convertor physical circuit layout is shown in Figure 3.4.3. Experimental work to optimise the circuit and achieve maximum η_{Conv} are detailed in Appendix A3.7.

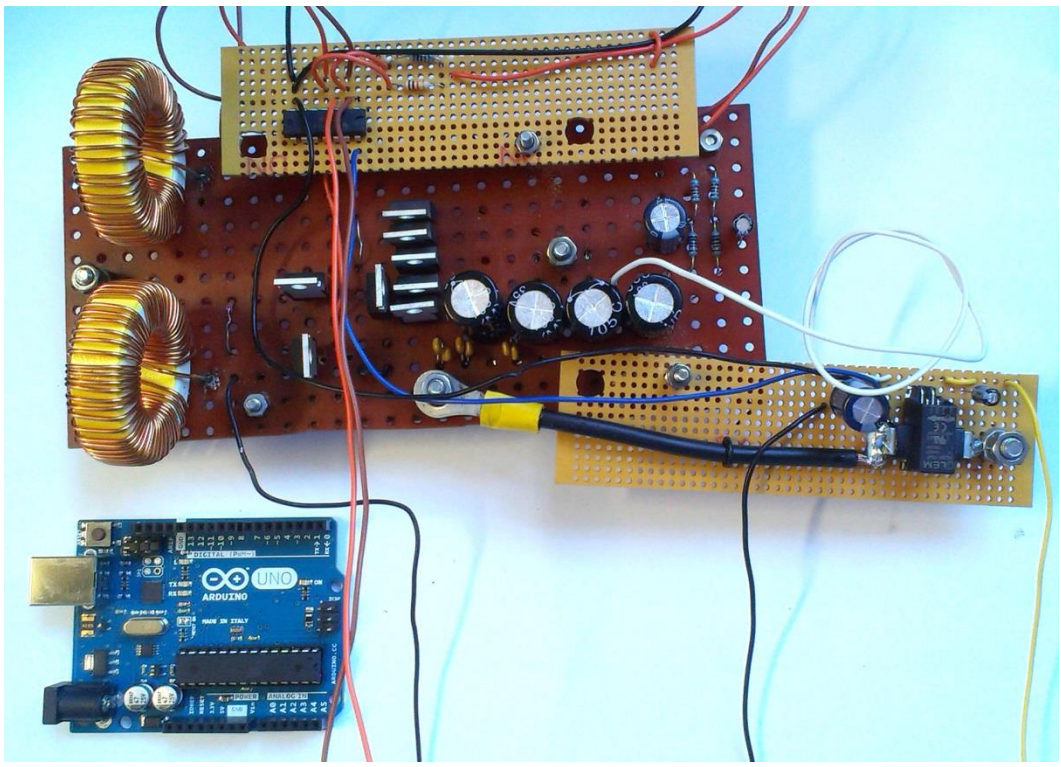

Figure 3.4.3 – DC-DC Step-up Converter Circuit

The Arduino and step-up circuit. The input and output terminals (+ve) are the two bolts to the left of the inductors and above the capacitors respectively. The WT ground bolt is situated below the capacitors (four electrolytic and six ceramic), connected to the current sensor (separate module), with a bolt on the far right to ground the ES. Five diodes are shown in the centre and three MOSFETs left of centre (switching, SR MOSFET, and one reserved for work discussed in Subchapter 3.7). Two voltage dividers for measurement on V_{in} and V_{out} are to the right of the circuit. The top module is the line driver. Additional capacitors were used for smoothing of the voltage/current measurement signals. Black wires were ground for the various components. Other wiring provided the two PWM and V/I measurement signals etc.

The Arduino Uno provided simple logic control for converter function. The analogue-to-digital (ADC) 10-bit converter has resolution of approx. 4.9 mV [151]. When reducing voltages, e.g. with a 4:1 voltage divider circuit, resolution becomes ≈ 20 mV (±10 mV) (unsuitable for certain sensors). Measurement of V_{ES} was not accurate for indication of P_{ES} for the HCS function. A current sensor (LEM HLSR 10P Hall effect sensor) was placed in the power circuit to measure I_{ES} to indicate P_{ES}. This sensor produced 2.5 V when I_{ES} = 0, increasing in steps of 80 mV A^{-1}, giving measurement accuracy ≈ 25 mA [152]. V_{In} and V_{Out} measurements involved a voltage divider circuit (40:10 kΩ). Real-time system data were monitored by PC connection to the Arduino in all testing work. Smoothing capacitors for the measurement circuits and use of code

to average several successive measurements were seen as critical to minimise error in the voltage and current measurement signals.

The Arduino demonstrated intermittent behaviour and several logic-type errors (apparent in three similar Arduino devices), discussed here to assist with further work using these devices. Intermittent behaviour was demonstrated when connecting to a new PC, or when using different USB connections on the same PC. For example, if the Arduino was initially set-up on one USB port it would then not operate on another port on the same PC. Voltage readings were occasionally inaccurate. The Arduino would often stop responding or erroneously report code errors during its verification process. It may occasionally fail to upload code, or occasionally stop functioning such as loss of pin output (particularly PWM pins) during use, making it appear unsuitable for continual operation/monitoring etc. Online support for the Uno was much more apparent than for the Leonardo (with slightly different pin assignments etc), used in later work. Arduino datasheets [151] explain several errors typical in measurements (also possible in more advanced controllers), illustrated in Figure 3.4.4. It would be advised to take these points into consideration during further experimental work using an Arduino. Absolute accuracy is comprised by all of the following errors:

- Quantisation error (ADC resolution, i.e. 4.9 mV)
- Offset error (the deviation of the first transition (0 to 1) compared to the ideal)
- Gain error (incorrect digital output per unit of voltage)
- Integral non-linearity (slight deviation of the amount of voltage variation that produces a change of value from the ADC, i.e. a change in gain error)
- Differential non-linearity (DNL, the maximum deviation of the interval between two adjacent transitions).

Arduino Uno PWM channels are 8-bit digital 5 V outputs, giving 255 units of resolution for the D value between 0-100%. In order to set-up the SR MOSFET, two PWM signals were required. A line driver circuit was used in this work to pull-up the PWM signal to suitable voltages for SR V_{GS}, discussed in Appendix A3.7.5. The PWM signal for the main switching MOSFET was set as D, and the SR MOSFET inverted such that its duty D_{SR} = 255 – D. The exact timing of the MOSFET switching had to be investigated to compensate for difference in ON- and OFF-state rise and fall times. PWM timing was adjusted to compensate for this as discussed in Appendix A3.7.5.

MPPT function for this controller was achieved via a simple HCS algorithm. The controller was set to measure I_{ES} and seek the optimum value by continual variation of D in 1.6% step size (4 increments within 8-bit/255 PWM output). The iteration frequency was set at 1 Hz.

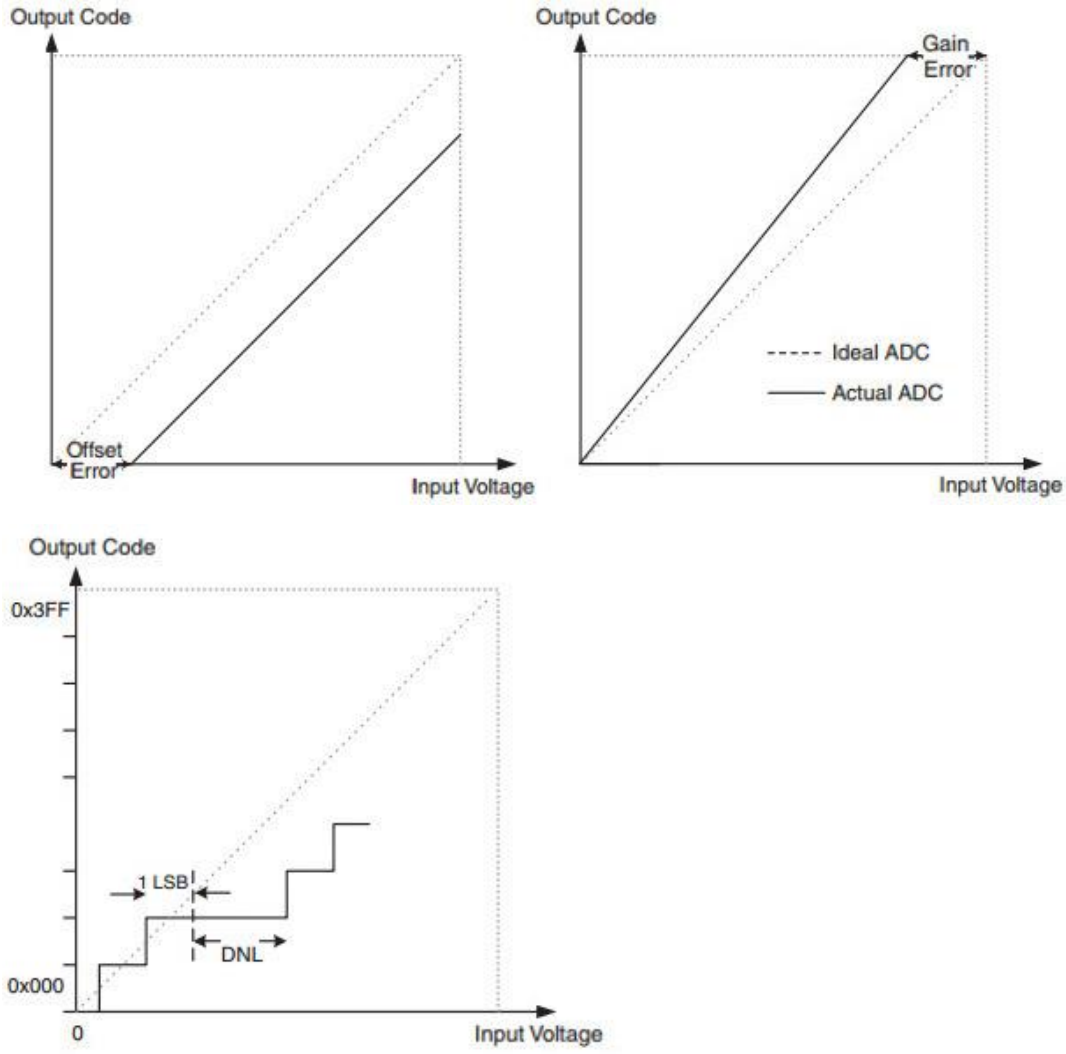

[151]

Figure 3.4.4 – Typical Measurement Error from an Arduino Controller

The digital output code (i.e. 0-1023) from a pin reading may contain error due to five factors. Four are demonstrated above with input voltage and output code data.

3.4.4 Conventional DC-DC Converter Test Experiment Results and Discussion

The DC-DC converter step-up circuit was tested with the WT and ES through a range of v (0-8 ms^{-1}). Further testing used a power supply (equivalent to 8-12 ms^{-1}). A resistive load was used to prevent damage to the ES in experimental work > 10 ms^{-1}. It is important to note that slight variation of data from test to test occurred due to natural variation of air density and measurement accuracy etc. Overall efficiency (η) of the

WT-ES system can be calculated from the enthalpy of the produced H_2 (i.e. ΔH_{Meas}, the enthalpy of the measured H_2 volume) and wind energy (i.e. $E_w = ½\rho A v_{RMC}{}^3 t$), thus

$$\eta = \frac{\Delta H_{Meas}}{E_W} \qquad \text{Eq 3.2}$$

The performance of the converter and MPPT function was however of specific interest in this work, requiring comparison of P_{ES} to the maximum power available from the WT when correctly loaded (i.e. P_{MPP} at the particular v). This is essentially comparison to an ideal converter. It was not possible to measure P_{MPP} precisely due to natural wind variation even at steady-state using a fan, or repeatable variable wind trends. Evaluation of MPPT function is therefore relative and inexact in this work. Converter efficiency, η_C, was considered in terms of the three aspects discussed in Section 3.3.4. This firstly included power transfer efficiency (η_{Conv}) previously defined (Eq 3.1). In this work the controller power (P_{Ctrl}) was provided by an external source, which would be powered by the WT in a real scenario and thus had to be considered in the efficiency calculations. Finally the performance of the MPPT function (η_{MPPT}) was compared to the ideal, calculated from pre-established ideal WT P-V data compared to the test data. Measured P_{WT} was essentially compared to the known P_{MPP}, which can be computed at steady-state (v = constant) to good accuracy, and thus η_{MPPT}, although in real wind conditions this would be challenging due to the continual/random variation of v. It is clear that η_{MPPT} would be lower during variable v compared to steady-state due to incorrect perturbations etc. Overall converter efficiency consisting of three factors was therefore calculated from the following overall expression:

$$\eta_C = \left(\frac{P_{ES}}{P_{WT}}\right)\left(\frac{P_{WT} - P_{Ctrl}}{P_{WT}}\right)\left(\frac{P_{WT}}{P_{MPP}}\right) = \frac{P_{ES}(P_{WT} - P_{Ctrl})}{P_{MPP}P_{WT}} \qquad \text{Eq 3.3}$$

Test data considering η_{Conv} are shown in Figure 3.4.5. The η_{Conv} component reached a maximum of 97.3% at $v \approx 7.3$ ms^{-1} ($D = 0$) in this data. Clearly η_{Conv} increases as $D \rightarrow 0$. When $v \approx$ 6.3-7.3 ms^{-1} the increase in η_{Conv} when $D = 0$ outweighs reduction of η_{MPPT} within this range. Therefore the controller was observed to divert to $D \approx$ 0-4% when v > 6.3 ms^{-1}, improving η_C. SR improved η_{Conv} by 1-2% in this work depending on the circuit condition. The Arduino and line driver power demand was significantly above the norm found in literature (such as ≈ 150 mW for a controller with similar function

[127]), due to inefficient power use within the Arduino and the inefficient nature of the line driver and external power supply circuit. In a sophisticated controller, P_{Ctrl} would be assumed ≈ 150 mW. This value was used for P_{Ctrl} to provide efficiency data more applicable to that expected with a state-of-the-art logic controller. MOSFET demand was tested, presenting loads of approx. 1, 9 and 25 mW at V_{GS} = 5, 15 and 25 V respectively (f = 7.8 kHz). MPPT function and η_{MPPT} were assessed at steady v. After several iterations (depending on the magnitude of change from the previous v value) the controller kept the WT above 95% of P_{MPP} (average η_{MPPT} ≈ 98%). Its performance with variable v would be poor and it was clear that variable step size and some intelligent logic would be essential to reach and maintain close to the correct D value, reducing error from rotor inertia and false positive readings etc as previously discussed. A sample of MPPT test data is shown in Figure 3.4.6. Spurious voltage readings from the Arduino are apparent in this data. V_{WT}, I_{WT} and v measurements were used to determine P_{WT}, P_{MPP} and thus η_{MPPT} as discussed previously. η_{Conv} data, P_{Ctrl} (150 mW) and η_{MPPT} (≈ 98%) therefore give the η_C trend of this power converter shown in Figure 3.4.7. η_{MPPT} approached ideal when v ≈ 7.6 ms^{-1} for this WT-ES circuit at D = 0. For this reason, η_C reaches a maximum of 95.5% at v ≈ 7.6 ms^{-1}.

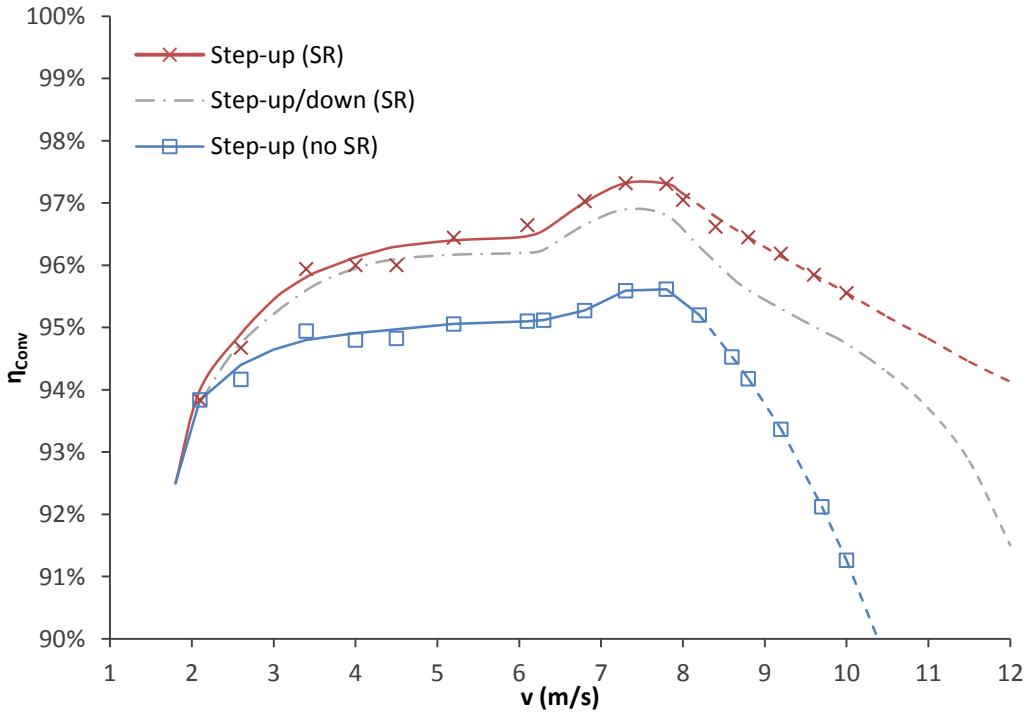

Figure 3.4.5 – DC-DC Converter Power Transfer Efficiency Test Data (η_{Conv})

Data for the step-up DC-DC converter compares η_{Conv} with/without SR and in step-up/down topology, for v = 2-12 ms^{-1}. Maximum η_{Conv} is shown at approx. 7.3 ms^{-1}.

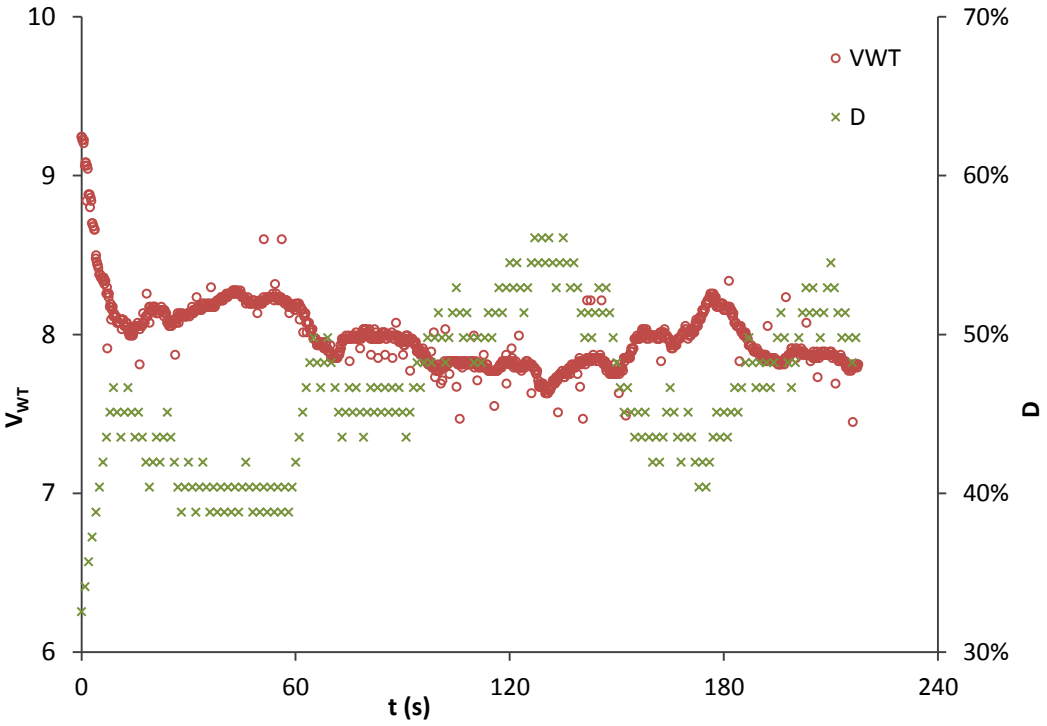

Figure 3.4.6 – Hill-Climb Search MPPT Data

A sample of wind turbine voltage and converter duty value are shown over time, at v = 3.5 ms^{-1}. Ideal V_{WT} = 8 V and ideal D = 50%. The degree of variation indicates the effectiveness of the MPPT function.

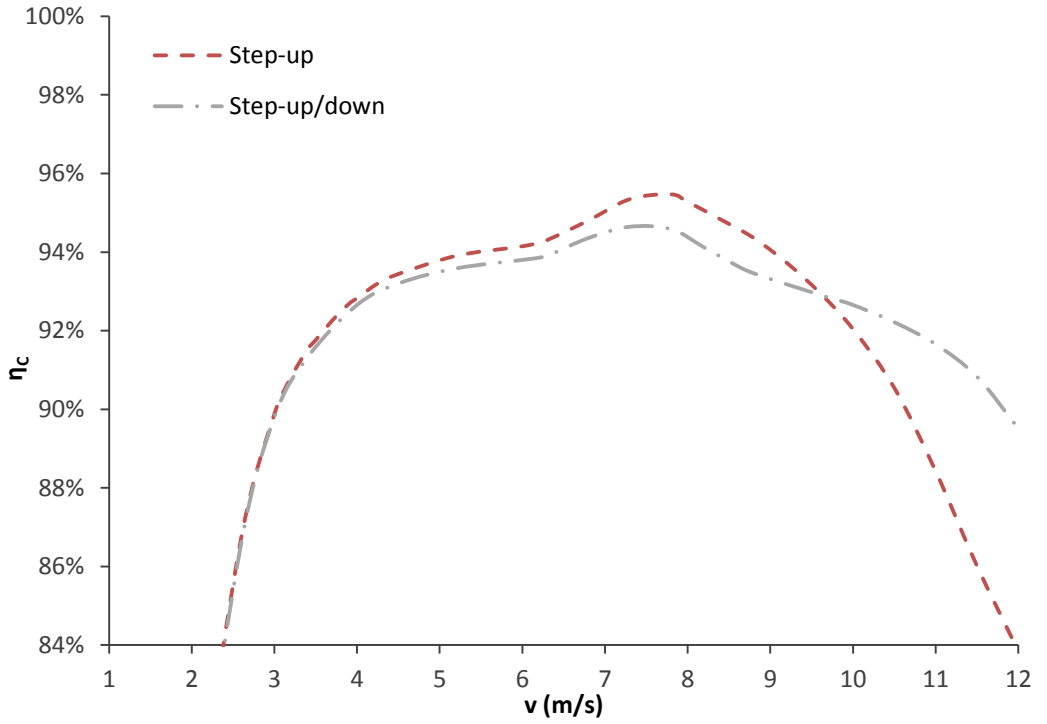

Figure 3.4.7 – DC-DC Converter Overall Efficiency Data (η_C)

The overall converter efficiency considering MPPT effectiveness is calculated from test data, showing maximum η_C = 95.5% at $v \approx$ 7.6 ms^{-1} for this system.

WT data indicates that the system cut in would occur at $v \approx 1.8$ ms^{-1} although power would be trivial in this region. Below the cut in the WT would not produce sufficient power above P_{Ctrl}. Above 12 ms^{-1} the power converter would become inefficient (particularly with only step-up function). Use of the step-up circuit rather than step-up/down appears slightly more preferable for the test conditions at reasonably low v, although the wind trends at a particular location and other parameters would have to be considered prior to final selection of topology. Step-up/down enables MPPT function when $v > 9$ ms^{-1} in this WT-ES set-up, whereas step-up would be fixed at $D = 0$ in this range, resulting in power loss. In a real scenario, a larger ES would be preferable if the WT was likely to frequently experience $v > 10$ ms^{-1}, due to the low ES rating. This and the topology selection would also depend on various other factors such as availably of initial capital and expectation of H_2 production, any other power loads on the WT etc.

3.4.5 Conventional DC-DC Converter Experiment Summary

The conventional DC-DC converter circuit with an HCS MPPT algorithm was tested in various steady-state wind conditions. Overall conversion efficiency was determined from the power transfer efficiency of the circuit (influenced by circuit/component quality, D etc), controller power demand, and MPPT algorithm effectiveness. Despite relative simplicity, reasonable efficiencies were obtained generally with η_C = 92-96% as shown in the data. The Arduino provided variable PWM and simple logic function to operate the HCS algorithm, although with limitations and inaccuracy. A more refined controller would be preferred for further work, supporting SR function at 25 V and with lower power demand etc. The converter circuit components were fine-tuned within the restraints of the equipment available to produce the highest η_{Conv} possible in the test range. The converter allowed cut-in of the WT-ES system at $v \approx 1.9$ ms^{-1}. MPPT function was tested in steady wind conditions. The HCS algorithm would need considerable improvement to maintain high efficiency in unsteady conditions (variable step size, compensation for rotor inertia and other methods as previously discussed). Further testing in variable wind conditions would be required to optimise HCS function. The controller and circuit demonstrate a very cheap, simple and reasonably efficient power converter, to enable wind-powered H_2 production, which could be scaled to operate with various micro/small WT-ES systems.

3.5 Solar-Powered Electrolysis using Direct Connection

3.5.1 Overview of Solar Electrolysis using Direct Connection

Similarities of I-V characteristics of the PV module and PEM EC tested in earlier work indicated direct connection would be feasible to create a simple solar-H_2 production system. This may permit reasonably high efficiency, equivalent to or greater than that which would be obtained using a DC-DC converter discussed in Subchapter 3.4. The performance of a micro PV-EC test set-up using the PV module and EC tested in Subchapters 2.2 and 3.2 is discussed here. This is modular and could be scaled without significant change in characteristics. The performance of this PV-EC set-up then was compared to the indicated performance of a similar set-up using a DC-DC converter. DC-DC converter performance (e.g. η_{Conv}) was taken from testing carried out in preparation for the work discussed in Sections 3.4.3-3.4.5. Direct connection is simple, requiring no controller and minimal circuitry, and is a desirable strategy for first consideration for a PV-ES system, particularly for low-cost micro/small scale systems.

Direct connection of PV to an ES has been discussed previously by various authors [142] [153-155]. It is generally considered only in grid-independent installations, since use of power converters would be essential where grid connection is involved to allow import/export of power to/from the ES/PV, and so the PV-ES system would be usually be set to operate through these power converters. The main convention for large PV-ES systems is use of DC-DC converters, and generally grid-tied (with DC-AC converters) to optimise use of the PV energy (grid export during intense irradiance etc) and also to potentially enable grid balancing using the ES. Work elsewhere reports improved overall efficiency of the PV-ES system being possible from direct connection, with lower cost per unit H_2 due to the lower system cost and higher H_2 output [153]. Similar to that discussed for the WT-ES, the overall efficiency is a measure of the H_2 production enthalpy and solar energy (E_S) incident on the area of the PV, where

$$\eta = \frac{\Delta H_{Meas}}{E_S} \qquad \text{Eq 3.4}$$

With direct connection, the electrical conversion efficiency $\eta_C \approx \eta_{MPPT}$ (= P_{ES}/P_{MPP}), since the circuit is virtually ideal excluding any essential circuitry. The key criterion for direct connection is selection of the PV and ES, ensuring that their I-V trends match.

3.5.2 Solar Electrolysis Direct Connection Experimental Method

This work used the four-cell microcrystalline PV module (0.02 m^2) described in Subchapter 3.2. One PEM EC described in Subchapter 2.2 was directly connected to the PV module. Measurement of the I-V trend during testing in variable solar irradiation conditions was carried out. Due to limitations of the range of irradiance during testing, some data was produced with PV power simulated by a DC power supply, observing the exact I-V trends of the PV module from previous testing.

3.5.3 Solar Electrolysis Direct Connection Experiment Results and Discussion

Test data for this experiment are shown in Figure 3.5.1. Data show five solar irradiances (175-940 W m^{-2}) with the PV MPP curve, EC curve, and lines representing where P_{EC} ≈ 90% of P_{MPP}. Since there is no controller, η_{MPPT} is the only concern to define η_C and is calculated from the power delivered to the EC (P_{EC}) compared to the maximum power available from the PV (P_{MPP}) at the specific irradiance value (and T_{Cell}). Data show P_{EC} remaining close to the 90% region and reaching much closer to P_{MPP} as intensity increases. The effective trend of η_{MPPT} (= η_C) is shown more clearly in Figure 3.5.2, where improvement would be possible with more optimal matching of the devices. The PV:EC ratio of 4:1 results in $V_{PV} \approx V_{MPP} - 0.25$ V. The EC is also overrated for the PV module tested here, since it can handle two times the maximum PV current. Therefore doubling the PV module (i.e. parallel connection of two) would improve the system matching. With a scaled-up system of identical PV (doubled) and ES of several identical cells as tested here, a ratio of 3.8 PV:EC would result in more efficient operation, shown in the data in Figure 3.5.2. This ratio could be achieved with a PV module of 42 cells coupled to an ES of 11 cells for example. Based on this and performance of the DC-DC converter tested in Subchapter 3.4, it is shown that direct connection strategies are likely to be superior in terms of efficiency and specifically cost per unit H_2. Different PV/ES equipment would require slightly different ratios, also depending on irradiance trends. Circuit losses would also need consideration in a real scenario for correct selection of equipment and ratios. It has been discussed in Subchapter 3.3 that WTs presently generate slightly cheaper electrical energy than PV. For this reason and due to resources, further work involving PV-ES systems was not carried out. Observing ΔH_{Meas} and E_S (and PV area), or η_C and efficiencies of the PV and EC, the overall solar-H_2 conversion efficiency in this work is indicated as $\eta \approx$ 12-13%.

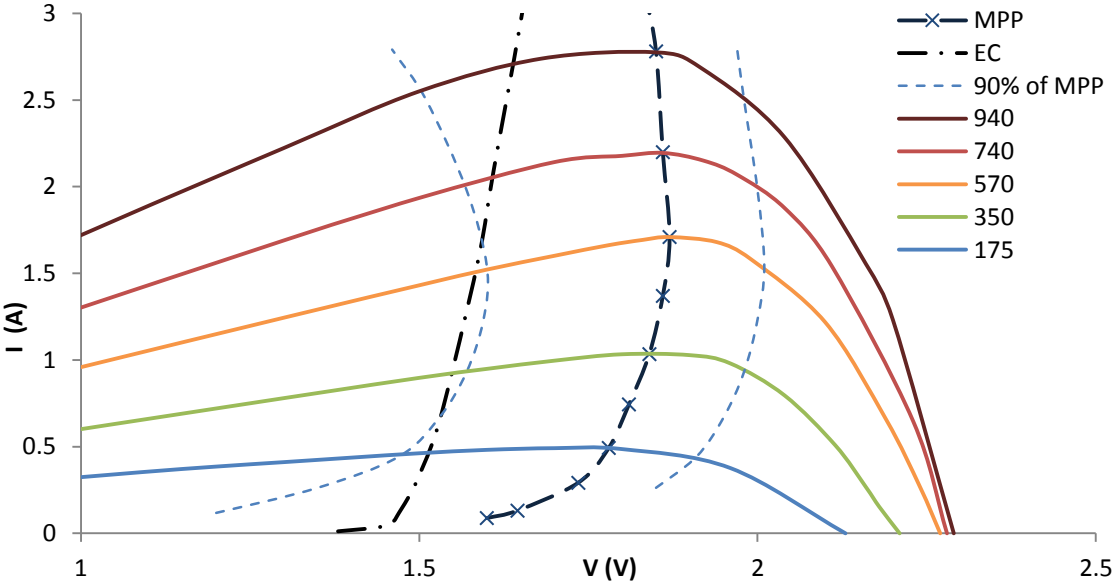

Figure 3.5.1 – PV-EC Direct Connection Test Data (I-V)

PV I-V and MPP trends for various irradiance intensities are shown, compared to the EC I-V curve, indicating direct connection feasibility. 90% of MPP lines are overlaid.

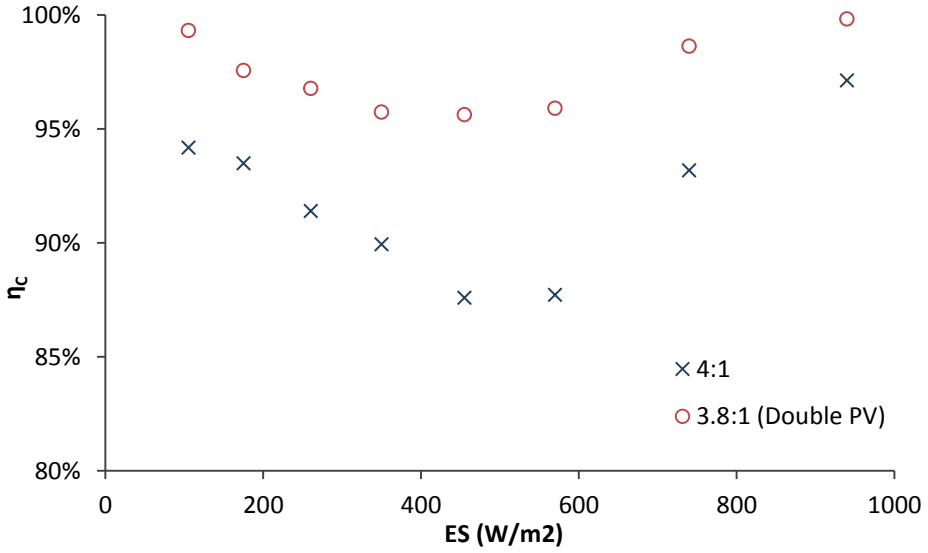

Figure 3.5.2 – PV-EC Direct Connection Overall Power Conversion Efficiency Data (η_C)

The direct connection circuit efficiency, η_C (essentially equivalent to η_{MPPT}), is shown compared to an optimised direct connection system of doubled PV and 3.8:1 ratio.

3.5.4 Solar Electrolysis Direct Connection Experiment Summary

Direct connection of PV to an ES for a grid-independent system is clearly feasible with high circuit efficiency (e.g. > 96%) when scaled correctly, shown here and elsewhere (e.g. [142]) to be cheaper and more efficient than an equivalent circuit using a DC-DC converter. This demonstrates a simple, robust and relatively efficient method for micro/small solar-H_2 production, where $\eta \approx$ 12-13%.

3.6 Wind-Powered Electrolysis using a Cell Selection Power Converter

3.6.1 Overview of Cell Selection Power Converter

A novel circuit to connect a micro WT to an ES and provide simple, cheap and efficient power control and MPPT function is presented here. Through investigation of WT and EC I-V trends (such as that of the D400 etc), it was noticed that voltage control of the D400 was a simple underlying method for MPPT. The D400 demonstrated regions of approx. 1-2 V width at constant v where there was no significant difference of P_{WT}, where V_{WT} could be e.g. 15-17 V at v = 6.4 ms^{-1} and the WT would remain practically at its MPP. For this reason it was identified that the number of active ECs (within an ES) loaded to the WT could provide a simple strategy for MPPT and optimised WT operation, replacing a DC-DC converter circuit. This is somewhat analogous to direct connection as previously discussed for PV. Cell selection in this manner was not considered for PV-ES operation due to limited range of V_{MPP} evident for PV modules. There is no significant apparent issue with operating a reduced number of cells within an ES. This would not be possible for a battery for example due to cell charge states.

This power control strategy based on cell number (n) variation was investigated using the D400 WT and eight-cell alkaline ES. The ES was assembled so that individual cells were electrically accessible. A MOSFET switching circuit was set-up to allow cell selection (in larger systems this could be replicated with relays for example). It was determined that bypassing individual cells with MOSFETs was the most practical arrangement for achieving variable n, rather than trying to electrically remove cells from the circuit. MPPT function was achieved by selecting a certain n to provide the most optimal configuration at the particular v value. Selection of n defines a narrow voltage range for the WT, due to the steep I-V trend of the ES. Control of this required test data from the WT and ES, which was available from previous testing. Data of this sort was coded in the form of a table of upper and lower I_{ES} limits assigned to each n value. When above or below this range, the controller would change n accordingly. When operating, a reading of I_{ES} (and n) would then allow the controller to determine the optimal n for the instantaneous condition. In the higher v ranges the full eight cells (n = 8) would become directly connected to the WT. In general, a relatively high n would be preferred in each case due to η_{ES} being relative to the active surface area and number of cells [55] [68], taken into account when defining the upper

and lower limits of I_{ES}. This MPPT function would require test data (not always available or desirable for systems) requiring a test procedure to establish the limits of I_{ES} for each n value. For an eight-cell ES this would be relatively simple and limits could be estimated/extrapolated once the first few limits had been established (which would be very convenient when testing in a real wind scenario). The circuit for this converter is shown in Figure 3.6.1, and basic logic function of the controller in Figure 3.6.2.

The ultimate function of this circuit was to produce maximum H_2 from the WT power and at the lowest cost. This was expected to be possible due to the simple and efficient circuit and an effective MPPT method, potentially keeping the overall system as close as possible to maximum efficiency. The overall converter efficiency was calculated in a similar method to the previous work (Eq 3.3). η_{Conv} is practically ideal during normal operation and this term was not considered directly as before. The controller was powered by an external source for convenience as in previous tests. Now however the ES requires consideration since η_{ES} was affected by n. This was factored into η_C when $n < 8$ with a term to consider the relative η_{ES} value, $\eta_{ES\text{-}R}$. The η_C value was now effectively based on η_{MPPT}, P_{Ctrl}, and $\eta_{ES\text{-}R}$, where

$$\eta_C = \left(\frac{P_{WT}}{P_{MPP}}\right)\left(\frac{P_{WT} - P_{Ctrl}}{P_{WT}}\right)(\eta_{ES-R}) = \eta_{ES-R}\frac{(P_{WT} - P_{Ctrl})}{P_{MPP}} \qquad \text{Eq 3.5}$$

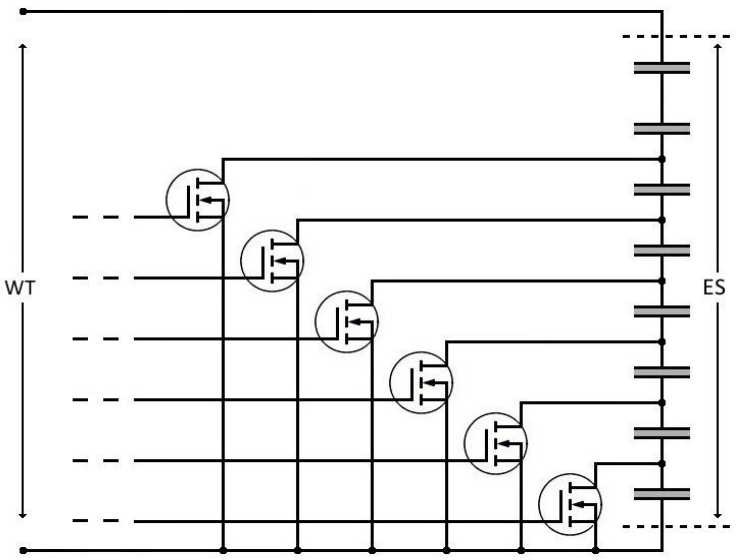

Figure 3.6.1 – Basic Circuit Diagram of Cell Selection Power Converter
The circuit relies on a MOSFET bank to select the number of ES active cells (n), providing variable loading and MPPT function. Dashed lines (MOSFET gates) are connected to individual controller unit output pins (e.g. an Arduino in this work).

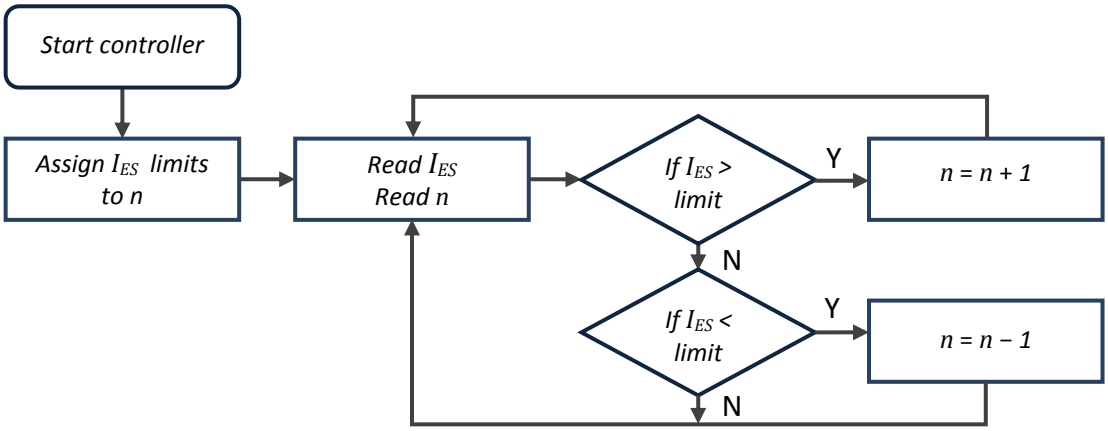

Figure 3.6.2 – Basic Logic Function of Cell Selection Converter

The logic function is relatively simple, where the controller checks n and I_{ES}, compares I_{ES} to limits (predetermined for the n value), and varies the n value accordingly.

3.6.2 Cell Selection Converter Experimental Method

The cell selection power converter circuit was set-up with the D400 micro WT and eight-cell alkaline ES, demonstrating a simple alternative to the conventional DC-DC converter/HCS MPPT function. Similar to the DC-DC converter testing, pre-inspection of the WT and ES ratings, I-V ratings curves/trends were essential in order to set-up the system correctly. The general function of the logic controller was to:

- Monitor the instantaneous I_{ES} and n value
- Compare to lookup data for the specific n configuration
- Select the n value determined by lookup data, outputting to the relevant MOSFET

As shown in Figure 3.6.1, the MOSFETs provided bypass circuits, operated individually by the controller (dashed lines). Cell selection was performed by bypassing a certain number of cells via a MOSFET. One MOSFET would be required for each assigned n value, excluding the maximum, and in this WT-ES setup a MOSFET was not used for the first cell (operation of one cell was not practical). Six MOSFTS were therefore used, allowing selection of two to eight active cells. An Arduino Leonardo was used to provide MOSFET control and MPPT lookup function, with a separate 5 V output for each MOSFET to enable individual switching. A data table of I_{ES} limits for each n value was programmed into the controller. The algorithm first measured I_{ES} and also determined the n value. It then computed 'If' statements to identify the upper and lower I_{ES} limits for the particular n value active, and whether I_{ES} was below, within, or above these limits. If below, the controller would reduce n by 1 (switching on the

corresponding MOSFET, n – 1). Likewise, if above, the controller would increase n by 1. If within the limits the algorithm would restart after a small delay. After any change of n, the controller would delay for several seconds before restating the algorithm, to enable the WT to settle to its new load condition.

There was concern with sudden switching of ECs in and out of the WT load circuit, which could cause mechanical or generator damage over time. This issue was suppressed using a resistor-capacitor (RC) circuit to slope V_{GS}, enabling the MOSFET to reach ON- or OFF-state gradually (over 100 ms, or longer). Test data for I_{DS} and V_{GS} trends over time for the MOSFET used in this work with variable RC circuits are shown in Appendix A3.8. From this data it was clear that the delay with reaching V_{GS} thresholds for MOSFET switching (i.e. V_{GS} > 2.4 V to reach ON-state) would not allow optimal MPPT function. Analogue/variable outputs were not available from the Arduino, so the RC circuit was modified with use of pedestal voltages via pull-up/pull-down resistors to keep the OFF- and ON-state V_{GS} values very close to the threshold. This was set to V_{GS} = 1.4 or 3.4 V for the particular MOSFET used in this work. This meant that when the n value was changed, the ON-state of the appropriate MOSFET would start almost immediately, reaching full ON-state within 0.3 seconds, thus allowing the WT MPPT control to act quickly but with the RC circuit able to prevent excessive sudden load changes. Without the voltage pedestal the RC circuit would otherwise cause significant delays before the MOSFETs would start to change state (> 0.5 s), with less effective MPPT function. Example data for the pedestal voltage testing is shown in Figure 3.6.3, using a 33 kΩ, 10 µF RC circuit (V_{GS} and I_{DS} are linked as shown previously in Figure 3.4.1 and in Appendix A3.8). The concept of variable cell number and regular switching of n appear to have no negative effects or hindrance on the integrity of a basic ES.

Higher R and lower C were preferred in the RC circuit to minimise charge drawn from the controller. It was also important that the MOSFET entering OFF-state took slightly longer than the one entering ON-state. There must be one MOSFET active to avoid open circuit condition, since entering open circuit and then sudden loading would be damaging to the WT generator and rectifier. This was achieved within the data in Figure 3.6.3 by virtue of the chosen pedestal levels. The physical circuit used for this power converter is shown in Figure 3.6.4.

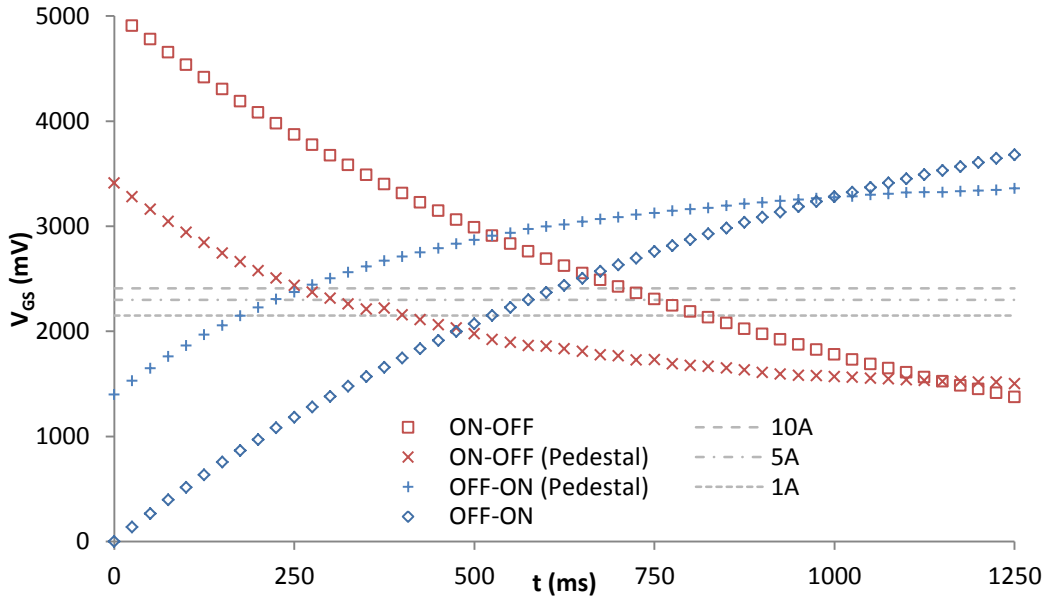

Figure 3.6.3 – MOSFET Gate-Source Voltage Testing with Pedestal Voltage

Data compares normal RC-circuit MOSFET operation (V_{GS} = 0-5 V) to a voltage pedestal circuit (V_{GS} = 1.4-3.4 V). With the latter, switching is gradual but with less time delay. V_{GS} levels at which permitted I_{DS} reaches 1, 5 and 10 A are shown.

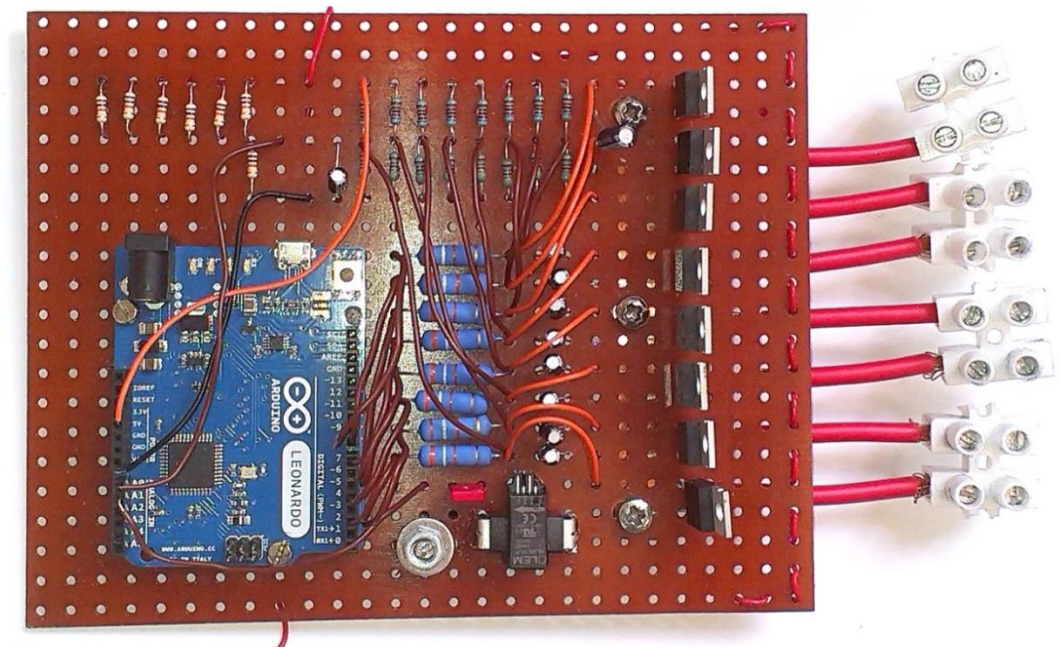

Figure 3.6.4 – Cell Selection Converter Circuit

The resistors to the top left formed a voltage divider for measurement of $\boldsymbol{V_{WT}}$. The 16 resistors above centre formed the voltage pedestal circuit (requiring a 5 V supply from the Arduino). The RC circuit was in the centre. Eight MOSFETs were situated to the right providing connection for up to eight cells. The current sensor was situated to the bottom of the circuit image, next to the earth bolt. The MOSFET source pins were soldered to a thick copper strip (on underside) running to the current sensor. The WT was directly connected to the ES as previously shown in Figure 3.6.1.

P_{Ctrl} would be slightly reduced with this controller since it would not be operating two PWM outputs. Cell selection would occur within a minimum of a few seconds and MOSFET power demand would therefore be much lower compared to use within a DC-DC converter. Use of lower quality MOSFETs than in the previous work would be possible with this circuit due to the more favourable operating conditions (e.g. no high-frequency switching, low V_{DS} etc), therefore offering some simple practical advantages.

The WT P-v trends were first investigated to determine the nature of the cell selection and to set lookup data for MPPT function. This initial test data is shown in Figure 3.6.5, showing η_{MPPT} > 95% in the test range up to 10.7 ms^{-1}. Switching to a higher n at slight expense of η_{MPPT} was favourable due to larger relative increase in η_{ES} available at the higher n, (i.e. higher $\eta_{ES\text{-}R}$) therefore allowing higher η_C. The relative factor $\eta_{ES\text{-}R}$ was determined from investigation of the ES, shown in Figure 3.6.6, as a function of v for the D400 WT. Adjustment to the I_{ES} limits was then made favouring higher n as implied from test data, to maximise η_C. For other WT-ES systems this convertor could be scaled accordingly, to the point where n becomes very high and impractical etc.

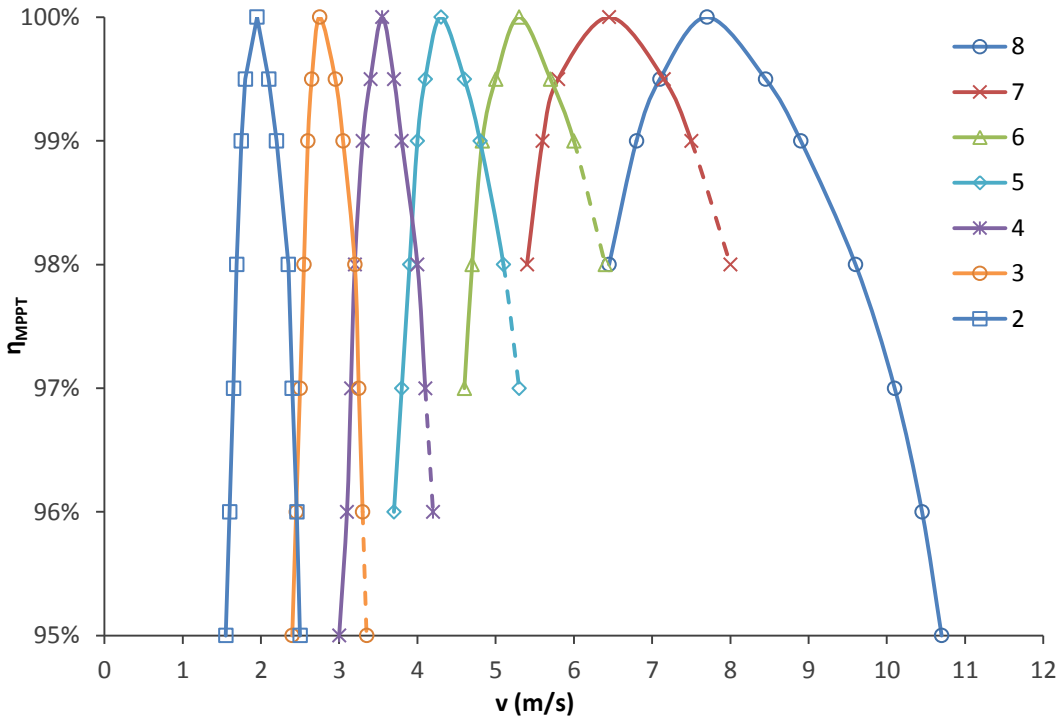

Figure 3.6.5 – Wind Turbine Maximum Power Point Tracking via Cell Selection
Performance of the D400 (η_{MPPT}) loaded with 2-8 cells is shown, for v = 1.5-10.7 ms^{-1}. Dashed lines show where the higher n value would in fact be selected to maximise η_C (due to the relative gain of $\eta_{ES\text{-}R}$ being greater than the loss of η_{MPPT}).

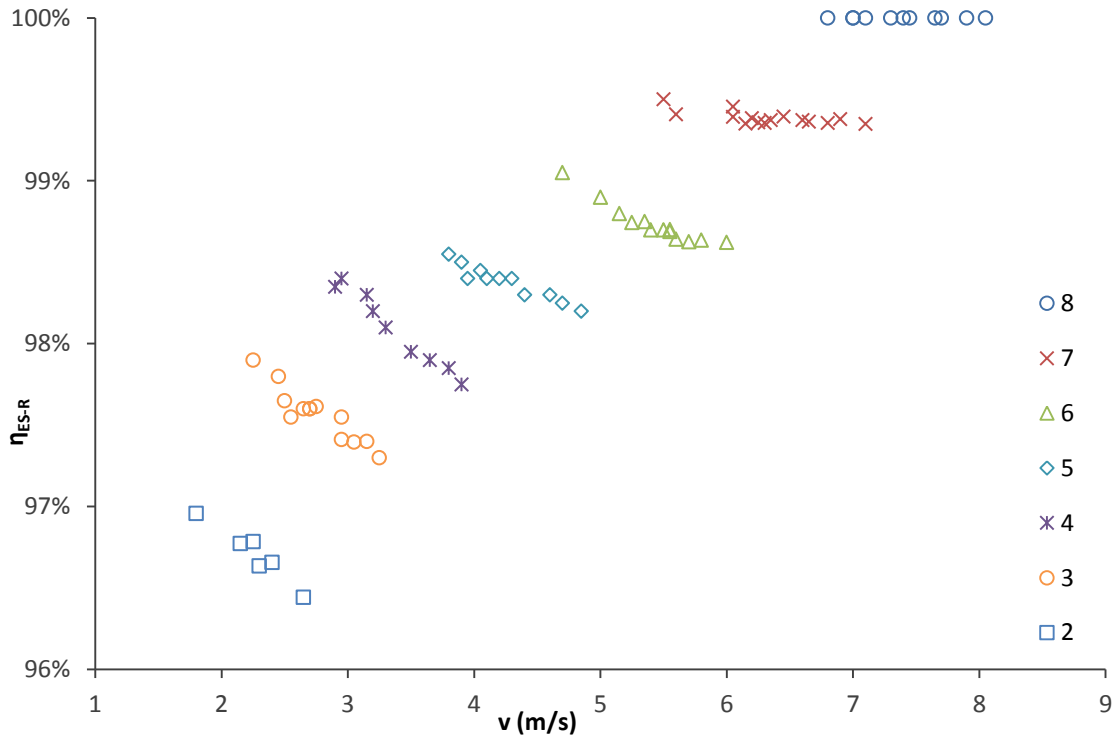

Figure 3.6.6 – Relative Electrolyser Efficiency with Reduced Cell Number
The relative ES efficiency ($\eta_{ES\text{-}R}$) trends with varying n are shown for a sample of test data, by wind velocity. This data was used to define lookup table limits, considering relative trends of $\eta_{ES\text{-}R}$ and η_{MPPT} to assist with finding maximum η_C.

3.6.3 Cell Selection Converter Experiment Results and Discussion

The cell selection controller was tested in similar conditions to the conventional DC-DC power converter. As a method for MPPT, cell selection kept the WT at η_{MPPT} > 98% when v > 4.7 ms^{-1} to above the WT test limits. MPPT function became ideal at approx. 7.7 ms^{-1}. From v ≈ 4.7-9.6 ms^{-1}, η_{MPPT} averaged > 99%, which was superior to the HCS algorithm. Test data used to determine MPPT function is shown in Figure 3.6.7.

Setting I_{ES} limits for the lookup table was relatively simple and could be done accurately with sample data for the WT and ES. The MPPT function of this controller was managed somewhat intrinsically by the ES load, particularly when n = 8 due to similarities with the WT at MPP and ES I-V trends. MPPT function was very effective for this reason. Although this controller was tested in relatively slowly changing v, it was clear that it could maintain effective MPPT function in variable conditions.

The algorithm was further enhanced with additional routines, such as use of delays, an 'over limit' coefficient, and ability to change n by more than one increment following a single measurement (such as following sudden change in v or power-on etc). In the

case where I_{ES} was measured beyond its limit, the controller would delay one second and measure I_{ES} again. If I_{ES} remained beyond the limit the controller would then vary the n value appropriately. If in the first measurement I_{ES} was over the limit by the coefficient, the delay and additional measurement would be bypassed and n would change immediately (by several increments in the case of the initial measurement following power-on). These routines would allow n to vary more quickly in very variable conditions, depending on the pre-set delay/coefficient etc, but would also be less prone to constant variation during slightly variable conditions or small changes in v. Very frequent reading of I_{ES} (e.g. 200 ms) allowed the controller to observe trends and intelligently influence any change of n. Further work would be required to optimise delays/coefficients and other logic functions for variable wind conditions.

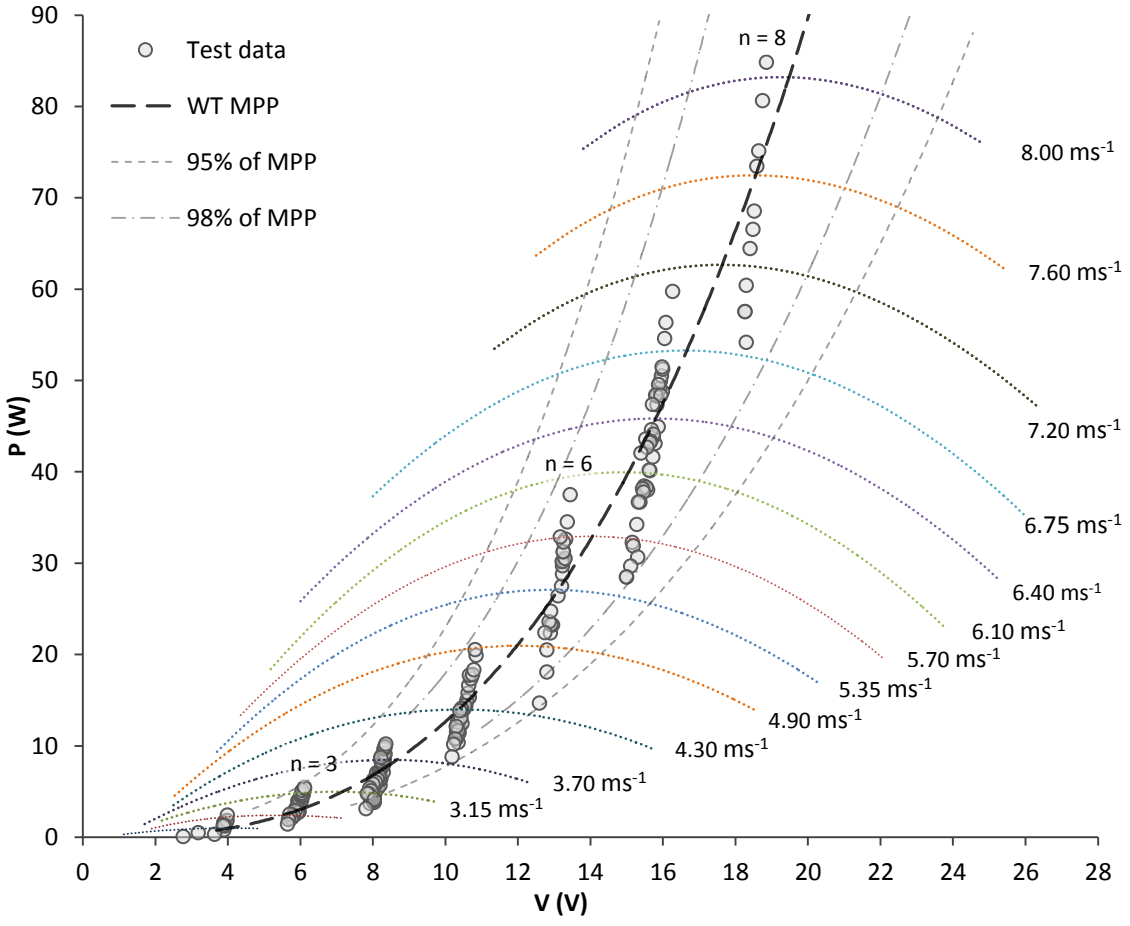

Figure 3.6.7 – Cell Selection Converter Test Data (*P-V*)

Power-voltage test data for this converter circuit, using the D400 WT and ES with variable n, shows η_{MPPT} is kept > 98% in the higher wind velocity ranges (i.e. > 4.7 ms^{-1}). This is superior to the HCS algorithm tested for the conventional DC-DC converter.

A simple mathematical function was also investigated to allow setting of I_{ES} limits with input of a small amount of test data. This would require some further work to determine its effectiveness. In principle this would allow setting of limits based on a second order I-V trend with two or three coefficients. An intelligent MPPT function to operate without initial lookup data could also be investigated. This could for example operate for a short duration in a mode similar to HCS, by variation of n, to hunt for the MPP and then store optimal I_{ES} limits for each n value into a table. Thus, initial lookup data is not essential for this converter.

Data for the overall power converter performance efficiency is shown in Figure 3.6.8, compared to earlier work with the conventional DC-DC converter with HCS.

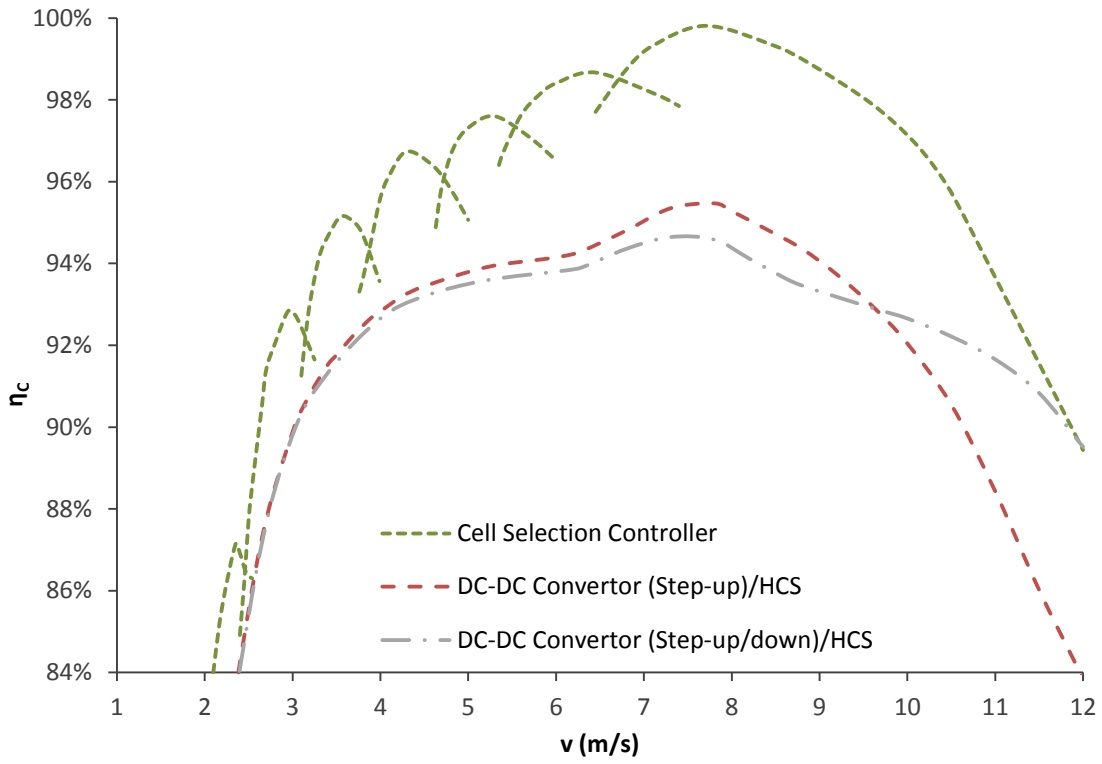

Figure 3.6.8 – Cell Selection Overall Converter Efficiency Data (η_C)

Test data for the novel cell selection converter overall efficiency, η_C, is quite variable due to the cell selection function. Data indicates significant superiority compared to the conventional converter performance in the test ranges of v = 2-12 ms^{-1}.

Some issues were identified with this circuit in its basic form. Firstly, two of the cells would always be active and may be prone to more wear and earlier failure. Depending on wind conditions, the distribution of cell use would vary and this may not be of concern. When using only two or three cells, I_{ES} would be very low and wear may not

be an issue. However, the cells could be manually repositioned following occasional servicing of the ES, allowing sharing of the additional susceptibility to unbalanced cell usage/wear. The circuit could also be modified to allow reverse cell selection, starting at the other end of the ES and progressing in the opposite direction, i.e. inverting the distribution of use. Additional MOSFETs, or simply an interchangeable module, could be used to achieve this such as the modified circuit shown in Figure 3.6.9. For example the controller could switch from one bank of MOSFETs to the other over set periods of time, or the module could be manually changed periodically. The second MOSFET bank would require higher V_{GS}, due to the source pin positions in the circuit at higher potential than circuit ground (this could be achieved with various techniques such as a higher output voltage from the controller). Alternatively this issue could simply be ignored accepting that certain cells may be more susceptible to wear.

This circuit would suit alkaline or PEM cells. It may be of significant benefit to an alkaline ES since it would allow operation at lower P_{ES} (lower v), since there would be a much reduced lower power limit (originating from the 20% lower limit to I_{ES} applying to only one cell rather than eight). Use of PGM/PEM cells would result in smaller voltage steps and may allow more precise MPPT function, requiring further investigation. This circuit would be more suited to micro scale due to the high voltages (e.g. 240 V) evident with larger WTs, involving large n values that may not be practical.

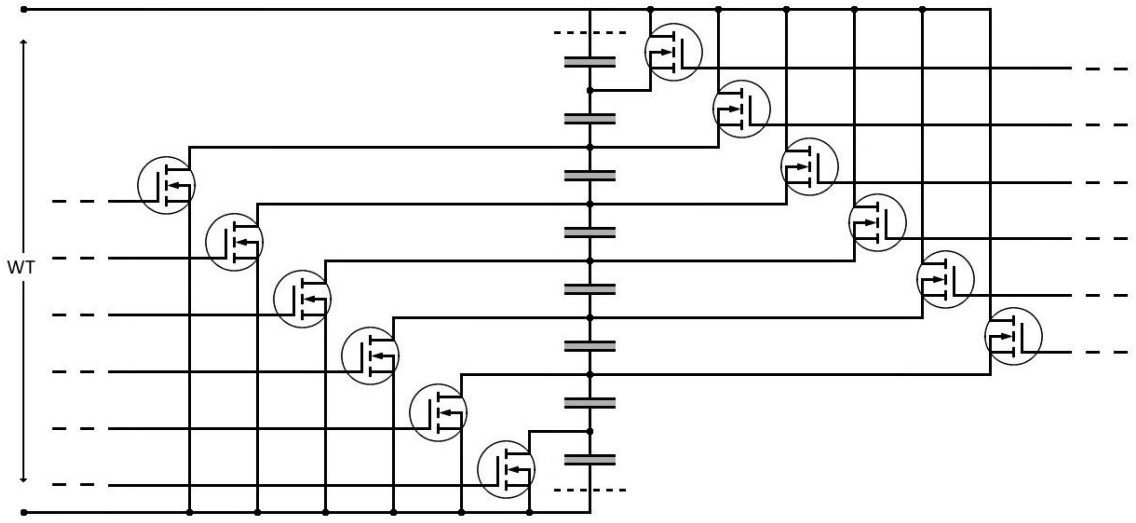

Figure 3.6.9 – Modified Cell Selection Circuit (Additional MOSFET Bank)
An example strategy is shown using additional MOSFET positions to reverse cell selection order, to limit premature wear on certain cells.

3.6.4 Cell Selection Converter Experiment Summary

Novel, cheap, simple and robust power control for micro WT-ES coupling, analogous to direct connection, was demonstrated with the cell selection controller. This had minimal circuit loss compared to conventional switched-mode DC-DC power conversion. The aim of this circuit and controller was to achieve maximum efficiency and minimise H_2 production cost. Similar to the previous work it was more practical to test the effective overall efficiency of the controller (with precise measurement of V and I, rather than the overall system based on inexact measurement of v and H_2 volume etc), which could then be compared to the DC-DC converter testing. The power conversion efficiency and MPPT function of this controller were both superior overall to the conventional DC-DC power converter with HCS in the test range. Efficiency trends were quite complex with this device due to the variable n and $\eta_{ES\text{-}R}$. The circuit was virtually ideal with only one MOSFET as a series component when n < 8. When n = 8 the circuit was direct connection, achieving almost ideal overall controller operation when $v \approx 7.8$ ms^{-1} in this work due to exact matching of WT output at P_{MPP} to the ES. MPPT required a lookup table from test data (fairly simple for an eight cell ES), allowing superior MPPT performance to that shown from HCS. Accurate data for the overall system would be preferable for optimal MPPT function.

3.7 Wind-Powered Electrolysis using a Hybrid DC-DC Converter

3.7.1 Overview of Hybrid DC-DC Power Converter

The benefits of direct connection and a lookup algorithm evident from the cell selection controller were further considered for modifications to a DC-DC converter. These two techniques were used to build another novel power converter circuit for enhanced WT-ES efficiency, maintaining some of the benefits of direct connection and the convention of DC-DC converters, offering an option also suited to higher voltage WTs than only micro scale.

From the DC-DC converter testing it was clear that when a certain point was reached where the required step-up magnitude was small, the losses from the step-up action became greater than the loss from not matching the MPP, since reduced D values improved η_{Conv} (ideally D = 0). For this reason the controller would benefit from diverting to D = 0 at a lower v than principally indicated from only the WT/ES I-V data

trends, which was demonstrated in the initial DC-DC converter testing in Subchapter 3.4. In the case of the DC-DC controller with HCS, this would require coding to disable the HCS function and maintain D = 0 while I_{ES} was above a threshold, or alternatively when D < 10% it could divert to D = 0 for a certain duration and continue to monitor I_{ES} (while above a threshold) for example. If the I_{ES} value fell below the threshold the HCS function could restart. The threshold in this case would occur at approx. 6.4 ms^{-1} by observation of the data in Figure 3.4.6. In this scenario the benefits of direct connection could then be gained if the DC-DC converter circuit incorporated a MOSFET to form a direct connection between the WT and ES (when $D \rightarrow 0$). The MOSFET would be activated as required by a separate output pin from the controller to provide a much lower ESR pathway eliminating the loss of the converter inductor in suitable ranges of v. Due to the improved η_{Conv} this could be activated at a slightly lower v than indicated in the earlier DC-DC converter testing (e.g. 6.3 ms^{-1}) and still have positive effects on overall efficiency. This direct connection MOSFET was one addition to the hybrid DC-DC converter considered to improve η_{Conv} and η_C. Clearly the simple 'inverting' type step-up/down topology would not accommodate this MOSFET.

A further possible improvement evident from earlier work would be to use another cell selection strategy, to reduce the D value. The ES could be split into two separate units, using a heavy duty MOSFET to connect them (in series), having very little effect on the ES performance. In the lower v ranges, an additional two MOSFETs could be used to connect the two ES units in parallel. The modified ES would halve the effective V_{ES} and allow considerable reduction in D in those ranges (with increased η_{Conv}). This would also present a second range of v for use of the direct connection MOSFET (i.e. when $V_{MPP} \approx ½V_{ES}$). The hybrid circuit incorporating these modifications is shown in Figure 3.7.1. Insignificant additional loss would be added to the ES part of the circuit as a result of these modifications, but reasonable gains in η_{Conv} would be possible (η_{MPPT} would not be significantly affected by these topology modifications). For improved MPPT function, a lookup algorithm was programmed into the controller observing data from previous testing. Lookup data values were created by initial mapping of I_{ES} for varying v and D, obtaining the mathematical trend of MPP, i.e. D_{MPP} for measured I_{ES} values. Alternatively the D_{MPP}-I_{ES} trend could be mapped with a lookup table (where the D_{MPP} value in steps of 5% for example could be assigned to I_{ES} bands).

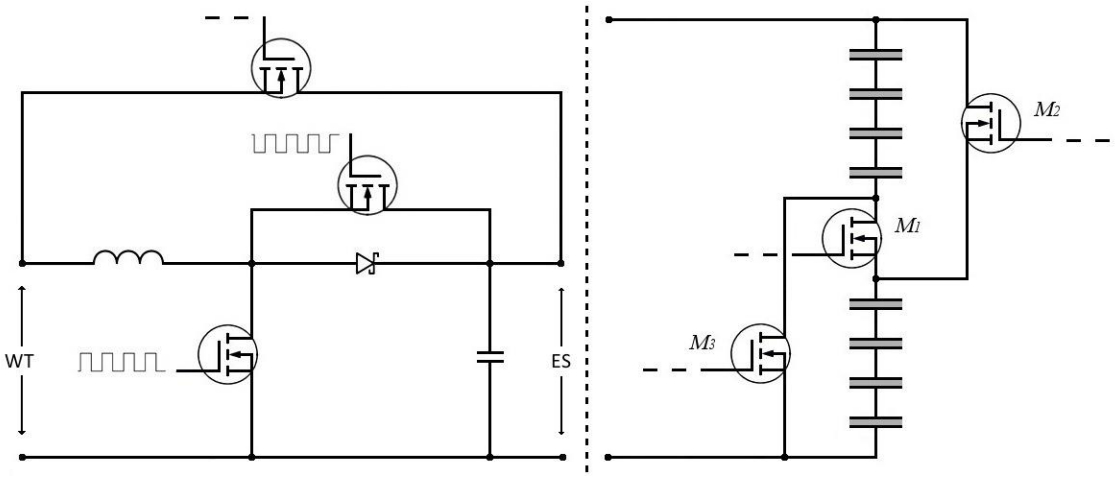

Figure 3.7.1 – Hybrid DC-DC Converter Circuit
This circuit features a direct connection MOSFET (top) and variable ES. Three MOSFETs (M_1, M_2, M_3) permit selection of eight series cells, or two parallel sets of four in series.

This novel converter therefore consists of a conventional DC-DC converter circuit (step-up) with the addition of a direct connection MOSFET in parallel with the inductor/diode/synchronous MOSFET used in two v ranges, a dual ES selection configuration and lookup MPPT function. These modifications were expected to allow improved η_{Conv} and more effective MPPT function (improved η_{MPPT}) during variable v conditions. Overall power conversion efficiency (η_C) was calculated in the same method as previously discussed for the DC-DC converter, allowing comparison to the previous DC-DC converter and cell selection performance.

3.7.2 Hybrid DC-DC Converter Experimental Method

The D400 WT was coupled to the hybrid DC-DC converter and modified ES circuit (Figure 3.7.1) for testing at various steady-state and some changing v values. The MPPT algorithm was set-up using a sample of initial test data. This and the general function of the algorithm are shown in Figures 3.7.2-3.7.3. From the data, when I_{ES} < 2.2 A an empirical trend expressed as D_{MPP} = -0.95 $I_{ES}^{-0.70}$ + 0.52 I_{ES} + 0.83 was observed. When I_{ES} > 2.2 A or if I_{ES} = 0 A, D_{MPP} reverted to zero for this set-up. The controller therefore dynamically computes D_{MPP} from measurement of I_{ES} and progresses towards the MPP. The D value cannot necessarily move by the exact increment anticipated due to the fact that I_{ES} will vary as D is varied, and thus D_{MPP} will vary. The controller used a suitable increment fraction to avoid error in this work. For example, after a measurement of I_{ES}, if D_0 < D_{MPP} then D_1 should progress towards D_{MPP} by a factor of 0.9 (i.e. D_1 = 0.1 D_0 + 0.9 D_{MPP}), where D_0 and D_1 are the zeroth and

first iterations. If $D_0 > D_{MPP}$ then D_1 should progress towards D_{MPP} by a factor of 1.0 (i.e. $D_1 = D_{MPP}$). Typically D_1 became very close to D_{MPP} and $D_2 \approx D_{MPP}$.

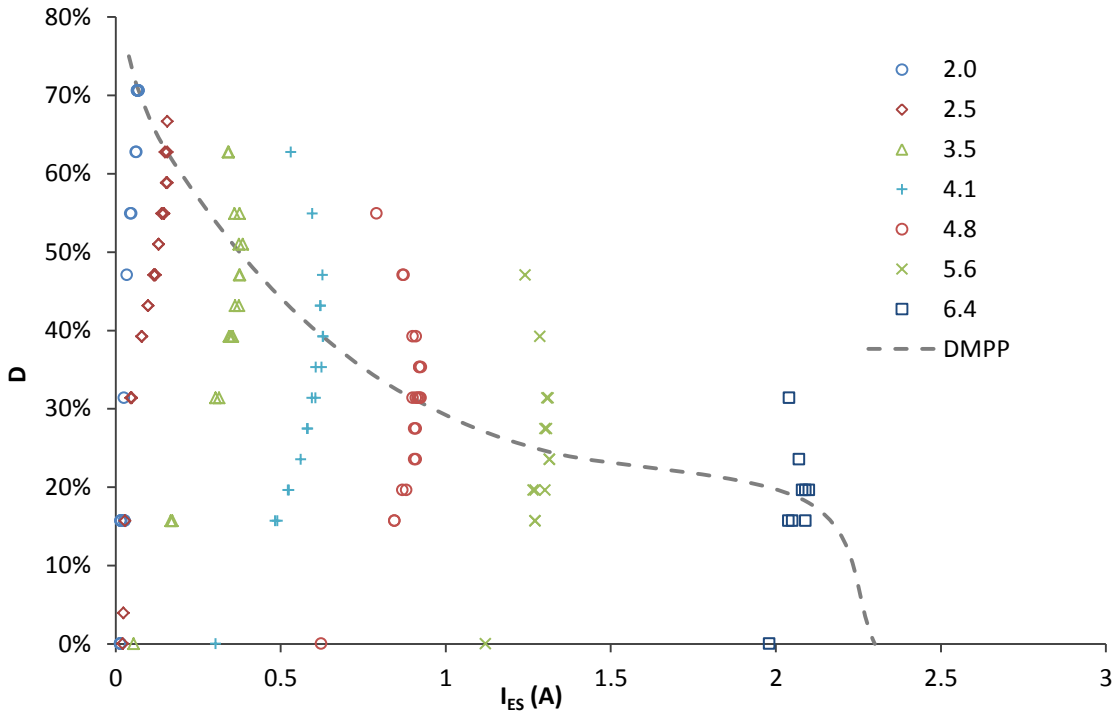

Figure 3.7.2 – Hybrid DC-DC Converter Data (D-I_{ES} and D_{MMP})
Test data from v = 2.0-6.4 ms^{-1} show the trend of I_{ES} with changes of D. The ideal D trend (D_{MPP}) is overlaid.

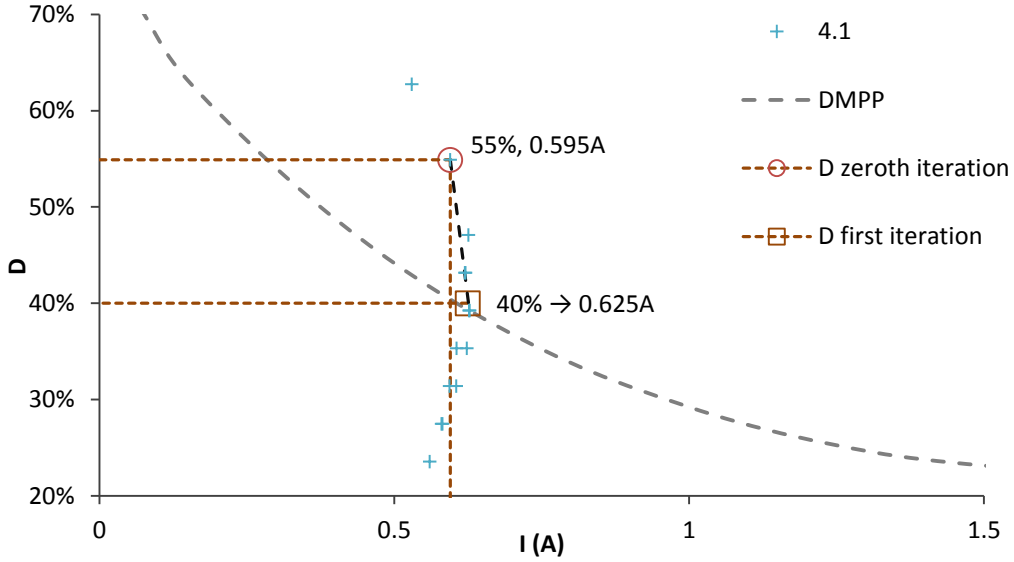

Figure 3.7.3 – Hybrid DC-DC Converter MPPT Function Example
D moves towards calculated D_{MPP} by a certain fraction, accounting for change in I_{ES} induced. After the first iteration, D becomes very close to D_{MPP}, as shown.

3.7.3 Hybrid DC-DC Converter Experiment Results and Discussion

Test data is shown in Figure 3.7.4 for η_{Conv} compared to the conventional DC-DC converter. A small I^2R loss was apparent in the data as a result of two series MOSFETs in the circuit. Data demonstrated regions where the direct connection MOSFET was active, which increased η_{Conv} towards ideal. In the remaining regions where the direct connection MOSFET was not active, the converter displayed similar η_{Conv} values as seen with the data for the conventional DC-DC converter(s). P_{Ctrl} was considered similar to the previous controllers (150 mW).

MPPT function was observed to be consistently close to ideal in steady-state test data, limited only by slight natural variation in v as expected, possible lookup data error, and measurement error from the Arduino. Test data indicated that the lookup algorithm used with this controller was superior to HCS even with somewhat basic function and inexact lookup data. Further testing (e.g. direct comparative testing with an HCS controller and further refinement of this algorithm), or testing of a similar/more refined lookup algorithm in naturally varying wind would be required as further work.

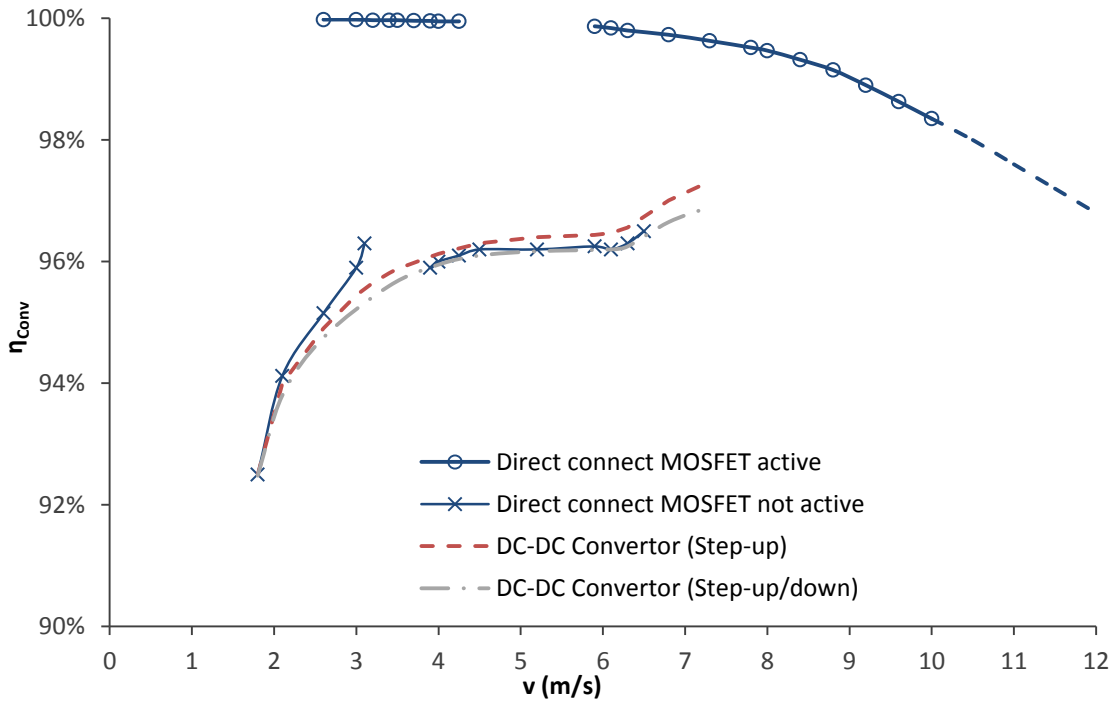

Figure 3.7.4 – Hybrid DC-DC Converter Power Transfer Efficiency Test Data (η_{Conv})

A complicated η_{Conv} efficiency trend was observed with this converter circuit due to the direct connection MOSFET ranges (brining η_{Conv} close to 100%), and normal converter function otherwise similar to previous data for the conventional converter.

Data for η_C is shown in Figure 3.7.5 with comparison to the previous data. The hybrid DC-DC converter shows significant improvement from the conventional DC-DC converter. Comparison of the hybrid to the cell selection converter data is inexact; however, performance of these two novel converters appears approx. equivalent.

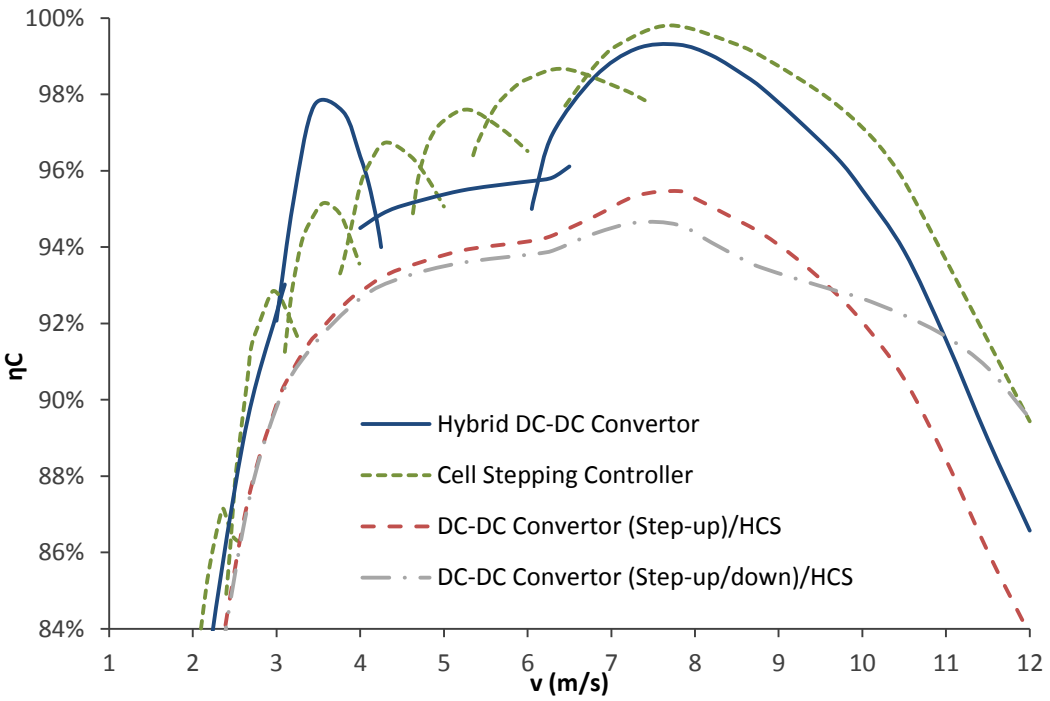

Figure 3.7.5 – Hybrid DC-DC Converter Overall Efficiency Data (η_C)
Data sets are shown for the overall conversion efficiency of the three converters. The cell selection and hybrid converters are superior to the conventional convertor. This is in part due to the improved power conversion efficiency (η_{Conv}) and improved MPPT function (η_{MPPT}).

3.7.4 Hybrid DC-DC Converter Experiment Summary

The novel hybrid DC-DC converter with MPPT function based on lookup data demonstrated improved η_C compared to conventional DC-DC converter testing, and similar η_C to the cell selection circuit. The direct connection MOSFET was a simple modification that could be used as a practical/effective improvement to a DC-DC converter (if selection ranges permitted, i.e. a region where D = 0). The variable ES arrangement provided some improvements in lower v ranges but was less effective/practical as a modification than the direct connection MOSFET. This was due to only low power occurring in the low ranges benefited by the dual cell range as tested here. This could be further investigated for 12 ECs or where large ranges of selection magnitudes were encountered for example. Also, use of different cell

arrangements could be considered (e.g. four and eight series cells, giving three direct connection ranges). The lookup MPPT algorithm based on the D_{MPP}-I_{ES} data trend was superior to HCS in all test conditions, and of similar performance to the lookup method used with the cell selection controller. This converter and the cell selection converter both demonstrate simple, robust and relatively efficient methods for micro/small renewable H_2 production from wind energy. Considering data for the WT, ES and the novel power converters, in this work the overall energy conversion is $\eta \approx 20\%$ when $v \approx$ 3-6 ms^{-1}, dropping to $\eta \approx 15\%$ when $v \approx 10$ ms^{-1}.

3.8 Summary

This work investigated WT and PV outputs and converter circuits for connection to an ES to enable renewable H_2 production. Important factors were the overall efficiencies, maximum H_2 production, and ultimately the lowest cost per unit H_2. Practical factors discussed here were power matching, power conversion, MPPT, and keeping circuits simple/robust/low-cost. DC-DC converters with HCS/P&O algorithms are common for micro/small WT/PV systems, although not optimal particularly in varying conditions. Lookup MPPT functions are superior, although require reasonably accurate data. More advanced algorithms may form system data through periods of HCS etc.

A novel cell selection circuit with a lookup algorithm demonstrated superior overall performance to a conventional DC-DC converter with HCS in this work. A hybrid circuit with a direct connection MOSFET, variable cell configuration and lookup also performed superiorly. These circuits demonstrate possible routes towards low-cost H_2 production, at micro/small scale. Cell selection shown in this work is more suited to micro WTs (avoiding 240 V etc). The hybrid converter topology would however potentially suit larger WTs, e.g. 50 kW. The dual ES configuration tested in this work enabled lower D values, slightly enhancing overall efficiency, although this may be impractical in some cases. The lookup MPPT functions (based on variation of n or D) were clearly beneficial for η_{MPPT} and considered here as almost ideal at steady v in the case of the D_{MPP}-I_{ES} algorithm. In variable v conditions these would both remain superior to HCS, although establishing the exact performance would require further testing in variable conditions (also with consideration of rotor inertia etc).

4. Biological H_2 Production via Mixed-Acid Fermentation

Research was carried out in collaboration with Frank Sargent Group (FSG), College of Life Sciences, University of Dundee, involving practical investigation of biological H_2 production processes by dark (mixed-acid) fermentation using *Escherichia coli* (E. coli). Physical aspects of the process were investigated and are presented as the following:

- An overview of mixed-acid fermentation of glucose and the H_2-releasing pathways/enzymes of E. coli
- An energy and cost analysis of the specific process investigated in this work
- Discussion of practical modifications required for improved (renewable) H_2 production in order to potentially reach commercial stage.

4.1 Mixed-Acid Fermentation of Glucose by E. coli

4.1.1 Overview of Mixed-Acid Fermentation

The biological process of dark fermentation of glucose by certain anaerobic and facultative enteric bacteria can produce H_2 along with CO_2 or other products [156]. Biological production of H_2 by E. coli was first achieved in the 1930s, hence this particular bacteria and process is well researched and characterised. The metabolic process requires several steps and pathways, many of which are well understood, although there does still remain some ambiguity across literature about certain components within the reaction.

Fermentation of E. coli is anaerobic, forming several intermediate acids and the term 'mixed-acid' fermentation is often used rather than 'dark', since it may occur in natural light. Mixed-acid fermentation uses various enzymes and metabolic pathways within bacteria such as E. coli to break-down simple carbohydrates such as glucose ($C_6H_{12}O_6$) to release H_2. Processes can use largely existing technology [156], and are potentially low-cost, sustainable and environmentally friendly biological processes, suitable for decentralised H_2 production units operating with various biomass/sugar wastes for example [157-159]. Importantly, when using sustainable waste biomass/ sugars, these are renewable H_2 production processes. It is however apparent from the literature that several aspects require significant improvement to become viable as low-cost commercial renewable H_2 production pathways.

Suitable bacteria may be classified by their sensitivity to O_2 (strict anaerobes or facultative enteric bacteria etc) and temperature requirements (mesophiles or thermophiles). The fermentation process is therefore ideally controlled in terms of temperature and pressure etc. Glucose and growing media mixed with the bacteria provide energy, nutrients and the physical source of hydrogen, which allow the bacteria to exist, multiply and release H_2. The media is mechanically mixed during the process to maximise use of glucose and nutrients, requiring energy input. Descriptions of the process found in biological literature are quite detached in format, style and terminology from what is encountered with processes of physical science, and differ from source to source (the process as explained in [157] and [160] for example).

E. coli is a rod shaped gram negative bacteria, a very diverse species within the enterobacteriaceae family. They divide by binary fission every 20 minutes in suitable conditions in order to multiply and propagate [161] [162]. They measure approx. 0.5-1.0 µm in diameter and 2 µm in length and have an inner and outer membrane. Harmless wild-type strains are found in gut flora and may assist with certain digestive functions. Hence they have become evolved to thrive at 37°C and studied to great extent over past decades. An anaerobic environment stimulates H_2 production. Of the various biological H_2 production methods (discussed in Appendix A1.3.10), dark fermentation appears the most promising due to the theoretical H_2 yields and rate of reaction, since photofermentation may require large areas to gather enough light.

There are various types of bacteria and strict anaerobes such as *Clostridium sp*. that can naturally provide higher amounts of H_2 per unit of glucose than E. coli. A great deal of research has previously been carried out with anaerobic bacteria [163]. *Clostridium* is well described in literature and naturally has a maximum yield of 4 mol H_2 mol^{-1} $C_6H_{12}O_6$, which is higher than the maximum of 2 mol H_2 applicable to enteric bacteria. These have been directly compared by Hua et al for example [164]. E. coli is however well understood and has been researched extensively [156]. Ongoing synthetic biology work has been carried out in FSG, hence there was familiarity with various types of E. coli and potential to significantly modify it during this research. Unfortunately biological H_2 production processes are as yet very inefficient and it is generally agreed throughout literature that yields as low as 4 mol H_2 mol^{-1} $C_6H_{12}O_6$ will not be suitable for commercial application of these processes [165] [166]. Therefore E.

coli must see significant modification before it can become viable. Strict anaerobes are very sensitive to O_2 and in the case that they become exposed their H_2 production ceases and does not return. They are also more sensitive to pressure than enteric bacteria. Therefore fermentative processes with strict anaerobes may not be practical, whereas E. coli is less sensitive and despite requiring anaerobic conditions to produce H_2 it can return to production following brief exposure to O_2 [159].

The mixing tank and media must be sterilised, by autoclaving or filter sterilisation of media for example prior to the process commencing, ensuring that no competing bacteria, viruses and fungi can co-exist in the media. Autoclaving involves steam immersion of the media vessel at slight pressure in an autoclave chamber. The fermentation process can occur on a batch or continual basis. In the case of laboratory experiments it is usually a single batch process, i.e. the media is prepared, the tank and media are sterilised, a sample of bacteria is added and the process observed for at least 24 hrs (while production is occurring). Continual processing is more appropriate to commercial production [166]. This involves running the process for long periods of time but draining some of media (dead bacteria and various waste products) and then replenishing, providing continual H_2 production. The metabolic pathways that perform the H_2-releasing reactions are the main factor in terms of the kinetics and overall H_2 yields etc. With E. coli the process produces CO_2 in molar proportion to H_2, along with acetate and traces of other products including lactose, sucrose and ethanol [159]. The gases form in the media and mixer tank headspace; hence exit tubes are used to vent the two gases. In lab work the flow rate of these gases can be accurately monitored.

Several practical and energy-based issues are evident with small or pilot scale mixed-acid fermentation processes, which prevent economical H_2 production. The main objectives of this research here have been to analyse these issues from a practical, energy and cost perspective and consider what modifications could be implemented in order to improve viability of the process. The reaction fundamentals and pathways were initially investigated, such that a quantitative physical understanding of the process and its limitations could be achieved, examining the critical factors that prevent it from becoming economically feasible, specifically as a renewable H_2 production pathway. This research was alongside synthetic biology work within FSG to improve the kinetics of E. coli in the H_2 production role. It is clear that biological

aspects are the primary drawback in terms of performance and viability of the process. The majority of research required is therefore within biology and outside of the scope of this thesis. This chapter briefly discusses biological aspects in order to explain their nature, but focusses upon practical limitations with existing methodologies. Main issues for mixed-acid fermentation are summarised by the following:

- Low H_2 yields (typically < 2 mol H_2 mol^{-1} $C_6H_{12}O_6$) and slow production rates
- Low efficiency (due to heating, stirring and control input versus H_2 output)
- Control of competing reactions (synthetic enhancement of pathways required)
- Control of competing bacteria (autoclaving etc is required)
- Limitations with direct use of complex sugars and various waste materials

4.1.2 The Metabolic Processes and Pathways

The basic fermentation process with glucose and a 'wild type' E. coli appears quite simple in principle although there is a great deal of complexity within the various metabolic reactions and there is not an exact and agreed-upon chemical formula for the overall process apparent in literature. This is because the reaction can take several pathways and what is experimentally evident is a mixture of end products, which are hard to quantify when mixed with used media etc. There are however ideal metabolic routes understood for maximum H_2 production that are sought, which may be influenced by something as simple as p and T etc. Evidently there are a number of competing reactions within the mixed-acid fermentation process that lower the H_2 production. In the case of E. coli these are well-understood [160] [167]. The overall preferential chemical reaction can be generalised by the following:

$$\text{Glucose} \rightarrow 2\text{Pyruvate} + 2\text{NADH} + 2\text{ATP}$$

$$2\text{Pyruvate} \rightarrow 2\text{Acetyl coenzyme A} + 2\text{Formate}$$

$$2\text{Formate} \rightarrow 2H_2 + 2CO_2$$

The metabolic pathways are shown schematically in Figure 4.1.1. One main challenge for improving the process is to modify the bacteria to remove competing reactions. Formation of CO_2 and acetate from fermentation of E. coli are however required under present pathways in order for H_2 production to be possible. Biological H_2 production methods fundamentally rely on the presence of an H_2 metabolising enzyme [168]. This key component in E. coli is the formate hydrogenlyase enzyme complex (FHL), which

catalyses the reversible oxidation of H_2 [167]. As a precursor, formate (HCOOH) is therefore required, which is cleaved by the FHL to produce H_2 and CO_2 in equal molar proportions [157]. CO_2 is therefore tied-in with H_2 production from formate, so this (and acetate) cannot be easily removed from the metabolic process.

Hydrogenases have been classified into either three or four groups according to metals thought to be at their active sites, such as: [FeFe] hydrogenases; [iFe] hydrogenases; [i] hydrogenases; metal-free hydrogenases [158] [168]. FeFe are most commonly found in various bacteria and algae, although E. coli has the NiFe hydrogenase [158]. Prior to formate, pyruvate is oxidised (forming acetyl-CoA and formate). The enzyme responsible is the pyruvate formatelyase [157]. Pyruvate results from glycolysis, where glucose is reduced to the acid phosphoenol-pyruvate and then pyruvate via a multi-enzyme metabolic reaction, involving activation by a source of two phosphate groups. The solid lines in Figure 4.1.1 are reactions that must occur along with H_2 to allow the reaction to proceed (either 1 ethanol or 1 acetate can be produced from each glucose molecule), whereas broken lines are unhelpful competing reactions. If the latter are eliminated (and acetate is optimised over ethanol) then 2 mol H_2 mol^{-1} $C_6H_{12}O_6$ can occur. These include removal of lactate/succinate formation and H_2 uptake.

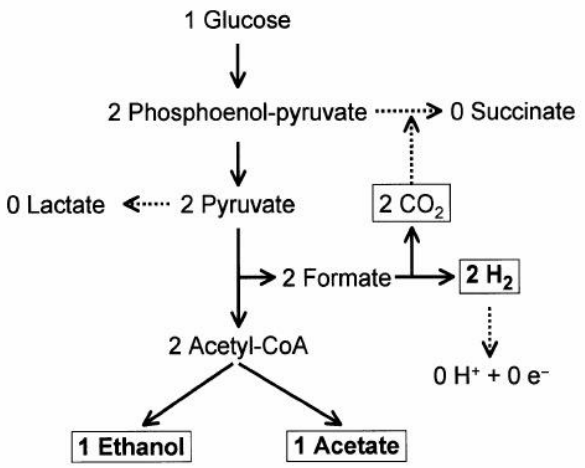

[167]

Figure 4.1.1 – E. coli Metabolic Scheme for Mixed-Acid Fermentation of Glucose
Redwood et al [167] provide a useful schematic for the metabolic processes within E. coli. H_2 production is linked with CO_2 due formate, and relies on other reactions.

In earlier work, usually only 1 mol H_2 mol^{-1} $C_6H_{12}O_6$ has been evident, mostly due to the competing reactions, although it is certainly possible to remove these [167]. For example, uptake of H_2 can be eliminated [167]. The FHL has at least three known isoenzymes: Hyd-1; Hyd-2; Hyd-3. Hyd-1 and Hyd-2 are known to cause H_2 uptake, whereas Hyd-3 (and possibly a Hyd-4) is responsible for H_2 production [167] [169] [170]. The role of Hyd-2 is thought to catalyse the oxidation of extraneous H_2, with the resulting electrons eventually producing succinate, thus allowing E. coli to use H_2 as an energy source during growth on non-fermentable carbon compounds [170]. Clearly work has been undertaken to eliminate Hyd-1 and Hyd-2 activity and promote Hyd-3 or other H_2 producing pathways. Other competing pathways can be removed by various synthetic biology processes. The exact nature of the steps to achieve this fall outside of the scope of this thesis. However, an overview of metabolic engineering and the biological 'toolbox' available is discussed by Abo-Hashesh, Wang and Hallenbeck [171]. E. coli has been mapped diagrammatically by various sources such as Berríos-Rivera et al [172], which is displayed in Appendix Figure A4.1.1 showing the layout of its various enzymes. Hyd-3 of the FHL complex is known to be physically located on the wall of the inner membrane [170]. From this diagram the ethanol route is shown to compete directly with formate, hence production of acetate is required.

E. coli cannot generally metabolise sugars more complex than glucose, such as sucrose, as discussed by Penfold et al [173]. In order to do so, a pre-metabolic process is required (to form glucose from a more complex substance) or hydrolysis of sucrose for example [174]. It is essential that biological H_2 production can operate with industrial wastes (which may contain sucrose and fructose or more complex carbohydrates) to create renewable pathways. Earlier work to investigate the ability of E. coli to be modified (using the pUR400 plasmid) such that it could utilise sucrose resulted in some success, and this has been considered more feasible than using a pre-metabolic process, such as an whole cell yeast invertase process to form glucose and fructose from sucrose [173] [175]. From another aspect, the initial concentration of glucose in the media affects the H_2 flow rate and overall yield. Earlier work has demonstrated a particular optimal concentration of glucose in the media for maximum production per mol [176]. Production rate is however likely to improve with higher concentrations. By adding fructose (50-50) with glucose, the production rate was seen to increase

compared to what was measured with only the glucose component, but potentially the same H_2 could be produced from the media per unit of glucose as per experiments of lower concentrations. This indicated that a mixture of sugars may overcome the saturation effect of glucose alone [175]. This may be due to metabolic pathways becoming altered at higher concentrations, such as towards production of ethanol [176]. The effects of glucose concentration and temperature during fermentation of a BL-21 strain of E. coli have been previously demonstrated, shown graphically in Figure 4.1.2 [176]. The BL-21 strain is an example of a modified E. coli with H_2 production of 3.12 mol H_2 mol^{-1} $C_6H_{12}O_6$ in estimated yields. This is very high in comparison to theoretical limits and other work, indicating replacement of the intrinsic H_2 metabolic pathway. The source does lack convention with energy calculations however, which may indicate credibility issues with the data. There are clearly a large number of variables and practicalities that affect fermentation and give disparity between measurements. Practical experimental H_2 production data is discussed in the next section along with data from various reference sources.

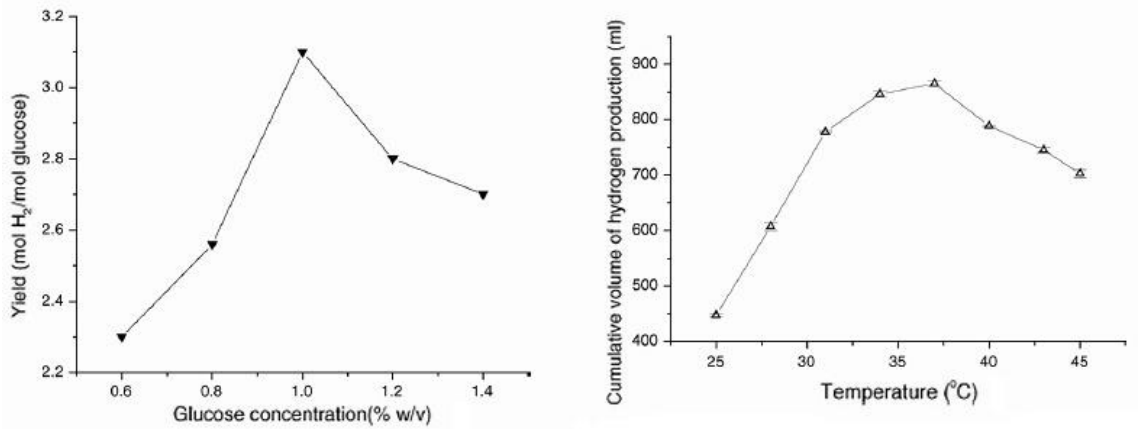

[176]

Figure 4.1.2 – Glucose Concentration and Temperature Effects on Hydrogen Yields
H_2 production trends are shown from work elsewhere with varying initial media concentration of glucose and variation of process temperature.

4.1.3 Characteristics of Hydrogen Production from Mixed-Acid Fermentation

H_2 production is a function of several factors, specifically the bacteria type and its pathways or activity. For a certain bacteria, production yield/rate can also vary by several environmental and physiological factors, namely bacteria population, pH, availability of glucose and certain nutrients, p and T etc [177]. Observations of

experimental fermentation with a wild-type E. coli give the characteristic exponential plot of population. Growing media is usually a form of lysogeny broth (LB), containing 10 g tryptone, 5 g yeast extract, 5 g NaCl per litre for example. This media provides the essential micro and macro nutrients and sources of C and N required for the bacteria to grow. Once introduced to a fermenter tank, the bacteria population experiences an initial acclimatisation period where the bacteria adjust to the new environment. This results in a slight reduction of population and lasts for approx. 2 hrs. The bacteria will propagate when the correct conditions are present, such as availably of nutrients, acclimatisation, correct p and T etc. Therefore after 2 hrs the population will begin to increase exponentially (binary division every 20 mins). In a fermentation tank the nutrients will deplete relatively quickly, at which time the bacteria enter a stationary phase, where some natural death will occur along with some growth, therefore population will remain fairly constant. As nutrients become fully depleted the bacteria enter an exponential decline. Bacteria population can be measured by the OD_{600} spectrophotometer technique [162]. This subjects a sample of the populated media to a light source of 600 nm and measures the optical density, which is proportional to population. Conversion from OD_{600} to population is shown graphically in Appendix Figure A4.1.2 [162] [178]. Example population data from is shown in Figure 4.1.3. The overall growth process is illustrated further in Appendix Figure A4.1.3.

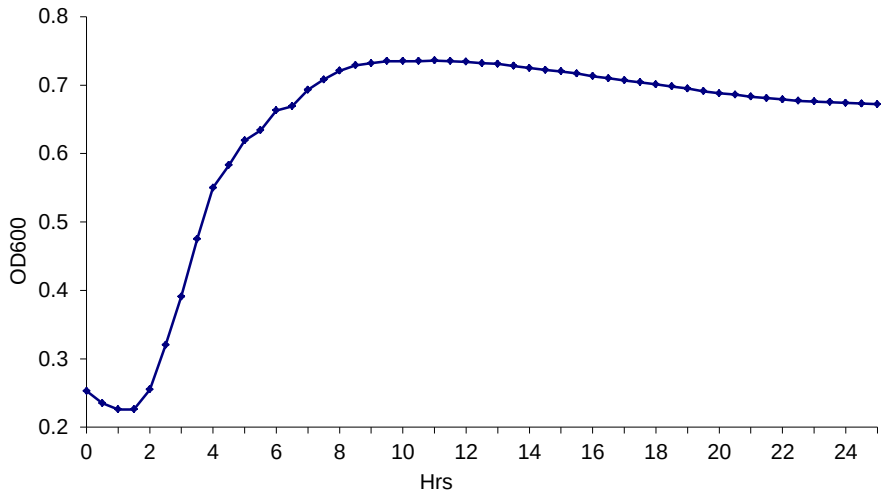

Figure 4.1.3 – Experimental Fermentation OD_{600} Data (E. coli wild-type MG059e1))
E. coli population within the fermenter have been counted with the OD_{600} technique, showing the exponential growth trend i.e. from 1-4 hrs. Where OD_{600} = 7.3, population $\approx 6\times10^{8}$ ml^{-1}. After approx. 12 hrs the population enter exponential decline.

4.2 Experimental Mixed-Acid Fermentation

4.2.1 Preparation and Experimental Method

Two sets of experiments were conducted, with a wild-type E. coli and with an experimental hybrid with optimised metabolic pathways (modification carried out by a collaborative research student within FSG). More than one modified E. coli was investigated although experimental work here refers to a strain assumed to have had successful removal of H_2 uptake enzymes, succinate and lactate pathways. The process was also optimised to suppress ethanol production (at the time of experiment this modified E. coli had not been formally named or classified). Removing CO_2 production had also been achieved in other experimental work in FSG, but resulted in very low yields of H_2. This was expected since it is part of the FHL reaction. The modified strain was developed as part of ongoing work to completely re-map the metabolic pathway to further improve H_2 production rates and maximum yields, to ultimately attempt to surpass the 2 mol limitation. This may have included an alternative precursor to H_2, i.e. without dependence on formate, without FHL, possibly without the existing glycolysis pathway. Specifically, metabolic engineering of various E. coli strains and directed protein evolution was carried out to integrate synthetic hydrogenase activity. Approaches included the construction and expression of active H_2-producing synthetic chimeric metalloenzymes, combining the catalytic activity of two different enzymes (thiosulfate reductase from Salmonella and E. coli Hyd-2). Although the FHL is represented by three (or four) hydrogenases, it actually consists of seven enzyme subunits and the reaction to produce H_2 occurs over two reactions. Concurrent work was also attempting to develop a biological process to metabolise chitin (shellfish waste) into fermentable sugar, therefore providing a potential sustainable H_2 pathway. Deletion of Hyd-1 and Hyd-2 uptake and competing pathways for lactate and succinate have been previously achieved and explained elsewhere in detail [166] [179] [180].

A Minfors 5 L fermenter was used for experimental procedures, shown in Figure 4.2.1. This features a temperature-controlled tank with mixing motor and control interface. A custom volumetric measurement device was set-up to measure H_2 production from the tank outlet. This counted instances of a volume of gas, determined by the size of a small container submerged in H_2O. When a certain volume of H_2 and CO_2 filled the

container it would rise out of the H_2O and release the gases. There were two containers positioned on a pivot mount; one would start to fill immediately after the other empties. This gave a numerical quantification of units of gas at 2.63 ml per count. Overall accuracy was determined to be ±2%. Leakage was tested prior to each experiment and determined to be < 5 ml hr^{-1}. A vapour trap was used in the gas outlet to collect any liquid present in the gas flow. The tank and media were autoclaved at 120°C for 20 mins. Fermentation involved the following preparation processes: selection of E. coli bacteria from low temperature storage; revival treatments/procedures carried out by FSG; injection into sterilised media.

Figure 4.2.1 – Minifors 5 L Biofermenter and Experimental Set-up
The fermenter, vapour trap and flowmeter used during this experimental work.

The fermenter was set to maintain 37°C and stirring at 3.3 rps. Growth of the bacteria within the fermenter tank proceeded under controlled anaerobic conditions. The heating element was rated at 700 W and the motor at 300 W in this fermenter, although they were not operated at these values during use. Investigation with power metering revealed that experimental work required approx. 100 W (45 W for heating power, 50 W for stirring and 5 W for the control interface). The process was started late in evenings so that production would be occurring during the following day, to

facilitate measurement and observation. Usually within 24 hrs the output had peaked and then became negligible. Three batch experiments were conducted with wild-type. Volumetric data was linked to a PC and exported in Excel format. Media used for wild-type experiments contained 20 g $C_6H_{12}O_6$ (0.111 mol) and 4 L H_2O mixed with 40 g peptone from casein, 20 g yeast extract and 20 g NaCl.

Further fermentation experiments were carried out with modified E. coli. Suitable data from this exceeding that of wild-type was not obtained as part of this research despite attempts. This was due to the volatility of the process and what appeared to be the additional instability and susceptibility of the modified bacteria. This further highlights the problematic nature of these processes as often described in literature [181]. Data was however captured independently by FSG and reported to extend close to the theoretical 2 mol limit. Investigatory work based on live fermentation processes specifically included observation of the following:

- Energy efficiency of process
- Effective H_2 cost

4.2.2 Fermentation Experiment Results and Discussion

Successful fermentation of wild-type E. coli labelled MG059e1 in single batch processes was achieved, shown in Figure 4.2.2 Data indicates a period of approx. 6 hrs until H_2 production is noticeable. Data is volumetric output, thus H_2 + CO_2 in equal molar proportions. 3380 mL was reached after 12 hrs, whereafter the flow rate became very low for these particular experimental conditions. It is assumed that virtually all of the glucose had been consumed at this stage (although the process continued for several more hours). The H_2 constituent volume was calculated by keeping molar equality and the fixed volume of 2.63 ml (measurement size), whereby partial pressures could then be adjusted (by van der Waals equation) to compensate for the physical amount of H_2 in the total volume. This however resulted in the actual amount of H_2 being within 0.1% of exactly 50% of the measured volume. Therefore, accounting for leakage and temperature at the volumetric measurement point, the typical H_2 produced in these experiments was determined to be 0.0691 mol (1.69 L). From a 20 g glucose source (0.111 mol) this represents 0.622 mol H_2 mol^{-1} $C_6H_{12}O_6$. This is slightly lower but almost equivalent to example data published for wild type, such as by Redwood et al [167]. 0.0691 mol H_2 equates to 19.8 kJ H_2.

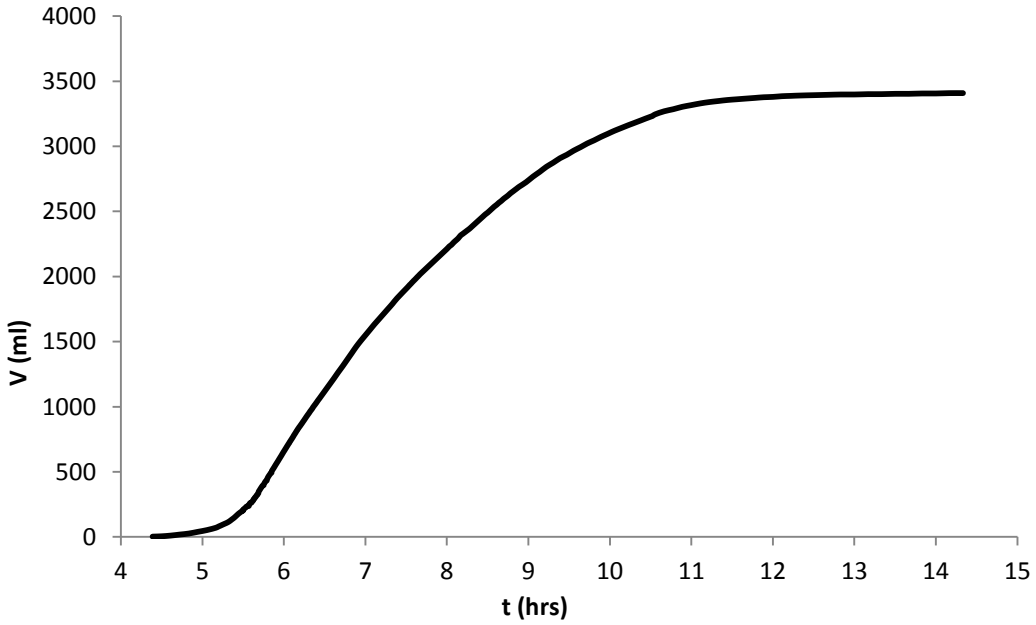

Figure 4.2.2 – Biological Hydrogen Production Data (E. coli wild-type MG059e1)
Volumetric measurement data for H_2 + CO_2 during active production over 24 hrs.

Experimental data for the modified E. coli investigated within this research remains unpublished, but is understood to approach the theoretical limit of 2 mol H_2 mol^{-1} $C_6H_{12}O_6$. Additionally there are claims of > 2 mol yields, for example 3.16 mol, by Chittibabu, Nath and Das [176] based upon modified E. coli. Energy analyses were therefore carried out with the experimental data, theoretical 2 mol data (which can be met with enhanced E. coli [156] [166]) and example published data of 3.16 mol [176]. Results are shown in Table 4.2.1. These efficiency calculations assume identical fermentation conditions and a period of 12 hrs (≈ 4320 kJ) for each species and consider the energy content of glucose (2808 kJ mol^{-1} [26]) and autoclaving (≈ 480 kJ), not including the energy content of the remaining media or intermediary/unwanted products. Efficiencies are very low, highlighting the challenge facing these processes.

E. coli type	Input	Output	η
Experimental (wild type), 0.622 mol H_2 mol	5112 kJ	19.8 kJ	0.39 %
Theoretical limit (unmodified), 2 mol H_2	5112 kJ	63.5 kJ	1.24 %
Published (modified), 3.16 mol H_2	5112 kJ	100 kJ	1.96 %

Table 4.2.1 – Efficiency Calculations for Batch Production of H2 (12 hr)
Efficiencies are shown for the experimental work and with two modified species.

The effective H_2 cost is very difficult to determine based on single batch fermentation, since a significant cost would be associated with the fermenter system and this would be spread across multiple batches or continual processes in a commercial scenario. A 5 L fermenter may cost from £4,000 to £15,000. The 20 g glucose and LB growing media used with the wild type were prepared by the lab services team in FSG who charge £6 for the 4 L prepared quantity. The cost of the autoclave is again difficult to establish. The electrical energy cost would be approx. £0.02 for a 20 min sterilisation, but the purchase of equipment would be £1,000+. Clearly the costs of H_2 under any of the three biological pathways exampled above, producing 0.14-0.71 g H_2, are several orders of magnitude greater than conventional methods such a SMR or electrolysis, which range from 2.8-4.7 \$ kg^{-1} H_2 (20-40 \$ GJ^{-1} H_2) [34]. As previously discussed, much of this deficit relates to biological aspects including kinetics, metabolic pathways and heat/stirring requirements within the process. There are however a number of practical, physical and economic improvements that can be attained alongside the biological work. These are discussed in the next subchapter.

4.3 Physical and Practical Enhancement of Mixed-Acid Fermentation

H_2 production is influenced by several complicated factors such as inoculum, substrate, reactor type, nitrogen, phosphate, metal ion, temperature and pH (discussed by Wang and Wan for example) [182]. These issues have been investigated along with a literature review of continuous fermentation processes and up-scaled fermentation.

4.3.1 Energy Efficiency Analysis

Lab-scale or experimental fermentation demonstrates very low process efficiency, associated with the low molar yields such as from glucose, although this is due to several specific factors. Investigation of the input energy revealed that a significant amount is used for heating and stirring. Experimental work elsewhere demonstrates that production is optimised at 37°C, and this is generally the case for most mesophilic bacteria [176]. Temperature is reported to be one of the most import factors with fermentation yields [182]. This suggests that either bacterium accustomed to thrive at ambient temperatures must be developed, or the process kept at 37°C. The later fits well with other industrial processes and waste heat. In most cases, heat sources below 150°C are not considered viable for steam generation (for turbines etc), and where it is

impractical to export low-grade heat for local space/water heating the heat is usually unwanted and dumped to atmosphere. It seems practical to locate fermenters in the vicinity of industrial sites where waste heat could be directly exported to the fermenter and eliminate the heat energy demand for the fermenter process. An example is the 4 MW gas generator CHP plant at UoD, which supplies electrical power and heat to university buildings, but also vents some low grade waste heat at the site. Locating a fermenter in or very near this building would therefore allow heating demand for biological H_2 production to be eliminated.

Development of fermentation processes operating with feeds of waste substances is quite well covered in literature by Guo et al [183] and Gioannis et al [184] and potential waste sources are also discussed elsewhere [171] [173] [185]. In the case where a substance is of no other practical use or value but can be fermented to produce H_2, then one has to question whether the energy value of that substance has bearing on the overall working efficiency of the fermentation process. In the case where a local source of waste material is abundant and made freely available, and if it can be directly fermented (without pre-treatments/invertase/hydrolysis processes etc) then it seems reasonable to discount the energy value of the substance from the overall effective working efficiency.

The effects of stirring action on overall yields of H_2 were one of a number of intended investigations within this research but were not completed due to resource constraints. Investigation into stirring has been carried out previously on different bacteria [186]. Experimental work with a wild type E. coli may not be of great significance, as individual bacteria and processes are likely to vary significantly from one another in terms of stirring variation. The primary role of stirring is to maximise the availability of the glucose and nutrients to the bacteria, although it is logical that reduced stirring would be sought in order to maximise process efficiency. It is understood from experimental work that the stirring action is not critical throughout the process and indeed not required at some stages. However, as indicated by Guo et al, the stirring action does have additional important roles, such as helping to control pH and improving the physical release of gases from the liquid media [183]. The use of sparging is discussed by Show, Lee, and Chang [177], using a gas such as N_2 to assist with purging H_2 from the media, but the negative effects of downstream separation

detract from the usefulness of the addition of this process. Stirring may therefore present one of the largest physical challenges for fermentation processes. This factor will have to be considered within the development of single optimised bacteria and managed such that the overall process is maximised in H_2 cost and energy terms.

The autoclave process is another significant drawback. Sterilisation of media to avoid unwanted microorganisms is one of the most important aspects of biofermentation and a significant cause of failure of growth or production in the case that it is not carried out properly [187]. Two approaches have been considered in the context of this research to reduce the energy and cost impact of autoclaving without compromising the process. Firstly, the media itself can be filter sterilised. The idea is microfiltration of the media (through a sub-micron filter of 0.2 μm) allowing media constituents to pass through but not bacteria or fungi etc. This occurs over reasonably short periods of time under slight pressure (which can be gravity fed). The fermenter tank itself must still be sterilised by autoclave or similar manner, or possibly chemical treatment. With continual processing, this would be carried out once within a long period of processing. For this reason the initial autoclave could potentially have quite minimal impact on the overall energy and cost input demand of the process. Another option to minimise autoclave and treatments is the development and use of more resilient bacteria. Mixed cultures (i.e. multiple types/strains) are one approach, which have been shown to be more practical and robust under non-sterile conditions [177].

Considering the aspects discussed in this section, the efficiency can be potentially classed as the ratio of optimised stirring (and some very minimal other demands), to H_2 output. The autoclave energy (and that of the glucose/media) may become quite negligible over long periods of continuous processing. In the case of the three data sets shown in Table 4.2.1, the input demand is now potentially an order of magnitude less at approx. 432 kJ over 12 hrs (stirring/energy demand ≈ 10 W). With continuous fermentation, the output would be greater, since the lag time would be much less, and more availability of glucose (continual feed) would increase production [177]. Therefore the outputs could reach 40 kJ, 127 kJ and 200 kJ for the three data sets over 12 hrs respectively. This implies potential efficiencies of 9.3%, 29.4% and 46.3%, and suggests efficiency of 58.6% at the theoretical 4 mol limit for strict anaerobes. This limit has in fact been demonstrated by hyperthermophilic bacteria at 70°C, stirring at

3.3 rps, which may demonstrate future feasibility for mesophilic bacteria at more reasonable conditions [156]. These figures represent a very significant increase from basic fermentation batch processes and it is recognised that the unreliable nature of fermentation make it very difficult to physically achieve the limits of optimisation. Reduced stirring would reduce the production rate and increase the time required and this would then have to be carefully investigated for the duration of the process stages such that optimal stirring could be established.

4.3.2 Cost Analysis

Lab fermentation is burdened by the cost of fermenter equipment and production scale (economies of scale etc). When moving towards commercial production these aspects would have to be addressed. For a refined process where the characteristics and optimum conditions for a certain bacteria were known then the use of a basic mixing tank would be applicable, since constant monitoring, control and intricate variation of the process would not be necessary. Mixing tanks are potentially very low cost. They are simply a glass or polymer tank with a stirring device, which could be internally mounted (such as at the top of the tank in head space) to avoid use of shaft seals such as with the Minifors fermenter. Over a long continual fermentation period the mixing tank cost would become quite minimal. Purchase of heat energy would not be required if the conditions described in Section 4.3.1 were observed, and stirring energy cost could be £0.01 for 12 hrs. The cost of glucose and growing media quoted (2012) at £6 for 4 L mixed comes from the lab services team in FSG. They report their product to be very competitive and would not provide a significant reduced cost for increased demand. Investigating the constituents they appear to be reasonably competitive (Sigma-Aldrich for example). It would be inevitably possible to source these wholesale at lower cost per unit elsewhere, provided that purchase scales were sufficiently high. £2.50 for a 4 L growing media mixture (glucose excluded) could be therefore taken as a more competitive reference price. Even by ignoring the cost of any other components of the process and making the assumption of the 4 mol theoretical limit of strict anaerobes, this sets a base cost of £2,790 kg^{-1} H_2. For the three data discussed previously the cost is £17,930 kg^{-1} H_2, £5,580 kg^{-1} H_2 and £3,550 kg^{-1} H_2 respectively, demonstrating that nutrient media alone is a restricting factor for the economics of basic fermentation processes. It is also apparent that super-

enhanced bacteria are not likely to be made freely available from biological research centres to commercial plants. Despite this high initial cost, a sample would only be required at the start of a continuous process. It is possible that future biological H_2 plants may have to be 'spin-outs' from research centres.

One quantitative approach within this research would be to compare fermentation to electrolysis. Both require electrical input and capital cost. For fermentation to become viable (in the case where all energy inputs are electrical) then it should operate at > 70% efficiency and have similar capital and running costs (maintenance, media, gas separation) to electrolysis, producing H_2 at similar overall unit cost. It is clear that even if a fermenter could be set-up with significantly less capital than an electrolyser, the fermentation system remains significantly more expensive in H_2 unit costs due to the cost of the media and overall efficiency inflicting higher energy requirements (stirring); the conclusion being that it does not seem possible to compete with electrolysis at present or in the near future. Thermodynamics and metabolic constraints suggest that it would be impossible to find a natural organism capable of the complete conversion of sugar-based substrates to H_2 by fermentation. The yield is so significant since the amount of H_2 is only a small proportion of the substrate in physical terms, and therefore it must be extracted to the maximum extent possible in order to make the process anywhere near viable in economic terms. Future possibilities include further metabolic engineering as previously discussed, or various two- or multi-stage systems to attempt to improve yields [156] [166]. The latter is discussed in the next section.

4.3.3 Combined or Sequential Two-Stage Fermentation

Mixed cultures and integrated processes combining dark and photofermentation have been shown elsewhere to potentially perform near maximum molar efficiency and could be more viable [168] [188]. There are two approaches to two-stage processes; combined fermentation or sequential fermentation [189]. When combined, this involves suspending two types of bacteria in one fermenter tank. When sequential, the two reactions occur in separate fermenters. The photofermentation process is fed by (liquid) output from the dark fermentation process. Combining processes in this way is generally regarded as one of the most plausible ways to maximise use of

glucose for biological H_2 production [189]. The pathway may involve the following reactions of dark fermentation first (at 4 mol H_2) and photofermentation second [165]:

$$C_6H_{12}O_6 + 2H_2O \rightarrow 2CH_3COOH + 2CO_2 + 4H_2$$

$$2CH_3COOH + 4H_2O \rightarrow 8H_2 + 4CO_2$$

The overall reaction producing 12 mol H_2 mol^{-1} $C_6H_{12}O_6$ is therefore:

$$C_6H_{12}O_6 + 6H_2O \rightarrow 6CO_2 + 12H_2$$

The second reaction is optimised to consume the waste product of the first reaction, thereby maximising the use of glucose and resources [156]. The bacteria from the first stage ideally require removal such as by filtration or centrifuge. Combined processes appear more beneficial, although data suggests that sequential fermentation produces higher yields. Combined processes with dark and photo bacteria must coexist and attempt to compromise the light levels and nutritional needs of both types of bacteria, which is understandably not ideal. Maximum yields for two-stage processes are reported as 7.1 mol H_2 mol^{-1} $C_6H_{12}O_6$ [165]. This therefore may show feasibility for fermentation once further advanced, refined and optimised [177]. For a hybrid system using photofermentation, more efficient photosynthetic bacteria must also be created and a sufficiently low cost transparent and hydrogen-impermeable photo-bioreactor [166]. Data for several two-stage processes are presented by Das and Veziroglu [165] and with extensive discussion by Redwood, Paterson-Beedle and Macaskie [188]. Further data tables for dark fermentation are published by Wang and Wan [182] and Das [190].

Another hybrid system suggested uses MECs to replace/support photofermentation. Similarly this could consume acetate and maximise production from an initial dark fermentation process. Presently the main drawbacks with MECs are the low current densities, relatively high applied voltages, and expensive cathode material [166]. Multi-stage processes have also been considered. These include dark fermentation occurring as a first stage, followed by photofermentation and MECs. The photofermentation process requires light, but the MEC does not; hence space can be optimised with maximum utilisation of available light by using photosynthetic bacteria supported by an MEC channel. It has been reported that NH_3 potentially produced in

the first stage suppresses the second stage, therefore requiring suitable anaerobic bacteria and/or treatment of the first stage output. Additional problems are also reported with the actual implementation, control and maintenance [18]. The waste products such as ethanol or acetate from a dark fermentation process may otherwise have to be considered as tradable products should that assist with profitability.

A further technique that was experimented with in FSG was the use of formate. As shown in Figure A4.1.1, this is both exported and absorbed by E. coli during its normal cycle. The ability to absorb format is therefore very effective and when subjected to increased levels of formate in the media the E. coli quickly export H_2. This is more effective than glucose in terms of the time taken to start H_2 production and the mass of H_2 produced per unit of source material. Formate has therefore been considered as a possible substance to support fermentation. However, the initial glucose and media would still be required in order for the E. Coli to begin to thrive, and there are various problems apparent such as the effect on pH from adding formate [191] [192]. It is generally agreed that use of glucose is preferred over formate [179].

4.3.4 Carbon Dioxide Removal

Little attention within the literature has been given to CO_2 produced during fermentation processes. The initial source of the carbon is fixed within the glucose or waste sugar source, which is destined for eventual biodegradation and natural release of CO_2. Therefore, fermentation is not a net contributor of CO_2 although it may have the effect of accelerating a natural decomposition process. The exact effect of this would be difficult to quantify, but in any case biological fermentation processes are not likely to bear any impact on global CO_2 release and uptake. Concern is therefore with removal of CO_2 from the H_2 gas flow for practical reasons. The use of gas chromatography/mass spectrometry (GC-MS) for quantificational analysis of the gas product was investigated. These are well-established techniques. GC consists of a capillary column that separates the gas molecules, based on their individual characteristic retention to a surface material and the difference in time they take to move through a column. MS ionises individual gas molecules and determines their type via charge-mass ratio. The use of both stages allows accurate and quick identification of gas samples. GC has been previously used within FSG to confirm products from the mixed-acid fermentation experiments.

Storage of H_2 or use in a FC is not practical while it contains CO_2. Clearly chemical or adsorptive H_2 storage could not accommodate CO_2. Also, a FC only vents a tiny amount of its H_2 input, to prevent build-up of impurities in the anode electrode. However, if this contains 50-50 H_2-CO_2, then there would be significant release of CO_2 and H_2 during use in order for the FC to run continuously. CO_2 is not reported to cause significant degradation of FC catalysts. At high temperatures (such as with solid oxide FCs discussed in Appendix A2.1) the reverse WGS reaction may occur producing CO, which does significantly and irreversibly affect the integrity of FC catalysts. Reverse WGS is thermodynamically unfavourable and not likely to occur at the temperature range of PEM FCs, but the reaction is however promoted by Pt present at the electrodes. CO is not reported to be produced naturally during fermentation. CO_2 separation techniques would however be required for the H_2 + CO_2 output gas [193].

Industrial CO_2 removal generally involves scrubbing solutions such as amines, hydroxides, or PSA, PrOx or methanation processes (introduced in Appendix A1.3.1), or permeable membranes for gas separation [194-197]. The chemical processes are relatively cheap and effective, but require treatment to recover the solution for further use. The cheapest hydroxide NaOH involves difficult heat treatments to release CO_2, which is not favourable for this application (the idea here is not to create additional waste or require heat). PSA is used for commercial scrubbing. This is based upon the tendency of gases to adsorb onto materials (such as zeolites) at different pressures. The stream of gas can passed through adsorbent beds and recycling the pressure such that one gas is adsorbed and then released separately. Membranes are typically based upon precious metals such as Pd, or ceramics. While these membranes are now starting to become practical, they remain expensive. The CO_2 is simply released after separation. In this work several CO_2 removal strategies were practically investigated. Removing CO_2 using a simple NaOH scrubbing solution was attempted as a baseline experiment, involving flow of the fermenter gas output through a 1 litre vessel containing a 1 mol NaOH solution in H_2O. Due to the variable nature of H_2 + CO_2 production during experimental batch fermentation, the free flow rate was carefully measured immediately prior to and after the scrubbing experiment times, to determine the expected natural flow rate during the scrubbing. Any observed flow rate reduction during scrubbing with the NaOH solution was therefore converted into

a scrubbing percentage value. The process was observed under three different experimental conditions: free flow; H_2O scrubbing; NaOH scrubbing. Reduction in measured flow rate during scrubbing was due to CO_2 absorption, natural variation and the small amount of water head (25 cm) known to suppress H_2 formation [177]. Therefore H_2O scrubbing was also carried out to assist with calibrating results and identifying the reducing effects of pressure. Flow was known to be following an exponential decline gradient and this was considered within the data. Various synthetic wool samples were investigated and used to diffuse the gas flow and enhance CO_2 absorption. Data in Table 4.3.1 indicated maximum CO_2 scrubbing of approx. 89.4%, falling to 53.7% in further tests. H_2O scrubbing alone appeared to induce a significant reduction in flow rate (-21.8%), which indicated that H_2 production was being decreased by the additional pressure and/or that H_2O itself was having some scrubbing effect. Based on this data and the known limitations such as pressure, chemical scrubbing does not appear practical for a fermenter scenario.

Flow Rate Data	
Free flow	0.2466 ml s^{-1}
H_2O + synthetic wool	0.1981 ml s^{-1}
NaOH + synthetic wool	0.1325 ml s^{-1}
Free flow	0.1805 ml s^{-1}
NaOH + synthetic wool	0.0998 ml s^{-1}
NaOH + synthetic wool	0.0485 ml s^{-1}
No Scrubbing	0.0663 ml s^{-1}

Table 4.3.1 – Flow Rate Data during Chemical Scrubbing of CO_2
Volumetric data indicating effects of H_2O/NaOH scrubbing with/without flow diffusion.

Algae are known to be a significant sink of CO_2. Use of green algae has also been discussed as a potentially economical and sustainable method for direct H_2 production, in terms of water utilisation as a renewable resource and recycling CO_2. The strong inhibition effect of generated O_2 on the hydrogenase is (conversely) the major drawback to the process [165]. Algae capable of H_2 production were not available to this research and have not been further reviewed in that role here. However, the idea of passing the product gas from a fermentation process through a series of algae tanks was considered as a method of removing CO_2. Algae may potentially therefore have

two important roles in H_2 production processes. Experimental work to determine the CO_2 uptake characteristics of a mixture of algae was carried out. This involved subjecting four algae tanks to CO_2 exposure with monitoring and also investigation of the physical and practical aspects that would be involved with creating an operational algae CO_2 sink. The algae were obtained from The Scottish Association for Marine Science (SAMS), Oban, Argyll, in 2010. They included two salt water algae and two fresh water algae samples. Of the salt water algae, one was a micro algae. Their individual CO_2 uptake characteristics were measured with a CO_2 and O_2 probe in the tank headspace above the water (Alba interface and logger, DJB Microtech Ltd). Data was obtained revealing the cyclical nature of CO_2 uptake, due to natural light variation. Effective CO_2 uptake by algae would only therefore occur when exposed to daylight.

Algae were proposed to be grown in an array of tubes or tanks, of wide area but low water depth/head. This was to allow the outlet from the fermenter to enter the algae tank at the bottom and filter through long diffused algae-impregnated channels, so that the CO_2 content would have maximum exposure to the algae and H_2O, yet the pressure would be low, indicating requirement for large flat tanks. As discussed, the fermentation process cannot be subjected to pressure in the outlet tube if maximum H_2 is sought. The gas was observed to form concentrated bubbles rather than a diffused mixture. This would limit the uptake. Therefore a range of high surface area materials such polymers in the micron range were inserted into the region of the inlet of the tanks to diffuse the gas flow and attempt to maximise CO_2 extraction. Experimental data involving approx. 50 g of each of the four algae samples indicated that ambient CO_2 levels in headspace of 35 ml reduced from approx. 400 ppm to 200 ppm during the course of 12 daylight hours. The CO_2 would be retained in small quantities by the H_2O, which would be slowly consumed by the algae. The exact mechanisms and kinetics of this would need further investigation. Exposure to a concentrated CO_2 source from fermentation would have to be investigated in order to quantify the exact amount of algae mass and type required. The uptake would only occur during daylight, which would need to be taken into account when considering two-stage processes involving photofermentation. Alternative simpler methods for H_2-CO_2 separation were investigated based on gravity separation. H_2 is much lighter than CO_2. Within a long vertically mounted tank a concentration gradient would be

expected, if the gases remained undisturbed. Suitable H_2 or CO_2 detection equipment was not available to this research and this technique was not properly tested, although investigation revealed that some gradient would form but not sufficient to consider as support for other separation techniques.

4.4 Summary

The H_2-producing ability of bacteria relies upon metabolic pathways and metal-dependent hydrogenase enzymes to decompose various sugars or H_2O. Future sources of renewable H_2 from biological processes may be possible with development of low-cost systems and pre-treatments, providing the complete, direct and efficient conversion of a broad range of waste streams and energy crops with extremely low energy demand [166]. These must occur at ambient temperatures or use low-grade waste heat. Several aspects of present fermentation processes must improve significantly, such as enhancement of metabolic pathways (particularly involving renewable wastes), greater stability, process simplification, reduced cost and increased efficiency. Currently reported limits of 4 mol H_2 mol^{-1} $C_6H_{12}O_6$ will not be sufficient for commercial renewable H_2 production, since for example other biofuels could be formed from the same substrates via other processes much more effectively [156]. The cost of the growing media, fermenter equipment, stirring energy input, CO_2 and waste media removal are significant issues preventing economic H_2 production from biological processes at present.

A precursor to commercialisation is the identification of the most suitable bacteria or platform(s) so that future research efforts are properly aligned. Subsequently, extensive metabolic enhancements, improved processing techniques (substrate concentrations, stirring etc) and simplified (i.e. low-cost) fermenter systems could be developed. Physical techniques to remove CO_2 such as separation, purification or scrubbing are not practical for fermentation processes, so should ideally be eliminated via metabolic pathway enhancement. Two-stage processes using waste products such as acetate from dark fermentation demonstrate improved overall efficiency and yields and may be a more viable future fermenter platform. However, compared to wind or solar renewable H_2 production discussed in Chapters 2 and 3, it is evident that present fermentation processes are expensive, inefficient and not economically feasible.

5. Photocatalytic Water Splitting Materials Processing

Production of H_2 from solar energy can be achieved by solar-powered electrolysis, PCWS/PEC cells, solar thermolysis and photobiological processes [198-203]. Mixtures of the above technologies are also evident, and solar energy can substitute other energy sources (renewable/non-renewable) to assist with H_2 production, such as solar thermal enhanced electrolysis [72] [204] [205]. Use of nanoscale materials processing was investigated for the production of photocatalytic surfaces for renewable H_2 production, involving the following:

- Deposition of nanoscale Ti coating onto a PEN substrate and laser processing to form a Ti/TiO_2 catalyst of high surface area
- Synthesis of CNTs for increased substrate surface area (in preparation for further materials processing/deposition).

5.1 Laser Processing of Ti/TiO_2 Photocatalytic Water Splitting Substrates

5.1.1 Overview of Nanoscale Materials Enhancement of PWCS

Of the main processes for H_2 production using solar energy resources, PV-electrolysis is clearly the most practical and technology-ready at present. Of the other (non-biological) processes, work with PCWS in nanoscale materials context was considered worthy here for practical investigation. PCWS has generally considered use of TiO_2 materials, due to stability, being non-corrosive, environmentally friendly and relatively low cost [206]. As discussed previously, there are fundamental problems with PCWS including, E-H pair recombination, H_2-O_2 recombination, limitation to UV, and the separation of H_2 and O_2. The active surface area of the catalyst is an important aspect influencing the performance of the process [205-207]. The catalyst material may be in the form of a suspended powder or surface coating on a substrate material (in H_2O), but in either case nanoscale technology has been of key interest [200] [206]. Research efforts to improve PCWS have included chemical additives and photocatalyst modification techniques [207] [208]. Several examples of these are discussed elsewhere, such as by Ni et al [206]. Chemical additives may include electron donors (sacrificial reagents or hole scavengers) to prevent rapid electron-hole recombination. This may be a hydrocarbon that can be oxidised (irreversibly) by photo-generated VB holes to enhance separation. Strongly reducing CB electrons can then reduce protons

to H_2. Methanol or ethanol are two examples of compounds used, needing to be continually added since they are consumed in the reaction (and may also contribute additional hydrogen to the reaction). Interestingly, pollutants (such as oxalic acid, formic acid) may form suitable electron donors, showing potential for pollutant decomposition within photocatalytic H_2 production reactions [206]. It is also reported that addition of carbonate salts could significantly enhance H_2/O_2 production stoichiometrically. Addition of Na_2CO_3 was found to be effective for H_2 production using Pt-loaded TiO_2 and in other work with TaO_5 and ZrO_2 described elsewhere [206]. This was understood to be due to the surface formation of several carbonate species. These consumed photo-generated holes, forming radicals that were found to be beneficial for photo-excited E-H separation.

In other work, noble metal loadings (Pt, Au, Pd, Rh, Ru, Ni, Cu, Ag) have been reported as very effective photocatalyst modification techniques (co-catalysts) in particular for enhancement of TiO_2 [206]. This is due to the Fermi level of the noble metals being lower than that of TiO_2. For this reason, photoelectrons can be transferred from the CB of TiO_2 to the noble metal particles, while the photogenerated VB holes remain in the TiO_2. This greatly reduces recombination and the overall efficiency of the reaction. Transition/rare earth metal ion doping has also been attempted in previous work reported by Ni et al [206]. This was found to bring the response of TiO_2 into the visible spectrum due to the metal ions being incorporated into the TiO_2 lattice, forming impurity energy levels in the band gap of TiO_2. This can also create electron or hole 'traps', but which are transferred to the surface. Therefore doping is kept close to the surface and optimised, avoiding deep doping that may result in recombination centres [206]. Anion doping has been reported in more recent work (with N, F, C, S etc), also able to move the response of TiO_2 into visible spectrum. Anions are less likely to form recombination centres [206]. Further methods for using visible light have been previously discussed and illustrated previously in Section 2.2.13 and Figure 2.2.8, including the two-step photoexcitation mechanism between different photocatalysts, and a single visible light responsive catalyst [207]. An example of this is use of a GaN:ZnO solid solution loaded with RuO_2 co-catalyst. Visible light separation of H_2O using this material is possible due to the band structure of the solid, described by Abe

[207]. Co-catalysts are considered for promoting the splitting reaction and not reformation and are a very important area of research within PCWS/PEM reactions.

Despite a multitude of attempts to enhance the H_2 production of TiO_2 and similar photocatalysts, production rates are still relatively low due to recombination, back reaction and inefficient use of visible light [206]. TiO_2 remains one of the most interesting photocatalysts despite these intrinsic material deficiencies. Its development to reach commercial H_2 production scale from sunlight will rely on overcoming these issues. A further approach, as discussed by Ahmad et al [200] is the use of CNTs. These are reported to have ability to increase visible light absorption, increase surface area, and reduce recombination. This is suggested to be due to cooperative reactions induced between oxides and carbon phases [200]. Previous work reports use of CNTs leading to up to 10 times increased photocatalytic activity in a methanol aqueous solution, compared to TiO_2 alone, and similar data is reported in other work [200]. For this reason, the synthesis of CNTs was investigated here for enhancement of PCWS. This was also considered previously for enhancement of EC/FC electrodes, where it was expected to increase surface area of cells and lead to improved distribution of catalysts and improved cell efficiency. There would likely be issues of stability requiring further investigation. A CNT synthesis process is discussed in Subchapter 5.2, which could be adapted for use within the context of both ECs/FCs and PCWS/PEC processes. Use of nanoscale deposition and laser processing were first investigated to produce an enhanced Ti/TiO_2 substrate with increased/dispersed TiO_2 coating, discussed in Section 5.1.2.

5.1.2 Laser Processing of Ti/TiO_2-Coated Substrate Experimental Method

The production of a flat substrate of large specific surface area (TiO_2) was considered in this work (rather than use of suspended power etc). This first involved selection of a substrate, where PEN polymer was initially considered suitable to undergo experimental materials processing. A sputter deposition process first was carried out to form a nanoscale Ti layer of 20 nm on one side of the PEN substrate. This was then processed by excimer laser to produce a dispersed Ti/TiO_2 coating. Laser power was lowered to 224 mJ (16 kV) for this work. Laser annealing proceeded at 20-60% intensities, with pulse width of 20 ns, frequency of 25 Hz and movement of 2 mm s^{-1} as in previous work here. Later experimental work involved thicker Ti coatings (40 nm).

5.1.3 Laser Processing of Ti/TiO_2-Coated Substrate Results and Discussion

Laser processing in this manner was an alternative process to more conventional methods discussed elsewhere, such as sol-gel techniques [209], or where laser deposition processes are instead involved [210]. The formation of TiO_2 was expected to occur while laser annealing in air/O_2. Reports of increased anatase and rutile phases (rather than amorphous phases) occurring with laser deposition of TiO_2 were found in literature, and with these phases being considered preferable for photocatalytic activity [210] [211]. SEM micrographs (at 5 kV, ×1000 magnification) are shown in Figure 5.1.1 for four samples. The higher intensities resulted in complete ablation of the Ti. Lower intensities (20/30%) show some Ti in a dispersed form on the PEN surface, which was the intended result for this processing.

(a) 20%

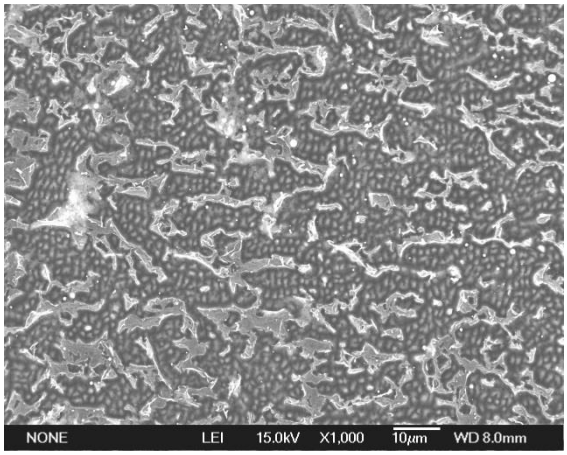

(b) 30%

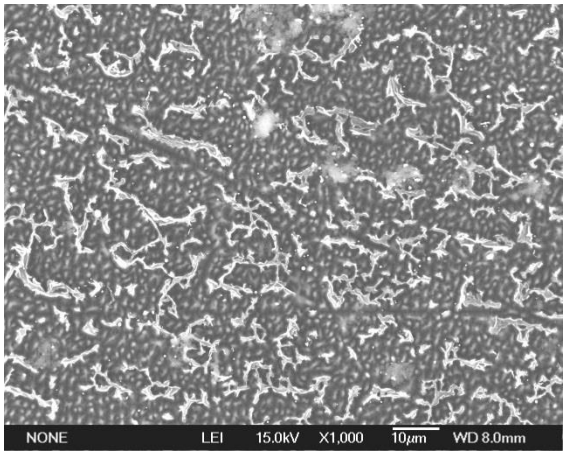

(c) 50%

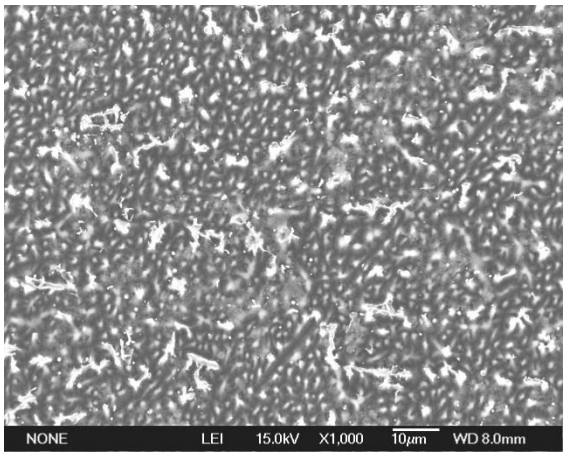

(d) 60%

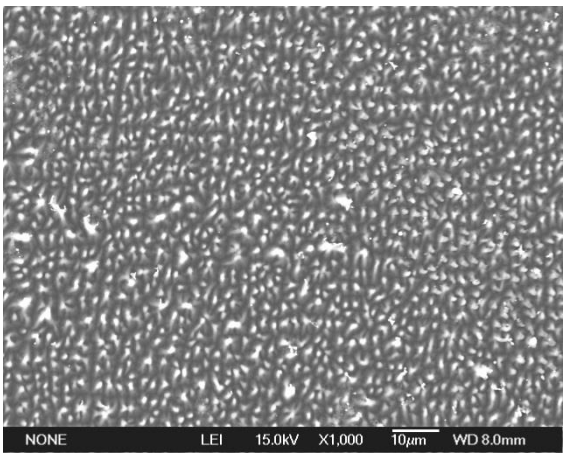

Figure 5.1.1 – SEM Micrographs of Laser Processed 20 nm Ti/TiO_2-Coated PEN
Higher laser intensities, (a) and (b), resulted in complete Ti ablation. Lower intensities, (c) and (d), show some Ti in a more suitable dispersed form on the PEN surface.

In this and previous work it was observed that the desired intermediate stage between no material modification and complete ablation was experienced in a relatively narrow range of laser intensities. For example, in this work laser annealing of a 20 nm Ti coating at 60% (of 224 mJ, 2 mms^{-1}) produced complete ablation, whereas 20% was just low enough to allow most of the material to remain. Although lower intensities were not easily available, it was possible that the equivalent of 10% would result in little or no surface annealing. There were practical measures available to further reduce the laser intensity such as lowering the substrate position and using semi-transparent shields (such as layers of Nafion between the laser emitter and substrate). Unlike in the previous work, this could not be in contact with the substrate since the presence of O_2 was critical. The PEN substrate was intended for analysis by XPS and later testing under natural and artificial UV light, although these activities were not possible during this research due to equipment outage or non-availability. XPS would allow surface composition analysis of the PEN to identify Ti and TiO_2 compositions (via chemical shift as discussed in Appendix Section A1.2.4). EDX was consequently used during SEM imaging to confirm the existence of Ti. The EDX scanning depth was approx. 100-500 times deeper than the Ti/TiO2 coating so only traces were detected. This was obviously not useful for TiO_2 detection due to O existing in the PEN material and appearing in composition data. Lighter areas in the micrographs were confirmed as Ti/ TiO_2. The stability of the Ti/TiO_2 coatings would require further investigation, and ultimately to confirm the ability of this substrate to perform the PCWS reaction.

5.1.4 Laser Processing of Ti/TiO_2-Coated Substrate Summary

A Ti-coated PEN substrate was produced via sputter deposition and laser processed to form a dispersed Ti/TiO_2 coating of increased active surface area. This was intended for further investigation of PCWS. Several Ti thicknesses and laser intensities were attempted to seek an optimal surface coating in terms of (minimal) ablation and maximum surface area. The exact composition of the Ti catalyst following laser annealing was unconfirmed although expected to be mostly TiO_2 (from previous work with Ti and similar metals undergoing laser annealing). However, in the event that this modified substrate would show improved H_2 production under suitable irradiation, this technique could be further investigated as a method for single-step large-area material processing to produce substrates with nanoscale Ti coatings.

5.2 CNT Synthesis for Enhanced Photocatalytic Water Splitting Substrate

5.2.1 Overview of CNT Synthesis

Further attempts to produce a PCWS substrate with high surface area were considered using CNTs. These were intended to be grown on a substrate to form a high surface area layer followed by, for example, the deposition of a Ti/TiO_2 layer, which could possibly be further enhanced by laser processing.

CNTs have been discussed extensively in literature since their discovery in 1991, with their properties and synthesis such as via PECVD being the subject of several research/review papers [212-214]. These nanostructures have been considered in several interesting H_2-based applications, notably H_2 storage, ECs/FCs, PCWS/PEM cells, and also reforming processes [68] [200] [215-218]. An example comparative case involving electrolysis with and without use of CNTs on the anode reported increased current density with the use of CNTs compared to graphite electrodes (at the same overpotential) [216]. In other work, use of CNTs on carbon cloth were reported to enhance the electrochemical activity and performance of a FC, understood to be due to their excellent electron transfer kinetics [218].

Use of TiO_2 nanotubes has been previously considered in work with alkaline electrolysis assisted with photocatalysis in a PEC [201]. The cell closely resembled an EC with a diaphragm, with the schematic and data for this cell shown previously in Appendix A1.3.10 and A1.3.11. The anode was exposed to UV light (365 W), resulting in 118% increase in H_2 production from the cell and a 14.5% reduction in V_{Cell}. While this is clearly of significance and demonstrating the effects of a TiO_2 nanotube photocatalyst anode, it has to be questioned whether the amount of UV light used in this experiment is practical, since this would require approx. 9.5 m^2 of collector area to harness this amount of UV in AM 1.5 sunlight (assuming 4% of 1000 W m^{-2}), and thermal effects may have had significant influence in the experiment.

Use of CNTs has also been considered in work elsewhere for photocatalysis, in H_2 production and water purification applications [219-222]. For example, MWCNTs have been previously mixed with Ti powder in various treatments and oxidation to form a stable Ti coating [219]. These were suspended in a solution under UV light, where it was proposed that the decomposition of a methylene blue aqueous solution was

improved in visible light as a result of the use of these MWCNTs. In other recent and extensive work by Miranda et al [220], a variety of TiO_2/CNT composites were prepared by a hydration/dehydration procedure and investigated for surface roughness and micropore structure. The efficiency of the oxidation of caffeine was evaluated by sample homogeneity, where photocatalytic efficiency was seen to correlate with the preparation, but where it was also suggested that further work to identify the activity and stability of these samples was necessary [220].

Work similar to what is proposed here was carried out by Yu et al [221], where TiO_2-CNT arrays were formed on a substrate via a CVD process. A CNT layer was first grown on a Ti substrate and then a TiO_2 layer of varying thickness was deposited over the CNTs. The TiO_2 layer thickness affected the photocatalytic activity, where 100 nm TiO_2 was suggested by Yu et al as most efficient for charge separation, and optimised TiO_2-CNT heterojunction arrays displayed apparently higher photoresponse than that of TiO_2 nanotube arrays [221]. Similarly, Li et al [222] suggested that combining CNTs with TiO_2 promoted the E-H separation in experimental PCWS/PEM, depending on the quality of the CNT-TiO_2 interfacial contact and morphological and surface properties of the nanocomposites. A uniform and well-defined TiO_2 (antase) layer was formed (by a sol-gel method, using three different Ti precursors) on individual MWCNTs, producing a mesoporous nanocomposite film. This was analysed by various techniques to inspect the textural, crystallographic and optical properties of the composites. Photocatalytic activity and photocurrent was found to vary by precursor and layer thickness, where a thinner TiO_2 (5-15nm) layer provided enhanced photocatalytic activity in the test range, and higher CNT content in the composites correlated with higher photocurrents in a PEC reaction [222].

5.2.2 CNT Synthesis Experimental Methods

Details of the different CNT synthesis processes have been introduced in Section 3.4.1 and are described elsewhere in detail [223] [224]. These include arc discharge, laser ablation and CVD/PECVD processes. In this work CNT synthesis was investigated and attempted via PECVD processes. Si and Si/SiO_2 wafers were used for test substrates. It was understood that surface transition metal catalysts would be required for this process (without this, amorphous carbon (a-C) would be the likely result), and also that the catalyst must be in the form of nanoparticles rather than a film. The particle size

has also been linked to CNT diameter in several previous works. Metal used in previous work have typically included Fe, Ni, Co, Mo [212].

Several PECVD processes were attempted to achieve CNT synthesis and simplify the process in terms of CNT density, low material use, heating/energy requirements etc. In each case Ni was used to form the nanoparticle catalyst. This was achieved by initial sputter deposition of Ni onto a crystalline Si wafer in the first set of experiments. Later experiments used buffer layers of Ta, and then later a Si/SiO_2 (undoped) wafer. The PECVD vacuum chamber was equipped with an RF electrode (13.56 MHz), gas inlets/outlets with mass flow control and two vacuum pumps. The substrate was fixed to a heating element bracket, with a thermocouple, and inserted into the PECVD chamber. An electrical heating element provided temperatures of approx. 600°C (powered by a DC source at 4 V, 11 A). This was later replaced by a custom element made from 1.2 mm Kanthal wire (FeCrAl) cut and formed using a simple custom jig, allowing higher process temperatures and elements of variable size (at virtually no cost). The catalytic surface for intended CNT synthesis was exposed to the plasma source. The thermocouple was calibrated prior to each process. Readings were with accuracy of ±15°C. Initial base pressure in all experiments was < 210 Pa (1.6 Torr).

The chamber was prepared by N_2 flushing for 30 minutes to remove O_2 at 333 Pa (2.5 Torr). The PECVD process was performed in three stages: two NH_3 annealing/plasma processes; CNT deposition. The first stages used NH_3 to break the surface film of Ni and form dispersed (catalyst) nanoparticles. This has been explained in previous literature as one method to achieve this, and another is using a buffer layer of a non-catalyst metal. The latter tends to form an alloy with dispersed regions of the catalyst metal (during sputter deposition etc). Catalyst particle size has correlated with film thickness (and therefore nanotube diameter) in work elsewhere [212]. The plasma annealing process involved 20 minutes of NH_3 flow without RF power, then 6 minutes of NH_3 flow with RF power (160 W). NH_3 flow rates of 0.5 ml s^{-1} (30 sccm) were used and chamber pressure maintained at 210 Pa for the plasma annealing processes. The chamber then remained for 30 minutes to reach maximum T (approx. 600°C). A low-pressure flow of C_2H_2 (acetylene) and NH_3 (diluent gas, to prevent excessive a-C) into the chamber provided the CNT deposition process (with RF power = 200 W). The chamber finally received 2 minutes of NH_3 flow in each case then returning to ambient.

5.2.3 CNT Synthesis Experiment Results and Discussion

Six CNT synthesis experiments were attempted. Process pressures of 130-2700 Pa (1-20 Torr) were used (based on previous work and literature [212]). General process conditions were as stated in Section 5.2.2. Substrates were examined by SEM/EDX following the PECVD processes. SEM micrographs are shown in Figures 5.2.1-5.2.6. A summary of process conditions is shown in Table 5.2.1.

CNT synthesis was not successful in experiment 1 (Figure 5.2.1). It appeared that a-C formed (or possibly silicon carbide), in dots of 50-150 nm. The micrograph of this experiment shows the Ni to have formed squares of 250-450 nm, as a result of the plasma annealing (which was reasonably successful). A sufficient source of carbon was clearly present. Lack of CNTs was considered due to low process temperature.

Experiment 2 used a 50 nm Ta buffer layer on a Si substrate. While this was not within convention to use another transition metal, it was understood that catalytic activity of Ni was greater than that of Ta (apparent from previous experimental CNT synthesis using the same equipment). Deposition of a 5 nm layer of Ni on Ta would likely form regions of the more effective Ni catalyst, limiting CNT growth sites to these regions. Some CNTs were visible under SEM (Figure 5.2.2).

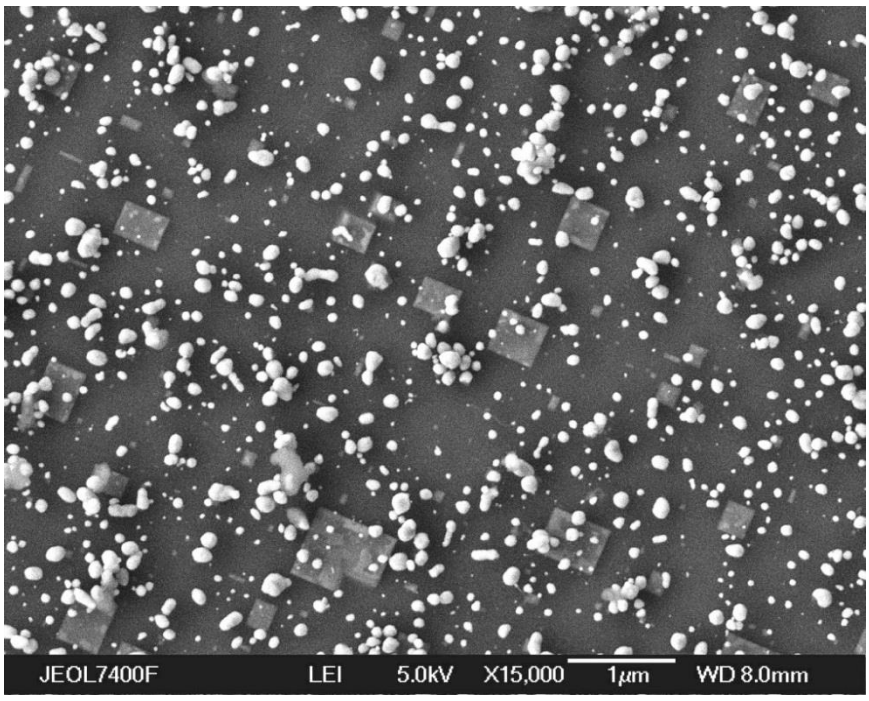

Figure 5.2.1 – Micrograph of CNT Synthesis Experiment 1 (Si wafer, Ni)
This Si substrate shows regions of a-C (round) and Ni (square), no CNTs.

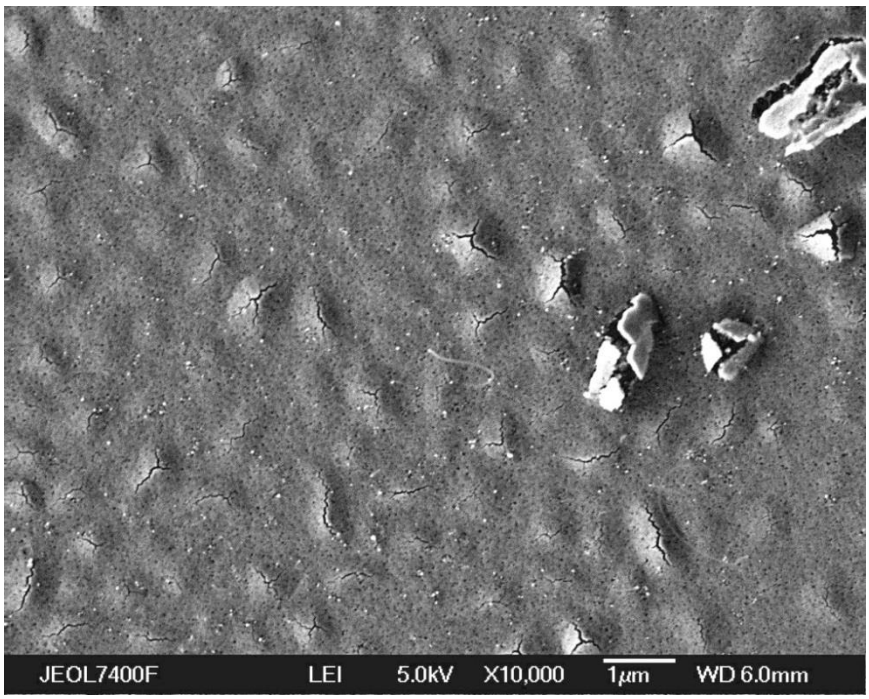

Figure 5.2.2 – Micrograph of CNT Synthesis Experiment 2 (Si wafer, Ni/Ta)
This Si substrate shows surface breakdown of the Ta buffer, traces of CNTs and a-C.

There was some breakdown of the surface (likely of the Ta layer). The distribution of Ni was not clear (white dots were likely a-C). The T readings during this process at the CNT growth stage were only 487-493°C, which was understood to be too low for CNT synthesis. Temperatures > 800°C are generally considered preferable (which is often incompatible with the substrate or other components in terms of melting temperatures etc) [214]. It is well recognised that higher T favours SWCNTs (generally preferred) [214] [224]. Microwave plasma CVD processes elsewhere have achieved synthesis of MWCNTs reported as low as 450°C [213], and SWCNTs at 550°C using a radio frequency magnetron PECVD [214]. From these and other previous work, it was understood that the process temperature was likely not high enough. A target of 600°C was sought, which was considered reasonable in this context [212] [224]. Temperatures generally refer to the substrate surface, although specifically the temperature of the catalyst metal is the important factor, and that of the plasma [213]. The process was attempted again with modifications to the mounting bracket to reduce heat conduction away from the substrate. The element was operated at its rated limit in the previous experiments so it was preferred not to simply increase applied power. Since the heating element was virtually in direct contact with the substrate it was suspected that current loss (through the substrate) was occurring.

This indicated that the electrical properties of SiO_2 would be preferential (i.e. an electrical insulator). By reducing the gas flow in this experiment (affecting the chamber pressure) the removal of heat from the chamber was reduced and T remained higher. Flow rates were kept reduced for the remaining experiments. Pressure and flow rates were understood to be some of several processing conditions that could be experimentally varied to enhance the process [225]. The growth stage process time was increased, expecting to support more dense CNT growth. The substrate was identical to that of experiment 2. The process temperature at the growth stage reached 605-645°C. A significant increase of CNTs was seen under SEM (Figure 5.2.3) and on most of the substrate surface. It was then evident that low T was a significant reason for poor results from previous attempts. Further improvements to the heating element and mounting bracket to increase T were considered.

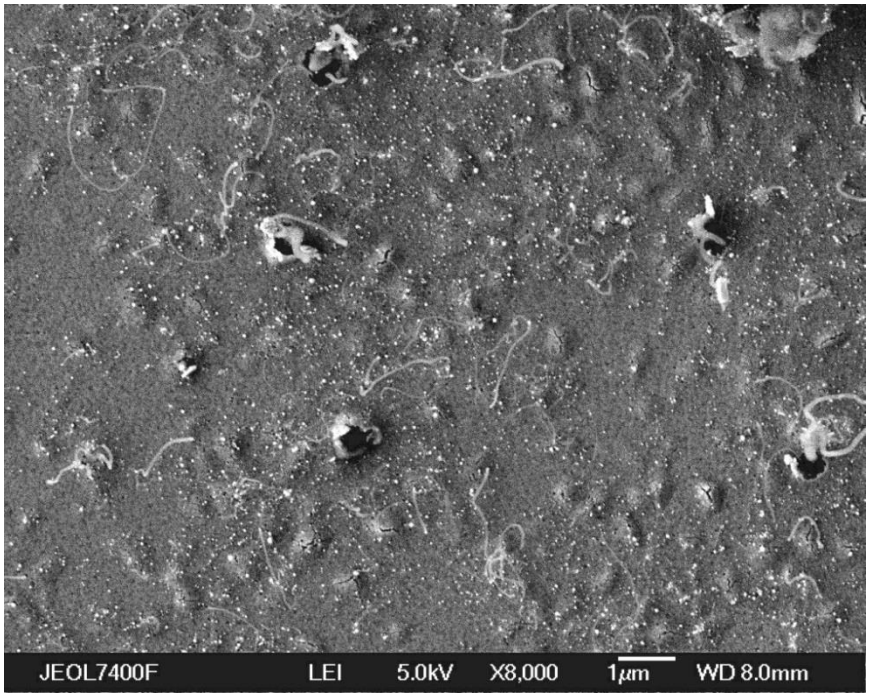

Figure 5.2.3 – Micrograph of CNT Synthesis Experiment 3 (Si wafer, Ni/Ta)
This Si substrate shows surface breakdown of the Ta buffer, traces of CNTs and a-C.

It was also noticed during experiment 3 that RF power was interfering with electrical metering and may have caused inaccuracy with reading of T via the thermocouple etc. A substrate with a SiO_2 surface was considered to be more suitable (insulating properties, stability etc), although this material had not initially available to this work (requiring a process temperature of 1100°C to produce). A Si/SiO2 substrate was later

obtained and the process was attempted two times with 8 nm Ni. Both were unsuccessful, forming a-C (Figures 5.2.4-5.2.5), largely due to heating failure. The second attempt (experiment 5) had CNT growth stage time increased to 480 seconds.

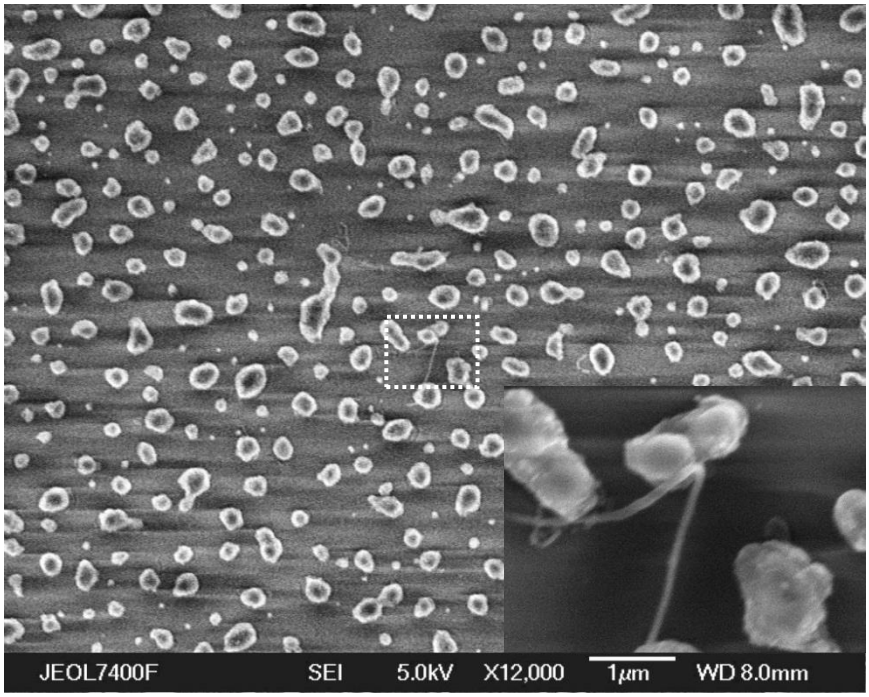

Figure 5.2.4 – Micrograph of CNT Synthesis Experiment 4 (SiO_2 wafer, Ni)
This SiO_2 substrate shows a-C and traces of CNTs, no surface breakdown.

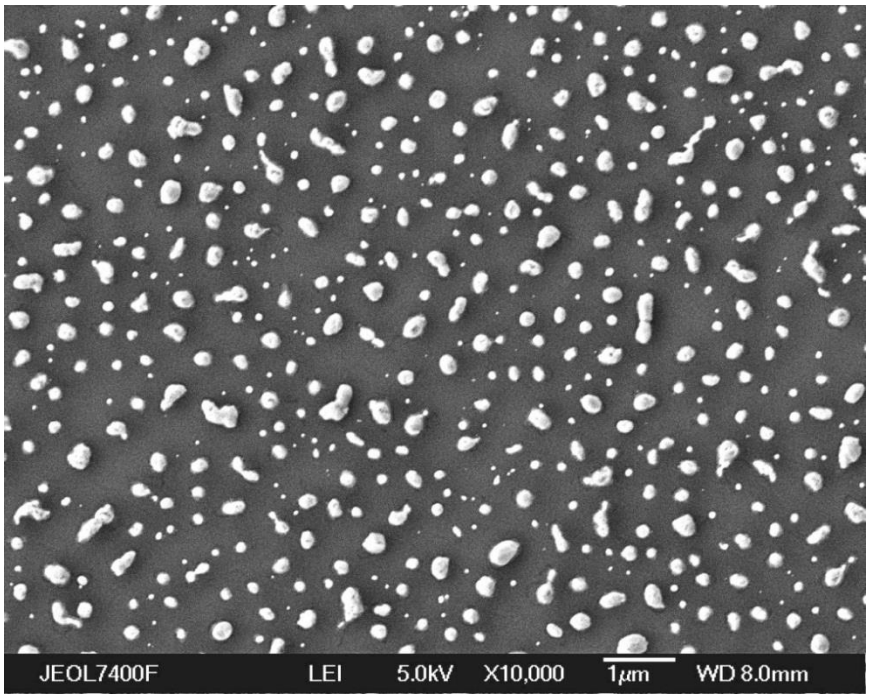

Figure 5.2.5 – Micrograph of CNT Synthesis Experiment 5 (SiO_2 wafer, Ni)
This SiO_2 substrate shows a-C, no traces of CNTs, no surface breakdown.

A modified heating element was formed from Kanthal wire, adjusted and optimised to suit the requirements of the bracket/substrate and the DC supply. It was identified (from basic electrical principles) that wire temperature was proportional to current density squared, and the physical amount of wire (i.e. length of wire in the region of the substrate, or R) also affected the heat/power dissipation. The element was carefully formed to enable increased physical amount of wire, placed directly behind the substrate with concentration of wire at the target area. This element allowed increased V and I (8.5 V, 15 A) and increased heating, and therefore increased T. The Kanthal wire had specific resistance of 1.5 Ω m^{-1} (at 25°C). The length of the wire was experimentally adjusted to suit the heating power and T requirements. Connective cabling was also improved to reduce losses. Reduced gas flow was maintained to minimise heat loss from the chamber. This process then resulted in dense CNT growth on the substrate (Figure 5.2.6), providing a very high surface area as anticipated.

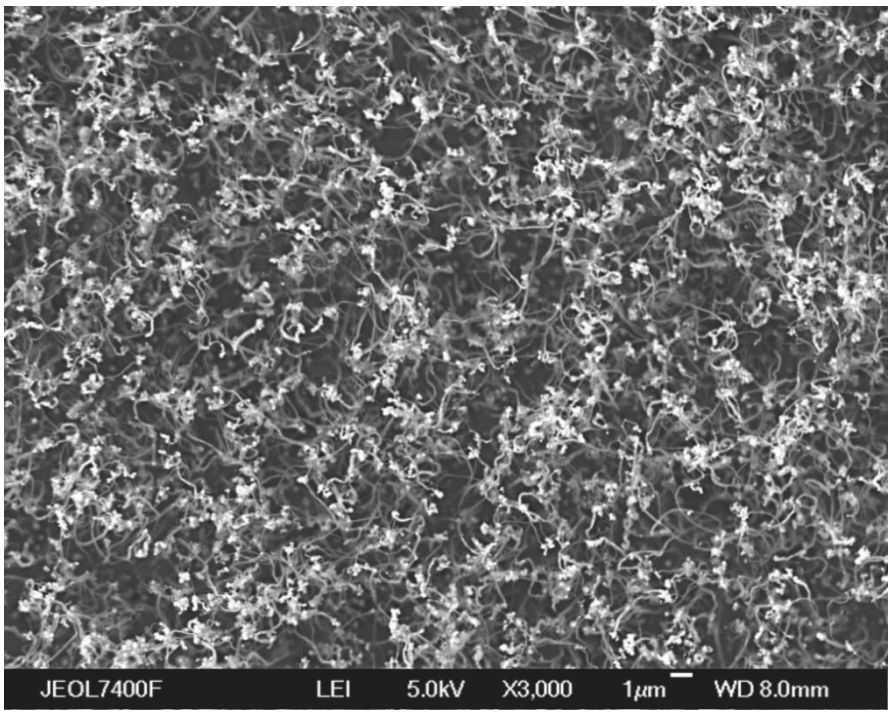

Figure 5.2.6 – Micrograph of CNT Synthesis Experiment 6 (SiO_2 wafer, Ni)
This SiO_2 substrate shows dense CNTs (likely MWCNTs).

The previous experiments demonstrated effective dispersed coatings of Ni were resulting from the NH_3 plasma. Use of Ta did not appear particularly beneficial in these processes. The final experiment achieved sufficient temperature amongst the other necessary conditions, resulting in the synthesis of a dense coating of CNTs.

Exp. No.	Catalyst Ni (nm)	Buffer Ta (nm)	T anneal (°C)	T dep (°C)	C_2H_2 (mL s^{-1})	NH_3 (mL s^{-1})	p dep (Pa)	t dep (s)
1 (Si)	8	-	570	520	1.33	0.33	730	300
2 (Si)	5	50	565	490	1.33	0.33	730	300
3 (Si)	5	50	590	625	1	0.25	270	360
4 (SiO_2)	8	-	590	625	1	0.25	270	360
5 (SiO_2)	8	-	589	574	1	0.25	400	480
6 (SiO_2)	8	-	567	645	1	0.25	400	480

Table 5.2.7 – Table of CNT Synthesis Process Conditions
Details are tabulated for experiments 1-6. Flow rates are 'standard' i.e. relative to STP.

5.2.4 CNT Synthesis Experiment Summary

Experiments to produce CNTs by PECVD were attempted observing critical processing conditions such as presence of a dispersed nanoparticle catalyst (Ni) and sufficient temperature (of the catalyst/plasma). NH_3 plasma annealing resulted in suitably dispersed Ni. Use of a Si/SiO_2 wafer was beneficial in this work due to its lower electrical conductivity (where previous Si substrates were likely conducting current and reducing the temperature of the heating element). C_2H_2 provided a source of carbon, with a NH_3 diluent gas. The most critical factor to allow formation of CNTs in this experimental work was substrate temperature > 625°C.

5.3 Summary

Production of a dispersed TiO_2 photocatalyst substrate was achieved via nanoscale materials processing. CNT synthesis was also achieved on a SiO_2 substrate via a refined PECVD process. These substrates would be suitable for investigation of H_2 production rates, co-catalysts etc, in PCWS/PEC reactions. For example, the CNTs could be coated with Ti and laser processed (or use of sol-gel TiO_2 formation processes etc) leading to a very high active surface area potentially providing enhanced photocatalytic activity.

There are various PCWS/PEC reaction methodologies; however, they are known to be restricted due to recombination, use of UV light, gas separation and other practicalities. At present these processes do not demonstrate effective low-cost renewable H_2 production from solar energy, and are unlikely to be competitive with conventional solar-powered electrolysis processes as discussed in Subchapter 3.4.

6. Conclusion and Recommendations for Further Work

6.1 Conclusion

Replacements are impending for fossil fuels in automotive, grid energy, space heating and industrial applications etc, where renewable H_2 may be an acceptable energy vector. H_2 must be energetically extracted from hydrogen-containing resources. Its volumetric energy density is low, restricting conventional storage. There is inadequate present H_2 infrastructure. H_2 markets are expanding, although use of FCs is restricted by the cost of PGMs. The hydrogen economy is therefore developing at a moderate pace although its future structure remains somewhat uncertain. It requires competitive renewable H_2 production, effective storage, distribution networks and developed end-use platforms. Global H_2 production has reached 100×10^6 tonnes yr^{-1}, almost entirely from hydrocarbon reforming for industrial markets (requiring CO/CO_2 removal for FC applications), reported at 2.8-4.7 \$ kg^{-1} (2010). Only a fraction is used for automotive applications. Cost targets for 2017 set by the USDoE are 2.0-4.0 \$ kg^{-1}, within reach of existing processes. ATR is relatively compact, practical and with lower capital cost, likely to expand into the H_2 production mix in the near-term. Pyrolysis can decompose hydrocarbons to H_2 and C avoiding significant CO_2 emission. BG and CoG processes are likely to expand, particularly where waste heat can be exported (CHP). Renewable H_2 (via electrolysis and BG etc) only accounts for a small fraction of global production. Growth in H_2 demand can be satisfied by existing processes, allowing renewable H_2 to expand into these markets.

Blending H_2 within existing gas networks is one strategy where H_2 can substitute other fuels. Compressed H_2 storage is suitable for many stationary applications, whereas LH_2 is suited to high performance applications. Cryocompression combines compression and LH_2, retaining some inefficiency but superior storage density. Hydrides (of B, Li, N, Mg, Al etc) present high hydrogen densities although are yet to combine sufficient kinetics, uptake at ambient p/T, reversibility or efficiency (thus more suited to single-use). Forming liquid fuels from renewable H_2 is an attractive concept. H_2 cost will eventually reach parity with fossil fuels although competing with battery technology and biofuels etc. H_2 may inevitably be inconvenient and application-dependent (based on technological developments, practicalities, economics and government policy).

ECs (PEM and alkaline) and FCs (PEM) were investigated in this work, observing electrochemical, efficiency and practical aspects. Electrolysis potentially permits efficient H_2 production from electrical energy. Cell reactions have had extensive investigation of catalysts in other work (particularly for the OER), since PGM cost is a significant issue for PEM technology. An EC was created using Ni catalysts (much cheaper than PGMs) and Nafion, involving sputter deposition and laser processing techniques. Test data indicated Ni to be an active catalyst, where Ni on Nafion (or on mesh) produced slightly improved cell performance compared to stainless steel mesh. A 1 nm Ni layer sputtered onto Nafion was found superior in this work compared to 2 nm (although influenced by cell integrity). Novel laser processing of 60 nm Ni on Nafion produced a high surface area of dispersed catalyst; however, testing revealed instability of the coating and inferior performance to unprocessed 1 nm Ni on Nafion.

Renewable H_2 production from wind, solar and biomass resources was considered in this work. Biological H_2 production, specifically mixed-acid fermentation of glucose using E. coli, presents fundamental biological issues (such as low specific H_2 yields, CO_2 production, instability, limited use of renewable feedstocks etc), significant cost and low efficiencies. These are likely to prevent biological H_2 production processes achieving low-cost H_2 production from renewable resources in the near-term. Processes may become more viable with two-stages, such as dark fermentation and photofermentation etc. Photocatalysis processes (various methods of) were researched, revealing low efficiencies, limited use of visible light and recombination/ separation issues restricting application. Photocatalytic materials were produced in this work via laser processing of Ti-coated PEN substrates. A SiO_2 substrate was coated with CNTs via PECVD. These substrates invite further investigation to form and characterise photocatalysts of high surface area/activity for solar-H_2 production via PCWS/PEC processes.

With the exception of BG processes not practically investigated here, wind- and solar-powered electrolysis have been considered the most suitable for low-cost renewable H_2 production at present. Solar energy can also provide heat for electrolysis and thermochemical decomposition cycles, reducing conventional energy requirements. Wind energy is relatively cheap, matching conventional grid energy production costs in many sites (i.e. 0.04 \$ kWh^{-1}). Large grid-connected WTs are preferable, allowing

economies of scale and superior capacity factors etc. Grid-connected WT-ES systems can support balancing of grid energy supply/demand. Micro/small WTs may be grid-independent. WTs and PV require effective control (e.g. of voltage) for maximum power delivery. In a WT/PV case study it was observed that profitability related critically to the siting and equipment integrity (determining energy production), and incentives and on-site energy demand (determining effective energy value).

DC-DC power convertors for micro/small wind- or solar-powered electrolysis were experimentally investigated. Conventional converters were observed to be relatively expensive devices. Correct scaling of WT/PV and ES systems was considered critical to optimise system efficiency and ultimately H_2 cost. MPPT function is mostly based on HCS/P&O for micro/small systems, although algorithms based on lookup data are known to be preferable (requiring system data). Testing of a simple DC-DC convertor and HCS indicated overall efficiency being dependent on three components: circuit power transfer; controller power demand; MPPT effectiveness.

A novel power converter using cell number selection and a lookup MPPT algorithm based on ES current ranges for each cell number was investigated. This demonstrated superior efficiency for the micro WT-ES system tested. A novel hybrid DC-DC convertor was also manufactured using a direct connection MOSFET, MPPT based on lookup, and a variable ES circuit. The hybrid convertor performed with similar efficiency to the cell selection convertor, particularly due to the MOSFET and lookup algorithm (relatively simple to implement). This hybrid converter would be practical for systems of for example 1-50 kW scale, where grid-connection may be involved. Converter efficiencies were approx. 92-95% in the mid ranges for the conventional DC-DC converter, but approx. 94-99% for the novel converters. These converters were of very low cost compared to commercial devices of similar rating. Overall wind-H_2 conversion efficiencies in this work were $\eta \approx$ 20% when $v \approx$ 3-6 ms^{-1}, dropping to 15% when $v \approx$ 10 ms^{-1}, although higher efficiencies would be expected at larger scale.

PV-EC testing with a correctly scaled direct-connected system indicated high efficiency would occur without use of a DC-DC converter. This would very likely offer a low-cost solar-H_2 production route outperforming use of a DC-DC converter in many scenarios. Indicated overall solar-H_2 efficiency was $\eta \approx$ 12-13% at most irradiance values.

From the methods investigated in this work, large grid-connected WT-ES systems (in suitable locations) are suggested to provide the cheapest renewable H_2 production route, also potentially providing grid balancing. For small-scale systems with relatively high cost, reducing the number of conversion steps and simplifying processes (i.e. simple, cheap power conversion) would reduce H_2 production costs.

6.2 Recommendations for Further Work

Deposition of PGM catalysts of thicknesses 3-100 nm onto Nafion would be recommended to investigate optimal catalyst coatings. A stable test cell would be sought with accurate flow measurement to quantify relative performance of each thickness. This may also depend on conditions such as the mesh catalyst, Nafion thickness, operating conditions etc, which would require further consideration. Investigation of laser processing of thicker catalyst coatings would also be recommended to support more accurate work as carried out here. Investigation of strategies to improve stability and further modify catalyst surfaces would be of interest. Similar work could also be attempted for an alkaline cell, with a dispersed Ni coating on electrodes and/or diaphragm if practical.

Testing of micro WTs would be more accurate if a lathe with torque measurement was used to turn the generator, providing accurate efficiency data for various rotational velocities and loadings of the generator etc. This would facilitate measurement of rotor efficiency, and allow a simulation of the generator/rotor performance to be established. For the power converters investigated in Subchapters 3.4 and 3.6-3.7, measurement of MPPT performance and converter efficiency would benefit from testing in variable (i.e. real) conditions. This is very difficult and impractical due to natural variation over time and unrepeatability, difficulties with placing identical WTs very close to one another, and also exact measurement of H_2 flow rates. Tests of this nature would however prove the performance of the algorithms presented in this work. Alternatively a test facility with an exact programmable wind velocity pattern, or more practically a power supply simulating the output of a WT during changing wind trends would be beneficial. Wind is however randomly variable, making exact measurement and comparison of MPPT algorithms inevitably challenging. Further improvement to the MPPT algorithms including an integrated HCS function to support

lookup data during changes of p/T and component wear etc would assist with maintaining optimal MPPT over long periods.

There have been modifications to the basic programmes discussed in Subchapters 3.6-3.7, such as programming the controller to observe the changing trend of wind to assist correct variation of n (to avoid constant switching etc) and coefficients to assist with variation of D to optimise selection of D_{MPP}. These and similar coding/routines could be further investigated and refined to improve the function of the two novel convertors. The lookup algorithms discussed here are deliberately simple and low level; they would benefit from more advanced coding to allow facilitated adjustment to refine and adapt to different WTs. A more refined controller than an Arduino would be recommended for further work to avoid logic errors etc. Pilot testing of a larger scale system would be beneficial to further explore the practicality/economics of optimised WT/ES operation with AC/grid components. A closer investigation of power electrical components for grid-coupling of large WT/ES systems, and the nature of grid balancing, would be necessary to refine the practicalities and economics of systems of large scale. The work in the case study reported in Appendix 3.5 could also be extended to investigate WT/PV payback times across the UK for example.

It was suggested in Section 4.3.1 that use of waste heat would benefit fermentation processes. These processes were observed to be very unpredictable and to respond notably to temperature changes. This may have practicalities and as a result it would be necessary to investigate industrial sites to determine whether these would in fact be suitable to supply heat to a fermenter, in particular for processes using enhanced bacteria that may have very different or sensitive temperature requirements.

Use of XPS facilities to perform surface analysis of the composition of Ti/TiO_2 substrate coatings produced in this work would determine whether these processes are beneficial for production of TiO_2 photocatalysts. In addition, access to a facility (e.g. a UV light source) to test various modified surfaces involving large surface area coatings of TiO_2 would be necessary to assess their performance.

Appendices

Appendix A1.1 – Physical Principles of Hydrogen Energy

A1.1.1 Hydrogen Energy Fundamentals

Hydrogen exists as a light gas (H_2) in any naturally occurring free state. It is non-toxic and odourless. It is highly combustible with oxygen (releasing energy in this reaction without CO_2 etc). H immediately forms diatomic hydrogen (H_2) with weak covalent bonds. Free hydrogen always therefore exists as H_2. The basic process of energy exchange requires O_2 for the reaction

$$H_2\,(g) + ½O_2\,(g) \rightarrow H_2O\,(l)$$

where proceeding to H_2O releases (-)286 kJ mol^{-1} H_2 [26]. This energy (enthalpy) value assumes standard temperature and pressure (STP) of the reactants/products (discussed in A1.1.3 and A1.1.4). Negative enthalpy denotes enthalpy is released in the process (exothermic). The reverse reaction forming H_2 and O_2 requires 286 kJ mol^{-1} (endothermic). The reaction is non-spontaneous, requiring energy to proceed in either direction, making it relatively controllable [27]. Energy can therefore be added to a reserve of H_2O to form H_2 (and O_2). The H_2 can be stored (and the O_2 released). H_2 can then be reacted with O_2 to release energy and form H_2O similar to conventional hydrocarbon fuels but excluding CO_2 emission. This is the fundamental principle of hydrogen energy.

Since H_2 is not abundant in a free state, it must be produced from a source and then reacted to re-release energy. H_2 is therefore an energy storage medium. Data for the physical properties of H_2 are shown in Tables A1.1.1 and A1.1.2. In comparison to conventional fuels, H_2 contains between two to three times more energy per unit mass (for example CH_4 = 55.0 MJ kg^{-1}, H_8C_{18} (octane) = 47.9 MJ kg^{-1}). However, it is a light gas with a low volumetric energy density, very low compared to liquid fuels (CH_4 = 40.0 kJ L^{-1}, H_8C_{18} = 38.0 MJ L^{-1} at STP) [26].

Physical Property	Value
Standard molar enthalpy of combustion ΔH	285.8 kJ mol^{-1}
Enthalpy by mass *(gravimetric energy density)* ΔH_M	141.8 MJ kg^{-1}
Enthalpy by volume *(volumetric energy density)* ΔH_{Vol}	11.67 kJ L^{-1}
Gibbs free energy ΔG	237.1 kJ mol^{-1}
Density ρ	0.08234 g L^{-1}
Molar volume Vol_M	24.48 L mol^{-1}
Molar mass M_M	2.016 g
Relative molecular mass u	2.016

[26]

Table A1.1.1 – Physical Properties of H2 at STP

Physical properties of H_2 extracted from text by Atkins [26].

T (K)	p (atm)	V (L)	n (mol)	M (g)	ΔH (kJ)
298.15	1	1	0.04085	0.08234	11.67
273.15	1	1	0.04458	0.08988	12.74
298.15	0.9869	1	0.04031	0.08127	11.52
273.15	0.9869	1	0.04400	0.08870	12.58
298.15	1	24.48	1	2.016	285.8
273.15	1	22.43	1	2.016	285.8
298.15	0.9869	24.81	1	2.016	285.8
273.15	0.9869	22.73	1	2.016	285.8
298.15	1	12,145	496.1	1000	141,795
273.15	1	11,127	496.1	1000	141,795
298.15	0.9869	12,306	496.1	1000	141,795
273.15	0.9869	11,275	496.1	1000	141,795

Data derived from [26]

Table A1.1.2 – Extended H_2 Physical Properties (from van der Waals Equation of State)

Extended H_2 physical properties relevant to this work, computed using van der Waals equation of state (Eq A1.1.1).

A1.1.2 Isotopes of Hydrogen

The most common isotope of hydrogen, ^1H, having one proton and one electron (can be known as protium), accounts for nearly all natural hydrogen (99.985 atomic%) [226]. As discussed, monatomic ^1H does not exist freely since H atoms quickly form H_2. Most H for consideration here is in the form of H_2O in water bodies. Other natural isotopes with one or two neutrons are known as deuterium (^2H) and tritium (^3H).

Deuterium (D) is stable and accounts for 0.02% atomic percent of hydrogen. H_2O with a high constitution of deuterium atoms is known as 'heavy water' (which can be artificially produced), traditionally used as a neutron moderator (and coolant) in some nuclear reactors instead of normal water or graphite [227]. With two ^2H atoms rather than two ^1H, the greater molecular weight of the water (20u versus 18u) explains the term 'heavy water', about 11% greater mass due to the two additional neutrons.

Tritium (T), exists in trace amounts and is radioactive, decaying to ^3He through beta decay (half-life 12.32 years) [226]. Other heavier isotopes have been formed artificially, for instance by nuclei bombardment of tritium, but decay (to tritium) in a matter of zeptoseconds. The word 'hydrogen' is often used in text in a general manner, or to mean either elemental hydrogen H, or its usual form of diatomic hydrogen gas H_2. Within this thesis, H implies elemental hydrogen (99.985% ^1H). H_2 implies diatomic hydrogen (gas). The next section discusses the effects and conventions of temperature and pressure on the physical properties of H_2.

A1.1.3 Temperature, Pressure and the van der Waals Equation of State

During research it was evident that different conventions for pressure (p) and temperature (T) exist for standard reactions. STP has been stated in most recent good publications as 298.15 K (25 °C) and 1 atm (1.01325 bar) [26]. This is very appropriate for laboratory experimental work. However, STP was noted to be defined as 273.15 K and 1 bar by the International Union of Pure and Applied Chemistry (IUPAC) [228], or other combinations as discussed in [229] and [230]. 1 bar would be convenient in industrial/engineering processes where high p values are experienced, measured in bar; however, a vast amount of processes occur at 1 atm. At least two conventions have thus remained. The pressure difference (1.3%) is not particularly significant, although the temperature difference is (8.4%). The use of per mol, per kg and per L and the above conventions have been resolved in Table A1.1.2 (necessary when handling data from various sources). STP is taken as 298.15 K and 1 atm throughout this thesis. H_2 at 273.15 K has a greater energy density by volume (+9.15%) when compared to that of an equivalent volume at 298.15 K, due to the slight increase in compaction with the lower T. Increasing p also has similar effect. At 290-310 K, H_2 can be treated as virtually an ideal gas and therefore the ideal gas equation can allow sufficient corrections to enthalpy by volume (ΔH_{Vol}) values for shifts in p and T.

However, adjustment of H_2 data for this research was completed with accuracy using the van der Waals equation of state

$$\left[p + \frac{an^2}{Vol^2}\right](Vol - nb) = nRT \qquad \text{Eq A1.1.1}$$

with coefficients a and b being 0.244 L^2 atm mol^{-2} and 0.027 L mol^{-1} respectively for H_2, and the gas constant R = 0.08206 L atm K^{-1} mol^{-1} [26]. For O_2, the a and b coefficients are 1.360 L^2 atm mol^{-2} and 0.032 L mol^{-1}; for CO_2, 3.59 L^2 atm mol^{-2} and 0.043 L mol^{-1} respectively [26]. Note that in this thesis 'Vol' is used for volume due to later work and formulae involving voltage (V) and volume (Vol) in the same discussions/contexts.

The two coefficients account for real gas deviations from ideal: a, the slight reduction in actual volume available to a store of gas, due to its own physical molecular size; b, the slight decrease in pressure observed due to the effect of attractive interactions between molecules. To explain, at standard p and T, the volume of the actual gas molecules (the excluded space) is quite negligible when compared to the complete volume occupied by the gas. But as the density of the gas molecules increases (i.e. with increasing p and/or reducing Vol), the actual physical space occupied by the molecules eventually becomes a significant fraction of the complete volume. Excluded space is larger than the actual molecule diameter due to small-radius intermolecular repulsion forces. And, because of large-radius intermolecular *attraction* forces, the collision speed against the container walls appears less. Therefore a slight reduction in pressure is observed. At high T and low p, however, the molar volume is so large that an^2/Vol^2 becomes negligible and nb can also be ignored. Therefore the van der Waals equation of state can be reduced to that of an ideal gas under those conditions. Furthermore, within the normal range of p and T, the van der Waals equation of state is considered exact (for H_2 and most normal gases) within 4 significant figures [26]. When measuring by Vol, the enthalpy value (ΔH_{Vol}) is relative to conditions of p and T, which must be considered for calculations. Based on the van der Waals equation at STP, H_2 has a molar volume (Vol_M) of 24.48 L and therefore ΔH_{Vol} = 11.67 kJ L^{-1}. There are however alternative conventions relating to enthalpy, free energy and physical state, as discussed in the next section.

A1.1.4 Enthalpy, Entropy, Gibbs Energy and Physical State

Values for enthalpy are typically expressed kJ mol^{-1} in physical chemistry and biology, or MJ kg^{-1} in more applied or engineering contexts. Since physical measurements are often by volume, kJ L^{-1} is very convenient. Convention for the enthalpy of the standard H_2-O_2 reaction is well defined, by Atkins etc [26]. H_2 and O_2 are both required for the exothermic combustion reaction. H_2 is conventionally considered to hold the 'enthalpy', since the H_2 is classed as the fuel source and the O_2 simply a free oxidant. Hence, the term 'enthalpy of combustion of H_2' (or heat of combustion) is used, and rarely '…of H_2 and O_2'. The definition of enthalpy change is the sum of the change in internal energy (U) and change in pressure–volume of the reactants during a reaction, therefore

$$\Delta H = \Delta U + \Delta(pVol) \qquad \text{Eq A1.1.2}$$

U is an extensive property, including the kinetic and potential energies of the electrons and atomic nucleus of the gas species. In the case of H_2 (diatomic) it can have rotational, vibrational or translational energies, and $pVol$ is the work done by the gas on the surroundings to physically exist in that space [231]. However, in combustion such as inside an engine cylinder, p and Vol both vary and $\Delta pVol$ will therefore be a difference of the two products from the initial to final stage along some pathway (automatically taking into account the energy lost and gained as expansion work). At constant p, which is often the case (atmospheric gases, biological processes etc)

$$\Delta \mathrm{H} = \Delta U + p\Delta Vol \qquad \text{Eq A1.1.3}$$

ΔU can be defined as

$$\Delta U = w + q \qquad \text{Eq A1.1.4}$$

where w is the transfer of work (within the gas) and q is the transfer of heat. Importantly, q can be considered as disorderly motion, and w as orderly motion [26]. At constant Vol (since no work can transfer)

$$\Delta U = q \qquad \text{Eq A1.1.5}$$

At constant p

$$\Delta U = q - p_{Exp}\Delta Vol \qquad \text{Eq A1.1.6}$$

and thus (from Eq A1.1.3)

$$\Delta H = q \qquad \text{Eq A1.1.7}$$

Where p_{Exp} is the pressure of the internal system (at which expansion work is done, and in this case equal to p). It is not possible to measure the actual H or U values for a sample of gas. The ΔH or ΔU values however are relatively easy. ΔH of a reaction can be measured by monitoring ΔT that occurs following a reaction at constant p, using a adiabatic flame calorimeter [230], or using a bomb calorimeter, a device in which heat is transferred (and measured) at constant Vol. The latter will only provide ΔU, but $\Delta pVol$ can be substituted sufficiently with $nR\Delta T$ (from the ideal gas equation) [26]. The enthalpy of combustion can also be understood from reference data values, by calculating the difference of the standard enthalpies of formation (ΔH_F) of the products and reactants (Hess's law) [26] [27]. The value of ΔH is concurred by either method above. In the case of combustion of H_2 and O_2, the reactants are H_2 (g) and $½O_2$ (g), and the product is H_2O (l) in the standard reaction:

$$H_2\,(g) + ½O_2\,(g) \rightarrow H_2O\,(l)$$

The final result of the reaction is the same irrespective of the path(s) of the reaction. This is an important concept that is often omitted in discussion, particularly of electrolysis and fuel cell processes. There are different conventions in literature relating to this reaction. It is noted that, in the above reaction, going from left to right, H_2O can form at a range of values of T, p, and either gas or liquid state. An energy process involving this reaction, which for example results in the H_2O reaching a high T and gas phase, may not be able to take useful energy from the later cooling or condensation. The STP heat capacities of H_2O are 75.3 J K^{-1} mol^{-1} (l) and 36.2 J K^{-1} mol^{-1} (g) and the enthalpy of vaporisation (+) or condensation (-), ΔH_{Vap}, is 40.7 kJ mol^{-1}) [26]. Therefore if the product exits the reaction at a higher energy state by virtue of its T, p, or physical state, then the ΔH available to the reaction is reduced. However, the properties of the reaction and ΔH have not changed, simply the nature of the process being that it does not extract all of the useful energy. This has been manipulated for processes in the past, resulting in lower values for ΔH being substituted into efficiency calculations. This practice is unhelpful and incorrect for full energy analysis. This thesis strictly observes the correct convention and absolute values. It is shown in

Chapter 2 that the basic fuel cell reaction cannot extract useful work equivalent to ΔH. This is due to entropy (S), physical phase, and other losses. It has been important to understand entropy in the context of this research, or within energy physics, thermodynamics or physical chemistry. Entropy holds definitions in terms of statistical mechanics or thermodynamics. The Boltzmann equation provides the statistical definition

$$S = kln(W) \qquad \text{Eq A1.1.8}$$

where k is Boltzmann's constant and W is the number of different ways in which the energy of the system can be achieved by rearranging the atoms or molecules among the states available to them [230]. Avogadro's number (N_A), R and k are linked by $R = N_A k$ [231]. The Boltzmann equation infers that a perfectly ordered system where there is only one state has zero entropy, since $W = 1$ and hence $S = 0$. With the number of states known, the entropy of a sample of gas can be calculated. The definition of S within thermodynamics originates from the Carnot cycle [26]. Again, it is more practical to consider ΔS rather than S, whereby for a reversible transfer of heat (q_{Rev})

$$\Delta S = \frac{q_{Rev}}{T} \qquad \text{Eq A1.1.9}$$

At constant p

$$\Delta S = \frac{\Delta H}{T} \qquad \text{Eq A1.1.10}$$

A useful way to consider this is the fact that heat flows from hot to cold and never the opposite. At molecular level this makes perfect sense since molecules with high kinetic energy will transfer to those with low kinetic energy statistically much more often than the reverse. A change in entropy is therefore proportional to the energy transfer that takes place making use of disorderly motion. Since a high T infers more disorderly motion present within the process, it follows that for a quantity of energy stored at high T, there is less significance from the added disorder, and therefore less entropy per unit of energy than there would be for the same quantity of energy stored at lower T, hence the T term in Eq A1.1.10 [230]. This infers that spontaneous exchange of energy will occur between bodies of different T, leading to an increase of S. The net result of any reaction is therefore the tendency for S of a gas and its surroundings to

stay the same or increase. Basic principles such as force, momentum, potential and kinetic energy drive the spontaneous nature of change, such as from hot to cold or the expansion of a gas into a region of lower pressure, not the change of energy itself. The apparent driving force for the spontaneity of reactions to proceed is the tendency for energy and matter to become disordered and entropy to increase [26].

In the H_2 reaction, the overall ΔS value is negative (-163.4 J K^{-1} mol^{-1}), since the reactants are gases (with high S) and the product is liquid (with lower S). This does not contradict the previous statements, but that the surroundings must be taken into consideration. The formation of H_2O causes the surroundings to be disordered in some way and expand into the space formed from gases becoming a compact liquid. ΔH has therefore been supplied to and taken from the surroundings, therefore there must also be ΔS, as defined by Eq A1.1.10. The reaction results in ΔS of the surroundings increasing by 958.7 J K^{-1} mol^{-1}, therefore the net increase of entropy ΔS_{Net} = +795.3 J K^{-1} mol^{-1}, as shown in Table A1.1.3 for the $H_2 + ½O_2 \rightarrow H_2O$ reaction. This ΔS value must be taken into account when considering real processes, as it represents a limit to the transfer of useful energy and therefore the limit of the efficiency of a system.

Species	ΔS (J K^{-1} mol^{-1})
H_2 (g)	130.7
O_2 (g)	205.1
H_2O (l)	69.9
H_2O (g)	188.8
Reaction (net)	(+)795.3

[26]

$$\Delta S = \sum S(\text{products}) - \sum S(\text{reactants})$$

= 69.9 – (130.7 + ½×205.1) J K^{-1} mol^{-1}

= -163.4 J K^{-1} mol^{-1}

$$\Delta S(surroundings) = -\frac{\Delta H}{T}$$

= 285.8 ×10^3 J mol^{-1} / 298.15 K

= +958.7 J K^{-1} mol^{-1}

Therefore net ΔS = +795.3 J K^{-1} mol^{-1}

Table A1.1.3 – Hydrogen-Oxygen Reaction Entropy Change (with calculation)

The Gibbs energy (ΔG) is a state function that considers the 'free' ΔH taking into account ΔS [231], where

$$\Delta G = \Delta H - \Delta(TS) \qquad \text{Eq A1.1.11}$$

and at constant T

$$\Delta G = \Delta H - T\Delta S \qquad \text{Eq A1.1.12}$$

It is derived from ΔG that a maximum amount of useful work (w_{Max}) can be obtained from this reaction [26]. Observing Eq A1.1.4 and Eq A1.1.12, at constant T and p, for an infinitesimal change

$$dG = dw + dq + pdVol - TdS \qquad \text{Eq A1.1.13}$$

Within the dw term, there may be internal expansion work (-$pdVol$) and non-expansion work ($d'w$). Non-expansion work is the free energy that is available for useful work, such as electrochemical work within a fuel cell. Therefore

$$dG = -p_{Exp}dVol + d'w + dq + pdVol - TdS \qquad \text{Eq A1.1.14}$$

By considering a reversible process where $dq = TdS$, and $p_{Exp} = p$ (constant), then

$$dG = d'w \qquad \text{Eq A1.1.15}$$

therefore

$$\Delta G = w'_{Max} \qquad \text{Eq A1.1.16}$$

This concept is fundamental to the discussion of fuel cell efficiency explained within Chapter 2. Specifically this applies to the maximum electrical energy available from a fuel cell reaction. In practical terms, the ΔH value can be divided into useful work, other work, and heat. Useful processes may therefore be fundamentally limited by the w'_{Max} component and thus ΔG. At STP, constant T and p, ΔG = -237.1 kJ mol^{-1} for the H_2 reaction, which is 83.0% of ΔH [26]. To conclude this, it is noted that there is a convention where ΔH may be referred to as the 'higher heating value' (HHV), and a 'lower heating value' (LHV) then used as an arbitrary alternative. A 'LHV' has been found defined or used as ΔH - ΔH_{Vap} or ΔG in numerous texts [11] [15]. In discussion of energy and efficiencies of processes, the use of the LHV is not accepted as correct in

good literature [27]. This appears as somewhat of a bad legacy and from lack of attention to the fundamentals of the energy process. In more recent years this has been partly the fault of some deficient publications by the US Department of Energy.

The next section briefly disuses the *quantum mechanical* energy states of the H atom.

A1.1.5 Quantum Mechanical Energy States of the Hydrogen Atom

The H atom has several permitted energy levels. The emission spectrum of the H atom has five series (named Pfund, Brackett, Paschen, Balmer and Lyman). As a light source, due to collision ionisation, H_2 is converted to H (in a spectral tube). Electrons from the H atoms are excited to higher energy levels through collisions. On returning to lower energy levels the atoms emit light of frequency given by the energy difference of the two states ($E = hf$), the *Bohr frequency condition*. The Balmer series is the only one within the visible range, of which four of the spectral lines are clearly visible. After the fourth line, the emission is weak and tending towards UV. The Balmer lines begin at 656 nm and converge at 300 nm. The discrete lines exist due to the quantisation of energy of an electron in the H atom, fitting the Bohr model. The energy E_n of a permitted electron orbit is given by [26]:

$$E_n = -\tfrac{1}{8}\frac{e^4 m_e}{\varepsilon_0^2 h^2 n^2};\ \ n = 1, 2, 3 \ldots \qquad \text{Eq A1.1.17}$$

where ε_0 is the permittivity of free space, e and m_e are the electron charge and rest mass. The emitted light can therefore have frequencies (f_{nm}) obtained from

$$f_{nm} = \tfrac{1}{8}\frac{e^4 m_e}{\varepsilon_0^2 h^3}\left(\frac{1}{n^2} - \frac{1}{m^2}\right);\ \ n, m = 1, 2, 3 \ldots \qquad \text{Eq A1.1.18}$$

This can be represented by an expression with the use of the Rydberg constant, R_{th}. Substituting for λ, one obtains

$$\lambda = \left[R_{th}\left(\tfrac{1}{n^2} - \tfrac{1}{m^2}\right)\right]^{-1} \qquad \text{Eq A1.1.19}$$

where

$$R_{th} = \tfrac{1}{8}\frac{e^4 m_e}{\varepsilon_0^2 h^3 c} \qquad \text{Eq A1.1.20}$$

R_{th} has a value of 1.097×10^7 m^{-1}. The n and m series must proceed with $m > n$. The Balmer series occurs where n = 2. The associated energy is the ionisation energy (or binding energy) for an electron in the nth permitted orbit. The quantum mechanical structure of the H atom is based on Rutherford's *nuclear model*. The Schrödinger equation can be solved to determine the binding energy levels (relative to a proton and infinitely distant stationary electron), within appropriate boundary conditions, such that the wavefunction must not become infinite and that it must repeat itself as the nucleus/proton is circled around. From these boundary conditions, only certain energy levels can occur, which is in accordance with the observed spectroscopic emission lines. The binding energy can be calculated by means of the equation

$$E_n = -R_{th}hc\frac{1}{n^2} \qquad \text{Eq A1.1.21}$$

The ground state (n = 1) is therefore found to be 13.59 eV. Figures A1.1.1 and A1.1.2 graphically show the H spectra and binding energy levels.

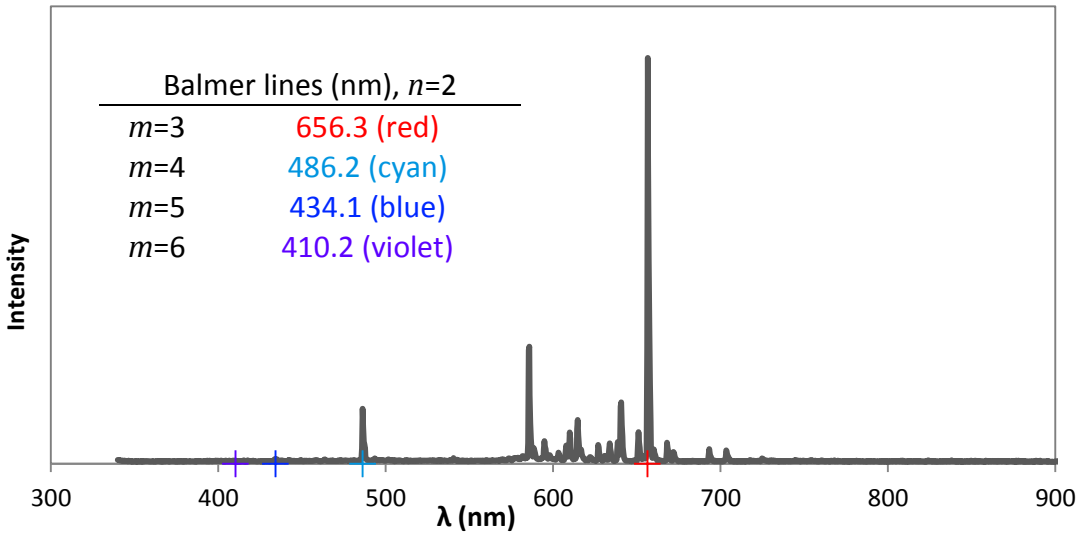

Figure A1.1.1 – Atomic Hydrogen Spectra
Graphical data of intensity against wavelength for first four Balmer lines produced from H tube and MeasureSpec optical fibre spectrometer. Additional lines (i.e. 585 nm) are from the H_2 molecule, having rotational and vibrational components.

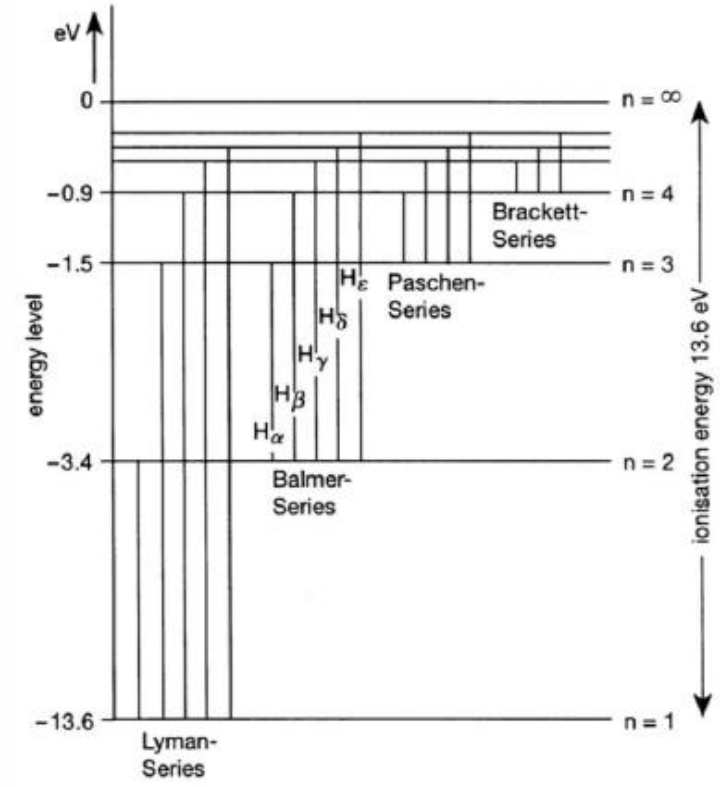

Representative of that shown in [26]

Figure A1.1.2 – Atomic Hydrogen Energy Levels
H energy levels showing five series, where H_α, H_β, H_γ etc label the permitted energy levels in the Balmer series for example. These can be reproduced using Eq A1.1.19.

Appendix A1.2 – Nanotechnology

Research for this thesis involved use of nanotechnology as a supporting novel theme. Nanotechnology offers significant scope for improvement of material properties, processing and imaging/analysis techniques, such as 'single-step' deposition and processing of catalytic layers onto electrolyser/fuel cell membranes/electrodes or photocatalysts for example. This research involved use of:

- Scanning electron microscopy (SEM)
- Atomic Force Microscopy (AFM)
- Transmission Electron microscopy (TEM)
- Energy-dispersive X-ray spectroscopy (EDX)
- X-ray photoelectron spectroscopy (XPS)
- Sputter deposition and plasma-enhanced chemical vapour deposition (PECVD)
- Excimer laser processing

A1.2.1 Scanning Electron Microscopy

SEM techniques can provide nanometre resolution of samples [232]. They operate with a high voltage electron gun within a column (to provide a source of high velocity electrons to strike a target sample) and electron detectors (to detect the electrons deflected from the sample). The electrons are accelerated under a potential of 1-30 kV, and collimated by electromagnetic condenser lenses, focussed by an objective lens, and finally rastered across the sample surface by the scanning coils. Secondary electrons (SE) and backscattered electrons (BSE) are emitted from the sample (from the spot irradiated by the electron beam), which are collected by the detector(s) and used to generate image data. The column and detector arrangement and nature of SE/BSE emission are shown in Figure A1.2.1.

Therefore, SEM relies on a beam of electrons striking the sample surface and being deflected onto a detector to provide the same role as light incident on a sample and reflected to a viewing lens in the case of optical microscopy. Optical microscopes are ultimately limited by the wavelength of visible light (≈ 550 nm) and numerical aperture (maximum NA ≈ 1.5) of the lens, whereas an SEM can resolve 1000× beyond that [233].

The Jeol JSM 7400F is a field emission high resolution SEM, used for this research (integrated with EDX capability, which uses the secondary processing/display). This SEM was operated with two computer processing systems and two displays, where real-time digital imagery could be obtained (display size = 32×24 cm, 1280×1024 pixels). The imaging process is generated by a point to point method, where an electron beam scans across the sample and produces point information to the detector, which is then processed and sent to the display. The JSM 7400F detectors are analogue devices. The sample image data is generated in a continuous analogue stream, as shown in Figure A1.2.2, and then converted to digital, pixel by pixel, rather than as one complete ‘full-field’ image at a time. This scanning action allows a small beam and detector to produce a relatively large and detailed image.

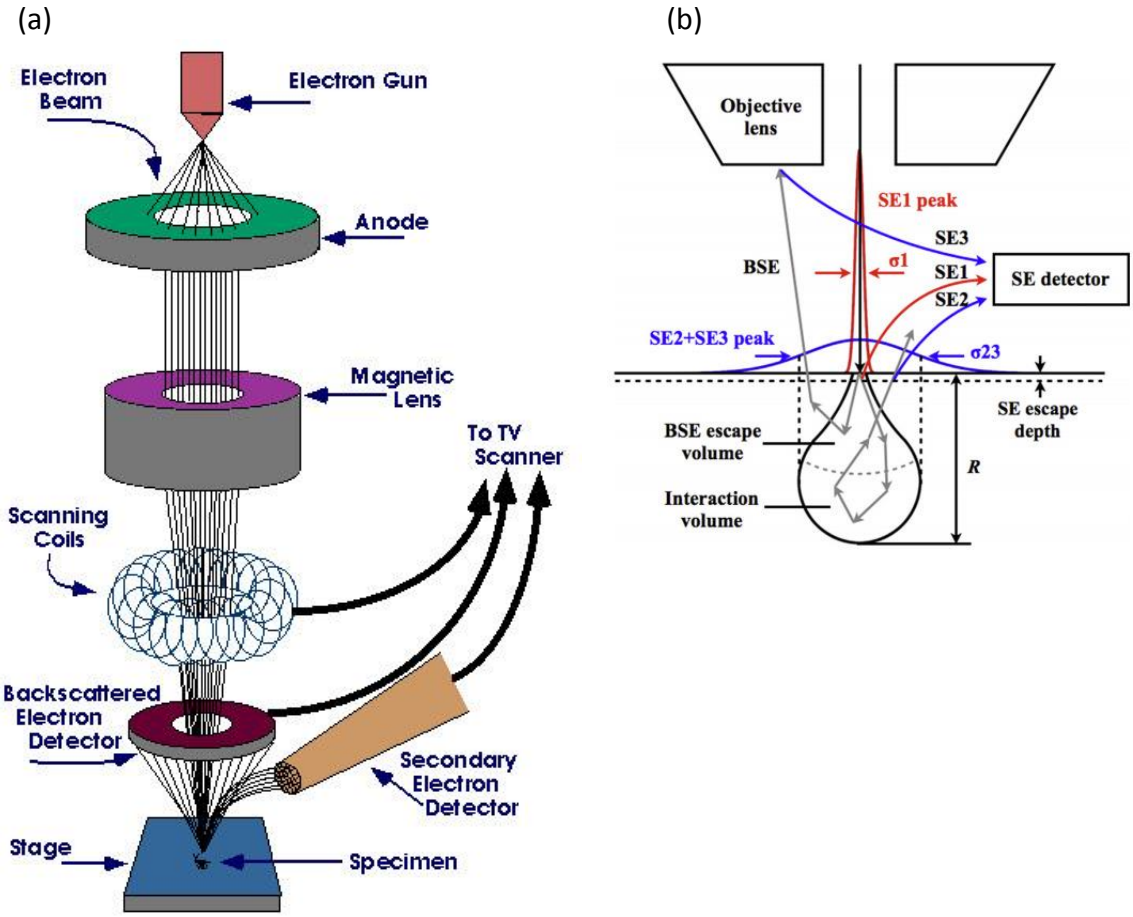

[234-236]

Figure A1.2.1 – Scanning Electron Microscope Column & Detector Arrangement
In (a), an SEM column is shown from the top-mounted electron gun, two detectors, through to the sample holder at the bottom stage. In (b), the depth of interaction with the sample of secondary electrons (SE) and back-scattered electrons (BSE) is shown.

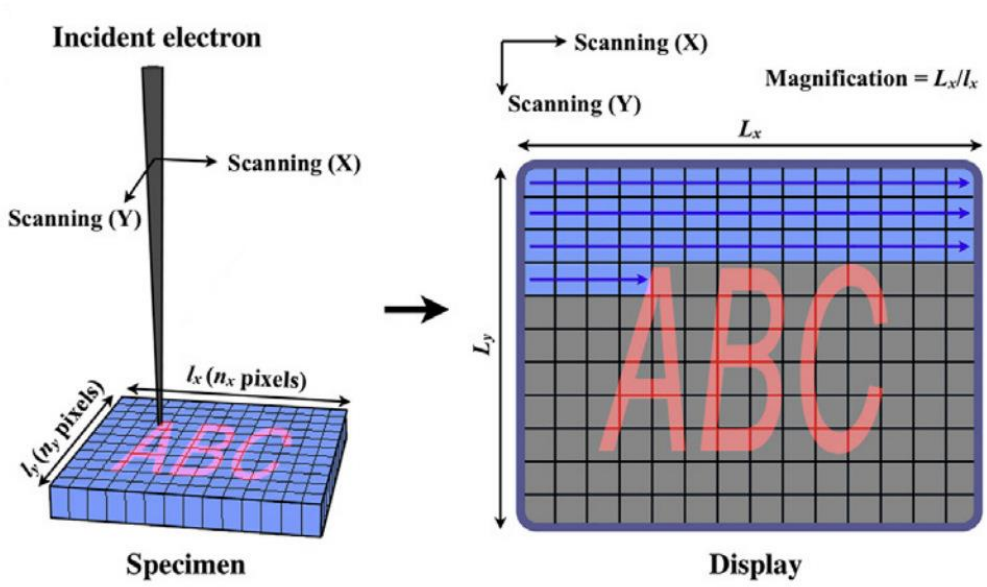

[236]

Figure A1.2.2 – Scanning Electron Microscope Imaging Process
SEM imaging is formed from scanning of an electron beam across the sample surface.

Maximum resolution is stated as $\times 10^6$, 1 nm [234], although it is necessary to clearly distinguish sample features on the monitor and this requires a reasonable cluster of pixels. At full magnification, one pixel width can therefore represent a dimension ≈ 0.25 nm. Resolution of one's eye and the ability to perceive fine detail is termed *resolving power*. The smallest separation between two points able to be detected is termed the *limit of resolution*. This is due to the physical size of the eye (≈ 2 cm), with spacing of receptors at the centre of the retina ≈ 3 μm (the most sensitive region, consisting only of cones). Assuming it necessary to fully span two receptors and that an object/image is brought as close to the eye as possible (≈ 20cm) remaining in focus (the *near point*), then this corresponds to approx. 50 μm [237]. Thus viewing a monitor (48cm, 1280×1024) at 60 cm just allows the eye to resolve individual pixels.

More recent versions of this SEM (JSM 7500F etc) utilise higher resolution displays up to 5120x3840. Ultimate limitation arises from the size of the scanning electron beam and the quality of the detectors. For the JSM 7400F the beam size can be reduced to ≈ 0.1 nm. The beam must be less than half of the size of a feature in order to resolve it. Therefore, taking into consideration any error probable at this limit of operation, the scanning system can reasonably resolve features of 1 nm on a sample and generate reasonable image data from a 0.25×0.25 nm region of the sample to a screen pixel.

The sample must be fixed to a loading platform, in a vacuum condition (10^{-4} Pa) to prevent electrons striking air molecules and affecting the scanning process. The shape of the electron beam can also be adjusted to correspond to varying altitudes of the sample. The vacuum is held in the lower part of the sample chamber by a beryllium disc. This is to prevent the entire column dumping pressure when the sample is exchanged.

In this research the JSM 7400F was used for the following analyses:

- Imaging/EDX of scrubbing material properties (size, form, etc)
- Imaging of E. coli bacteria
- Imaging/EDX of carbon nanotube synthesis on Si and SiO_2 substrates
- EDX of Ni electrode plates (from alkaline electrolyser)
- Imaging/EDX of PEN substrates with laser processed Ti/TiO_2 surface
- Imaging/EDX of Nafion substrates with laser processed Ni surface

A1.2.2 Atomic Force Microscopy

AFM and TEM facilitates were available in the NMRL for this research. Both of these microscopy systems are capable of producing micrographs with sub-nanometre resolution [232] [238-241]. AFM operates using an atomic-sized probe on a cantilever, which can be moved along the surface of the sample recording changes of topology, as shown in Figure A1.2.3. There are three main modes of AFM operation:

- Contact mode (i.e. operating with physical repulsion from the surface atoms to provide a reading of the surface)
- Tapping mode (where the probe is oscillated up and down on the surface and records the relative change of oscillation; specifically the forces required to maintain a constant oscillation)
- Non-Contact mode (which avoids physical contact with the surface and relies on weak repulsion forces close to the surface to vary the resonant frequency of the cantilever. The correction of this provides the reading).

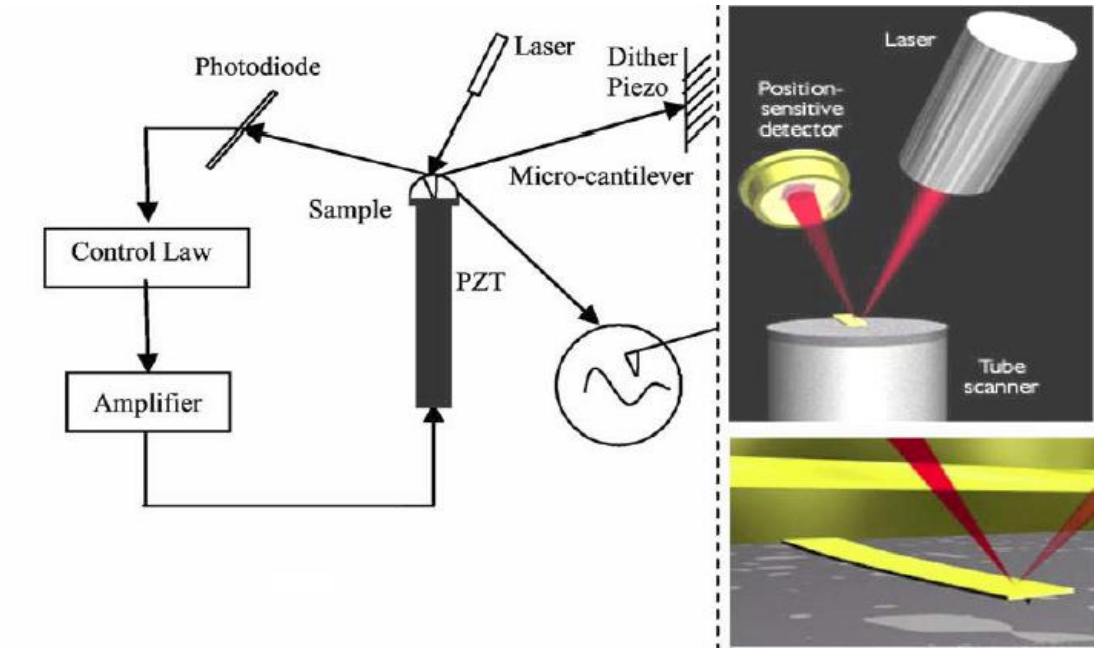

[241]

Figure A1.2.3 – Schematic of Atomic Force Microscope Laser/Cantilever/Detector
AFM uses a laser reflected from the surface of a micro-cantilever moved along the sample surface. A photodiode maps the laser beam and therefore the changing surface topology, allowing an image of the sample to be formed.

The latter two AFM modes minimise damage to the sample and probe. Tapping mode is specifically useful for measuring a sample where some moisture may exist on its surface. The process does not require vacuum conditions, therefore it is useful for imaging of biological materials [241]. Both AFM and TEM are capable of very high resolution processes, which can resolve individual atoms [232].

A1.2.3 Transmission Electron Microscopy

TEM is similar in principle to SEM, but relies upon a beam of very high velocity electrons striking the surface, penetrating the sample, which can then be detected below the sample (rather than by deflection, such as in the case of SEM). The working difference between TEM and SEM are the requirement for a thinner sample (to allow transmission of electrons) in the case of TEM, the higher accelerating voltages (100 kV compared to 10 kV for SEM), and the higher resolution of TEM (typical working resolutions of 0.1 nm rather than 1nm). SEM is however more versatile and less destructive, being able to image larger areas, provide additional surface analysis (such as EDX), and work with much larger/thicker samples due to only requiring the deflection of electrons.

A1.2.4 Energy Dispersive X-ray Spectroscopy/X-ray Photoelectron Spectroscopy

EDX capability was provided for this research integrated within the JSM 7400F SEM. The principle of EDX and XPS is to produce surface elemental composition analysis of a sample. The JSM 7400F within EDX function produces a digital/graphical report of atomic and mass percent/distribution of elements of the sample surface under examination, relative to approx. 5 µm depth and a surface area from approx. 1 nm^2 to several mm^2 as required. The EDX function of the JSM 7400F is not described in detail within the manual although its function is fairly standard. The EDX function shares the same electron gun as the SEM (having the two devices housed together is quite practical for a modern SEM). Samples are targeted with a pulsed electron beam. As a result of pulsed electrons striking the surface of the sample material, characteristic X-rays are emitted from the surface. Characteristic X-rays occur due to outer electrons of the atoms on the sample's surface becoming ionised by the high energy electrons from the electron beam [242]. The ionised and excited atom can then reduce to a lower energy level if for example an outer shell electron has been removed and then filled by another electron from a higher energy state. The release of energy emits an

X-ray photon. Each element therefore has a characteristic X-ray emission spectrum, based on the permissible energy levels. The previous Figure A1.2.1 shows a volume of the material where secondary and backscattered electrons may be released from during SEM mode. This entire volume can generate X-rays for the EDX analysis. This therefore provides composition analysis up to depth of approx. 5 µm.

The X-rays are mapped by a Si(Li) drift detector through a three-stage process [243]. The detector is based on a p-n junction with a high voltage bias across it (such as 1 kV). An example drift detector is shown in Figure A1.2.4. The purpose of the Li is to widen the p-n transition region to improve the X-ray capture ability of the detector [233]. An X-ray ionises one of the atoms within the semiconductor crystal, transferring charge proportional to the X-ray energy in the form of electron-hole pairs. This may be thousands of electron-hole pairs, when considering that the effective bandgap of the detector is 4 eV and an X-ray may have 8,000 eV. The charge displacement is then converted into an amplified voltage signal by the FET preamplifier and then the signal is fed into a pulse processor for measurement. Therefore the X-rays striking the detector can be analysed based upon comparison of their energies to that of reference data for elements. The EDX output is a count of X-rays matching known data and therefore individual elements and overall composition percentages can be determined. The process requires very high accuracy and must minimise background noise, from thermally generated electron hole pairs, low energy X-rays etc. Noise reduction is achieved by cooling the detector to approx. 140 K [233]. Most materials have more than one characteristic X-ray energy level, which assists accurate detection. Analysis of the two lightest solid elements within a material sample is not practical partly due to the use of Be within the detector to form a seal (to prevent any moisture condensing on the detector; Be transmits most X-rays except very low energy ones), which leads to interference with EDX function. The lightest detectable element is B. Therefore EDX operates on the principle of electron bombardment of a sample to produce X-rays, which can be quantifiably measured and mapped in order to determine the composition of the surface of the material. The data is based upon pure elemental composition, not being specific to the structural form and bonding between the elements. For example, TiO_2 reports as Ti and O by elemental composition, but it would not be possible to determine the actual form (i.e. TiO_2 or simply Ti and O etc).

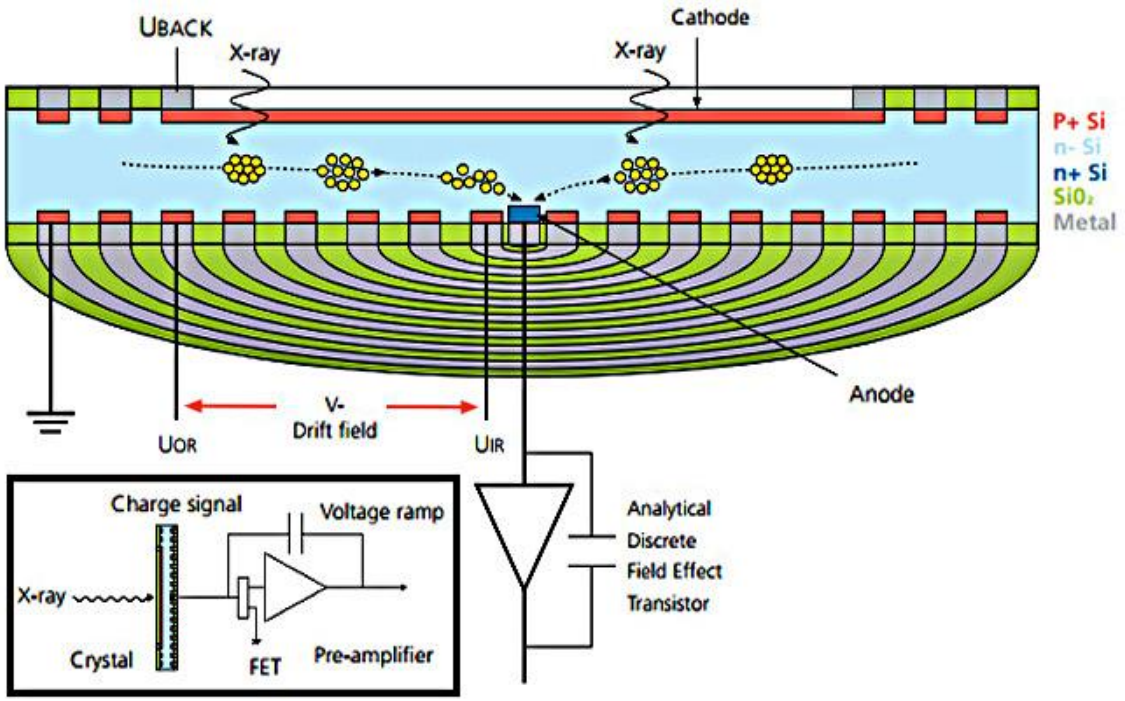

[243]

Figure A1.2.4 – Si(Li) Drift Detector and Voltage Amplifier
X-rays are mapped by charge proportionality in the drift detector and amplified to produce a signal suitable for the EDX detector.

For XPS, a much shallower sample analysis depth is typical. In the case of the VG HB 100 device (located in NMRL), the surface analysis is most pertinent to a depth of approx. 2-10 nm. In addition, XPS can determine the nature of the material composition, as in the TiO_2 example above. XPS functions with X-ray-to-electron generation, the opposite approach to EDX. The device targets the sample with a specific X-ray emitted from an excited metal source (Mg or Al), which excites electrons from within the surface atoms of the sample. Some of the electrons that absorb the X-ray energy release from their atom (photoelectrons) and some escape from the surface of the material (photoemission), with energy levels therefore equal to that of the source X-ray minus the binding energy and material work function [244]. Therefore the binding energy can be established from the maximum kinetic energy of an emitted electron. The maximum values occur from the surface atoms, whereas further below the surface the electrons tend to collide and lose energy. Therefore the detected energy levels of the electrons span a range of values, but peaking and sharply falling at a certain point, indicating the binding energy. The process requires ultra-high vacuum conditions to prevent the electron losing energy via collisions with air

molecules. The choice of X-ray source and energy value is such that it is sufficiently high enough to excite core-level electrons of all elements (> 1 keV), be a relatively clean X-ray (i.e. monochromatic), the characteristic X-ray linewidth should be narrow in comparison to the core-level linewidths and chemical shifts to be observed, and the material is practical (i.e. conductive, stable etc). This results in only two materials being suitable; Mg and Al, whose X-ray energies and linewidths (K_α) are 1253.6 eV, 0.70 eV, and 1486.6 eV, 0.85 eV respectively [244]. The use of both Mg and Al as X-ray source materials is common. The photoionisation of the atoms also causes 'Auger electrons'. This refers to the phenomenon of electrons being ejected from the atom rather than a photon when lower energy bands are filled by a higher energy electron. The energy of which will be constant when either X-ray source is used. Therefore when the source X-ray is changed, the data will be handled with a different value and the Auger electrons will therefore appear to change in energy, whereas the photoelectrons will remain constant. This allows the sample data to be determined with the identification of the unhelpful Auger peaks, which may be similar to photoelectron peaks in one of the X-ray modes and difficult to distinguish [244].

The detection of electron (kinetic) energy is achieved with a hemispherical energy analyser [245], shown in Figure A1.2.5. This device employs two concentric curved electrodes that enclose the path of the electron. A potential is applied across the two electrodes, such that an electron will have a specific tendency to curve its pathway between the electrodes. The kinetic energy will determine the distance that the electron can travel, whether it strikes an electrode or reaches the sensor positioned between the electrodes at the end of the path. By varying the potential, the device can scan through the range of electron energies, whereby the intensities of each energy level can be mapped. Ultimately this leads to a distribution of intensity versus energy level. The energy levels are produced with various peaks, where the binding energy of the element can be identified. In addition, in order to detect the nature of the elements, such as individual atoms or bonded structures such as TiO_2, the distribution can be observed in terms of the *chemical shift* [245]. It was observed during the early development of XPS analysis that materials with the same composition would display slightly different binding energies, depending on the oxidations state, lattice position etc. This effect can be modelled with some simplicity

by considering the atom to be a hollow sphere with (valance) charge (q) on the surface and therefore the potential is equal at all points inside, where r is the average valance orbital radius [245]. If q or r change then q/r changes proportionally/inversely etc, and therefore the binding energy (E) of a core atom i changes, observing that

$$E_i = E_i^0 + kq_i + \sum_{(i \neq j)} \frac{q_i}{r_{ij}} \qquad \text{Eq A1.2.1}$$

where E_0 is a reference energy value and j represents the surrounding atoms, of distance r_{ij}. The exact nature of the shift needs to account for polarising effects. Values for chemical shift are documented and graphically represented in text [246]. The depth of detection is limited due to electrons having several orders of magnitude more tendency to be stopped than that of the X-rays. Only near-surface electrons are likely to escape the solid [244]. This gives a range of energy values within the data for a sample, but significantly it results in peaks forming, which are weighted by those atoms nearest the surface. As an approx. principle, electrons with E = 50-1000 eV will generally not proceed past 2-10 atomic layers (≈ 0.4-2.0 nm) without losing energy through inelastic scattering (represented by an exponential decay function, by depth, E, material properties etc) [244]. They will therefore not contribute to the peak (and may not contribute at all). However, the practical aspect of XPS is that the percentage of elements and compounds of an element can be determined fairly simply based on understandable binding energy and binding energy shifts.

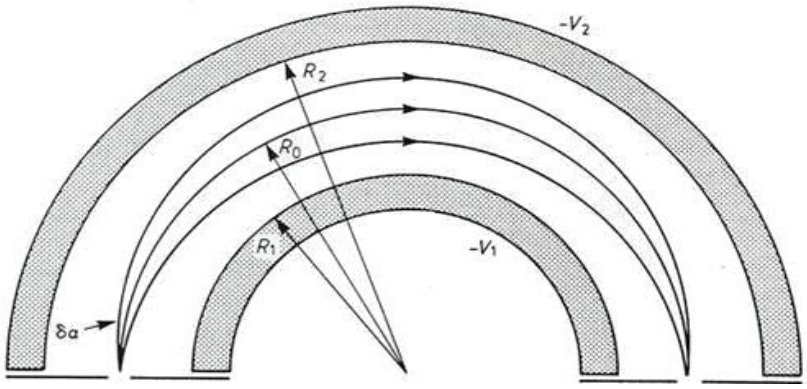

[245]

Figure A1.2.5 – Hemispherical Electron Energy Analyser
Hemispherical electron energy measurement used in an XPS. Correct voltage applied between outer/inner hemispheres permits the electron to reach the detector at the end (not colliding with surfaces). Electron energy can thus be measured by voltage.

A1.2.5 Sputter Deposition/Plasma-Enhanced Chemical Vapour Deposition

Two methods were used in this research for nanoscale material deposition. Sputter deposition was one process, employing a target (source) material that is bombarded with high energy ions in order to release atoms, which then deposit a thin film onto a substrate [247]. Generally metallic targets are used, such as Ni, Ti, Ta, etc, depending on the application. There are a range of different types of sputtering processes. The one used for this research was (planer) DC magnetron sputtering. Planer or cylindrical terminology refers to the orientation of the magnets [247]. The other main types are RF magnetron, ion beam, and DC diode (most basic) or RF diode sputtering processes. Processes generally involve an evacuated chamber with presence of an inert gas such as Ar, or Kr or Xe for deposition of heavier elements. All are fairly similar in principle. The deposition process is commenced with the bombardment of a cathode target material plate with energetic ions generated in a glow discharge plasma, which eject atoms from the target material. A plasma is defined as a state of matter following where a gas has been subjected to energy (thermal, electric, magnetic) such that a significant amount of molecular bonds are broken and electrons dissociated, forming a mostly positively ionised gas species and electrons [248].

The promotion of chemical reactions by plasmas is based on two functions: firstly, the formation of chemically active species used for layer formation as a result of inelastic collisions of precursor molecules with energetic particles (mainly electrons) formed in the plasma. Secondly, delivery of energy to the substrate for enhancement of surface processes such as nucleation, particle migration and heterogeneous kinetics. Plasma parameters therefore determine the composition, structure and properties of deposited layers [249]. The ejected atoms from the source material can therefore deposit onto the nearby surfaces, namely the substrate, providing the very thin material coating. Secondary electrons are also emitted from the target surface as a result of the ion bombardment, which play an important role in maintaining the plasma. A basic sputtering process operates with very low deposition rates, low ionisation efficiencies and high substrate heating effects. Magnetron sputtering has been developed to overcome these issues [250]. The use of a magnetic field parallel to the target surface can constrain secondary electron motion to the region of the target. The magnets are arranged in such a way that one pole is positioned at the central axis

of the target and the second pole is formed by a ring of magnets around the outer edge of the target. Trapping the secondary electrons in this way increases the probability of an ionising electron–atom collision occurring, resulting in a dense plasma forming in the target region [251]. This leads to increased ion bombardment of the target, giving higher sputtering rates and higher deposition rates at the substrate [250]. DC magnetron sputtering offers faster deposition than the basic DC diode process.

With DC sputtering processes, high voltages are used to create a potential difference between the plasma region and the target material, resulting in positive ions being accelerated from the plasma towards the target, with energies relative to the amount of potential. Magnetron sputtering also allows a reduction in the voltage (from 2-3 kV to 500 V) [250]. Sputtering is most suited to producing thin material films (i.e. < 1 μm). DC magnetron sputtering can typically provide deposition rates of 0.1-10 nm s^{-1} and uniformity of coating within a few percent [252]. A typical planer magnetron sputtering device (inside a vacuum chamber) schematic is shown in Figure A1.2.6.

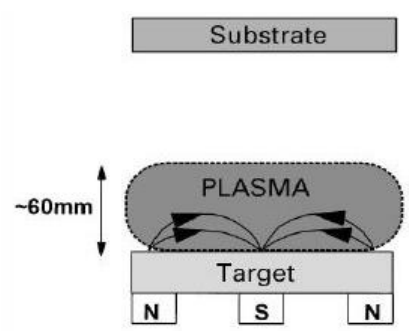

[250]

Figure A1.2.6 – Conventional (Planer) DC Magnetron Sputter Deposition Device
A typical sputter deposition arrangement is shown, where a substrate is positioned close to a target material that is bombarded with ions to remove atoms (within a plasma region), depositing a fine layer onto the substrate and nearby surfaces.

The DC magnetron sputter deposition process used in this research consisted of a low pressure chamber at 1×10^{-3} Pa. A high voltage DC supply (approx. 500-1000 V) was used, typically controlled to limit at 0.5 A. Allowing higher currents increased the deposition rate; however, a good balance of the coating bonding/integrity versus deposition rate/time was realised at approx. 0.5 A. The process was water cooled.

Deposition thickness could be determined via the piezoelectric properties of a quartz crystal installed in the chamber (fairly standard practice in these devices) [253]. The sensor is in the form of a crystal wafer with conductive electrodes on its two faces, positioned close to the substrate, receiving an equivalent coating of the material. The measurement is based upon change of oscillating frequency. As the coating on the crystal increases, the oscillating frequency changes proportional to the added mass of material. This change in frequency can be converted into a thickness readout. It is not exact and does require calibration. However, monitoring the deposition rate with this technique and co-observation of current and time allows a fairly practical method of achieving the required thicknesses. In addition, the process operates for a few moments with the crystal and substrate shielded (from the metallic atoms), which allows the process to establish a steady state and also allows the Ar ions to perform a cleaning action onto the surfaces. When ready, the substrate and crystal become unshielded and steady deposition occurs. This is particularly relevant to very quick/thin depositions, allowing good control of deposition uniformity and thickness.

A plasma-enhanced CVD process was also used during this research for carbon nanotube (CNT) synthesis. In a basic CVD process, a thin film is formed on a material through gas phase and substrate surface chemical reactions. If these reactions are stimulated by plasma, the process is 'plasma-enhanced' [254]. PECVD is preferential over CVD in certain deposition processes, such as to lower substrate temperature (permitting processes that would otherwise not be possible due to melting points of semiconductor materials etc) [249]. The PECVD process involves a 'source' gas, a monomer such as C_2H_2 (in the case of deposition of CNTs) or for example $SiH_4 + O_2$ (for SiO_2 deposition), which is fed into a vacuum chamber. The source gas supplies the physical source of material to be deposited onto the substrate. Growth of material on the substrate is considered to occur predominantly due to radicals, although the exact processes remain unclear in literature [248] [249]. The source gas is accompanied by a carrier or diluent gas (NH_3 in the case of this research). The primary role of the carrier/diluent is to provide a controlled inert environment, to increase the homogeneity and stability of the plasma, and to enhance the source gas excitation [248]. Use of NH_3 is in fact also understood to catalytically promote the CNT synthesis reaction [255]. Plasma was generated by applying a 13.56 MHz frequency electric field

across two electrodes surrounded by the gases. To deposit material, the substrate (with catalytic coating) was attached to one of the electrodes. Material deposition (or CNT synthesis etc) then naturally commences due to the plasma being in the vicinity of the catalyst layer. Further details and discussion of the specific PECVD processes used in this research are contained in Chapter 5. PECVD and sputter deposition processes are discussed in detail in literature elsewhere [248] [249] [254] [255].

Thermal evaporation is an alternative and fairly simple deposition process available. This involves a simple vacuum vessel and a crucible, containing a heating element such as a W (Tungsten) coil. A metal sample can be placed in the crucible and vaporised, such that is performs a thin even coating on the surroundings. This includes the substrate, mounted above the crucible, and also any exposed areas of vessel interior. The process is therefore simple but not efficient in terms of the material usage, since a vast amount of material is not deposited on the substrate. For example the use of Pt with this process would be inefficient in cost terms. It is also necessary to remove the waste material from the vessel after use, which can be difficult. Therefore use of this process was generally not considered during this research.

A1.2.6 Excimer Laser Processing

Modification of thin surface layers can be achieved using UV laser processing techniques, such as by a Kr-F excimer laser used within this research. The laser functions with three gases: Kr; F; Xe. The UV photon emission occurs due to the temporary formation of excited states of the noble gas (induced by a high voltage across two electrodes), with either itself or another gas, in this case F (mostly). The electrodes are relatively large, with round edges to assist with the uniform electric field and uniform excitation. The unstable bound molecule then returns to a more stable state (separate gases) and releases a photon. The Xe acts as a (noble) buffer gas during the process. It may also be excited, but its purpose is to act as a bridge to transfer energy. The process therefore forms excited complexes and ‘dimers’ (of Kr), hence the origin of the term ‘excimer’ [256]. Excimer lasers are almost ideal sources for these surface modification processes, due to the high photon energy (248 nm), short pulse lengths (such as 10-50 ns), and in terms of their highly multimode/incoherent beam [256] [257]. The energy levels of the photons of excimer lasers allow photodissociation of target surface molecules and/or absorption of energy

within the material. The short pulse length aids the ablation of a region of the surface with low damage to the surrounding material, which is important for substrates with low melting points. Surface processing may be micromachining (to form holes/drilling etc), ablation of regions of material (lithography), recrystallisation, surface preparation, doping, medical procedures (such as cutting skin tissue, with greatly reduced scarring) [258] [259], formation of oxides, or to restructure the surface and form nanoscale regions of surface coating (catalysts). The latter two were processes employed within this research. Pulse repetition can be from a few Hz to several KHz. The efficiency of laser devices in terms of electrical power demand compared to the energy of the output beam, at present, is low (1-3%) [257]. Absorption depth of a 248 nm (Kr-F) laser is, for example in Si, approx. 5.5 nm [258]. A schematic of the basic excimer laser generation process is shown in Figure A1.2.7. The gaseous mixture is corrosive and the system/pipework requires stainless steel coating. It also tends to form unwanted species, hence the need for a recirculation and filtering. The process employs a capacitor bank to provide high voltages to start the process, after which the gases mixture become more conductive and the excitation continues. A system of mirrors is used to reflect the photons onto the target [256].

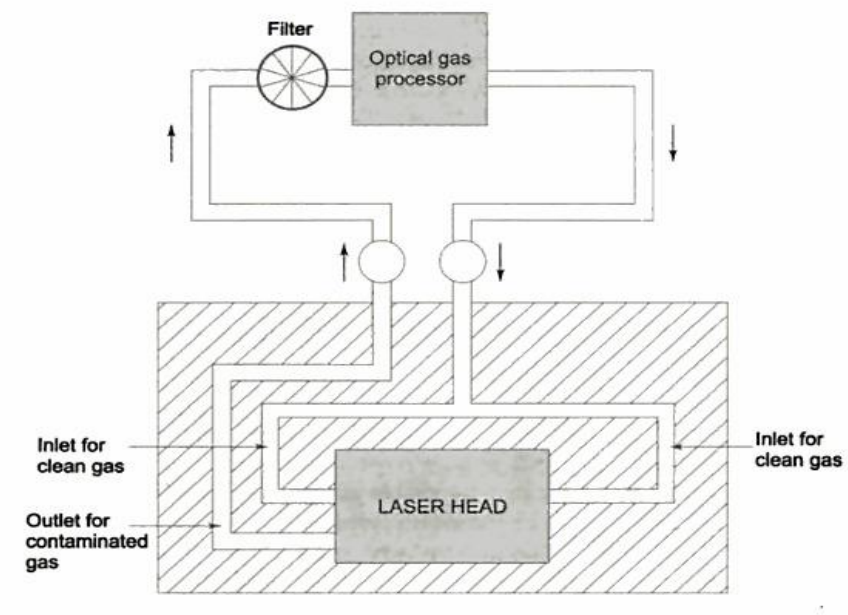

[256]

Figure A1.2.7 – Basic Schematic of Excimer Laser UV Photon Generation Process
Typical excimer laser set-up, with controlled gas flow through the laser head, forming excited states and emitting UV (induced by high voltage electrodes).

Appendix A1.3 – Hydrogen Production Methods

A1.3.1 Steam Reforming

SR processes involve the thermal reaction of a hydrocarbon source with steam in the presence of a catalyst. The process requires T >180°C for oxygenated hydrocarbons such as methanol, or > 500°C for natural gas and conventional hydrocarbons. Commercial reactors operate in the region of 600-900°C and 1-40 bar in the case of CH_4 reforming [260]. A typical SR system is exemplified in Figure A1.3.1. The chemical process for methanol (endothermic, +49.2 kJ mol^{-1}) [43], is as follows:

$$CH_3OH + H_2O \rightarrow CO_2 + 3H_2$$

Or for conventional hydrocarbons (alkanes):

$$C_mH_n + mH_2O \rightarrow mCO + (m + ½n)H_2$$

Thus, for CH_4 (+206.2 kJ mol^{-1}) [42]:

$$CH_4 + H_2O \rightarrow CO + 3H_2$$

The CO and H_2 product (synthesis gas or 'syngas') from the initial reforming can be further processed to produce more H_2 (+ CO_2) in a WGS reaction (-41.2 kJ mol^{-1}) [261]:

$$CO + H_2O \rightarrow CO_2 + H_2$$

Therefore the final reaction for CH_4 is (253.1 kJ mol^{-1}):

$$CH_4 + 2H_2O \rightarrow CO_2 + 4H_2$$

Catalysts for the WGS reaction include Fe, Cu, Zn, C, Al, Ni, Ce [261]. Syngas can also be used in alternative secondary reactions to form liquid fuels, such as through Fischer-Tropsch (F-T) synthesis, as discussed in Appendix A1.7 (however, the high ratio of H_2 to CO from the SMR processes is not preferred for F-T) [33]. WGS increases the overall chemical conversion process efficiency. Without WGS it is limited at 78.8%, whereas with WGS it appears near unity, based on ΔH of 890.0 kJ mol^{-1} and 1140 kJ mol^{-1} for CH_4 and $4H_2$ [26] (discounting the H_2O and CO_2 components). However, due to the heat/energy input requirements and other losses and observing thermodynamic irreversibly of the process, real efficiencies are typically reported in literature at 75%

and limited at approx. 85% [15] [33] [37]. WGS typically occurs firstly at a high T reactor and then low T reactor, achieving less than 1% CO concentration. Copper is a typical catalyst for the WGS reaction [33]. SR processes are used mainly with natural gas (mainly CH_4). Nickel is used as a catalyst, or precious metals such as platinum or rhodium (group VIII metals). The benefits of the use of precious metals are limited in conventional reactors due to mass and heat transfer limitations. Catalysts must have high activity, high thermal stability and mechanical strength. Iron is oxidized rapidly, cobalt cannot withstand the partial pressures of steam and hence Ni is currently the standard in industry [33] [262]. Microchannel-based reactors have been developed to improve performance in terms of these limitations [42]. However this tends to revert towards the use of expensive group VIII catalysts such as Rh and has led to the pursuit of less expensive catalysts such as Co-based [33]. The H_2O:CH_4 feed ratio is kept high to reduce coke formation (at 2.5-3:1) [262].

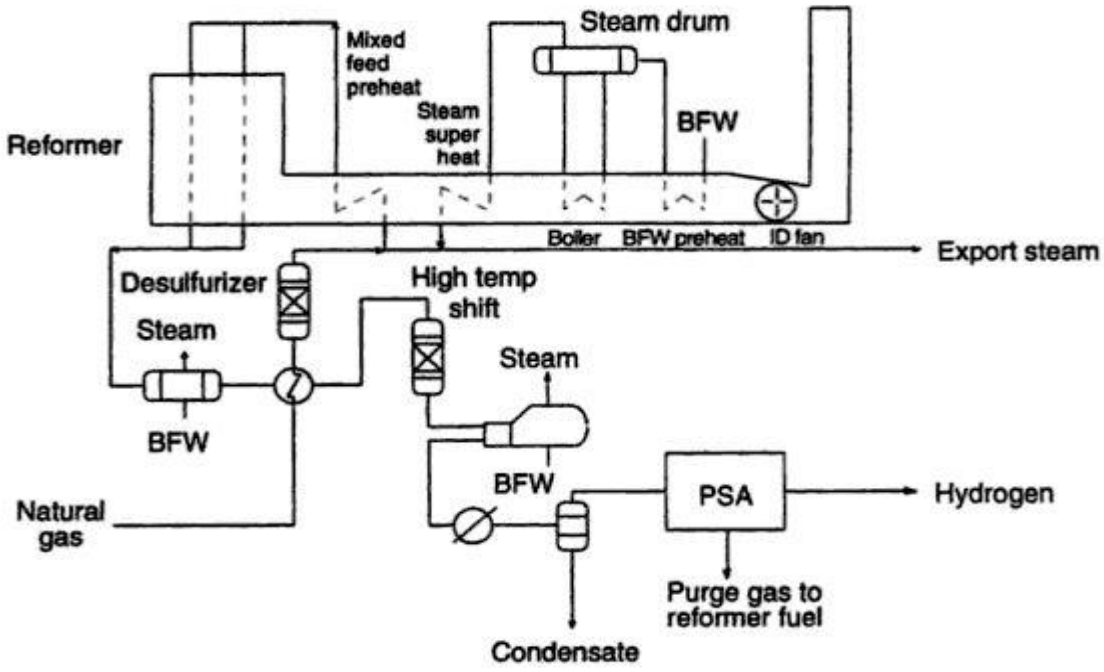

[19]

Figure A1.3.1 – Steam Reforming Process Systematic
Example schematic of SR process, including natural gas feed, desulphurisation, WGS reforming, PSA for purification, and H_2 outlet.

Further reactions to purify the H_2 to a greater extent are PrOx, methanation, or PSA. PrOx involves carefully measured addition of air, which adds complexity to the system and can result in combustion of the H_2. Methanation does not require air, although

PrOx is reported to be preferable. Catalysts for these reactions also belong to group VIII (Pt, Ru, Rh). Alternatively, PSA processes (now established in industry) or membranes (newer approach, typically with ceramics or Pd) can be used to purify the H_2 further, reaching > 99.999% [33] [37]. These processes all require additional energy so a purity-efficiency trade-off etc exists.

Desulphurisation exists to remove sulphur from the natural gas source to avoid contamination of the reformer catalyst [263]. These are typically in the form of chemical processes such as hydrosuphurisation (HDS), or alkylation. HDS hydrogenates the S-containing species within the gas and results in formation and release of H_2S [33]. Alkylation is a pilot-scale process at present where the S-containing molecules are increased in mass to allow separation via distillation [33]. Adsorptive processes involve activated carbons, zeolites etc, to adsorb the S-containing molecule. Alternatively a Ni surface can be used, to form NiS [33].

The overall SMR reaction forms 4 H_2 and 1 CO_2 per CH_4. Overall CO_2 production per H_2 including the process heating etc depends on several factors such as the individual reactor, efficiency, hydrocarbon type, heating source and its CO_2 footprint, process T etc [264]. SMR processes are responsible for a significant amount of CO_2 emissions, reported to have been approx. 3% of global industrial sector emissions in studies through 2005-2008 [36]. Example data is reported to be in the region of 9.3-13.9 kg CO_2 kg^{-1} H_2 (0.42–0.63 mol CO_2 mol^{-1} H_2) [263] [264]. SMR also produces significant NO_x due to the interaction of O and N within the heating/burner stage [44]. A review of the SR process losses and emissions is given by [36] [265] [263] [266]. There is also interest in small-scale reformers to convert hydrocarbons or biofuels into H_2 for direct use in a fuel cell at distribution units. These two process stacked together potentially offer a more practical and efficient way to store and produce electrical energy from these sources over conventional processes (such as use of the hydrocarbon in a conventional combustion engine etc) [267]. SMR has been reported to produce approx. 240 $\times 10^9$ m^3 yr^{-1} H_2 based on a share of 48% of global production in 2008 [15] and has reached an estimated 48 $\times 10^6$ tonnes yr^{-1} (540 $\times 10^9$ m^3 yr^{-1}) as of 2013.

A1.3.2 Partial Oxidation

POX and catalytic POX (CPOX) are alternative thermal reforming processes to SR. Some of the hydrocarbon is initially combusted with O_2 in a reactor to produce heat and the products H_2O and CO_2 [44]. For example (-802.3 kJ mol^{-1}) [268]:

$$CH_4 + 2O_2 \rightarrow CO_2 + 2H_2O$$

This is followed by reactions involving H_2O and CO_2 to produce H_2 (as syngas) [269]:

$$CH_4 + H_2O \rightarrow CO + 3H_2$$
$$CH_4 + CO_2 \rightarrow 2CO + 2H_2$$

This is followed by WGS. POX relies on high process T (often > 1000°C), whereas CPOX is intended to for lower T. Catalysts are based on Ni, Co, Fe, Cu, and Rh, Ru, Ir, Pt [33] [269] [270], with Ru being slightly cheaper than Rh and of similar reactivity. Ni is not significantly less reactive yet 100 times cheaper [271]. It is argued that CPOX of CH_4 offers 30% cost reductions compared to SR, and does not emit NO_x since burners are not used [44]. In addition, POX processes favour the production of syngas, due to the H_2:CO ratio of approx. 2 [44]. The very high T can lead to localised hot areas (due to the highly exothermic decomposition of CH_4) and subsequent degradation/melting of the catalyst [269]. Coking of the catalyst can occur due to cracking (+75.6 kJ mol^{-1}) and Boudouard reactions (-172.4 kJ mol^{-1}) reactions [44] [268]:

$$CH_4 \rightarrow C + 2H_2$$
$$2CO \rightarrow C + CO_2$$

This is known to affect mostly Ni catalysts, hence a trade-off exists between the use of Ni and the expensive group VIII metals mentioned previously [44]. The exact set of reactions that occur are slightly uncertain and can vary. The idealised POX reaction for the production of syngas would be (-35.7 kJ mol^{-1}) [44]:

$$CH_4 + ½O_2 \rightarrow CO + 2H_2$$

It has been the subject of a significant amount of research as to whether this reaction can be solely catalysed [269].

There are around 10 reactions that occur, including the above reactions, WGS, and:

$$CH_4 + O_2 \rightarrow CO_2 + 2H_2$$

$$CO + ½O_2 \rightarrow CO_2$$

$$H_2 + ½O_2 \rightarrow H_2O$$

Desulphurisation is also required at the inlet to reduce degradation of the catalysts. POX and CPOX processes are estimated to produce approx. 30% of global H_2, based on reforming of CH_4 and heavier hydrocarbons (oils), 150 $\times 10^9$ m^3 yr^{-1} H^2 [15] and an estimated 30 $\times 10^6$ tonnes yr^{-1} (330 $\times 10^9$ m^3 yr^{-1}) as of 2013.

A1.3.3 Autothermal Reforming

ATR is a combination of SR and POX. An initial POX/CPOX reaction process provides heat, which is then transferred to a catalytic region within the reformer where the endothermic SR reaction occurs [33]. The process provides its own heat (as the name suggests) and is therefore more compact and requires lower capital cost. It can also be started and stopped quickly and is suitable for upscaling. The process requires careful control in terms of the O:hydrocarbon and C:H_2O ratios. Efficiencies are reported in the region of 60-75%, which is comparable with POX/CPOX, but slightly below that of SR. For these reasons it is expected that autothermal reforming will grow, particularly where there is demand for syngas for F-T synthesis processes [44] [268].

A1.3.4 Pyrolysis

Pyrolysis or thermal decomposition of hydrocarbons is a further reforming process that can produce H_2 [272] or bio-oil in 'fast' pyrolysis [273]. This process is used widely across industry in a number of roles, such as the decomposition of biomass, transformation of oils to lighter hydrocarbons (cracking), waste disposal, formation of C-based materials [33]. The significance in the H_2-forming role is the reduction in CO_2 or CO emission (due to no O_2) versus that of SR or POX, since the process forms carbon in a solid form that can be sequestered relatively easily. The basic reaction for pyrolysis of CH_4 is as follows (+75.6 kJ mol^{-1}) [44]:

$$CH_4 \rightarrow C + 2H_2$$

A reforming process similar to pyrolysis, typically used with CH_4 or biogas (CH_4 + CO_2), is referred to as CO_2 reforming or dry reforming [274]. It is followed by the WGS

reaction. It is an alternative process for low CO_2 formation of H_2 or syngas. However, the high amount of C formation inherently leads to coking. Also, the relatively low initial H:CO ratio (one) is reported to be not ideal for syngas (despite WGS being performed as a secondary reaction to increase the ratio) [262]. The basic CO_2 reforming reaction for CH_4 is as follows (+247.0 kJ mol^{-1}) [273]:

$$CH_4 + CO_2 \rightarrow 2CO + 2H_2$$

Use of pyrolysis processes for the processing of hydrocarbons and biomass, for H_2 formation and within other roles, are expected to grow within industry [264]. The formation of bio-oils from pyrolysis are reported to be hindered by limited use and difficulty in downstream processing, which have so far restricted the wide application of biomass pyrolysis technology [275].

A1.3.5 Plasma Reforming

Plasma reforming proceeds under the equivalent basic chemical reactions as the previous reforming processes. Plasma is generated to drive the reforming reaction. This forms H, OH, O radicals and electrons, which cause reduction and oxidation reactions to proceed. There are thermal and non-thermal processes; non-thermal are reported to be far more efficient [33]. Plasma reforming has some advantages over the larger reforming processes, such as very fast start-up, higher efficiency (non-thermal processes), low cost (due to minimal catalyst required), low deterioration/coking, ability to operate at lower temperatures, more confinement, and high productivity particularly from heavy hydrocarbons.

Disadvantages include electrical requirements and issues of electrode erosion [33] [276-278]. The compactness and fast start-up leads to the possibility of distributed or mobile reforming processes, to produce H_2 on demand from a hydrocarbon source [279-281]. Without catalysts, the process also becomes sulphur tolerant [33]. Thermal plasma reforming processes involve significant heating and then also cooling for the electrodes. Non-thermal processes do not require the hydrocarbon to be heated significantly [281].

There are four main types of non-thermal process: gliding arc plasma; dielectric barrier discharge; microwave plasma; corona discharge [33]. Literature suggests that the

gliding arc plasma process is the most efficient [280]. Plasma reforming can also be incorporated into other reforming processes, such as SR, POX, ATR, pyrolysis (mostly POX and ATR) [33] [281].

A1.3.6 Aqueous Phase Reforming

Production of H_2 by APR was first published in Nature (2002), where it was demonstrated that oxygenated hydrocarbons (ethylene glycol, methanol) and sugars (glucose) could produce an H_2-rich gas. The process proceeded at near 500 K in a single-reactor APR process, using a platinum-based catalyst. H_2 constituted 50% of the product gas. The remainder was gaseous alkanes and CO_2 [282]. In comparison to other biomass processes such as enzymatic decomposition of sugars, SR of bio-oils and gasification processes, APR potentially relieves issues of low H_2 production rates and complex processing requirements [283]. Selectivity for H_2 production increases when molecules that are more reduced than sugars are used, with ethylene glycol and methanol being almost completely converted into H_2 and CO_2. APR does not require vaporisation of H_2O or the oxygenated hydrocarbon. It also occurs at low temperatures, such that WGS is thermodynamically favoured, leading to relatively low levels of CO [284] [285]. A catalyst for H_2 production must facilitate C–C bond cleavage and promote removal of adsorbed CO species by the WGS reaction, but the catalyst must not facilitate C–O bond cleavage and hydrogenation of CO or CO_2 [284]. Naturally, alternative catalysts to Pt, such as Ni, Pd, Rh, Ru, Co and Cu have been researched [283-287]. For example, use of Ni as a replacement for Pt, in a bimetallic catalyst such as Pt–Ni, supported by Al, is shown to lower activity for reforming of glucose, but to cause no significant decrease in activity for ethylene glycol even after decreasing the Pt content by 33% [284]. This indicates that with the right combination of metals, a highly active catalyst can be synthesised at lower cost than solely Pt. As an example process, glycerol (the main co-product of biodiesel production) is considered as a promising source to produce H_2. The APR process for glycerol has the following overall stoichiometric reaction [287]:

$$C_3H_8O_3 + 3H_2O \rightarrow 3CO_2 + 7H_2$$

This may take place via the intermediate formation of CO (converted to CO_2 by WGS):

$$C_3H_8O_3 \rightarrow 3CO + 4H_2$$

Again, this process could serve further synthesis reactions such as F-T. It is therefore feasible that catalytic APR processes may start to become useful for the generation of H_2-rich gaseous fuel from waste carbohydrates and biomass.

A1.3.7 Ammonia Reforming

Ammonia (NH_3) is a commercial chemical of high hydrogen content. It is a gas at STP but forms liquid, for example when compressed to approx. 10 atm or cooled to 240 K [230] [288]. Although ammonia is actually manufactured industrially from reformed H_2 and atmospheric N_2 (thus a significant demand market for H_2 as stated in Section 1.2.5), it can also be decomposed back to H_2. The NH_3 reforming reaction is the following (+46.1 kJ mol^{-1}) [26]:

$$2NH_3 \rightarrow 3H_2 + N_2$$

The NH_3 reforming process is carried out at approx. 775 K or above (to fully decompose the NH_3 feedstock) within a chamber equipped with a catalyst bed, similar to most other reforming processes. Ru or Ir are typical catalysts. Work on Pt, Pd Rh and Ni is also contained within literature [288] [289]. At temperatures below 775 K without catalysts, it is reported that no significant reforming is observed [289].

Therefore NH_3 can potentially be used as a liquid fuel for the storage and transportation of hydrogen and then reformed to produce H_2 on demand. The limitations of this system are the overall efficiency, since the H_2 must first be produced, synthesised to NH_3 and then back to H_2. However, being a liquid, NH_3 does offer a potential solution to H_2 storage issues, and infrastructure for storage, transportation and handling of NH_3 is already established [33]. Therefore, NH_3 could be stored at pressures of around 20 atm and handled similarly to LPG fuel. Drawbacks to the use of NH_3 are mainly with its toxicity, although leak detection would be simple due to its strong odour [33] [111].

Its lack of development at present however, seems to also be due to the carbon-intensive process within which it is produced (involving SMR etc), and low overall efficiency of the multi-step process to reproduce H_2. There is not currently a suitable fuel cell system available to use NH_3; however, NH_3 would be suited for use in an internal combustion engine (ICE). It is reported to be slightly less efficient as an ICE

fuel compared to diesel or petroleum, for reasons such as high auto-ignition temperature (924 K for NH_3 versus 527 K for diesel) leading to incomplete combustion and emission of NH_3 [289]. This would also not gain the efficiency advantages of fuel cells versus ICEs, one fundamental aspect of the hydrogen economy discussed in Subchapter 1.2. Forming NH_3 into H_2 to operate a fuel cell or direct use of NH_3 in an ICE are therefore the main interests of NH_3 in the energy context. The former remains as basically an inefficient overall method for energy transfer and storage to produce final H_2 at a demand site, which would rely upon mass production of cheap renewable H_2 to be practical, and the latter would also be based around cheap renewable H_2 being reformed into an acceptable (liquid) but non ideal ICE fuel [289]. The product of NH_3 reforming, N_2, is benign for fuel cells, which may negate the use of purification etc [288], although NH_3 itself is very damaging to the polymer electrolyte membrane (PEM) used in a fuel cell [46]. There is little commercial interest or development of NH_3 within the energy or transportation context at present.

A mobile NH_3-H_2 reformer is one option for using NH_3 as a storage medium for on-demand H_2 on-board a vehicle [289] [290]. While this is not an efficient process overall, it may act as a possible substitute for the transition from diesel or petroleum towards use of H_2, overcoming some of the storage and infrastructure holdbacks. The use of exhaust heat to assist the process has previously been proposed. For a diesel engine, the exhaust temperature is typically under 675 K. Therefore input of air/O_2 to the reformer to allow combustion of the NH_3 in an autothermal reaction to further increase the process temperature can also be implemented [289].

A1.3.8 Gasification

Coal gasification (CG) is one of the main current sources of H_2 [15]. The process can occur at a range of temperatures generally from 700-1000 °C [29]. Higher temperatures promote faster/preferable reactions (up to the reasonable temperature limits of the system) with higher H_2 proportion of the product gas (and generally higher conversion process efficiency) [94] [291]. The overall process of CG is not particularly efficient (generally <50%), whereas biomass gasification (BG) efficiency is generally superior and potentially a source of renewable H_2 [33] [94]. The process can be applied to various wastes and biomass feedstocks, such as animal and agricultural wastes, wood and crop (such as corn) wastes, aquatic plants, herbaceous species,

waste paper [33]. Gasification is not always associated with the reforming reactions within literature, yet it is very similar. It includes equivalent reactions as discussed within pyrolysis, POX and SR. However, gasification extends further, applying to a wider range of feedstocks/biomass. In comparison to pyrolysis, gasification processes are focussed upon H_2 or other gaseous or hydrocarbon production where the C component of the feedstock is reformed into CO or CO_2, whereas pyrolysis forms C (coke) and H_2 in its primary reaction.

The gasification process is not always described with exactness within literature due to variations of processes and feedstock composition etc [291]. There are several stages to the process [292]. It firstly involves a drying phase to remove moisture from the feedstock. Unlike pyrolysis of a gas, there will naturally be a small amount of air/H_2O within the CG and BG process. The pyrolysis reaction then occurs to reduce the feedstock to mainly C, H_2, hydrocarbon gases and liquid tars. Process heat is often taken from partial combustion or POX of the feedstock (producing CO) or external heating (from combustion of feedstock). The process continues with a WGS reaction and also reforming reactions, Boudouard and methanation, but producing mainly CO_2, CO, H_2 and another gas or H_2O depending upon the gasification medium and feedstock. The composition of the product gas obtained from the process does also depend on several parameters such as feedstock moisture, p and T, process kinetics and gasifier design etc. Gasification mediums can be air, O_2, steam, CO_2 or mixtures of these. Air is common but the N_2 content leads to a lower enthalpy value of the product gas/syngas. Use of steam or O_2 (at greater cost) offer a higher value, such as 10-15 kJ L^{-1} compared to 3-6 kJ L^{-1}, for steam and N_2 gasification product gases respectively.

Combustion/POX of feedstock drives the reaction (not possible with steam or CO_2 gasification mediums) and also generates H_2O and CO_2 for further reduction reactions. Use of CO_2 as the gasifier or a mixture of mediums offers the ability to produce further syngas from the C, CH_4, tar and char species, through Boudouard and WGS/reverse-WGS reactions during the process (catalysed by Ni/Al), and is therefore prominent within literature [94] [292]. CO_2 within the product gas is usually released (or fed back through the reaction). Different reactor types include: fixed bed; fluidised bed (most suited to biomass); drop tube furnace; wire mesh. Catalysts used within gasification

are generally Group VIII [291]. Pure H_2 is obtained by a gas separation process, or syngas is used for further processing (F-T etc) [33].

Coal gasification and biomass gasification are established processes and are likely to form significant roles in the future of H_2 energy. Use of coal and biomass in co-gasification (CoG) also has presence within the literature. The differences between coal and many biomass feedstocks are reported conveniently by Emami-Taba et al [29]. Changing the feedstock type has significant effect on parameters such as gas constituents, C conversion, gas/tar yields, efficiency, ΔH, and the release of H_2S/NH_3 [94]. There are some advantages to the co-process reported, such as efficiency improvement of the gasification of low grade coal by the addition of pine chips [94]. In general, various process conditions appear to be optimised with the addition of biomass feedstock due to its physical form and composition etc. It is quite frequently reported that increased use of biomass generally leads to decreased H_2 and more CO, CO_2, within the product gas [94]. Carbon conversion (defined as the C content of the feedstock that is converted to CO, CO_2, CH_4) increases with the use of biomass, which is attributed to its higher reactivity, producing more free radicals and increasing reaction kinetics [94].

Biomass gasification is therefore a possible route towards renewable H_2 production but clearly there remains optimisation of the process required and in the case of CG or CoG the carbon aspects will need better managed if this is to offer an advantageous near- or medium-term pathway. The integrated gasification combined cycle integrates a steam CG process in a combined heat and power facility. It is currently considered the cleanest and one of the most efficient coal fuelled techniques [32].

A1.3.9 Electrolysis of Water

Electrolysis is an established electrochemical process for decomposition of H_2O into H_2 and O_2 [68]. A simple electrolyser consists of cells containing two submerged electrodes with an electrical potential applied, which separate the constituents of H_2O by electrical force. The overall reaction is as follows (+285.8 kJ mol^{-1}) [26]:

$$H_2O \rightarrow H_2 + ½O_2$$

In practice, the process does not proceed at a significant rate until excess energy is applied in the form of an overvoltage (i.e. > 1.48 V per cell) due to system losses. However, this produces heat and the process becomes more favourable as the H_2O temperature increases, leading to a reduced overvoltage. The process is therefore naturally efficient. Electrolysis requires a catalyst (such as Pt, Ni) and an electrolyte to proceed, which is based mainly upon alkaline (ion conducting), polymer (proton conducting), or ceramic solid oxide (oxide ion conducting) electrolytes. Coupled with a renewable energy resource such wind or solar, electrolysis can therefore provide very low carbon renewable H_2 production (a small amount of carbon is attributed to the present manufacture and installation of the devices). Critically, this can combine variable renewable electricity with energy storage provision and also accommodate surplus electrical grid energy. Coupling these requires understanding of the electrical characteristics of both systems. Research of this nature is the main element of this thesis and presented in Chapters 2 and 3.

Electrolysis is occasionally associated with hydrolysis, but despite similarity in the implied meanings the processes are quite separate. Electrolysis in the context of this thesis involves the splitting of H_2O into H_2 and O_2 by use of electricity, which is the most fundamental type of electrolysis process, although electrolysis is also used for the splitting of other substances such as salt water into H_2, Cl and NaOH, etc. Hydrolysis is actually referring to the splitting of 'a substance', such as a carbohydrate, 'using H_2O'. Hydrolysis is therefore not a process where significant H_2 production is anticipated. There have been attempts to use catalytic hydrolysis chemical processes to produce H_2 from aqueous $NaBH_4$ solutions containing various concentrations of NaOH [293] [294]. This process is more in the context of chemical storage of H_2 rather than a process for significant production of H_2. These are therefore discussed briefly in Appendix A1.5.

A1.3.10 Biological Hydrogen Production

Biological H_2 production includes a number of processes, mainly based upon use of anaerobic bacteria (fermentation) or algae (photolytic processes) and relying upon the presence of an H_2 metabolising enzyme [18] [168] [295]. The physical source of hydrogen may be from H_2O, or biomass/carbohydrates (glucose/$C_6H_{12}O_6$) in aqueous environments [33]. The processes generally occur near ambient temperature and pressure [165].

BioH_2 production processes can be categorised by the following [18]:

- Dark fermentation
- Photofermentation
- Direct biophotolysis
- Indirect biophotolysis
- Bio water-gas shift
- Microbial electrolytic cell

Some of these processes may also be combined (hybrids) [165]. Dark fermentation includes use of certian bacteria, such as *Enterobacter cloacae*, *Enterobacter aerogenes*, *Clostridium sp.*, *Bacillus sp.*, and *Escherichia coli* (E. coli), and also certain algae [18]. Hydrogenase enzymes are the key element for catalysing the formation of H_2 (by combining protons and electrons) [295]. The use of E. coli in dark fermentation processes with glucose has been the subject of physical research for this thesis, further discussed in Chapter 4. It is termed 'dark' since the process is not driven by solar energy. The overall fermentation reaction for strict anaerobic bacteria produces a maximum of $4H_2$ from glucose [165]:

$$C_6H_{12}O_6 + 2H_2O \rightarrow 2CH_3COOH + 2CO_2 + 4H_2$$

The other main products are acetic acid and CO_2 in stoichiometric quantities as shown above. However, for facultative enteric bacteria, including E. coli, the maximum yield is only $2H_2$ [165]. The overall processes are not simple and there are competing reactions, such as for succinate, lactate and ethanol in the case of E. coli [168].

Photofermentation includes bacteria such as *Rhodobacter sphaeroides*, *Rhodobacter capsulatus*, *Rhodobacter sulfidophilus*, *Rhodopseudomonas palustris* and *Rhodospirillum Rubrum* [295]. Nitrogenase is the main enzyme responsible in molecular H_2 formation within these anoxygenic reactions. Glucose, fatty acids and similar sources can be used for H_2 production by these bacteria. Use of acetic acid is more routine, which is a product of dark fermentation. Hence the two fermentation processes are often used together [165] [296]. The process does not require intense light levels, but does require strict environmental conditions [295].

An example reaction from acetic acid is as follows:

$$CH_3COOH + 2H_2O \rightarrow 4H_2 + 2CO_2$$

Fermentation processes are considered to be more productive than photolysis (see Table A1.3.1), although the maximum yields, overall efficiency, production rate and economics are the main challenges still apparent in order to allow biological H_2 production to become up-scaled and commercialised [18] [165] [296] [297].

Direct biophotolysis is based mostly upon use of cyanobacteria or algae, such as the common green algae *Chlamydomonas reinhardtii*, or *Scenedesmus obliquus, Chlorococcum littorale, Platymonas subcordiformis* and *Chlorella fusca*, or *Anabaena cylindrica* (cyanobacteria), which are known to harness solar energy to drive the decomposition of H_2O to produce H_2 [165]. The algae metabolic process generates H^+ ions in the medium and uses a hydrogenase enzyme to produce H_2, with electrons that are donated from the photolysis reduction reaction. This occurs under anaerobic conditions, or when too much energy is captured. The photolysis reaction comes from the algae's ability to perform photosynthesis, hence some O_2 is produced [165] [297].

Indirect biophotolysis is based upon use of cyanobacteria, such as *Anabaena sp*., *Calothrix sp*. or *Oscillatoria sp*., and involves a series of four steps: production of biomass (glucose/acetic acid) by photosynthesis; biomass concentration; dark aerobic fermentation to produce 4 mol H_2 mol^{-1} glucose in the bacteria/algae cells with 2 mol of acetate; conversion of acetate to H_2 [18] [165] [198]. Nitrogenase and hydrogenase are both used during the process. The overall general reaction is as follows [198]:

$$12H_2O \rightarrow 12H_2 + 6O_2$$

Compared to fermentation, the biophotolysis processes may appear to offer more benefits in the long term, since they only require H_2O and sunlight, two enormous free reserves, whereas fermentation processes require certain biomass (waste). However, biophotolysis does not produce H_2 at significant rates and requires large surface areas to collect sufficient light [297]. Key areas for research are to modify algae/bacteria so that the majority of the solar energy is diverted to H_2 production, or to reduce sensitivity to O_2 (which builds-up and slows the reaction). Achieving continuous production is clearly another drawback with the use of natural light.

Biological WGS can be performed by certain photoheterotrophic bacteria, which can grow in dark conditions using only CO as a feed source, such as *Rhodospirillum rubrum*, *Rubrivivax gelatinosus* and *Carboxydothermus hydrogenoformans* [18]. They oxidise CO to CO_2, following the WGS reaction and thus releasing H_2, using enzymes rather than metal catalysts [33]. The process can be achieved at anaerobic near-ambient conditions and is quite favourable, occurring at a relatively fast rate. The process needs careful control of light, nutrient and CO levels if it is to continue for a reasonable length of time. These processes currently remain at laboratory scale [18].

Use of a microbial electrolytic cell (MEC) is a further biological approach to H_2 production (microbial electrohydrogenesis) [18] [33], which is based on the reverse process of a microbial fuel cell (MFC), and obeying similar principles to electrolysis of water as discussed in the previous section and Subchapter 2.1 etc. The MEC process remains anaerobic, whereas an MFC has an exposed cathode. The cell is represented in Figure A1.3.2. Bacteria such as *Geobacter*, *Shewanella sps*. and *Rhodoferax ferrireducens* are used [294]. The MEC may typically use a polymer electrolyte membrane (similar to a normal electrolyser), gas diffusion membrane or be operated without a membrane [18] [298]. The cell is intended for use with products that cannot be broken down by dark fermentation, such as butyrate, ethanol, acetate, etc, since the processes would not be spontaneous (-ΔG) and energy would therefore have to be applied. One option is photofermentation, another is a MEC where the energy comes in the form of a voltage applied to the cell electrodes. However, the MEC process can also be used with glucose or glucose-containing substrates [165]. The reaction for acetate producing hydrogen carbonate and $4H_2$ is as follows [298]:

$$CH_3COO^- + 4H_2O \rightarrow 2HCO_3^- + H^+ + 4H_2$$

The minimum reaction potential has been calculated by the ΔG value (+104.6 kJ mol^{-1}), which equates to 0.14 V. However, as discussed in Chapter 2.1 and acknowledged by Logan et al [298], calculation must consider $T\Delta S$, thus equating to use of ΔH to derive the minimum potential, also giving consideration to various overpotentials. Voltage > 0.2 V per cell would be expected for this reaction to proceed by a measureable amount. Production of H_2 at 0.5 V and STP would give an electrical efficiency of approx. 300% from the cell. MECs are therefore also suitable for hybrid biological

processes, involving dark fermentation of glucose as a first step providing waste organic compounds, which can undergo the MEC process. The voltage can be provided (or offset) by a renewable resource such as wind or solar for a fully renewable H_2 production process.

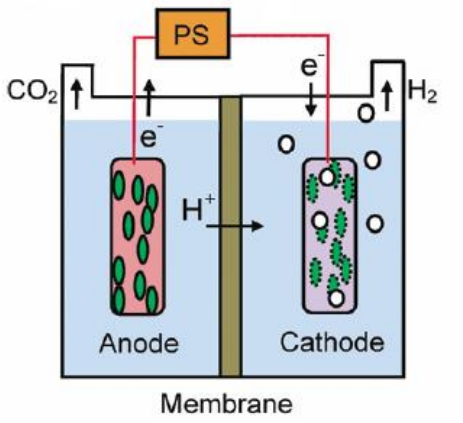

[298]

Figure A1.3.2 – Microbial Electrolytic Cell Schematic
The microbial cell contains two electrodes submerged in H_2O, with a small potential applied. Green ovals represent bacteria (in previous work they have been detected on each electrode, although their function is not yet fully understood).

An approx. comparison of the six biological H_2 processes is provided in Table A1.3.1, using reasonable samples of production rates [33]. There are also additional indirect routes to H_2 production via processes such as anaerobic digestion with reforming of intermediate biogas [111] although these are not identified as significant H_2 production pathways at present.

System	H_2 synthesis rate mmol H_2 L^{-1} h^{-1}
Dark fermentation	8.2-121
Photo-fermentation	0.16
Direct photolysis	0.07
Indirect photolysis	0.355
Biological WGS	96
Microbial electrolysis	5.8

[33]

Table A1.3.1 – Approximate Comparison of Published Biological H_2 Production Rates
Comparative data from literature for the six biological process discussed in this work.

A1.3.11 Thermochemical Decomposition of Water

H_2O can be decomposed into H_2 and O_2 at very high temperatures via thermal decomposition (TD) processes (or water thermolysis) [199] [299]. This process can in theory be performed with heat from concentrated solar energy, or from another reaction such as nuclear fission (this may be referred to as supercritical extraction etc) [204] [300]. The use of solar energy or waste thermal energy can also assist electrolysis of water, by reducing the electrical energy requirement [72], or may also drive or supplement heat for hydrocarbon reforming by conventional reactions, leading energy, cost, and CO_2 emissions reductions [299]. Therefore, there are a number of pathways for solar, waste or non-waste thermal energy to take part in TD reactions for H_2 production. Interest here is with the use of concentrated solar energy (or heat from other renewable resources), waste or low carbon energy, and TD of H_2O rather than of hydrocarbons. Direct thermolysis of H_2O is not thermodynamically favourable below approx. 4400 K, above that which can be contained with conventional materials and catalysts, and not feasible in terms of thermodynamic efficiency due to considerable radiated heat loss etc [301] [302]. It is observed not to be practical > 2500 K, due to material issues and the cost of very high solar energy concentration, therefore a significant amount of the H_2O (vapour) entering the reactor will be heated but not undergo decomposition, which is very inefficient [302]. Multiple-step decomposition allows lower temperatures: hydrogen production; oxygen production; materials regeneration [199]. Layouts of a single-stage and two-stage reactor heated by concentrated solar collectors are shown in Figure A1.3.3.

For the single-stage process, the reactor cavity is divided by a porous ceramic membrane into two chambers. The membrane is heated by concentrated solar radiation to a high temperature. Steam is introduced into the front chamber. Adjacent to the membrane surface it heats up and undergoes partial dissociation, forming a mixture of H_2O, HO, H, O, H_2 and O_2. Part of the mixture (+H) diffuses through the membrane (stream Y).

For a two-stage reactor, the cavity is divided by an outer and an inner membrane into three consecutive chambers. Three gas streams emerge (usually below 1300 K). Stream X is enriched in O, stream W with H, Z is intermediate (which eventually exchanges heat with the inlet flow) [302]. These processes are both not direct

thermolysis, as they form H_2 and O_2 by partial decomposition [303]. Lower pressure favours the reaction. At 0.05 bar, 2500 K, 25% of the H_2O is reported to dissociate, while all of it must be heated [302]. With improvements, the efficiency is reported to reach 40%, but clearly there are significant thermodynamic issues with these processes, which prevent commercial viability at present [302]. Also, effective gas separation practices for the process are reported to be a significant challenge [304]. Figure A1.3.4 shows the effects of p and T on the decomposition fraction of H_2O.

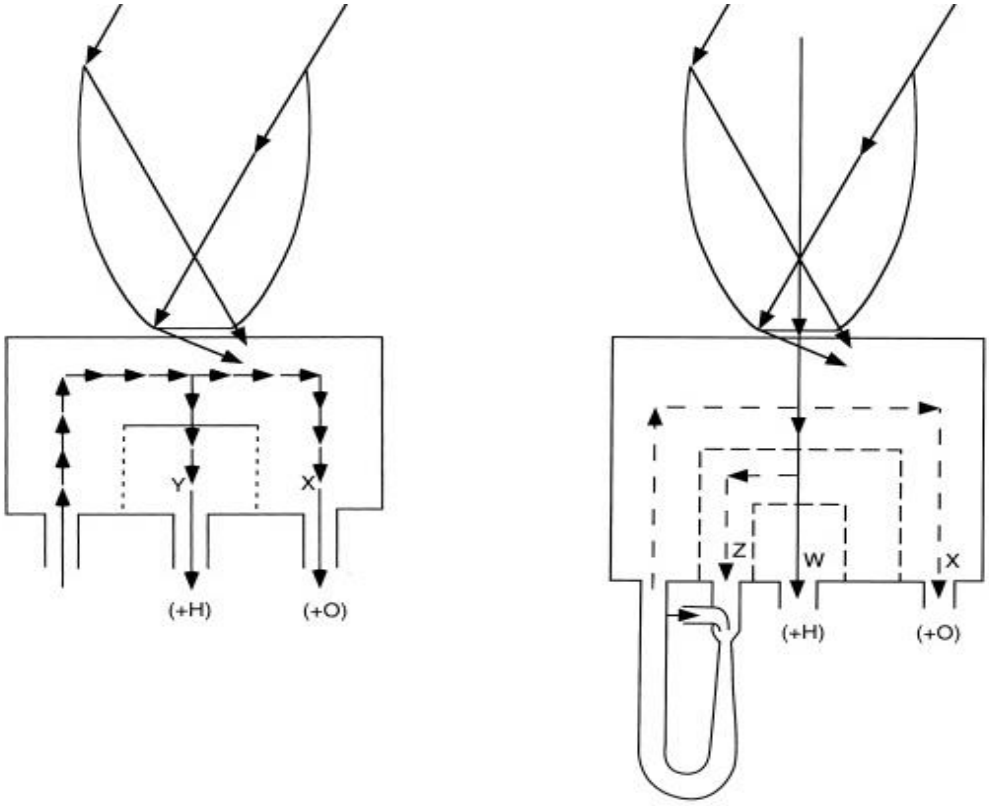

[302]

Figure A1.3.3 – Single-Stage and Two-Stage Solar Thermal Decomposition Reactors
Single-stage and two-stage TD reactors, showing reactor cavities situated below parabolic solar concentrator dishes.

Metal oxide cycles are another TD approach [303]. Advantages are further T reduction and fewer stages. The process generally involves two steps (where M is a metal):

$$M_xO_y \rightarrow M_xO_{y-1} + ½O_2$$

$$M_xO_{y-1} + H_2O \rightarrow H_2 + M_xO_y$$

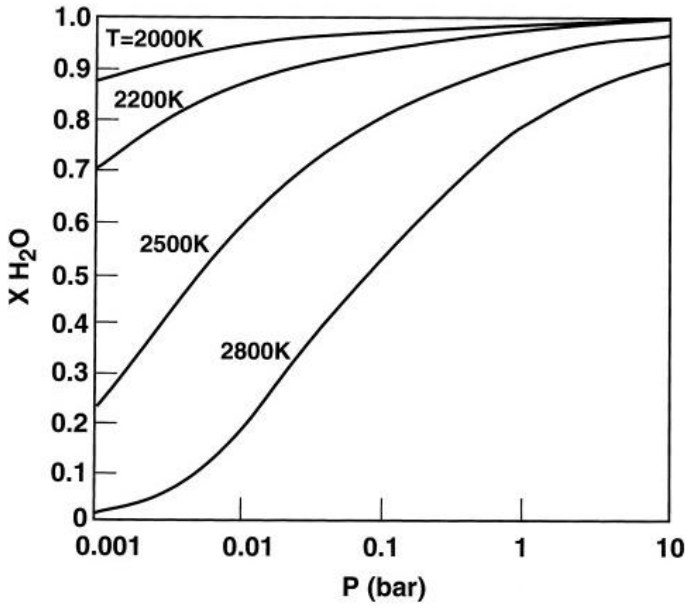

[303]

Figure A1.3.4 – Pressure and Temperature Effects on Steam Thermal Decomposition
Graph of H_2O proportion (X) that does not decompose during the reaction, by p and T.

The two stages are dissociation and water reduction. Data for the thermodynamics of metal oxidation is shown in Figure A1.3.5, for Zn/ZnO, Mn_2O_3/MnO, Fe_3O_4/FeO [303]. These chemical TD processes show thermodynamic favourability at much lower T than for H_2O, such as 1750 K for Mn_2O_3/MnO.

There are other cycles such as sulphur iodine and hybrid sulphur, shown in Figures A1.3.6 and A1.3.7, which are reported to be the most favourable, occurring between 725-1075 K. The latter is a combination of thermochemical decomposition and electrolysis [32] [111] [305]. Optimum thermal efficiencies of these reactions are reported generally < 55%.

The net chemical process for these reactions is the same as shown previously for electrolysis of H_2O. Multiple stage, metal oxide or thermochemical processes are possibilities for the future. These are not yet suitable for commercial scale. Use of solar, nuclear, waste or combinations of these heating sources are however credible options for promoting conventional reforming processes or electrolysis in the near term, and thermal decomposition in the long term.

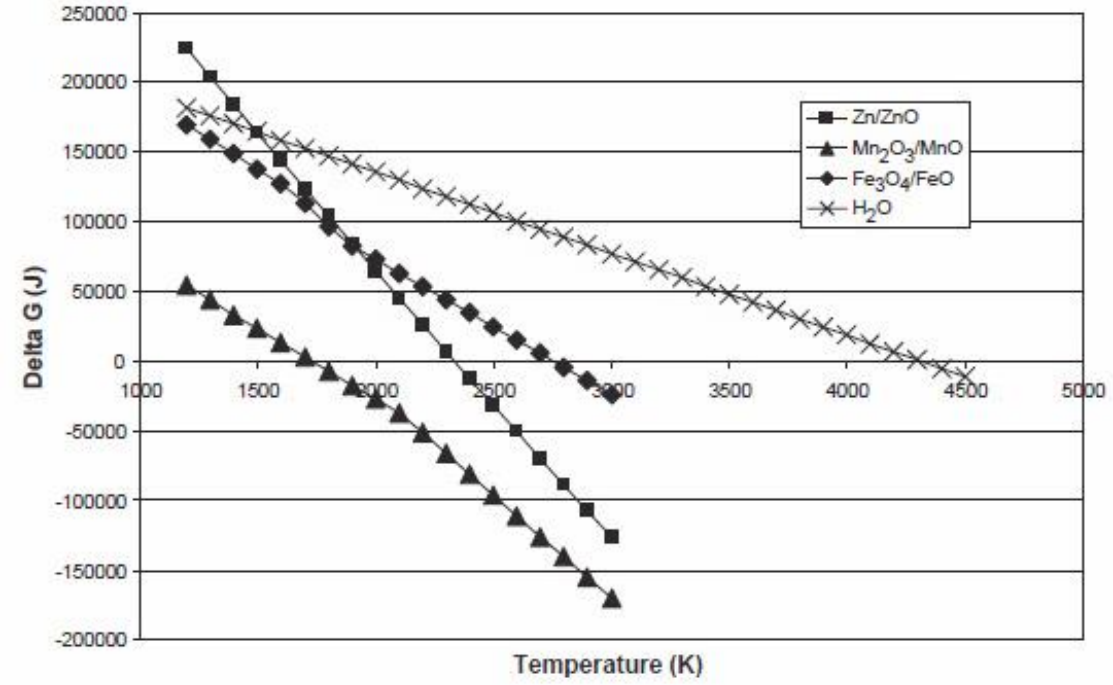

[303]

Figure A1.3.5 – Thermodynamics of Thermal Decomposition with Metal Oxides
Equilibrium temperatures for three metal oxides are shown to be lower than H_2O.

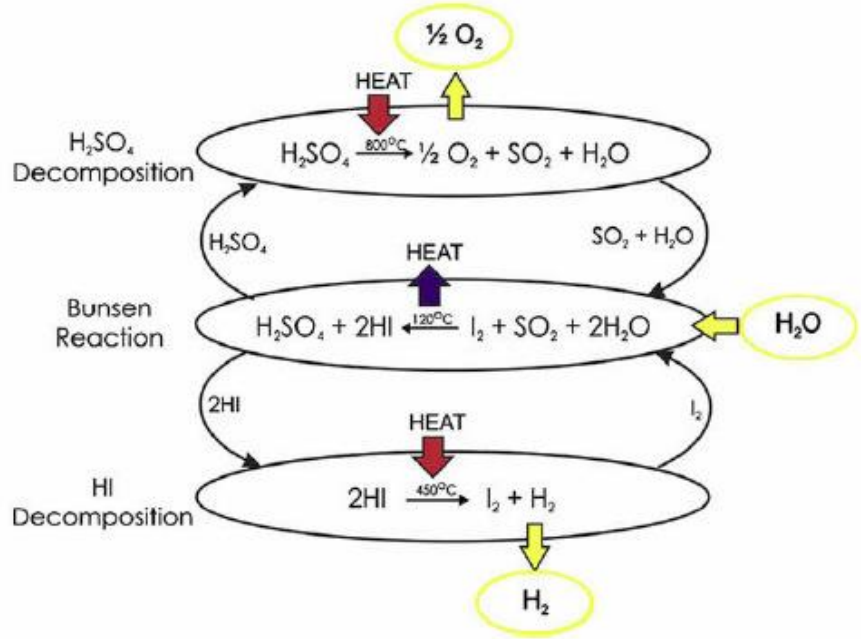

[111] [32]

Figure A1.3.6 – Sulphur Iodine Thermochemical Cycle

- Bunsen reaction – H_2O is reacted with I_2 and SO_2 (exothermic, 400 K)
- H_2SO_4 decomposes to SO_2 in a 2-stage reaction (725 K and >1075 K, endothermic)
- Decomposition of 2HI to H_2 and I_2 (slightly endothermic)

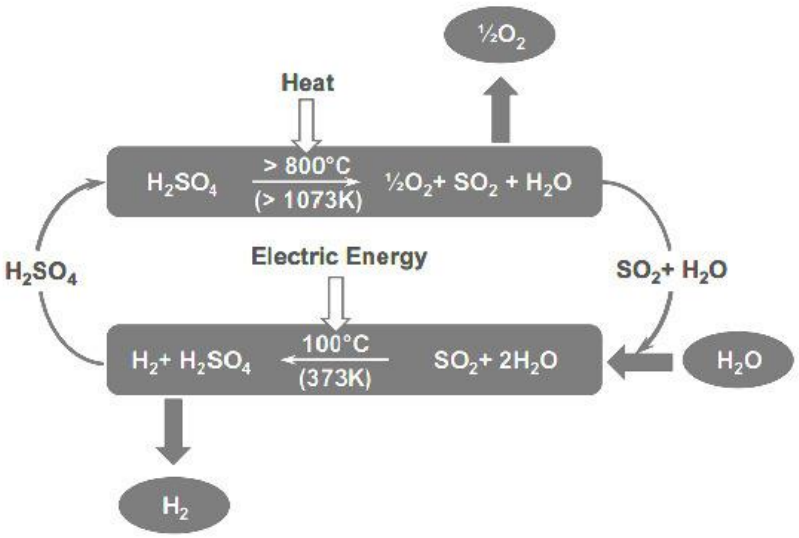

[304]

Figure A1.3.7 – Hybrid Sulphur Thermochemical Cycle

- Electrolysis of $2H_2O + SO_2$ forming $H_2 + H_2SO_4$ (360-373 K)
- Decomposition of H_2SO_4, forming O_2 (1075 K, endothermic)

A1.3.12 Photocatalytic Water Splitting and Photoelectrolysis

Water splitting to produce H_2 and O_2 can be achieved via photocatalytic processes utilising solar energy [206] [207]. It has also been attempted to combine photocatalytic and electrolysis-type photoelectrochemical (PEC) processes, often termed photoelectrolysis [33]. These are both 'artificial photosynthesis' processes and potentially promising methods for renewable H_2. Photocatalytic water splitting (PCWS) and other PEC processes have been described in literature since 1972 and are typically based upon use of TiO_2 catalytic electrodes. While there are other options such as CdS and SiC, oxides and TiO_2 in particular are considered more stable, non-corrosive, environmentally friendly, abundant and cost effective. The PCWS process is illustrated in Figure A1.3.8. It requires the photogeneration of electron-hole (E-H) pairs. When a photon of sufficient energy strikes a TiO_2 (semiconductor) electrode, an electron-hole pair can form. They may recombine, or migrate to the electrode surface where they can react with adsorbed H_2O (reduction/oxidation). Key aspects are the active surface area, hence nanoscale surfaces are used. Also, the conduction band (CB) and valance band (VB) levels are significant. The CB level should be more negative than the reduction potential of H_2O to initiate production of H_2, since electrons (in the CB) reduce H^+ to form H_2, while the VB should be more positive than the H_2O oxidation potential to from O_2 [206] [207].

There are four significant challenges with this process [206] [207]:

- The recombination of photo-generated electron/hole pairs within the electrode
- The recombination of H_2 and O_2 (to reform H_2O)
- Only solar UV light can be used (4%) with TiO_2, due to its band gap (3.2 eV)
- Final separation of the H_2 and O_2 products from the H_2O medium

In order to overcome these issues, there are two main groups of approaches: chemical additives (addition of electron donors/hole scavengers, addition of carbonate salts); photocatalyst modification techniques (noble metals loading, metal ion doping, anion doping, dye sensitisation, composite semiconductors, metal ion-implantation) [200] [206]. Example electron donors are sacrificial reagents or hole scavengers such as certain hydrocarbons. These can enhance electron-hole separation by acting irreversibly with holes, improving efficiency. The electron donors require replenishment to continue H_2 production. Enhanced production has also been reported by the addition of Na_2CO_3. This is understood to form radicals that consume holes and promote electron-hole separation. Use of noble metals such as Pt, Au, Pd, Rh, Ni, Cu and Ag tend to hold the electron but the hole remains within the TiO_2. The result is a promoted reaction and reduced recombination. In addition, dye sensitisation (with redox property and visible light sensitivity) can be used to add electrons to the CB, thus improving the efficiency [206].

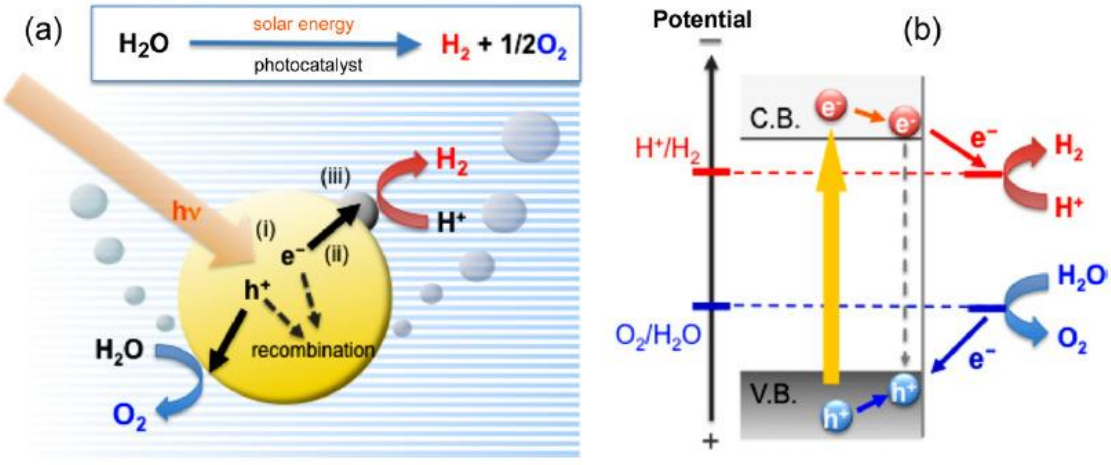

[207]

Figure A1.3.8 – Photocatalytic Water Splitting Reaction and Band Diagram
In (a) photocatalytic sites form surface E-H pairs, which can split H_2O, creating O_2 + H_2, and (b) the necessary material CB and VB levels are shown (for redox to occur).

There are two main strategies within the attempts to use visible light [207]. One is a two-step photoexcitation (similar to natural photosynthesis 'Z scheme') using two different photocatalysts. The PCWS reaction is therefore performed in two stages; one for H_2 and another for O_2 evolution. These are combined using a shuttle redox couple in the solution. In the H_2 reaction, the photoexcited electrons reduce H_2O to H_2. Holes in the valence band oxidise the reductant to an oxidant. The oxidant is reduced back to the reductant by photoexcited electrons generated over an O_2 evolution photocatalyst, where the holes oxidise H_2O to O_2.

The second method attempts to perform a single-step PCWS reaction using a single visible-light responsive photocatalyst. Few stable semiconductors can absorb visible light and have a sufficiently high potential for PCWS, therefore materials have to be developed/engineered to have a narrow band gap, to be stable under solar irradiation/UV light, and have suitable CB and VB levels as discussed previously. Unfortunately there remains to be only a few reliable engineered photocatalysts for the one-step PCWS reaction under visible light, one recent example being a WO_3 electrode (efficiency reported as 3.76 %) [208]. The band diagrams for these two reactions are shown in Figure A1.3.9.

Separation of the products can be achieved by diffusion membranes, diaphragms etc. It is also reported that an electron mediator (Fe^{2+}/Fe^{3+}) and proton conduction membrane (Nafion) can be used to provide separation from twin H_2 and O_2 electrodes, and for reduced back reaction/recombination [306]. Various oxides, nitrides, sulphides, carbides and phosphides have been reported to perform the PCWS reaction. The quantum efficiency (only reported as high as 5.9%) of these processes is a 'bottleneck' to its commercial application, where 10% is regarded as the minimum [307]. Using an array of PCWS processes driven by solar energy is however a promising and potentially renewable future source of H_2.

PCWS is further discussed in Chapter 5, where practical investigation of large surface area TiO_2 electrode formation from nanoscale deposition and laser processing is considered.

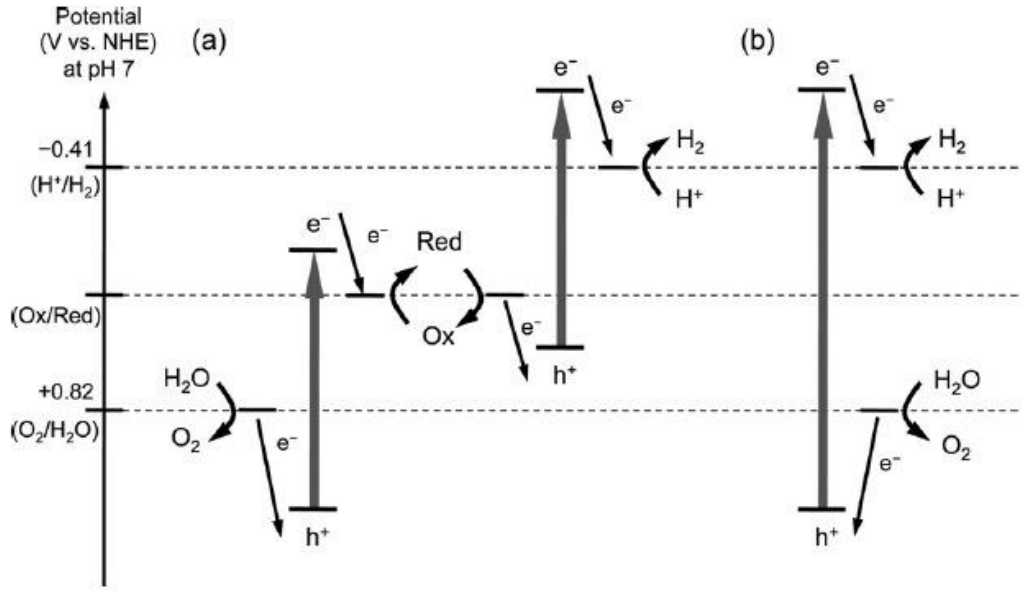

[207]

Figure A1.3.9 – Band Diagram of Two-Step (a) and Single-Step (b) PCWS Reactions
Band diagram showing (a) two-step and (b) single-step PCWS reactions.

PEC processes are based upon electrolysis with the addition of a photocatalyst and light source (to improve electrical efficiency), or PCWS with the addition of an electrolysis reaction to improve kinetics and provide separation (there is often crossover in literature with the definition of these processes and under which process they belong) [207]. An example PEC device is shown in Figure A1.3.10, with TiO_2 nanotube enhanced Ni electrodes, NaOH electrolyte and perfluorosulfonic acid ionic membrane (180 µm thickness) [201]. The increase of H_2 production from the combined process in Figure A1.3.10 has been shown to be quite significant with the addition of light (UV), displayed in Figure A1.3.11. The data for 1.6 V (and other data from this source from 0-1.6 V) shows negligible H_2 production in comparison. At 2.0 V and with UV light the production rate is significantly improved, showing the relevance of both of these factors [201]. However, PCWS/PEC processes compete with more conventional solar photovoltaics and electrolysis to provide solar H_2 production (which is approx. 10-13% efficient), hence the 10% target apparent for PEC technologies. PEC processes and the other decomposition processes discussed through Sections A1.3.9-A1.3.12 generally require pure/distilled H_2O. A table of approx. efficiencies (if known) and status for the main H_2 production processes are listed in Table A1.3.3. Efficiency values stated are referring to what may be theoretically possible in the event that they reach commercial development [33].

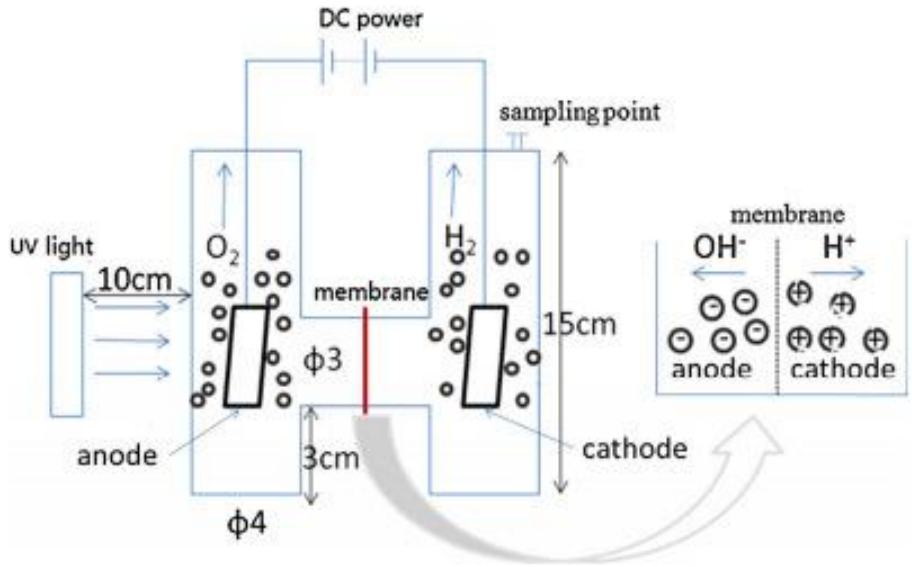

[201]

Figure A1.3.10 – Electrolysis + Photocatalytic/Photoelectrochemical Cell Schematic
Example PEC with use of UV light and catalyst-coated electrodes to enhance an (alkaline) electrolysis reaction. A membrane is used to separate the H_2 and O_2.

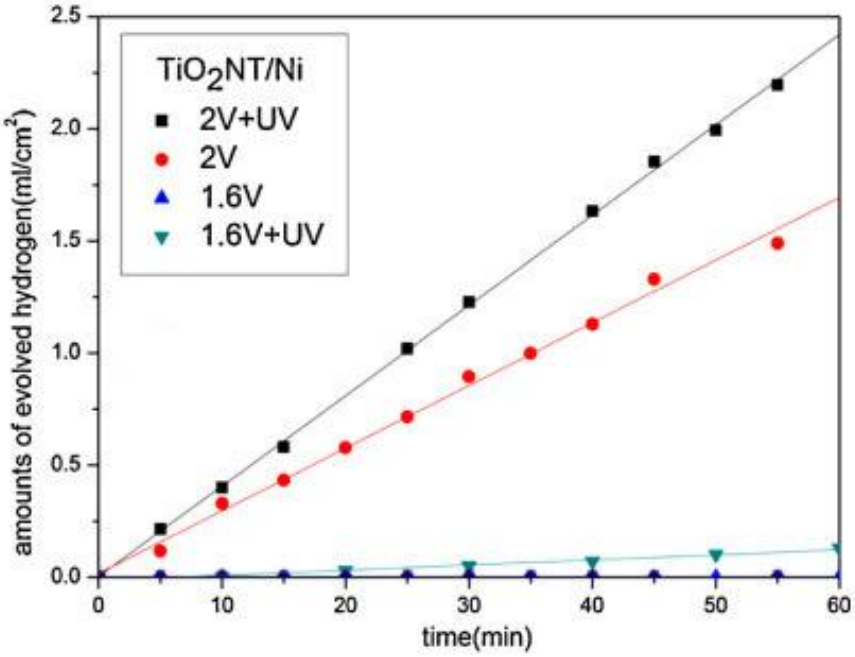

[201]

Figure A1.3.11 – Photocatalytic Enhanced Electrolysis under UV Light
Specific H_2 production data (ml cm^{-2} surface area) from PEC described in Figure A1.3.10

Process	Feed stock	Efficiency	Feasibility
Steam reforming (SR)	Hydrocarbons	70–85%	Commercial
Partial oxidation (POX)	Hydrocarbons	60–75%	Commercial
Autothermal reforming (ATR)	Hydrocarbons	60–75%	Near term
Plasma reforming	Hydrocarbons	9–85%	Long term
Aqueous phase reforming (APR)	Carbohydrates	35–55%	Medium term
Ammonia reforming	Ammonia	–	Near term
Biomass/Coal gasification (BG/CG)	Biomass/Coal	35–50%	Commercial
Photolysis	H_2O Sunlight	0.5%	Long term
Dark fermentation	Biomass	30–80%	Long term
Photo fermentation	Biomass + sunlight	0.1%	Long term
Microbial electrolysis cells	Biomass + elec	78%	Long term
Alkaline electrolyser	H_2O + elec	60–70%	Commercial
PEM electrolyser	H_2O + elec	65–85%	Very near term
Solid oxide electrolyser	H_2O + elec + heat	40–60%	Medium term
Thermochemical water splitting	H_2O + heat	–	Long term
Photoelectrochemical water splitting	H_2O + sunlight	12.4%	Long term

[33]

Table A1.3.3 – Hydrogen Production Processes, Efficiency and Feasibility
Summary data from literature for H_2 production processes discussed in this work.

Appendix A1.4 – Conventional Hydrogen Storage

A1.4.1 Compressed Storage

Storage of H_2 under high pressure within cylinders is currently the cheapest and most effective conventional mechanical method for stationary and automotive applications [15]. For portable/automotive applications, there are clearly limits with the use of high pressure storage, since increased p brings increased weight to the tank. Compressed storage tanks have been traditionally metallic (steel, aluminium) for thermal conductivity, but more recently carbon fibre reinforced plastic (CFRP) composites due to strength issues and safety standards. Unfortunately the CFRP materials do not have the high thermal conductivity required and must be kept under 358 K, which slows the refilling process [46]. There are however raised safety concerns in the event of exposure to fire, since this will weaken the mechanical properties of a CFRP tank.

There are mainly two types of compressed storage tank in use for automotive applications. These are CFRP (type IV) and metal-lined CFRP (type III). The latter is generally preferred, having a compromise of Al and CFRP properties, but at greater

cost and lower capacity [46]. Use of tensile internal struts is one example of attempts to reduce tank weight but maintaining strength, to further increase storage capacity; however, manufacturing and durability improvements of such tanks remain in progress for them to become viable [308]. There has also been recent interest in hollow glass microspheres (HGMs) to provide H_2 storage [309]. These have a unique structure of interconnected pores in microsphere walls, which can absorb, retain and release hydrogen. Dimensions of HGMs are 10-100 μm, with wall thickness of 1-2 μm and pores on the microsphere walls of 100-500 nm. HGMs have advantages over other storage methods, for example they are easy to handle at atmospheric p and T, can be packed in cartridges from which H_2 can be released, they are also cheap, reusable and recyclable. Storage in HGMs occurs from diffusion of H_2 through the heated porous walls (uptake occurs at high p and T); on cooling, the H_2 is retained inside. To release requires slight heating. However, glass does not conduct heat favourably, which can result in slow or partial uptake. These thermodynamic/kinetic factors and fairly low capacity are however currently of high research interest, such as addition of metals such as Fe, Co or Zn to improve thermal conductivity [309].

CFRP tanks are typically rated at 350 or 700 bar (these are design assumptions based on USDoE and industry input). The higher p improves volumetric density but not gravimetric, since material weight increases by a greater factor [310]. Systems also incorporate various sensors/gauges/transducers, solenoid control valves, pressure regulators, ports and relief components (balance of plant, around one fifth of total system weight). Base cases for CFRP type IV single tank storage systems are reported to be 5.5 wt% for 350 bar and 5.2 wt% for 700 bar. These may increase to 6.0 wt% and 5.9 wt% respectively with further improvements to the CFRP properties (strength of composite) and reduction of minimum base p from 20 bar to 3 bar. The H_2 occupies approx. 70-81% of the actual volume of the tank. For type III, the base figures are 4.2 wt% and 3.6 wt% for 350 and 700 bar single tanks. For dual tank systems, these figures are all slightly lower [310]. At 350 and 700 bar, base volumetric densities have been reported for CFRP type IV as 0.0176 and 0.0263 kg H_2 L^{-1} respectively. These values may reach as high as 0.0188 and 0.0278 kg H_2 L^{-1} respectively with the improvements discussed above. Use of type III brings little effect to the volumetric density at 350 bar but slight reduction at 700 bar [309]. Costs of 342 £ kg^{-1} (520 $ kg^{-1})

are reported for a 5.6 kg tank (350 bar, type IV); approx. 75% of this results from the CFRP material (>100 times the value of the H_2 that it can store) [310]. For stationary applications using Al tanks, costs are lower, 0.14-0.40 £ kg^{-1} (0.21-0.60 $ GJ^{-1}) [15].

Compressed storage of H_2 offers the best compromise of capacity, simplicity and cost at present for automotive applications [48]. Use of rigorously tested type IV 700 bar tanks are scheduled for the next batches of H_2 FCVs scheduled to be released over the coming years [311]. Until these benchmarks can be significantly outperformed, use of CFRP will continue, although propagation of hydrogen in automotive markets will be restricted from the storage perspective.

A1.4.2 Liquefaction

Cryogenic storage of H_2 in liquid form (LH_2) occurs at 20 K. Formation of LH_2 has been achieved effectively since as early as 1900, such as with the Claude cycle, and expanded significantly in the 1950s for the US space programme [312]. LH_2 itself exists at 0.07 kg L^{-1} (10 MJ L^{-1}). In comparison to compressed storage, liquefaction can achieve approx. twice the volumetric density [46]. Despite the superior volumetric storage, very large amounts of energy are required to create LH_2 (for example 50 MJ kg^{-1}, three times that which is required to compress H_2 to 690 bar). Additionally, LH_2 boils very easily during storage and refilling etc. Evaporation (0.3-3.0% per day) leads to very high pressures occurring over time (boil-off), which require venting and monitoring [311] [313]. The vessel also requires very high performance thermal insulation to reduce conduction, convection and radiated heat transfer, consisting of alternating metallic and thermally insulated polymer or glass films. As a result of these properties and ancillary components, an example LH_2 storage tank system of combined 90 kg weight contains 4.6 kg LH_2 (5.1 wt%) [46]. The physical amount of storage of LH_2 borders on what is satisfactorily for automotive applications; however, the fundamental energy and monetary cost of LH_2 and practical issues as discussed have kept development of LH_2 restricted and it will not likely reach commercial usage in automotive applications. LH_2 will however likely remain within static storage or rocket fuel markets for the foreseeable future [311]. Combination of LH_2 with compression technology (cryocompression) however has seen significant research interest, discussed in the next section.

A1.4.3 Cryocompression

Significant recent developments in conventional storage systems use a hybrid of compressed LH_2, cryogenic H_2 or two-phase systems [46]. Compressed LH_2 can achieve 0.087 kg L^{-1} at 237 atm (24% improvement on LH_2 at 1 atm). As LH_2 vaporises, heat to provide ΔH_{Vap} is extracted from the LH_2, but the rate of heat entering the vessel obviously exceeds this heat extraction. Conventional LH_2 vessels can generally withstand 6 bar. Increased p allows less cooling or venting loss since the vessel can vent H_2 at higher T. Also, by allowing higher T, LH_2 enters a mixed phase as it vapourises at increasing p, as shown in Figure A1.4.1. As T rises, the LH_2-phase and H_2-phase densities merge to a common value; the physical distinction between LH_2 and H_2 disappears (critical point). H_2 in the tank can be kept at very high p, allowing the H_2 to exist at 30% of the density of LH_2 [311]. Cryocompression therefore improves venting loss and ultimately offers improved volumetric density (and safety); therefore it offers significant potential and may become established in commercial markets. This is supported by testing of a Toyota Prius, which as of 2013 demonstrated the longest unrefuelled distance travelled by a FCV. Comparison of a 71 L / 102 kg (5.6 kg H_2) compressed LH_2 tank to USDoE targets revealed the following [46]:

- Gravimetric density of 5.5 wt% meets 2017 target. Increased p and use of Al for outer shell material are reported to allow the vessel to meet the ultimate target.
- The tank had a volumetric density of 0.0418 kg H_2 L^{-1}, and potentially reaching 0.0478 kg H_2 L^{-1}. This meets the 2017 target but not the ultimate target.
- Cost was approx. two times USDoE targets.
- Efficiency – due to use of LH_2, at 41.4% this tank could not meet the 60% target.

Compressed cryogenic H_2 offers another potential method to increase storage density by a factor of three compared to conventional compressed storage, but omitting the energy cost of creating LH_2. Using liquid N_2, a tank of H_2 can be cooled to 77 K. For example, at 740 atm, 4.1 kg can be stored within 100 L at ambient T; however, at 77 K, only 148 atm is required. This may therefore offer another storage mechanism to improve capacity. The addition of thermal insulation does add weight and volume to the tank unfortunately; hence this storage method remains under development [46].

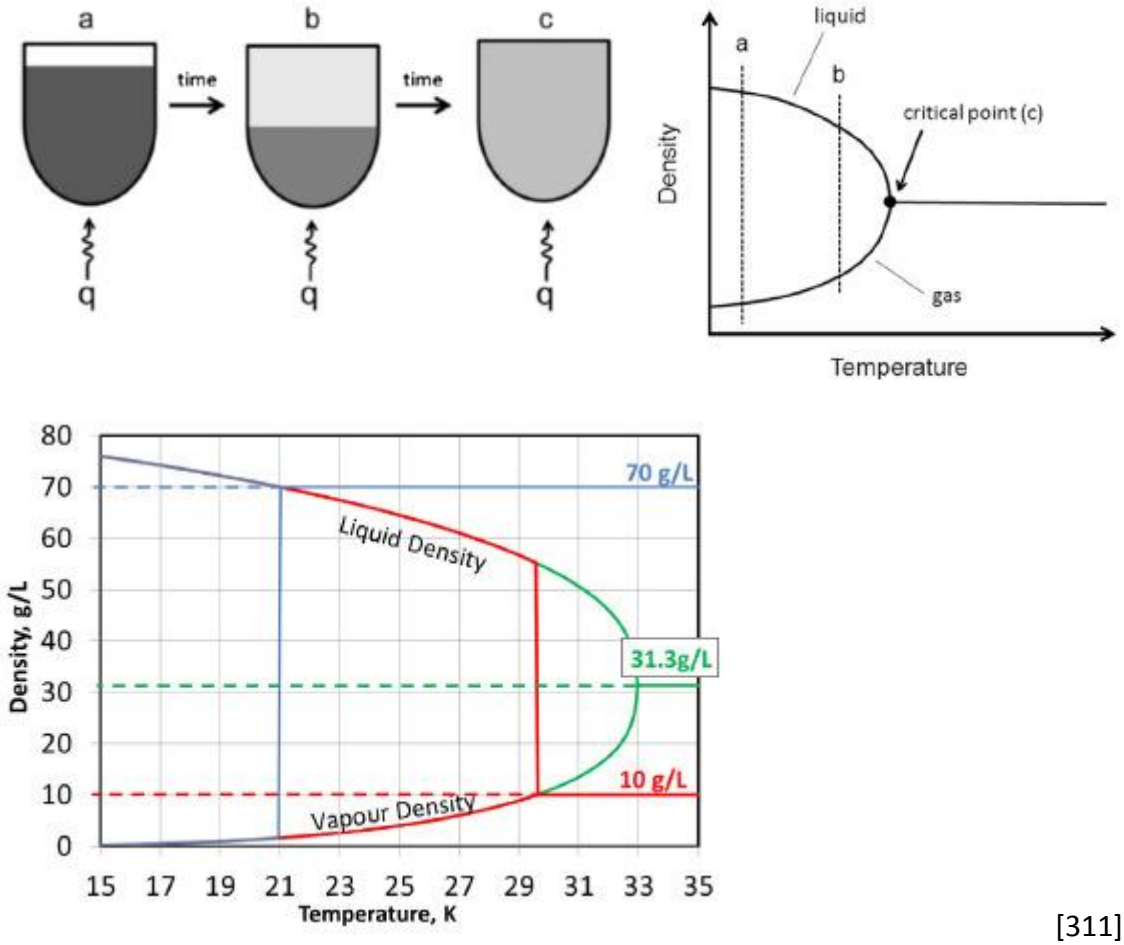

[311]

Figure A1.4.1 – Phase Change in Cryocompressed LH_2/H_2 Vessel
LH_2 enters a mixed phase in a cryogenic vessel as T and p are allowed to increase, permitting higher density than compression alone and more practicality than LH_2.

Appendix A1.5 – Metal/Chemical Hydrides

Metal or chemical hydrides are materials that contain chemically bound hydrogen. They are formed at elevated temperatures with strong bonds (high bonding enthalpies), from light materials (the first 20 elements). For these reasons they are not reversible at low temperatures or easily recharged on-board a FCV, but they can exceed capacities of conventional storage methods [313]. Hydrides have received a considerable amount of research effort [46] [313] [314]. There are several hydride materials and chemical mechanisms described in literature; categorisation differs between sources but can be generally fitted conveniently into the following:

- Metal hydrides
- Complex metal hydrides
- Non-metal/chemical hydrides

A1.5.1 Metal Hydrides

Metal hydrides involve one or more light metals to form a host structure to absorb H. Considering various chemical characteristics, Li, B, C, Mg and Al are the most promising [50]. The absorption process first involves H_2 transitioning to a film of physisorbed H_2 (van der Waals forces, approx. 1-10 kJ mol^{-1}) on the surface of the metal(s) (at radius of approx. one H_2 molecule). H_2 then dissociates to H (436 kJ mol^{-1}), interacting with several surface molecules (Leonard Jones 6-12 potential). The dissociation barrier is overcome to form a chemisorbed state on the surface (40-60 kJ mol^{-1}), and the H atom can diffuse into the bulk material, occurring quickly even when T = ambient. This forms an M-H phase ('α phase', where M represents a metal). The 'α phase' H concentration is p-dependent. A 'β phase' exists as the H atoms diffuse into the lattice and form the hydride compound. The diagram shown in Figure A1.5.1 demonstrates the basic hydride forming process [313]. Desorption is the reverse of this process. The transition from α to β phase is demonstrated in Figure A1.5.2 with isotherms, where C_H is the H concentration and T_C is the critical point where the phase is continuous.

The simplest hydrides with one metal are reported to be not particularly effective due to issues such as high T for H_2 desorption, slow kinetics and high reactivity to air/O_2 (forming a stable MgO material layer for example). The most notable of these are MgH_2 and AlH_3. MgH_2 has previously been reported to have the highest energy density of all reversible metal hydrides, at 7.6 wt% or 10.8 MJ kg^{-1}, requiring T = 300°C for H_2 desorption [50] [314] [315]. AlH_3 and some other hydrides have been reported to exceed that capacity, but reversibility and kinetics are issues [46]. MgH_2 has inadvertently set a benchmark for hydrides to match in terms of reversibility, capacity, cost (relatively low), but ideally provide desorption closer to ambient conditions, which would make the hydride suitable for on-board hydrogen storage.

As metal hydrides store hydrogen within the crystalline structure of the host, defects/vacancies within the material can improve the storage properties. Attempts to improve MgH_2 desorption T and kinetics have included mechanical ball milling with other elements as a pre-treatment to reduce the stability of hydride and to increase surface area. This induces thermodynamic and kinetic changes to the material, providing stable defects, phase change, and a crystalline or amorphous structure. In an amorphous structure, there is distortion and variation, therefore the binding energy

varies, allowing occupancy at lower p and T, although this may reduce the overall storage capacity. There is also the use of improved catalysts etc [50] [314]. Extensive data on MgH_2 and advanced hydride capacities/kinetics is provided by Sakintuna et al [314].

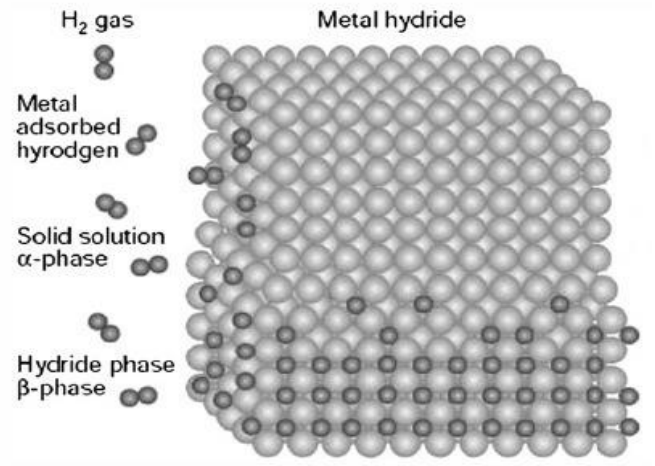

[313]

Figure A1.5.1 – Schematic of Metal Hydride Structure

H_2 molecules exist at the surface, forming an adsorbed (H_2) phase, then solid (H) α phase, then β phase (hydride where H atoms exist interstitially in the metal lattice).

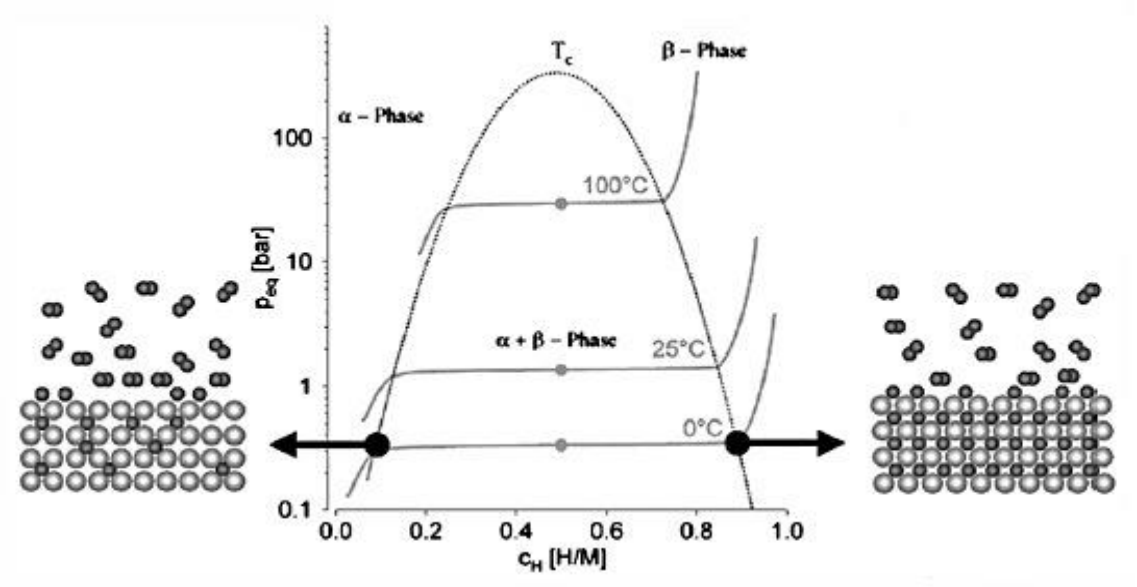

[313]

Figure A1.5.2 – Metal Hydride Isothermal Pressure-Composition Curves

Transition from α to β phase is shown occurring along isotherms. C_H is the H concentration and T_C is the critical point where the phase is continuous.

Intermetallic hydrides involving more than one metal provide H uptake at lower temperatures. The principle is to have one light rare earth or alkaline metal (providing the strong hydride bond) and a heavier transition metal forming an unstable hydride. The target for hydrides is T = 0-100°C and p = 1-10 atm [313]. Only a few hydrides can work in this range, as shown by the van't Hoff plots in Figure A1.5.3, which are intermetallic. Unfortunately the cost of many of these intermetallic hydrides is high and the gravimetric capacity low.

One of the most promising from those intermetallics shown in Figure A1.5.3 and now commercially available is $LaNi_5H_6$. Hydrides with more than two metals, often (heavier) metals such as Ti, V, Cr, Mn, Fe, Co, Pt and Ru are the subject of research and many of which are capable of improved kinetics. They can also incorporate hydrogenation catalysts such as Pd and Ni. The use of heavy metals limits the gravimetric capacity to approx. 3 wt% for reversible hydrides operating at ambient p and T [313]. Volumetric capacity is high for most metal hydrides; however, there is a compromise with gravimetric capacity, reversibility, kinetics, p/T, and cost.

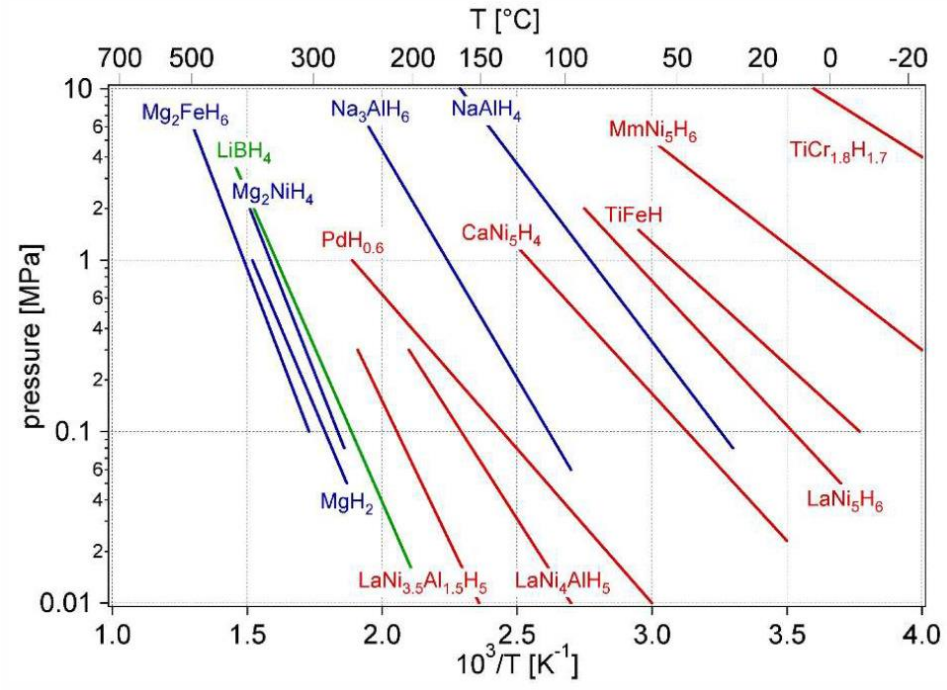

[316]

Figure A1.5.3 – Equilibrium Pressure and Temperature for Various Metal Hydrides
Various van't Hoff plots are shown for significant metal hydrides, where $LaNi_5H_6$ is one of the only showing potential for H uptake near ambient p and T.

A1.5.2 Complex Metal Hydrides

Complex hydrides differ from more simple metallic hydrides by the transition to an ionic or covalent compound upon hydrogen absorption. These include mainly alanates and borohydrides and have received considerable attention as hydrogen storage materials, potentially allowing up to 18 wt% and lower desorption T (150°C) [46] [313] [314]. Alanates have received the most attention recently, $NaAlH_4$ in particular. Reversible hydrogen storage of 4.2 wt% has been demonstrated with $NaAlH_4$ (doped with Ti) at 210°C, although kinetics were slow. However, variation of particle size, catalysts and dopants were shown to improve the kinetics substantially [313]. $NaAlH_4$ dehydrogenation occurs in two steps (37 and 47 kJ mol^{-1}) [313]:

$$3NaAlH_4 \rightarrow Na_3AlH_6 + 2Al + 3H_2$$
$$Na_3AlH_6 \rightarrow 3NaH + Al + 1.5H_2$$

The first step is limited at 3.7 wt% and can occur at just above ambient conditions. The second requires slightly above 100°C, giving a total of (theoretical limit) of 5.5 wt% [46]. Hydrogenation occurs at around 100 bar, 100°C however. The rate, high p, and stability are two significant issues requiring ongoing research (for example with ball milling/doping procedures and use of additional catalysts such as $Ti/TiCl_3$ and Zr, which permit much lower T) [50] [313].

Mg alanate ($Mg(AlH_4)_2$) exhibits high gravimetric capacity although it is less stable than $NaAlH_4$. Again this occurs in two steps:

$$Mg(AlH_4)_2 \rightarrow MgH_2 + 2Al + 3H_2$$
$$MgH_2 \rightarrow Mg + H_2$$

Peak decomposition of the first step has been found to occur at 163°C, releasing 6.6 wt%. The total theoretical limit for $Mg(AlH_4)_2$ is 9.3 wt%. Some important issues need to be addressed (using similar techniques as above) prior to practical application, including slow kinetics, reducing T (< 100°C), and the formation of stable MgH_2 and Al_2Mg_2 (negatively influencing hydrogenation) [313]. $LiAlH_4$ is an interesting alanate with a theoretical 10.5 wt% capacity (with issues of reversibility) [317], also known to release 3 wt% at 100°C. However, for all these hydrides there is a need for balance of doping etc to find a compromise for the overall cycle. The $Mg(AlH_4)_2$ system can

release 6 wt% hydrogen at 150 °C, although reversibility is still questionable. $NaAlH_4$ is unlikely to be fully adequate for mainstream automotive markets due to the wt% limit and its hydrogenation, under existing storage expectations.

Borohydrides are the other main group of complex hydrides. This includes $LiBH_4$ (potentially capable of up to 18.5 wt%) and $NaBH_4$. These hydrides require even higher dehydrogenation T (> 673 K), due to strong stable hydride bonds [46]. Therefore research is focussed upon reducing bonding enthalpies and improving kinetics [313]. The dehydrogenation reaction proceeds as follows [46]:

$$2LiBH_4 \rightarrow 2LiH + 2B + 3H_2$$

Due to lack of reversibility, $LiBH_4$ will probably only suit one-shot storage systems in the near future, but may contain up to for example 13.8 wt% [313]. Destabilising techniques have involved additives such as metals, metal oxides, $LiNH_2$, sulphides or other hydrides, doping (Ti), catalysis etc [46] [318]. H_2 can also be released by a hydrolysis reaction. However this is commonly used with $NaBH_4$, since it is slightly safer and occurs at ambient T (although it favours higher T) [293]. This involves Ni, Ru, F/Co or Pt catalysts with the following typical reaction (not reversible) [46] [293] [294]:

$$NaBH_4 + 2H_2O \rightarrow NaBO_2 + 4H_2$$

H_2 storage capacities with this are stated to reach approx. 7 wt%; however, it is reported that the high cost of $NaBH_4$ is the prohibiting factor at present [293] [294].

Two other complex hydride groups are amides/imides such as $LiNH_2$, and combinations of two metals (Li/Mg) [319]. $LiNH_2$ can reversibly store up to 6.5 wt% at 558 K [46]. $Mg(NH_2)_2$ is an alternative with lower reaction T. Although these are of interest, the reactions produce NH_3 as a by-product, which even at 0.1 ppm damages PEM FCs [46] [314]. Finally, the addition of MgH_2 to a $LiBH_4$ complex hydride has a destabilising effect, also creating an intermediate reaction that occur at approx. 240 K lower than for pure $LiBH_4$ [46]. This offers some improvement but the overall reaction T is still high and with slow kinetics. Use of $Mg(OH)_2$ additive has recently been published discussing a three-step reaction achieving 9.6 wt% at 500°C and with some reversibility [318]. Complex hydrides therefore demonstrate high capacities, but with complex multi-step mechanisms where it will be difficult to enhance all of the steps with one

dopant/ball milling process etc. They proceed typically at high T, with slow kinetics and stability and reversibly issues, also involving expensive materials. Theoretical storage limits for various complex hydrides are shown in Table A1.5.1 [320].

Hydride	wt%	Availability
$KAlH_4$	5.8	J. Alloys Compd. (2003) 353, 310
$LiBH_4$	18.5	Commercially available
$Al(BH_4)_3$	16.9	J. Am. Chem. Soc. (1953) 75, 209
$LiAlH_2(BH_4)_2$	15.3	British Patents 840 572, 863 491
$Mg(AlH_4)_2$	9.3	Inorg. Chem. (1970) 9, 325
$Mg(BH_4)_2$	14.9	Inorg. Chem. (1972) 11, 929
$Ca(AlH_4)_2$	7.9	J. Inorg. Nucl. Chem. (1955) 1, 317
$NaAlH_4$	7.5	Commercially available
$NaBH_4$	10.6	Commercially available
$Ti(BH_4)_3$	13.1	J. Am. Chem. Soc. (1949) 71, 2488
$Zr(BH_4)_3$	8.9	J. Am. Chem. Soc. (1949) 71, 2488

[320]

Table A1.5.1 – Theoretical Storage Limits for Complex Hydrides
Summary data from literature for known complex hydride storage capacity (wt%).

A1.5.3 Non-metal/Chemical Hydrides

There remain several hydrides that are not based upon metals (or metals do not form the main part of the hydride). These are known to offer weaker bonding, allowing use of lighter materials, including hydrides of B, C or N [46]. Storage in the form of hydrocarbons would be an obvious choice since it would fit the existing fuel infrastructure. Release of H_2 from hydrocarbon reforming has been discussed in Appendix A1.3. The formation of hydrocarbons is discussed in Appendix A1.7, as part of Fischer-Tropsch synthesis. Chemical hydrides of B and N are the main interest (some of which fall within discussion of complex hydrides). There remain several other chemical or non-metal hydrides, such as NH_3BH_3 (ammonia borane) with a theoretical capacity of 19.6%, hence it has received significant interest. Dehydrogenation occurs over several reactions (at T = 363-423, 423, 423 and 773 K respectively):

$$NH_3BH_3 \rightarrow {}^1\!/_x\,(NH_2BH_2)_x + H_2$$
$${}^1\!/_x\,(NH_2BH_2) \rightarrow {}^1\!/_x(NHBH)_x + H_2$$
$${}^1\!/_x\,(NHBH)_x \rightarrow {}^1\!/_x\,(NBH)_x + ½\ H_2$$
$${}^1\!/_x\,(NHBH) \rightarrow {}^1\!/_x\,(NB)_x + H_2$$

Each of these reactions releases unwanted NB/NBH products. Two methods to address this have been achieved: reacting with metals; hydrolysis/alcoholysis processes. Reacting with Li to form $LiNH_2BH_3$ allows release of 11 wt% at 368 K [46]. The hydrolysis reaction is seen to be relatively clean, simple and fast:

$$NH_3BH_3 + 2H_2O \rightarrow NH_4BO_2 + 3H_2$$

This produces possibly the most effective hydride available in recent literature. Data for several B and N hydrides are shown in Figure A1.5.4 [321].

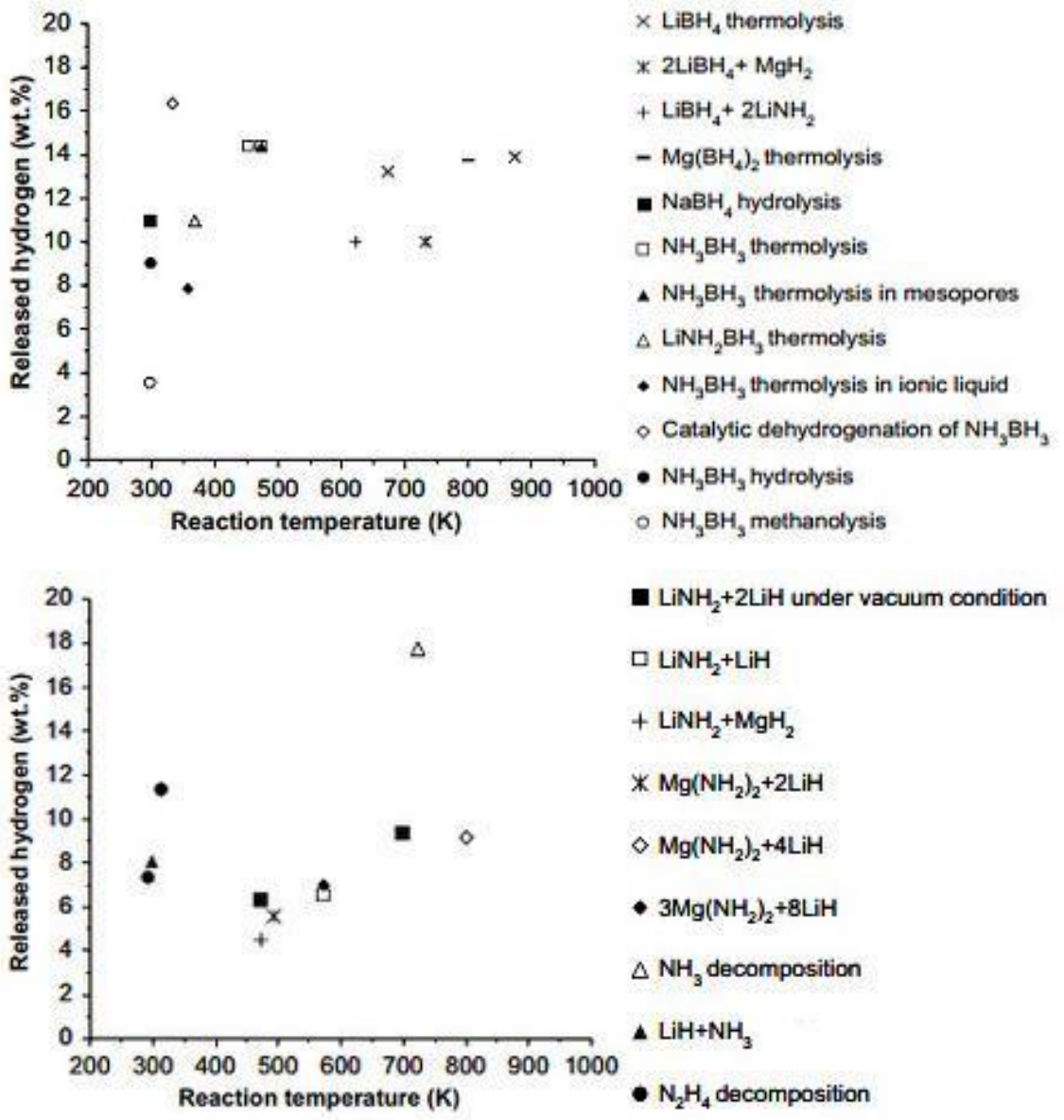

[321]

Figure A1.5.4 – Hydrogen Storage wt% in Boron and Nitrogen Hydrides
Hydrogen storage wt% data is shown for chemical hydrides based on B and N.

$Li_3N/LiNH_2$ (lithium nitride) offers another chemical hydride option with a theoretical capacity of 11.5 wt% [322]. This reaction has been observed for over a century, which is known to be reversible and occurs in two steps, demonstrating 9.3 wt% at 528 K:

$$LiNH_2 + LiH \rightarrow Li_2NH + H_2$$
$$Li_2NH + LiH \rightarrow Li_3N + H_2$$

Approximately 6.3 wt% is released under high vacuum (T < 528 K). Increasing to 593 K allows complete dehydrogenation [322]. The reaction has been shown with the characteristics in Figure A1.5.5. This has demonstrated a fairly complicated reaction and issues of stability/rehydrogenation and reversibility (requiring high T etc) have been apparent. To some extent this has been resolved with partially oxidising the material. The reaction has also shown slightly improved wt% and dehydrogenation T with use of a $TiCl_3$ catalyst and substitution of $LiNH_2/LiH$ with Mg [321].

Use of NH_3 and N_2H_4 are also interesting for chemical hydrides. NH_3 has existing infrastructure/production means and a high density, 17.7 wt%. The dehydrogenation reaction has been shown in Section A1.3.7. It is an endothermic reaction, possibly at too high T for general use. However, similarly to as discussed previously, this can be combined with LiH permitting up to 8.1 wt% at ambient T and 5 bar, therefore having significant interest for future practical use. The reaction is reversible (and $LiNH_2$ an store another 8.1 wt% hydrogen at 573 K at 5 bar) [321]. The first reaction is:

$$NH_3 + LiH \rightarrow LiNH_2 + H_2$$

N_2H_4 (hydrazine) can provide 12.6 wt%. It can be synthesised by two reactions, one involving NH_3. It dehydrogenates with the following reaction:

$$N_2H_4 \rightarrow N_2 + 2H_2$$

Reaction T must be controlled to promote H_2, rather than NH_3 formation. This leads to a complicated selectively, since at high T (> 673 K) NH_3 may dehydrogenate etc [321]. Ni/SiO_2 and Ir/Al_2O_3 are two catalysts that are reported to promote this reaction. It must be stressed than the formation of NH_3 with any of the N hydrides must be eliminated or removed to allow use of fuel cells. This is perhaps the main obstacle for

these particular chemical hydrides at present and hence delaying their use [46] [321]. NH_3 itself may however take on very important hydrogen storage roles.

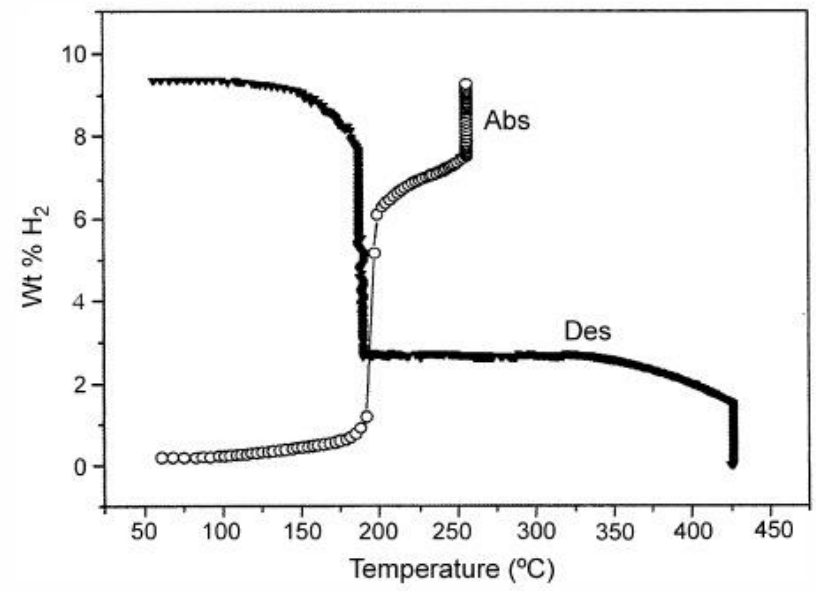

[322]

Figure A1.5.5 – Li_3N Hydrogen Absorption/Desorption
Graphical data for H_2 absorption/desorption (wt%) is for shown for Li_3N samples

Appendix A1.6 – Carbon Nanostructures and Adsorption Materials

Adsorption of H_2 onto large surface area nanostructures saw significant interest following reports of exceptionally high storage in single-walled CNTs (5-10 wt%) [323] and graphite/carbon nanofibres (GNFs) (67.55%) [215] [324] in the late 1990s. These wt% calculations were later disregarded with error assumed to be related to H_2O in the H_2 gas or measurement system for example [313] [325]. Adsorption mechanisms involve weak bonding of H_2 onto the host material, generally requiring cryogenic T and high p. Use of adsorbents with compressed cryogenic H_2 technology (as discussed in Section A1.4.3) has also seen recent research interest. CNTs, activated carbon (AC) and metal organic framework (MOF) compounds have seen significant interest, along with zeolites, clathrates and microporous polymers [46] [311].

Adsorption arises from van der Waals attractions of H_2 molecules onto the sorbent surfaces (relatively weak binding energies of 2-10 kJ mol^{-1} H_2) [311]. This storage mechanism is based upon physisorption, whereas hydride formation is based upon

chemisorption (although physisorption does occur in the initial stages of hydride formation).

A combination of long-range attractive, dispersive or van der Waals interactions, and short-range repulsive interactions occur between the H_2 and adsorbent surface, which can be represented by the Leonard Jones 6-12 potential. The attractive interaction originates from long-range forces produced by charge distribution of the H_2 and atoms and the adsorbent surface. At close range, the repulsion force becomes significant (and increase rapidly); hence there is a certain intermolecular distance where a minimum potential energy is reached, occurring at approx. one molecular radius from the adsorbent surface [313]. H_2 remains diatomic, on the host surface (not incorporated into the crystal lattice as in the case of chemisorption), bonding is reversible and kinetics are seen to be fast [311] [313]. However, the bonding is weak so T must remain low (small increases lead to desorption) and storage at ambient T is impeded. Adsorbent materials therefore need to be cooled (< 100 K) for significant storage of H_2.

Adsorption relies on two mechanisms: initial adsorption of H_2 along the immediate surface; mass transfer and subsequent retention of H_2 within internal spaces. Once one layer of H_2 forms on the adsorbent surface, the binding energy of the second layer becomes similar to the ΔH_{Vap} H_2 [313]. This is much higher than that of the first layer, so adsorption at T > 20 K (T_{Vap}) generally only allows a monolayer. The surface area includes internal micro pores within which the material that can retain H_2. Storage capacity therefore has a composite and complex dependency upon surface area/topology/chemical composition, and p and T. Carbon nanostructures have received significant attention due to their relatively low cost, low density, high surface area, extensive pore structure, wide variety of structural forms, chemical stability and versatility [215] [313]. The main H_2 adsorbent materials are reviewed in this appendix:

- Carbon nanostructures
- MOFs
- Zeolites
- Clathrates

A1.6.1 Carbon Nanostructures

Carbon nanostructures include H_2 adsorption onto AC, CNTs, GNFs, carbide-derived carbons and ordered porous carbons etc. AC is of interest due to its relative ease of manufacture and its chemistry being well-understood. This material contains very small graphite crystallites and amorphous carbon with pore diameters typically < 1nm, forming specific surface areas ≈ 3000 m^2 g^{-1}. Graphite has a multiple sheet-like structure (with hexagonal molecular rings forming the sheets) and weak van der Waals bonding the sheets above and below. AC is produced from C-rich organic materials by thermal/chemical method. Ball milling of graphite can also produce a high surface area material [223]. Adsorption within AC relies upon large surface area, appearing proportional to this and micropore area/volume (favouring narrow micropores, < 2nm) [215] [325]. Figure A1.6.1 shows this trend for various CNT/graphite/AC samples at 77 K and 298 K; as discussed previously, H_2 is assumed to store as a monolayer at T > 20 K [316]. A reasonable amount of data indicates that capacities of approx. 2.5 wt% are attainable for AC at 77 K (p = 1-10 atm) and up 5.5 wt% (p ≈ 60 atm). At T = ambient a maximum of 0.5 wt% is observed even at high p [215]. There are claims that an AC (type KUA5) can permit up to 6.8 wt% at ambient and 493 atm (significantly exceeding conventional compressed storage), although this does not appear independently confirmed. There are also H_2 recoverability issues with similar ACs such as type AX-21 [46]. Other data has demonstrated what appears to be the best performing commercial AC, Maxsorb, at 0.67 wt% (ambient) and 5.7 wt% (77 K), p = 30 bar [215].

Graphene is a single sheet of graphite, having a chemical formula of $C_{60}H_{20}$ for example (since H tends to occupy the 'dangling bonds' at the edges) [223]. Graphene does not exist naturally, as it would tend to form tubes or spheres etc. If the graphene sheet contains pentagonal (or heptagonal) rings it would be classed as fullerene. Theoretically, the maximum H_2 storage on graphene is approx. 3 wt% (based on specific surface area of 1315 m^2 g^{-1}), achievable only at very low T. This value would have to reach 3290 m^2 g^{-1} in order to match the 7.5 wt% USDoE target, but in practice > 4000 m^2 g^{-1} would be required based on extrapolation of data (Figure A1.6.1) [223].

CNTs, first discovered in 1991, are effectively graphene rolled up to form a tube with diameter ≈ 1nm for single-walled (SWCNTs) and up to 30 nm for multi-walled CNTs (MWCNTs, containing multiple tubes stacked inside each other). Lengths are usually in

the mm range. The CNT ends close with hemispherical fullerene-like structures, and can be opened by chemical or ultrasound treatment, or closed with thermal treatment. Formation of CNTs requires evaporation of C to create single atoms and molecules, condensing to form CNTs [223]. Synthesis techniques can be:

- Arc discharge between two C electrodes (produces large quantity of impure CNTs)
- Laser ablation of graphite (at 1200°C, 0.67 bar of inert gas such as Ar, He).
- CVD/PECVD, with varying amounts of catalyst material.

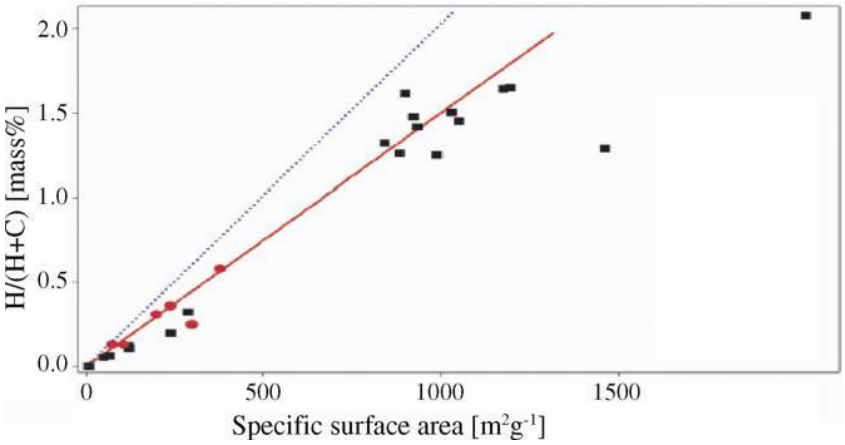

[316]

Figure A1.6.1 – Adsorption wt% of Hydrogen Proportional to Surface Area
Samples are at 298 K (red circles) and at 77 K (black squares); dotted line represents the calculated amount of H_2 that would exist in a monolayer at the substrate surface.

In the case of CNT synthesis by laser ablation, if Co/Fe/Ni are mixed with the graphite, SWCNT are formed; with pure graphite, MWCNTs are formed. For CVD/PECVD, the catalyst also has a large influence on the type and quality of CNT formed [223]. CNTs are often described within literature as expensive to produce; however, subjected to some customisation and use of basic materials the process can be relatively cheap and simple. Synthesis of CNTs was carried out by PECVD for applications within photocatalysis. The process is discussed in Chapter 5. There are also GNFs, which are not hollow and have been considered as adsorptive H_2 storage materials in literature. These are manufactured via heat treatments using carbon and catalyst particles, and provide good surface areas and interaction sites for H_2 sorption. Fullerene spheres also appear in literature but have generally not provided notable H_2 storage; these materials are not reviewed in this thesis.

Although CNTs are generally considered superior to ACs (partly due to their structure being practically known), with higher H_2 coverage per unit area, there is not credible evidence of storage ability that can suit USDoE requirements (or that which is superior to ACs) [215]. Significant issues are metallic impurities (from synthesis process) and defects, affecting their structure and performance. There is extensive coverage of CNTs within literature in this topic and research is ongoing; more recent papers discuss CNTs of various different types, sizes, additives, pre-treatment and packing arrangements. SWCNTs, generally larger ones, are preferable, since they have larger specific surface area and can potentially allow storage along the central axis [46] [326]. This is best achieved by opening the CNT ends by an oxidative treatment for instance [223]. Data for near ambient T and practical p ranges is sought (since cooling to 77 K etc is not feasible), although this is not published in abundance. There is a limit to p since physical damage may occur to the CNT structure and packing [223]. General trends of T and p are shown in Figure A1.6.2 [223]. H_2 storage data for CNTs generally concludes that there they are limited to approx. 1wt% at T = ambient, p = 100 bar. There are several original papers and reviews indicating that values of 2.0-6.3 wt% have been achieved at p = 40-148 bar; open-tipped CNTs have shown possibly the best performance for H_2 storage, of 6.46 wt% (at 77 K, 100 bar) [215] [313]. At 77 K it is implied that up to 8 wt% could be reached, although this is yet to be demonstrated and verified independently [215] [313].

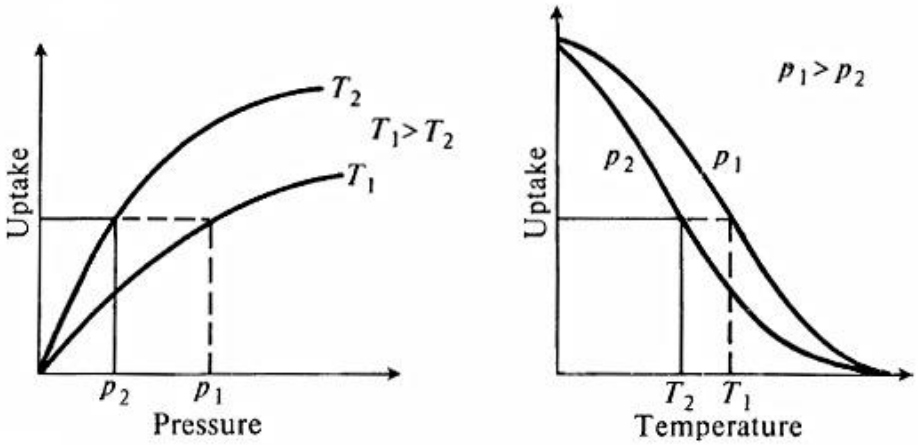

[223]

Figure A1.6.2 – Adsorptive H_2 Uptake with Temperature and Pressure Variation
Graphical example data trends demonstrating H_2 uptake increasing with p and decreasing with T in adsorptive materials.

Additional measurement of CNTs by ion beam analysis of samples has not found H_2 storage exceeding 1 wt%. It is generally accepted that claims above 1 wt% are not reproducible and that measurement error is a large factor, and that the USDoE target of 7.5 wt% will not be reached at reasonable conditions of T and p by storage based on CNT adsorption [215] [327]. There is however a small amount of ongoing work with CNTs and it may be that breakthroughs allow a significant increase in their storage capacities, such that they may serve certain H_2 storage applications [46].

A1.6.2 Metal Organic Frameworks

MOFs are high surface area crystalline microporous metal structures with networks of pores and channels, often with quite complex chemical formulas. Surface areas are typically > 3000 $m^2\ g^{-1}$, having reached up to 7140 $m^2\ g^{-1}$ experimentally, and with a theoretical limit of 14600 $m^2\ g^{-1}$ [328]. MOFs have received significant research interest as H_2 adsorbent materials since pioneering work in 2003 [328]. They are synthesised preferably from light elements with one atom thick highly segmented walls. Example metals are Zn (most common), Li, Na and Mg and Fe, and heterometallic structures. Al and monovalent cations ($^{1+}$) (K, Na, Li) however are not usually used due to susceptibility to hydrolysis and forming oxides [46]. Pore size is one critical factor, and this is known to be optimal when the same size as the van der Waals diameter of H_2. A number of techniques have been attempted to achieve this ideal diameter, such as use of a 'guest' material located within the pores to reduce the diameter and offer additional adsorption sites. This must have low vapour pressure so that it does not desorb during removal of H_2. An example material is fullerene spheres [46]. Other options include mixing with another framework, forming an optimised interweaved or bridged MOF. Three MOF structures are shown in Figure A1.6.3 [328].

Example data indicated that IRMOF-11 can store 1 wt% at T = ambient, p = 47 atm. It has been reported that a CeZn MOF has demonstrated 0.86 wt% at ambient/33.5 atm. An upper limit is presently considered as 7.5 wt% for MOFs under high p (which exceeds that of ACs); however, there are claims of almost 9 wt% at 77 K, 56 bar with MOF NU-100 [46] [313] [328]. Data for a four-fold interpenetrated MOF claims to be 1.12 wt% at T = ambient, p = 48 atm. Storage of 2.47 wt% has been claimed at 1 bar (77 K) [313]. However, a maximum capacity of 4 wt.% was reported for a bridged MOF

structure, IRMOF-8, by hydrogen spillover using carbon bridges. This data was obtained at 298 K, 100 bar [313].

MOFs therefore represent a very interesting and promising class of material, with the possibility of achieving considerable H_2 storage by adsorption that may eventually approach gravimetric targets of the USDoE at near ambient conditions. They do however suffer from low volumetric density in comparison to other adsorbents. Much further research is anticipated for MOFs to overcome these issues, such as strategies for the design of MOF nanostructures with optimised high surface areas/topology/reactivity, pores of appropriate dimension, open metal sites, large free volumes, suitable crystal density, larger bonding ΔH, inclusion of metal nanoparticles etc [215] [313] [328]. Like all adsorbents, MOFs show preference for low T and high p. At low p, H_2 uptake is influenced by pore size, but at high p it is dependent on surface area and pore volume [328].

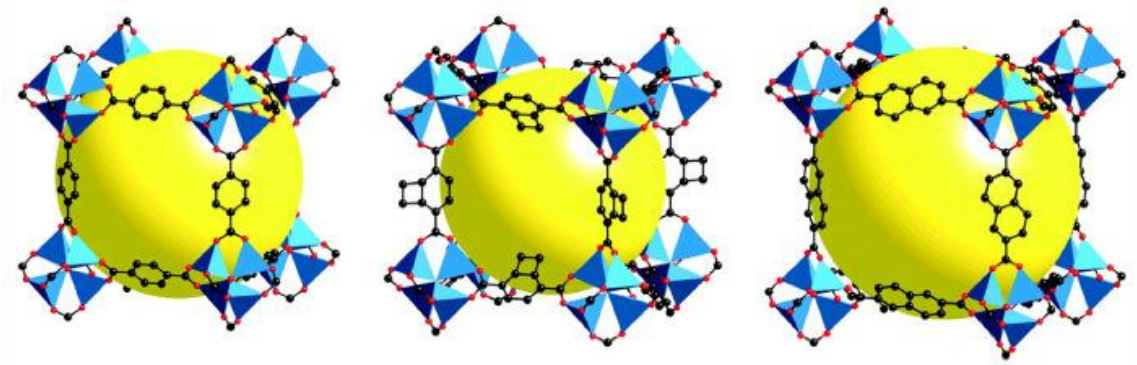

[328]

Figure A1.6.3 – MOF Structures
Blue polyhedrons represent Zn, black spheres represent C, red spheres represent O. The yellow sphere represents the space for H_2 (specifically the largest sphere that would fit in the cavities without touching the van der Waals atoms of the frameworks).

A1.6.3 Zeolites

Zeolites are microporous crystalline aluminosilicates formed from SiO_4 and AlO_4 tetrahedra, first synthesised in the mid-1900s. There are over 200 zeolitic materials, which are often classified by pore size, although the above is of central interest within the context of H_2 storage. This is due to the controllable diameter of the material cages and channels, high stability and low cost. They also contain isolated and exposed cations that are reported to potentially act as H_2 binding sites [46] [313] [325].

The mechanisms of storage in zeolites and their performance are similar to other adsorbents, although generally slightly less wt% is observed. This is due to the relatively dense frameworks and low pore volumes of zeolites compared to optimised nanoporous carbons and MOFs, indicating that zeolites will probably not achieve H_2 storage that can satisfy USDoE targets and will therefore not likely not find roles in automotive applications. The highest uptakes found in literature are for Ca-X zeolite, with a capacity of 2.19 wt% at 15 bar, and 2.55 wt% for Na-X at 40 bar, both at 77 K. H_2 uptake of 0.6 wt% was obtained for the H-YZ zeolite (surface area of 710 $m^2\ g^{-1}$) at 1 atm (77 K) [325]. A maximum of 0.6 wt% was obtained for a Li-LSX zeolite sample at 298 K. The capacity in LSX by bridged hydrogen spillover was also investigated, where the capacity was enhanced to 1.6 wt% (100 bar), representing the highest observed storage at ambient T for zeolites [313].

A1.6.4 Clathrates

The main remaining group of H_2 adsorbents are clathrates, which are chemical compounds consisting of a lattice of one compound trapping a second compound. The idea of trapping is to overcome the low binding energies of physisorption. The simplest clathrates are based on H_2O, CH_4 and NH_3. Work over the last 20 years has demonstrated storage in $H_2(H_2O)_2$, $H_2(H_2O)$ and $(H_2)_4(CH_4)$, equivalent to 5.3, 11.2 and 33.5 wt% respectively (reaching above USDoE gravimetric and volumetric targets in the second two materials). However, these require extremely high P (such as 2467 atm) to synthesise the compounds (and use of CH_4 is not desirable in this context). Clathrates however do offer some potential. They have theoretical capacity of 5.6 wt% at 59-118 atm, 263 K. They are inherently safe (due to H_2O contained within the compound), low cost and environmentally benign [46]. There are three common types of clathrate hydrate structures: sI hydrate (consisting of two 5^{12} cages and six $5^{12}6^2$ cages in a unit cell; sII hydrate (sixteen 5^{12} cages and eight $5^{12}6^4$ cages); sH hydrate (three 5^{12}, two $4^35^66^3$, and one $5^{12}6^8$ cages). These are shown in Figure A1.6.4 [313]. The type of crystalline structure of the clathrate hydrate depends on the size of the guest (stored) molecule. Small guests usually generate sI and sII; larger guests generate sH.

To store H_2 at lower p, it has been shown that tetrahydrofuran (THF) as a guest component may stabilise the clathrate at 280 K, 50 bar. Powder X-ray diffraction measurements confirmed that the same sII binary clathrate hydrate forms as reported

in previous work. Raman spectroscopy suggested that most large cages of the clathrate were filled with THF; in contrast, H_2 molecules most likely occupied only small cages. THF can considerably decrease p but its presence leads to a significant decrease in the H_2 capacity [313].

It has been reported that capacities in THF-containing clathrates can however be increased up to 4 wt% (277.3 K, 120 bar) by adjusting the composition to allow H_2 to enter both the larger and the smaller cages. However, in a later study the capacity of binary THF-H_2 clathrate hydrate (sII) was found to be approx. 1 wt% at p < 600 bar, corresponding with stoichiometric calculations for one H_2 per small cavity. In this study the storage was not increased upon reproducing the same conditions, indicating that THF is a favourable guest for large cages and H_2 occupancies there cannot be achieved at moderate p. Recent studies of semi-clathrate hydrates of quaternary NH_3 compounds demonstrated stability at ambient p and T, and capacities 10 times greater than that of binary H_2-THF clathrates previously reported. There is clearly further room for development with this system to optimise p, T, kinetics, and practicalities of the clathrate synthesis.

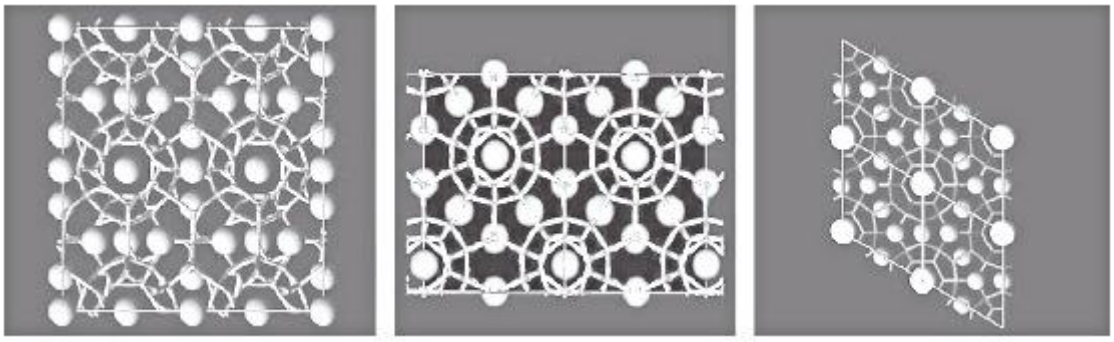

[313]

Figure A1.6.4 – Structure of Clathrates (sI, sII, sH)
The complex structure of three common clathrates.

In general, most H_2 storage data for adsorbents is measured by a manometric method, which measures the change of p of a fixed sample volume during the charging of a system. Further H_2 is added to the sample volume and the process is repeated. The reverse process is used to measure desorption. Gravimetric methods are also used, which involve a highly sensitive microbalance to measure the weight change of a sample as a function of the change in p [325]. It is often noted within review literature

that there lacks proper consistency of testing and of measuring procedures, and lack of reproducibility in many of the works published on adsorption materials. Data for identical systems has been shown to vary between test sites. Data would be more comparable if measured in terms of deliverable H_2 capacity at standardised conditions, although it would be difficult to establish these conditions in a meaningful way since delivery p may vary between systems etc [325]. In addition, much of the simulation work provides very variable results that often do not correlate with physical testing [215] [313] [329] [330]. Broom and Book provide [325] good discussion and data for various other less common adsorbent materials. Raising p excessively at ambient T is not shown to allow adsorbents to match the storage observed at 77 K [215].

Appendix A1.7 – Alternative Hydrogen Storage

Fuel in liquid form compatible with existing infrastructure and produced from H_2 (renewable H_2 in the future) would be a much more expedient storage option. FCVs must compete with various biofuel energy systems or battery/hybrid vehicles as technologies develop. It seems logical that a solution would be a catalytic reformer to produce hydrocarbons from renewable H_2 and atmospheric CO_2, powered by renewable resources. This perhaps deserves equal research attention to that of H_2 storage methods. There exists the well-established process of F-T synthesis briefly introduced in Chapter 1, which reforms H_2 and CO into hydrocarbons, which could supplement existing fuels within the medium-term. F-T was first achieved in Germany the 1920s, but has received renewed interest in the search for low-carbon and alternative fuel production. The idea here is to use CG, BG, CoG and other H_2/syngas production process, and later with increasing amounts of renewable H_2, to develop a renewable fuel reforming system based on F-T synthesis. This process could feasibly assist development of H_2 production/infrastructure. The basic chemical process is

$$n\mathrm{CO} + 2n\mathrm{H_2} \rightarrow (\text{-}\mathrm{CH_2}\text{-})_n + n\mathrm{H_2O}$$

where a range of fuels are synthesised [331]. Current use is mainly with CG and SMR plants, in South Africa (such as Sasol, producing 36% of the country's fuel competitively), a region where coal for example is relatively abundant and cheap but oil is not. ATR is actually preferred in terms of the H_2-CO ratio. These overall

processes may be known as coal to liquid (CtL), gas to liquid (GtL) or biomass to liquid (BtL). Rauch et al and Davis describe several commercial/demonstration CtL, GtL and BtL plants, reviewing their operation and chemistry (including selection of p, T, fluid dynamics, catalysts etc) [331] [332]. There are clearly significant opportunities for CtL in China and the USA for example. F-T plants are not ideal and have high capital expenditure and maintenance costs, and have been affected by volatility in oil and gas prices in the past.

There are a number of reactions in the F-T process. The basic process integrated with BG is shown in Figure A1.7.1. Syngas production has been discussed in Appendix A1.3. Particular interest is with BG (with steam gasification agent, rather than air/CO_2 etc) and BtL. Since BG produces CO_2 and small amounts of light alkanes, H_2S, NH_3, alkali and aromatics etc amongst the syngas, this undergoes an initial cleaning stage and other reforming/WGS reactions. This may be necessary to produce an optimised H_2-CO ratio of 2.1 (higher than the typical case for BG syngas) [333]. The range of products can be represented by the modified Anderson-Schulz-Flory (ASF) distribution

$$m_n = A\alpha_1^{n-1} + B\alpha_2^{n-1} \qquad \text{Eq A1.7.1}$$

where m_n represents the molar selectivity of a hydrocarbon with n carbon atoms and α the chain growth the probability of the synthesis; A and B are coefficients [331]. Optimising for petroleum must either increase α, or otherwise deviate or interfere with the process from the distribution entirely. This has been attempted by catalyst synthesis (such as addition of alkali metals), development of high and low T F-T processes (HTFT/LTFT), or using chemical additives [334].

Catalysts such as Ni, Co, Fe and Ru may be used, which assist with cleaving of the C-O bond. Ru is especially active, but approx. 50,000 times more expensive than Fe. Ni is very active for breaking the C-C bond and for hydrogenation, so its selectivity towards CH_4 is very high. Fe promotes petroleum, whereas Co promotes diesel, heavier alkanes and waxes; Fe and Co are therefore both suitable catalysts. HTFT at 300-340°C promotes petroleum, or LTFT at 180-250°C promotes synthesis of 'green' diesel ($C_{10}H_{22}$-$C_{19}H_{40}$) or waxes [335]. Conditions of p (0.5-1000 atm), T, syngas composition and catalysts can be optimised to allow reasonable selectivity for certain hydrocarbons and alcohols etc [331].

Undesired products also form (aldehydes, ketones, esters etc), but F-T fuel produces no SO_x and limited NO_x. The final products are upgraded to improve quality (such as catalytic isomerisation and breaking long chains by hydrocracking). Combining BG and F-T processes seems beneficial, although F-T involves highly exothermic reactions and heat removal is required. Syngas production is reported as > 60% of the F-T process cost [335].

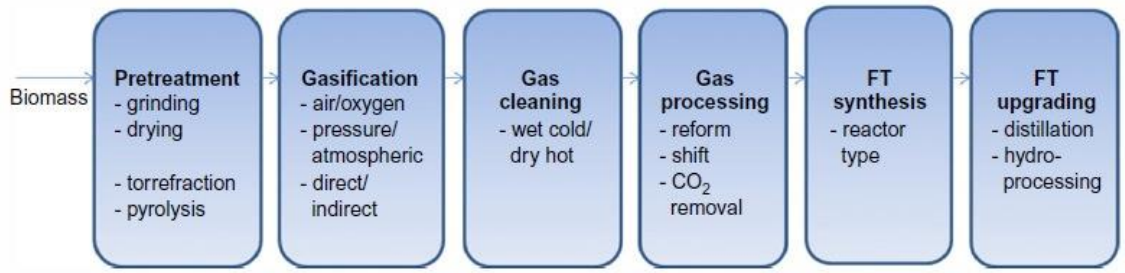

[331]

Figure A1.7.1 – Biomass-to-Liquid (via Fischer-Tropsch Synthesis)
Main stages of biomass-to-liquid fuel production via BG syngas production followed by F-T synthesis and upgrading.

A list of example reactions and product distributions are shown below [331]:

Desired:

nCO + $(2n + 1)H_2 \rightarrow C_nH_{2n+2} + nH_2O$ (alkanes)

nCO + $2nH_2 \rightarrow C_nH_{2n} + nH_2O$ (alkenes)

nCO + $2nH_2 \rightarrow C_nH_{2n+2}O + (n - 1)H_2O$ (alcohols)

Other possible reactions:

$2CO + H_2 \rightarrow (-CH_2-) + CO_2$ (-204 kJ mol^{-1})

$3CO + H_2 \rightarrow (-CH_2-) + 2CO_2$ (-244.5 kJ mol^{-1})

$CO2 + H_2 \rightarrow (-CH_2-) + H_2O$ (-125.2 kJ mol^{-1})

$CO + H_2O \rightarrow H_2 + CO_2$ (-39.8 kJ mol^{-1}, reverse WGS)

Undesired:

nCO + $(2n - 1)H_2 \rightarrow C_nH_{2n}O + (n - 1)H_2O$ (aldehydes, ketones)

nCO + $(2n - 2)H_2 \rightarrow C_nH_{2n}O_2 + (n - 2)H_2O$ (carboxylic acids)

The F-T process combined with BG is therefore suggested as a near- to medium-term effective substitute fuel solution, to supplement existing infrastructure with a synthetic fuel based on biomass and H_2. This could progress with renewable H_2 in the medium-

term, such as from wind-powered electrolysis, to upgrade the H_2-CO ratio from BG reforming processes. In addition, catalytic reforming of CO_2 to produce CO could be developed, such as through biological processes or the reverse Boudouard reaction (although this particular reaction does have a high ΔH requirement of +172.4 kJ mol^{-1}).

A typical product distribution separated by p and T, and an example of modified ASF distribution is shown in Figure A1.7.2.

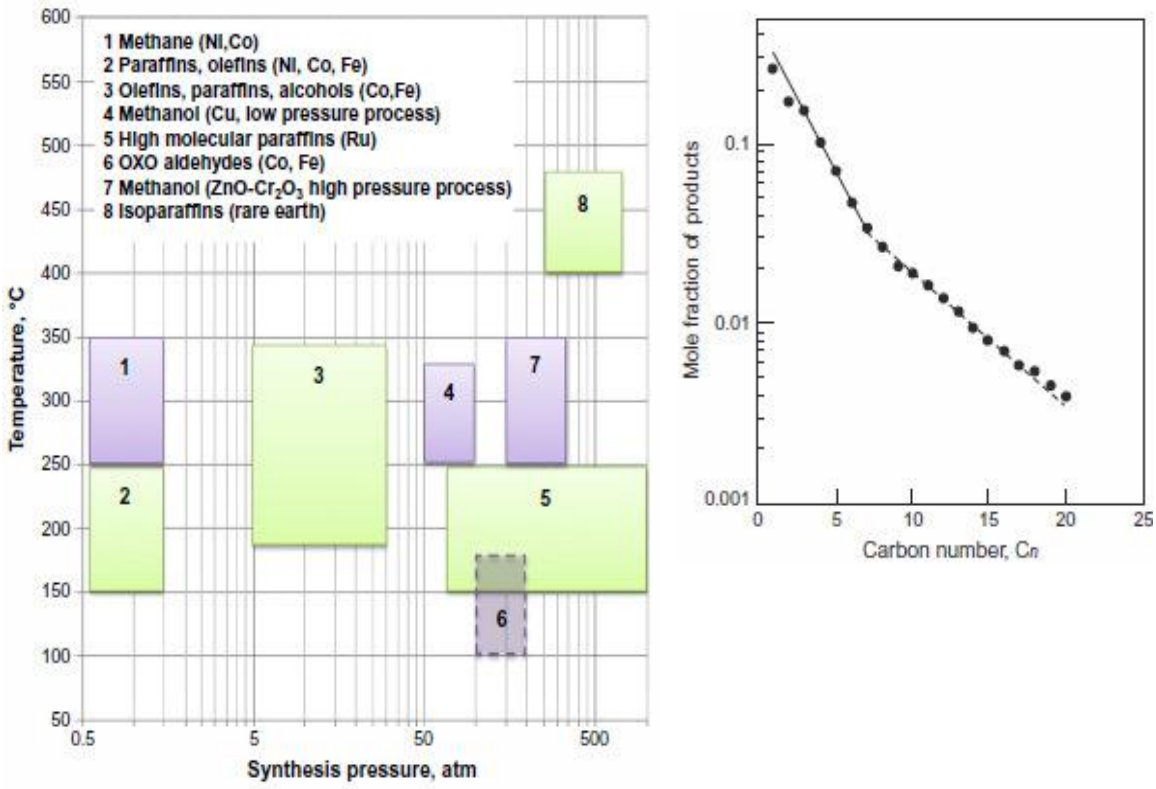

[331]

Figure A1.7.2 – Typical F-T Product Distribution and Modified ASF Distribution

A log graph of T and p for the F-T process shows the bands of certain alkanes, paraffins, alcohols etc, indicating suitable catalysts. The mol fraction of products is also graphically shown from the modified ASF distribution, by carbon number (C_n).

Appendix A2.1 – Electrolyser/Fuel Cells

A2.1.1 Electrolyser/Fuel Cell Overview

Electrolysis and the earliest electrochemistry began at the turn of the 1800s. Faraday later established quantitative relationships between charge and mass formation [72]. By the 1900s large-scale electrolysis was operated for H_2 production for industry and later ammonia production for fertilisers etc (now Haber-Bosch processes) [39]. There are now six main types of EC/FC, differing by electrolyte type, electrochemistry and operating temperature [39]:

- Polymer electrolyte membrane (PEM) (H^+, < 100°C)
- Alkaline (OH^-, < 200°C)
- Solid oxide (O^{2-}, 600-1000°C)
- Phosphoric acid (H^+, 150-220°C)
- Molten carbonate (CO_3^{2-}, 600-700°C)
- Direct methanol (H+, 400°C)

The first commercial alkaline electrolysers where produced from 1927 (Norsk Hydro) and the first PEM electrolysers from 1966 (General Electric) [72]. Modern industrial/commercial electrolysis mainly involves grid-powered alkaline electrolyser stacks (the energy source is therefore dependent upon the breakdown of generation within the local grid). Alkaline electrolysers are established and relatively cheap electrochemical devices, using Ni catalysts [64]. PEM cells require expensive Pt-group metal (PGM, including Ru, Rh, Pd, Os, Ir, Pt) catalysts [68].

A simple EC or FC is essentially the same and can in principle proceed with either reaction (depending on whether either a sufficient external potential source or load is applied across the cell electrodes, and whether H_2O or H_2/O_2 is available), although most stacks are dedicated to one reaction and the reverse will be very limited (surrounding electrodes with H_2O prevents the FC reaction etc). Discussion in this work is focussed on the EC reaction, although the FC reaction can be inferred from the reverse of this. In an EC the anode is +ve (O_2) and cathode –ve (H_2) (whereas for FCs the cathode is +ve and anode –ve). The reaction occurring in PEM cells (acidic/H^+ reaction) is slightly more simple compared to alkaline cells. For the reaction to proceed in a PEM EC, it is required that H_2O surrounds the anode and a potential

applied of typically > 1.48 V. This is a fundamental aspect of EC discussion (and similarly for a FC), which has been often considered under different conventions within literature. For these reasons, the underlying electrochemistry aspects are defined and given detailed explanation in the main body of this thesis in Subchapter 2.1.

Literature concerning PEM cells is much more abundant than that of alkaline cells, and specifically for PEM FCs. Amongst other reasons, this is likely due to industrialised H_2 production from SMR and other reforming, and the relative prosperity of alkaline electrolysers. Improvement of FCs in terms of cost, stability and efficiency (novel/improved catalysts and membrane assemblies etc) will bring a significant boost to the hydrogen economy such as within automotive systems or mobile power sources. PEM cells are likely to be the main focus for these roles in the near future and there is a considerable amount of ongoing research in this field [68].

Alkaline FCs are reported to be highly efficient due to the nature of the cathode reaction [27], although the hydroxide (OH^-) within the electrolyte is intolerant to CO_2 due to formation of CO_3^{2-}, therefore atmospheric air is unsuitable. They also form H_2O in the electrolyte (anode) following the H_2-O_2 reaction, which must be removed to prevent dilution. Alkaline FCs do not require PGM catalysts and therefore offer certain benefits, but are generally considered impractical due to the sensitivity to CO_2 and the electrolyte/H_2O management [336]. For these two reasons, there has been much more recent research effort in PEM FC technology.

Of the other cells types, solid oxide fuel cells/electrolysers cells (SOFCs/SOECs) are of the most interest, since their first reports in the 1980s and particularly in recent years [68]. There is significant research interest in SOFCs at the University of St Andrews and University of Birmingham. These cells operate at > 600°C using a ceramic electrolyte. Since the charge carrier through the electrolyte is O^{2-}, they can consume H_2, CH_4 or CO (and syngas) as a fuel source in the FC reaction [27]. Although these cells can achieve high efficiencies (particularly with heat recovery), they require time to heat-up with inherent losses and impracticalities, and there are also issues of instability [64]. SOECs are suited to stable power plant usage and have potential for large-scale H_2 production where temperature and rapid start-up is not such an issue.

Low cell voltages are preferable for ECs, whereas increasing/maintaining cell voltages is a key aspect for FCs. PEM EC research became motivated by cost rather than efficiency, which is partly why the performance of ECs has not significantly improved over the last few decades [68]. Cell characteristics are quantified in terms of current density (*j*) and voltage (at a certain *j*, indicative of efficiency). Multiple cells are formed into stacks to step-up voltage and operate at suitable levels (the cells are configured physically/electrically into series).

Maximum current handling is proportional to cell surface area (and availability of H_2 + O_2 in the case of FCs) [27]. Similar to WT and PV systems, there are several factors such as rating, cost per Watt etc applicable to an electrolyser stack (ES). These would need consideration when pairing to a power source. In particular, power density and practicalities such as p and T (H_2 storage, stack cooling etc) are of significance for FCs in mobile applications. An ES would need individual consideration depending on the nature of the application, power source(s), centralised or decentralised generation, grid-dependent or grid-independent etc [67].

Much consideration has been given to WT and PV as power sources for electrolysis [63] [67] [337-339]. In remote regions with abundant wind/solar resources, ECs coupled to WTs/PV could provide heating/cooking fuel, electrical energy storage/provision from electrolyser/FC cycles, or vehicle fuel. In particular, this could offset reliance on diesel generators in some remote locations [339]. This is of direct interest in the UK, for example on islands such as the Isle of Eigg with its autonomous renewable energy system (Eigg Electric), backed-up by diesel generators. Larger renewable-H_2 systems would be able to trade H_2 as a marketable fuel/commodity. This could also draw from the grid when off-peak, assisting with grid stabilisation. H_2 supplied by a PEM EC in particular is of much higher purity than that from reforming processes, therefore with higher value and direct access to existing medical, chemical and FC markets etc without extensive purification [64] [67]. Critically it does not contain CO.

FCVs compete with ICE vehicles of relatively low efficiency; hence automotive use is currently a very feasible application albeit with some storage limitations as explained in Appendices A1.4-A1.6 [337]. As discussed in Subchapter 2.1, the efficiency of FCs

are relatively low in comparison to ECs and presently this limits economical use of H_2 in direct EC-FC cycles for electrical energy storage. However, with future developments and increased deployment of WT and PV technology and other renewables, becoming more wide-spread and eventually providing cheap/excess energy, the need for grid storage/stability should eventually allow the use of H_2 EC/FC energy storage cycles in certain scenarios [67]. Therefore, in the longer term with foreseeable reductions in EC/FC costs, H_2 energy storage can be a convenient supporting mechanism for grid energy.

A2.1.2 Electrolyser/Fuel Cell Component Overview

Research for this thesis is centred upon electrolysis within the context of renewable H_2 production from wind and solar energy resources, therefore naturally PEM and alkaline cells have been considered to the greatest extent. Figure A2.1.1 shows the basic cell arrangements for PEM and alkaline cells.

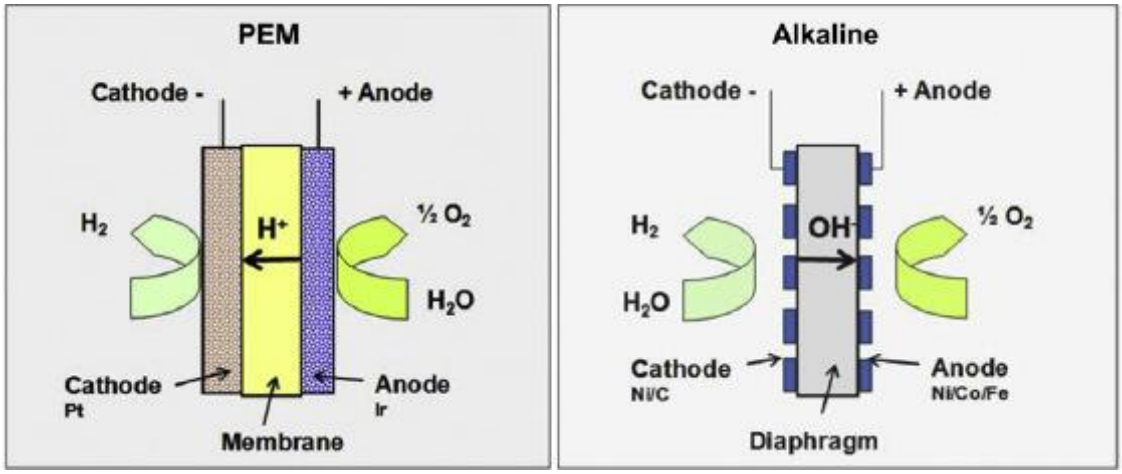

[68]

Figure A2.1.1 – Polymer Electrolyte Membrane and Alkaline Cell Schematics
The basic schematic of PEM and alkaline ECs are shown. Key physical differences are the membrane/diaphragm and catalyst. The half reactions are also different.

PEM electrodes are typically formed from carbon, titanium or stainless steel with micromesh current collectors (Ti) [68]. The catalysts are deposited directly onto the membrane or onto mesh facing the membrane. In the electrolysis reaction, Pt is typically used for the cathode and Ir/Ru/Pt for the anode. The membrane electrode assembly (MEA) is bonded together. The PEM material may extend partially into the mesh due to its plasticity. The intersection between the PEM and electrodes requires

certain basic properties for either reaction: large surface area; electrical conductivity (of the electrode); porosity (allowing mass transport of $H_2/O_2/H_2O$); physical contact with the membrane (allowing H^+ conduction); catalytic activity [55]. This function and the PEM molecular structure are shown diagrammatically in Figure A2.1.2 (in FC mode). Nafion® is the conventional material for PEM cells, manufactured by Dupont in several thicknesses.

Alkaline cell electrodes are formed from porous carbon or nickel for both the anode and cathode. Silver is often used as a catalyst in alkaline FC cathodes (cheaper than PGMs) [336]. A diaphragm is used in alkaline cells, in a similar role as the PEM. The diaphragm conducts OH^- ions, but does not permit H_2O, H_2, O_2 or electrons, thus it provides a pathway for the reaction and separation of H_2 and O_2.

Zirfon® diaphragms are commonly used at present (replacing asbestos-based diaphragms of the 1970-1980s etc). These are composed of ZrO_2 particles embedded in a polysulphone matrix. These components together ensure a very stable and hydrophilic diaphragm, which may be used in aggressive environments such as 10 mol KOH aqueous solutions in an H_2/O_2 atmosphere, 90°C, 1 MPa etc [341].

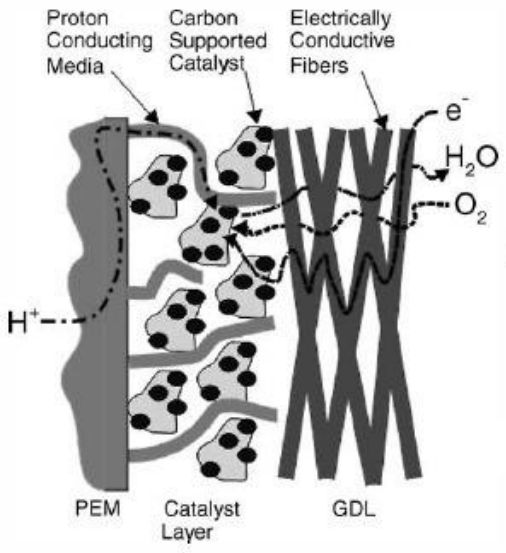

(a)

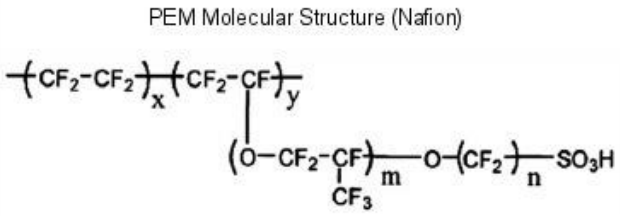

(b)

[55] [70]

Figure A2.1.2 – PEM-Catalyst-Electrode Interaction Schematic and Nafion Structure
The physical nature and interaction of the membrane, catalyst and electrode are shown for a FC (a) where GDL is the gas diffusion layer analogous to a current collector on an EC. In (b), Nafion with for example 0.175 mm thickness, the coefficients would be: $m \geq 1$; $n = 2$; $x = 5\text{-}13.5$; $y = 1000$ [70] [342]

PEM ECs have from the 1970s seen batches of significant research effort in terms of catalysts, electrodes and membranes. A very useful review is provided by Carmo et al [68], discussed here. Early work highlighted PGM cost and investigated catalyst activities and characteristics. The O_2 evolution reaction (OER, anode/+ve) has required more attention than the H_2 evolution reaction (HER, cathode/-ve). OER catalyst research has involved investigation mainly of Ru, Ir and Pt, and later binary/tertiary catalysts. Some of this has considered liquid acidic electrolysis, since the chemistry is similar considering the acidic nature of a PEM. Ru and Ir were noted to have higher activities than Pt for the OER. It is understood that use of Pt (and Pd) causes an oxide film that adversely affects the electrocatalytic activity.

Unfortunately the preferable metal Ru (RuO_2) is observed to corrode with oxygen evolution, likely forming RuO_4 (that may enter the membrane). Introducing Ir into the Ru catalyst structure has been shown to significantly reduce corrosion. Besides Ru, Ir provides the most superior catalytic OER activity, but Ir does not present the corrosive properties of Ru. Therefore modern cells have adopted Ir/IrO_2 catalysts and research activity is now based on this benchmark.

For the HER, Pt is generally used (where Pt or Pd are considered the most optimal, and Ni has some activity although inferior to PGMs). Carbon-supported Pt nanoparticles are reported to be the state-of-the-art for FC catalysts, technology that has been borrowed for ECs. CNTs can be used as supports due to their high conductivity, corrosion resistance and surface area [216]. Recent work has also involved use of various (cheaper) supporting metals/oxides, involving Sn, Ta, Nb. Early ECs had high PGM catalyst loadings, particularly of Pt on the cathode (later found to be unnecessary), demonstrating lower cell voltages than alkaline cells of the time. Catalyst loadings for ECs are now generally 0.5-1.0 mg cm^{-2} Pt (cathode) and 2 mg cm^{-2} IrO_2 (anode). Pt is prone to poisoning by various metals (fortunately IrO_2 and RuO_2 are not) [343]. This is due to the reversible potential of Pt being +ve of the HER [68].

Important features of the membrane are: stability; mechanical strength; corrosion resistance; high proton conductivity [68]. It should also remain hydrated, which is maintained from H_2O evolution in FC reactions and from H_2O containment in ECs [70]. The PEM EC reaction only consumes H_2O from the anode side, although having the

membrane fully immersed is practical and beneficial i.e. to prevent the FC reaction occurring (since the gases will rise quickly and not remain in contact with the membrane to potentially undergo the FC reaction). Importantly, Nafion membranes have optimal proton conductivity at 80°C and this is therefore normally the target condition for cells [70] [342]. Membrane dehydration, reduction of conductivity, decreased affinity for water, loss of mechanical strength (due to softening of the polymer backbone) and increased parasitic losses (high fuel permeation) are observed at T > 80°C. Nafion conductivity data trends are provided elsewhere [70].

Cell electrodes (separator plates) and current collectors have to provide suitable porosity and stability, where a number of factors are considered. These include: corrosion resistance (due to overpotentials, presence of O_2 etc); conductivity; mechanical support (they support the membrane, which may encounter high differential pressures); water/gases must counter flow unrestricted around the catalyst sites; maintain an even current distribution to avoid hot spots. Current collectors are therefore typically prepared from sintered Ti powder, forming layers of approx. 0.8-2.0 mm with porosity of 20-50%, pore sizes of 5-30 µm, resistance of 5-10 mΩ cm. In FCs, due to the less corrosive environment, carbon materials are used. Separator plates are usually Ti, stainless steel or graphite, but these are prone to gradual degradation.

The MEA is assembled from the PEM, current collectors and separator plates pressed together. A balance of conductance and mass transport ability/microporosity is critical [68]. It has been reported elsewhere that MEAs perform slightly superior with catalytic layers deposited directly onto the membrane surface rather than onto the current collector surfaces, possibly due to the difference in electrode active area contacting the membrane [75]. This may also give slight improvements in durability [68]. Catalyst deposition techniques are discussed further in Subchapter 2.3.

Appendix A3.1 – Wind Energy

A3.1.1 Wind Energy Overview

Wind energy has been harnessed for as early as 2000 BC with early sailing vessels, simple drag turbine devices in the Afghan highlands from around 700 BC and extensive ancient wind milling in Persia [39] [344]. Early devices had an axis vertical to the wind, analogous to a simple modern vertical axis wind turbine (VAWT). The horizontal axis wind turbine (HAWT), having an axis of rotation parallel to the ground in line with the wind, is understood to have first been used the beginning of the second millennium in Persia, Tibet and China, spreading to Europe by the 1100s [345]. From then WTs continually increased in size, efficiency and deployment. They were used across industries such as milling and pumping, reaching a peak in the 1800s, but then declining due to industrialisation. The earliest achievement of wind-electricity is understood to have been by pioneering Scottish academic James Blyth (1887) with a cloth sail VAWT of 10 m height and 8 m width, powering a dynamo for lighting [346]. In 1891 electrical wind power was also developed in Denmark. The advent of aerofoils and two world wars hastened further improvement, and by the 1950s WTs had become the forerunners to the modern HAWT [344].

Wind energy received renewed interest following the oil price rises in the 1970s. Global wind power capacity was only 1.9 GW in 1990 but has grown to exceed 318 GW by the end of 2013 [87]. The recent trend of deployment is illustrated in Figure A3.1.1. Besides hydro, wind energy is regarded as the most cost-effective renewable electrical energy and is likely to remain so for the foreseeable future, potentially < 0.04 \$ kWh^{-1} (< £0.03 £ kWh^{-1}) [111] [112]. Hence there is significant interest with wind energy as a source for renewable H_2 production via electrolysis processes. Electrolysis loading was in fact achieved with some of the earliest use of WTs in 1891 to 1902, as an energy storage mechanism for lighting [104].

WTs range in size, style and shape, and arbitrary size classifications have evolved (of various conventions). An example is shown in Table A3.1.1 [347]. Rated power is based upon a measured performance at a specific wind velocity, typically 12 ms^{-1}, indicating a benchmark performance for the WT [99] [348]. Alternatively, rated power has also been found used in the context of the actual electrical generator rated power

(i.e. its near-maximum such as for the WES 80 WT [348]). Standardised performance tables are not apparent, particularly for micro/small WTs. This may be due to the difficulties of gathering exact performance data or lack of enforced legislation. During physical testing (Subchapter 3.1), it was clear that micro WT datasheets are often erroneous and that the micro/small WT industry would benefit from some standardisation. The Electrotechnical Commission international standard IEC61400 deals with technical specifications and build requirements for WTs. The largest commercial WT found in the literature (2014) is the 7.58 MW rated Enercon E-126, with a 127 m diameter rotor [87] [349]. The following sections briefly explain the operation of WTs and key concepts for maximum energy generation.

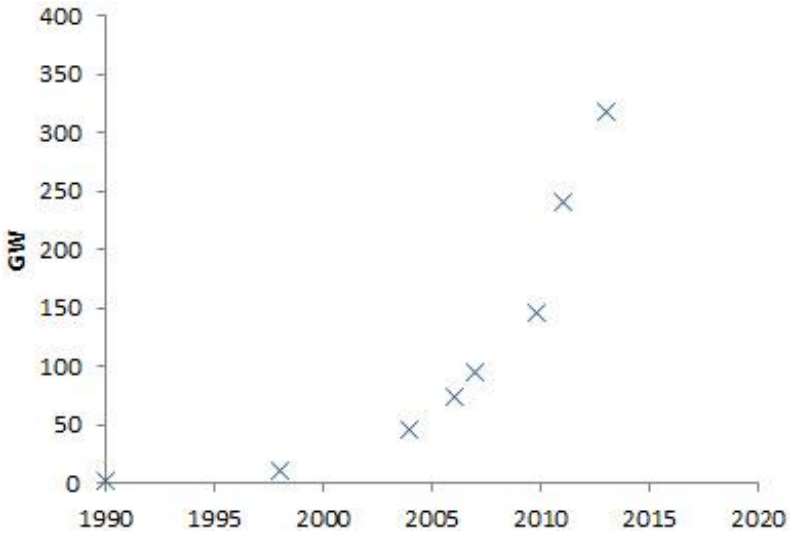

[17] [87] [112] [350-353]

Figure A3.1.1 – Reports of Cumulative Global Wind Turbine Installed Capacity
Reports from various literature sources have been combined to produce graphical trend of the rapid growth of wind energy installed capacity since 1990.

Size	Rated Power	Diameter	Swept Area	Height	Efficiency
Micro	< 1.5 kW	< 3 m	< 7 m^2	< 15 m	20-30%
Small	1.5-50 kW	3-16 m	7-200 m^2	10-35 m	25-35%
Medium	50-500 kW	16-36 m	200-1000 m^2	30-75 m	30-45%
Large	> 500 kW	> 36 m	> 1000 m^2	> 75 m	40-50%

[347]

Table A3.1.1 – Approximate Size Classification for Horizontal Axis Wind Turbines
Some arbitrary size classifications are shown for HAWTs, by rating, swept area etc.

A3.1.2 Wind Energy Derivations

Wind energy is extracted from the kinetic energy of moving air. It is reported that approx. 2-3% of solar energy reaching the earth is converted to the form of wind from thermal effects causing atmospheric circulation [39] [111]. Kinetic energy of wind is a function of velocity and obviously the highest average velocities acting on a WT rotor are sought for maximum energy extraction. Therefore a great deal of significance rests with the actual WT location and wind velocity trends [350]. The power output from a WT is most useful in electrical form, for grid power etc. There are therefore distinct mechanical and electrical features of a WT. The most relevant elements are briefly discussed in this section, to support discussions later in this thesis.

Movement of air has kinetic energy by virtue of its mass and velocity (E_K = ½mv^2). For calculating wind power, the m term is converted into mass flow, of air density, ρ, rotor interaction (swept) area, A, and velocity, v, where

$$\frac{m}{t} = \rho A v \qquad \text{Eq A3.1.1}$$

and therefore for wind power,

$$P_{Wind} = ½\rho A v^3 \qquad \text{Eq A3.1.2}$$

Air density is determined from p and T (where $\rho = Mp/RT$ and $M \approx 0.029$ kg mol^{-1}), therefore $\rho \approx 1.18$ kg m^{-3} near sea level at 25°C, 1 atm [354], although ρ reduces with increasing humidity levels since the density of water vapour is lower than that of air. Use of an anemometer can determine v trends at a WT site and thus indicate potential P_{Wind} available (in W m^{-2} etc). Maximum WT power extraction is lower than P_{Wind} and the conventional extraction limit is based upon Betz theory, which is discussed by Manwell, McGowan and Rogers [345] or Gipe [354]. Betz theory assumes that kinetic power (mechanical) is extracted as wind passes through an actuator disc similar to a HAWT rotor in a steady state dynamic control volume, with reduction in v from v_1 to v_2 from upwind of the rotor to downwind. Betz stipulates that values of p, ρ and T remain constant at the initial and final points (which are reasonable considering the relative pressures/forces that wind can deliver versus ambient pressure ≈ 101 kPa). Therefore mass flow continuity requires an increase from A_1 to A_2 to permit a decrease from v_1 to v_2. In reality there must be a small increase in p and ρ immediately before

the disk/rotor and a small decrease immediately after, but which must return to ambient further downwind. Betz derives the power extraction limit by letting the actuator disc regulate mass flow from fully unrestricted to fully restricted. This equates to axial induction, α, in the case of a real rotor, which is the effective velocity reduction factor from upwind to the rotor in the control volume, where

$$\alpha = \frac{v_1 - v}{v_1} \qquad \text{Eq A3.1.3}$$

Power extraction results from force (F, or thrust) applied at the disc at velocity v, where v = ½(v_1 + v_2), and $P = Fv$. This translates to torque (τ) and rotational velocity (ω) of a real rotor (where $P = \tau\omega$). The F or τ component acting on a disc/rotor is resultant from the change of momentum/energy of air mass through what is effectively a long cylinder of moving mass gradually amalgamating with the ambient surroundings far upwind and downwind. The small pressure differential on either side of a rotor allows torque. Force can be defined by the Bernoulli function through the control volume experiencing reduction in v, assuming negligible change in p and ρ upwind to downwind, where [39]

$$p_1 + \tfrac{1}{2}\rho v_1^2 = p_2 + \tfrac{1}{2}\rho v_2^2 \qquad \text{Eq A3.1.4}$$

$$F = \tfrac{1}{2}\rho A(v_1^2 - v_2^2) \qquad \text{Eq A3.1.5}$$

The disc/rotor area forms A. Maximum F occurs at the limit when v_2 = 0, but mass flow ceases and therefore v and P = 0. At $v_2 = v_1$, similarly F and P = 0. A range of P occurs as v_2 varies from v_1 to 0. Peak power of $^{16}/_{27}$ (59.3%) of the theoretical kinetic power defined in Eq. A3.1.2 occurs when α = ⅔, equating to v_2 = ⅓v_1 and v = ⅔v_1, where the F component is $^{8}/_{9}$ of maximum. The maximum power point (MPP) is the Betz limit, which is a fundamental extraction limit applying to all WTs. A Betz flow diagram is shown in Figure A3.1.2. The upper grey lines indicate the propagating trend of the wind passing over the turbine rotor when at the MPP. Further lines show the changing trends of wind flow that occur under Betz theory while α is varied from minimum induction ($\alpha \approx 0$, $v_2 \approx v_1$) to maximum ($\alpha \approx$ ½, $v_2 \approx 0$). Since surrounding air flow interacts downstream, values of p, ρ and v eventually return effectively to the ambient conditions. The trend of P_{Mech} with α and the $^{16}/_{27}$ limit is shown in Figure A3.1.3.

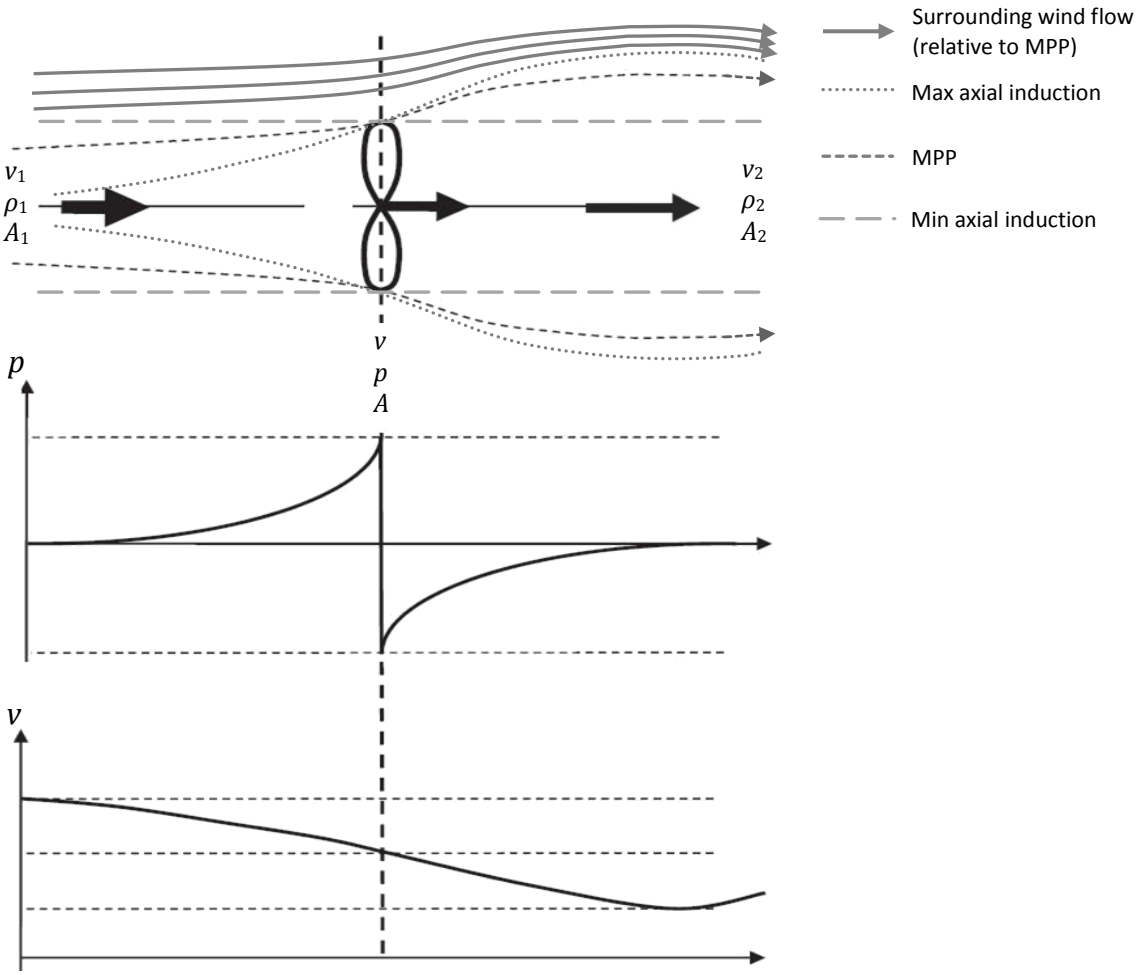

[345] [354]

Figure A3.1.2 – Betz Flow Diagram

A modified version of the classic Betz flow diagram is shown with the implied airflow indicated around the rotor and changes in relative p and v shown in graphs below.

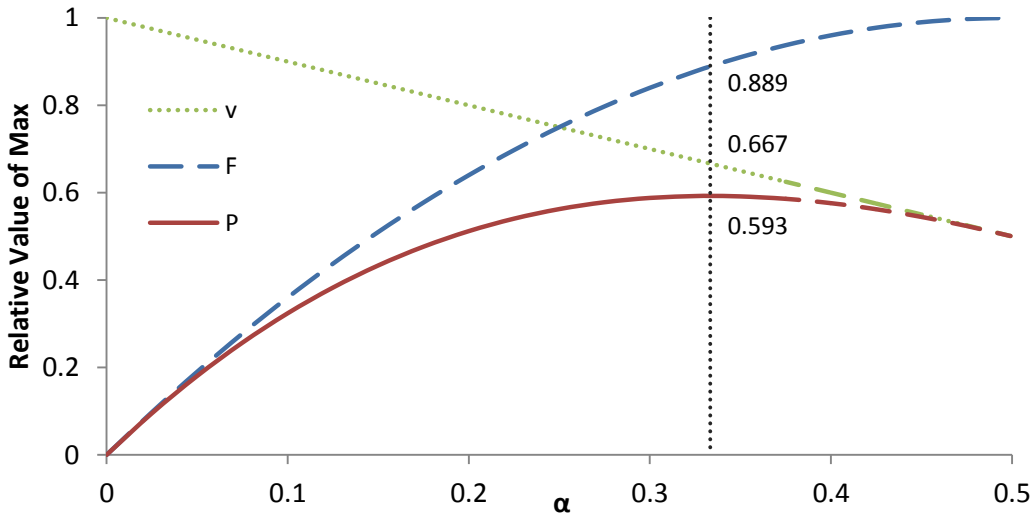

Figure A3.1.3 – Theoretical Betz Extraction Limit by Axial Induction

Implied v (at rotor), F and P produced from theoretical calculations by varying α, indicting the limit of P (0.593) at α = ⅓ and lack of Betz validity when $\alpha \rightarrow$ ½.

The limit can be derived mathematically such as by solving the differential equation for P with respect to the mass flow or v ratio (v_2/v_1) [354]. By letting k = ½ρA, the wind power equation becomes simplified to

$$P = Fv = ½\rho A v^2 v = kvv^2 \quad \text{Eq A3.1.6}$$

The limit of P exists where the v reduction is optimal. P can be expressed as a function of v_1 and v_2 (where v = ½(v_1 + v_2)) and therefore

$$P = kv(v_1^2 - v_2^2) \quad \text{Eq A3.1.7}$$

$$= ½k(v_1 + v_2)(v_1^2 - v_2^2) \quad \text{Eq A3.1.8}$$

$$= ½k(v_1^3 + v_2 v_1^2 - v_1 v_2^2 - v_2^3) \quad \text{Eq A3.1.9}$$

Maximum P is found when v_2 is a certain ratio of v_1, occurring when

$$\frac{dP}{d\,(v_2/v_1)} = 0 \quad \text{Eq A3.1.10}$$

This is solved easily by letting v_1 = 1 and v_2 vary from the limits 0-1, thus

$$(1 - 2v_2 - 3v_2^2) = 0 \quad \text{Eq A3.1.11}$$

$$(v_2 + 1)(v_2 - ⅓) = 0 \quad \text{Eq A3.1.12}$$

Therefore with a solution at v_2 = ⅓. The extraction component of the maximum theoretical power, C_P, can then be defined as

$$C_P = \frac{v(v_1^2 - v_2^2)}{v_1^3} = 4\alpha(1 - \alpha)^2 \quad \text{Eq A3.1.13}$$

giving $^{16}/_{27}$ at the maximum. Similarly for the force component, C_F, on the disc/rotor

$$C_F = \frac{(v_1^2 - v_2^2)}{v_1^2} = 4\alpha(1 - \alpha) \quad \text{Eq A3.1.14}$$

giving $^{8}/_{9}$ at the maximum. The same theory was actually derived five years earlier by a lesser known British scientist Frederick Lanchester, a colleague of Betz [354]. It is therefore often referred to more correctly as the Betz-Lanchester limit. Values of P, v, F, ω and τ are fundamental to the discussions of wind energy, mechanical and electrical power, which therefore involve voltage (V) and current (I).

Theory formulates only a power *extraction limit* applicable to an idealised WT device. Real WT operation varies in many aspects, since Betz makes several assumptions:

1. airflow beyond the outer edges of the rotor, upwind and downwind, not being affected by the existence of the WT rotor (the swept area and control volume conventions are inexact)
2. flow being steady state, homogenous, incompressible (no change in ρ) within an impermeable control volume
3. ambient air pressure having no effect at ends or throughout the control volume
4. wind travelling orthogonally at velocity v through area A, and that A is exactly inverse to v
5. zero friction/drag/losses (such as at the blade tips)
6. an actuator disc being identical to a rotor (a rotor has a nose cone, does not have infinite blades/solidity, is flexible, airflow may be obstructed by a tower, there are non-ideal blade conditions towards the centre of the rotor, there may be yaw error, etc)
7. the rotor operating with v exactly at the midpoint of v_1 and v_2 (this is unlikely)
8. the exiting airflow not rotating (wake rotation)
9. the WT continuing to operate at the exact MPP (which is virtually impossible due to constant variation of v)

The theory is strictly invalid when $v_2 = 0$ and becomes increasingly unreliable as $v_2 \to 0$ ($\alpha \to ½$), since $A_2 \to \infty$ and $P \to 0$ [345]. The error is highlighted by dashed lines on Figure A3.1.3 for v and P where $\alpha \to 0.5$ (i.e. $v_2 \to 0$). The exact nature of this error is complicated and a satisfactory analysis was not found in literature. Further investigation is outside of the scope of this thesis, but it is clear that $v \to 0$ when $v_2 \to 0$ and the unaccounted effects on Betz-Lanchester theory likely result in the limit being slightly reduced and found at a slightly lower α ($v < ⅔v_1$). Further investigation of the theory in terms of reduction from v_1 to v_2 resulting in v = mean (v_1, v_2) reveals that A and v would have to remain strictly inversely proportional (since mass flow contains A and v terms) and v reduction strictly linear, requiring a constant F, or some complicated function of these variables. F and the deceleration may not be constant and there is no exact start and end point, therefore there is further dispute as to whether $v = ⅔\ v_1$ at rotor position at a theoretical limit.

Due to $P \propto v^3$, v values acting on the WT rotor are of utmost significance for maximum energy production at a WT site. Wind is known to increase with height above ground. An empirical power law explained by Gipe [354] gives approximation for v at height h, with reference to a sample height and velocity, h_0, v_0, where α is a terrain roughness coefficient (Table A3.1.2 lists typical wind shear exponents):

$$\frac{v}{v_0} = \left(\frac{h}{h_0}\right)^{\alpha} \qquad \text{Eq A3.1.15}$$

Terrrain	Wind Shear Exponent, α
Ice	0.07
Snow on flat gorund, calm sea	0.09
Coast with onshore winds	0.11
Snow-covered crop stubble	0.12
Cut grass	0.14
Short grass, open field/landscape	0.16
Crops, tall grass	0.19
Hedges	0.21
Scattered trees and hedges	0.24
Trees, hedges, a few buildings	0.29
Suburbs	0.31
Woodlands	0.43

[354]

Table A3.1.2 – Terrain Wind Shear Exponents (α)
Typical wind shear exponents for different terrain are listed, for use in Eq A3.1.15.

Pressure and temperature change with ambient variation and with altitude. Density is proportional to p and T^{-1}. Ambient p may vary by approx. 6.5%. Temperature reduces at approx. 6.5°C per 1000m [355]. Ambient T may vary by approx. 15% annually observing limits of -10 to 35°C (for most densely inhabited parts of the world). For the majority of time it is observed that p = 1000-1026 mbar, and T = 5-20°C in a location such as the UK, therefore T will dictate most of the ambient change in ρ. Extreme highs of p and lows of T and vice versa rarely occur simultaneously in the UK. With increasing altitude, the decreasing p component will outweigh the decreasing T and therefore ρ reduces. The highest ρ values occur at sea level, whereas v increases with height and therefore a compromise is necessary for energy density. The normalised trend of p, T and ρ with altitude from sea level is shown in Figure A3.1.4.

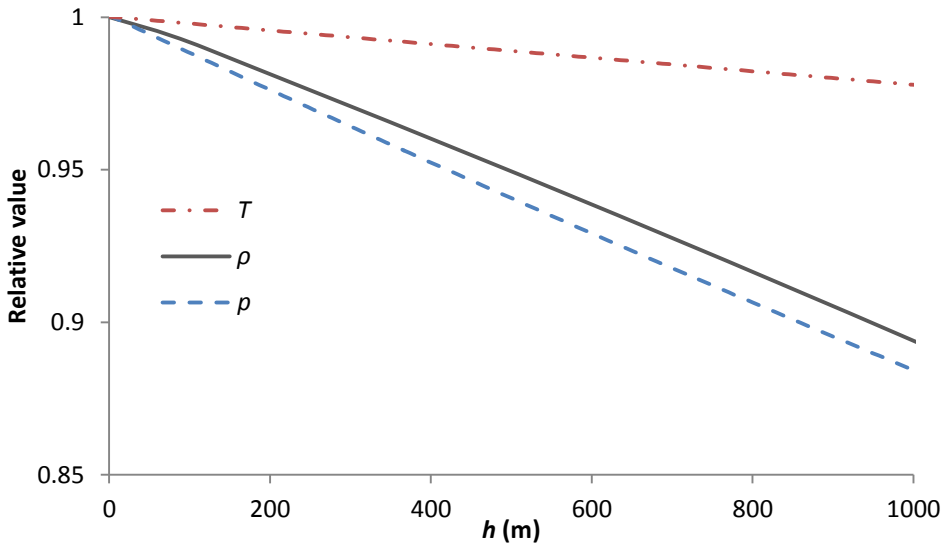

[355] [356]

Figure A3.1.4 – Relative Air Pressure, Temperature and Density Variation with Altitude
Air density decreases with altitude (h). However, v tends to increases with h and therefore a balance is required (e.g. tower of 60m on exposed low-altitude hilltops).

In terms of analysing wind velocity data for a potential WT site, since there is a cubic function of v in relation to P, the site energy is not proportional to a simple mean average v. Discrete v values and their durations can be converted to a root-mean-cube (RMC) average, providing one v value that can produce the correct average wind power for the site. The RMC average can be calculated in a trapezoidal manner over time (t), putting v into equal bands and observing the amount of time within that band. For example, v_1 can be the median (0.5 ms^{-1}) of a band of 0-1 ms^{-1} and multiplied by the time duration of that band (t_1), therefore producing v_{RMC} values from

$$v_{RMC} = \sqrt[3]{[(v_1^3 t_1 + v_2^3 t_2 \ldots + v_n^3 t_n)/t]} \qquad \text{Eq A3.1.16}$$

This allows one value to represent an extensive set of v data for power or energy calculations. The bin sizes must be suitably narrow to avoid error.

However, as is discussed, WT extraction is not directly proportional to v^3 due to various losses mainly within the generator. There are also limits to the operation of a WT that exclude some of the very low v conditions (cut in) and limit or exclude high v conditions (cut out, furling, pitching out, or other generator/rating limits). Wind of rapidly changing v does not result in the same level of efficiency in terms of power extraction by a WT as that of steady v. This is due to the inability of a WT to quickly

change ω to the optimised value during changeable conditions due to rotor inertia and electronic factors, discussed in Chapter 3. Therefore a gradually changing wind of a certain average power may in fact result in more electrical energy produced by a WT than that of a higher average power wind consisting of rapidly changing v values. Averages of any nature may not therefore be particularly accurate other than for benchmarking a WT site.

Wind trends can also be represented by a Rayleigh or Weibull probability distribution function, which can closely resemble wind trends over time at a site [354]. Weibull is preferred as it has a shape parameter and scale parameter. Two values can therefore present an extensive set of data. Again, these are not particularly accurate and do not account for the degree of changeability of the wind.

A3.1.3 Wind Turbine Component Discussion

The critical component in terms of extracting power (mechanical) is the rotor. In-depth explanation of blade element momentum theory, aerodynamics, boundary layers and commercial rotor/blade form is outside of the scope of this thesis but covered elsewhere, such as by Manwell, McGowan and Rogers [345]. The basic rotor function can be explained with some simplicity however. Blade form is typically based on standard aerofoils, where the lift:drag characteristics and optimal angle of attack are known. Rotor aerofoils are positioned at very low pitch angles (to the direction of rotation). The resultant wind vector from lateral movement of the blade through air with rotation and the wind create the *apparent* wind and an angle of attack different (more optimal) than indicated by the pitch. Lift force is defined as the component of force perpendicular to the apparent wind, whereas drag is parallel to the apparent wind [345]. These components are shown in Figure A3.1.5. Lift force results from air accelerating around the leading edge of the top of the aerofoil and decelerating as it reaches the trailing edge. This creates a reduced pressure region along the upper surface and a net lift force. As the angle of attack is increased, up to a limit, lift increases. Drag results from these pressure distributions and friction from the air passing over the aerofoil surface. A net force therefore exists from lift and drag components. Some lift and drag occurs at zero angle of attack due to aerofoil shape.

As the blade cuts through air at speeds far in excess of v, the angle of attack approaches optimal values for the aerofoil in terms of lift:drag ratio (maximum is sought for efficiency). Aerofoil blades are thick at the inner blade for strength but thin at the outer blade to maximise this ratio. They are usually manufactured from CFRP [345]. A certain fixed pitch angle for a blade therefore potentially achieves optimal power extraction throughout the range of v (theoretical scenario). Example aerofoil lift and drag coefficient data is shown in Figure A3.1.6. Three sample aerofoils are shown in Figure A3.1.7. Blades can be divided into elements along the length of their radius, r, to compute the various force components. Since the elements will travel at different relative speeds (depending on their r position) this requires different pitch for each element such that optimised angle of attack can be maintained along the blade length [345]. For a rotor, $P \propto A$, therefore the outer elements are responsible for the most power provision (observing an r^2 function of element area) and are prioritised.

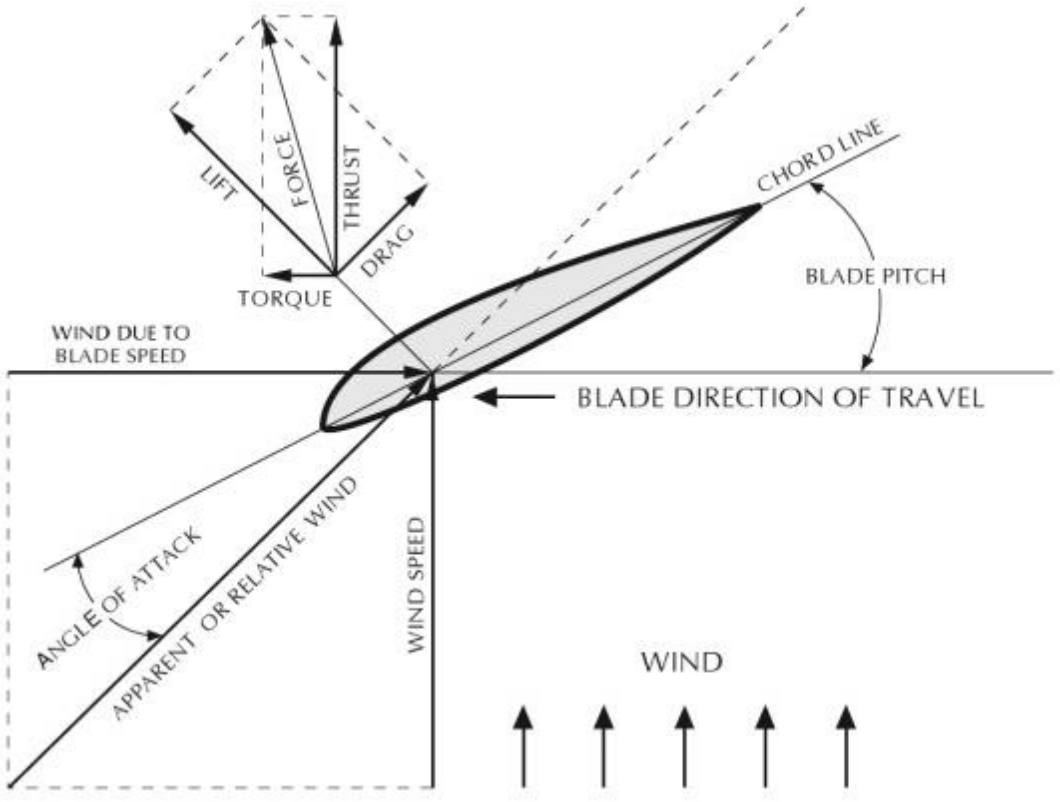

[354]

Figure A3.1.5 – Aerofoil Force Components

Critical aerofoil components lift and drag convert to τ and v at the rotor driveshaft. Apparent wind is defined by the vector sum of blade velocity and actual wind.

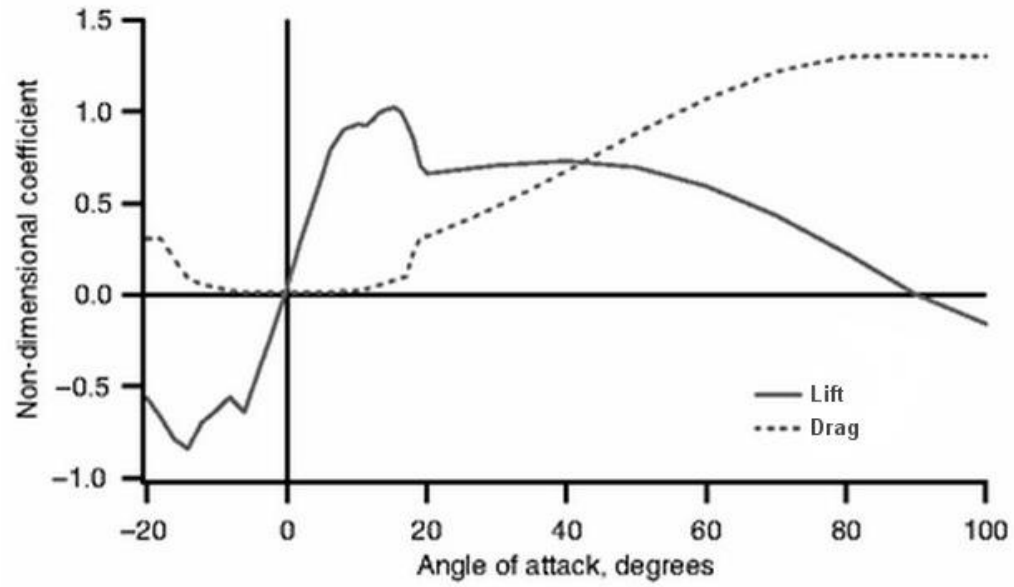

[345]

Figure A3.1.6 – Lift and Drag Coefficents for a Sample Aerofoil (S809)
Example aerofoil lift/drag data. The maximum ratio occurs at approx. 5°.

[345]

Figure A3.1.7 – Sample Aerofoils
Three sample aerofoils are shown for general indication of blade cross section.

Several variable factors are apparent from these discussions and it is clear that a certain fixed ratio of blade speed or ω to v is required to align these factors. Loading of the rotor will reduce ω from its maximum for a given v, since there is finite τ available from the wind-rotor forces. Loading is therefore a key variable to control the blade speed to v ratio. The convention is to observe the tip-speed ratio (TSR, λ) referenced to the speed of the blade tip ($r\omega$) in comparison to v, where

$$\lambda = \frac{r\omega}{v} \qquad \text{Eq A3.1.17}$$

Since Betz suggests α = ⅔ at optimum extraction, $\omega \approx$ ⅔ of maximum is expected from theory. Operating a rotor at the optimal TSR is considered a key factor in literature for maximising (mechanical) power, such as by Baroudi, Dinavahi and Knight [116]. The exact TSR for a particular rotor is based upon aerofoil shape, pitch and blade number. Blade number is therefore also a key factor. The trend for large turbines is three blades, although this is not strictly for theoretical power reasons. It is observed that

for torque to be put onto a rotor there must be an opposite reaction induced in the form of rotation of the near downwind airflow, known as wake rotation mentioned previously. This constitutes a loss of kinetic energy, therefore in real WTs τ must be demoted and ω promoted from the ideal scenario in order to optimise P [345].

Since individual blades interact with airflow to produce τ, fewer blades result in lower τ, higher ω, and less wake rotation (since wake rotation is considered proportional to τ). Basic theory therefore indicates one-bladed rotors may be the most optimal, although this is not the case. There are serious asymmetrical force and yaw issues with one-bladed WTs. Two-bladed WTs are more practical, and can be manufactured/transported/installed potentially for less than three-bladed WTs (requiring less blade material, and since they rotate faster this can reduce gearbox requirements). Aerodynamic and fluid mechanic computations indicate that a larger relative chord size is more optimal for two blades compared to three, and this is welcomed for the increase in strength [107]. This is due to the Reynolds number being proportional to chord and ω and maintaining the solidity of the rotor [39] [357]. Despite this, two-bladed WTs are reported to operate at 1-3% less efficiency (per unit of area) than three-bladed WTs due to other aerodynamic factors, with the exact amount depending on the operating conditions such as TSR etc [357]. Other issues affecting two-bladed WTs are rotor noise, tower shadow and mechanical factors, and appearance. Noise is known to be relative to tip speed, and therefore a faster two-blade WT would potentially produce more noise. If the TSR is kept constant for smaller WTs with smaller r, then ω must be greater. There are therefore potential safety issues with micro two-bladed WTs operating at fast tip speeds near to habitats (this is one reason why micro WTs typically have three to six blades). Another significant issue is the effect of the blade passing in front of the tower, where the upper blade experiences more wind force than the lower blade, creating a significant bending force on the rotor shaft and fluctuating loads every half cycle, therefore leading to early shaft/mount and gearbox fatigue. This fatigue is much reduced with three-bladed WTs. Mounting two blades during construction, particularly offshore, is easier since this can be achieved in one lift operation. However, a teetering mechanism (a pivoting blade mount) tends to be used for the hub to minimise fatigue effects, which adds cost and is not mature for large variable pitch rotors [357]. Finally, it is understood that the

form of three-bladed WTs is favourable in terms of public perception. Therefore over the last two decades of expedited WT development, particularly for larger devices, three blades have generally been favoured. Despite the slight reduction in efficiency, small/medium two-bladed WTs have also become popular due to potentially lower costs per unit of energy from the lower relative installed costs.

To operate a WT rotor at its optimal power, in mechanical terms, it is important to observe optimal α, TSR and pitch, amongst other factors. However, when a WT is grid connected it may have to stay close to one value for ω, which can therefore result in efficiency loss since the ω value will not remain ideal for the range of v. This can be compensated partially by variable pitch, so that the optimal angle of attack is maintained throughout the range of v. Variable pitch can also provide feathering during very strong winds (to limit power and/or prevent damage) and provide a mechanism to stop the rotor (during periods of low grid power demand). Electrical power from a WT is more relevant than mechanical power however. The extensive properties of generators are discussed elsewhere and outside of the scope of this thesis. They are typically 3-phase devices. They are explained from basic principles of electricity and magnetism, such as Ampere's and Faraday's laws [345]. Specifically, current creates a magnetic field of flux density B, and a changing magnetic field inducts an emf into a coil (or conductor). Emf (V) is proportional to the rate of change of magnetic flux (Φ, or BA), where N is the number of turns in the coil of area A

$$V = -\frac{d(NBA)}{dt} \qquad \text{Eq A3.1.18}$$

The negative sign convention indicates that the emf opposes the direction of that which created it (Lenz's law). A conductor segment dl forced through a magnetic field will have current induced in it according to the following vector equation

$$dF = Idl \times dB \qquad \text{Eq A3.1.19}$$

The cross product signifies that the conductor is at right angles to the field when the force is greatest (F is perpendicular the field and conductor) [345]. Rotation of the B-field from the generator rotor (ω) cutting through stator coils therefore creates emfs. Force is induced to the rotor from the current through the stator coils. Therefore, observing equations A3.1.18 and A3.1.19 it is understood that $\omega \propto V$ and $\tau \propto I$

(accounting for generator losses). These are two very important relationships for consideration when maximising electrical power from a WT.

The function of a permanent magnet synchronous generator (PMSG) such as those most commonly found in micro/small WTs is quite simple. Larger WTs use electromagnets and asynchronous (induction) generators (AGs), which are reported to be more rugged, cheaper, and easier to connect to AC electrical grids. AGs are either of squirrel cage (SQAG) type, which have conducting bars rather than rotor windings, or wound rotor (WRAG) type. SQAGs have been traditionally more common due to cost and ruggedness aspects. However, WRAGs are reported to be more suitable for variable-ω rotor operation than SQAG and may therefore see greater preference in the future [345]. AGs require an external source of reactive power and a constant frequency source to control ω. They also require correction of their power factor (with capacitance at their connection to the grid). The stator of an AG has multiple windings, arranged such that the phase-displaced currents produce a rotating magnetic field at exactly the synchronous speed (depending on the grid frequency and number of poles). If the rotor turns faster than the synchronous speed it inducts an elevated voltage in the stator and current flows to the grid. The ratio of the difference in speed is termed slip, which will generally be 2% [345]. These large AGs cannot naturally permit a range of ω and hence variable pitch is used to reduce losses and/or a DC-DC link is implemented. In the case of WRAGs this is reported to be easier, requiring power converters of one-third capacity. For SQAG the cost of implementing electronic converters is high, brings additional losses and there may be insignificant gains in overall efficiency. Therefore the main reason may be to avoid high fatigue associated with constant ω operation (due to high τ values encountered) [345].

Large two-speed AGs have been achieved with dual generators or dual stator windings (with different number of poles). Also, variable-speed AGs are becoming more established with electronic controls to allow increased slip, offering 10-20% ω variation, reducing mechanical stress and increasing WT efficiency [358]. Micro/small WTs usually have PMSGs and fixed pitch and therefore rectification and DC-DC converters for variable ω operation are essential and well established, since they are often used with DC loads such as battery charging circuits. There is therefore a division in power control concepts for micro/small and medium/large WTs. Micro/small WTs

have been practically investigated as part of this research and further discussion is focussed on that relating to PMSG, variable ω, fixed-pitch devices. Discussion of power control for these devices is a key component of this research, in Subchapters 3.4 and 3.7-3.8. Where DC rectification is required at this scale, 3-phase diode rectifiers are typically used, shown in Figure A3.1.8.

There are certain conventions present across literature and repeated discussion of TSR and pitch angle for all WT sizes [116]. However, Narayana et al illustrate very plainly that electrical power is not strictly proportional to mechanical power from the rotor due to electrical generator losses, demonstrating that TSR is not an exact principle for maximising electrical power [102]. High generator efficiency and suitable power rating are clearly of importance. Practical aspects of micro WTs and actual performance data were not found well explained across literature. Micro/small WTs are predominantly fixed-pitch variable ω devices, unlike larger WTs that are more often described.

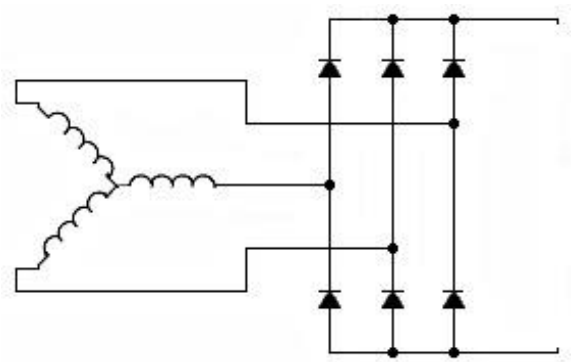

[97] [122]

Figure A3.1.8 – 3-Phase Diode Bridge Rectifier
3-phase AC sources such as a WT can be rectified to DC with a simple diode bridge.

Appendix A3.2 – Wind Velocity Measurement

Investigation of wind measurement devices and good practice was carried out, since accurate measurement was essential for this work. There are four main types of anemometer by principle of operation, and there may be several forms/shapes/sizes of device within these types. Ultrasonic anemometers are a key technology. They typically use four probes positioned in the airflow measuring the speed of sound between one probe to each of the other three. Since there is a change in the speed of sound depending on relative air movement, this difference between each

measurement is computed into a net wind velocity (and direction). They have no moving parts and compensate for variable p, T and ρ, providing exact measure of v. Cupped anemometers are cheap and simple and unaffected by sudden wind direction changes. The principle is similar to a tiny VAWT where ω of the rotor is measured, observing that $\omega \propto v$. Cupped anemometers are not significantly affected by p, T or ρ, since the force required to turn the rotor is small (v is therefore measured to reasonable accuracy). This is convenient for measurement of v in the general case, but where v is used to calculate potential wind power and ρ needs to be taken into account then it is preferable to have the exact v and ρ values, rather than a slightly offset v value not fully compensating for changes in ρ from the ambient reference. Cupped anemometers are reliable and convenient for most scenarios. Thermal mass flow devices operate by measurement of relative cooling of an exposed heated wire. The wire may conduct a certain current at a certain temperature, and when cooled by airflow this current changes due to temperature-related conductance properties of the wire. This can be compared to an identical but unexposed wire and the difference in conductance converted into a v value. These are reasonably accurate, although they do not always compensate exactly for p, T and ρ. They essentially measure current change, proportional to mass flow, converted to a v value.

A manometer operates on the same principle as an aircraft pitot-static probe for measurement of air speed at altitude. A manometer measures the dynamic air pressure by pointing a small probe directly into the wind. Ambient pressure is measured by a static port on the side of the probe. Velocity creates a differential pressure, which displaces water height in a column and v is measured in terms of this displacement (mm). Observing Eq A3.1.5, the change in pressure experienced with v is

$$\Delta p = ½\rho v^2 \qquad \text{Eq A3.2.1}$$

$$v = \left(2\frac{\Delta p}{\rho}\right)^{½} \qquad \text{Eq A3.2.2}$$

where 1 mm H_2O = 9.81 Pa. The ρ value is required for accurate measurement. From Eq A3.2.2, it is evident that ambient p is the equivalent to approx. 408 ms^{-1}. During real operation of a WT rotor, typical Δp values experienced are therefore quite insignificant in comparison to ambient p.

Appendix A3.3 – Wind Turbine Test Data

Data from various micro WT testing work are included in this appendix.

D400

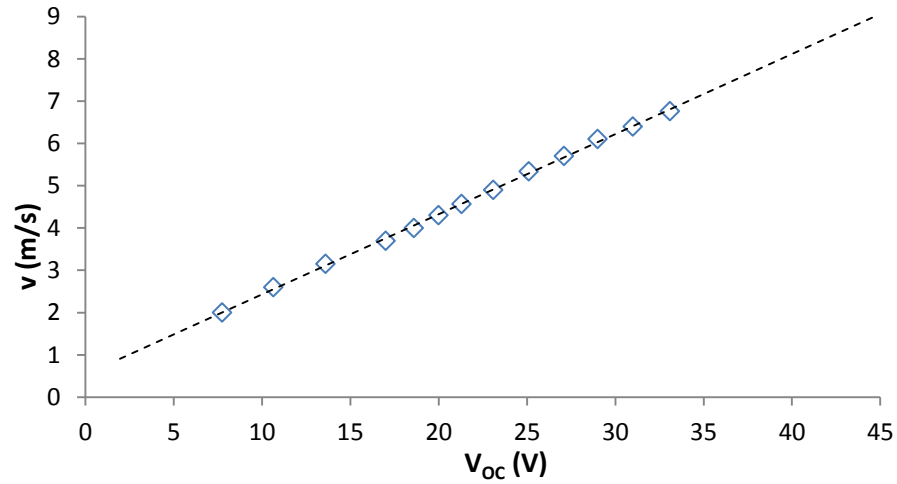

910-F

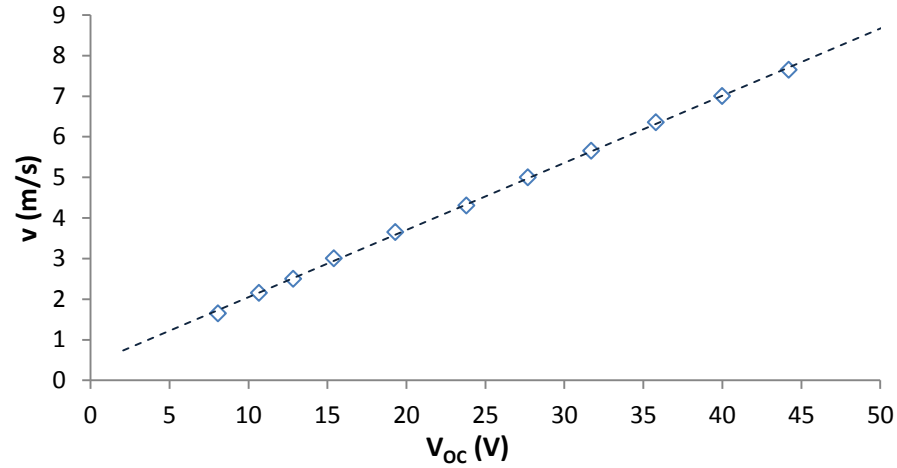

V30

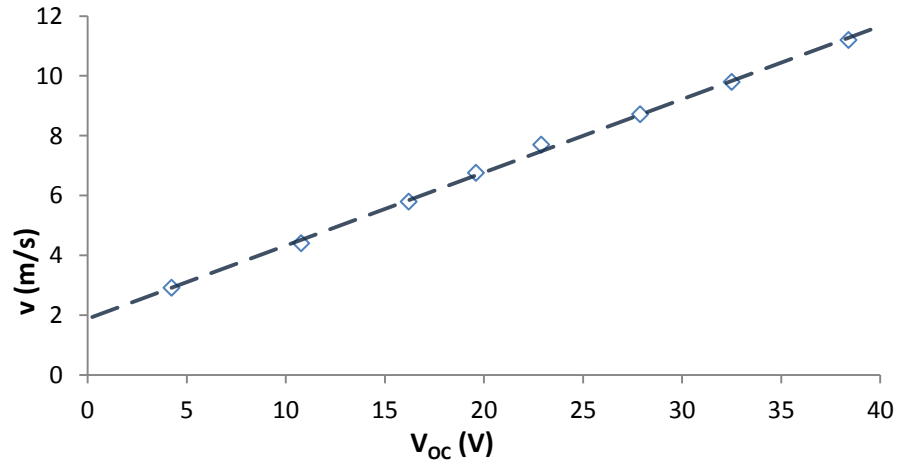

Figure A3.3.1 – Wind velocity-voltage data (v-V_{OC})

Open circuit voltage for the three WTs was recorded for known wind velocities. These data sets were used during later testing to confirm v without use of an anemometer.

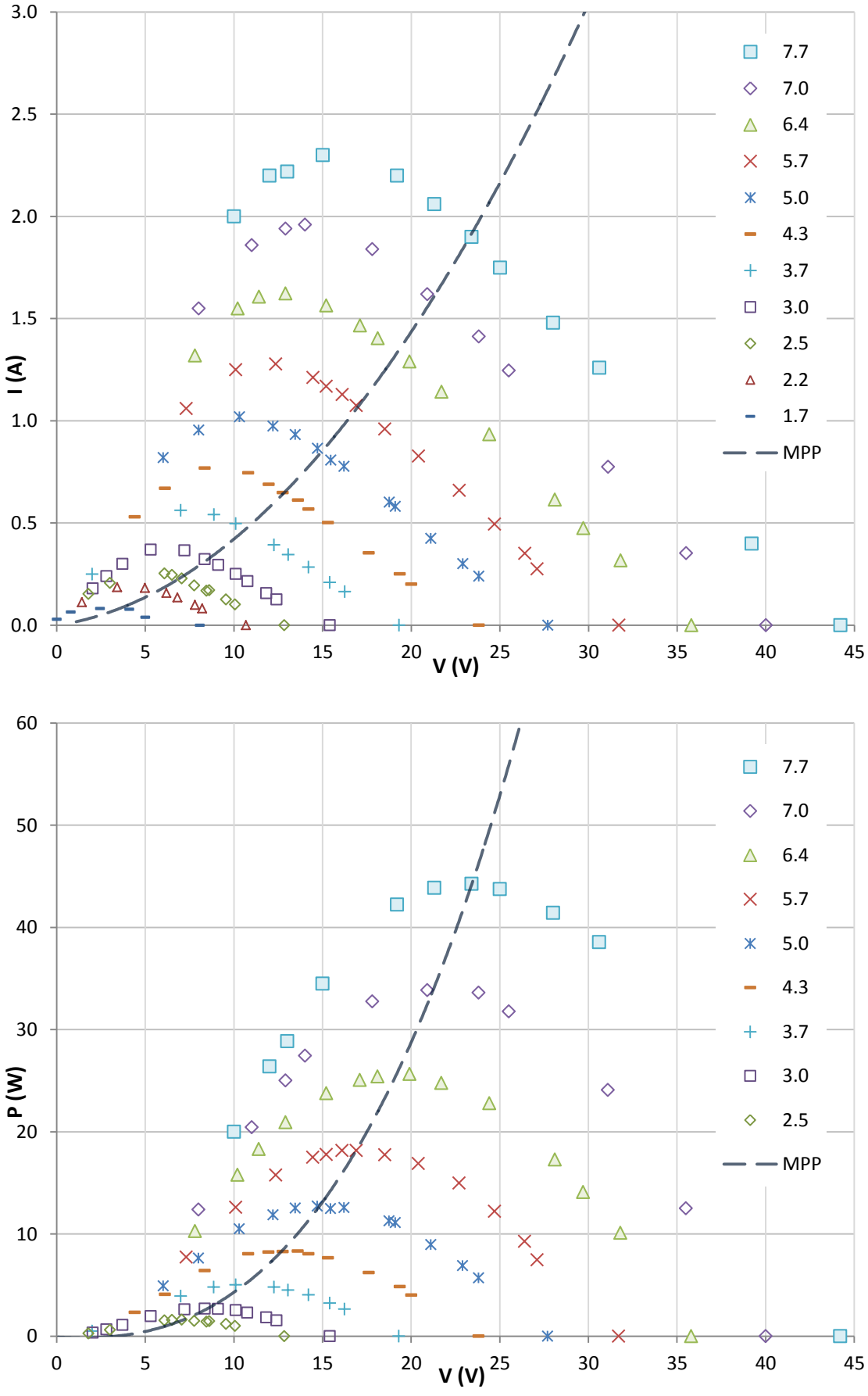

Figure A3.3.2 – 910-F HAWT Test Data (*I*-*V* and *P*-*V*)

Power-voltage and current-voltage data for 910-F HAWT testing (v = 1.7-7.7 ms^{-1}).

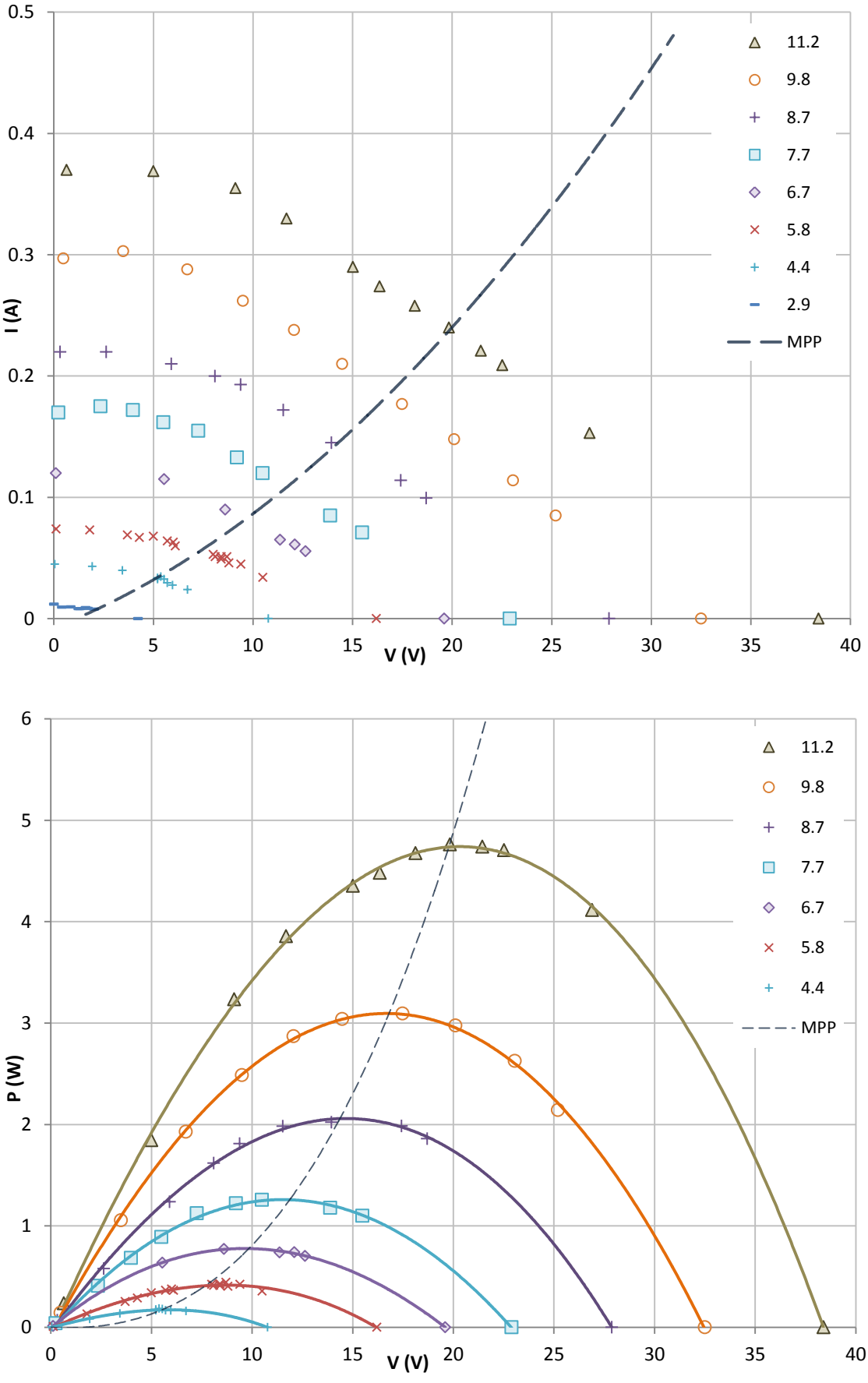

Figure A3.3.3 – V30 VAWT Test Data (*I-V* and *P-V*)

Power-voltage and current-voltage data for V30 VAWT testing (v = 4.4-11.2 ms^{-1}).

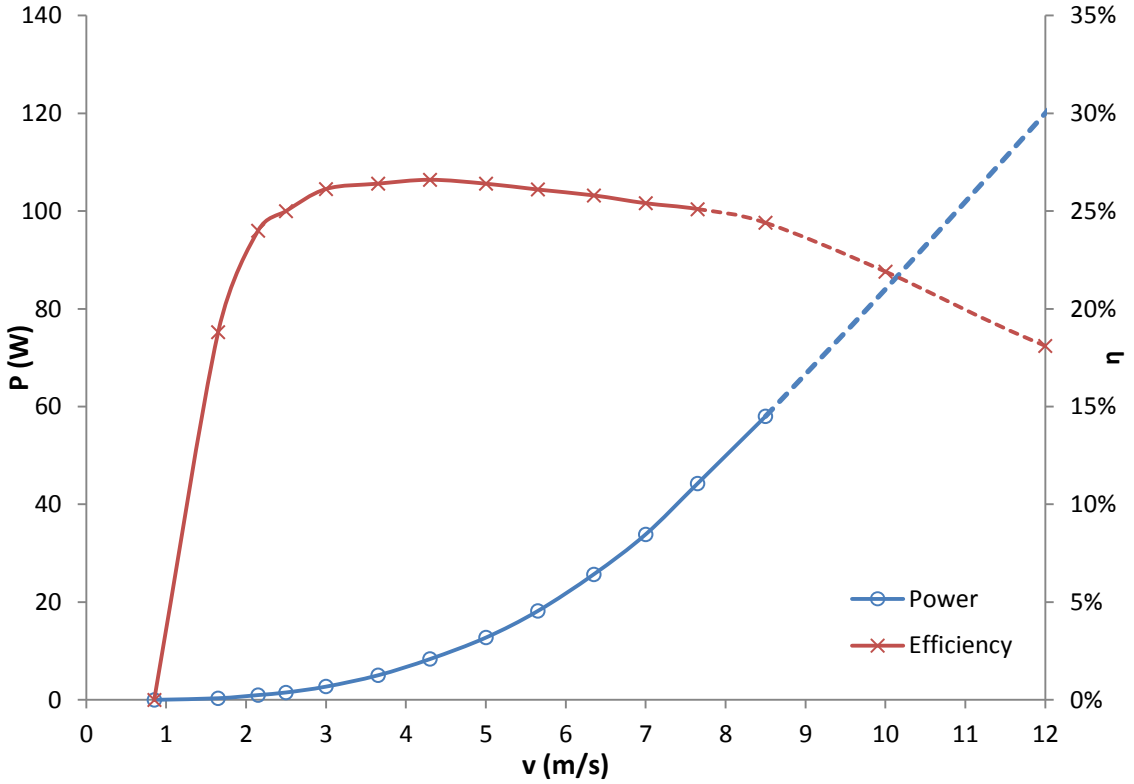

Figure A3.3.4 – 910-F HAWT Test Data (P-v)

Power-velocity and efficiency data for 910-F HAWT testing.

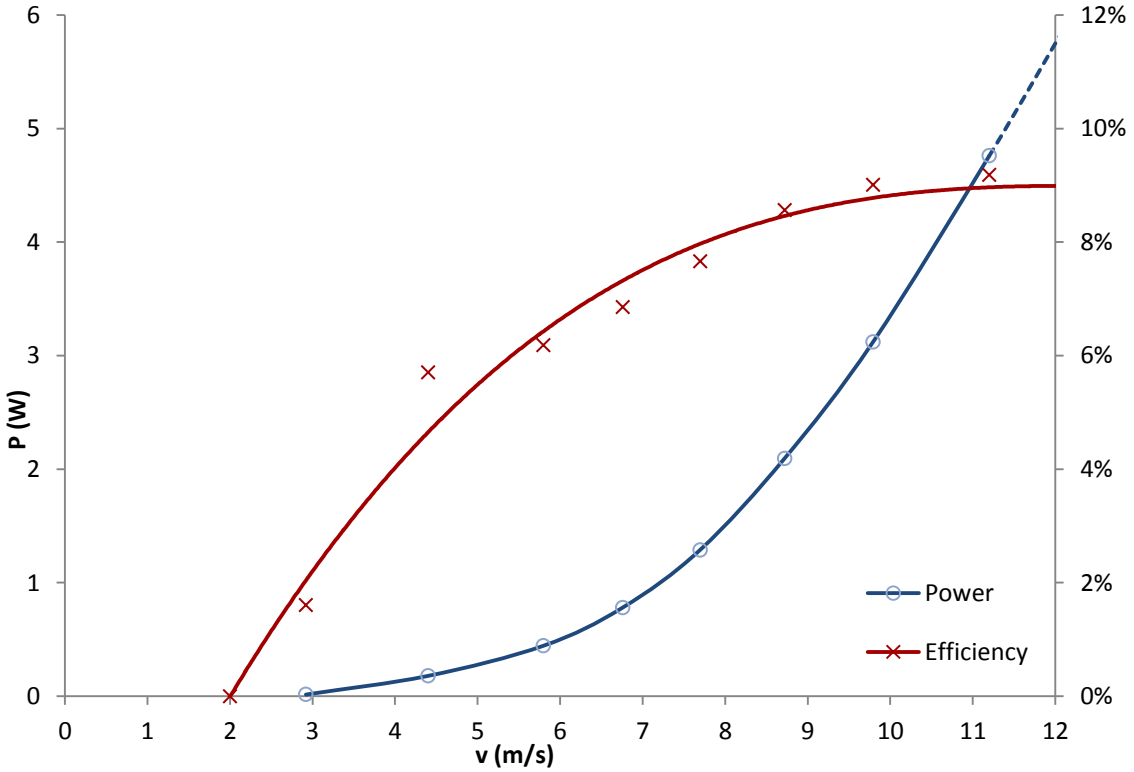

Figure A3.3.5 – V30 Test Data (P-v)

Power-velocity and efficiency data for V30 VAWT testing.

Appendix 3.4 – Solar Photovoltaic Energy

A3.4.1 Solar Photovoltaic Energy Overview

The photovoltaic effect was discovered as early as 1839 by Becquerel. The first proper PV cells were produced later, such as by Fritz in 1883, and cells involving copper oxide in the 1920s, of 1% conversion efficiencies [39] [359]. Silicon cells were developed from 1941, reaching 11% efficiency by 1954 (Bell Laboratories). The space revolution in the 1950s and 1960s was a main driving force for further development and commercialisation of this technology [359]. Early work was based upon maximising efficiency, whereas research moved towards reducing cost from the 1970s onwards. Growth of 35-40% per year of installed PV capacity has generally been sustained since 2007, as shown in Figure A3.4.1 [39] [87] [360]. By the end of 2013, 139 GW of global installed capacity was reported, 81.5 GW in Europe [87] [360]. For the years following 2013 slower growth has been expected due to reduced financial incentives (in Europe), as discussed in Subchapter 5.3. Germany held the largest installed capacity in 2013 (26% of global), followed by China (13%), Italy (13%), Japan (10%) and USA (9%). The UK had 2% in 2013 [360]. China and the USA both have significant off-grid capacity (with requirement for storage). Global PV capacity is expected to reach 220 GW by 2016 and grow at 50 GW per year, although future markets are uncertain due to changes in incentives and emergence of new countries into PV energy [360].

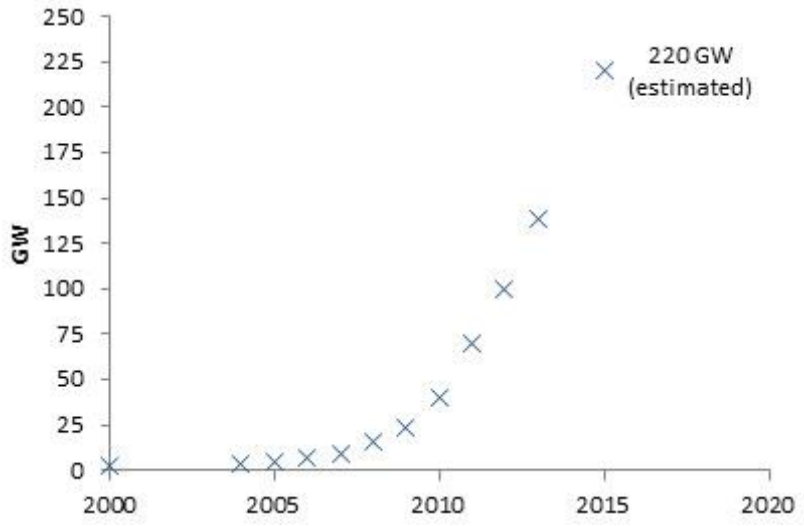

[39] [87] [360]

Figure A3.4.1 – Reports of Global Photovoltaic Installed Capacity
Various sources provide historical data for installed PV capacity, presented here.

Recent years have seen very significant changes in PV capacity and growth of individual countries. Italy grew from negligible installed capacity in 2007 to 13% of Europe's capacity by 2013 (with PV responsible for 7.5% of Italy's electrical energy). Similarly, Germany dominated Europe by capacity in 2007, but was demoted to 30% by 2013. Growth in both of these countries reduced considerably in 2013. The Global Market Outlook Report 2014-2018 [360] discusses extensive data trends not reported here. The majority of installed PV capacity is based on single junction crystalline Si cells [361]. The USA, Japan and Europe have played significant roles in production in previous years, although China is now the biggest manufacturer, responsible for 67% of PV cell production in 2013 (a total of 87% was manufactured across Asia) [87]. Early cells were crystalline Si, although there are now three broad classifications of PV: crystalline material; amorphous thin films; organic polymers [39]. Crystalline Si accounts for approx. 85% of all PV production and installed capacity. Despite the increasing presence of large area thin film technology, market trends favouring crystalline Si have remained steady in very recent years [87] [361]. The pursuit of cheaper materials (despite its abundance, Si has high cost due to purification processes and competing electronics industries), cheaper manufacturing (less heat treatment) and increased efficiency are the main driving forces for current PV research [39].

Other materials most commonly used are amorphous silicon (a-Si:H) and compounds of cadmium telluride (CdTe), cadmium sulphide (CdS), copper indium gallium selenide (CIGS), gallium arsenide (GaAs) and cuprous sulphide (Cu_2S) [361] [362]. Use of thin films, multi junctions, dye-sensitised cells and nanotechnology have been methods to increase cell performance and/or reduce materials/cost [202]. Interest in this work is with Si crystalline cells due to their market presence and availability etc. Crystalline Si cells offer between 15-20% conversion efficiency, compared to 5-7% for thin film, although the latter are cheaper and offer slightly cheaper energy unit costs [39] [361] [363]. Crystalline cells are single crystal and polycrystalline, where the latter is less efficient (≈ 15%) but of lower cost per Watt. The cost aspect has dominated installation decisions and growth in recent years (polycrystalline has taken a larger market share). The difference in cost and performance originate from the manufacturing processes. Both involve high purity Si from extensive heat treatments. This involves removing oxygen and CO_2 and further treatments including the floating zone technique where a rod of Si is passed continually through a heated zone in one

direction to create a pure and impure end. The impure end is then discarded. Pure polycrystalline Si material can be cast directly into ingots, whereas production of single crystal Si follows with the Czochralski process, where a crystal seed of Si is introduced to heated polycrystalline Si and 'pulled' out resulting in the formation of a large pure single crystal ingot of Si. The ingots are cut into wafers, doped to create the necessary p-n junction and formed into cells. The cells receive metal contacts antireflective coatings and are assembled into PV modules [364]. Polycrystalline cells do not require the single crystal growth step and therefore have a simpler manufacturing process and lower production cost. As they consist of a number of small crystals there is greater carrier loss by recombination and they have slightly lower efficiency [39]. The energy required to manufacture crystalline Si cells can be regenerated by the cell in two to three years, compared to one year for thin film cells [362]. Grid connection is understood to be the most effective, feasible and economic use of PV at present. Stand-alone systems relying on battery storage, or conversion to hydrogen, are also of interest [359]. Connection of PV to electrolysers for H_2 production is possible with similar DC-DC converter techniques as discussed for WTs, or in fact by direct connection (which is not practical for WTs) [142]. For this reason PV-electrolysis systems are perhaps preferred from a technical point of view.

3.4.2 Fundamentals of Photovoltaic Energy

PV materials involve p-n junctions. N-type doping is achieved with group V elements such as As or Sb, which act as electron donors. P-type doping involves group III elements such as Ga or In, which act as acceptor holes [362]. When a photon enters PV material, it may be reflected, absorbed, or transmitted. If absorbed by a valence electron and the photon energy is greater than the band gap energy (E_G), the electron can jump into the conduction band. The electric field from the p-n junction separates the electron-hole pair created and causes a current to flow through an external circuit [362]. The electron or hole carriers may not negotiate the entire field region at the p-n junction. In particular, the minority carriers have a finite lifetime and may recombine, reducing the current flow. Only one electron-hole pair is normally permitted per photon regardless of energy. Photons with energy < E_G do not create electron-hole pairs. Photons with energy > E_G do, depositing any remaining energy thermally [39]. There are therefore two fundamental efficiency limits based upon the material absorbency and band gap. Assuming a single junction PV cell operates ideally, the

maximum electrical energy extracted is based upon the amount of photons generating carriers at the junction (not being reflected or transmitted) minus any thermal energy from high energy photons > E_G. Approx. half of solar energy is visible and UV (380-750 nm and 10-380 nm respectively) [39]. Radiation below 280 nm is absorbed by the earth's atmosphere [365]. Band gaps of various PV materials are shown in Table A3.3.1. The performance of single junction Si cells is limited to approx. half of the energy of the solar spectrum (which can be absorbed by the material). There is basic proportionality between the number of photons and available cell current, where the specific ratio per unit area depends on the above factors. There are also further loss mechanisms that further limit cell efficiency in terms of voltage etc. Maximum cell photocurrent, I_p, can be represented by electron charge e, the incident photon flux with energy above the band gap, φ, and area A, where [39]:

$$\mathrm{I_p} = e\varphi A \qquad \text{Eq A3.4.1}$$

Single junction cells are understood to be fundamentally limited at approx. 33% efficiency by the Shockley-Queisser limit [366]. This refers to the maximum electrical energy extraction of a cell with ideal band gap (1.34 eV) under full sunlight at air mass 1.5 (1000 W m^{-2}). The band gap of Si (1.1 eV) is less, but only slightly limits efficiency. Three techniques are found in literature to overcome the Shockley-Queisser limit: carrier multiplication; spectrally selective beam splitting; thermo-photovoltaic cells [39]. Multi junction cells are of particular interest (spectrally selective beam splitting), involving two or more layers of cells with different band gaps formed into a cascaded cell [366]. The upper layer absorbs the highly energetic photons efficiently (since it can generate a higher voltage from its higher band gap), and lower layers absorb the remainder. Theoretical single junction material but with two band gaps (multiband) and thermal upgrading of photons are other approaches discussed elsewhere [39] [367]. Energy components relating to the solar spectrum and theoretical limits of various advanced cell types and a recent efficiency achievement are shown in Figure A3.4.2. Air mass is a very important factor, determined mainly by sun elevation. The physical mass of air causes scattering of photons. Where air molecules have a diameter < λ, Rayleigh scattering occurs, whereas when the diameter > λ, Mie scattering occurs. The latter is more related to air pollution, and the contributions of both types therefore vary by location. Cloud cover and moisture also have significant

effects. When the sun is at its zenith with clear sky, AM = 1.0, whereas in typical conditions in the developed regions of the Northern Hemisphere this value is considered AM =1.5 (1000 W m^{-2}), relating to an elevation of 41.8°. Above the atmosphere AM = 0 (1360 W m^{-2}) [39] [110]. Warm, sunny, dry sites with unpolluted air (and ideally higher altitudes) are therefore preferable for PV installations.

Material	$E_G\ (eV)$	λ (=hc/E_G) (nm)	Region
Ge	0.66	1870	IR
Si	1.12	1110	IR
GaAs	1.42	870	NIR
CdTe	1.44	860	NIR
a-Si:H	1.7-1.8	730	Vis

[368]

Table A3.4.1 – Band Gaps of Common Photovoltaic Materials
Band gap data (at 300 K) from literature is shown for five common PV materials.

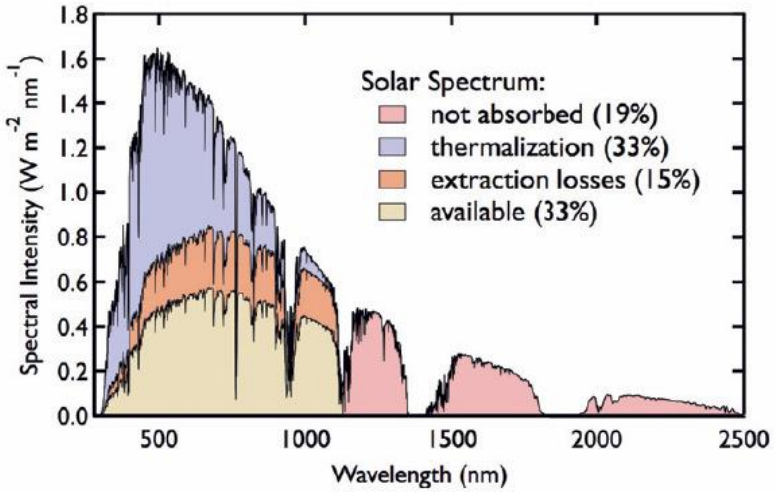

(a)

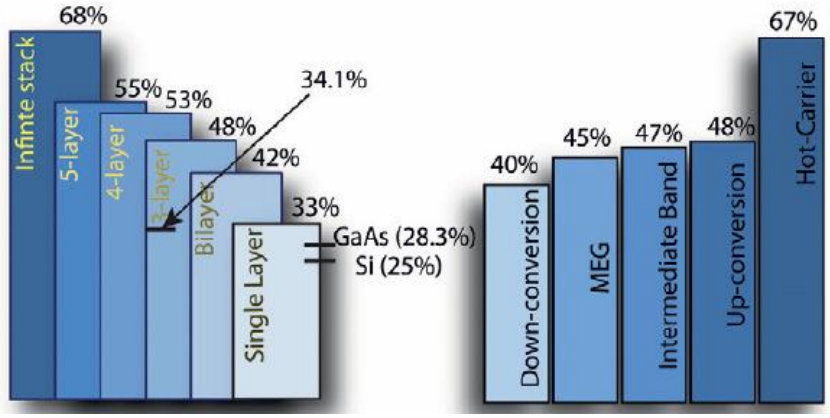

(b)

[369]

Figure A3.4.2 – Crystalline Silicon Spectral Losses and Various Advanced PV Cell Limits
In (a), spectral intensity and absorption bands, by wavelength are shown, and in (b) theoretical limits are shown, with some recent achievements.

Voltage is defined from cell band gap, doping/carrier concentration, recombination and T_{Cell} etc [39] [359]. V_{OC} for a crystalline Si cell reaches 0.6 V in typical irradiance [369]. *I-V* characteristics of a cell can be represented by an equivalent electrical circuit such as Figure A3.4.3, where I_d is the diode current, R_{sh} the shunt resistance (usually very large), R_s the effective series resistance and R_d the load [359]. Diffusion voltage V_D (resulting from the electric field across the p-n region) can be defined from acceptor and donor dopant concentrations, n_A and n_D, and intrinsic carrier density, n [110]:

$$V_D = \frac{kT}{e}\ln\left(\frac{n_A n_D}{n^2}\right) \qquad \text{Eq A3.4.2}$$

Carrier density n is directly related to the band gap and falls exponentially with increasing E_G. In turn, V_{OC} relates to V_D. *I-V* characteristics can be explained from the basic diode equation, where I_s is the reverse saturation current (and $V = V_D$) [39]

$$I_d = I_s\left[\exp\left(\frac{eV}{kT}\right) - 1\right] \qquad \text{Eq A3.4.3}$$

From the equivalent circuit, photocurrent I_p is shared between I_d and I, therefore [39]

$$I = I_p - I_d = I_p - I_s\left[\exp\left(\frac{eV}{kT}\right) - 1\right] \qquad \text{Eq A3.4.4}$$

Voltage can also be expressed from I by inverting Eq. A3.4.4:

$$V = \frac{kT}{e}\ln\left[\frac{I_p - I}{I_s} + 1\right] \qquad \text{Eq A3.4.5}$$

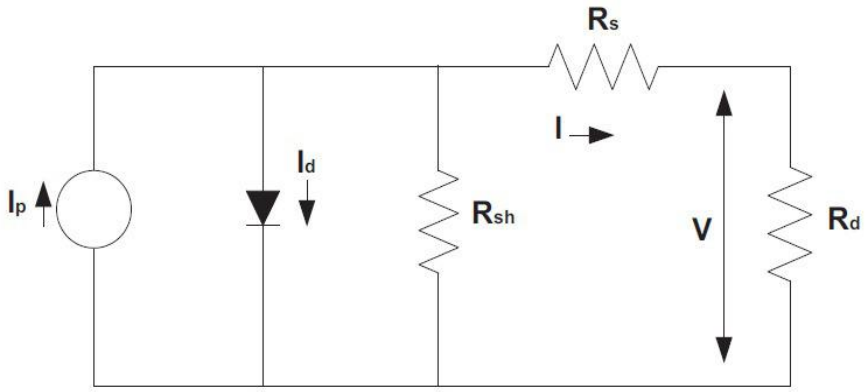

[359]

Figure A3.4.3 – Simplified Equivalent Circuit of a Photovoltaic Cell

A PV cell can be represented approximately as a current source with internal resistances R_{sh}, R_s and a diode with current I_d.

Considering R_{sh}, R_s and a diode non-ideality factor m (between 1-5, < 2 for most PV cells), Eq A3.4.4 becomes [110] [370]

$$I = I_p - I_s\left[\exp\left(\frac{e(V+IR_s)}{mkT}\right)-1\right]-\frac{V+IR_s}{R_{sh}} \qquad \text{Eq A3.4.6}$$

Ignoring the R_{sh} term (often insignificant), power can therefore be expressed as

$$P = VI_p - VI_s\left[\exp\left(\frac{e(V+IR_s)}{mkT}-1\right)\right] \qquad \text{Eq A3.4.7}$$

Cell performance varies with temperature, specifically I_s, by the following function where T_c is a reference temperature and I_c the reverse saturation current at T_c [359]:

$$I_s = I_c\left(\frac{T}{T_c}\right)^3 \exp\left[\left(e\frac{E_G}{k}\right)\left(\frac{1}{T_c}-\frac{1}{T}\right)\right] \qquad \text{Eq A3.4.8}$$

Typical trends based on these equations are shown in Figure A3.4.4 and A3.4.5. The theoretical MPP can be found for example when dP/dV = 0. Important features are therefore I_{SC}, V_{OC}, and I_{MPP}, V_{MPP}, which determine the cell 'quality' or fill factor (FF)

$$FF = \frac{I_{MPP}V_{MPP}}{I_{SC}V_{OC}} \qquad \text{Eq A3.4.9}$$

and with known irradiance, E_s (W m^{-2}) and cell area, A, the efficiency is therefore [110]

$$\eta = \frac{FFV_{OC}I_{SC}}{E_SA} = \frac{P_{MPP}}{E_SA} \qquad \text{Eq A3.4.10}$$

The latest published PV cell performance benchmarks across all the technology types are held by the US National Renewable Energy Laboratory (NREL) [371]. At the time of writing, claims of 38.8% are the highest for (four) multi junction cells, or 46.0% with use of a solar concentrator. Thin film single junction GaAs cells have been reported at 28.8%. The reason for GaAs being of high efficiency but thin film is due to the band gap and being a direct semiconductor, with a much higher absorption coefficient than crystalline Si [110]. For Si, 25.0% (27.6% with concentrator) has been reported for single crystal and 20.4% for polycrystalline. CIGS thin film has reached 21.7% (23.3% with concentrator) and a-Si:H at 13.4%. 11.9% has been achieved with dye-sensitised

cells. Other emerging technologies have reached 10-12%, but 20.1% in the case of perovskite cells, showing potential for commercial use in the near term.

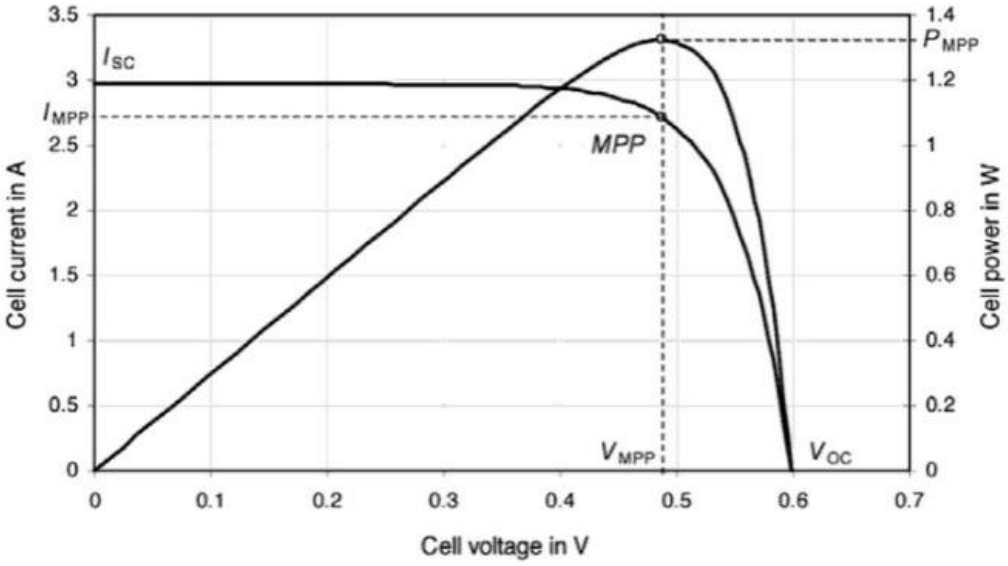

[110]

Figure A3.4.4 – Example PV Cell *I-V*, *P-V* Curves

Current- and power-voltage trends are shown for an example PV cell test at an arbitrary irradiation value. I_{SC}, V_{OC} are the maximum current and voltage (at short and open circuit). I_{MPP}, V_{MPP} and P_{MPP} are the current, voltage and power at the MPP.

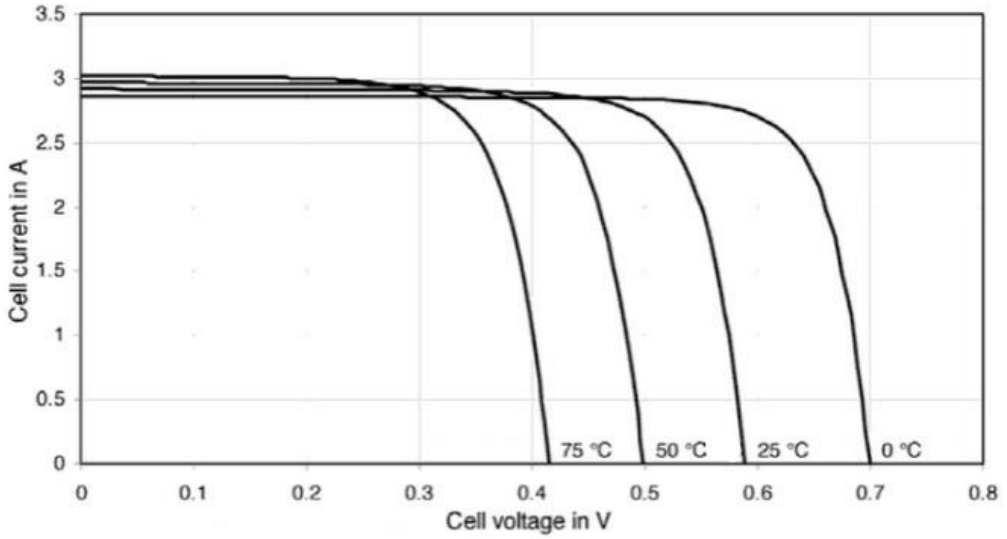

[110]

Figure A3.4.5 – Example PV Cell *I-V* Variation with Temperature

Cell voltage is shown to decreases significantly as temperature rises from 0-75°C. Conversely, current increases (by a much smaller relative amount).

Appendix A3.5 – Wind and Solar Case Study: Cypex, Dundee

Cypex is a small biological processing unit in Dundee with a A 74 kW WES 80 WT and 17 kW PV array installed on- site. These were investigated as a case study. Data was kindly made available by the owner (Dr Mike Voice). Specifications and data are shown in Figures A3.5.1-A3.5.5 and Table A3.5.1.

WT:
WES 80 HAWT (74 kW @ 12 ms^{-1})
Approx. 400 V (3-phase AC)
Commissioned May 2009
Installed cost: £200,000
Rotor: 2-blade
Hub height: 30 m
Ø / area: 17.9 m / 251.6 m^2
η (rated): 28%
η (max): 35%
ROC/LEC incentive

PV:
17 kW (polycrystalline Si) PV
Commissioned July 2012
Installed cost: £34,000
FIT incentive

Figure A3.5.1 – Cypex Wind Turbine and Solar PV Installation Specifications

Year	Wind, MJ (kWh)	Payment	Solar, MJ (kWh)	Payment
1	104,486 (29,024)	£ 5,220		
2	132,638 (36,844)	£ 5,965		
3	159,833 (44,398)	£ 7,627		
4/1	98,003 (27,223)	£ 4,923	53,276 (14,799)	£ 3,743
5/2	130,291 (36,192)	£ 5,960	51,849 (14,402)	£ 3,805
6/3 (incomplete)	98,644 (27,401)	≈ £ 4,500	33,589 (9,330)	£ 2,628
Average (approx)	124,200 (34,500)	£ 6,000	52,920 (14,700)	£3,800

Table A3.5.1 – Cypex Case Study Data Summary
Summary of annual energy and financial data for the Cypex WT and PV installations.

The data values for the WT and PV in Table A3.5.1 take into account all the incentives/tariffs and the savings from reduced import of electricity at the site (£0.1259 kWh^{-1}). The unit has a high electricity demand (for cooling etc) and much of the generated power is consumed on site.

The WT was registered under the ROC arrangements of the time and what has actually followed has been a mixture of irregular payments that do not necessarily fall within the corresponding year of generation. Data for the WT is reported as per the generating timescale for these payments. A comparison to present FIT structure indicates similar revenue would be gained if the installation was commissioned in 2015.

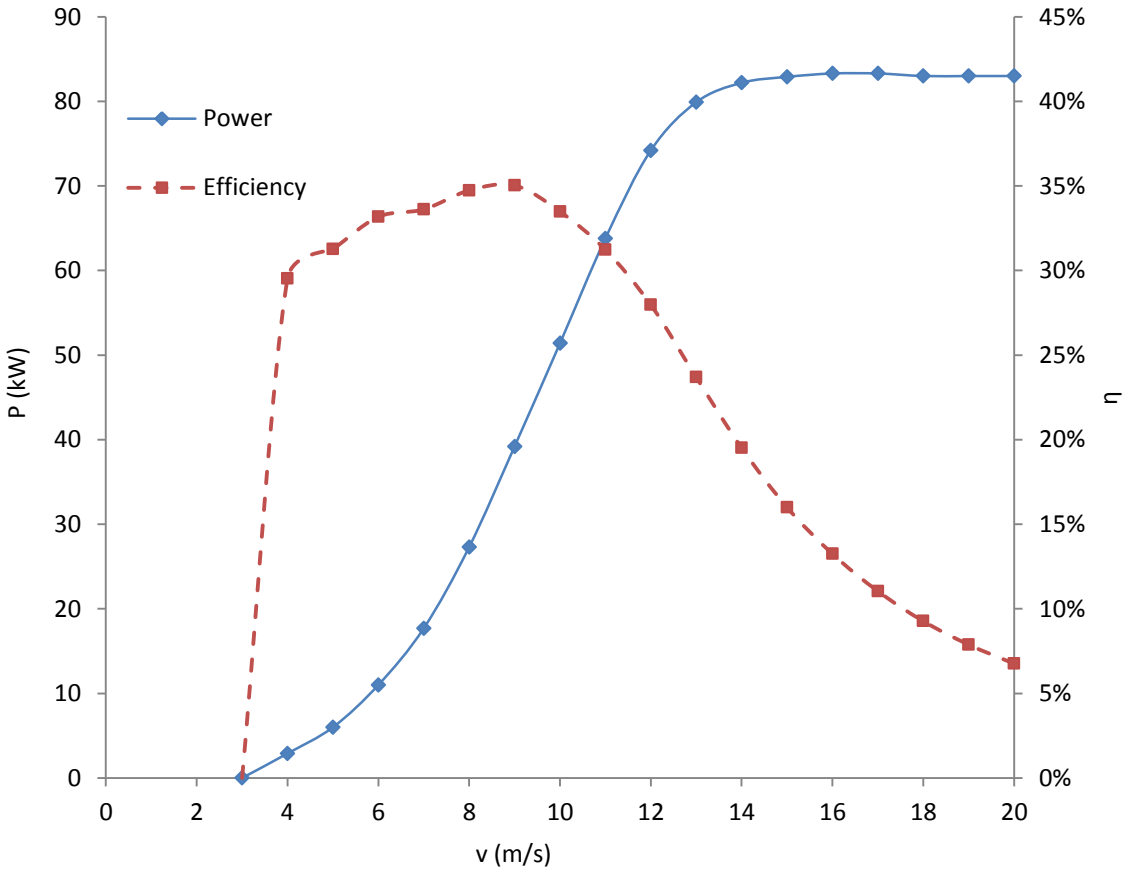

[348]

Figure A3.5.2 – WES 80 Power and Efficiency Curve

The power-velocity and efficiency curves are shown for the WES 80 WT. Peak power is indicated at 14 ms^{-1}, with maximum efficiency (35%) occurring at 9 ms^{-1}.

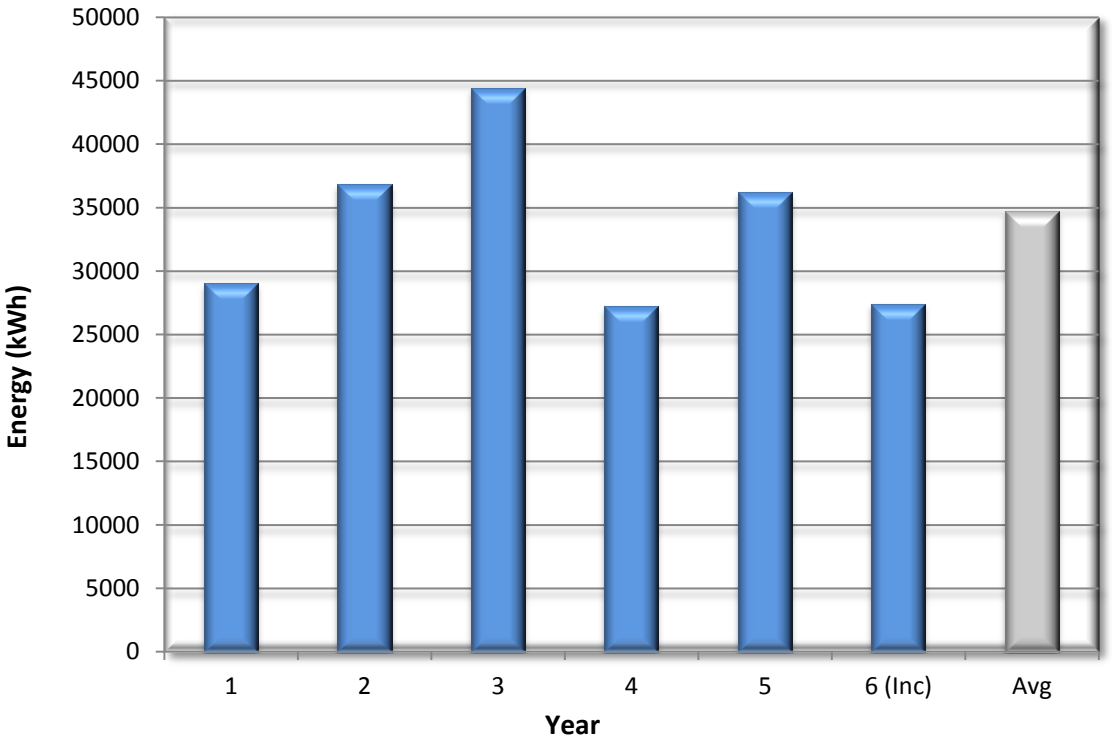

Figure A3.5.3 – Cypex Wind Turbine Yearly Performance Data

WES 80 WT yearly energy generation (kWh) is shown. Year 3 (May 2011 to May 2012) was clearly above average, whereas year 4 (May 2012 to May 2013) was poor.

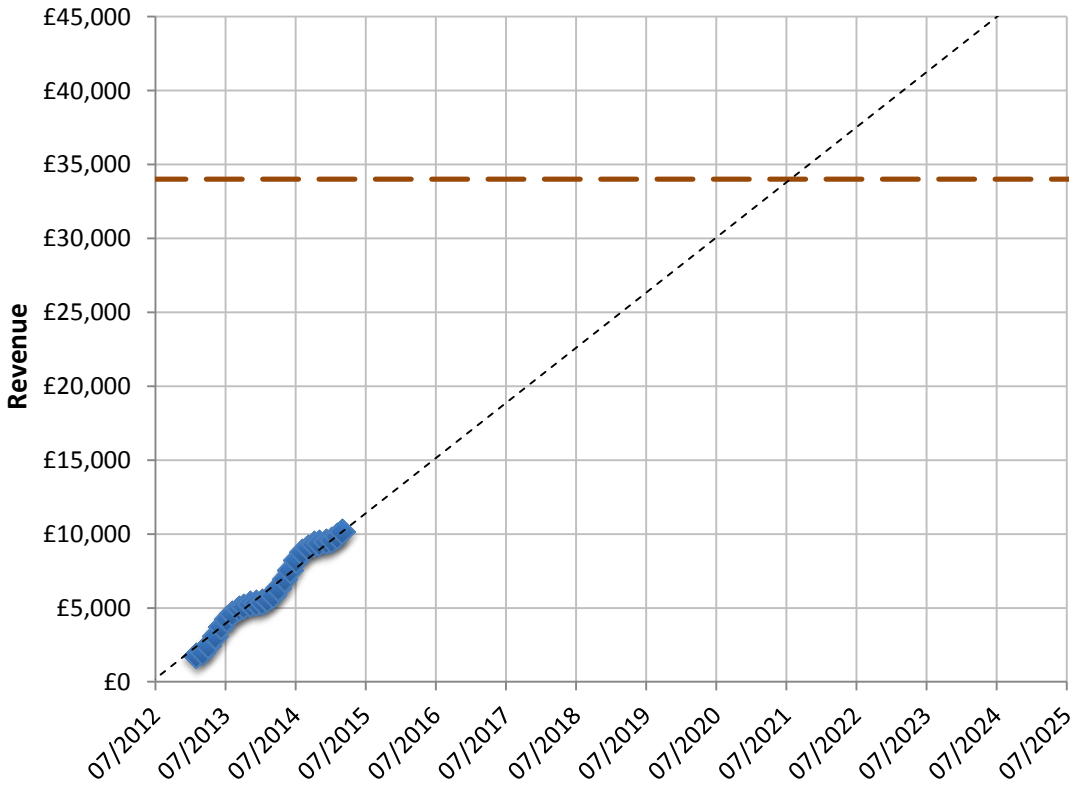

Figure A3.5.4 – Cypex Solar PV Revenue Data and Payback Trend

Extrapolation of PV data indicates payback will be reached in 2021 (nine years).

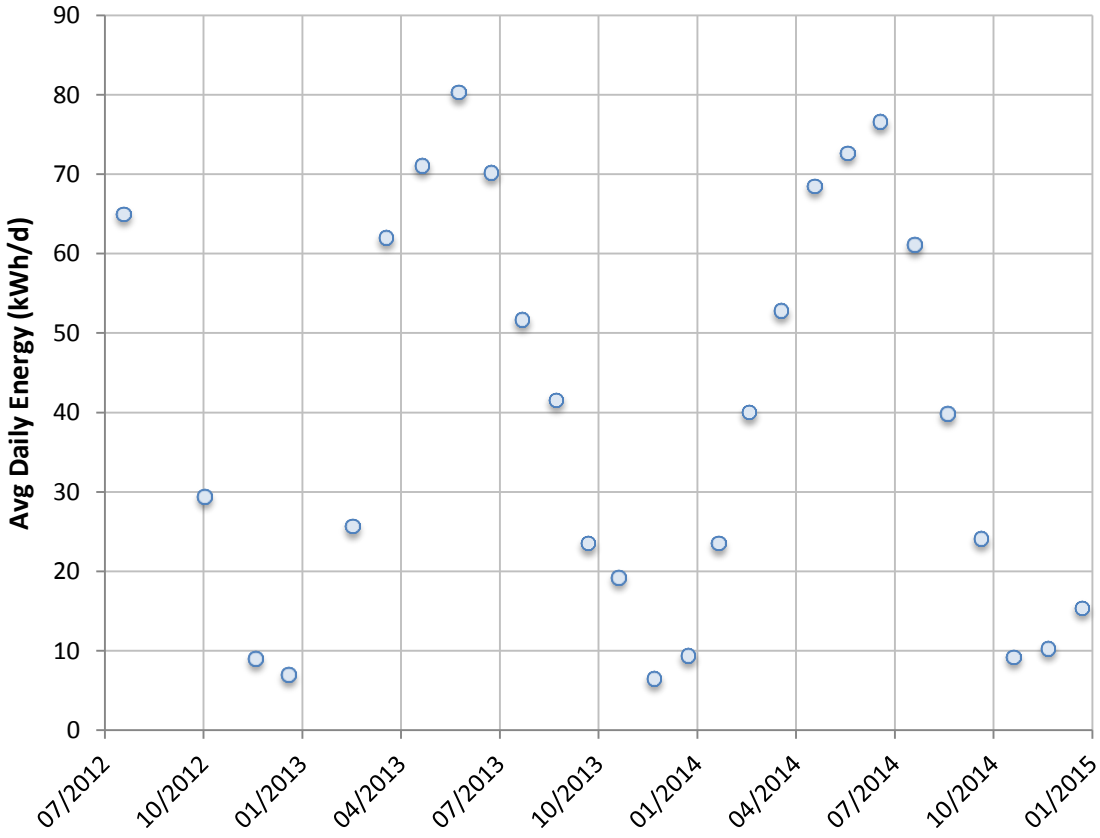

Figure A3.5.5 – Cypex Solar PV Performance Data Example Daily Averages
The cyclical nature of PV generation is shown. Clearly mid-summer is significantly more productive (≈ 80 kWh day^{-1}) than mid-winter (≈ 7 kWh day^{-1}) at UK locations.

The WES 80 was installed for £200,000 (including equipment, mast, power converter/inverter, mount, earth works, cabling and certain maintenance activities). The installation was part-funded with a £68,000 grant and a £100,000 interest-free loan (eight-year, £12,500 yr^{-1}. The initial cost to Cypex was £32,000 and the effective overall cost to Cypex is £132,000. In 2015 an equivalent installation would cost £100,000-£150,000 (minus any grants), due to significant reductions in equipment and installation costs from better market competition and changes in economic factors [87], representing 1350-2000 £ kW^{-1} (2000-3000 $ kW^{-1}). The £12,500 repayments have benefited from an effective deduction due to compound inflation maintaining 1-5% (average 3%) until early 2015 (the six-year point). CPI/RPI/RPU inflation measures have remained fairly equivalent during these six years [372]. Inflation in 2015 has approached 0%, likely to remain as such for two years.

Inflation has therefore created an effective reduced repayment amount equating to approx. £88,600. This indicates a total effective cost of 188,600, of which £120,600 is

paid by Cypex. ROC/LECs are index linked, but have required ongoing negotiation to obtain payments. 2010 was noted to have been an unusually poor year for wind energy, from weather data and a review of other WT installations in Scotland [109]. The payback time for the WT installation only considering the £120,600 is estimated at 20 years (or 31 years if £188,600), which is poor for a medium WT. The main reason is due to the high purchase cost and poor wind trends at the site. Predominant WSW winds are indicated from weather data; however, there are large buildings directly to the ENE and the ground also rises in the direction of these buildings. A high wind shear is expected and the 30 m WT hub is therefore too low for economical power extraction. Considering a wind shear exponent of 0.31, the WT performance would likely increase by 20-30% if the hub height was 40 m. It is understood that the original plans were for 40 m but this was reduced to 30 m due to proximity to nearby residences. The installers appear to have not closely measured/considered wind trends at the site. After the 25-year point the installation could feasibly be reconditioned and continue to operate. Based on the data, the WT capacity factor ≈ 5.3% and energy unit cost ≈ 0.22 £ kWh^{-1} (0.33 $ kWh^{-1}) over the initial 25 years.

The 17 kW PV installation was commissioned in July 2012, receiving FIT payments and almost three years of data were available at the time of writing. The PV was funded by an interest-free loan (eight-year). Inflation brings the initial payment of £34,000 to an equivalent of approx. £32,500 at the eight-year point. A similar installation in 2015 could be achieved for £25,000-30,000 due to increased market sector competition and lower equipment costs [87]. The FITs (export tariff) are index-linked, therefore the repayments have varied but have averaged at £0.15 kWh^{-1}. The repayment timescale is estimated at eight to nine years, after which an earning of approx. £3,800 (index linked) will be made for the remaining lifetime of the installation. Based on the data, the PV capacity factor in the first two years ≈ 9.8% (859 kWh kWp^{-1}) and unit cost ≈ 0.09 £ kWh^{-1} (0.13 $ kWh^{-1}) over 25 years.

The data in this case study for the WT is not indicative of a typical installation of this rating, based on data reported elsewhere such as the Renewables 2014 Global Status Report [87]. The PV is however reasonably as anticipated. This demonstrates that equipment/installation costs, site conditions, demand and incentives are key components of the viability for a renewable energy installation.

Appendix A3.6 – DC-DC Power Converters

Basic DC-DC convertor circuits for step-up, step-down, and both, are shown in Figure A3.6.1. These circuits require a square wave signal generator (variable pulse-width) to provide ON/OFF switching of the MOSFET. When the MOSFET cycles ON/OFF the inductor undergoes charge/discharge cycles (which are fairly linear) [150]. In each case, the inductor provides the temporary energy store (magnetic) to enable the step up/down function, effectively delivering units of additional voltage or current to the circuit. The capacitor provides stability to the circuit during the switching cycles, where it may provide all of the output power for short instances (practically there may be a bank of several large capacitors in parallel). Cycle frequencies are typically 10-100 kHz, where charge/discharge is relatively small to minimise DC ripple and losses.

For the step-up circuit, during MOSFET ON (inductor charging), the load is isolated from the input and the capacitor provides power to the load. The diode prevents the capacitor returning current to the inductor/input part of the circuit. When the MOSFET is cycled to OFF, the inductor (discharging) holds voltage across it in series with the input, allowing a stepped-up voltage to reach the capacitor/load. The circuit therefore delivers higher output voltage, with V_{out}/V_{in} determined by the % ON (duty, D) of the PWM switching signal. At minimum duty cycle (0%) the inductor becomes a series (resistive) component of the circuit (R_L, in mΩ) and no stepping occurs.

In the step-down circuit with the MOSFET ON (inductor charging) the load is powered (through the inductor) and the capacitor is charged. When the MOSFET is OFF, the inductor maintains current through its part of the circuit (discharging via the diode) to power the load, assisted by the capacitor (parallel). The orientation of the inductor opposes the input voltage while charging and results in a reduced output voltage being maintained, but increased current due to the parallel inductor/capacitor. In both cases, pulse-width modulation (PWM) controls the voltage stepping magnitude [97]. The ratio of ideal step-up/step-down is related to D by the following functions [97]:

$$\frac{V_{Out}}{V_{In}} = \frac{1}{1-D} \qquad \text{(step-up)} \quad \text{Eq A3.6.1}$$

$$\frac{V_{Out}}{V_{In}} = D \qquad \text{(step-down)} \quad \text{Eq A3.6.2}$$

(a) Step-up (boost)

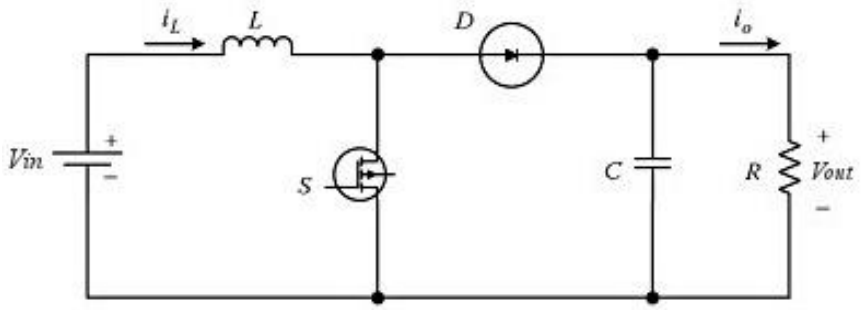

(b) Step-down (buck)

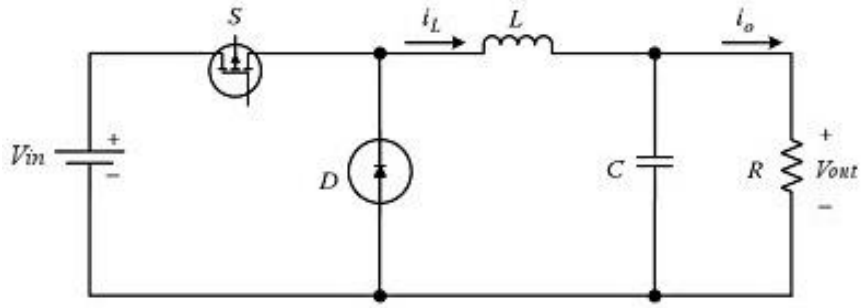

(c) Step-up/down (buck-boost, non-inverting)

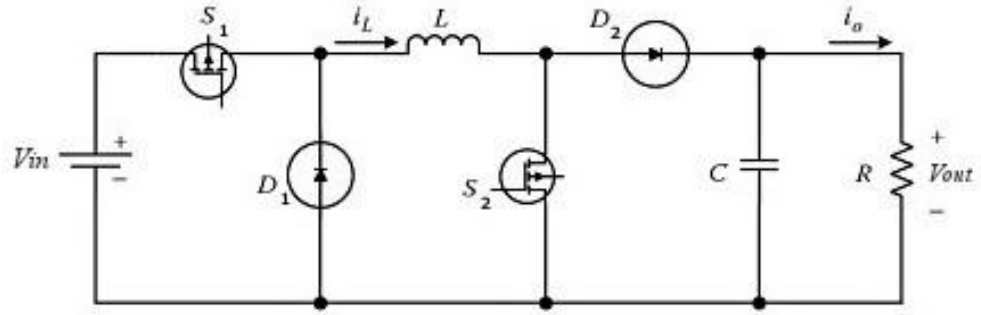

[97] [150]

Figure A3.6.1 – Inductive DC-DC Voltage Converters

Three circuits operated by a square wave signal generator provide (a) step-up, (b) step-down, and (c) both step-up and step-down (without inverting votlage). L, D, S, C and R represent the inductor, diode, MOSFET, capacitor and load respectively.

Step-up is achieved by increasing D from 0%. For step-down, D starts at 100% and is reduced towards 0% to reduce V_{Out}. Step-up limits and non-ideality exist mainly from inductor and MOSFET losses such as R_L, illustrated in Figure A3.6.2 [150]. D should be controlled dynamically (load-dependent) to achieve the correct stepping. When stepping up, the effective loading of the input is increased. Conversely, when stepping down, the effective loading is reduced. Variable stepping function of DC-DC converters

provides the platform for conventional MPPT of WT and PV systems, with variable duty % to vary the effective load and control I-V trends to operate at maximum power through a range of conditions [117]. To enable stepping in both directions (buck-boost), two PWM signals would be required, independently operating the MOSFETs as shown in Figure A3.6.1(c). Another option is the more simple 'inverting' type DC-DC converter, but not considered suitable for the work here [121]. When stepping up, the S_1 MOSFET would remain ON (100%) and S_2 would operate as with the normal step-up circuit (0-100%). Likewise, when stepping down, S_2 would remain OFF and S_1 would be operated (100-0%). S_1 would never reach 0% and S_2 100% since these would result in open circuit and short circuit in the step-down and step-up circuits respectively.

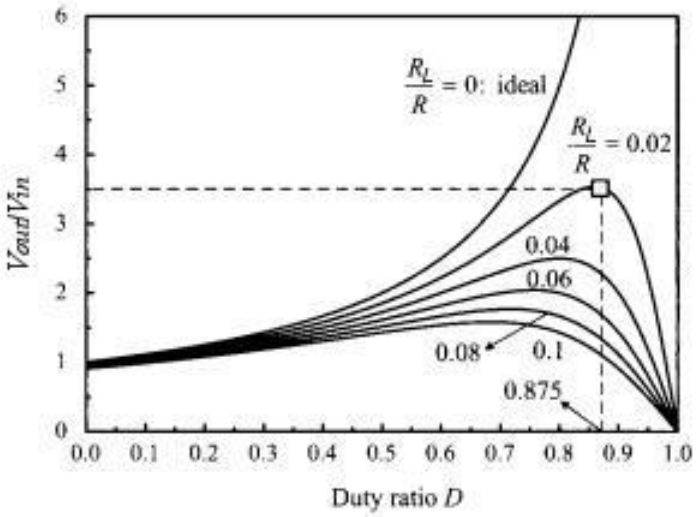

[150]

Figure A3.6.2 – Typical Limits for Inductive DC-DC Step-up
Circuit ideality reduces as $D \rightarrow$ 100%. Step-up is limited (e.g. < 3.5). Data here assumes constant load current (I_{out}). Losses depend on loading (R), inductor ESR (R_L) and other circuit component integrity etc.

Capacitive DC-DC converters were also investigated as an alternative to inductive converters, allowing higher step-up values. Their function is somewhat similar, although they have not been found in use for power/renewable applications due to lower efficiency. A charge pump capacitive voltage stepping circuit with one 'flying capacitor' (C_1) is shown in Figure A3.6.3 [145]. C_1 is charged by the input and placed in series to provide output voltage of almost double the input (the opposite occurs for step-down). S_1 and S_2 ON-state provide charging of C_1. S_3 and S_4 ON-state provide discharging. S_3 and S_4 are OFF-state when S_1 and S_2 are ON-state and vice versa.

More capacitors can be added to create very large stepping. The capacitive circuit requires two MOSFETs plus another two per flying capacitor, making it slightly impractical. When $D \approx 0$ or 100% the circuit controller must put S_1 and S_3 ON-state to enable current flow (since the capacitor becomes a DC block).

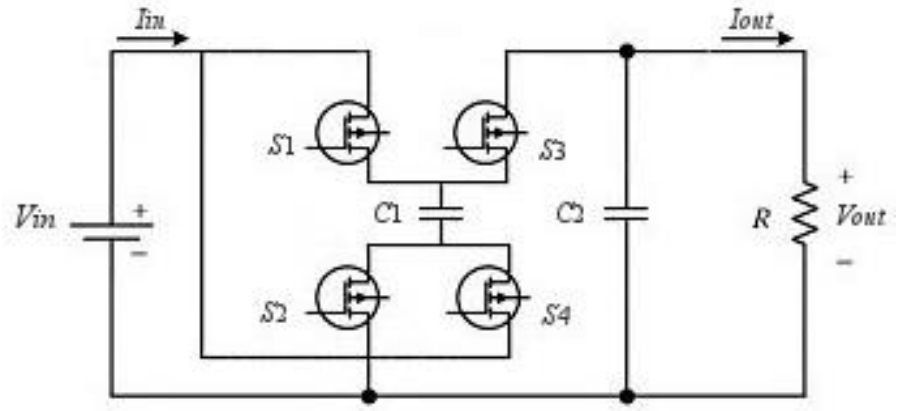

[145]

Figure A3.6.3 – Basic Capacitive DC-DC Stepping Circuit (Charge Pump)

Capacitor C_1 is charged in parallel with input voltage V_{in} (MOSFETs S_1 and S_2 ON-state), and discharged in series (MOSFETs S3 and S4 ON-state) to step up voltage out, V_{out}. V_{out} can reach approx two times V_{in}, and current out I_{out} is half of current in I_{in}.

Appendix A3.7 – Optimisation of Conventional DC-DC Converter

A3.7.1 Inductor

Five inductor ratings were tested with two 100 and 220 µH inductors placed singly or in series/parallel configurations. The inductors were toroidal with insulated copper coil wound over an iron core. Tests were of L = 50, 100, 200, 220 and 440 µH at a range of power levels and step-up values. The inductance value determines the rate at which the coil resists the change of current (from a change of voltage across it, either from an external source or its own magnetically inducted emf). Inductor losses were understood to be from ohmic loss and reactance (X_L, due to the switched mode operation), forming the ESR. X_L is a ratio of the amount of self-induced emf that opposes any change in current (this emf is what provides the step-up of V). X_L remains constant at fixed f and D. Changing D allows X_L to change, which in turn allows a higher or lower V_L for the I_L value [373]. The larger inductor was of higher power rating and was preferable. At very low D values, the two 100 µH in parallel (L = 50 µH) performed well, but conversely they were the worst-performing at high D. This was

due to the relatively high conductance but low inductance. Choice of inductor would ideally be made following investigation of the typical circuit operating conditions. Two 220 µH inductors in series (440 µH) was determined optimal for this circuit for the WT-ES operating ranges. A single 440 µH (or larger) inductor of better quality (e.g. thicker copper wire) would further improve performance. Test data is shown in Figure A3.7.1. There are endless test conditions concerning V_{In}, V_{Out} and I_{In}, I_{Out}, so a fixed input was maintained and variable D applied (with variable load) for comparative tests. Data at lower I give higher η_{Conv} (less I^2R losses). Since the diode had a voltage drop of 0.3 V, for data without SR η_{Conv} is further decreased at low V. Losses increase with increased D mainly due to increasing loss through the MOSFET circuit. The magnitude of stepping for a certain D also depends upon I. At low I the step-up is greater.

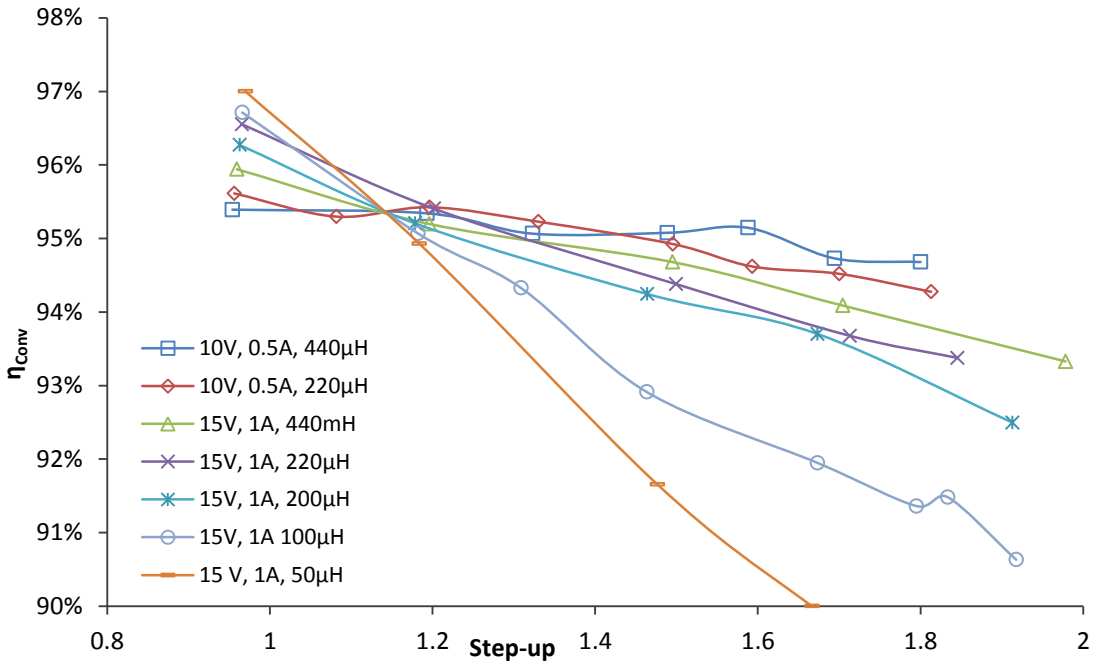

Figure A3.7.1 – Inductor Rating Experimental Test Data
Data for power conversion efficiency (η_{Conv}) by voltage step-up factor is shown for various inductor ratings (50-440 µH). Larger inductance aids larger step-up, but typically reduces η_{Conv} in lower step-up ranges (due to larger ESR).

A3.7.2 Frequency

The Arduino is a 1 kHz chipset but can be modified to produce PWM signals of 3.9, 7.8 31.3 and 62.5 kHz. A square wave signal generator (of similar current rating) was initially used to investigate the effects of f on η_{Conv}. Example data is shown in Figure A3.7.2 (at V_{GS} = 5 V, 10 V), indicating the optimum for the particular configuration

occurring at $f \approx 15$ kHz. The closest f value available from the Arduino was 7.8 kHz (a 5 V), although 7.8 or 31.3 kHz were both considered optimal. 7.8 kHz was used for ongoing tests (although requiring a further check due to the slightly different maximum current delivery from the signal generator and Arduino, affecting η_{Conv}). V_{GS} = 10 V is shown to be preferable in the data, as this moves the MOSFET through the relatively high R_{DS} region more quickly. As a result, 10 V favours slightly higher f (20-25 kHz) and also produces higher η_{Conv}.

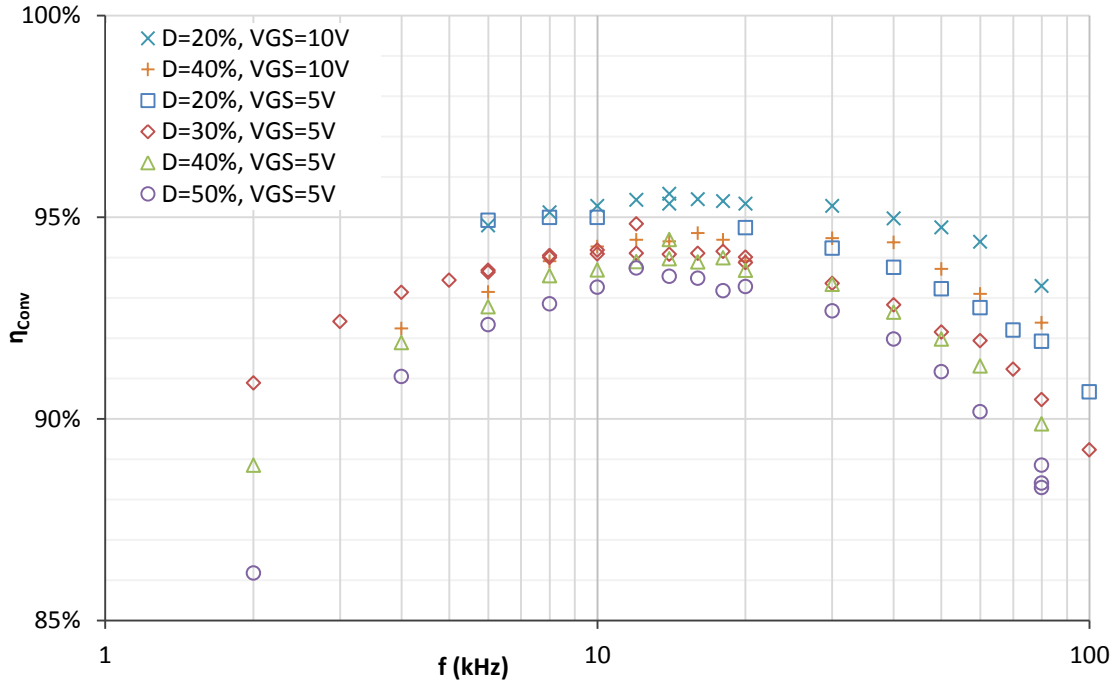

Figure A3.7.2 – PWM Signal Frequency Tests
η_{Conv} was investigated at PWM frequencies of 2-100 kHz. Max η_{Conv} was found at $f \approx 15$ kHz. Later work using the Arduino was set at 7.8 kHz (closest available frequency).

A3.7.3 Capacitor

Capacitance was formed with electrolytic capacitors (220 µF) and ceramic capacitors (2.2 µF). Test data for varying capacitance (electrolytic) and for various V_{In} and I_{In} conditions are shown in Figure A3.7.3. Electrolytic capacitors of 10, 22 and 47 and 100 µF and series capacitor configurations were tested (to obtain smaller C values). There was little difference in η_{Conv} apparent when C > 220 µF except at high I_{In} ranges. The regions < 220 µF are shown dashed. The final controller was set-up with four parallel 220 µF capacitors and six ceramic 2.2 µF capacitors to maintain practicality and to minimise ESR from the capacitive part of the circuit. Testing was carried out with the ES and a purely resistive load (labelled as ES and R in the legend of Figure A3.7.3). Data

indicated effective capacitance ≈ 5 µF in the ES (resulting from its electrode plates). This was apparent due to offset of approx. 5 µF in the η_{Conv} data for the ES and R loads (for example, the ES data remained above 85% when C = 0). Measurement of ES capacitance is quite complicated due to electrolyte concentration gradient across multiple cells, and V_{ES} etc (since H_2 formation will commence when V_{EC} > 1.5). Reactive power at the ES was checked and determined negligible. Work to investigate voltage or current ripple was not essential here due to the nature of the load. Selection of L and C rating can also be dealt with theoretically, described elsewhere in various application reports [373] [374], although physical testing is more applicable to this work due to component tolerances and other practical factors. For example, the minimal value of L to achieve a specific inductor current ripple (ΔI_L) can be calculated mathematically by considering f and the range of V and I [373]:

$$L = \frac{V_{Out}(V_{In} - V_{Out})}{\Delta I_L f V_{In}} \qquad \text{Eq A3.7.1}$$

ΔI_L can be estimated from [374]:

$$\Delta I_L \approx 0.3\, I_{Out} \qquad \text{Eq A3.7.2}$$

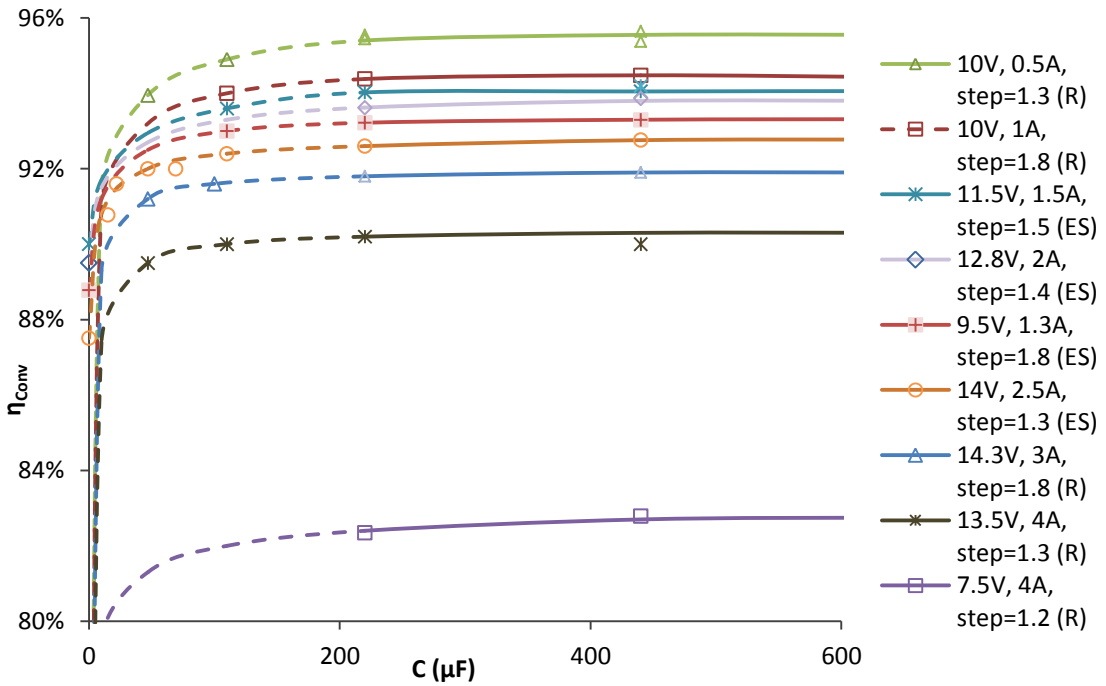

Figure A3.7.3 – Capacitor Rating Tests

Varying capacitance was tested to determine the optimal (minimum) rating. Data < 220 µF are shown dashed. R and ES refer to testing with resistive or ES circuit loading.

A3.7.4 Diode

Diode voltage drops were investigated in a test circuit and also in the DC-DC converter by oscilloscope. The final circuit used five Schottky diodes (10 A rating) in parallel for minimum voltage drop, representing similar performance to one larger/higher quality diode. Use of one superior diode would be preferred to prevent thermal runaway. This occurs due to diodes becoming better conductors with increasing T, which would occur with increased I, so there is then possibility of one diode heating faster and taking more current, with then further increase of T, and so on, with the thermal runaway leading to lowered performance and possible damage. Experimental work was below 10 A. Diode and synchronous MOSFET voltage drop data is shown in Figure A3.7.4. Voltage drop with five diodes was approx. 0.3-0.4 V within experimental ranges. Further parallel diodes would not give significant improvement. The MOSFET is far superior within this range (< 0.16 V) and for this reason an SR circuit was set-up.

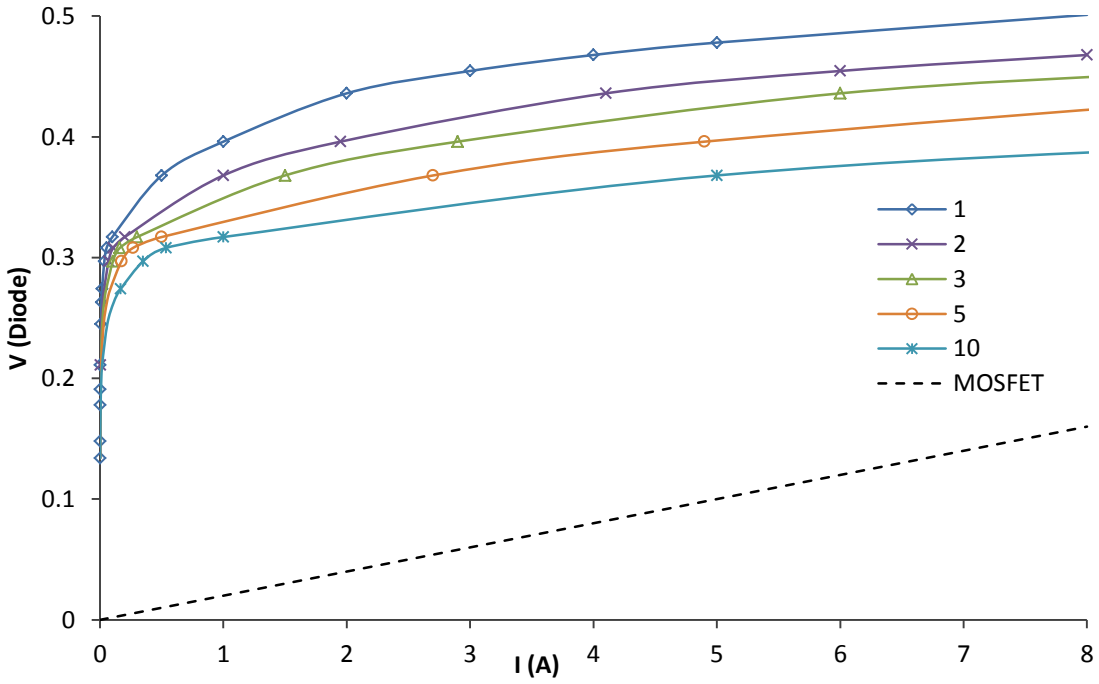

Figure A3.7.4 – Diode Voltage Drop Tests (Forward Bias)
1-10 Schottky diodes were tested for voltage drop at varying currents. A MOSFET is shown for comparison, highlighting the benefits of synchronous rectification.

A3.7.5 MOSFET (Switching and Synchronous Rectification)

MOSFETs of the lowest R_{DS} rating (at V_{GS} = 5 V) and highest quality available to this work were used. These were Fairchild FQP85N06 N-Channel MOSFETs (85 A I_{DS}, 60 V

V_{DS} ratings, with V_{GS} trends shown in Subchapter 3.4 (Figure 3.4.1). Their V_{DS} rating had to be above the levels expected (i.e. > 20 V). It was discovered that a circuit fault or disconnection of the ES would result in very high output voltages occurring momentarily in the circuit, potentially damaging the MOSFET. Highest V_{DS} rating was sought to prevent this, which naturally resulted in high I_{DS} rating. V_{GS} of 5 V had to allow full ON-state although it was more practical for this to be achieved at V_{GS} < 4 V. Several MOSFETs were tested and that with the lowest R_{DS} resulted in the highest η_{Conv}. Each had a different C_{GS} and required different PWM frequency for optimised use in these circuits (dependent on the maximum current delivery from the PWM signal). Characteristics were measured by oscilloscope, specifically the V_{GS} trend, to determine rise and fall times to assist with work to incorporate SR MOSFET.

The switching MOSFET was operated directly from the Arduino (5 V). The SR MOSFET PWM voltage signal was pulled-up to suitable levels (such that V_{GS} > V_{Out}) with an external power supply, operating through a line driver chip (Texas Instruments SN7407N). The power supply was regulated suitably through a resistor (approx. 0.2-1.0 kΩ). The pull-up circuit is shown in Figure A3.7.5. In a commercial DC-DC converter a higher voltage PWM would simply be used rather than a pull-up/line driver, which was not however possible in this experimental work.

Use of a SR MOSFET and line driver/pull-up circuit produced a slight inexact matching of the SR MOSFET function in terms of the rise/fall times, becoming out of synchronisation with the switching MOSFET. With exact synchronisation of the PWM signals, the rising MOSFET would not reach ON-state until after the falling MOSFET would reach OFF-state. This was due to the OFF-state being initiated by effectively grounding the gate pin (no current limit), whereas ON-state is reached by delivery of current from the PWM signal (limited to 40 mA in the case of the Arduino and line driver circuits). Failure to correctly observe these ON-/OFF-state timings could result in short-circuit or open circuit conditions. To avoid this, the PWM signals were offset by a small delay allowing the SR MOSFET to come fully OFF-state before the switching MOSFET reached ON-state.

Similarly, the switching MOSFET needed to come fully OFF-state before the SR MOSFET came fully ON-state. This was achieved by programming the controller to reduce D_{SR}.

This effectively advanced the OFF-state timing for the SR MOSFET (where the units of D_{SR} were equal to 1/(7800×255) seconds, considering f = 6.8 kHz and resolution = 255). The other delay conveniently occurred within this circuit due to the slight delayed response of the line driver circuit, slowing the ON-state of the SR MOSFET in comparison to the switching MOSFET.

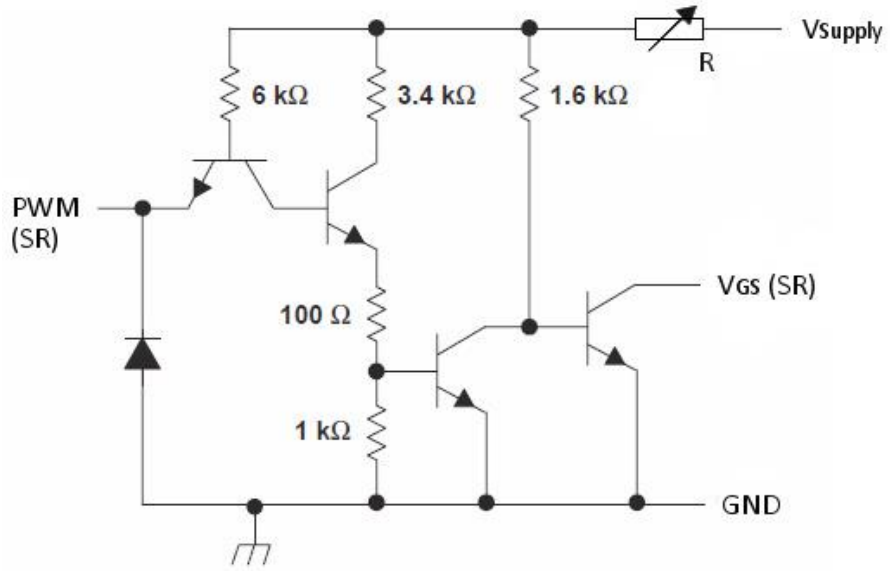

Figure A3.7.5 – Line Driver Circuit for V_{GS} Pull-up

The Arduino SR PWM signal (5 V) was pulled-up using a line driver circuit so that V_{GS} > V_{Out} to permit correct operation. This circuit was mounted on the DC-DC converter as a separate module and powered by a variable (25 V) external power supply in this work. A variable resistor was used to regulate the pull-up voltage and current to avoid damage to the line driver. This circuit was purely to assist the Arduino providing sufficient SR PWM voltage, representing a more suitable controller with 20 V PWM etc.

General circuit optimisation was achieved with heavy copper tracks and thick wiring. Wire length and connections were kept minimal. These were considered a suitable match for the test range. Earlier WT test work (Figure 5.1.11) indicated V_{MPP} ≈ 5-18 V within this range. Similarly, ES test work (e.g. Figure 2.2.8) indicated V_{Cell} ≈ 1.9-2.3 V. For eight cells this would be approx. 15-18 V. The DC-DC converter would therefore not require step down, operating with a step-up magnitude between one and three.

Appendix A3.8 – MOSFET Testing with RC Circuits

MOSFET test data with variable RC circuit components are shown in this appendix.

OFF- to ON-state (0-5000 mV V_{GS}):

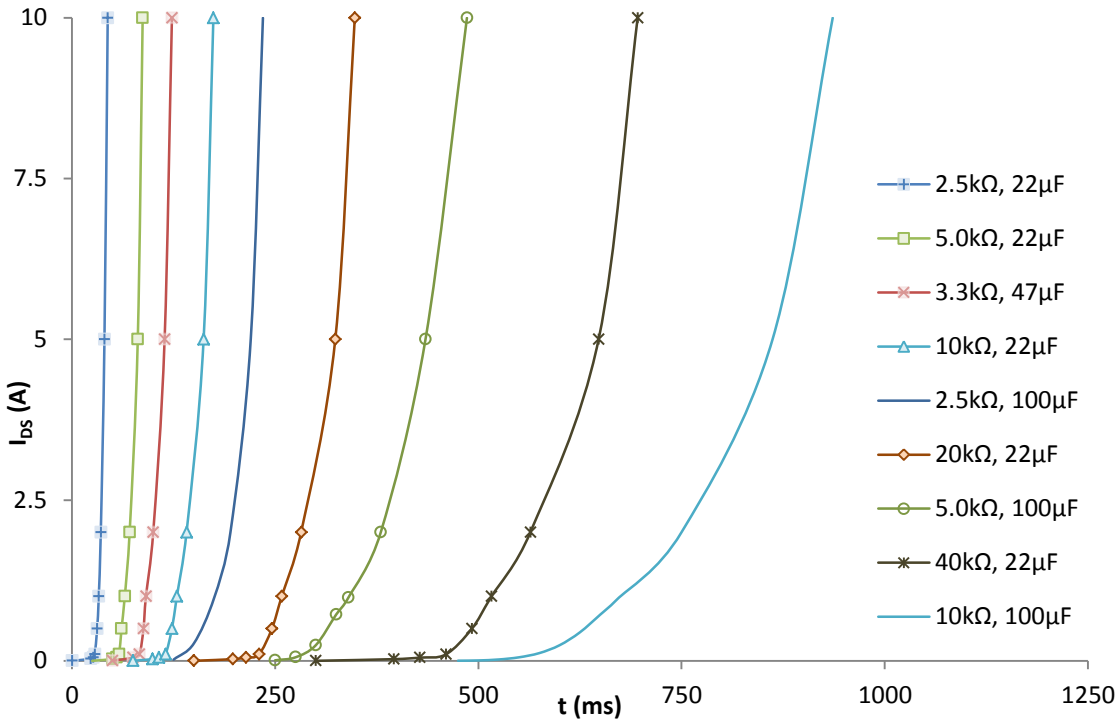

ON- to OFF-state (5000-0 mV V_{GS}):

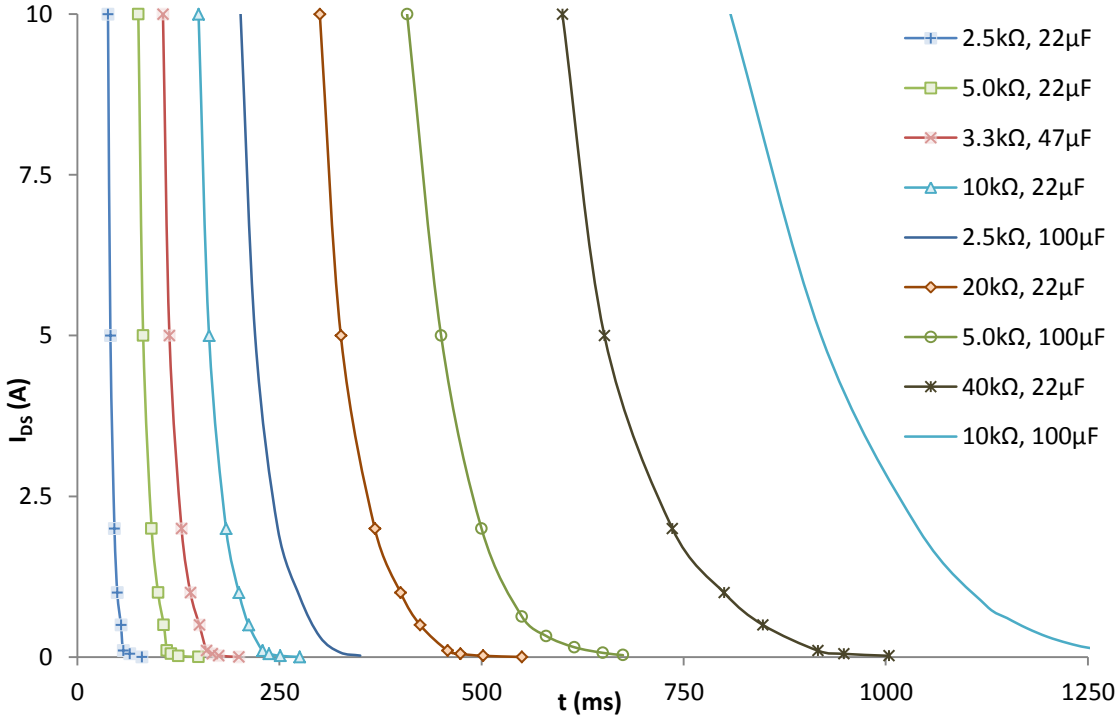

Figure A3.8.1 – MOSFET Switching Rate Testing (I_{DS} trends)

I_{DS} levels over time from change of state are shown for various RC circuit components.

OFF- to ON-state (0-5000 mV V_{GS}):

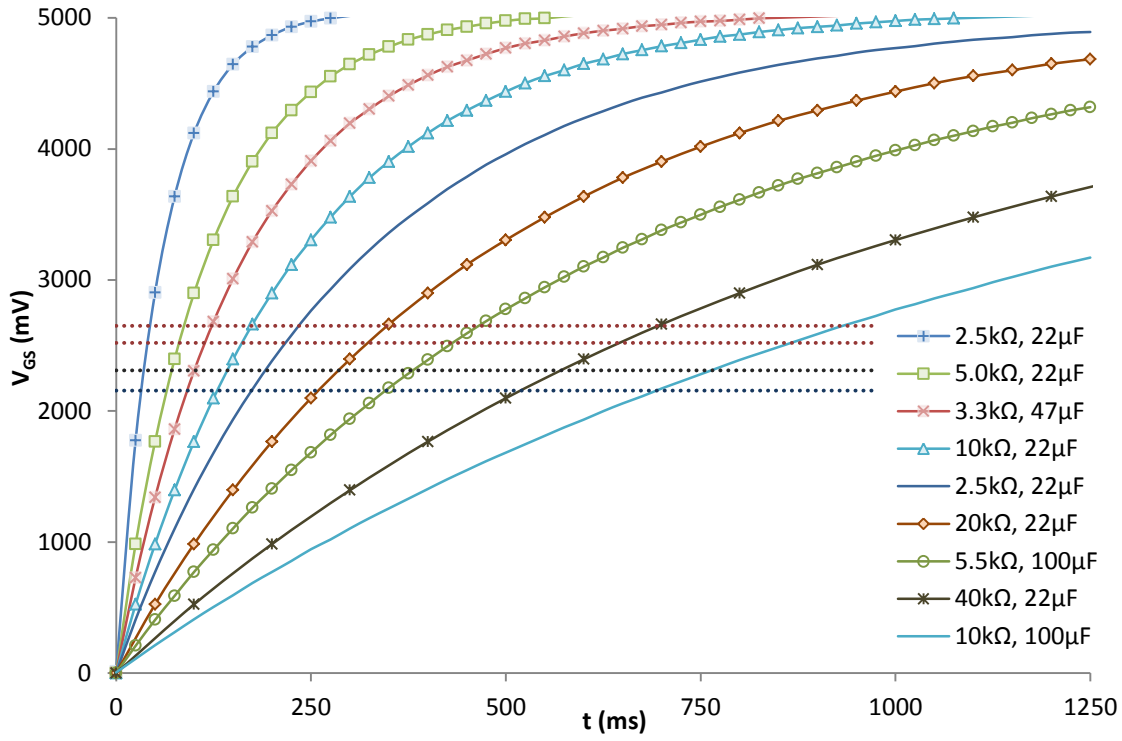

ON- to OFF-state (5000-0 mV V_{GS}):

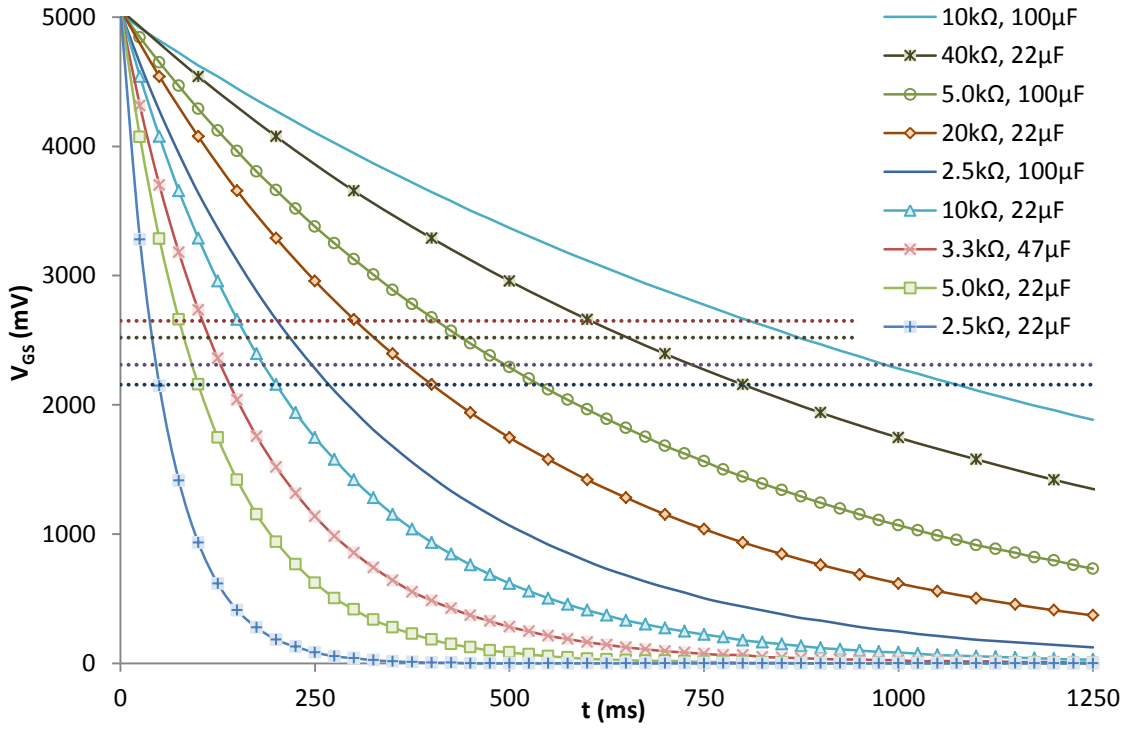

Figure A3.8.2 – MOSFET Switching Rate Testing (V_{GS} trends)

V_{GS} levels over time from change of state are shown for various RC circuit components. Horizontal lines represent V_{GS} reaching levels to permit 1, 2, 5 and 10 A I_{DS}.

Appendix A4.1 – E. coli Growth Experimental Work

This appendix contains supplementary material to support discussion within Chapter 4 of the main body.

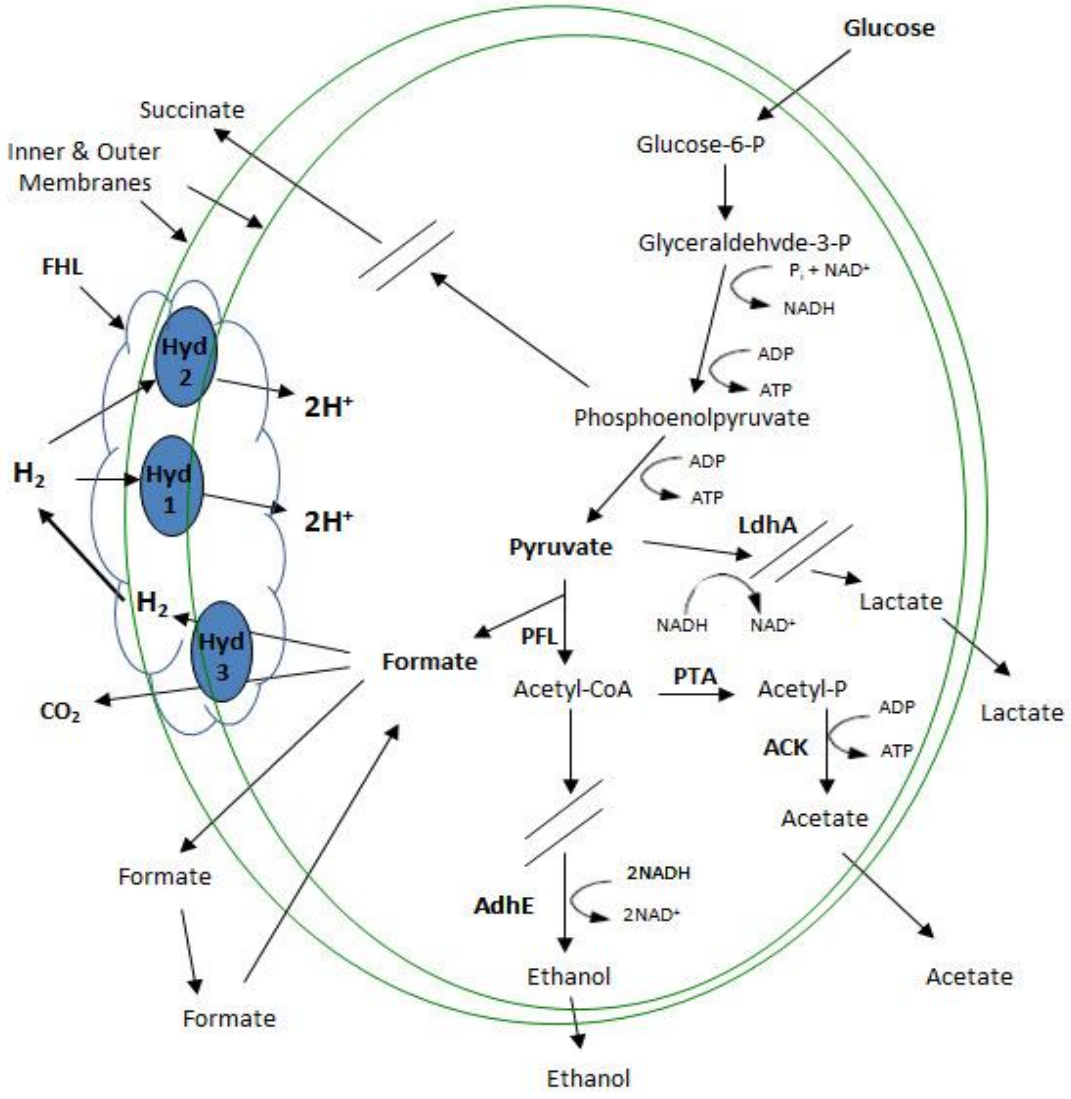

[172]

Figure A4.1.1 – Graphical Layout of Metabolic Activity in E. coli

Metabolic pathways in E. coli have been mapped in various other works. Several pathways are shown. The H_2 pathway relies on formate and requires ethanol production, but competes with succinate, acetate and lactate. H_2 production critically relies on the Hyd 3 enzyme within the formate hydrogenlyase complex. Work has been carried out in FSG to successfully eliminate competing pathways as shown by diagonal lines above. The effects of removing the ethanol pathway was also removed to investigate the effects

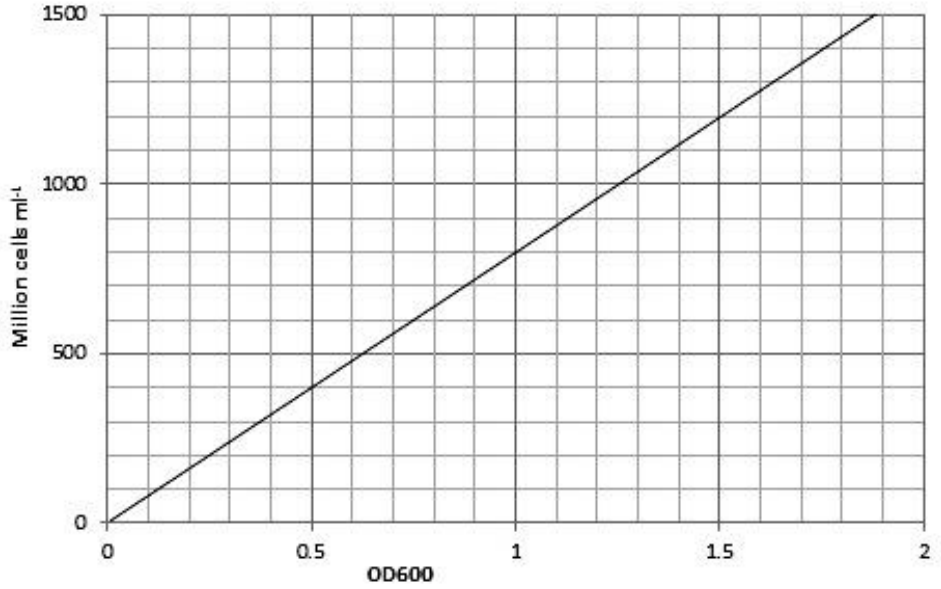

[162] [178]

Figure A4.1.2 – Population-OD_{600} Conversion Graph
Approximate E. coli population from OD_{600} reading.

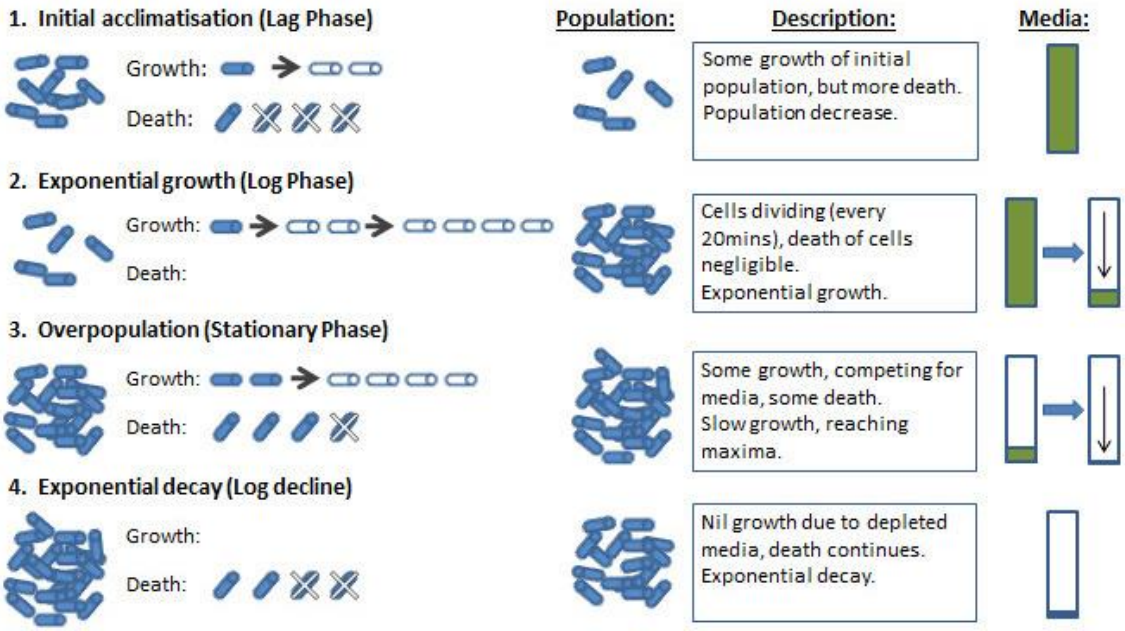

Figure A4.1.3 – E. coli population Growth/Decline during Fermentation
A simple schematic shows the E. coli growth and decline stages, population and media consumption as observed in this work.

References

[1] F H Cocks, *Energy Demand and Climate Change: Issues and Resolutions*, Wiley (2011) 3527644598

[2] T M Letcher, *Change In Future Energy (2nd Ed), Ch 1 - Introduction with a Focus on Atmospheric Carbon Dioxide and Climate*, p3-16, Elsevier (2014) 9780080994246

[3] *L M Gandia, G Arzamendi, P M Dieguez, Renewable Hydrogen Energy: An Overview, in Renewable Hydrogen Technologies (Production, Purification, Storage, Applications and Safety), Ch1 Renewable Hydrogen Energy*. Elsevier, 2013

[4] R S Dhillon, G von Wuehlisch, *Mitigation of global warming through renewable biomass*, Biomass and Bioenergy 48 (2013) 75–89

[5] M H McCay, *Future Energy Improved: Sustainable and Clean Options for our Planet*, 2014, 23 495-510

[6] International Energy Agency, *World Energy Outlook 2011: Executive Summary*; OECD/IEA: Paris, 2011.

[7] *IPCC. Climate change 2001: impacts, adaptation and vulnerability*. *Report of the working group II*. Cambridge University Press (2001) 967.

[8] *IPCC. Climate change 2007. Impacts, adaptation and vulnerability, Summary for policymakers and technical summary, WG II contribution to the AR4*. Cambridge University Press (2007) 93

[9] T F Stocker et al, *IPCC Climate Change 2013: The Physical Science Basis. Working Group 1 (WG1) Contribution to the Intergovernmental Panel on Climate Change (IPCC) 5th Assessment Report* (AR5), Cambridge University Press (2013)

[10] S Dunn, *Hydrogen futures: toward a sustainable energy system*, International Journal of Hydrogen Energy 27 (2002) 235-264

[11] G Marbán, T Valdés-Solís, *Towards the Hydrogen Economy?*, International Journal of Hydrogen Energy 32 (2007) 1625-1637

[12] P Moriarty, D Honnery, *Hydrogen's role in an uncertain energy future*, International Journal of Hydrogen Energy 34 (2009) 31-39

[13] K Mazloomi, C Gomes, *Hydrogen as an energy carrier: Prospects and challenges*, Renewable and Sustainable Energy Reviews 16 (2012) 3024-3033

[14] D K Ross, *Hydrogen storage: The major technological barrier to the development of hydrogen fuel cell cars*, Vacuum 80 (2006) 1084-1089

[15] M Balat, *Potential Importance of Hydrogen as a Future Solution to Environmental and Transportation Problems*, International Journal of Hydrogen Energy 33 (2008) 4013-4029

[16] M Granovskii, I Dincer, M A Rosen, *Life cycle assessment of hydrogen fuel cell and gasoline vehicles*, International Journal of Hydrogen Energy 31 (2006) 337-352

[17] P Moriarty, D Honnery, *Intermittent renewable energy: The only future source of hydrogen?*, International Journal of Hydrogen Energy 32 (2007) 1616-1624

[18] O Bičáková, P Straka, *Production of hydrogen from renewable resources and its effectiveness*, International Journal of Hydrogen Energy 38 (2012) 11563-11578

[19] H H Gunardson, *Industrial Gases in Petrochemical Processing: Chemical Industries*, CRC Press (1997) 1420001159

[20] T Ohta, *Solar-Hydrogen Energy Systems (An Authoritative Review of Water-Splitting Systems by Solar Beam and Solar Heat: Hydrogen Production, Storage and Utilisation)*, Elsevier (1979), Ch 2, 25-33, 978000227139

[21] W M Haynes, *CRC Handbook of Chemistry and Physics*, 95th Ed, CRC (2014) 1482208679

[22] S Ahmed, A Aitani, F Rahman, A Al-Dawood, F Al-Muhaish, *Decomposition of hydrocarbons to hydrogen and carbon*, Applied Catalysis A: General 359 (2009) 1-24

[23] M Dan, L Senila, M Roman, M Mihet, M D Lazar, *From wood wastes to hydrogen – Preparation and catalytic steam reforming of crude bio-ethanol obtained from fir wood*, Renewable Energy 74 (2015) 27-36

[24] T Keskin, P C Hallenbeck, *Hydrogen production from sugar industry wastes using single-stage photofermentation*, Bioresource Technology 112 (2012) 131-136

[25] M Balat, M Balat, *Political, economic and environmental impacts of biomass-based hydrogen*, International Journal of Hydrogen Energy 34 (2009) 3589-3603

[26] P W Atkins, *The Elements of Physical Chemistry*, 3rd Ed, p31-33, 47-53, 66-74, 78-92, 158, 234, Oxford (2001) 0198792905

[27] R O'Hayre, S Cha, W Colella, F Prinz, *Fuel Cell Fundamentals*, Wiley (2009), 9780470258439

[28] J Bockris, *The hydrogen economy: Its history*, International Journal of Hydrogen Energy 38 (2013) 2579-2588

[29] L Emami-Taba, M F Irfan, W M A Wan Daud, M H Chakrabarti, *The effect of temperature on various parameters in coal, biomass and CO-gasification: A review*, Renewable and Sustainable Energy Reviews 16 (2012) 5584-5596

[30] J W Kim, K J Boo, J H Cho, I Moon, *Key challenges in the development of an infrastructure for hydrogen production, delivery, storage and use*, In Advances in Hydrogen Production, Storage and Distribution, Ch1, Woodhead Publishing (2014), 3-31, 9780857097682

[31] L Barreto, A Makihiraa, K Riahia, *The hydrogen economy in the 21st century: a sustainable development scenario*, International Journal of Hydrogen Energy 28 (2003) 267-284

[32] R Elder, R Allen, *Nuclear heat for hydrogen production: Coupling a very high/high temperature reactor to a hydrogen production plant*, Progress in Nuclear Energy 51 (2009) 500-525

[33] J D Holladay, J Hu, D L King, Y. Wang, *An overview of hydrogen production technologies*, Catalysis Today 139 (2009) 244-260

[34] R G Lemus, J M M Duart, *Updated hydrogen production costs and parities for conventional and renewable technologies*, International Journal of Hydrogen Energy 35 (2010) 3929-3936

[35] R Kothari, D Buddhi, R L Sawhney, *Comparison of environmental and economic aspects of various hydrogen production methods*, Renewable and Sustainable Energy Reviews 12 (2008) 553-563

[36] R Soltani, M A Rosen, I Dincer, *Assessment of CO2 capture options from various points in steam methane reforming for hydrogen production*, International Journal of Hydrogen Energy (2014)

[37] N Hajjaji, M-N Pons, A Houas, V Renaudin, *Exergy analysis: An efficient tool for understanding and improving hydrogen production via the steam methane reforming process*, Energy Policy 42 (2012) 392-399

[38] K C Mondal, S Ramesh Chandran, *Evaluation of the economic impact of hydrogen production by methane decomposition with steam reforming of methane process*, International Journal of Hydrogen Energy 39 (2014) 9670-9674

[39] A V Da Rosa, *Fundamentals of Renewable Energy Processes*, 3rd Ed, Academic Press (2012), 0123972191

[40] A Giaconia, *10 - Thermochemical production of hydrogen,* In Advances in Hydrogen Production, Storage and Distribution, Woodhead (2014) 263-280, 9780857097682

[41] D Fino, *4 - Hydrogen production in conventional, bio-based and nuclear power plants, In Advances in Hydrogen Production, Storage and Distribution*, Woodhead (2014) 85-122, 9780857097682

[42] E Simsek, M Karakaya, A K Avci, Z Ilsen Onsan, *Oxidative steam reforming of methane to synthesis gas in microchannel reactors*, International Journal of Hydrogen Energy 38 (2013) 870-878

[43] A Iulianelli, P Ribeirinha, A Mendes, A Basile, *Methanol steam reforming for hydrogen generation via conventional and membrane reactors: A review*, Renewable and Sustainable Energy Reviews 29 (2014) 355-368

[44] A C W Koh, L Chen, W Kee Leong, B F G Johnson, T Khimyak, J Lin, *Hydrogen or synthesis gas production via the partial oxidation of methane over supported nickel–cobalt catalysts*, International Journal of Hydrogen Energy 32 (2007) 725-730

[45] D Mori, K Hirose, *Recent challenges of hydrogen storage technologies for fuel cell vehicles*, International Journal of Hydrogen Energy 34 (2009) 4569-4574

[46] D J Durbin, C Malardier-Jugroot, *Review of hydrogen storage techniques for on board vehicle applications*, International Journal of Hydrogen Energy 38 (2013) 14595-14617

[47] A Lappas, E Heracleous, *Production of biofuels via Fischer-Tropsch synthesis: biomass-to-liquids*, *Ch 19*, in Handbook of Biofuels Production, Woodhead (2011), 493-529, 9781845696795

[48] S W Jorgensen, *Hydrogen storage tanks for vehicles: Recent progress and current status*, Current Opinion in Solid State and Materials Science 15 (2011) 39-43

[49] D Pukazhselvan, Vinod Kumar, S.K. Singh, *High capacity hydrogen storage: Basic aspects, new developments and milestones*, Nano Energy (2012) 1, 566–589

[50] Z Guo, C Shang, K Aguey-Zinsou, *Materials Challenges for Hydrogen Storage*, Journal of the European Ceramic Society, 28 (2008) 1467-1473

[51] http://energy.gov/sites/prod/files/2014/03/f12/targets_onboard_hydro_storage.pdf, accessed Jan 2015

[52] M P de Wit, A P C Faaij, *Impact of hydrogen onboard storage technologies on the performance of hydrogen fuelled vehicles: A techno-economic well-to-wheel assessment*, International Journal of Hydrogen Energy 32 (2007) 4859-4870

[53] G Mulder, J Hetland, G Lenaers, *Towards a sustainable hydrogen economy: Hydrogen pathways and infrastructure*, International Journal of Hydrogen Energy 32 (2007) 1324-1331

[54] P Agnolucci, W McDowall, *Designing future hydrogen infrastructure: Insights from analysis at different spatial scales*, International Journal of Hydrogen Energy 38 (2013) 5181-5191

[55] S Litster, G McLean, *PEM fuel cell electrodes*, Journal of Power Sources 130 (2004) 61-76

[56] http://www.itm-power.com/news-item/injection-of-hydrogen-into-the-german-gas-distribution-grid, accessed December 2014

[57] http://www.nrel.gov/docs/fy13osti/51995.pdf, accessed December 2014

[58] T Hua et al, *Status of hydrogen fuel cell electric buses worldwide*, Journal of Power Sources 269 (2014) 975-993

[59] M Felgenhauer, Thomas Hamacher, *State-of-the-art of commercial electrolyzers and on-site hydrogen generation for logistic vehicles in South Carolina*, International Journal of Hydrogen Energy 40 (2015) 2084-2090

[60] S Verhelst, R Sierens, *Hydrogen engine-specific properties*, International Journal of Hydrogen Energy 26 (2001) 987-990

[61] S Verhelst, T Wallner, *Hydrogen-fueled internal combustion engines*, Progress in Energy and Combustion Science 35 (2009) 490-527

[62] H Fayaz, R Saidur, N Razali, F S Anuar, A R Saleman, M R Islam, *An overview of hydrogen as a vehicle fuel*, Renewable and Sustainable Energy Reviews 16 (2012) 5511-5528

[63] T Smolinka, E T Ojong, J Garche, *Ch 8 - Hydrogen Production from Renewable Energies-Electrolyzer Technologies*, In Electrochemical Energy Storage for Renewable Sources and Grid Balancing, Elsevier Amsterdam (2015), 103-128, 9780444626165

[64] A Ursúa, L M Gandía, and P Sanchis, *Hydrogen Production From Water Electrolysis: Current Status and Future Trends*, Proceedings of the IEEE (2012) 100 2;410-426

[65] H Zhang, G Lin, J Chen, *Evaluation and calculation on the efficiency of a water electrolysis system for hydrogen production*, International Journal of Hydrogen Energy 35 (2010) 10851-10858

[66] O Atlam, M Kolhe, *Equivalent electrical model for a proton exchange membrane (PEM) electrolyser*, Energy Conversion and Management 52 (2011) 295-2957

[67] K Zeng, D Zhang, *Recent progress in alkaline water electrolysis for hydrogen production and applications*, Progress in Energy and Combustion Science 36 (2010) 307-326

[68] M Carmo, D L Fritz, J Mergel, D Stolten, *A comprehensive review on PEM water electrolysis*, International Journal of Hydrogen Energy 38 (2013) 4901-4934

[69] S K Mazloomi, N Sulaiman, *Influencing factors of water electrolysis electrical efficiency*, Renewable and Sustainable Energy Reviews 16 (2012) 4257-4263

[70] S Peighambardoust, S Rowshanzamir, M Amjadi, *Review of the proton exchange membranes for fuel cell applications*, International Journal of Hydrogen Energy 35 (2010) 9349-9384

[71] A Buttler, R Koltun, R Wolf, H Spliethoff, *A detailed techno-economic analysis of heat integration in high temperature electrolysis for efficient hydrogen production*, International Journal of Hydrogen Energy 40 (2015) 38-50

[72] P Millet, S Grigoriev, *Chapter 2 - Water Electrolysis Technologies*, In Renewable Hydrogen Technologies, Elsevier Amsterdam (2013), 19-41, 9780444563521

[73] N A Kelly, *Ch 6 - Hydrogen production by water electrolysis*, In Advances in Hydrogen Production, Storage and Distribution, Woodhead Publishing (2014), 159-185, 9780857097682

[74] Jianlu Zhang, H Zhang, J Wu, Jiujun Zhang, *Ch 6 - Hydrogen Crossover*, In PEM Fuel Cell Testing and Diagnosis, Elsevier Amsterdam (2013), 171-185, 9780444536884

[75] S A Grigoriev, P Millet, S A Volobuev, V N Fateev, *Optimization of porous current collectors for PEM water electrolysers*, International Journal of Hydrogen Energy 34 (2009) 4968-4973

[76] E Slavcheva , I Radev, S Bliznakov, G Topalov, P Andreev, E Budevski, *Sputtered iridium oxide films as electrocatalysts for water splitting via PEM electrolysis*, Electrochimica Acta 52 (2007) 3889-3894

[77] S Marini, P Salvi, P Nelli, R Pesenti, M Villa, M Berrettoni, G Zangari, Y Kiros, *Advanced alkaline water electrolysis*, Electrochimica Acta 82 (2012) 384-391

[78] A Minguzzi, F-R Fan, A Vertova, S Rondinini, A J Bard, *Dynamic potential-pH diagrams application to electrocatalysts for water oxidation*, Journal of Chemical Science (2012) 3;217

[79] R G Compton, C E Banks, *Understanding Voltammetry*, World Scientific (2011), 53-55, 1848165862

[80] Jianlu Zhang, H Zhang, J Wu, Jiujun Zhang, *Ch 5 - Membrane/Ionomer Proton Conductivity Measurements*, In PEM Fuel Cell Testing and Diagnosis, Elsevier Amsterdam (2013), 143-170, 9780444536884

[81] M Shen, N Bennett, Y Ding, K Scott, *A concise model for evaluating water electrolysis*, International Journal of Hydrogen Energy 36 (2011) 14335-14341

[82] Z Dülger, K R Özçelìk, *Fuel economy improvement by on board electrolytic hydrogen production*, International Journal of Hydrogen Energy 25 (2000) 895-897

[83] A C Yilmaz, E Uludamar, K Aydin, *Effect of hydroxy (HHO) gas addition on performance and exhaust emissions in compression ignition engines*, International Journal of Hydrogen Energy 35 (2010) 11366-11372

[84] N Nagaia, M Takeuchia, T Kimurab, T Oka, *Existence of optimum space between electrodes on hydrogen production by water electrolysis*, International Journal of Hydrogen Energy 28 (2003) 35-41

[85] F Allebrod, C Chatzichristodoulou, P L Mollerup, M B Mogensen, *Electrical conductivity measurements of aqueous and immobilized potassium hydroxide*, International Journal of Hydrogen Energy 37 (2012) 16505-16514

[86] O Edenhofer et al, *Renewable Energy Sources and Climate Change Mitigation: Special Report of the Intergovernmental Panel on Climate Change*, Cambridge University Press (2011) 1139505599

[87] Renewables 2014 Global Status Report, http://www.ren21.net/ren21activities/globalstatusreport.aspx, accessed March 2015

[88] B Sørensen, *Origin of Renewable Energy Flows, Chapter 2, In Renewable Energy, 4th Ed*, Academic Press, Boston (2011), p35-204, 9780123750259

[89] I López et al, *Review of wave energy technologies and the necessary power-equipment*, Renewable and Sustainable Energy Reviews 27 (2013) 413-434

[90] A Falcão, *Wave energy utilization: A review of the technologies*, Renewable and Sustainable Energy Reviews 14 (2010) 899–918

[91] M Ishak Yuce, A Muratoglu, Hydrokinetic energy conversion systems: A technology status review, Renewable and Sustainable Energy Reviews 43 (2015) 72-82

[92] S Rehman, L M Al-Hadhrami, M M Alam, *Pumped hydro energy storage system: A technological review*, Renewable and Sustainable Energy Reviews 44 (2015) 586-598

[93] R Shortall, B Davidsdottir, G Axelsson, *Geothermal energy for sustainable development: A review of sustainability impacts and assessment frameworks*, Renewable and Sustainable Energy Reviews 44 (2015) 391-406

[94] L Emami-Taba, M F Irfan, W M Ai Wan Daud, M H Chakrabarti, *Fuel blending effects on the co-gasification of coal and biomass - A review*, Biomass and Bioenergy 57 (2013) 249-263

[95] P Coker, J Barlow, T Cockerill, D Shipworth, *Measuring significant variability characteristics: An assessment of three UK renewables*, Renewable Energy 53 (2013) 111-120

[96] J U Aluya, O L Garraway, *Nanotechnology, Solar, Wind, and Hybrid Alternative Energy: Global Leadership Perspectives*, Author House (2010), 9781452004297

[97] Y-S Lee, M H L Chow, *Power Electronics Handbook (3rd Ed.)*, 149-181, Butterworth-Heinemann (2011), 9780123820365

[98] T Matsukawa, M Shioyama, K Shimada, T Takaku, C Neumeyer, S Tsuji-Iio, R Shimada, *Application of parallel connected power-MOSFET elements to high current d.c. power supply*, Fusion Engineering and Design 58–59 (2001) 63-67

[99] Datasheet for the Eclectic Energy D400 wind turbine - www.duogen.co.uk/ page21.html, accessed March 2015

[100] www.marlec.co.uk/products/windchargers, accessed March 2015

[101] www.forgenrenewables.com/buy-products/wind-turbines/vertical-axis, accessed March 2015

[102] M Narayana, G A Putrus, M Jovanovic, P S Leung, S McDonald, *Generic maximum power point tracking controller for small-scale wind turbines*, Renewable Energy 44 (2012) 72-79

[103] D Yogi Goswami, F Kreith, *Handbook of Energy Efficiency and Renewable Energy*, p17/14, CRC Press (2007), 1420003488

[104] E Hau, H von Renouard, *Wind Turbines: Fundamentals, Technologies, Application, Economics*, Springer Science & Business Media (2013), 3642271510

[105] S Eriksson, H Bernhoff, *Loss evaluation and design optimisation for direct driven permanent magnet synchronous generators for wind power*, Applied Energy 88 (2011) 265-271

[106] S A Rolland, M Thatcher, W Newton, A J Williams, T N Croft, D T Gethin, M Cross, *Benchmark experiments for simulations of a vertical axis wind turbine*, Applied Energy 111 (2013) 1183‑1194

[107] P J Schubel, R J Crossley, *Wind Turbine Blade Design*, Energies (2012) 5;3425-3449

[108] I Ross, A Altman, *Wind tunnel blockage corrections: Review and application to Savonius vertical-axis wind turbines*, Journal of Wind Engineering and Industrial. Aerodynamics 99 (2011) 523-538

[109] www.wunderground.com/personal-weather-station/dashboard?ID=IDUNDEE1, accessed various

[110] V Quaschning, *Understanding Renewable Energy Systems*, Earthscan (2005), 1844071286

[111] N Z Muradova, T Nejat Veziroğlu, *''Green'' path from fossil-based to hydrogen economy: An overview of carbon-neutral technologies*, International Journal of Hydrogen Energy 33 (2008) 6804-6839

[112] M A Delucchi, M Z Jacobson, *Providing all global energy with wind, water, and solar power, Part II: Reliability, system and transmission costs, and policies*, Energy Policy 39 (2011) 1170-1190

[113] C L Benson, C L Magee, *On improvement rates for renewable energy technologies: Solar PV, wind turbines, capacitors, and batteries*, Renewable Energy 68 (2014) 745-751

[114] www.gov.uk/feed-in-tariffs/overview, accessed April 2015

[115] www.fitariffs.co.uk, accessed April 2015

[116] J A Baroudi, V Dinavahi, A M Knight, *A review of power converter topologies for wind generators*, Renewable Energy 32 (2007) 2369-2385

[117] M A Abdullah, A H M Yatim, C W Tan, R Saidur, *A review of maximum power point tracking algorithms for wind energy systems*, Renewable and Sustainable Energy Reviews 16 (2012) 3220-3227

[118] A Khalilnejad, G H Riahy, *A hybrid wind-PV system performance investigation for the purpose of maximum hydrogen production and storage using advanced alkaline electrolyzer*, Energy Conversion and Management 80 (2014) 398-406

[119] M E Sahin, H I Okumus, M T Aydemir, *Implementation of an electrolysis system with DC/DC synchronous buck converter*, International Journal of Hydrogen Energy 39 (2014) 6802-6812

[120] F Valenciaga, C A Evangelista, *Control design for an autonomous wind based hydrogen production system*, International Journal of Hydrogen Energy 35 (2010) 5799-5807

[121] M Korpa, C J Greiner, *Opportunities for hydrogen production in connection with wind power in weak grids*, Renewable Energy 33 (2008) 1199-1208

[122] J G García Clúa, R J Mantz, H De Battista, *Evaluation of hydrogen production capabilities of a grid-assisted wind-H2 system*, Applied Energy 88 (2011) 1857-1863

[123] E Koutroulis, K Kalaitzakis, *Design of a Maximum Power Tracking System for Wind-Energy-Conversion Applications*, IEEE Transactions on Industrial Electronics, 2006; 53(2):486-494

[124] M H Taghvaee, M A M Radzi, S M Moosavain, H Hizam, M Hamiruce Marhaban *A current and future study on non-isolated DC–DC converters for photovoltaic applications*, Renewable and Sustainable Energy Reviews 17 (2013) 216-227

[125] S Poshtkouhi, V Palaniappan, M Fard, O Trescases, *A General Approach for Quantifying the Benefit of Distributed Power Electronics for Fine Grained MPPT in Photovoltaic Applications Using 3-D Modeling*, IEEE Transactions On Power Electronics, 2012;27(11):4656-66.

[126] S Poshtkouhi, J Varley, R Popuri, O Trescases, *Analysis of Distributed Peak Power Tracking in Photovoltaic Systems*, IEEE International Power Electronics Conference (IPEC), 2010:942-947

[127] I Skaale, D J Pattersonb, H Pullen, *The development of a new maximum power point tracker for a very high efficiency, compound curve photovoltaic array for a solar powered vehicle*, Renewable Energy 22 (2001) 295-302

[128] R Kot , M Rolak, M Malinowski, *Comparison of maximum peak power tracking algorithms for a small wind turbine*, Mathematics and Computers in Simulation 91 (2013) 29-40

[129] S M Raza Kazmi, H Goto, H-J Guo, O Ichinokura, *Review and Critical Analysis of the Research Papers published till date on Maximum Power Point Tracking in Wind Energy Conversion System*, IEEE Energy Conversion Congress and Exposition (2010), 4075-4082

[130] I Kortabarria et al, *A novel adaptative maximum power point tracking algorithm for small wind turbines*, Renewable Energy 63 (2014) 785-796

[131] Q-N Trinh, H-H Lee, *Fuzzy Logic Controller for Maximum Power Tracking in PMSG-Based Wind Power Systems*, Advanced Intelligent Computing Theories and Applications. With Aspects of Artificial Intelligence. Lecture Notes in Computer Science 6216 (2010) 543-553

[132] S M Raza Kazmi, H Goto, H-J Gu, O Ichinokura, *A Novel Algorithm for Fast and Efficient Speed-Sensorless Maximum Power Point Tracking in Wind Energy Conversion Systems*, IEEE Transactions on Industrial Electronics (2011) 58 1;29-36

[133] A Reza Reisi, M Hassan Moradi , S Jamasb*, Classification and comparison of maximum power point tracking techniques for photovoltaic system: A review*, Renewable and Sustainable Energy Reviews 19 (2013) 433-443

[134] M A Eltawil, Z Zhao, *MPPT techniques for photovoltaic applications*, Renewable and Sustainable Energy Reviews 25 (2013) 793-813

[135] A Safari, S Mekhilef, *Incremental conductance MPPT method for PV systems*, IEEE 24th Canadian Conference on Electrical and Computer Engineering (CCECE) (2011), 345-347

[136] D Reddy Challa, I Raghavendar, *Implementation of Incremental Conductance MPPT with Direct Control Method Using Cuk Convertor*, International Journal of Modern Engineering Research 2 (2012) 6;4491-4496

[137] D Sera, L Mathe, T Kerekes, S V Spataru, R Teodorescu, *On the Perturb-and-Observe and Incremental Conductance MPPT Methods for PV Systems*, IEEE Journal of Photovoltaics 3, (2013) 1070-1078

[138] A G Moacyr et al, *Comparative Analysis of MPPT Techniques for PV Applications*, IEEE International Conference on Clean Electrical Power (ICCEP), 2011

[139] W-M Lin, C-M Hong, *Intelligent approach to maximum power point tracking control strategy for variable-speed wind turbine generation system*, Energy 35 (2010) 2440–2447

[140] J Brahmi, L Krichen, A Ouali, *A comparative study between three sensorless control strategies for PMSG in wind energy conversion system*, Applied Energy 86 (2009) 1565–1573

[141] M A Abdullah, A H M Yatim, C Wei Tan, *A Study of Maximum Power Point Tracking Algorithms for Wind Energy System*, IEEE Clean Energy and Technology (2011) 321–326

[142] R E Clarke, S Giddey, F T Ciacchi, S P S Badwal, B Paul, J Andrews, *Direct coupling of an electrolyser to a solar PV system for generating hydrogen*, International Journal of Hydrogen Energy 34 (2009) 2531-2542

[143] K Agbossou, S Kélouwani, A Anouar, M Kolhe, *Energy management of hydrogen-based stand-alone renewable energy system by using boost and buck converters*, IEEE Industry Applications Conference 4 (2004) 2786-2793

[144] V Samavatian, A Radan, *A novel low-ripple interleaved buck–boost converter with high efficiency and low oscillation for fuel-cell applications*, Electrical Power and Energy Systems 63 (2014) 446-454

[145] T V Breussegem, M Steyaert, *CMOS Integrated Capacitive DC-DC Converters*, Springer (2013) 121, 146144280X

[146] http://www.farnell.com/datasheets/1774698.pdf, accessed April 2015

[147] P Petit, M Aillerie, A Zegaoui, J-P Sawicki, J-P Charles, *Rdson behavior in various MOSFET families*, IEEE International Symposium on Industrial Electronics (ISIE) (2011), 353-357

[148] X Wu, Y Wang, Q Zeng, *Reliability of High Energy Density Ceramic Capacitors*, Procedia Engineering (2012) 45;998-1003

[149] P C Sen, *Power Electronics*, Tata McGraw-Hill Education (1987), 7-8, 0074624008

[150] B Choi, *Pulsewidth Modulated DC-to-DC Power Conversion: Circuits, Dynamics, and Control Designs* (IEEE), John Wiley & Sons (2013), 3-41-3-52

[151] http://www.atmel.com/images/doc8161.pdf - accessed June 2014

[152] http://docs-europe.electrocomponents.com/webdocs/1272/0900766b81272eb2.pdf - accessed June 2014

[153] T L Gibson, N A Kelly, *Predicting efficiency of solar powered hydrogen generation using photovoltaic-electrolysis devices*, International Journal of Hydrogen Energy 35 (2010) 900-911

[154] F Barbir, *PEM electrolysis for production of hydrogen from renewable energy sources*, Solar Energy 78 (2005) 661-669

[155] R García-Valverde, N Espinosa, A Urbina, *Optimized method for photovoltaic-water electrolyser direct coupling*, International Journal of Hydrogen Energy 36 (2011) 10574-10586

[156] P C Hallenbeck, M Abo-Hashesh, D Ghosh, *Strategies for improving biological hydrogen production*, Bioresource Technology 110 (2012) 1-9

[157] A Pandey, J-S Chang, P Hallenbeck, C Larroche, *Biohydrogen*, Newnes (2013), 111-115, 0444595481

[158] G Cai, B Jin, P Monis, C Saint, *Metabolic flux network and analysis of fermentative hydrogen production*, Biotechnoloigy Advances 29 (2011) 375-387

[159] V Martínez-Merino, María J Gil, A Cornejo, *Biological Hydrogen Production*, In Renewable Hydrogen Technologies, Ch 8, Elsevier (2013), 171-199, 9780444563521

[160] R G Sawers, *Formate and its role in hydrogen production in Escherichia coli*, Biochemical Society Transactions (2005) 33, 1

[161] W Margolin, *Themes and variations in prokaryotic cell division*, FEMS Microbiology Reviews 24 (2000) 531-548

[162] G Sezonov, D Joseleau-Petit, R D'Ari, *Escherichia coli Physiology in Luria-Bertani Broth*, Journal of Bacteriology (2007) 8746-8749

[163] M-L Chong, V Sabaratnam, Y Shirai, M A Hassan, *Biohydrogen production from biomass and industrial wastes by dark fermentation*, International Journal of Hydrogen Energy 34 (2009) 3277-3287

[164] C C Hua, A Giannis, C-L Chen, W Qi, J-Y Wang, *Comparative study of biohydrogen production by four dark fermentative bacteria*, International Journal of Hydrogen Energy 38 (2013) 15686-15692

[165] D Das, T Nejat Veziroglu, *Advances in biological hydrogen production processes*, International Journal of Hydrogen Energy 33 (2008) 6046–6057

[166] P C Hallenbeck and D Ghosh, *Advances in fermentative biohydrogen production: the way forward?*, Trends in Biotechnology (2009) 27 5;287-297

[167] M Redwood, I Mikheenko, F Sargent, L Macaskie, *Dissecting the roles of Escherichia coli hydrogenases in biohydrogen production*, FEMS Microbiology Letter 278 (2008) 48-55

[168] P Sinha, A Pandey, *An evaluative report and challenges for fermentative biohydrogen production*, International Journal of Hydrogen Energy 36 (2011) 7460-7478

[169] K Trchounian, A Trchounian, *Hydrogenase 2 is most and hydrogenase 1 is less responsible for H_2 production by Escherichia coli under glycerol fermentation at neutral and slightly alkaline pH*, International Journal of Hydrogen Energy 34 (2009) 8839-8845

[170] M J Lukey et al, *How Escherichia coli Is Equipped to Oxidize Hydrogen under Different Redox Conditions*, The Journal of Biological Chemistry 285 (2010) 6;3928-3938

[171] M Abo-Hashesh, R Wang, P Hallenbeck, *Metabolic engineering in dark fermentative hydrogen production; theory and practice*, Bioresource Technology 102 (2011) 8414-8422

[172] S J Berríos-Rivera, K-Y San, G N Bennett, *The Effect of NAPRTase Overexpression on the Total Levels of NAD, the NADH/NAD^+ Ratio, and the Distribution of Metabolites in Escherichia coli*, Metabolic Engineering 4 (2002) 230-237

[173] D W Penfold, C F Forster, L E Macaskie, *Increased hydrogen production by Escherichia coli strain HD701 in comparison with the wild-type parent strain MC4100*, Enzyme and Microbial Technology 33 (2003) 185-189

[174] F M Morsy, *Hydrogen production from acid hydrolyzed molasses by the hydrogen overproducing Escherichia coli strain HD701 and subsequent use of the waste bacterial biomass for biosorption of Cd(II) and Zn(II)*, International Journal of Hydrogen Energy 36 (2011) 14381-14390

[175] D W Penfold, L E Macaskie, *Production of H_2 from sucrose by Escherichia coli strains carrying the pUR400 plasmid, which encodes invertase activity*, Biotechnology Letters (2004) 26:1879-1883

[176] G Chittibabu, K Nath, D Das, *Feasibility studies on the fermentative hydrogen production by recombinant Escherichia coli BL-21*, Process Biochemistry 41 (2006) 682-688

[177] K-Y Show, D-J Lee, J-S Chang, *Bioreactor and process design for biohydrogen production*, Bioresource Technology 102 (2011) 8524-8533

[178] M Shuler, F Kargi, *Bioprocess Engineering: Basic Concepts*, 2nd Ed, Prentice-Hall (2002), 0130819085

[179] T Maeda, V Sanchez-Torres, T K Wood, *Metabolic engineering to enhance bacterial hydrogen production*, Microbial Biotechnology (2008) 1;30-39

[180] T Maeda, V Sanchez-Torres, T K Wood, *Enhanced hydrogen production from glucose by metabolically engineered Escherichia coli*, Applied Microbiol Biotechnology (2007) 77;879-890

[181] P Bakonyi, N Nemestóthy, V Simon, K Bélafi-Bakó, *Review on the start-up experiences of continuous fermentative hydrogen producing bioreactors*, Renewable and Sustainable Energy Reviews 40 (2014) 806-813

[182] J Wang, W Wan, *Factors influencing fermentative hydrogen production: A review*, International Journal of Hydrogen Energy 34 (2009) 799-811

[183] X Guo, E Trably, E Latrille, H Carrère, J-P Steyer, *Hydrogen production from agricultural waste by dark fermentation: A review*, International Journal of Hydrogen Energy 35 (2010) 10660-10673

[184] G De Gioannis, A Muntoni, A Polettini, R Pomi, *A review of dark fermentative hydrogen production from biodegradable municipal waste fractions*, Waste Management 33 (2013) 1345-1361

[185] I Kapdan, F Kargi, *Bio-hydrogen production from waste materials*, Enzyme and Microbial Technology 38 (2006) 569-582

[186] C-H Choua , C-W Wang, C-C Huang, J-J Lay, *Pilot study of the influence of stirring and pH on anaerobes converting high-solid organic wastes to hydrogen*, International Journal of Hydrogen Energy 33 (2008) 1550-1558

[187] B Junker et al, *Sustainable reduction of bioreactor contamination in an industrial fermentation pilot plant*, Journal of Bioscience and Bioengineering (2006) 102 4;251-268

[188] M D Redwood, M Paterson-Beedle, L E Macaskie, *Integrating dark and light bio-hydrogen production strategies: towards the hydrogen economy*, Reviews in Environmental Science and Biotechnology (2009) 8:149–185

[189] L Singh, Z A Wahid, *Methods for enhancing bio-hydrogen production from biological process: A review*, Journal of Industrial and Engineering Chemistry (2015) 21;70-80

[190] D Das, *Advances in biohydrogen production processes: An approach towards commercialization*, International Journal of Hydrogen Energy 34 (2009) 7349-7357

[191] E Seol, A Manimaran, Y Jang, S Kim, Y-K Oh, S Park, *Sustained hydrogen production from formate using immobilized recombinant Escherichia coli SH5*, International Journal of Hydrogen Energy 36 (2010) 1-6

[192] N Mnatsakanyan, A Vassilian, L Navasardyan, K Bagramyan, A Trchounian, *Regulation of Escherichia coli Formate Hydrogenlyase Activity by Formate at Alkaline pH*, Current Microbiology 45 (2002), 281-286

[193] C-N Lin, S-Y Wu, K-S Lee, P-J Lin, C-Y Lin, J-S Chang, *Integration of fermentative hydrogen process and fuel cell for on-line electricity generation*, International Journal of Hydrogen Energy 32 (2007) 802-808

[194] M Mahmoudkhani, D W Keith, *Low-energy sodium hydroxide recovery for CO2 capture from atmospheric air–Thermodynamic analysis*, International Journal of Greenhouse Gas Control 3 (2009) 4;376-384

[195] M Yoo, S-J Han, J-H Wee, *Carbon dioxide capture capacity of sodium hydroxide aqueous solution*, Journal of Environmental Management 114 (2013) 512-519

[196] K Ledjeff-Hey, J Roes, R Wolters, *CO -scrubbing and methanation as purification system for PEFC*, Journal of Power Sources 86 (2000) 556-561

[197] G T Rochelle, *Amine Scrubbing for CO2 Capture*, Science 325 (2009) 1652-1654

[198] M Y Azwar, M A Hussain, A K Abdul-Wahab, *Development of biohydrogen production by photobiological, fermentation and electrochemical processes: A review*, Renewable and Sustainable Energy Reviews 31 (2014) 158-173

[199] M A Rosen, *Advances in hydrogen production by thermochemical water decomposition: A review*, Energy 35 (2010) 1068-1076

[200] H Ahmad, S K Kamarudin, L J Minggu, M. Kassim, *Hydrogen from photo-catalytic water splitting process: A review,* Renewable and Sustainable Energy Reviews 43 (2015) 599-610

[201] H He, A Chen, M Chang, L Ma, C Li, *A feasible hydrogen evolution process of water electrolysis assisted by TiO2 nanotube photocatalysis*, Journal of Industrial and Engineering Chemistry 19 (2013) 1112-1116

[202] H Tributsch, *Photovoltaic hydrogen generation*, International Journal of Hydrogen Energy 33 (2008) 5911-5930

[203] L J Minggu, W R W Daud, M B Kassim, *An overview of photocells and photoreactors for photoelectrochemical water splitting*, International Journal of Hydrogen Energy 35 (2010) 5233-5244

[204] M F Orhan, I Dincer, M A Rosen, M Kanoglu*, Integrated hydrogen production options based on renewable and nuclear energy sources*, Renewable and Sustainable Energy Reviews 16 (2012) 6059-6082

[205] Z Wang, R R Roberts, G F Naterer, K S Gabriel, *Comparison of thermochemical, electrolytic, photoelectrolytic and photochemical solar-to-hydrogen production technologies*, International Journal of Hydrogen Energy 37 (2012) 16287-16301

[206] M Ni, M K H Leung, D Y C Leung, K Sumathy, *A review and recent developments in photocatalytic water-splitting using TiO2 for hydrogen production*, Renewable and Sustainable Energy Reviews 11 (2007) 401-425

[207] R Abe, *Recent progress on photocatalytic and photoelectrochemical water splitting under visible light irradiation*, Journal of Photochemistry and Photobiology C: Photochemistry Reviews 11 (2010) 179-209

[208] W Zhao, Z Wang, X Shen, J Li, C Xu, Z Gan, *Hydrogen generation via photoelectrocatalytic water splitting using a tungsten trioxide catalyst under visible light irradiation*, International Journal of Hydrogen Energy 37 (2012) 908-915

[209] A Ranjitha, N Muthukumarasamy, M Thambidurai , R Balasundaraprabhu, S Agilan, *Effect of annealing temperature on nanocrystalline TiO2 thin films prepared by sol-gel dip coating method*, Optik 124 (2013) 6201-6204

[210] L Zhao, M Han, J Lian, *Photocatalytic activity of TiO2 films with mixed anatase and rutile structures prepared by pulsed laser deposition*, Thin Solid Films 516 (2008) 3394-3398

[211] M-Y Hsu, N V Thang, C W, J Leu, *Structural and morphological transformations of TiO2 nanotube arrays induced by excimer laser treatment*, Thin Solid Films 520 (2012) 3593-3599

[212] M Meyyappan, L Delzeit, A Cassell, D Hash, Carbon nanotube growth by PECVD: a review, Plasma Sources Science and Technology 12 (2003) 205-216

[213] J I B Wilson, N Scheerbaum , S Karim , N Polwart , P John , Y Fan , A G Fitzgerald, *Low temperature plasma chemical vapour deposition of carbon nanotubes*, Diamond and Related Materials 11 (2002) 918-921

[214] E Ju Bae, Y-S Min, D Kang, J-H Ko, W Park, *Low-Temperature Growth of Single-Walled Carbon Nanotubes by Plasma Enhanced Chemical Vapor Deposition*, Chemistry of Materials 17 (2005) 20;5141-5145

[215] Y Yürüm, A Taralp, T Nejat Veziroglu, *Storage of hydrogen in nanostructured carbon materials*, International Journal of Hydrogen Energy 34 (2009) 3784-3798

[216] P K Dubey, A S K Sinha, S Talapatra, N Koratkar, P M Ajayan, O N Srivastava, *Hydrogen generation by water electrolysis using carbon nanotube anode*, International Journal of Hydrogen Energy 35 (2010) 3945-3950

[217] R Oriňáková, A Oriňák, *Recent applications of carbon nanotubes in hydrogen production and storage*, Fuel 90 (2011) 3123-3140

[218] H-Y Du, C-H Wang, H-C Hsu, S-T Chang, H-C Huang, L-C Chen, K-H Chen, *Graphene nanosheet CNT hybrid nanostructure electrode for a proton exchange membrane fuel cell*, International Journal of Hydrogen Energy 37 (2012) 18989-18995

[219] Y Cong, X Li, Y Qin, Z Dong, G Yuan, Z Cui, X Lai, *Carbon-doped TiO_2 coating on multiwalled carbon nanotubes with higher visible light photocatalytic activity*, Applied Catalysis B: Environmental 107 (2011) 128-134

[220] S M Mirandaa, G E Romanos, V Likodimos, R R N Marques, E P Favvas, F K Katsaros, K L Stefanopoulos, V J P Vilar, J L Fariaa, P Falaras, A M T Silva, *Pore structure, interface properties and photocatalytic efficiency of hydration/dehydration derived TiO2/CNT composites*, Applied Catalysis B: Environmental 147 (2014) 65-81

[221] H Yu, X Quan, S Chen, H Zhao, Y Zhang, *TiO_2-carbon nanotube heterojunction arrays with a controllable thickness of TiO2 layer and their first application in photocatalysis*, Journal of Photochemistry and Photobiology A: Chemistry 200 (2008) 301-306

[222] Z Li, B Gaoa, G Z Chena, R Mokaya, S Sotiropoulos, G L Puma, *Carbon nanotube/titanium dioxide (CNT/TiO_2) core-shell nanocomposites with tailored shell thickness, CNT content and photocatalytic/photoelectrocatalytic properties*, Applied Catalysis B: Environmental 110 (2011) 50-57

[223] R Ströbel, J Garche, P T Moseley, L Jörissen, G Wolf, *Hydrogen storage by carbon materials*, Journal of Power Sources 159 (2006) 781-801

[224] Y Ando, X Zhao, T Sugai, M Kumar, *Growing carbon nanotubes*, Materials Today 7 (2004) 10;22-29

[225] B B Wang, S Leeb, X Z Xu, S Choi, H Yan, B Zhang, W Hao, *Effects of the pressure on growth of carbon nanotubes by plasma-enhanced hot filament CVD at low substrate temperature*, Applied Surface Science 236 (2004) 6-12

[226] G L Miessler, D A Tarr*, Inorganic Chemistry*, 3rd Ed, Pearson Prentice Hall (2004)

[227] A Vértes, S Nagy, Z Klencsár, *Handbook of nuclear chemistry: Instrumentation, separation techniques environmental issues*, Volume 5, Springer (2003) 1402013175

[228] http://goldbook.iupac.org/S05910.html, accessed November 2014

[229] C Housecroft, E Constable, *Chemistry*, 3rd Ed, Pearson (2006), 18

[230] P W Atkins, *Physical Chemistry*, 5th Ed, Oxford (1994), 0198557310

[231] K Stowe, *An Introduction to Thermodynamics and Statistical Mechanics*, 2nd Ed, Cambridge (2007), 1139462857

[232] M Aindow, C J Kiely, *Electron Microscopy and Analysis 2001*, IOP (2001), 0750308125

[233] R Egerton, *Physical Principles of Electron Microscopy: An Introduction to TEM, SEM, and AEM*, Springer (2006), 0387260161

[234] Instruction Manual for JOEL JSM 7400F Field Emission Scanning Electron Microscope (published July 2003)

[235] Image obtained from http://www.purdue.edu/ehps/rem/rs/graphics/sem2.gif, representative of that contained in JOEL JSM 7400F user manual

[236] M Suga et al, *Recent progress in scanning electron microscopy for the characterization of fine structural details of nano materials*, Progress in Solid State Chemistry 42 (2014) 1-21

[237] H N Southworth, *Introduction to Modern Microscopy*, Wykeham Publications Ltd (1975) (no ISBN)

[238] D J Smith, *Progress & perspectives for atomic-resolution electron microscopy*, Materials Today 12 (2010) 1;10-16

[239] D J Smith, *Progress and problems for atomic-resolution electron microscopy*, Micron 43 (2012) 504-508

[240] J Barthel, A Thust, *Quantification of the Information Limit of Transmission Electron Microscopes*, Physical Review Letters (2008) 101

[241] N Jalili, K Laxminarayana, *A review of atomic force microscopy imaging systems: application to molecular metrology and biological sciences*, Mechatronics 14 (2004) 907-945

[242] D C Bell, A J Garratt-Reed, *Energy Dispersive X-ray Analysis in the Electron Microscope*, Garland Science (2003), 1135331405

[243] Extracted from http://www.oxford-instruments.com/OxfordInstruments/media/nanoanalysis/brochures%20and%20thumbs/OI_AppNote_SDD_Explained.pdf, accessed November 2014

[244] J M Walls, *Methods of Surface Analysis: Techniques and Applications*, CUP Archive (1990), 052138690X

[245] D Briggs, M P Seah, *Practical Surface Analysis: Volume 1 – Auger and X-Ray Photoelectron Spectroscopy*, 2nd Ed, Wiley (1996), 0471920819

[246] C D Wagner et al, *Handbook of X-ray Photoelectron Spectroscopy*, Perkin-Elmer, 1979 (no ISBN)

[247] K Wasa, M Kitabatake, H Adachi, *Thin film materials technology: sputtering of compound materials*, William Andrew (2004), 0815519311

[248] M M Hossain, *Plasma Technology for Deposition and Surface Modification*, Logos Verlag Berlin GmbH (2009), 5, 3832520740

[249] A C Jones, M L Hitchman, *Chemical Vapour Deposition: Precursors, Processes and Application*, Royal Society of Chemistry (2009), 494-495, 0854044655

[250] P J Kelly, R D Arnell, *Magnetron sputtering: a review of recent developments and applications*, Vacuum 56 (2000) 159-172

[251] C A Bishop, *Vacuum Deposition onto Webs, Films, and Foils, Ch 16 - Planar Magnetron Sputtering—Source Design and Operation*, William Andrew Publishing (2007), 297-324, 9780815515357

[252] G Bräuer, B Szyszka, M Vergöhl, R Bandorf, *Magnetron sputtering – Milestones of 30 years*, Vacuum 84 (2010) 1354-1359

[253] R V Stuart, *Vacuum Technology, Thin Films, and Sputtering: An Introduction*, Academic Press (2012) 0323139159

[254] Alexander Fridman, *Plasma Chemistry*, Cambridge University Press (2008), 541, 1139471732

[255] J-M Ting, S-H Lin, *Growth and characteristics of carbon nanotubes obtained under different C2H2/H2/NH3 concentrations*, Carbon 45 (2007) 1934-1940

[256] K R Nambiar, *Lasers: Principles, Types and Applications*, New Age International (2006), 501-502, 8122414923

[257] D W Bäuerle, *Laser Processing and Chemistry*, Springer (2011), 88, 3642176135

[258] R C Crafer, *Laser Processing in Manufacturing*, Springer (1992), 239-256, 0412415208

[259] H Y Zheng, Y C Guan, X C Wang, Z K Wang, *Tailoring material properties induced by laser surface processing ,in Laser Surface Engineering: Processes and Applications*, Woodhead (2015), 315-357, 9781782420743

[260] M El-Bousiffi, D Gunn, *A dynamic study of methane reforming*, *in Reaction Kinetics and the Development and Operation of Catalytic Processes*, Studies in Surface Science & Catalysis 133, Elsevier (2001), 247-254, 0080540295

[261] T L LeValley, A R Richard, M Fan, *The progress in water gas shift and steam reforming hydrogen production technologies - A review*, International Journal of Hydrogen Energy 39 (2014) 16983-17000

[262] S D Angeli, G Monteleone, A Giaconia, A A Lemonidou, *State-of-the-art catalysts for CH4 steam reforming at low temperature*, International Journal of Hydrogen Energy 39 (2014) 1979-1997

[263] B Chen, Z Liao, J Wang, H Yu, Y Yang, *Exergy analysis and CO2 emission evaluation for steam methane reforming*, International Journal of Hydrogen Energy 37 (2012) 3191-3200

[264] J Dufour, D P Serrano, J L Gálvez, J Moreno, C García, *Life cycle assessment of processes for hydrogen production. Environmental feasibility and reduction of greenhouse gases emissions*, International Journal of Hydrogen Energy 34 (2009) 1370-1376

[265] J C Meermana, E S Hamborg, T van Keulena, A Ramírez, W C Turkenburga, A P C Faaij, *Techno-economic assessment of CO2 capture at steam methane reforming facilities using commercially available technology*, International Journal of Greenhouse Gas Control 9 (2012) 160-171

[266] A P Simpsona, A E Lutz, *Exergy analysis of hydrogen production via steam methane reforming*, International Journal of Hydrogen Energy 32 (2007) 4811-4820

[267] D K Lee, K Y Koo, D J Seo, W L Yoon, *Analysis of design variables for an efficient natural gas steam reforming process comprised in a small scale hydrogen fueling station*, Renewable Energy 42 (2012) 234-242

[268] R Lødeng, E Bjørgum, B C Enger, J L Eilertsen, A Holmen, B Krogh, M Rønnekleiv, E Rytter, *Catalytic partial oxidation of CH4 to H2 over cobalt catalysts at moderate temperatures*, Applied Catalysis A: General 333 (2007) 11-23

[269] B C Enger, R Lødeng, As Holmen, *A review of catalytic partial oxidation of methane to synthesis gas with emphasis on reaction mechanisms over transition metal catalysts*, Applied Catalysis A: General 346 (2008) 1-27

[270] M W Smith, D Shekhawat, *Fuel Cells, Ch 5 - Catalytic Partial Oxidation*, Elsevier (2011), 73-128, 9780444535634

[271] S Freni, G Calogero, S Cavallaro, *Hydrogen production from methane through catalytic partial oxidation reactions*, Journal of Power Sources 87 (2000) 28-38

[272] N Muradov, *Hydrogen via methane decomposition: an application for decarbonization of fossil fuels,* International Journal of Hydrogen Energy 26 (2001) 1165-1175

[273] A V Bridgwater, *Review of fast pyrolysis of biomass and product upgrading*, Biomass and Bioenergy 38 (2012) 68-94

[274] F Rahmani, M Haghighi, Y Vafaeian, P Estifaee, *Hydrogen production via CO2 reforming of methane over ZrO2-Doped Ni/ZSM-5 nanostructured catalyst prepared by ultrasound assisted sequential impregnation method*, Journal of Power Sources 272 (2014) 816-827

[275] M Puig-Arnavat, J Carles Bruno, A Coronas, *Review and analysis of biomass gasification models*, Renewable and Sustainable Energy Reviews 14 (2010) 2841-2851

[276] C Du, D Huang, J Mo, D Ma, Q Wang, Z Mo, S Ma, *Renewable hydrogen from ethanol by a miniaturized nonthermal arc plasma-catalytic reforming system*, International Journal of Hydrogen Energy 39 (2014) 9057-9069

[277] C M Du, J M Mo, J Tang, D W Huang, Z X Mo, Q K Wang, S Z Ma, Z J Chen, *Plasma reforming of bio-ethanol for hydrogen rich gas production*, Applied Energy 133 (2014) 70-79

[278] P W E Blom, G W Basson, *Non-catalytic plasma-arc reforming of natural gas with carbon dioxide as the oxidizing agent for the production of synthesis gas or hydrogen*, International Journal of Hydrogen Energy 38 (2013) 5684-5692

[279] L Bromberga, D R Cohna, A Rabinovicha, J Heywood, *Emissions reductions using hydrogen from plasmatron fuel converters*, International Journal of Hydrogen Energy 26 (2001) 1115-1121

[280] T Paulmier, L Fulcheri, *Use of non-thermal plasma for hydrocarbon reforming*, Chemical Engineering Journal 106 (2005) 59-71

[281] G Petitpas, J-D Rollier, A Darmon, J Gonzalez-Aguilar, R Metkemeijer, L Fulcheri, *A comparative study of non-thermal plasma assisted reforming technologies*, International Journal of Hydrogen Energy 32 (2007) 2848-2867

[282] R D Cortright, R R Davda, J A Dumesic, *Hydrogen from catalytic reforming of biomass-derived hydrocarbons in liquid water*, Nature 418, 964-967

[283] G Wen, Y Xu, H Ma, Z Xu, Z Tiana, *Production of hydrogen by aqueous-phase reforming of glycerol*, International Journal of Hydrogen Energy 3 (2008) 6657-6666

[284] A Tanksale, Y Wong, J N Beltramini, G Q Lu, *Hydrogen generation from liquid phase catalytic reforming of sugar solutions using metal-supported catalysts*, International Journal of Hydrogen Energy 32 (2007) 717-724

[285] R R Davda, J W Shabaker, G W Huber, R D Cortright, J A Dumesic, *A review of catalytic issues and process conditions for renewable hydrogen and alkanes by aqueous-phase reforming of oxygenated hydrocarbons over supported metal catalysts*, Applied Catalysis B: Environmental 56 (2005) 171-186

[286] B Roy, K Loganathan, H N Pham, A K Datye, C A Leclerc, *Surface modification of solution combustion synthesized Ni/Al2O3catalyst for aqueous-phase reforming of ethanol*, International Journal of Hydrogen Energy 35 (2010) 11700-11708

[287] Yong Guo et al, *Hydrogen production by aqueous-phase reforming of glycerol over Ni-B catalysts*, International Journal of Hydrogen Energy 37 (2012) 227-234

[288] T V Choudhary, C Sivadinarayana, D W Goodman, *Production of COx-free hydrogen for fuel cells via step-wise hydrocarbon reforming and catalytic dehydrogenation of ammonia*, Chemical Engineering Journal 93 (2003) 69-80

[289] W Wanga, J M Herreros, A Tsolakis, A P E York, *Ammonia as hydrogen carrier for transportation; investigation of the ammonia exhaust gas fuel reforming*, International Journal of Hydrogen Energy 38 (2013) 9907-9917

[290] J H Kim, D H Um, O C Kwon, *Hydrogen production from burning and reforming of ammonia in a microreforming system*, Energy Conversion and Management 56 (2012) 184-191

[291] M F Irfan, M R Usman, K Kusakabe, *Coal gasification in CO_2 atmosphere and its kinetics since 1948: A brief review*, Energy 36 (2011) 12-40

[292] M Puig-Arnavat, J Carles Bruno, A Coronas, *Review and analysis of biomass gasification models*, Renewable and Sustainable Energy Reviews 14 (2010) 2841-2851

[293] D Hua, Y Hanxi, A Xinping, C Chuansin, *Hydrogen production from catalytic hydrolysis of sodium borohydride solution using nickel boride catalyst*, International Journal of Hydrogen Energy 28 (2003) 1095-1100

[294] S C Amendola et al, *A safe, portable, hydrogen gas generator using aqueous borohydride solution and Ru catalyst*, International Journal of Hydrogen Energy 25 (2000) 969-975

[295] H Argun, F Kargi, *Bio-hydrogen production by different operational modes of dark and photo-fermentation: An overview*, International Journal of Hydrogen Energy 36 (2011) 7443-7459

[296] P C Hallenbeck, *Fermentative hydrogen production: Principles, progress, and prognosis*, International Journal of Hydrogen Energy 34 (2009) 7379–7389

[297] K Y Show, D J Lee, J H Tay, C Y Lin, J S Chang, *Biohydrogen production: Current perspectives and the way forward*, International Journal of Hydrogen Energy 37 (2012) 15616-15631

[298] B E Logan et al, *Microbial Electrolysis Cells for High Yield Hydrogen Gas Production from Organic Matter*, Environmental Science & Technology 42 (2008) 23;8630-8640

[299] A Steinfeld, *Solar thermochemical production of hydrogen–a review*, Solar Energy 78 (2005) 603-615

[300] A. H. Abedin, Z. Wang, M. A. Rosen, *Heat extraction from supercritical water-cooled nuclear reactors for hydrogen production plants*, International Journal of Hydrogen Energy 37 (2012) 16527-16534

[301] A. Giaconia, *Thermochemical production of hydrogen*, In Advances in Hydrogen Production, Storage and Distribution, 10; 263-280, Woodhead (2014), 9780857097682

[302] A Kogana, E Spiegler, M Wolfshtein, *Direct solar thermal splitting of water and on-site separation of the products. III. Improvement of reactor efficiency by steam entrainment*, International Journal of Hydrogen Energy 25 (2000) 739-745

[303] C Perkins, A W Weimer, *Likely near-term solar-thermal water splitting technologies*, International Journal of Hydrogen Energy 29 (2004) 1587-1599

[304] S Z Baykara, *Experimental solar water thermolysis*, International Journal of Hydrogen Energy 29 (2004) 1459-1469

[305] M B Gorensek, W A Summers, *Hybrid sulfur flowsheets using PEM electrolysis and a bayonet decomposition reactor*, International Journal of Hydrogen Energy 34 (2009) 4097-4114

[306] S-C Yua, C-W Huanga, C-H Liaoa, J Wua, S-T Chang, K-H Chen, *A novel membrane reactor for separating hydrogen and oxygen in photocatalytic water splitting*, Journal of Membrane Science 382 (2011) 291-299

[307] R Yerga, M Alvarez-Galvá, F Vaquero, J Arenales, J Fierro, *Hydrogen Production from Water Splitting Using Photo-Semiconductor Catalysts*, In Renewable Hydrogen Technologies, Elsevier (2013) 3;43-61, 9780444563521

[308] M Doyoyo, N Faure, *Pressure Vessels with Reinforcing Space-Filling Skeletons*, Journal of Pressure Vessel Technology 130(3) (2008) 031210

[309] Sridhar Dalai et al, *Fabrication of zinc-loaded hollow glass microspheres (HGMs) for hydrogen storage*, International Journal of Energy Research (2015) 1099-114X

[310] T Q Hua et al, *Technical assessment of compressed hydrogen storage tank systems for automotive applications*, International Journal of Hydrogen Energy 36 (2011) 3037-3049

[311] G Petitpas et al, *A comparative analysis of the cryo-compression and cryo-adsorption hydrogen storage methods,* International Journal of Hydrogen Energy 39 (2014) 10564-10584

[312] S Krasae-in, J H Stang, P Neksa, *Development of large-scale hydrogen liquefaction processes from 1898 to 2009*, International Journal of Hydrogen Energy 35 (2010) 4524-4533

[313] X Hu et al, *Hydrogen Adsorption and Storage*, In Coal Gasification and Its Applications, Elsevier (2011), 9780815520498

[314] B Sakintuna, F Lamari-Darkrim, M Hirscher, *Metal hydride materials for solid hydrogen storage: A Review*, International Journal of Hydrogen Energy 32 (2007) 1121-1140

[315] L Kustov et al, *Hydrogen storage materials*, Focus Article (Mendeleev Communication) (2014) 24, 1-8

[316] A Züttel, *Materials for hydrogen storage*, Materials Today 6 (2003) 9;24-33

[317] J Ares Fernandez et al, *Mechanical and Thermal Decomposition of $LiAlH_4$ with Metal Halides*. International Journal of Hydrogen Energy 32 (2007) 1033-1040

[318] J Ares et al, *Influence of Impurities on the Milling Process of MgH_2*, Journal of Alloys and Compounds 434–435 (2007) 729-733

[319] Y Liu et al, *Reversible hydrogen storage behavior of $LiBH_4$-$Mg(OH)_2$ composites*, International Journal of Hydrogen Energy 39 (2014) 7868-7875

[320] J Ritter et al, *Implementing a Hydrogen Economy*, Materials Today 6 (2003) 9;18-23

[321] T Umegaki et al, *Boron- and nitrogen-based chemical hydrogen storage materials*, International Journal of Hydrogen Energy 34 (2009) 2303-2311

[322] H Langmi, G McGrady, *Non-hydride Systems of the main group elements as hydrogen storage materials,* Coordination Chemistry Reviews 251 (2007) 925-935

[323] A Dillon et al, *Storage of hydrogen in single-walled carbon nanotubes*, Nature 386 (1997) 377-379

[324] A Chambers et al, *Hydrogen storage in graphite nanofibers*, Journal of Physical Chemistry B 102 (1998) 4253-4256

[325] P Broom, D Book, *15 - Hydrogen storage in nanoporous materials*, In Advances in Hydrogen Production, Storage and Distribution, Woodhead (2014), 410-450, 9780857097682

[326] X Ye et al, *A nanocontainer for the storage of hydrogen*, Carbon 45 (2007) 315-320

[327] C Liu et al, *Hydrogen storage in carbon nanotubes revisited*, Carbon 48 (2010) 452-455

[328] H W Langmi et al, *Hydrogen Storage in Metal-Organic Frameworks: A Review*, Electrochimica Acta 128 (2014) 368-392

[329] B Kuchta et al, *Numerical estimation of hydrogen storage limits in carbon-based nanospaces*, Carbon 48 (2010) 223-231

[330] Y Chen et al, *Mechanics of hydrogen storage in carbon nanotubes*, Journal of the Mechanics and Physics of Solids 56 (2008) 3224-3241

[331] R Rauch, A Kiennemann, A Sauciuc, *Fischer-Tropsch synthesis to biofuels (BtL process)*, In The Role of Catalysis for the Sustainable Production of Bio-fuels and Bio-chemicals, Chapter 12, Elsevier (2013), 397-443, 9780444563309

[332] Burtron H Davis, *Fischer–Tropsch synthesis: current mechanism and futuristic needs*, Fuel Processing Technology 71 (2001) 157-166

[333] M Tijmensen, A Faaij, C Hamelinck, M van Hardeveld, *Exploration of the possibilities for production of Fischer Tropsch liquids and power via biomass gasification*, Biomass and Bioenergy 23 (2002) 129-152

[334] J M Bucher, J W Schwank, *The effect of downstream synthesis gas feeding on Fischer–Tropsch product distributions*, Fuel Processing Technology 90 (2009) 1009-1015

[335] Editorial, *Present and future applications of the Fischer–Tropsch process*, Applied Catalysis A: General 276 (2004) 1–3

[336] E Gulzow, M Schulze, U Gerke, *Bipolar concept for alkaline fuel cells*, Journal of Power Sources 156 (2006) 1-7

[337] K B Martin, S E Grasman, *An assessment of wind-hydrogen systems for light duty vehicles*, International Journal of Hydrogen Energy 34 (2009) 6581-6588

[338] W Isherwood et al, *Remote power systems with advanced storage technologies for Alaskan villages*, Energy 25 (2000) 1005-1020

[339] D Chade, T Miklis, D Dvorak, *Feasibility study of wind-to-hydrogen system for Arctic remote locations - Grimsey Island case study*, Renewable Energy 76 (2015) 204-211

[340] D C Young, G A Mill, R Wall, *Feasibility of renewable energy storage using hydrogen in remote communities in Bhutan*, International Journal of Hydrogen Energy 32 (2007) 997-1009

[341] P Vermeiren, J P Moreels, A Claes, H Beckers, *Electrode diaphragm electrode assembly for alkaline water electrolysers*, International Journal of Hydrogen Energy 34 (2009) 9305-9315

[342] B Smitha, S Sridhar, A A Khan*, Solid polymer electrolyte membranes for fuel cell applications – a review*, Journal of Membrane Science 259 (2005) 10-26

[343] Cheng et al, *A review of PEM hydrogen fuel cell contamination: Impacts, mechanisms, and mitigation*, Journal of Power Sources 165 (2007) 739-756

[344] T Ackermann, *Wind Power in Power Systems*, John Wiley & Sons (2012), 9781119942085

[345] J F Manwell, J G McGowan, A Rogers, *Wind energy explained: theory, design and application, 2nd Ed,* WILEY (2009), 0470686286

[346] http://www.oxforddnb.com/view/article/100957, accessed March 2015

[347] Various publications by RenewableUK, taking classifications from initial ofgem feed-in tariff size bands - http://www.renewableuk.com/en/publications/index.cfm/Small-Medium-Wind-Market-Report-2015, accessed March 2015

[348] Datasheet for the WES 80 wind turbine - www.windenergysolutions.nl/wes-80, accessed March 2015. Data also shown in Appendix 5.1

[349] Datasheet for Enercon E-126 wind turbine - http://www.enercon.de/en-en/66.htm, accessed March 2015

[350] G M Joselin Herbert, S Iniyan, E Sreevalsan, S Rajapandian, *A review of wind energy technologies*, Renewable and Sustainable Energy Reviews 11 (2007) 1117-1145

[351] S M Muyeen, A Al-Durra, J Tamura, Variable speed wind turbine generator system with current controlled voltage source inverter, Energy Conversion and Management 52 (2011) 2688-2694

[352] Wind Gains Ground, *Hitting 33 GW of Installed Capacity*, The Electricity Journal 34 (2010) 5;1-3

[353] P E Morthorst*, Capacity development and profitability of wind turbines*, Energy Policy 27 (1999) 779-787

[354] P Gipe, *Wind Power: Renewable Energy for Home, Farm, and Business*, 2nd Ed, Chelsea Green Publishing (2004), 1603581634

[355] C S Rao, *Environmental Pollution Control Engineering*, New Age International (2007), 9788122418354

[356] C Donald Ahrens, *Meteorology Today: An Introduction to Weather, Climate, and the Environment*, 10th Ed, Cengage Learning (2012), 1285400968

[357] C Bak, *Aerodynamic design of wind turbine rotors, Ch 3*, In Advances in Wind Turbine Blade Design and Materials, Woodhead Publishing (2013), p59-108, 9780857094261

[358] S A Kalogirou, *Wind Energy Systems*, In Solar Energy Engineering, Ch 13, 2nd Ed, Boston Academic Press (2014), p735-762, 9780123972705

[359] G K Singh, *Solar power generation by PV (photovoltaic) technology: A review*, Energy 53 (2013) 1-13

[360] http://www.epia.org/news/publications, accessed April 2015

[361] V V Tyagi, N A A Rahim, N A Rahim, J A Selvara, L Selvarai, *Progress in solar PV technology: Research and achievement*, Renewable and Sustainable Energy Reviews 20 (2013) 443-461

[362] S A Kalogirou, *Photovoltaic Systems*, Ch 9, In Solar Energy Engineering (2nd Ed), Academic Press Boston (2014) 481-540, 9780123972705

[363] B Parida, S Iniyan, R Goic, *A review of solar photovoltaic technologies*, Renewable and Sustainable Energy Reviews 15 (2011) 1625-1636

[364] Philip G. Jordan, *Solar Energy Markets*, Ch 1-2, Academic Press Boston (2014) 1-18, 9780123971746

[365] M Z Jacobson, *Fundamentals of Atmospheric Modeling*, Cambridge University Press (2005), p281, 0521548659

[366] J You, L Dou, Z Hong, G Lia, Y Yang, *Recent trends in polymer tandem solar cells research*, Progress in Polymer Science 38 (2013) 1909-1928

[367] S V Boriskina, G Chen, *Exceeding the solar cell Shockley-Queisser limit via thermal up-conversion of low-energy photons*, Optics Communications 314 (2014) 71-78

[368] S Kasap, P Capper, *Springer Handbook of Electronic and Photonic Materials*, Springer Science & Business Media (2006), 54, 0387291857

[369] O E Semonin, J M Luther, M C Beard, *Quantum dots for next generation photovoltaics*, Materials Today 15 (2012) 11

[370] J A Carson, *Solar Cell Research Progress*, Nova Publishers (2008), 25, 1604560304

[371] www.nrel.gov/ncpv, accessed April 2015

[372] www.ons.gov.uk/ons/dcp171778_358581.xml, accessed March 2015

[373] http://www.ti.com/lit/an/slva157/slva157.pdf (Texas Instruments application report), accessed April 2015

[374] http://www.onsemi.com/pub_link/Collateral/AND9135-D.PDF (ON Semiconductor application note), accessed May 2015